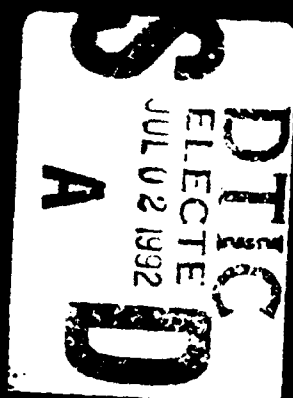Parkin
Hopster
Renard
Shinjo
Zinn

EDITORS

VOLUME 231

VOLUME 231

Magnetic Surfaces, Thin Films, and Multilayers

VOLUME 231

Magnetic Surfaces, Thin Films, and Multilayers

EDITORS

Stuart S.P. Parkin

Herbert Hopster

Jean-Pierre Renard

Teruya Shinjo

Werner Zinn

Magnetic Surfaces, Thin Films, and Multilayers

Magnetic Surfaces, Thin Films, and Multilayers

Symposium held April 29-May 2, 1991, Anaheim, California, U.S.A.

EDITORS:

Stuart S.P. Parkin
IBM Almaden Research Center, San Jose, California, U.S.A.

Herbert Hopster
University of California -Irvine, Irvine, California, U.S.A.

Jean-Pierre Renard
Universite Paris-Sud, Orsay, France

Teruya Shinjo
Kyoto University, Kyoto, Japan

Werner Zinn
IFF-KFA, Julich, Germany

Contents

*Invited Paper

*Invited Paper

*Invited Paper

PART IX: THIN FILM GROWTH

PART X: THIN FILM MAGNETISM

*Invited Paper

*Invited Paper

Preface

This symposium details recent developments in the magnetism of surfaces, thin films and multilayers. More than 20 invited contributions and more than 60 contributed papers attest to the great interest and vitality of this subject.

In recent years the study of magnetic surfaces, thin films and multilayers has undergone a renaissance, partly motivated by the development of new growth and characterization techniques, but perhaps more so by the discovery of many exciting new properties, some quite unanticipated. These include, most recently, the discovery of enormous values of magnetoresistance in magnetic multilayers far exceeding those found in magnetic single layer films and the discovery of oscillatory interlayer coupling in transition metal multilayers. These experimental studies have motivated much theoretical work. However these developments are to a large extent powered by "materials engineering" and our ability to control and understand the growth of thin layers just a few atoms thick. It is quite remarkable that the magnetic and transport properties of certain thin film and multilayered structures are sensitive to thickness variations on the scale of one atomic layer but even more so that we can actually engineer such structures. In terms of growth techniques, sputter deposition techniques are proving that they have an important role to play not simply for technological applications but for basic science studies. Indeed sputter techniques are a marvelous way to rapidly survey new materials systems and to study systematics of the dependencies of various physical properties on structure. The preparation of single crystal thin film layers and multilayers remains important for many studies, in particular, for properties dependent. Studies are just beginning on the magnetism of lower dimensional nano-structures including magnetic dots and arrays of magnetic dots, prepared, for example, by scanning tunneling microscopy techniques and by advanced lithographic capabilities. These studies obviously require engineering not just of layer thicknesses but of lateral dimensions as well. The properties of such structures are already proving to be of great interest.

An important development is the combination of powerful structural probes with advanced magnetic probes. Remarkable progress is being made in this way, for example, in understanding the origin of magnetic anisotropy at magnetic surfaces and interfaces. This subject continues to be of great importance. In recent years many new probes of magnetism have been developed. These include magnetic x-ray absorption and magnetic x-ray scattering to probe thin ferromagnetic and paramagnetic layers, a variety of spin polarized electron spectroscopies to probe surface magnetism and magnetic domain structures, spin polarized scanning tunneling microscopy to probe surface magnetic order and polarized neutron reflectivity and grazing angle diffraction to study magnetization profiles and magnetic surface ordering. These new techniques continue to reveal unexpected properties in many systems.

Many of these developments are described in these proceedings. We would particularly like to thank everyone who contributed to the symposium, particularly those who contributed to this volume.

Stuart Parkin
Herbert Hopster
Jean-Pierre Renard
Teruya Shinjo
Werner Zinn

November 1991

Acknowledgments

*Prior Materials Research Society Symposium Proceedings
available by contacting Materials Research Society.*

PART I

Review of Recent Developments

SURFACE, INTERFACE AND THIN-FILM MAGNETISM: AN OVERVIEW

L. M. FALICOV
Department of Physics, University of California, Berkeley CA 94720, and
Materials Science Division, Lawrence Berkeley Laboratory, Berkeley CA 94720.

ABSTRACT

A brief review of the state of the art in the field of surface, inter-
face and thin-film magnetism is presented.

INTRODUCTION.

Magnetism is an electronically driven phenomenon, weak compared with
electrostatic effects but subtle in its many manifestations. It is quantum-
mechanical in nature, with its origins in the existence of the electron spin
and in the Pauli exclusion principle. It leads to a large variety of short-
and long-range forces, and both classical and quantum-mechanical effects.
This last feature provides the richness of textures and properties
encountered in magnetic systems, from which useful engineering and technical
applications arise. In particular, with the information revolution and the
ever growing need to acquire, store, and retrieve information, the science
and technologies attached to magnetic recording have experienced an
explosive growth. Central to those pursuits is the materials science of
magnetism as it applies to surfaces, interfaces, and thin films [1].
Several technical developments are responsible for the intense activity
in this field. In addition to application-driven pressures, three major
advances are to be noted:
(1) The advent of new sample-preparation techniques which now permit
the manufacture of single-purpose devices to extraordinarily accurate
specifications; these techniques {Molecular Beam Epitaxy (MBE), Metal-
Organic Chemical Vapor Deposition (MOCVD), sputtering, lithography, etc.}
are becoming increasingly available and less expensive and have produced, in
addition to the obvious technological progress, a new branch of "pure"
science concerned with artificially made systems.
(2) The availability of better and sophisticated sample
characterization techniques, based mostly (although not exclusively) on
centrally located facilities. These techniques are based on x-ray and
ultra-violet photons (synchrotron sources), visible and infrared photons
(ordinary and free-electron lasers), neutrons (reactors and pulsed neutron
sources), and electrons of a variety of energies (electron microscopes of
several kinds; low-, intermediate-, and high-energy electron sources for
elastic and inelastic scattering experiments). To these should be added the
existence and ready availability of excellent controlled environments (good
vacuum and clean gaseous atmospheres; from very low to very high
temperatures; high and spatially very uniform magnetic fields).
(3) The increasing availability of fast, operationally inexpensive and
numerically intensive computers which have permitted the calculation of a
large variety of problems related to realistic systems, in complicated
geometries, with subtle quantum-mechanical effects, and/or for practical
devices.

OVERVIEW: THEORY.

Electronic calculations. The prediction of magnetic structures, in

4

bulk materials as well as in surfaces and interfaces, is still an imperfect science, even though enormous progress has been achieved [2]. Complex structures have been predicted for bulk, surface and composite structures. Many times such calculations agree with experimental results, but there are notable exceptions.

Calculated Fermi surfaces of magnetic metals show good agreement with experiment [3] in some cases (Fe), not as good [4-6] for others (Co, Ni). Reliable Fermi surfaces however are necessary for predicting as well as interpreting and understanding transport properties.

Systematic studies of a wide variety of physical and magnetic structures of surfaces and interfaces currently require more approximate methods of electronic structure calculations. If such methods are constructed to reproduce known experimental or ab initio results, predictions are, in general, quite reliable [7].

Critical phenomena. There are, in addition, fascinating surface effects related to a variety of critical phenomena: behavior and transitions involving the decay in short-range order [8], the interplay between surface and bulk effects [9] (including the persistence of order on surfaces at temperatures higher than the bulk Curie or Néel temperatures and various temperature dependences of the magnetization of the surface layers as compared to the bulk), and distinction between universal and non-universal behavior of magnetic overlayer systems when the coverage is fractional [10].

Transport properties. The study of transport properties in magnetic systems differs from that in any other material by the fact that it always takes place in the presence of an intrinsic, local magnetic field; in other words, it is always the study of galvanomagnetic properties, in particular magnetoresistance.

When a magnetic field is applied to a normal (i.e. not ferromagnetic) metal, the resistance is seen to increase with the intensity of the field, regardless of the relative orientation of the field with respect to the current and with respect to the crystallographic axes. This phenomenon, positive magnetoresistance, is very well understood, and for high-purity metals with a large electronic mean-free path, yields accurate and easily interpretable information about the electronic structure, the Fermi surface in particular, of the metal. Increases in resistance of many orders of magnitude are observed in particularly pure, single crystals at very low temperatures and high magnetic fields (typically 10 to 100 kOe). For polycrystalline samples and at normal temperatures more modest increases, typically of a factor of 2 to 10, are obtained for equivalent fields. Positive magnetoresistance can be interpreted, in general terms, by noting that in the presence of a magnetic field, electron trajectories become convoluted (e.g. helical), and the effective distance that an electron can transport charge before being scattered decreases as the magnetic field increases.

In ferromagnetic systems, which in the absence of an applied field consist of several magnetic domains, the phenomenon of negative magnetoresistance [11] is observed: the application of an external magnetic field decreases the resistance by up to an order of magnitude in fields as small as 100 Oe. The phenomenon is commonly interpreted based on two facts: (1) the spin-up and the spin-down electrons have different band structures and different phase space available for transport and for scattering; (2) the external field changes the domain structure, and produces a single-domain crystal. Under those conditions three effects take place. The electrons with different spin encounter different spatial arrangements which change with applied field; the electron trajectories, because of the presence of a now uniform internal field, become less convoluted; and the removal of Bloch walls eliminates a source of electron scattering [12]. All three effects result in longer mean-free paths upon application of a magnetic field, i.e. a negative magnetoresistance. Similar negative magnetoresistance effects have been found in multilayer systems, as

described below.

Micromagnetics. Micromagnetic theory provides a framework for predicting macroscopic magnetic phenomena, such as domain walls and hysteresis loops, in systems where the details of the atomic structure are not important [13]. Input to the calculations includes exchange parameters, crystalline anisotropy constants, and sample microstructure. It is a classical (i.e. non quantum-mechanical) many-body problem in which much of the computational expense comes from the long-range nature of the magnetostatic interaction. The memory dependence of the problem requires that the motion of the magnetization be traced in time to ensure accuracy. Various calculations, semi-quantitative in nature, have provided considerable insight. Quantitative accuracy is normally prohibitive.

OVERVIEW: SYSTEMS.

Surface and monolayer films. While it is possible for theorists to model ideal monolayers in computer simulations, it has proven an almost insurmountable challenge for experimentalists to grow idealized model systems in the laboratory. The issue is associated with the need for a substrate and the inability to realize free-standing monolayers. Interactions with the substrate dominate most properties of interest. For instance, Cu, Ag, and Au single crystals are good substrate candidates because of their filled d bands. But it is this characteristic that creates metallurgical problems: their lower surface free energies, compared to that of the magnetic elements, can provide thermodynamic driving forces for surface segregation, intermixing, etc.

Transition-metal substrates have higher surface free energies. However, hybridization between the magnetic d or f electron states and the substrate d electron states across the interface becomes a controlling factor. For instance, it has been shown that while fcc Fe(111) grows on Ru(0001) with an expanded in-plane lattice spacing that should promote ferromagnetism, the first two monolayers of Fe appear to be magnetically dead [14]. The in-plane expansion leads to an interplanar contraction and a strong Fe-Ru band hybridization precludes magnetic moment formation. For the Fe/Pd(100) system quite the opposite effect occurs. The strong d-d hybridization is predicted to induce ferromagnetism in the Pd substrate [15]. It is interesting to note that these trends are mirrored in the behavior of dilute Fe alloys in 4d-transition-metal hosts: Fe in Ru lacks a local moment, while Fe in Pd is the classic giant-moment system because of the polarization of Pd sites that extends many atomic shells away from the impurity site.

Surface perfection manifests itself in the quest to verify the theoretical predictions regarding possible ferromagnetism [16-18] at the {100} surfaces of Cr . This prediction also indicates that the moments are dramatically enhanced at the surface. The surface-ordering temperature is also raised, relative to the bulk Néel temperature of bulk Cr. The enhanced surface magnetism of Cr(100) leads to ferromagnetic (100) sheets that are coupled antiparallel to each other on adjacent layers. The problem is that if terrace widths at the surface are smaller than the domain-wall thickness, the surface becomes divided into antiparallel domains, and there is no net moment on a macroscopic scale. Since even a (100) surface well-defined by standard surface-science criteria does have step densities of order one per 100 Å, even with polarized-electron imaging of the domain structure the present resolution level (~ 500 Å) is insufficient to clarify this issue. It is expected that increased experimental resolution in imaging and an enhanced ability to create ultraflat surfaces will be forthcoming and will help resolve these problems.

Metastable epitaxial films. Elemental magnetic materials exist in a variety of crystallographic and magnetic phases. Thin-film growth of these

materials on crystal ine substrates allows the forces present at the interface to drive the film into specific crystallographic structures. These structures may be either a known high-pressure or high-temperature phase, or a phase not previously observed. Since the energies associated with a change in crystal structure (≈ 0.1 eV per atom) is of the same order of magnitude as energies associated with a change in magnetic structure (e.g. ferromagnetic to antiferromagnetic), often the magnetic properties of thin films dramatically depend on the growth conditions and structure of the substrates. These artificial magnetic materials, which are stabilized by their growth in thin film form, are referred to as metastable structures.

In addition to providing new structures these metastable phases provide stringent tests of calculational techniques used to predict structural and magnetic properties of magnetic materials. These techniques are capable of yielding the total energy of an elemental crystallographic system as a function of lattice structure and spacing, including a zero-temperature prediction of magnetic moment and magnetic arrangement. As an example, epitaxial growth of Fe on a Cu substrate has shown that either ferromagnetic or antiferromagnetic fcc Fe can be obtained depending on the detailed conditions of growth (substrate temperature, surface preparation, and surface cleanliness) [19]. Both faces are predicted by theoretical calculations [20]. This indicates that fine details of total energy calculations may be manifest in metastable thin films.

Another example of a metastable phase is given by the two cubic phases of Co. Face-centered-cubic Co is the high temperature ferromagnetic phase observed in nature; however, there is no naturally occurring bcc phase of Co. Experimentally, however, a bcc ferromagnetic phase [21] was successfully formed by epitaxial growth on GaAs. Total-energy calculations [20] yield tne bcc-Co phase with the observed lattice constant, and correctly predict it to be ferromagnetic.

There is also a theoretical indication that there should be bcc phases of Ni, both ferromagnetic and nonmagnetic, even though in nature Ni only appears in a ferromagnetic fcc phase. Body-centered-cubic Ni has been reported to be stabilized by epitaxial growth on a single-crystal surface of Fe(100). At this lattice constant, it is far from the metastable equilibrium value for the Wigner-Seitz radius indicated by the calculation, and the strong influence of the ferromagnetic substrate made magnetic characterization difficult.

Semiconducting substrates. Single-crystal semiconductor substrates provide a very attractive template for the epitaxial growth of metal films. In particular, a group consisting of Ge, GaAs, AlAs, and ZnSe all have lattice constants very close to 5.65 A. This is also very close to twice the latti e constant of bcc Co (2.82 A), bcc Fe (2.87 A), and bcc Ni (2.89 A), which should permit a c(2 x 2) reconstruction of the metal films upon these substrates. Although bcc Co has been successfully grown on GaAs [21] and bcc Fe on Ge, GaAs and ZnSe [22], there are important unresolved issues of interface chemistry with these systems.

Rare earths. The growth of rare earths provides a particularly fertile ground for the study of magnetic phenomena in thin films and their relationship to magnetism in reduced dimensionality. The main reason is that rare earths display a variety of systems which are chemically similar, span a large range of ionic radii and crystal structures, and present a wealth of magnetic structures including helical, ferromagnetic, antiferromagnetic, and cone magnetic structures. In addition, rare earths exhibit a great variability of thermodynamic phase diagrams ranging from complete immiscibility -- as is the case for many rare earths with transition metals -- to the formation of complete sets of solid solutions -- as is the case of two rare earths. The epitaxial growth of rare earths and transition metals is particularly challenging because of the high reactivity of the rare earths and tne high melting points of many of the transition metals. As a consequence, MBE is used for these systems, with special care

taken to avoid contamination. Generally it has been found that the growth of rare earths can be accomplished quite conveniently on a transition metal [23-25]. One reason that these systems can be grown with relative ease is that they do not form solid solutions in their phase diagram, and possibly this facilitates the growth of a segregated rare earth.

Oxides. One particular type of system which is of great importance and which has not been studied extensively is the growth of epitaxial oxides. Oxides in many cases exhibit interesting magnetic properties -- such as antiferromagnetism -- and are the basis for a variety of devices, especially when used in conjunction with a ferromagnetic material. The growth has usually been accomplished using oxygen sources in an MBE system, using reactive sputtering or laser ablation techniques. Nickel monoxide (NiO) and cobalt monoxide (CoO) single crystals have been prepared on MgO substrates by chemical vapor deposition [26]; titanium oxides were grown on sapphire by MBE [27]. Chemical vapor deposition was used to prepare a variety of thick oxide films, especially ferromagnetic compounds such as NiO, CoO, $Ni_xCo_{1-x}O$, and $REFeO_3$ (where RE is a rare earth) [28].

Multilayers. A large variety of multilayered systems have been grown: ferromagnetic-normal metals, ferromagnetic-superconducting, rare-earth-rare-earths, etc. The preferred growth method has been sputtering or MBE, although recently titanium-oxide-titanium superlattices have been grown by the chemical vapor deposition techniques.

Multilayered systems which are lattice-matched have been grown by thermal evaporation or MBE. The MBE grown, lattice-matched systems exhibit narrow x-ray diffraction lines comparable to the instrumental resolution. The lattice mismatched systems are generally textured and exhibit broader x-ray diffraction lines. However, questions regarding interfacial chemistry have not been fully addressed, because detailed understanding of roughness, disorder and interdiffusion is not yet available.

OVERVIEW: PHYSICAL EFFECTS.

Proximity effects. In some systems, interface effects of a purely magnetic origin extend beyond the interface and into the bulk, thus giving rise to proximity effects. Examples can be found in transition-metal systems where one side consists of a strong ferromagnet, such as Co, and the other side consists of an easily polarizable (almost magnetic) material, such as Pd, or a weakly magnetic material, such as Cr. The strong electron-electron interaction of the fully saturated ferromagnet, frustrated by a lack of $\underline{d}$ holes from producing a larger moment, induces through hybridization and exchange an additional magnetic moment in the $\underline{d}$ bands of the polarizable material. This effect is analogous to the polarization of the Fe atoms in dilute $\underline{Fe}$-Co alloys and the polarization of Pd atoms in dilute $\underline{Pd}$-Fe alloys. Theoretical and experimental studies of proximity effects in transition and simple metals have established a series of empirical rules that can be summarized as follows [29-31]:

1.- The magnetic moments of cobalt and nickel are virtually saturated; they can be only very slightly changed by their immediate environment. The fractional change, however, can be appreciable in nickel (which has a small moment of about 0.6 Bohr magnetons), but is negligible in cobalt.

2.- The magnetic moment of iron, which has only a moderate electron-electron interaction, can be appreciably affected by its immediate environment.

3.- Chromium, which is a weak magnetic ion, may have its moment profoundly altered by the presence of surfaces, interfaces, and both magnetic and nonmagnetic neighbors.

4.- The "almost magnetic" elements, vanadium and palladium, may acquire a sizeable magnetic moment in the proper environment.

5.- Free surfaces, which reduce the local bandwidth of a metal, tend to increase the magnetic moment of an element; hence the surface of chromium

has a much larger moment than the bulk [32,33], nickel tends to be marginally more magnetic at the surface [34], and it is possible that some crystallographic faces of vanadium exhibit a magnetic moment [29].

6.- Proximity of a nonmagnetic metal tends to suppress the magnetic moment of some elements; this effect depends crucially on the overlap of the wave functions between the $\underline{d}$ band of the magnetic metal and the conduction band of the nonmagnetic one.

7.4 The proximity of a strongly magnetic element tends to induce or enhance magnetic moments on the neighboring, susceptible elements. Thus iron becomes more magnetic in the proximity of cobalt [35], the enhanced moment of the chromium surface tends to propagate over several layers into the bulk [36], chromium acquires a large moment in the proximity of iron [32] and/or cobalt, and vanadium and palladium may develop sizeable magnetic moments in the proximity of iron and/or cobalt.

Exchange coupling across interfaces. Magnetic exchange coupling between ferromagnetic and antiferromagnetic layers was discovered and studied in various systems, e.g., the Co/CoO and $Ni_{81}Fe_{19}/Fe_xMn_{1-x}$ systems. In general there is a large discrepancy (of approximately two to three orders of magnitude) between theoretical estimates of the interfacial exchange coupling energy and the measured values. Although various models have been proposed to account for the large discrepancy between experiment and theory, none is yet fully accepted.

Not only do ferromagnetic/antiferromagnetic coupled systems display a fascinating range of properties, but the interfacial exchange coupling can be harnessed to study the properties of the antiferromagnetic layer. It is difficult to measure many fundamental magnetic properties of ultra-thin antiferromagnetic films, including for example their Néel temperatures, because of the difficulty of coupling to the sublattice magnetization. Most electron, optical and neutron scattering, and magnetic resonance techniques are incapable of examining antiferromagnetic thin films. Spin-polarized photoelectron diffraction is one of the few techniques with some potential for such studies [37].

The ferromagnetic layer in a ferromagnet/antiferromagnet couple forms a natural probe of the antiferromagnetic system. By monitoring the temperature at which the exchange bias field goes to zero the blocking temperature of the antiferromagnet can be determined. This temperature is slightly lower and closely related to the Néel temperature T_N of the antiferromagnet. At a temperature just below T_N the anisotropy of the antiferromagnetic layer becomes too weak compared to the exchange coupling energy to maintain the rigidity of the antiferromagnetic lattice, which thus becomes free to follow the magnetization of the ferromagnetic layer.

In contrast to the ferromagnetic/antiferromagnetic coupled systems, the magnitude of the exchange coupling in ferromagnetic/ferromagnetic systems can be very large. A wide variety of systems has been studied; they include, however, very few studies on well characterized single crsytals. Examples include single-crystal $\underline{bcc}$ Ni/Fe bilayers, polycrystalline $Ni_{81}Fe_{19}/Fe$ superlattices and a wide variety of amorphous rare earth-transition metal (RE/TM) alloy films coupled to other RE/TM alloys or polycrystalline films of Fe, Co or $Ni_{81}Fe_{19}$. The latter systems all have been developed for their posssible application in a variety of magnetic recording devices.

RKKY coupling. Bulk rare-earth elements and their alloys with yttrium exhibit complex spin arrangements caused by the combination of strong crystal field effects and the oscillatory exchange interaction modulated by the conduction electrons (Ruderman-Kittel-Kasuya-Yosida or RKKY interaction). Early work in rare-earth multilayers [38,39] demonstrated that RKKY polarization propagates across the rare-earth/yttrium (0001) interface, and thus it decays slowly enough to provide coherent exchange coupling across as much as 130 Å of Y. Spiral (transverse) and c-axis (longitudinal) polarizations are preserved. Intriguingly, the periodicity

of the spin polarization in the Y is that of dilute rare-earth-yttrium alloys, while that in the rare earth deviates from bulk values at low temperatures.

A model for RKKY coupling has been proposed [40]. Rare-earth sheets are required to be immersed in the Y conduction band, but to interact with the $\underline{s}$-$\underline{f}$ interactions appropriate to the rare earth. The polarization, therefore, is formed by the nesting features of the Y band structure. In the case of spiral structures, two transverse polarization waves, out of phase by one lattice spacing, are produced, thus providing a helical arrangement.

Experiments have explored the RKKY coupling across $(10\bar{1}0)$ and $(11\bar{2}0)$ interfaces. For Dy/Y the polarization is insufficient to bring the spiral order of successive rare-earth blocks into coherence but does provide adequate coupling to produce long-range ferromagnetic order in Gd superlattices. This may simply reflect the strongly anisotropic range of RKKY oscillations in Y but may also be evidence for total reflection of those conduction electrons most important in providing the RKKY coupling, as presented by the superlattice band approach of reference [40]. Other evidence for spin-dependent transmission has been seen in magnetotransport experiments in the Fe/Cr/Fe system.

Coupling through nonmagnetic layers. Great interest has developed in the last two years in the magnetic and magneto-transport properties of layers of ferromagnetic TM -- Fe, Co, Ni and the $Ni_{80}Co_{20}$ alloy in particular -- separated by layers of variable thickness of ordinary transition or noble metals metals (Cr, Ru, Re and Cu). Two related effects are found: (1) successive ferromagnetic layers couple variously in either antiferromagnetic and ferromagnetic arrangements, depending on the thickness and nature of the intervening non-ferrmagnetic metal; and (2) samples with antiferromagnetic coupling between successive layers exhibit either a small (e.g. Co/Ru) or a giant (Fe/Cr) negative magnetoresistance. These effects have been observed by a variety of techniques: spin-polarized electron-scattering [41], magneto-optic-Kerr-effect and Brillouin scattering studies [42, 43], galvanomagnetic measurements [44,45], magnetization studies [45,46], neutron diffraction [46] and ferromagnetic resonance [43] among others [47]. Various theoretical models have been proposed to account for these phenomena [48-54], although the coupling mechanism is, at present, not yet fully understood. It is apparently too large a coupling to be accounted for by magnetostatic effects, and although the coupling strength oscillates with normal-metal-film thickness, the period of the oscillation is much too large to be caused by RKKY, unless it is dominated by very small pieces of the normal-metal Fermi surface. The giant magnetoresistance found in the Fe/Cr multilayer samples is of great interest for potential recording head applications.

There have been numerous other studies of systems of the ferromagnet/ metal/ferromagnet type, ranging from attempts to vary the coercivity of ferromagnetic films by lamination for magnetic recording applications, to studies of single-crystal superlattices [55,56], such as Fe/Ag. Exchange coupling of successive Fe layers in this system has been inferred [56] from the temperature dependence of the magnetization at low temperatures. A calculation [57,58] of the temperature dependence of the magnetization in the spin-wave regime for an arbitrary multilayered magnetic structure has shown that there always exists a range of temperature for which the magnetization varies as $\alpha T^{3/2}$, where the coefficient α depends on the exchange coupling between the magnetic layers. The method of calculation can be applied to obtain the exchange coupling in ferromagnetic/metal/ ferromagnetic systems. In some fairly recent elegant experiments [59] the coupling between a surface layer of $Ni_{81}Fe_{19}$ and an underlying thick $Ni_{81}Fe_{19}$ layer (separated from each other by submonolayers of Ta) was obtained.

Tunneling between a spin-polarized superconducting film coupled to a

ferromagnetic layer has been extensively used to study the magnetic properties of thin ferromagnetic layers [60]. It has been proposed [61] that tunneling between two ferromagnets could depend on the relative alignment of the magnetization of the two ferromagnetic layers; this effect was subsequently observed [62] in the system Fe-Ge-Co. The magnitude of this magnetic tunneling-valve effect was found to be about half that expected from the spin polarizations in Fe and Co as deduced from tunneling [63] in ferromagnet/insulator/superconductor junctions. More recently, similar effects have been observed in [64] Ni/NiO/Co tunnel junctions.

Magnetoelasticity. The presence of strain has been used to modify the physical properties through the magnetoelastic effect. This is particularly important for materials such as rare earths and Laves-phase alloys, where magnetoelastic effects are large. This effect was observed in Dy super-lattices [65] and films [66], and in Er films and superlattices. Both Dy and Er epitaxial materials can be driven to ferromagnetism at a critical value of the applied field that depends on film thickness. In the case of Er, a variety of commensurable spin states are induced at low temperatures by fields below the critical value [67]. Bulk behavior is not recovered in films up to 1 μm thick. The treatment of this problem to date has relied on bulk values of the magnetoelastic coupling constants subject to rigid clamping assumptions.

Superlattice effects. Many of the effects described above can be conveniently studied in simple snadwiches or in multilayered films since the latter consist of a superposition of single films [68]. Moreover, multilayers provide the possibility of ex-situ studies without concern regarding contamination, since they can be grown very thick (~1 μm) compared to usual contamination depths. The drawback is, of course, that by its very nature any single, bi- or tri-layered film effect can only be obtained in a statistical sense, averaged over many repetitions of the system.

There is, however, a class of effects which cannot, even in principle, be observed in a small number of layers because they rely on the periodic nature of the multilayer. These are the so-called superlattice effects. These effects all rely on the presence of extended electronic states in the growth direction. However, all metal systems studied to date exhibit large amounts of interfacial scattering as indicated by the thickness-dependent resistivity [69]. Whether this scattering is sufficient to break down the existence of extended states perpendicular to the layers and in effect confines the electrons to individual layers is not clear.

A superlattice effect which does not require perfection at the atomic level is the development of magnon bands in ferromagnet/normal-metal superlattices [70]. The coupling in these types of superlattices depends on the long-range dipolar interaction which is not much affected by small amounts of disorder at an interface. The individual modes in each one of the magnetic layers spreads into bands of magnons as the intervening normal metal thickness is decreased.

ACKNOWLEDGMENTS

REFERENCES

[1]   For a comprehensive review of the field see L. M. Falicov, D. T. Pierce, S. D. Bader, R. Gronsky, K. B. Hathaway, H. J. Hopster, D. N.

Lambeth,, S. S. P. Parkin, G. Prinz, M. B. Salamon, I. K. Schuller, and R. H. Victora, J. Mater. Res. 5, 1299 (1990).

[2] V. L. Moruzz , J. F. Janak and A. R. Williams, Calculated Electronic Properties of Metals (Pergamon, New York, 1978).

[3] K. B. Hathaway, H. J. F. Jansen, and A. J. Freeman, Phys. Rev. B 31, 7603 (1985).

[4] C. S. Wang and J. Callaway, Phys. Rev. B 15, 298 (1977).

[5] T. Jarlborg and M. Peter, J. Magn. Magn. Mat. 42, 89 (1984).

[6] A discussion of some discrepancies between theory and de Haas - van Alphen data for Co may be found in: F. J. Himpsel and D. E. Eastman, Phys. Rev. B 21, 3207 (1980).

[7] See, for example, R. H. Victora in Magnetic Properties of Low-Dimensional Systems, edited by L. M. Falicov and J. L. Morán-López (Springer Verlag, Berlin-Heidelberg-New York-Tokyo, 1986), p. 25.

[8] J. M. Kosterlitz and D. J. Thouless, in Progress in Low Temperature Physics, edited by D. F. Brewer (North Holland, Amsterdam, 1978), Volume VII B.

[9] R. Lipowsky, Phys. Rev. Lett. 49, 1575 (1982); R. Lipowsky and W. Speth, Phys. Rev. B 28, 2983 (1983); R. Lipowsky, Z. Phys. B. 55, 345 (1984); R. Lipowsky, Phys. Rev. Lett. 52, 1429 (1984); R. Lipowsky, Phys. Rev B 32, 1731 (1985); R. Lipowsky, Ferroelectrics, 73, 69 (1987); R. Lipowsky in Random Fluctuations and Pattern Growth, ed. by H. E. Stanley and N. Ostrowsky (Kluwer Academic, Dordrecht, 1988).

[10] S. Dietrich, in Phase Transitions and Critical Phenomena, edited by C. Domb and J. L. Leibowitz (Academic Press, London, 1988), Volume 8, p. 1.

[11] G. R. Taylor, A. Isin and R. V. Coleman, Phys. Rev. 165, 621 (1968); R. V. Coleman, R. C. Morris, and D. J. Sellmyer, Phys. Rev. B 8, 317 (1973); R. W. Klaffky and R. V. Coleman, Phys. Rev. B 10, 4803 (1974).

[12] G. G. Cabrera and L. M. Falicov, phys. stat. solidi (b), 61, 539 (1974); ibid. 62, 217 (1974); G. G. Cabrera and L. M. Falicov, Phys. Rev. B 11, 2651 (1975).

[13] W. F. Brown, Micromagnetics (Wiley, New York, 1963).

[14] C. Liu and S. D. Bader, Physica B 161, 253 (1989).

[15] S. Blügel, M. Weinert and P. H. Dedericks, Phys. Rev. Lett. 60, 1077 (1988).

[16] G. Allan, Surf. Sci. 74, 79 (1978).

[17] D. R. Grempel, Phys. Rev. B 24, 3928 (1981).

[18] R. H. Victora and L. M. Falicov, Phys. Rev. B 31, 7335 (1985).

[19] W. A. A. Macedo and W. Keune, Phys. Rev. Lett. 61, 475 (1988).

[20] V. L. Moruzzi, P. M. Marcus, K. Schwarz and P. Mohn, Phys. Rev. B 34, 1784 (1986); P. M. Marcus, V. L. Moruzzi, Z. Q. Wang, Y. S. Li and F. Jena, in Physical and Chemical Properties of Thin Metal Overlayers and Alloy Surfaces, edited by D. M. Zener and D. W. Goodman, Materials Research Society Symposia Proceedings, volume 83 (Mat. Res. Soc., Pittsburgh, 1987) p. 21.

[21] G. A. Prinz, Phys. Rev. Lett. 54, 1051 (1985).

[22] G. A. Prinz, B. T. Jonker, J. J. Krebs, J. M. Ferrari and F. Kovanis, Appl. Phys. Lett. 48, 1756 (1986).

[23] D. Weller and S. F. Alvarado, J. Appl. Phys. 59, 2908 (1986).

[24] J. Kwo, D. B. McWhan, M. Hong, E. M. Gyorgy, L. C. Feldman and J. E. Cunningham, in Layered Structures, Epitaxy and Interfaces edited by J. M. Gibson and L. R. Dawson, Materials Research Society Symposia Proceedings, volume 37 (Mat. Res. Soc., Pittsburgh, 1985) p. 509.

[25] H. Homma, K. Yang, and I. K. Schuller, Phys. Rev. B 36, 9435 (1987).

[26] A. E. Berkowitz and J. H. Grenier, J. Appl. Phys. 36, 3330 (1965); J. Bransky, I. Bransky and A. A. Hirsch, J. Appl. Phys. 41, 183 (1970).

[27] K. B. Alexander, J. R. Conner, F. A. List, R. A. McKee, and F. J. Walker (private communication).

[28] A. Berkowitz (private communication).

[29] A. J. Freeman and C. L. Fu, in Magnetic Properties of Low-Dimen-
      sional Systems, edited by L. M. Falicov and J. L. Morán-López
      (Springer-Verlag, Berlin-Heidelberg-New York-Tokyo,1986) p. 16.

[30] D. S. Wang, A. L. Freeman and H. Krakauer, Phys. Rev. B 24, 1126
      (1981).

[31] L. M. Falicov, R. H. Victora and J. Tersoff, in The Structure of
      Surfaces, edited by M. A. Van Hove and S. Y. Tong (Springer-Verlag,
      Berlin-Heidelberg-New York-Tokyo. 1985) p. 12, and references therein.

[32] R. H. Victora and L. M. Falicov, Phys. Rev. B 31, 7335 (1985).

[33] L. E. Klebanoff, R. H. Victora, L. M. Falicov and D. A. Shirley,
      Phys. Rev. B 32, 1997 (1985).

[34] J. Tersoff and L. M. Falicov, Phys. Rev. B 26, 6186 (1982).

[35] R. H. Victora, S. Ishida and L. M. Falicov, Phys. Rev. B 30, 3896
      (1984).

[36] H. Hasegawa, J. Phys. F.: Met. Phys. 16, 1555 (1986).

[37] B. Hermsmeier, J. Osterwalder, D. Friedman, and C. S. Fadley, Phys.
      Rev. Lett. 62, 478 (1989).

[38] C.F. Majkrzak, J. W. Cable, J. Kwo, M. Hong, D. B. McWhan, Y. Yafet,
      J. V. Waszczak and C. Vettier, Phys. Rev. Lett. 56, 2700 (1986).

[39] M. B. Salamon, S. Sinha, J. J. Rhyne, J. E. Cunningham, R. W. Erwin,
      J. Borchers and C. P. Flynn, Phys. Rev. Lett. 56, 259 (1986).

[40] Y. Yafet, J. Kwo, M. Hong, C. F. Majkzak and T. O'Brien, J. Appl.
      Phys. 63, 3453 (1988)

[41] C. Carbone and S. F. Alvarado, Phys. Rev. B 36, 2433 (1987).

[42] P. Grünberg, R. Schreiber, Y. Pang, M. B. Brodsky and H. Sowers,
      Phys. Rev. Lett. 57, 2442 (1986); F. Saurenbach, U. Walz, L. Hinchey,
      P. Grünberg and W. Zinn, J. Appl. Phys. 63, 3473 (1988).

[43] B. Heinrich, Z. Celinski, J. F. Cochran, W. B. Muir, J. Rudd, Q. M.
      Zhong, A. S. Arrott, K. Myrtle, and J. Kirschner, Phys. Rev. Lett 64,
      673 (1990).

[44] M. N. Baibich, J. M. Broto, A. Fert, F. Nguyen Van Dau, F. Petroff,
      P. Etienne, G. Creuzet, A. Friederich and J. Chazelas, Phys. Rev.
      Lett. 61, 2472 (1988).

[45] S. S. P. Parkin, N. More, and K. P. Roche, Phys. Rev. Lett. 64, 2304
      (1990); S. S. P. Parkin, A. Mansour, and G. P. Felcher, Appl. Phys.
      Lett. (to appear); S. S. P. Parkin, R. Bhadra, and K. P. Roche
      (private communication); S. S. P. Parkin and D. Mauri (private
      communication).

[46] A. Cebollada, J. L. Martinez, J. M. Gallego, J. J. de Miguel, R.
      Miranda, S. Ferrer, F. Batallan, G. rillion, and J. P. Rebouillat,
      Phys. Rev. B. 39, 9726 (1989).

[47] See the various contributions included in these proceedings.

[48] H. Hasegawa, Phys. Rev. B 42, 2368 (1990); see also these proceedings.

[49] Y. Wang, P. M. Levy, and J. L. Fry, Phys. Rev. Lett. 65, 2732
      (1990); P. M. Levy, J. L. Fry, and E. C. Ethridge, these proceedings.

[50] D. M. Edwards, J. Mathon, R. B. Muniz, and M. S. Phan (private
      communication)

[51] G. Mathon, these proceedings.

[52] F. Herman, J. Sticht, M. Van Schilfgaarde, and M. Methfessel, these
      proceedings.

[53] P. J. Jensen, K. H. Bennemann, A. Mokrani, and H. Dreysse, these
      proceedings.

[54] D. Deaven and D. S. Rokhsar, Bull Am. Pys. Soc. 36, 844 (1991).

[55] B. T. Jonker, K. H. Walker, E. Kisker, G. A. Prinz, and C. Carbone,
      Phys. Rev. Lett. 57, 142 (1986).

[56] C. J. Gutierrez, S. H. Mayer, Z. Q. Qiu, H. Tang, and J. C. Walker,
      in Growth, Characterization and Properties of Ultrathin Magnetic
      Films and Multilayers, edited by B. T. Jonker, E. E. Marinero, and J.
      P. Heremans, Materials Research Society Symposia Proceedings, volume

151 (Mat. Res. Soc., Pittsburgh, 1989), p. 17.

[57] J. Mathon, Rep. Prog. Phys. $\underline{51}$, 1 (1988).

[58] J. Mathon and S.B. Ahmad, Phys. Rev. B $\underline{37}$, 660 (1988); J. Mathon, Physica $\underline{149B}$, 31 (1988).

[59] D. Mauri, D. Scholl, H.C. Siegmann, and E. Kay, Phys. Rev. Lett. $\underline{62}$, 1900 (1988).

[60] J. S. Moodera and R. Meservey, Phys. Rev. B $\underline{34}$, 379 (1986).

[61] J. C. Slonczewski, Phys. Rev. B $\underline{39}$, 6995 (1988).

[62] M. Julliere, Phys. Lett. $\underline{54A}$, 225 (1975).

[63] P. M. Tedrow and R. Meservey, Phys. Rev. B $\underline{7}$, 318 (1973).

[64] U. Gaefvert and S. Maekawa, IEEE Trans. Mag. $\underline{MAG-18}$, 707 (1982).

[65] R. W. Erwin, J. J. Rhyne, M. B. Salamon, J. Borchers, S. Sinha, R. Du, J. E. Cunningham and C. P. Flynn, Phys. Rev. B $\underline{35}$, 6808 (1987).

[66] K. Y. Yang, H. Homma, and I. K. Schuller, J. Appl. Phys. $\underline{63}$, 4066 (1988).

[67] J. A. Borchers, G. Nieuwenhuys, M. B. Salamon, C. P. Flynn, R. Du, R. W. Erwin and J. J. Rhyne, J. de Physique $\underline{49-C8}$, 1685 (1988).

[68] See for instance, I. K. Schuller and H. Homma, Mat. Res. Soc. Bulletin $\underline{XII}$, 1 (1987).

[69] See various articles in Physics, Fabrication and Applications of Multilayered Structures, edited by P. Dhez and C. Weisbuch (Plenum Press, New York, 1988).

[70] C. Colvard, R. Merlin, M. V. Klein and A. C. Gossard, Phys. Rev. Lett. $\underline{45}$, 298 (1980).

Novel Measurement Techniques

MAGNETIC DOMAIN IMAGING OF EPITAXIAL THIN FILMS BY SPIN-POLARIZED SCANNING ELECTRON MICROSCOPY

R. ALLENSPACH AND M. STAMPANONI
IBM Research Division, Zurich Research Laboratory, 8803 Rüschlikon, Switzerland

ABSTRACT

The formation of magnetic domains in thin epitaxial Co/Au(111) films is investigated by spin-polarized scanning electron microscopy. Three-monolayer films are shown to decay into out-of-plane domains of micrometer size. The transition from out-of-plane to in-plane magnetization at a crossover thickness of 4.5 layers is followed by imaging the domains, and the transition is shown to occur as a continuous rotation of the magnetization. The domain size in field-free-grown perpendicular films depends linearly on film thickness. From high-resolution line scans across magnetization reversals we determine the resolution in magnetic imaging to be better than 40 nm.

INTRODUCTION

Tailoring magnetic thin films and multilayers to reveal specific magnetic properties is a rapidly advancing art and maturing science [1]. In particular, growing epitaxial films of monolayer or near-monolayer thickness allows the investigation of two-dimensional ferromagnetism, and these results can be matched to their well-established three-dimensional counterparts. From a more applied point of view, thin films with large magnetic anisotropies perpendicular to the surface [2] will play a key role in future data storage devices. In particular, thin epitaxial cobalt films [1,3-8] are the most prominent representative of this class of materials. For a better understanding of the ferromagnetic properties of thin films and superlattices, novel magnetic characterization techniques are being developed which are highly sensitive to even very thin layers and likewise allow spatial resolution below the diffraction limit of light. In this paper we present a detailed study of magnetic domain imaging of epitaxially grown Co films [9] on Au(111) substrates with one of these techniques, namely spin-polarized scanning electron microscopy (spin-SEM [10] or SEMPA [11]). We studied the formation and growth of magnetic domains in films as thin as three monolayers. In addition, we investigated the switching behavior from perpendicular to parallel magnetization in such films, characterized at a domain size level. Finally we will present an example of very high-resolution domain wall imaging, thus showing the capabilities of this spin-polarized technique.

EXPERIMENTAL SETUP

The principle of domain imaging with spin-polarized electrons has been described previously [10,11]. Here we only summarize the most relevant points. An ultrahigh vacuum scanning electron microscope is used to produce a finely focussed beam of electrons which scans along the ferromagnetic sample. A huge number of low energetic secondary electrons is ejected, collected by a transfer optic and transferred to a spin detector, which is capable of analyzing the spin polarization $P = (N_\uparrow - N_\downarrow)/(N_\uparrow + N_\downarrow)$ where $N_\uparrow$ ($N_\downarrow$) is the number of electrons with spin parallel (antiparallel) to a given direction. The success of this spin-polarized SEM relies on

two facts, namely i) the high yield of low energetic (0 to 20 eV) secondary electrons, and ii) that the spin polarization for these electrons is proportional to the magnetization within the topmost three to five monolayers (ML) of a surface [12,13]. Hence this technique is particularly well suited to study thin magnetic films. By measuring the direction of P, we directly image the magnetization distribution in a thin film of a given ML thickness.

In our setup the electron microscope is equipped with a cold field emission gun of variable energy from 0.5 to 25 keV, with a minimum beam diameter of 5 nm. The spin detector, a high-energy (100 kV) Mott type, is capable of simultaneously measuring the out-of-plane and one in-plane polarization direction. We note that this feature is especially useful for the present study. It has been achieved by a particular geometric arrangement of energy analyzer, spin detection axes and sample normal.

THIN FILM GROWTH AND CHARACTERIZATION

The thin epitaxial cobalt films were grown in the same ultrahigh vacuum system as used for domain imaging by slow evaporation from a crucible heated by electron bombardment at a growth rate of 0.2 Å/min onto a single crystalline Au(111) substrate. The slow deposition rate seems to be one of the crucial parameters in growing well-ordered epitaxial metal films: This method gives an atom time to rearrange on the surface before additional atoms are deposited in its vicinity. On the other hand, a lower limit of the growth rate is given by the fact that, even in ultrahigh vacuum, contaminants from the residual gas are incorporated into the film during deposition. In our system, the pressure during evaporation was $< 5 \times 10^{-10}$ mbar, with a base pressure of 1×10^{-10} mbar. Film thicknesses have been determined independently by Auger spectroscopy and stylus profilometry as well as scanning force microscopy for thicker films, with agreement being within 15%. The growth characteristics have been investigated in detail earlier [3,5]. The interface is sharp on the atomic level; no interdiffusion is known to occur. The large lattice mismatch between Au(111) and Co(0001) of 14% causes stress at the interface, which is relieved by misfit dislocations. We monitored the quality of our films by low-energy electron diffraction (LEED). The sharp spots of the Au(111) substrate broaden for the first two monolayers (1 ML = 2 Å), and then sharpen again to produce the well-known sixfold symmetry characteristic of hexagonal (hcp) Co(0001) [14]. From LEED, we find a tensile strain in the surface plane of $\simeq 14\%$ for 1 ML and $\simeq 8\%$ for 3 ML compared to the Co bulk value, which is achieved at 6 ML; these values are in agreement with those found earlier [15]. Both evaporation and measurements have been performed at 300 K. We note that in Auger uptake curves (Auger signal vs. deposition time) we were not able to detect the notorious breaks indicating completion of the first individual layers as expected for ideal layer-by-layer growth [16]. We attribute this deficit to the fact that the growth of the first layers is not ideally layer-by-layer.

IMAGING OF MAGNETIC DOMAINS IN Co/Au(111) FILMS

Perpendicularly oriented domains in very thin films

The motivation for growing very thin cobalt layers on a (111)-oriented face-centered cubic (fcc) crystal stems from the fact that this orientation has the proper symmetry to allow Co to retain its easy magnetization direction as similar to bulk Co as possible. Bulk Co in its hcp phase has a crystalline anisotropy, hence favoring the magnetization to point along the c-axis. On a (111)-oriented fcc substrate, this direction is normal to the surface. Neglecting shape anisotropy for the

moment, Co films therefore should show a tendency toward perpendicular magnetization on such a substrate orientation, even without invoking Néel's surface anisotropy [17] or strain anisotropy [18].

This has in fact been observed for various systems such as Co/Au(111) [3-5], Co/Pt(111) [8], or Co/Pd(111) [6] by hysteresis loop experiments. We can easily observe the perpendicular easy magnetization axis without applying any external magnetic field by domain imaging. Figure 1a depicts the magnetic domain image for a 3-ML Co/Au(111) film, showing irregularly shaped domains with magnetization vectors along the surface normal. The simultaneously measured in-plane magnetization vanishes completely, see Fig. 1b. For comparison, Fig. 1c shows the simultaneously acquired electron intensity distribution, showing topographical contrast only at some small defects on an otherwise flat surface. The fact that the domains are fully out-of-plane stresses the importance of a highly uniaxial anisotropy for the magnetization direction in thin films [1,3-8]. The most remarkable fact and new finding in Fig. 1 is not this presence of a vertical magnetization, but its decay into a domain structure. In fact, classical theories [19] predict a single domain for thin films, because the saving in magnetostatic energy gained by the creation of up and down domains is not sufficient to compensate for the energy required to form domain walls, the former being proportional to the film thickness d^2, the latter to d. Experimentally, single-domain behavior has been indirectly inferred from hysteresis loops for various systems [20-22], and also directly observed for Co/Cu(100) films magnetized in-plane [23]. Contrary to these systems, we always find micrometer-sized domains in our out-of-plane magnetized films.

This is in apparent contradiction to a recent investigation of magnetization reversal in Au/Co/Au(111) sandwiches grown on glass [24]. However, their "as-grown single-domain state" might be brought about by a persisting small external magnetic field [25]. Our films, on the other hand, have been evaporated in a field-free configuration ($H < 1$ A/m), which produces truly demagnetized films.

Substrate or film imperfections are known to serve as pinning centers for domain walls. Interestingly, we found that the domain size of our films is much larger than the average step width of the substrate of $\simeq 50$ nm. Defects in the film can cause local alterations of the preferred magnetization axis. We note, however, that at extended irregularities visible in the topography we do not observe any

(a)   (b)   (c)
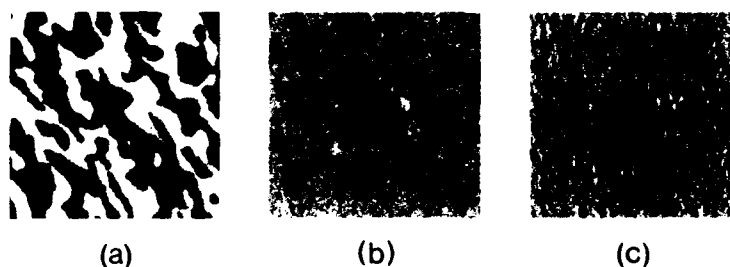
FIG. 1. (a) Magnetic domain image of a 3-ML Co/Au(111) film, showing out-of-plane domains with magnetization up (white) and down (black); (b) same as (a) for the corresponding in-plane magnetization. The gray scale varies from a spin polarization $P = -15\%$ (black) to $P = +15\%$ (white). (c) Simultaneously measured electron intensity distribution showing some local defects. Primary energy 5 keV, beam current 0.1 nA, scan area 20 μm × 20 μm.

variation. Specifically, we find no in-plane magnetization component. We conclude therefore that most surface imperfections do not influence domain formation.

The lowest-energy configuration of a ferromagnetic sample can be expected to be reached by annealing above the Curie temperature T_C and subsequent cooling in zero field. Upon annealing, we find that the location of the domains changes irregularly. In no case were we able to achieve a single-domain state. Hence we conclude that at room temperature the lowest-energy state of a 3-ML Co/Au(111) film is an irregular arrangement of vertical domains, with a typical domain size of some micrometers. We note that this result can explain why hysteresis loops in very thin Au/Co/Au layers display a strongly reduced remanent magnetization compared to saturation [26].

A recent elaborate calculation predicts domains even in ML films, based on a model including dipolar magnetic energy [27]. The relevant quantities are $\delta = w/D$ (w = domain wall width, D = domain size) and f, which is proportional to the ratio of uniaxial anisotropy to demagnetization energy. For domains to be present, f must be within the range $1 \lesssim f \lesssim 1.4$. The striking fact is that such a small variation of f causes δ to vary by more than six orders of magnitude. For $f > 1.4$, the domain size grows to macroscopic dimensions, thus appearing as as a single-domain state in domain microscopy. For our 3-ML film, our experiments determine $\delta < 0.02$, $D \simeq 2 \mu m$, and hence [27] $f \simeq 1.06$. Therefore finite domains can be expected. To our knowledge, Fig. 1 represents the first experimental support of the prediction that a very thin film with large perpendicular anisotropy has a multi-domain equilibrium state owing to the small dipolar magnetic energy. Much more work is required to test the implications of this novel view of regarding domain formation as being driven by dipolar energy. We postpone this discussion to a later chapter. Here we emphasize once more that no equilibrium domains can be found in in-plane magnetized systems such as Co/Cu(100) [23].

Magnetization direction switching

Any film magnetized vertically must change its magnetization direction at a critical thickness d_c, owing to the predominance of magnetostatic energy over anisotropy. This switching has been investigated earlier with hysteresis loop experiments [3,28]. The result is that near d_c, the out-of-plane remanent magnetization decreases, whereas the in-plane magnetization increases. Depending on substrate and film growth parameters, d_c varies between 0.5 and 1.9 nm [3,4,7]. The exact mechanism of such a transition, however, is not clear. The crucial question is whether the out-of-plane remanence decrease is due to a break-up into domains or to a rotation of the magnetization from out-of-plane towards in-plane. We emphasize that from hysteresis loops one cannot discriminate between a continuous rotation of the magnetization and only two allowed discrete values. It is the monitoring of the magnetization direction in a domain that allows us to conclude that the magnetization crossover takes place by a continuous rotation from 0° to 90°, within a thickness increase of 2 ML.

The experiment to obtain this result involves evaporation of a thin film whose thickness is subsequently increased in well-defined intervals. At each thickness, the *identical* position on the sample has to be probed. The results of such an experiment are displayed in Fig. 2 for a selected thickness range 3 ML $\leq d \leq$ 6 ML, each with the out-of-plane and one in-plane component. Below 2 ML we do not find magnetization at room temperature, in accordance with the observation that $T_C < 300$ K [3]. At 2 ML, very small domains ($\leq 0.5 \mu m$) with perpendicular magnetization begin to form (not shown). At 3 ML, an out-of-plane domain pattern similar to that in Fig. 1 is observed. One additional layer is sufficient to let the small

3 ML   4 ML   4.5 ML   5 ML   6 ML
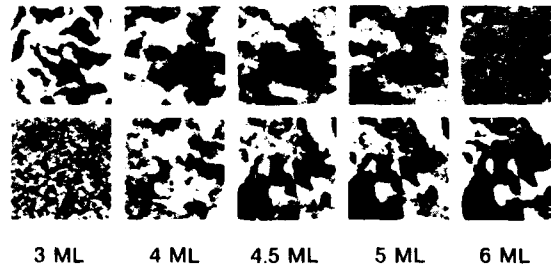
FIG. 2. Magnetic domain images for Co/Au(111) thin films, showing the evolution of domain size and switching behavior vs. film thickness. The pictures have been taken at identical positions on the sample between evaporation of additional layers. For each thickness, the upper image gives the out-of-plane and the lower the in-plane magnetization component (along the length of the page). Gray scales from black to white indicate magnitude of magnetization component along the measured axis; scan area $20\,\mu m \times 20\,\mu m$. Note the collapse of the small domains on proceeding from 3 ML to 4 ML.

domains coalesce into larger domains, and some faint contrast is already visible in-plane. The crossover thickness d_c is reached by evaporating an additional 0.5 ML. Another 0.5 ML forces the film to essentially switch in-plane. For $d \geq 6\,ML$, no perpendicular component is left within the statistical error of the experiment.

From Fig. 2 we are able to reconstruct the angle θ between surface normal and magnetization for each individual point. The results are summarized in Fig. 3. We find a continuous switching from out-of-plane to in-plane magnetization in a finite thickness interval of 2 ML [29]. Two recent calculations may shed some light on this finding, although one of them deals exclusively with fixed film thickness [30], whereas the other is only applicable far from the Curie temperature [31]. According to [31], the magnetization axis might rotate or jump into the plane at a finite, small
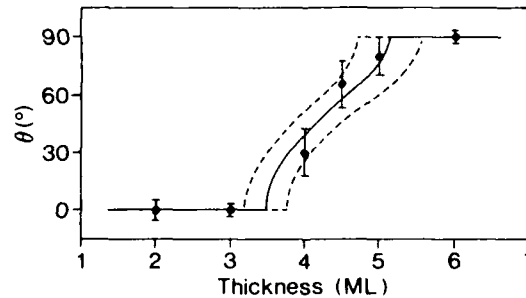
FIG. 3. Angular dependence of the magnetization direction vs. thickness derived from point-by-point analysis of Fig. 2. θ is the angle between surface normal and magnetization. The solid line represents the best fit for $\sin^2\theta = (\mu_0/2 \times M^2 - K_{1B} - K_S/d)/2K_2$, with the Co bulk values $M = 1440\,kA/m$, $K_{1B} = 412\,kJ/m^3$, $K_2 - 143\,kJ/m^3$, and the fit parameter $K_S = 0.62\,mJ/m^2$. For comparison, the dashed lines represent fits for $K_S = 0.57$ and $0.67\,mJ/m^2$, respectively.

temperature $\ll T_C$. However, this condition is not fulfilled in our case. In the following we outline how the tilted configuration can be understood by a simple energy consideration. The reason is the different angular dependence of the demagnetization energy and second hexagonal anisotropy constant K_2. The total energy $E = \mu_0/2 \times M^2\cos^2\theta + K_1\sin^2\theta + K_2\sin^4\theta$, with M as the magnetization and K_1, K_2 the uniaxial anisotropy constants, is minimized with respect to θ. Depending on the actual numbers, the solutions are $\theta = 0°$, $\theta = 90°$, and $\sin^2\theta = (\mu_0/2 \times M^2 - K_1)/2K_2$. Since K_1 may be split into bulk and surface contributions, $K_1 = K_{1B} + K_S/d$ [28,32], we can determine the uniaxial surface or interface anisotropy K_S from a fit to Fig. 3. Taking Co bulk values $M = 1440\,kA/m$, $K_{1B} = 412\,kJ/m^3$, and $K_2 = 143\,kJ/m^3$, the result is $K_S = 0.62 \pm 0.05\,mJ/m^2$, in good agreement with the $0.53\,mJ/m^2$ found earlier [28]. We also include in Fig. 3 the fits for $K_S = 0.57$ and $K_S = 0.67$, which should allow the reader to judge the quality of our estimate independently.

We emphasize that the phenomenological quantity K_S cannot give insight into the physical origin of the uniaxial anisotropy. The present understanding is that strain might be responsible for the out-of-plane anisotropy, although Néel's surface anisotropy cannot be excluded [7,8]. Experiments with unstrained hexagonal Co films would be highly desirable to solve this ambivalence. The task for the experts in metal epitaxy is to find the proper substrate that will allow ordered growth without alloying.

It might be instructive to summarize the essential ingredients leading to this continuous magnetization rotation in a finite thickness interval. The balance between magnetization and the first anisotropy constant K_1 determines the crossover thickness d_c because of the competition between demagnetization energy and anisotropy energy. The existence of a finite K_2 with a different angular dependence than M and K_1, on the other hand, determines the finite transition width responsible for the continuous rotation. To our knowledge, this is one of the first examples which clearly shows the importance of the second-order anisotropy constant, a constant that can usually be neglected in most calculations and experiments.

In addition, there must be at least one other crossover thickness with a drastic change in domain pattern, since the domain configuration for the infinite film thickness limit is known from bulk hcp-Co. We can extend Kittel's pioneering work [19] to estimate various relevant crossover thicknesses. As a first approximation we try four different domain arrangements, namely, single-domain out-of-plane, single-domain in-plane, multi-domain out-of-plane, and multi-domain out-of-plane with closure domains. We include an extra energy term describing surface anisotropy, $E_S = K_S/d$, with $K_S = 0.62\,mJ/m^2$ as in Fig. 3. The result — to be compared to Fig. 2 of [19] — is displayed in Fig. 4. A first crossover thickness occurs at 4.2 ML from out-of-plane to in-plane magnetization, in agreement with experiment. However, as mentioned above, classical theory predicts a single-domain state for both regions, in contrast to our measurement. An additional crossover from in-plane single-domain to out-of-plane multi-domain is predicted between 100 ML and 200 ML. Finally the transition taking place at $d \simeq 10^4\,ML$ (2 μm) leads to a multi-domain state with closure domains which minimize flux leakage out of the surface. This model might be oversimplified. In particular the intermediate state for $100\,ML < d < 200\,ML$ is likely to be replaced by a more complex domain pattern, as pointed out recently [33]. The firm fact is, however, that a transition will occur to a multi-domain configuration with closure domains. With our Co evaporators optimized for slow growth conditions, it is not feasible to grow an epitaxial film of micrometer thickness. However, we can simulate the thick film by an hcp Co single crystal, the equivalent orientation being (0001). The corresponding domain image nicely shows the complicated lace-like domain structure at the surface, produced by this stray field minimization, see Fig. 5. Note that we observe no in-plane sixfold symmetry, as has been claimed in an earlier

work on the Co(0001) surface [34]. Indeed one might only expect this in-plane symmetry if a small higher order term in crystalline anisotropy becomes relevant, a condition that does not seem to be fulfilled for Co [35]. This is corroborated by the situation shown in Fig. 1 that neither six- nor threefold symmetry is found in the domain pattern of the thin Co/Au(111) films.
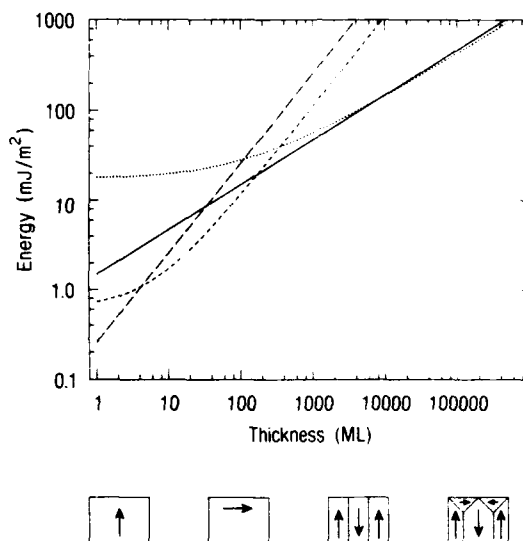
FIG. 4. Free energy vs. film thickness d for four different domain configurations, calculated following Kittel's model [19] and including a surface anisotropy energy $E_S = K_S/d$, with $K_S = 0.62\,mJ/m^2$. With increasing thickness, the lowest-energy configurations are single-domain out-of-plane (long-dashed), single-domain in-plane (short-dashed), multi-domain out-of-plane without closure domains (solid), and multi-domain out-of-plane with closure domains (dotted). A sideview sketch of the domain pattern is drawn at the relevant thickness interval.
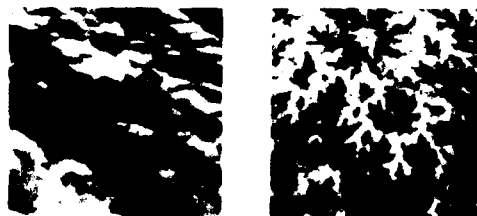
FIG. 5. Magnetic domain images for a bulk hcp-Co(0001) single crystal, showing the lace-like structure in the out-of-plane magnetization component (right) and the in-plane component (left) due to closure domains. Scan area 9 μm × 9 μm.

Dependence of domain size on film thickness

From Fig. 2 we see that the domain size D grows with increasing film thickness d, mainly by eliminating intermediate domains and walls. A domain growth with increasing film thickness was predicted long ago [19], with $D \sim \sqrt{d}$, provided that $D < d$. In our films, $D \simeq 1000\, d$, and the approximations in [19] are no longer valid. To our knowledge, the extreme case $D \gg d$ has not yet been tackled theoretically. The statistical evaluation of various films gives a roughly linear increase from $D \simeq 0.5\, \mu m$ at 2 ML to $D \simeq 4\, \mu m$ at d_c, and followed by a slow increase for thicker films. For films with $d \geq 10$ ML, we find elongated domains, which indicate an anisotropy within the film plane. Again, we emphasize that the results summarized in Fig. 6 represent the domain size for films grown in zero field. In contrast to films with $d \leq 3$ ML, films at d_c can be made single domain by magnetizing in a sufficiently high magnetic field [3]. Actually we find square hysteresis loops for films with $d = 8$ ML with *in situ* magneto-optical Kerr effect, and a coercive field of $H_C = 12$ kA/m. We verified the single-domain state over millimeter-sized areas. Thus the 3-ML film ground-state domain configuration is responsible for the *occurrence* of domains in films with $d > 3$ ML, whereas the *size* of the domains depends on d.
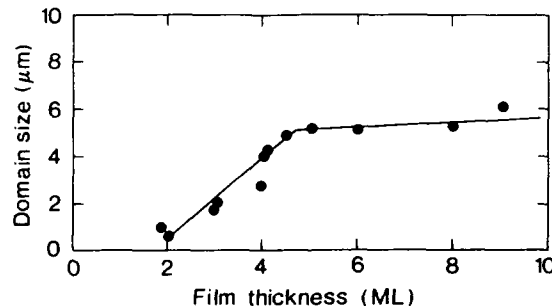
FIG. 6. Average domain size D vs. film thickness d for films evaporated in zero applied field. The two straight lines are drawn to guide the eye; they indicate a roughly linear dependence between D and d, and a break at crossover thickness.

High-resolution domain wall imaging

In this last chapter we would like to touch upon the high-resolution imaging capability of spin-SEM, a capacity to be exploited for direct testing of micromagnetic theories [36]. The reason is that, contrary to a quantity such as the domain size, which also depends on the magnetic history of the sample, the domain wall width w is given by material properties only (exchange and anisotropy constants, crystallographic orientation, film thickness). One can therefore expect to gain additional insight into these properties of thin films by measuring the domain wall width versus film thickness. An exploratory measurement for a 50-ML film is shown in Fig. 7. We identify a cross-tie wall [37] characterized by an in-plane magnetization rotation of oppositely oriented wall segments which separate the antiparallel magnetization direction of the adjacent domains. The narrower transition width along the wall is 40 nm as deduced from the line scan in Fig. 7, indicating that our probing diameter is below this value. The wall width itself is astonishingly large, $w \simeq 150$ nm. Note that Fig. 7 even shows the faint contrast
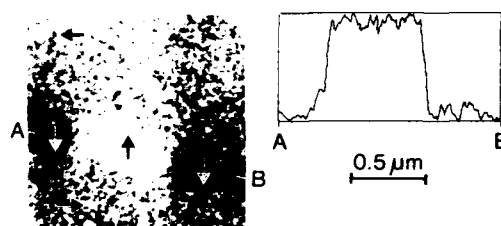
FIG. 7. High-resolution image of in-plane magnetization component in a 50-ML Co(0001) film and line scan along the cross-tie wall. The out-of-plane magnetization vanishes. Note the sharp transition between oppositely magnetized wall segments and the wide extension of a magnetization component into the adjacent domain which avoids magnetic singular es at the wall edge. Scan area 1.4 μm × 1.4 μm.

reminiscent of a cross-t wall within the domains adjacent to the wall, owing to flux closing of the wall segments.

An even more interesting task will be to resolve the walls in out-of-plane magnetized samples which are much thinner. An experimental determination of $w = w(d)$ for the out-of-plane magnetized films will provide a better foundation for the theory of domain formation [27]. The value of f derived from Fig. 1 predicts $w \simeq 10$ nm for $d = 3$ ML. Furthermore w is predicted to decrease as d increases. Experiments are under way to resolve these narrow walls as well.

CONCLUSIONS

In conclusion, we have investigated magnetic domains in thin epitaxial Co films grown on Au(111) single crystals. We do not find a single-domain state for the thinnest films investigated, but rather domains of micrometer size. This can be regarded as a first indication that the small magnetic dipolar energy might be responsible for domain formation in out-of-plane magnetized thin films. The transition from out-of-plane to in-plane magnetization is shown to occur smoothly within a narrow thickness region of 2 ML. This transition width allows the determination of the surface anisotropy constant K_S and indicates good agreement with values determined with independent methods. The domain size is found to depend linearly on film thickness. At room temperature, a multi-domain configuration is the ground state for a 3-ML film, whereas for films with $d \geq d_c$, the single-domain state can be reached by magnetizing the film in an external field. High-resolution spin-SEM allows us to find a transition width in domain walls which is appreciably smaller than that observed previously.

ACKNOWLEDGMENTS

REFERENCES

[1] For a comprehensive review on thin film magnetism, see Appl. Phys. A **49**, 437-629 (1989).

[2] J.G. Gay and R. Richter, Phys. Rev. Lett. **56**, 2728 (1986).

[3] C. Chappert et al., J. Magn. Magn. Mat. **54**, 795 (1986).

[4] F.J.A. den Broeder et al., Phys. Rev. Lett. **60**, 2769 (1988).

[5] C.H. Lee et al., Phys. Rev. Lett. **62**, 653 (1989).

[6] P.F. Carcia, A.D. Meinhaldt, and A. Suna, Appl. Phys. Lett. **47**, 178 (1985).

[7] C.H. Lee et al., Phys. Rev. B **42**, 1066 (1990).

[8] C.H. Lee et al., Phys. Rev. B **42**, 11384 (1990).

[9] R. Allenspach, M. Stampanoni, and A. Bischof, Phys. Rev. Lett. **65**, 3344 (1990).

[10] K. Koike, H. Matsuyama, and K. Hayakawa, Scanning Microsc. Suppl. **1**, 241 (1987).

[11] G.G. Hembree et al., Scanning Microsc. Suppl. **1**, 229 (1987).

[12] M. Taborelli, Ph.D. thesis, ETH No. 8545, Swiss Federal Institute of Technology (ETH), Zurich, Switzerland, 1988.

[13] D.P. Pappas et al., Phys. Rev. Lett. **66**, 504 (1991).

[14] G.L.P. Berning, Surface Sci. **61**, 673 (1976).

[15] C. Dupas et al., J. Appl. Phys. **67**, 5680 (1990).

[16] For a review see C. Argile and G.E. Rhead, Surf. Sci. Rept. **10**, 277 (1989).

[17] P. Bruno, J. Phys. F **18**, 1291 (1988).

[18] G.F. Dionne, Mat. Res. Bull. **6**, 805 (1971).

[19] C. Kittel, Phys. Rev. **70**, 965 (1946).

[20] T. Beier et al., Phys. Rev. Lett. **61**, 1875 (1988).

[21] M. Stampanoni et al., Phys. Rev. Lett. **59**, 2483 (1987).

[22] C. Liu, E.R. Moog, and S.D. Bader, J. Appl. Phys. **64**, 5325 (1988).

[23] H.P. Oepen et al., J. Magn. Magn. Mat. **86**, L137 (1990).

[24] J. Pommier et al., Phys. Rev. Lett. **65**, 2054 (1990).

[25] P. Bruno (private communication).

[26] J. Ferré et al., Appl. Phys. Lett. **56**, 1588 (1990).

[27] Y. Yafet and E.M. Gyorgy, Phys. Rev. B **38**, 9145 (1988).

[28] C. Chappert and P. Bruno, J. Appl. Phys. **64**, 5736 (1988).

[29] Note that the film thickness must be very uniform to lead to such a small transition width.

[30] D. Pescia and V.L. Pokrovsky, Phys. Rev. Lett. **65**, 2599 (1990).

[31] P.J. Jensen and K.H. Bennemann, Phys. Rev. B **42**, 849 (1990).

[32] The difference by a factor of 2 in the formula for K_1 is due to the fact that Ref. 28 deals with Au/Co/Au(111) bilayers in contrast to our Co/Au(111) film.

[33] A. Hubert (private communication).

[34] J. Unguris et al., Appl. Phys. Lett. **55**, 2553 (1989).

[35] E.P. Wohlfarth, in Ferromagnetic Materials, Vol. 1, edited by E.P. Wohlfarth, (North Holland, Amsterdam New York, 1980), Chapt. 1.

[36] M.R. Scheinfein et al., Phys. Rev. B **43**, 3395 (1991).

[37] S. Middelhoek, J. Appl. Phys. **34**, 1054 (1963).

SOFT X-RAY MAGNETIC SCATTERING STUDY
OF THIN FILMS AND MULTILAYERS

C.-C. KAO, E.D. JOHNSON, J.B. HASTINGS, D.P. SIDDONS

National Synchrotron Light Source

Brookhaven National Laboratory, Upton New York 11973

C. VETTIER

Institute Laue-Langevin, 38052 Grenoble CEDEX, France

Abstract

A brief discussion of the resonant magnetic scattering process is given. Results from recent studies of thin Fe films and Fe/Gd multilayers are used as examples to demonstrate the information can be obtained and the unique features of this technique: large resonant enhancement, sensitivity to magnitization, elemental specificity, and tunability of the penetration depth. Comparison is made with related techniques: magneto-optical Kerr effect, Faraday effect, and magnetic circular dichroism.

Resonant magnetic scattering

Recently, large resonant enhancement of the magnetic scattering cross section near an absorption threshold has been observed in Ho and UAs [1,2]. In favorable cases the magnetic scattering cross section can be comparable to that of charge scattering. These observations can all be explained by the resonant exchange scattering process [3]. To summarize briefly, the large resonant enhancement is the result of strong electric multipole transitions from atomic core levels to unoccupied states above the Fermi level, while the sensitivity to magnetization arises both from spin polarization and from exchange splitting of the conduction band. In fact, in many respects resonant magnetic scattering can be considered as a simple extension of normal magneto-optical

effects to higher photon energies. However, there is an important distinction between the two cases. At lower energies, especially when both the initial and final states are in the conduction band, the spin-orbit splitting is often small in comparison with the bandwidth of the joint density of states, which leads to partial cancellation of the magneto-optical effects. On the other hand, at higher energies where the spin-orbit splitting of the initial core state is typically much greater than the bandwidth of the conduction band, the cancellation is small, which in turn makes the observed magneto-optical effects much more pronounced [4].

In the remainder of this paper, we will limit our discussion to dipole transitions and to the transverse scattering configuration, where the magnetization of the sample is perpendicular to the scattering plane. For a complete analysis of multipole transitions and polarization dependence , see reference [3]. Following Hannon et al. [3], the scattering amplitude due to resonant exchange scattering in the transverse configuration, and considering only dipole transitions, is given by equation (1),

$$f_{E1}^{(res)} = \frac{3\lambda}{8\pi} \left\{ (\vec{e}_f \cdot \vec{e}_o) \left[F_{11} + F_{1-1} \right] - i \ (\vec{e}_f \times \vec{e}_o) \cdot \vec{z}_j \left[F_{11} - F_{1-1} \right] \right\}. \tag{1}$$

In equation (1), $\vec{e}_o$ and $\vec{e}_f$ are the polarization vectors of the incident and scattered beams, $\vec{z}_j$ defines the quantization axis, and F_{LM} is the resonant response, where L is the order of the transition (L = 1 for dipole transitions) and M is the change in angular momentum ($\Delta M = 0, \pm 1$). The first term is the usual resonant scattering amplitude in anomalous scattering and the second term is the linear magnetic term, which is proportional to the magnetization of the sample. Since ΔM equals -1 (+1) for left- (right-) circularly polarized light, the two terms in equation (1) can also be considered as the sum and difference of scattering due to left- and right-circularly polarized components of plane polarized light.

The relationships between resonant magnetic scattering and other related

techniques can be briefly summarized with the aid of equation (1). Resonant magnetic scattering makes use of the coherent interference between the second term and first term in equation (1), and measures the total scattering intensity. On the other hand, the Faraday effect and magnetic circular dichroism measure the real part and the imaginary part of the second term, respectively. Moreover, since the real and imaginary parts of the scattering factor are related through Kramers-Kronig relations, the results from Faraday effect and dichroism measurements can be interconverted by performing Kramers-Kronig analysis. With both the real and imaginary parts of the scattering factor, the resonant scattering intensity can also be obtained [5]. This unique possibilty of cross referencing results from three different experimental techniques provides not only a much more stringent test for these results, but also an opportunity for them to complement each other.

Case I: thin Fe film

The specular reflectivity of p-polarized soft x-ray near the Fe $L_{II,III}$ absorption edges was measured from a single crystal Fe film in the transverse configuration. The sample is a 35 Å thick single crystal of Fe(110) (17 atomic layers) deposited by molecular beam epitaxy on a (110) gallium arsenide substrate [6]. The effect of resonant exchange scattering manifests itself as changes in the specular reflectivity upon reversal of the direction of the magnetic field. To illustrate the effect better, an asymmetry ratio R defined as $R = \dfrac{I^+ - I^-}{I^+ + I^-}$ was derived as a function of photon energy, where I^+ and I^- are the measured specular reflectivity with the applied magnetic field parallel and antiparellel to the cross product of the polarization vectors of the scattered and the incident beams.

Figure 1 shows the asymmetry ratios as well as I^+ and I^- taken at a scattering angle of 35°. An asymmetry ratio as large as 13 % was observed. The effect should be even larger at larger scattering angles because the ratio of the angular dependent
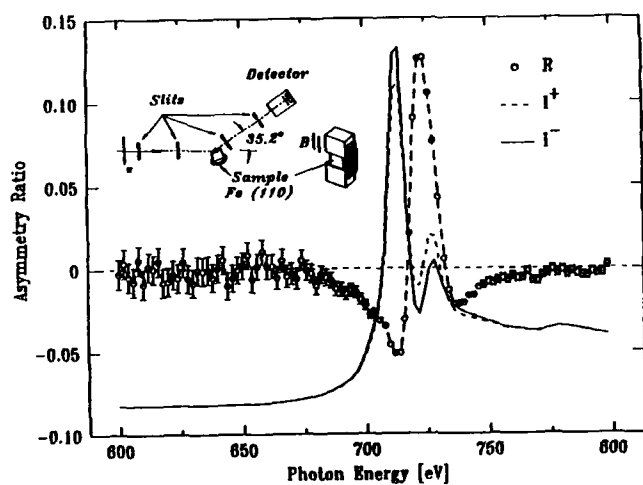
Fig. 1. Specular reflectivity of p-polarized light, I^+ and I^-, and asymmetry ratios R

measured from a 35 Å Fe(110) crystal.
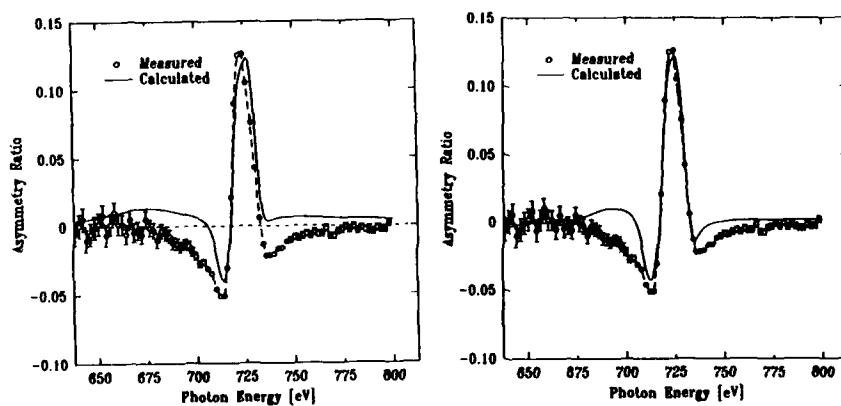
Fig. 2(a) Comparison between the measured and the calculated asymmetry ratios;

2(b) The same as 2(a) except a 5 Å thick oxide layer is included in the calculation.

parts, i.e. the ratio between the cross product and the dot product of the polarization vectors, is proportioal to tan(2θ).

The data agrees very well with an atomic-like model calculation based on the resonant exchange scattering process [7]. In this model, the 3d states of Fe are treated as atomic levels with an exchange splitting Δ. The resonant scattering amplitude then becomes

$$f_{E1}^{(res)} = F \ [\ (\vec{e}_f \cdot \vec{e}_o) \ n_h \ + \ i \ (\vec{e}_f \times \vec{e}_o) \cdot \vec{z}_j \ \frac{\mathbf{P}}{4} \ ],$$ (2)

with

$$\mathbf{P} = [\ \mathbf{n}_e - (\ \frac{\Delta}{\Gamma(\mathbf{x}(\alpha,\eta)-i)} \ ) \cdot \mathbf{n}_h \ ],$$ (3)

where F includes the radial part of the transition probability and the resonant denominator, $\frac{1}{\mathbf{x}(\alpha,\eta)-i}$, $\mathbf{n}_e$ is the net number of spin up electrons, $\mathbf{n}_h$ is the total number of holes in the 3d band, Γ is the total width of the excited state, and Δ is the exchange splitting. In the resonant denominator x is the deviation from the absorption edge energy in units of half widths, and is defined as

$$\mathbf{x}(\alpha,\eta) = \frac{[\ \varepsilon - (\ E_\eta - E_\alpha \ ) \ ]}{\Gamma/2},$$ (4)

where ε is the photon energy, and E_α, E_η are the energies of the ground state and the excited state respectively.

From equation (3), it is clear that the linear magnetic term is a function of both the spin polarization of the partially filled states and the exchange splitting of the unoccupied states. Given these functions, the specular reflectivity and asymmetry ratios

can then be calculated using the scattering amplitude in equation (2). Figure 2 (a) is a comparison of the calculated and the measured asymmetry ratios using the following parameters: $n_e = 1$, $n_h = 4$, $\Delta = 1.5$ eV, $\Gamma = 5.0$ eV. Better agreement between the calculated and the measured asymmetry ratios is obtained by including a 5 Å thick surface oxide layer as shown in Figure 2 (b).

Case II: Fe/Gd multilayer

Asymmetry ratios were also measured for a (32.4 Å Fe/ 32.7 Å)$_{22}$ multilayer near both the Fe $L_{II,III}$ edges and the Gd $M_{IV,V}$ edges as a function of photon energy and scattering angle [8]. Figure 3 shows the asymmetry ratios measured at 690 eV, about 17 eV below the L_{III} absorption threshold, as a function of wave vector transfer Q, $4\pi\frac{sin(\theta)}{\lambda}$, as well as the first order Bragg peak corresponding to the periodicity of the multilayer.

Since the wavelength of the photon is still much longer than the dimensions of the atomic states being excited, the standard Fresnel-Maxwell formulae used in the optical range are still applicable. Recently, several algorithms which allow arbitrary magnetization directions in the component layers have been developed to calculate the magneto-optical properties of these multilayer structures. For example, see Zak et al. [9] and references therein. In the following, a simpler algorithm specific to the transverse configuration used in the experiment is used to calculate the reflectivity of the Fe/Gd multilayer.

Figure 4 (a) is a comparison of the calculated and the measured asymmetry ratios around the first Bragg peak at 690 eV, while figure 4 (b) shows the calculated asymmetry ratios at the same energy for an extended range of Q. The agreement between the calculated and the measured asymmetry ratios in figure 4 (a) is not as good as in the case of the thin Fe film. However, the calculation does seem to reproduce the main features in the data: a major peak near the Bragg angle and a series of
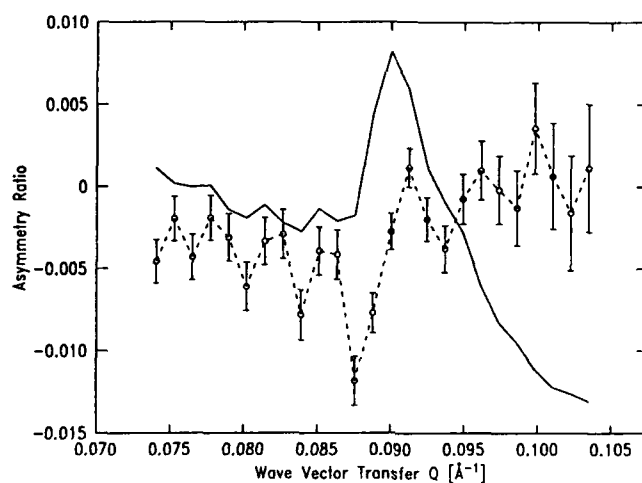
Fig. 3. Bragg scattering and asymmetry ratios from a (32.4 Å Fe/ 32.7 Å)$_{22}$ multilayer at 690 eV photon energy.
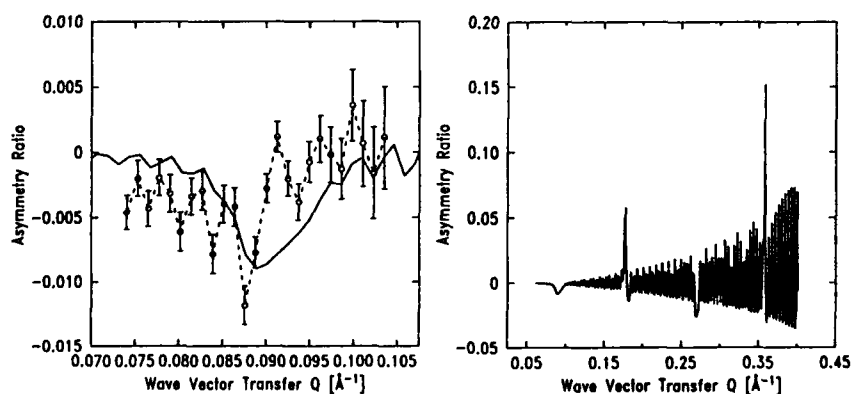
Fig. 4(a) Comparison between the measured and the calculated asymmetry ratios; 4(b) Calculated asymmetry ratios for an extended range of wave vector transfer Q.

high frequency oscillations. The high frequency oscillations in the asymmetry ratios are due to the finite number of layers in the sample. The spacing between these oscillations agrees very well with sampling depth of 22 layers. This demonstrates that the penetration depth of the photon can be extended to over one thousand angstroms by tuning the photon energy to slightly below the absorption edge, since the effects of resonant magnetic scattering can be still quite large before the absorption edge. In fact, these oscillations can serve as a measure of the penetration depth of the photons. From figure 4 (b), it can be further stated that in addition to the angular dependence of the resonant scattering, as observed in the Fe film, further enhancement of the effect was observed at the Bragg angles.

Conclusions

(1)From the analysis of resonant magnetic scattering, the criteria for large enhancement of the magnetic scattering cross section near an absorption edge are the following: the absorption edge involves some strong multipole transitions, large spin-orbit coupling in the initial state to avoid partial cancellation of the effect, strong spin polarization of the unoccupied states, and large exchange splitting. In the soft x-ray region, large effect can be expected from 3d transition ferromagnets and 4f rare-earth magnetic materials.

(2)The results from the thin Fe film demonstrate that important spectroscopic information about the electronic structure of magnetic systems can be extracted from magnetic scattering measurements. Further, the information obtained from resonant magnetic scattering and related techniques, Faraday effect and magnetic circular dichroism, can be considered as complementary to that from spin-polarized photoemission.

(3)The large resonant enhancement combined with the high photon flux available from synchrotron radiation sources makes this technique especially attractive for the

study of surface, interface, and thin film magnetism, and for the characterization of dilute magnetic samples.

(4)For multilayers consisting of 3d and/or 4f elements, large enhancement of the magnetic scattering cross section can be expected. Moreover, in cases where the wavelength of soft x-ray photon used in the excitation is comparable to the periodicity of the multilayer, the ordering and coupling of these multilayers can also be studied. Field dependent and temperature dependent studies of these systems should provide valuable information on the understanding of these interesting systems.

References

1. D. Gibbs, D.R. Harshman, E.D. Isaacs, D.B. McWhan, D. Mills, and C. Vettier, Phys. Rev. Lett. **61**, 1241 (1988).

2. E.D. Isaacs, D.B. McWhan, C. Peters, G.E. Ice, D.P. Siddons, J.B. Hastings, C. Vettier, and O. Vogt, Phys. Rev. Lett **62**, 1671 (1989).

3. J.P. Hannon, G.T. Trammell, M. Blume, and D. Gibbs, Phys. Rev. Lett. **61**, 1245 (1988), See also errata Phys. Rev. Lett. **62**, 2644 (1989).

4. J.L. Erskine, E.A. Stern, Phys. Rev. **B8**, 1239 (1973); Phys. Rev. **B12**, 5016 (1975).

5. C.-C. Kao, D.P. Siddons, (unpublished).

6. Sample kindly provided by G.A. Prinz of NRL.

7. C.-C. Kao, J.B. Hastings, E.D. Johnson, D.P. Siddons, G.C. Smith, G.A. Prinz, Phys. Rev. Lett. **65**, 373 (1990).

8. C.-C. Kao, E.D. Johnson, J.B. Hastings, C. Vettier, (to be published).

9. J. Zak, E.R. Moog, C. Liu, S.D. Bader, Phys. Rev. **B43**, 6423 (1991).

SPIN-POLARIZED SCANNING TUNNELING MICROSCOPY (SPSTM)

R. WIESENDANGER, D. BUERGLER, G. TARRACH, I.V. SHVETS, AND
H.-J. GUENTHERODT
University of Basel, Dept. of Physics, CH-4056 Basel, Switzerland

ABSTRACT

We report on a novel promising technique for the investigation of magnetic structures at surfaces at high spatial resolution, ultimately down to the atomic scale. This technique is based on the observation of vacuum tunneling of spin-polarized electrons by means of a scanning tunneling microscope (STM). We discuss appropriate probe tips for the spin-polarized STM (SPSTM) and describe initial experimental results. We further focus on the information obtained by SPSTM. Finally, the perspectives of SPSTM will be discussed.

1. INTRODUCTION

The development of magnetic storage devices with increasing storage density requires the understanding and control of magnetic structure at the submicrometer level. Accordingly, there is a demand for magnetic imaging techniques at high spatial resolution on a nanometer or even subnanometer scale. Scanning electron microscopy with polarization analysis (SEMPA) [1] and magnetic force microscopy (MFM) [2] so far offered the highest spatial resolution of some ten nanometers. SEMPA allows to image magnetic domain structures using any magnetization vector component on the sample surface. The experiment has to be performed in ultra-high vacuum (UHV) and the resolution is mainly determined by the primary electron beam diameter and the efficiency of the spin detector. In contrast, MFM probes the stray fields at magnetic surfaces via the magnetic dipole interaction between a magnetized tip and a magnetic sample. It can be performed even in air. The spatial resolution is limited by the weak decay of the magnetic dipole forces with increasing tip-surface separation. A magnetic interaction between a probe tip and a sample surface with a much stronger, preferentially exponential decay would be needed to considerably improve spatial resolution. Force microscopy involving magnetic exchange forces as well as electron tunneling involving spin analysis are promising techniques for magnetic imaging down to the atomic scale. Both types of experiments can only be performed in UHV with well defined tips and sample surfaces.

Here, we will concentrate on the discussion of spin-polarized scanning tunneling microscopy (SPSTM) based on the direct observation of vacuum tunneling of spin-polarized electrons by means of a scanning tunneling microscope [3]. After introducing the concept of SPSTM in section 2, we will describe the choice and the preparation of appropriate SPSTM probes

(section 3). In section 4, we will report on recent results of SPSTM experiments. The information obtained by SPSTM will be discussed in section 5 before concluding with the perspectives of SPSTM (section 6).

2. CONCEPT OF SPSTM

Spin-polarized tunneling experiments may be realized in different ways. For a superconductor-barrier-ferromagnet tunnel junction in a parallel magnetic field and at temperatures well below the superconductor transition temperature, the Zeeman split density of states of the superconductor can act as a spin detector for the tunneling current carriers from the ferromagnet as has been demonstrated for planar tunneling junctions with oxide barriers [4]. Alternatively, a ferromagnetic barrier, e.g. EuS, separating two non-ferromagnetic electrodes in zero applied field can act as a very efficient spin filter at temperatures well below the Curie temperature of the ferromagnet [5].

A magnetic valve effect has been predicted for tunneling junctions consisting of two ferromagnets separated by an insulating barrier [6]. By considering the electron spin, the conductance G of a ferromagnet-barrier-ferromagnet tunneling junction was shown to be modified by an additional factor:

$$G = G_0(1+P_{fb}^2 \cdot \cos\theta) \qquad (1)$$

where θ denotes the angle between the directions of the magnetization vectors within the two ferromagnets and P_{fb} is the effective polarization of the magnet-barrier interface; (the two ferromagnets were assumed to be identical). It can easily be verified that

$$P_{fb}^2 = P = (G_{\uparrow\uparrow} - G_{\uparrow\downarrow})/(G_{\uparrow\uparrow} + G_{\uparrow\downarrow}) \qquad (2)$$

where $G_{\uparrow\uparrow}$ ($G_{\uparrow\downarrow}$) is the conductance of the tunneling junction for the case of parallel (antiparallel) alignment of the magnetization vectors within the two ferromagnets. Therefore, by directly measuring the expression on the right hand side of equation (2), the effective polarization P can be obtained.

The STM-type configuration with one electrode being an atomically sharp probe tip offers the opportunity to measure P on a local scale, ultimately at the atomic level. This experiment does not necessarily require low temperatures as long as the conductance changes of the tunneling junction due to tunneling of spin-polarized electrons are readily detectable.

3. PROBES FOR SPSTM

By considering equation (1), it becomes clear that successful SPSTM experiments at room temperature can only be

performed if efficient sources (detectors) for spin-polarized electrons are employed as probe tips. Optically pumped semiconductors such as GaAs [7] are well known as sources of spin-polarized electrons. However, the spin-polarization of electrons from such sources is relatively low and the problems which arise by using these sources for SPSTM have already been discussed [8].

The most promising materials for SPSTM probe tips are the half-metallic ferromagnets [9] which show normal metallic behaviour for one spin direction, while being insulators (or semiconductors) for the opposite spin direction. Therefore, a spin polarization of 100% at the Fermi level can be expected. Some Mn-based Heusler alloys such as XMnSb (X=Ni,Co,Fe,Pt) [9,10], as well as $CuCr_2S_4$ [11], Fe_3O_4 [12], CrO_2 [13], NiUSn [14] and $KCrSe_2$ [15] were theoretically predicted to be half-metallic ferromagnets. Some of these materials have Curie temperatures well above room temperature and therefore are expected to provide ideal spin filters for room temperature SPSTM experiments.

For our first successful observation of vacuum tunneling of spin-polarized electrons by means of STM [3], we have used a CrO_2 tip. The preparation of these CrO_2 tips has already been described [3]. Briefly, a polycrystalline CrO_2 film with in-plane magnetization was grown on a Si(111) substrate. Subsequently, the substrate was scribed and cleaved to give a tip shape. Finally, the Si substrate at the foremost end of the tip was etched back in a $HF-HNO_3$ solution which preferentially dissolves the silicon. The overhanging CrO_2 film tip which can freshly be broken in-situ then provided the magnetic probe for SPSTM experiments. Single crystal CrO_2 whisker tips might be used as well. Though the half-metallic behaviour of CrO_2 is still a matter of debate, it has experimentally been verified by means of spin-resolved photoemission that electrons with a spin polarization of 80-100% originate from states between 1.5 eV and 3 eV below the Fermi level [16]. For other materials which were predicted to be half-metallic ferromagnets, such a high spin-polarization has not yet been experimentally confirmed.

Apart from half-metallic ferromagnets, it is also worth to consider Fe, Co or Ni for use as SPSTM tips. Since these materials easily oxidize and surface magnetism critically depends on the existence of oxide layers, it is necessary to prepare such tips in-situ in UHV. We have recently developed a generally applicable in-situ tip preparation technique which is illustrated in Fig. 1. A polycrystalline, 0.25 mm diameter wire is electrochemically etched until a constriction of 20-100 μm diameter is formed (Fig. 1a). The top part is fixed in the tip holder of the STM whereas the bottom part is fixed in another tip holder on top of a standard sample holder. The two parts can finally be pulled apart in the UHV chamber at a background pressure of $1 \cdot 10^{-11}$ mbar. The cleanness of the obtained tips (Fig. 1b) at the foremost end is only limited by the amount of bulk impurities. The microtips formed at the foremost end of the
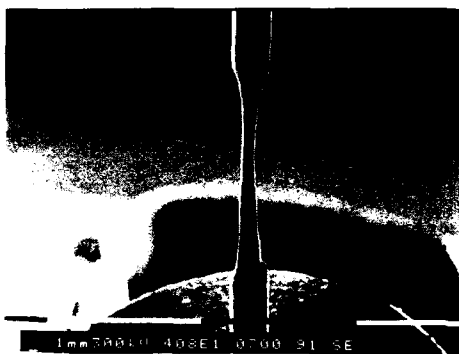
Fig. 1a:
Fe wire (0.25mm diameter)
electrochemically etched
in 4% HCl solution until
a constriction of 100 μm
(in this case) is formed.

Fig. 1b:
Fe tip which resulted by
pulling the wire shown in
Fig. 1a into two parts.

Fig. 1c:
Higher magnification
image of the left Fe
minitip in Fig. 1b.

Fig. 1d:
Higher magnification
image of the microtips
formed at the foremost
end of the Fe tip. Note
that the tip axis is
along the image diagonal
in Figs. 1b-d.

tips (Figs. 1c and 1d) reproducibly have a radius of curvature of 10 nm or even less. The formation of microtips with such a small radius of curvature does not depend on the diameter of the original constriction. Atomic resolution on the Si(111)7x7 test surface can routinely be achieved with these tips as demonstrated in Fig. 2.

Tips of antiferromagnetic materials such as Cr or NiMn with atomic resolution capability have also been produced by using the preparation technique described above. Antiferromagnetic tips are desirable for SPSTM experiments on ferromagnetic samples in order to exclude the influence of magnetic dipole forces between tip and sample on the experimental results [17,18]. Interestingly, half-metallic antiferromagnets without a spontaneous magnetization but with 100% spin polarization of the charge carriers at the Fermi level might exist [9], which would be particularly promising for SPSTM experiments.
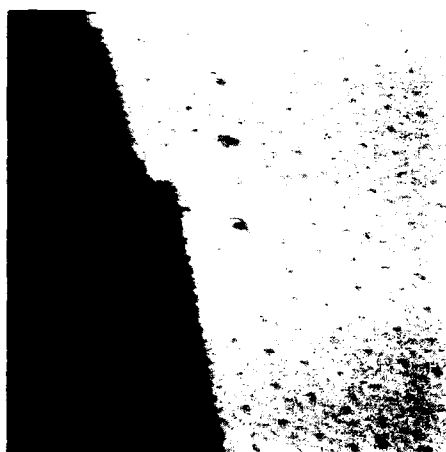
Fig. 2a:
STM image (top-view, grey scale) of the Si(111)7x7 surface obtained with a tip prepared according to the procedure illustrated in Fig. 1. Atomic resolution is achieved on both sides of a monatomic surface step. Imaged surface area: 31 nm x 33 nm, sample bias voltage: +2.0 V, tunneling current: 1 nA.
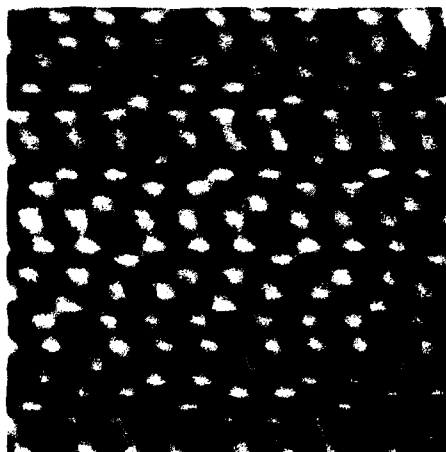
Fig. 2b:
STM image of the Si(111)7x7 surface at higher magnification. The tunneling parameters were identical to those of Fig. 2a.

4. SPSTM EXPERIMENTS

SPSTM experiments can be performed either without [3] or with [19] an applied magnetic field. In the latter case, magnetic field modulation and lock-in detection techniques are useful for measuring the small spin-polarized tunneling signal. Static SPSTM experiments are based on the additional contribution of spin-polarized tunneling to the normal non-polarized tunneling signal which is used to image the "topography" of the sample surface in conventional STM studies. The effective polarization of the tunneling junction can be extracted by recording the deviations from the topography as measured with a non-magnetic probe tip according to equations (1) and (2).

In our initial SPSTM experiment performed with a CrO_2 tip [3] we used the topological antiferromagnetic structure of the Cr(001) surface [20] as a magnetic test structure on a nanometer scale. Successive ferromagnetic terraces on the Cr(001) surface are predominantly separated by monatomic surface steps as verified by STM studies with a non-magnetic tungsten tip [3,21]. Therefore, the ferromagnetic terraces are alternately magnetized according to the antiferromagnetic structure of Cr. By operating the STM at a constant tunneling current with a CrO_2 tip, the separation between tip and sample surface had to be adjusted depending on the direction of magnetization of the terraces relative to the magnetization direction within the tip (Fig. 3). Consequently, alternating step-height values were obtained with the CrO_2 tip [3]. Based on the measured deviation $\Delta s = \Delta s_1 + \Delta s_2$ from the topographic step-height value h, the effective polarization P was calculated according to the equation [3]:

$$P = (\exp(A\sqrt{\phi}\Delta s)-1)/(\exp(A\sqrt{\phi}\Delta s)+1) \qquad (3)$$

where ϕ denotes the independently measured mean local tunneling barrier height and $A = 1.025$ eV$^{-1/2}$ Å^{-1}. The derived value of P was $(20 \pm 10)\%$ for the CrO_2-vacuum-Cr(001) tunneling junction.
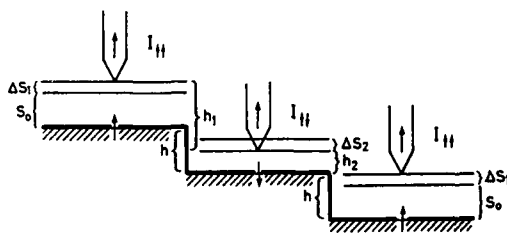
Fig. 3:
Schematic drawing of a ferromagnetic tip scanning over alternately magnetized terraces separated by monatomic steps of height h. An additional contribution from spin-polarized tunneling leads to alternating step heights $h_1 = h + \Delta s_1 + \Delta s_2$ and $h_2 = h - \Delta s_1 - \Delta s_2$.

Recently, we have performed similar experiments with Fe tips which were in-situ prepared according to the procedure described in section 3. We were again able to image the terraces separated by monatomic steps on the Cr(001) surface as shown in Fig. 4. However, a significant deviation of the measured monatomic step-height values from the topographic step-height value could not yet be found. This negative result might be explained by a lower spin polarization of electrons originating from the Fe tips compared to the CrO_2 tips.

We want to emphasize that according to equation (1), SPSTM is mainly sensitive to the surface spin component along the magnetization direction in the tip. For the CrO_2 as well as for the Fe tips used in our experiments, shape anisotropy is likely to force the magnetization direction to lie along the tip axis. Therefore, it is assumed that mainly the out-of-plane surface spin component is probed as schematically depicted in Fig. 3. A complementary experiment can be performed with a SPSTM sensor probing the in-plane surface spin component [19].

Fig. 4:
STM image (top-view, grey scale) of the Cr(001) surface obtained with a Fe tip prepared according to the procedure illustrated in Fig. 1. Imaged surface area: 37 nm x 40 nm, sample bias voltage: +0.04 V, tunneling current: 1 nA.

5. INFORMATION FROM SPSTM

As we have seen, SPSTM can provide information about the local value of the effective polarization P of a tunneling junction. It should be emphasized that the value of P is characteristic for the whole tunneling junction (including the type of electrodes as well as their separation). By changing one of the electrodes or the distance between the electrodes, the effective polarization P will generally be affected. Additionally, the effective polarization P depends on the applied bias voltage in the SPSTM experiment. In the limit of vanishing applied bias voltage, it has been shown [6] that the effective polarization P of the tunneling junction can be factorized into two polarizations characterizing the two electrodes. However, for a finite applied bias voltage, density-of-states effects have to be taken into account. In Fig. 5 we present a simple calculation of the local effective polarization P as a function of the applied bias voltage for the CrO_2-vacuum-Cr(001) tunneling junction. The calculation is based on published density of states for CrO_2 [13] and Cr(001) [22] and the absence of spin scattering has been assumed. The calculation is simplified in the sense that the different contributions of s-, p-, and d-states were not treated separately. However, our simple calculation already reveals the important fact that the value and even the sign of P depends critically on the applied bias voltage. Though initially, this seemed to be a further complication for the interpretation of SPSTM results, the bias dependence of P may allow to derive information on the local spin-dependent electronic structure of one electrode, ultimately on the atomic scale, provided that the spin-dependent electronic structure of the other electrode is already known.

A dependence of P on the separation of both electrodes can result from different decay constants of s-, p-, and d-type electronic states. It is important to realize that STM probes only the tails of the wavefunctions of those electronic states that have significant overlap with the tip. Therefore, a direct comparison with results of spin-polarized photoemission, for instance, is generally not possible.
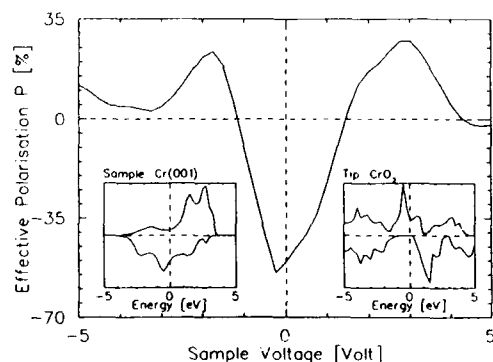
Fig. 5:
Effective local spin polarization of the CrO_2-vacuum-Cr(001) tunneling junction as a function of sample bias voltage. The insets show the spin-up (upper part) and the spin-down (lower part) density of states for CrO_2 and the Cr(001) surface.

6. CONCLUSIONS

SPSTM has the potential to reveal valuable information about surface magnetic properties down to the atomic scale. Particularly the extension of conventional scanning tunneling spectroscopy (STS) [23] to spin-resolved scanning tunneling spectroscopy (SRSTS) by measuring the bias dependence of the effective polarization might lead to spatially resolved information about the local spin-dependent electronic structure. Applications of SPSTM might include antiferromagnets, spin density wave systems, magnetic semiconductors, magnetic impurities in semiconductors, domain wall structures, magnetic clusters on surfaces [24], magnetic thin films at the early stage of growth, and artificial magnetic nanostructures (either MBE-grown magnetic superlattices [25] or magnetic nanostructures written by the STM itself [26]). SPSTM performed at low temperatures is also promising for probing properties of superconductors, particularly the novel high-T_c superconductors.

REFERENCES

[1] G.G. Hembree, J. Unguris, R.J. Celotta, and D.T. Pierce, Scanning Microscopy Suppl. 1, 229 (1987).
[2] D. Rugar, H.J. Mamin, P. Guethner, S.E. Lambert, J.E. Stern, I. McFadyen, and T. Yogi, J.Appl.Phys. 68, 1169 (1990).
C. Schoenenberger and S.F. Alvarado, Z.Phys. B80, 373 (1990)
[3] R. Wiesendanger, H.-J. Güntherodt, G. Güntherodt, R.J. Gambino, and R. Ruf, Phys.Rev.Lett. 65, 247 (1990).
[4] P.M. Tedrow and R. Meservey, Phys.Rev.Lett. 26, 192 (1971).
P.M. Tedrow and R. Meservey, Phys.Rev. B7, 318 (1973).
R. Meservey, Phys.Scr. 38, 272 (1988).
[5] J.S. Moodera, X. Hao, G.A. Gibson, and R. Meservey, Phys.Rev.Lett. 61, 637 (1988).
[6] J.C. Slonczewski, J. de Physique C8, 1629 (1988).
J.C. Slonczewski, Phys.Rev. B39, 6995 (1989).
[7] D.T. Pierce and F. Meier, Phys.Rev. B13, 5484 (1976).
[8] D.T. Pierce, Phys.Scr. 38, 291 (1988).
[9] R.A. de Groot, F.M. Mueller, P.G. van Engen, and K.H.J. Buschow, Phys.Rev.Lett. 50, 2024 (1983).

46

R.A. de Groot and K.H.J. Buschow,
J.Magn.Magn.Mat. 54-57, 1377 (1986).
R.A. de Groot, Physica B, (1991), in press.
[10] J. Kübler, Physica 127B, 257 (1984).
[11] J.J. Horikawa, T. Hamajima, F. Ogata, T. Kambara,
and K.I. Gondaira, J.Phys. C15, 2613 (1982).
[12] A. Yanase and K. Siratori, J.Phys.Soc.Jpn. 53, 312
(1984).
[13] K. Schwarz, J.Phys. F16, L211 (1986).
[14] R.C. Albers, A.M. Boring, G.H.O. Daalderop, and
F.M. Mueller, Phys.Rev. B36, 3661 (1987).
[15] J. Dijkstra, C.F. van Bruggen, C. Haas, and
R.A. de Groot, Phys.Rev. B40, 7973 (1989).
[16] K.P. Kämper, W. Schmitt, G. Güntherodt, R.J. Gambino,
and R. Ruf, Phys.Rev.Lett. 59,2788 (1987).
[17] R. Wiesendanger, D. Bürgler, G. Tarrach, A. Wadas,
D. Brodbeck, H.-J. Güntherodt, G. Güntherodt,
R.J. Gambino, and R. Ruf, J.Vac.Sci.Technol. B,
(1991), in press.
[18] A.A. Minakov and I.V. Shvets, Surf.Sci.Lett. 236,
L377 (1990).
[19] M. Johnson and J. Clarke, J.Appl.Phys. 67, 6141
(1990).
[20] S. Blügel, D. Pescia, and P.H. Dederichs,
Phys.Rev. B39, 1392 (1989).
[21] R. Wiesendanger and H.-J. Güntherodt, Surf.Sci. 235,
1 (1990).
[22] G. Allan, Surf.Sci. 74, 79 (1978).
[23] R.J. Hamers, Annu.Rev.Phys.Chem. 40, 531 (1989).
R.M. Tromp, J.Phys.: Condens.Matter 1, 10211 (1989).
[24] P.N. First, J.A. Stroscio, R.A. Dragoset, D.T. Pierce,
and R.J. Celotta, Phys.Rev.Lett. 63, 1416 (1989).
[25] S.S.P. Parkin, N. More, and K.P. Roche,
Phys.Rev.Lett. 64, 2304 (1990).
[26] U. Staufer, L. Scandella, and R. Wiesendanger,
Z.Phys. B77, 281 (1989).
D.D. Awschalom, M.A. McCord, and G. Grinstein,
Phys.Rev.Lett. 65, 783 (1990).

Spin Polarized Spectroscopies

SPIN POLARIZED PHOTOEMISSION STUDIES OF SURFACES AND THIN FILMS

PETER D. JOHNSON, N.B. BROOKES and Y. CHANG
Physics Dept., Brookhaven National Laboratory, Upton NY 11973.

ABSTRACT

Spin polarized photoemission is used to study the magnetic states associated with the clean iron (001) surface. These studies reveal evidence for a minority spin surface state in agreement with a first principles calculation. Studies of the same surface with silver and chromium epitaxial overlayers reveal evidence for interface states derived from this state found on the clean surface. In the case of the silver overlayer the binding energy of the new state is found to be dependent on the layer by layer thickness of the overlayer. With chromium overlayers the binding energy for the same interface state does not show the same thickness dependence. However a second interface state is observed immediately below the Fermi level. These changes in the interfacial electronic structure have implications for any modelling of magnetic coupling in multilayers dependent on the magnetic properties of the interface.

INTRODUCTION.

In recent years there has been a marked increase in research activity in the general area of surface magnetism including the magnetic properties of surfaces [1], thin films [2] and multilayers [3]. Much of the work in the latter area has been motivated by the observation that in certain transition metal multilayers, an example being the Fe/Cr system, alternate ferromagnetic layers may be made to align either parallel or anti-parallel depending on the thickness of the intervening layer [4]. Further in the same systems enhanced magnetoresistance effects have also been observed [5]. The period of the oscillations is not easily explained by a simple RKKY type interaction and hence several explanations have been proposed for the phenomena. One model proposes that the oscillations in the coupling reflect size quantization of hole states trapped in the nonmagnetic medium between the layers [6]. An alternative model relies on coupling of states localized in the interface through hybridization with conduction electrons in the intervening layer [7]. Clearly a better knowledge of the spin dependent electronic structure of these materials will be of benefit in any attempt to elucidate the correct mechanism.

Spin polarized photoemission with the capability of identifying two and three dimensional electronic states represents an excellent tool for such studies. The technique is however limited by the mean free path or escape depth of the photoelectrons. This limitation makes it more difficult to study directly the multilayer systems. However the interfaces may be studied by growing them in-situ using molecular beam epitaxial growth methods.

In this paper we describe spin polarized photoemission experiments, which examine the magnetic structure of the clean iron (001) surface and modifications to this structure through the growth of thin film overlayers of silver and chromium. We are able to show that, as predicted, magnetic surface states or
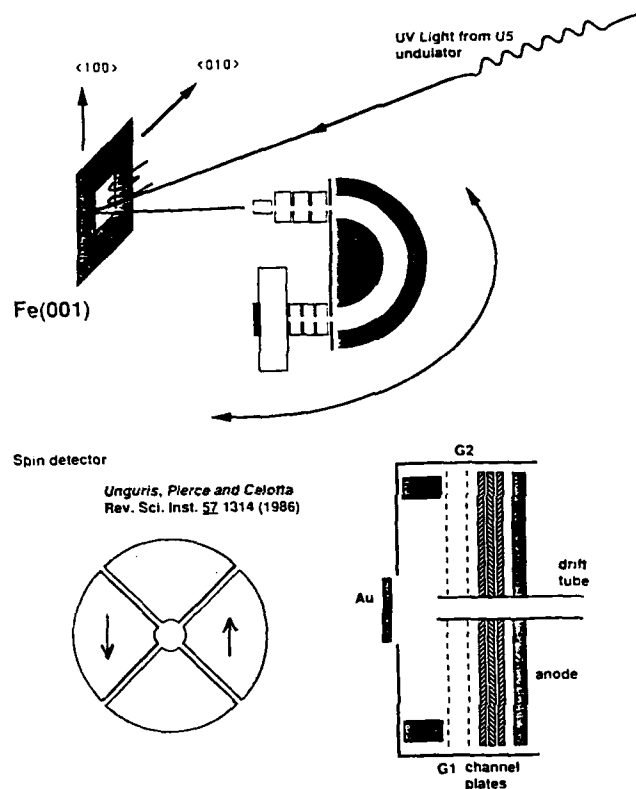
Fig.1 Schematic diagram of the apparatus used for spin polarized photoemission. Upper level: light from the U5 undulator excites photoelectrons which are detected by a hemispherical electron spectrometer. This analyser is coupled via an exit lens to a spin detector. Lower level: arrangement of the spin detector of the type described by Unguris et al. (ref. 9). G1 and G2 represent energy selecting retard grids. Four discrete anodes collect the scattered electrons as indicated at the lower left side.

resonances exist at the iron (001) surface. With the deposition of epitaxial overlayers these states appear to become more localized in the interface region. As the thin film grows the interface states are found to be continuously sensitive to the changing boundary conditions, particularly in the case of the iron-silver interface where each newly deposited silver layer results in a discrete new binding energy for the state. For the chromium-iron interface two new states are observed with one state sitting immediately below the Fermi level. The important conclusion of these studies is that both the electronic and magnetic properties of an interface may be modified by the presence of a nonmagnetic overlayer.

EXPERIMENTAL.

The experiments described in this paper were carried out on a spin polarized photoemission facility [8] established on the U5 UV undulator at the NSLS. Shown schematically fig. 1, a commercial hemispherical electron spectrometer, equipped with a low energy spin detector of the type described by Unguris et al. [9] is mounted on a goniometer allowing the full flexibility of angle resolved measurements. Measurement of a spin dependent asymmetry in the scattering of low energy, 150 eV, electrons from a polycrystalline gold target is used to determine the polarization of the photoemitted electrons. The low efficiency or figure of merit of the spin detector, 10^{-4}, is more than compensated for by the high photon flux available from the undulator. The experimental chamber is also equipped with Low Energy Electron Diffraction (LEED) and Auger Electron Spectroscopy (AES) for surface characterization.

Fcc silver and bcc chromium have a nearly perfect lattice match for growth on a bcc iron (001) substrate, the appropriate interatomic spacings being 2.88, 2.86 and 2.87 Å respectively. The metal overlayers were produced from electron beam evaporators with deposition rates monitored by both AES and by
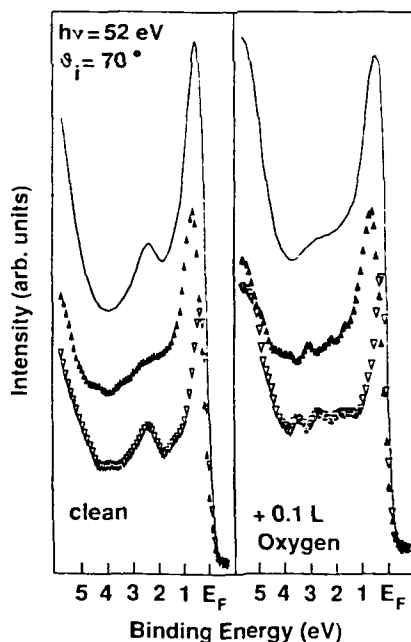
Fig.2. Photoemission spectra recorded for emission along the surface normal from the clean Fe(001) surface and the same surface following exposure to 0.1 L of oxygen. Solid and open triangles indicate the spin resolved majority and minority spin spectra respectively. The incident photon energy was 52 eV with an angle of incidence corresponding to p-polarized light.

evaporating directly into a quadrupole mass spectrometer. Silver films were deposited on an iron (001) substrate at room temperature but in order to study the same interface it was found to be necessary to evaporate iron films on a silver (001) substrate at a lower temperature of approximately 160 K. Chromium films were evaporated on the iron substrate at the slightly elevated temperature of 70 C. Thin iron films were subsequently deposited on these chromium films at room temperature.

RESULTS.

Studies of the clean Fe(001) surface, fig. 2, reveal evidence for a minority spin surface resonance at the center of the zone, approximately 2.7 eV below the Fermi level. As evidenced in fig. 2, the surface designation reflects the sensitivity of the state to adsorption or contamination. Comparison with first principles calculations shows this state to be largely d in character but with some admixture of s and p states [10]. At the center of the zone, where no absolute bandgap exists, the state is essentially a bulk band "resonating" in the surface region. Farther out in the zone, at the $\bar{X}$ point, a band gap exists and it becomes a surface state. Fig. 3 shows charge density plots for the state at the center and edge of the zone [11], clearly demonstrating the difference in localization between the two points. Although predicted theoretically, no majority counterpart for this state is clearly observed. However the calculations suggest that such a state may possibly be dispersed over a larger range of binding energies.

Deposition of silver on this surface quenches the minority surface peak but

$\bar{\Gamma}$ minority
surface resonance

$\bar{X}$ minority
surface state
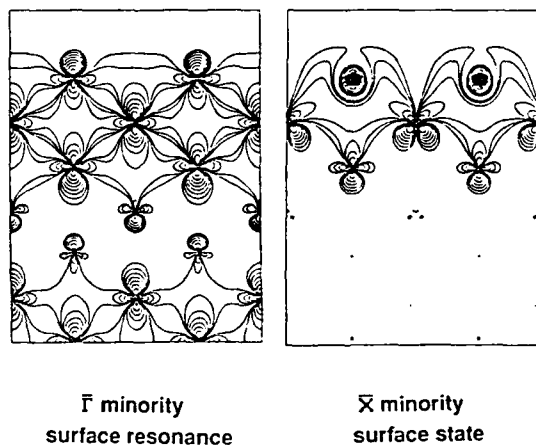
Fig. 3 Calculated charge density plots for the minority surface resonance at the center of the zone and for the same state at the zone boundary where it falls within a bulk band gap. The calculation is for a 13 layer slab with the surface at the top of the figure and the center or bulk at the bottom. The cut is in the (110) plane.
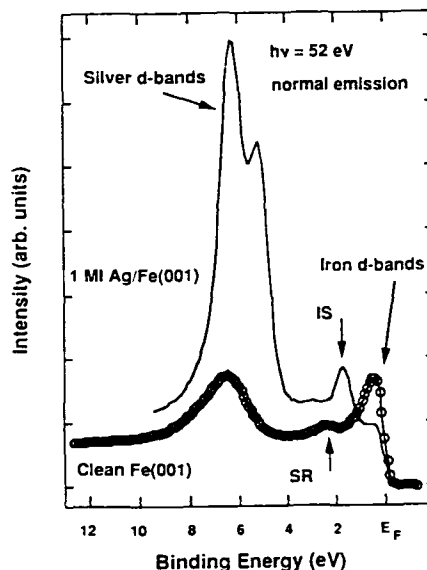
Fig. 4 Photoemission spectrum recorded along the surface normal following the deposition of 1ML of silver on the Fe(001) surface. For comparison the spectrum recorded from the clean surface is also shown. IS indicates the interface state and SR the surface resonance on the clean surface. The two spectra, both recorded with an incident photon energy of 52 eV, are not normalized with respect to each other.

a new feature is observed at a lower binding energy [12]. Shown in fig. 4, the latter peak is observed to undergo a maximum in intensity at a silver coverage corresponding to one monolayer, as calibrated by AES. LEED studies of this overlayer system show a good p(1x1) pattern throughout the initial growth. The new peak observed in the photoemission spectrum, fig. 4, is identified with an interface state predicted in a first principles calculations for this overlayer system [13].

With subsequent growth of the silver thin film, the "interface" state is observed to move towards the Fermi level in a series of discrete steps, fig. 5, each step reflecting the layer by layer growth. Spin polarization analysis indicates that in all cases the interface state is of minority spin character [12] and thus suggests that the state is derived from the minority spin surface state observed on the clean surface. The interface state is also observed when an iron monolayer is deposited on a silver (001) surface [14]. However in that case the state is less well resolved and it is not possible to detect any movement reflecting subsequent layers. The experimentally observed dispersion of the Ag/Fe(001) interface state away from the center of the zone is in reasonable accord with the predictions of the calculation [14].

Shown in figure 6, Chromium overlayers deposited on Fe(001) again result in the formation of an interface state derived from the surface state associated
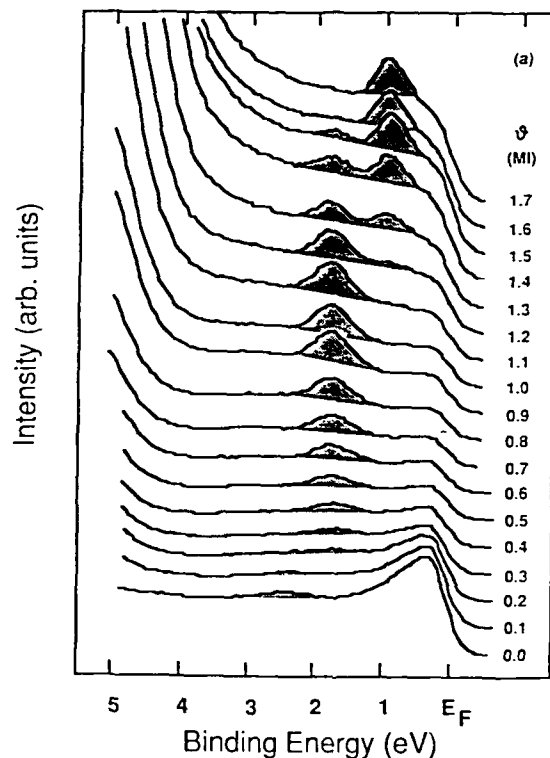
Fig. 5. Photoemission spectra recorded along the surface normal from a series of silver coverages deposited on Fe(001). The different coverages are indicated. The *incident photon energy* energy is 52 eV and the angle of incidence corresponds to p-polarized light.

with the substrate [15]. However unlike the silver overlayers the presence of chromium now causes the surface resonance to move further from the Fermi level rather than towards it with the absolute magnitude of the shift being smaller than that observed for silver. The spin integrated spectra of fig. 6 also show an increase in the intensity of emission immediately below the Fermi level. A spin polarized spectrum, fig. 7, recorded following the deposition of one monolayer of chromium shows the interface state at a binding energy of 2.7 eV to be entirely of minority spin character, identical to the interface states observed for the silver overlayers. The spin resolved spectrum shows that the new intensity appearing below the Fermi level is also of minority character. Both the spectra in fig.6 and the spectrum in fig.7 are recorded with the light at an angle of incidence corresponding to p-polarization. We note that in this photon energy range near the center of the zone a peak below the Fermi level is found in the minority spectrum of clean iron. However in that case, because of the symmetry
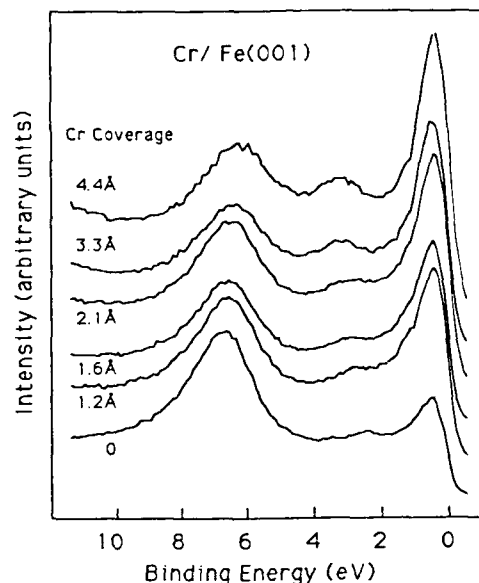
Fig. 6. Spin integrated photoemission spectra recorded from Cr deposited on Fe(001) as a function of Cr coverage. The incident photon energy is 52 eV and the angle of incidence corresponds to p-polarized light.

of the initial state, the intensity is a maximum for s-polarized rather than p-polarized incident light.

With thicknesses of chromium beyond 2.0 Å the spin integrated spectra in fig. 6 show the evolution of the peak at approximately 3.0 eV binding energy into the chromium surface resonance equivalent to that observed on the clean iron surface. Interestingly, a spin polarized photoemission study of this feature [15] shows no particular polarization indicating that if the Cr(001) surface is ferromagnetic as calculated [16], the presence of steps and terraces masks any possible observation [17].

As noted in the introduction, other experiments have previously shown that iron overlayers deposited on the chromium films may show a parallel or antiparallel magnetic alignment with the iron substrate depending on the thickness of the intervening chromium layer [4]. Figure 8 shows spin resolved photoemission spectra recorded from iron films, 3.3 and 3.9 A thick, grown on chromium films 3.2 and 8.2 A thick, respectively. These spectra clearly show the reversal of polarization associated with the antiparallel alignment on the thicker chromium layer. They also provide some indication that the local moment on the iron for the two systems must be similar in that exchange split counterparts are placed at approximately the same binding energies of 0.5 and 2.5 eV.

DISCUSSION.

The sensitivity to the presence of adsorbates of the minority feature observed in the spin resolved spectra, fig.2, and the close agreement to
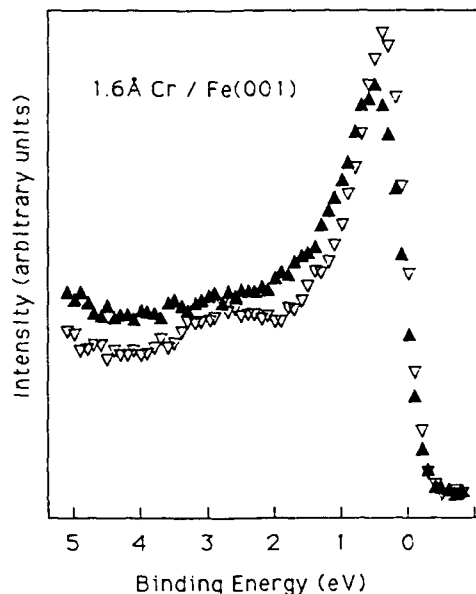
Fig. 7. Spin polarized photoemission spectrum recorded from approximately one monolayer of chromium on Fe(001). The photon energy for this spectrum is 52 eV and the angle of incidence corresponds to p-polarized light.

calculation supports its identification as a surface state. As noted above, the state is a resonance rather than a pure surface state. Such a state is also predicted in a simple tight binding calculation using a nonorthogonal basis set [12]. The latter calculation is a layered scheme with parameters taken from the tabulations, fitted to bulk calculations, provided by Papaconstantopoulos [18]. The modelling was extended to thin overlayers by scaling the respective parameter sets according to the scheme of Andersen [19]. Using such a method a calculation for a silver monolayer on iron (001) found an interface state in close agreement with both experiment and first principles calculation.

The tight binding simulation suggests that with the formation of the interface, a state is formed with 70% of its weight on the surface iron atoms and 30% on the silver monolayer. On the silver side the state has approximately 50% d character, the rest being s and p character. At the same time the modelling indicates that with the formation of the interface, the state becomes more localized within the surface layers of the iron substrate. Thus the decay of the resonant state back into the bulk of the material is reduced. A similar phenomena was previously observed in an inverse photoemission study of an unoccupied interface state in the Nb(110)/palladium interface [20]. In that study it was also shown theoretically that the presence of the palladium tended to localize a niobium surface resonance into the interface region.

Simulations of the chromium monolayer find that, as in the case of silver, the clean iron surface resonance is both localized and shifted by the presence of the overlayer. In agreement with the experiment the interface state is now at a higher rather than lower binding energy. The calculation now finds that the chromium component of the interface state is nearly 80% d in character. This
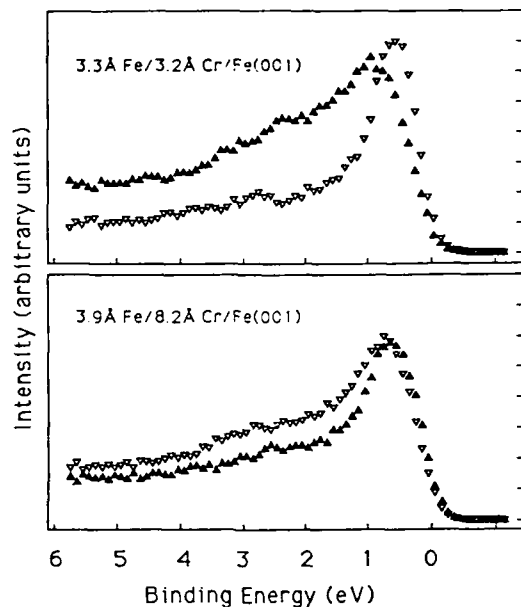
Fig. 8. Spin polarized photoemission spectra recorded from thin iron films of thickness approximately 3.5 Å grown on different thicknesses of chromium. As in previous spectra the photon energy is 60 eV and the angle of incidence corresponds to p-polarized light. The different thicknesses of chromium are indicated in the two panels.

increase in the d component probably reflects the fact, unlike silver, the chromium has unfilled d bands. At the same time the modelling also finds another interface state pulled down below the Fermi level. Unlike the higher binding energy interface state, which is d_{z^2} in character this second state has d_{xz} character. It is derived from an unoccupied surface state sitting immediately above the Fermi level on the clean iron surface.

To summarize, for both the silver and chromium films the presence of the overlayer appears to localize states within the interface, at least in terms of the decay length into the substrate. These magnetic states, having a well defined spin character, also have weight on the overlayer sites. However it is difficult on the basis of the present experiments to make any quantitative statements regarding the possible existence or size of magnetic moments on the overlayer atoms. In the case of silver, the interface states show well defined binding energies reflecting the thickness of the overlayer film. Thus the presence of the overlayer modifies both the electronic and magnetic properties of the interface. Any modelling that reflects the electronic structure of the interface should allow for the possibility of such changes. One further consideration is the probability of a distinct face dependence for the surface states and surface resonances from which the interface states are derived.

58

ACKNOWLEDGEMENTS.

REFERENCES.

1. A.J. Freeman, C.L. Fu, S. Ohnishi and M. Weinert, Chapter 1 in "Polarized Electrons in Surface Physics", Ed. by R. Feder, (World Scientific, Singapore 1985).
2. "Magnetism in Ultrathin Films", Special Issue of Appl. Phys. A49, Ed. D. Pescia (1989).
3. L.M. Falicov, D.T. Pierce, S.D. Bader, R. Gronsky, K.B. Hathaway, H.J. Hopster, D.N. Lambeth, S.S.P. Parkin, G. Prinz, M. Salamon, I.K. Schuller and R.H. Victora, J. Mater. Res. 5, 1299 (1990).
4. P. Grunberg, R. Schreiber, Y. Pang, M.B. Brodsky, and H. Sowers, Phys. Rev. Lett. 57,2442 (1986).
5. M.N. Baibich, J.M. Broto, A. Fert, F. Nguyen Van Dau, F. Petroff, P. Etienne, G. Creuzet, A. Friederich, and J. Chazelas,Phys. Rev. Lett. 61,2472 (1986).
6. D.M. Edwards and J. Mathon, to be published.
7. Y. Wang, P.M. Levy and J.L. Fry, Phys. Rev. Lett. 65,2732 (1990).
8. P.D. Johnson, S.L. Hulbert, R. Klaffky, N.B. Brookes, A. Clarke, B. Sinkovic, N.V. Smith, M.J. Kelly, D.T. Pierce· R. Celotta and M.R. Howells, to be published.
9. J. Unguris, D.T. Pierce and R.J. Celotta, Rev. Sci. Inst. 57, 1314 (1986)
10. N. Brookes, A. Clarke, P.D. Johnson and M. Weinert, Phys. Rev. B 41, 2643 (1990).
11. M. Weinert, private communication.
12. N. Brookes, Y. Cnang and P.D. Johnson, submitted to Phys. Rev. Lett.
13. S. Ohnishi, M. Weinert and A.J. Freeman, Phys. Rev B 30, 36 (1984).
14. N. Brookes, Y. Chang, P.D. Johnson and M. Weinert, to be published.
15. Y. Chang, N. Brookes and P.D. Johnson, to be published.
16. e.g. P.H. Victora and L.M. Falicov, Phys. Rev B 31, 7335 (1985).
17. S. Blugel, D. Pescia and P.H. Dederichs, Phys. Rev B 39, 1392 (1989); R. Wiesendanger, H.-J. Guntherodt, G. Guntherodt, R.J. Gambino and R. Ruf, Phys. Rev. Lett. 65,247 (1990).
18. D.A. Papaconstantopoulos, "Handbook of the Band Structure of Elemental Solids",(Plenum Press 1986).
19. O.K. Andersen and O. Jepsen, Physica B 91, 317 (1977).
20. X. Pan, P.D. Johnson, M.Wenert, R.E. Watson, J.W. Davenport, G. W. Fernando and S.L. Hulbert, Phys. Rev. B 38, 7850 (1988).

SPIN POLARIZED PHOTOEMISSION FROM FE ON CU(100)

D.P. PAPPAS*,K.-P. KÄMPER**, B.P. MILLER**, H. HOPSTER**
D.E. FOWLER*, A.C. LUNTZ*, C.R. BRUNDLE*
Z.-X. SHEN***
    *IBM Research Division, Almaden Research Center, 650 Harry Road, San Jose, CA 95120-6099
    **Dept. of Physics, University of California, Irvine, CA 92717
    ***Stanford Electronics Laboratory, Stanford, CA, 94305

ASTRACT

The spin resolved electronic structure of ultra-thin Fe films on Cu(100) was investigated using spin polarized angle resolved photoemission spectroscopy. An exchange splitting of the Fe Δ_5 band of 2.5 eV is observed for photon energies between 20 and 30 eV. A peak at 6 eV binding energy which has been previously identified as a many-electron resonance was observed only after contamination of the films with oxygen. In addition, the spin dependent attenuation lengths for electrons in Fe were measured at 11, 19, and 40 eV above E_f. The attenuation length for the minority spin electrons was found to be shorter than that of the majority spin electrons. The difference between the two attenuation lengths was shown to increase at low energy. Short attenuation lengths of ≈ 3 monolayer were measured at 11 eV. The large increase of the attenuation length at low energy which is expected from the "universal curve" is not observed in Fe.

INTRODUCTION

The addition of spin analysis to electron spectroscopy allows for the separation of the majority and minority spin contributions in spectra from ferromagnetic samples. This provides information about the spin resolved electronic structure of materials as well as the spin dependence of electron scattering in the material. Recent studies using spin polarized versions of secondary electron emission spectroscopy (SPSEES) [1], and angle resolved photoemission spectroscopy (SPARPES) [2] indicate that the information depth (i.e. the depth in the sample from which most of the detected electrons originate) at low energies is quite small in the 3-d transition metals, on the order of a few ML. The short information depth makes spin polarized electron spectroscopy a sensitive technique for investigating ultra-thin ferromagnetic overlayers such as Fe, Ni, and Co on a wide variety of substrates.

In particular, the system Fe on Cu(100) is interesting because the fcc phase of Fe, which is the equilibrium structure of Fe between 1184 K and 1665 K, can be stabilized at low temperature on Cu(100). This is based on detailed LEED I-V curve analysis [3] and the close match of lattice constants between fcc-Fe and Cu (3.65 vs. 3.61 Å). Theoretical band structure calculations for fcc-Fe show that it may occur in three magnetic states, either anti-ferromagnetic (AFM), FM with high moment ($\approx 2.2\mu_B$), or FM with a low moment ($\approx 1.5\mu_B$) [4, 5]. The use of spin polarization analysis in photoemission is needed in order to identify the spin character of the observed energy bands of the Fe films. A direct comparison between experiment and theory can then be made.

The information depth plays a important role in all electron spectroscopies. It can be characterized by an energy dependent attenuation length (λ) of so called "hot" electrons, i.e. electrons with $E > E_f$. λ is typically measured by the overlayer method, whereby the intensity of a source of electrons of fixed energy, e.g. an Auger transition or photoemission peak from the substrate, is monitored for different thicknesses and fit to an exponential decay. Using SPARPES, the spin resolved λ's can be found by measuring the polarization of an initially unpolarized beam after it has traversed a ferromagnetic film, giving

$$I_{\uparrow,\downarrow} = \frac{I_0}{2} \exp(\frac{-d}{\lambda_{\uparrow,\downarrow}}),$$ [1]

where the ↑ and ↓ refer to electron moment parallel and anti-parallel with the magnetization, respectively. Considerable work has been done to determine the energy and material dependence of λ. The energy dependence of λ is often displayed as a "universal curve" [6], which indicates that there should be a large increase in λ at low electron energy for all materials. This behavior is not well established experimentally, and our results indicate that the increase at low energy is not universal with respect to attenuation in Fe. The material dependence of λ should be strongest in the low energy regime ($E < 50$ eV), where, e.g., the hot electrons begin to interact strongly with the bandstructure of the solid [7]. The additional electron spin polarization information obtained from SPARPES allows one to identify the type of scattering which is dominant at different energies, i.e. spin dependent vs. spin independent scattering. For example, inelastic scattering in Fe due to the creation of electron-hole pairs (Stoner excitations), would be strongly spin dependent, while a spin independent inelastic processes would be, e.g., phonon scattering.

In the absence of elastic scattering, λ and the inelastic mean free path (IMFP) would be identical [8]. However, it has been estimated that elastic scattering causes about a 30% discrepancy between λ and the IMFP for the 68 eV Auger electrons in aluminum [9]. Elastic scattering effects may occur at low energies in Fe as well [10]. For example, SPLEED from bcc-Fe [11] shows a 1 eV wide, 20% reflection peak centered at 6 eV scattering energy. Elastic scattering can also be strongly spin dependent [12, 13]. The measured spin averaged and spin resolved λ's are therefore a combination of the elastic mean free paths (EMFP's) and the IMFP's.

APPARATUS AND SAMPLE PREPARATION

The experiments were conducted in a UHV chamber which was equipped with LEED and Auger electron spectroscopies for sample characterization. The SPARPES apparatus consists of a 90° spherical energy analyzer and a medium energy retarding potential Mott analyzer. The electron optics were built so that the photoemitted electrons could be directed either into the Mott analyzer where the perpendicular and one of the in-plane components of polarization were measured, or directly into an electron multiplier to avoid the low efficiency of spin analysis. Specta could then be obtained either in a low resolution ($\Delta E \approx 1 eV$) spin resolved mode or a high resolution ($\Delta E \approx 0.1 eV$) spin integrated mode, respectively. Photoemission was conducted both with a resonance lamp and synchrotron radiation from a toroidal grating monochromator beamline at Stanford Synchrotron Radiation Laboratory. All photoemission electron spectra were taken in normal emission, with the radiation incident at 45° off normal. The incident light had both s- and p-character.

Ultra-thin Fe films were deposited by sublimation from a chunk of 99.999% pure Fe heated by electron bombardment. The only contamination apparent in the Auger spectra was oxygen, of ≈1% equivalent ML coverage. The films were evaporated at low substrate temperature to avoid intermixing and were then annealed to 300 K to improve the structural quality [14]. The LEED patterns show strong wings on the (10) and (11) spots, with intensity maxima near the 4th or 5th order position. The Fe-layer thicknesses were determined by calibrating the Auger Fe and Cu peak-peak intensities against a quartz crystal microbalance. The geometry factor between the thickness monitor and sample deposition rates was determined by substituting a glass slide for the sample, growing a thick (1000 Å) film, and measuring its thickness with optical interferometry. The magnetic properties of this system have been studied previously [15, 16]. The remanent magnetization of the films was checked by measuring the spin polarization of the secondary electrons. The films were ferromagnetic with remanence perpendicular to the plane of the film for thickness d < 6.5 ML, and in-plane for d > 6.5 ML.

RESULTS

Photoemission results taken without spin analysis from thick Fe films (d≈30 ML) are presented in Fig. 1. These films are thick enough that there is negligible contribution to the spectra from the Cu 3d peak. For photon energy hν = 20-30 eV, there are three distinct features within 5 eV of E_f. Comparing the peak positions from Fig. 1 to calculated spin resolved fcc-Fe bandstructures in Ref. [4, 5], the peak at 3 eV can be attributed to the Fe Δ_5 state. A slight dispersion of about 0.5 eV toward E_f is observed between hν = 30 and 22 eV, which is also in accord with the calculations. The SREDC's in Fig. 2 confirm the majority spin character of the 3 eV peak. The two peaks close to E_f, one at or just below E_f and one at 1 eV below, can be definitively identified as minority and majority spin states, respectively. Considering the selection rules for normal emission in photoemission [17] and the calculated fcc-Fe bandstructures, the minority and majority spin states are identified as Δ_5 and Δ_1 states. It is stressed here that the spin resolved EDC's are essential for unambiguously determining the spin character of these peaks.

30 ML Fe on Cu(100)
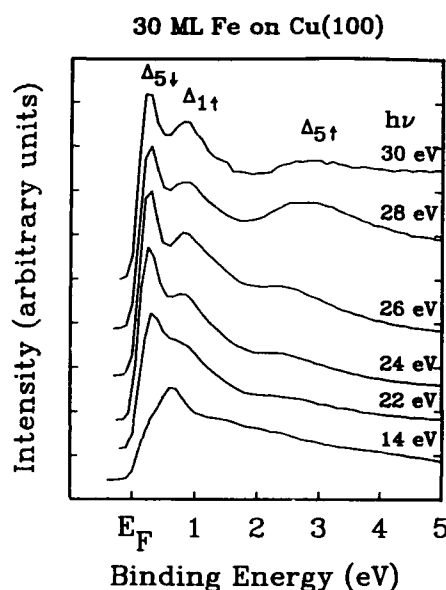
FIG. 1. Photoemission intensity versus binding energy for a thick (≈30 ML) Fe/Cu(100) film.

From the identification of the $\Delta_{5\uparrow}$ and $\Delta_{5\downarrow}$ peaks, we derive an exchange splitting of ~2.5 eV. This is comparable to the splitting seen in bcc-Fe, which has a moment of 2.1 μ_B. We conclude that the thin films of Fe are in a high moment state. This is corroborated by the spin resolved bandstructure calculations in Ref. [4] where the splitting near the Γ point for low- and high-moment fcc-Fe goes from 1.6 to 2.5 eV. We note here that the complex LEED pattern for these Fe films may indicate a distortion or reconstruction of the lattice, either of which could influence the electronic structure of the films in relation to the calculated bandstructures.

A dramatic loss of intensity in the $\Delta_{5\downarrow}$ peak is observed between hν = 22 and 14 eV, which is consistent with the energy band crossing E_f. The analogous band crossing observed in bcc-Fe occurs between hν = 33 and 35 eV [18]. For transitions into a free electron-like final state in the second Brillioun Zone, this indicates that the Δ_5 band must cross E_f more than halfway across the first BZ. The calculated fcc-Fe bandstructures, on the other hand, show the Δ_5 state crossing

FIG. 2. The spin resolved intensity energy distribution curves (SREDC's) from a thick (≈30 ML) Fe/Cu(100) film.

E_f much closer to the zone center. Considering the small dispersion of these bands, it is clear that a slight shift of the calculated fcc-Fe d-bands towards higher binding energy would drastically change the position of the Fermi energy crossing in k-space.

In addition, we find no evidence of the extra peak at 6 eV (which was reported in Ref. [19]) in spectra taken from clean Fe/Cu(100) films. However, a similar peak was observed if the films were grown with an oxygen partial pressure of 4×10^{-10} Torr. Subsequent exposure to .05 L O_2 substantially increased the size of the peak. We therefore conclude that the 6 eV feature observed in Ref. [19] is most likely due to oxygen contamination.
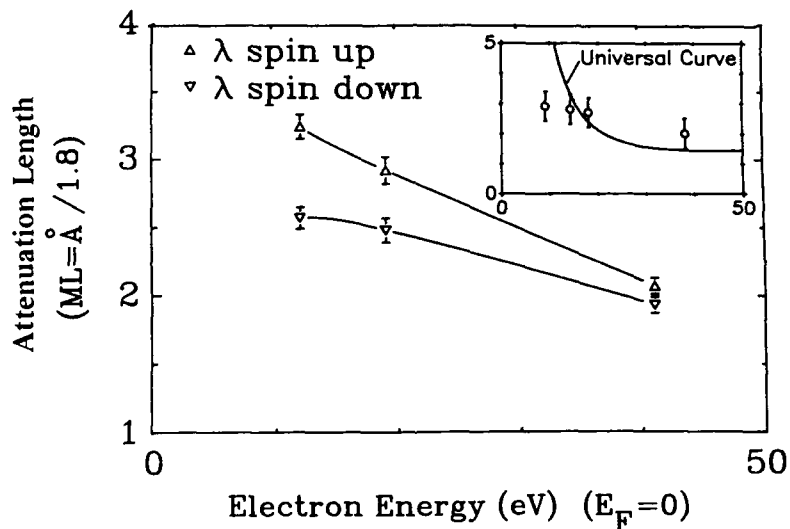
FIG. 3. Spin dependent λ's determined from the spin polarized photoemission spectra. The inset shows the measured spin averaged λ compared to the universal curve.

The second main focus of this work was the measurement of the attenuation lengths of low energy electrons in the Fe films. If $\lambda_\uparrow$ and $\lambda_\downarrow$ are not too different (as it turns out), the double exponential decay is experimentally indistinguishable from a single exponential decay with $\lambda_{av} = \frac{1}{2}(\lambda_\uparrow + \lambda_\downarrow)$. The λ's shown in the inset of Fig. 3 were obtained by measuring the Cu 3d intensities in the photoemission spectra without spin analysis after successive Fe evaporations. For comparison, the "universal curve" from Ref. [6] is also plotted. While there is good agreement at the higher energies, the large increase at low energy in Ref. [6], which is based mainly on data taken from Au, Ag, and Al (all of which have a low density of states near E_f), is not observed in Fe.

Spin resolved photoemission results are shown in Fig. 4 for hv = 14, 22, and 44 eV along with a reference spectrum from the bare Cu at each energy. The Cu photoemission features are clearly identifiable in the Fe/Cu spectra and show the well known dispersion of the Cu bands. The polarization of the Cu 3d electrons (after subtracting the Fe background) can be related to the exponential attenuation by

$$P(Cu) = \frac{I_\uparrow - I_\downarrow}{I_\uparrow + I_\downarrow} \simeq \frac{1}{2} \frac{e^{-d/\lambda_\uparrow} - e^{-d/\lambda_\downarrow}}{e^{-d/\lambda_{av}}} . \qquad [2]$$

The following net Cu polarizations are obtained as an average over several films of thicknesses around 4 ML:20% at 14 eV, 12% at 22 eV, and 5% at 44 eV photon energy. These polarization values can be converted into spin dependent attenuation lengths by combining Eq. 2 and the following approximation for the total Cu 3d intensity,

$$I_{Cu} = \frac{I_0}{2} (e^{-d/\lambda_\uparrow} + e^{-d/\lambda_\downarrow}) \simeq I_0 e^{-d/\lambda_{ave}}. \quad [3]$$

to give

$$\frac{1}{\lambda_{\uparrow,\downarrow}} = \frac{1}{\lambda_{ave}} - \frac{\ln(1 \pm P)}{d}. \quad [4]$$

The values thus obtained for the $\lambda_{\uparrow,\downarrow}$ are shown in Fig. 3 for the three energies used. The spin resolved data show that the λ of minority spin electrons remains nearly constant down to low energies, while there is a slight increase in the λ of the majority electrons. Also, $\lambda_\uparrow > \lambda_\downarrow$, as expected from SPEELS data from bcc-Fe surfaces [20], where strong evidence for electron-hole pair creation (i.e. Stoner excitations) is seen in the energy loss spectrum. This will tend to filter out the minority spin electrons at low energies, since there is a higher number of empty minority states near E_f to scatter into than empty majority states. Short attenuation lengths due to inelastic exchange scattering of low energy electrons in the transition metals Ni, Gd, and Ce (which all have a high DOS near

FIG. 4. The SREDC's from Fe films on Cu(100) at three different photon energies. Also shown for comparison are the intensity spectra of the clean Cu surface (not to scale).

E_f, in contrast with Al, Au, and Ag), has also been reported in Ref. [21]. We therefore believe that this scattering mechanism is important, if not dominant, at very low energy in the transition metals and accounts for the observed short attenuation lengths.

SUMMARY

This study has focused on two main points, the spin resolved electronic structure of Fe films grown on Cu(100) and the spin dependent attenuation lengths of low energy electrons in Fe.

We have shown that observed structure in SPARPES agrees reasonably well with ab-initio electronic structure calculations for the high moment state of fcc-Fe [4, 5] We have measured the apparent exchange splitting in the thick Fe films, and find that $\Delta E \simeq 2.5$ eV. This is taken to prove that the Fe exists in a high moment state. The photoemitted feature related to the Δ_1 band crosses E_f at an incident photon energy which is $\simeq 15$ eV lower than for bcc-Fe. The effect of oxygen contamination was found to result in a prominent peak at about 6 eV binding energy.

Secondly, we have shown that in Fe, λ does not increase substantially for electron energies going down from 40 to 9 eV. Conversely, the difference between the majority and minority electron attenuation increases with decreasing energy, with $\lambda_\uparrow > \lambda_\downarrow$. This can be explained by noting that the cross-section for electron-hole pair excitations increases at low energy.

REFERENCES

1 D.L. Abraham and H. Hopster, Phys. Rev. Lett. **58**, 1352 (1987).
2 D.P. Pappas, K.-P. Kämper, B.P. Miller, H. Hopster,, D.F. Fowler, C.R. Brundle, A.C. Luntz, and Z.-X. Shen, Phys. Rev. Lett. **66**, 504 (1991).
3 S.H. Lu, J. Quinn, D. Tian and F. Jona, Surf. Sci. **209**, 364 (1989).
4 D. Bagayoko and J. Callaway, Phys. Rev. B **28**, 5419 (1983).
5 V.L. Morruzzi, private communication.
6 M.P. Seah and W.A. Dench, Surf. and Interf. Analy. **1**, 2 (1979).
7 D.R. Penn and S.M. Girvin, Phys. Rev. Lett. **55**, 518 (1985).
8 A. Powell, Jour. Elec. Spec. and Relat. Phen. **47**, 197 (1988).
9 A. Jablonski., Surf. Sci. **188**, 164 (1987).
10 M. Gokhale and D.L. Mills, to be published.
11 D. Tillmann, R. Thiel and E. Kisker, Z. Phys. B **77**, 1 (1989).
12 H. Hopster, D.L. Abraham and D.P. Pappas, J. Appl. Phys. **64**, 5927 (1988).
13 D.A. Steigerwald, I. Jacob and W.F. Egelhoff, Jr., Surf. Sci. **202**, 472 (1988).
14 C. Liu, J.F. Cochran and S.D. Bader, Phys. Rev. Lett. **60**, 2422 (1988).
15 D.P. Pappas, K.-P. Kämper, H. Hopster,, Phys. Rev. Lett. **64**, 3179 (1990).
16 J. Hermanson, Solid State Commun. **22**, 9 (1977).
17 E. Kisker, K. Schröder, W. Gudat and M. Campagna, Phys. Rev. B **31**, 329 (1985).
18 A. Amiri Hezaveh, G. Jennings, D. Pescia, and R. F. Willis, K. Prince, M. Surman, and A. Bradshaw, Solid State Comm. **57**, 329 (1986).
19 J. Kirschner, Phys. Rev. Lett. **55**, 973 (1985).
20 F. Meier, G.L. Bona and S. Hüfner, Phys. Rev. Lett. **52**, 1152 (1984).

THEORETICAL STUDIES OF SPIN DEPENDENT SCATTERINGS OF ELECTRONS FROM FERROMAGNETIC SURFACES AND ULTRA THIN FILMS

A. ORMECI, M. P. GOKHALE, BURL M. HALL AND D. L. MILLS
Department of Physics, University of California, Irvine, CA 92717

ABSTRACT

We summarize results of our recent theoretical studies of spin dependent scattering of electrons from ferromagnetic surfaces. We obtain an excellent account of both the energy and angle variation of the exchange asymmetry reported by Waller and Gradmann in their SPLEED study of the Fe(110) surface, and of spin dependent asymmetries in the transmission of photoelectrons through an ultra thin film of Fe on Cu(100). Potentials supplied by Fu and Freeman enable us to account for the data, with use of ground state potentials generated by *ab initio* methods.

I. Introduction

Much of our information on microscopic aspects of the magnetism at surfaces and in ultra thin films is generated through various spin polarized electron spectroscopies. Quantitative interpretation of the data generated by these methods requires the development of theories sufficiently complete that the unknown parameters relate only to the structure or the nature of the magnetism in the samples of interest, i.e., the calculations should be based on parameter free ionic potentials, etc. In this paper, we summarize recent calculations that meet these constraints, and which provide a fully quantitative account of existing data. We discuss also the implications of our results.

Our calculations are based on the muffin tin approach, and the relativistic multiple scattering methods developed in the pioneering work of Feder.[1] Within each muffin tin, we imbed spherically symmetric potentials which describe moment bearing Fe atoms; the potentials thus have the form $V(r)I + B(r)\sigma_z$, with $V(r)$ and $B(r)$ both spherically symmetric. Both $V(r)$ and $B(r)$ are the spherically symmetric pieces of the ground state potentials generated by Fu and Freeman [2], in their *ab initio*, fully self consistent study of Fe surfaces. Our only adjustment is our method of simulating enhanced moments near the surface. We do this by replacing, in layer ℓ, $B(r)$ by $(\mu_\ell / \mu_\infty)B(r)$, with μ_∞ the bulk Fe moment, and μ_ℓ that in layer ℓ. Calculations using full layer dependent, non-spherical potentials are underway, and will be reported elsewhere. We take the complex inner potential to be spin independent, and modeled in the manner now standard in the literature on low energy electron diffraction.

II.   Exchange Asymmetries in Spin Polarized Low Energy Diffraction (SPLEED): The
      Case of Fe(110)

A quantity of central interest in SPLEED measurements is the exchange asymmetry A_{ex},
which provides a direct measure of the exchange coupling of the beam electron to the moments in
the surface layers of the substrate. With reliable potentials in hand, one can hope to extract
information on the magnitude of the surface moment from such data.

In the experiment, a spin polarized electron beam strikes the surface, and the total
scattered current is measured in the specular direction, or a Bragg direction. (Here we discuss
only data on the specular beam; for Fe(110) comparison between theory and experiment for the
$(1\bar{1})$ beam is given elsewhere. [3]) Let $I(\sigma\mu)$ be the intensity when the beam polarization is
parallel $(\sigma=\uparrow)$ or antiparallel $(\sigma=\downarrow)$ to $\hat{y}$, and $\mu=\uparrow,\downarrow$ denotes whether the substrate moment
is parallel or antiparallel to $\hat{y}$. The scattering plane is the xz plane. Then we have[1]

$$A_{ex} = \left(I(\uparrow\uparrow)+I(\downarrow\downarrow)-I(\uparrow\downarrow)-I(\downarrow\uparrow)\right) \Big/ \left(I(\uparrow\uparrow)+I(\downarrow\downarrow)+\cdots I(\downarrow\uparrow)\right).$$

Gradmann and Waller [4] have reported a most remarkable and complete study
of A_{ex}, for the Fe(110) surface. They measure the variation of A_{ex} with angle of incidence θ
(measured with respect to the surface normal), for many beam energies between 50eV and
130eV. In what follows, we compare our theoretical calculations with their data.

In Fig. (1), we reproduce from ref. [3] a comparison between theory and experiment
for A_{ex} for the beam energy of 62eV. The data are the squares, and the solid line the theory
based on the picture of enhanced moments in the surface (19.4% in the outer layer, 6.8% in the
second, 2.7% in the third and 1.4% in the fourth) put forward by Fu and Freeman.
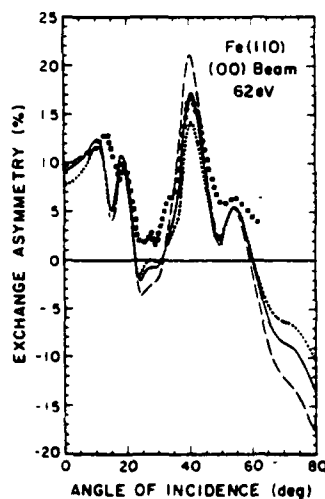
Fig. (1): Comparison between the data of
Waller and Gradmann (squares) and the theory for A_{ex}
at 62eV, using the Fu-Freeman model of enhanced
surface moments (solid line). The dotted curves are
calculations of A_{ex} assuming no enhanced moment in
the surface, and the dashed curve comparison between
the model proposed by Tamura et al. (ref. 5), where
the surface moment is enhanced by 40% over the bulk.
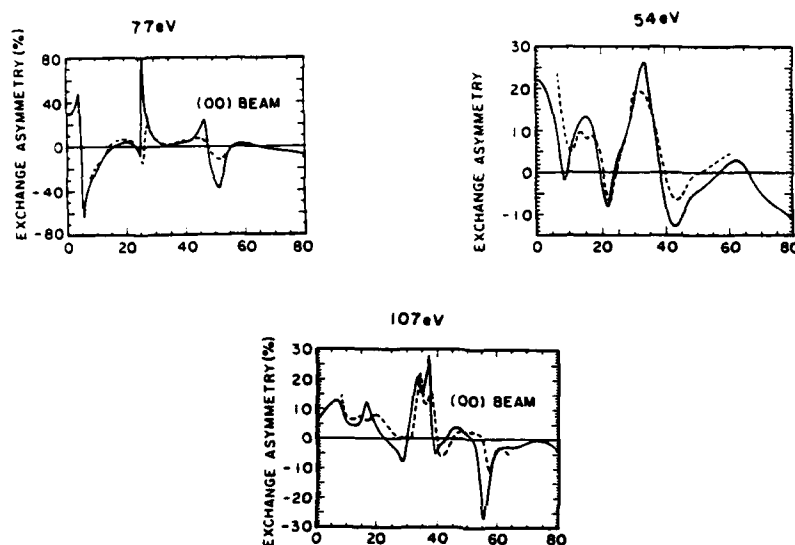
Fig. (2): Comparison between the calculated exchange asymmetry for the specular beam (solid line) for the model put forward by Fu and Freeman, and the data of Waller and Gradmann (dashed line).

In Fig. (2), at three additional energies, we show comparison between theory and experiment for the angular variation of A_{ex}.

In our view, agreement between theory and experiment is excellent, at all energies. We have by now surveyed virtually the entire data set in the extensive measurements of Waller and Gradmann, to find comparable agreement at all energies. The reader must keep in mind that we have here an absolute comparison between theory and experiment; we have adjusted no feature in the potential, nor adjusted the scale factor in the data to bring the two close at some particular energy or angle, as is done commonly in LEED analyses where the experimentalist cannot supply accurate absolute scattering intensities. Since A_{ex} is an intensity ratio, the experimenter needs relative and not absolute intensities to determine A_{ex}.

The next question is whether we can use data on A_{ex} to inquire into the possible presence of enhanced surface moments. Fig. (1) is encouraging; the dotted curve describes A_{ex} for the case where no enhanced moments are present, and the dashed curve our prediction for a model put forward in ref. [5] (40% enhancement of surface moment). The solid line (Fu and Freeman picture) would seem preferred.

We do not show several models in Fig. (2) because at these energies, there is a more modest dependence of A_{ex} on surface moment profile; we can draw no confident conclusions

from these data. We are then led to inquire if one can locate additional beam energies where A_{ex} exhibits substantial sensitivity.

This issue has led us to develop a method we call the ΔT expansion [6], in which the spin dependent piece of the electron-surface scattering is expanded in powers of $\Delta\mu_\ell = \mu_\ell - \mu_\infty$, the difference between the moment in layer ℓ and that in the bulk. With this method, and a criterion we have developed to locate regimes of energy and angle where sensitivity to surface moment is high, we can scan a large region of the relevant parameter space very quickly. In the energy regime explored by Waller and Gradmann (50–130eV beam energy), we find only one other "window" (~52eV) where sensitivity to surface moment is comparable to that at 62eV. The account of the data provided by the model of ref. [5] would seem a bit better than that of Fu and Freeman, though the differences are not large.

Thus, while our analysis leads us to conclude there are indeed enhanced moments in the Fe(110) surface, it is difficult for us to differentiate conclusively between the two pictures that have been discussed.

It is the case that we obtain an excellent account of the data with ground state potentials generated from *ab initio* methods adjusted only to simulate enhanced surface moments. We believe such calculations, particularly in combination with the ΔT expansion can guide future experiments, so focus can be placed in those energies and angles where one realizes particular sensitivity to surface moment. We understand that greater precision in the measurement of A_{ex} can now be realized [7]; uncertainties the order of 20% are sufficient to obscure differences between different models of surface magnetic moment profiles.

It is our hope that these remarks will stimulate new experimental studies.

III.   Spin Dependent Electron Transmission through Ultra Thin Ferromagnetic Films:
        Evidence for Spin Dependent Electron Mean Free Paths?

The calculations above employ a spin independent complex inner potential, and assume the potential imbedded within the muffin tins is real. The analysis thus presumes the inelastic contributions to the electron mean free path to be spin independent. While this allows us to carry out calculations with no adjustable parameters, this picture can be questioned. In ref. [5], for example, within each muffin tin, the authors imbed a spatially varying complex and energy dependent supplement to their ground state potential. This is described by a phenomological form designed to account for spin dependent transitions of intra atomic character, induced by the beam electron.

Pappas and collaborators [8] have reported an elegant photoemission study which bears on this issue directly. Their sample is four monolayers of Fe, deposited on Cu(100). Electrons are excited from the Cu 3d bands, and the authors measure the dependence of the intensity on the spin orientation of the photoemitted electron, to find electrons with spin antiparallel to the Fe magnetization are transmitted with less intensity than those with spin parallel to the Fe magnetization. They argue the mean free path of the minority spin photoelectrons is shorter than that of those polarized in the majority spin direction, a very reasonable conclusion consistent with

qualitative arguments advanced elsewhere [1]. From the data, at three energies in the range 10–40eV above they extract the spin and energy variation of the apparent electron mean free path from the spin asymmetry in the transmissivity.

We have interpreted the data within a different framework. Even in the absence of electron attenuation, the transmissivity of the Fe film will be spin dependent, because of spin dependence in the elastic scattering produced by the exchange coupling between the photoelectron spin, and that of the Fe spins. We have used the model of section II to calculate the transmissivity, to find very good agreement with both the magnitude and energy variation reported in ref. [8], in our picture where the inner potential is assumed spin independent, and no additional spin dependent loss mechanisms are introduced. The details are described elsewhere [9].

When the results of this study are set alongside those summarized in section II of the present paper, we conclude that at least for Fe, an excellent account of the spin dependence of low energy electron scattering from the surface follows from the use of high quality ground state potentials, in combination with standard complex inner potentials such as those employed commonly in conventional LEED and photoemission studies. We thus have a basis for the fully quantitative analysis of data generated by spin dependent electron spectroscopies, where the uncertainties reside in the aspects of greatest interest, the magnetic properties of only the outermost atomic layers.

References

1.   R. Feder, Chapter 4 in Polarized Electrons in Surface Physics, edited by R. Feder (World Scientific, Singapore, 1985)
2.   C. L. Fu and A. J. Freeman, J. Magn. Mater. 69, L1 (1987). Each Fe atom is represented by the potential in the mid plane of their model slab, with the effect of surface moments simulated as described in the text.
3.   Alim Ormeci, Burl M. Hall and D. L. Mills, Phys. Rev. B42, 4524 (1990).
4.   G. Waller and U. Gradmann, Phys. Rev. B26, 6330 (1982); G. Waller, Ph.D. Thesis, Universität Clausthal, 1986 (unpublished).
5.   E. Tamura, R. Feder, G. Waller and U. Gradmann, Physics Status Solidi (b) 157, 627 (1990).
6.   Alim Ormeci, Burl M. Hall and D. L. Mills, Phys. Rev. B (to be published).
7.   H. Hopster, private communication.
8.   D. Pappas et al., Phys. Rev. Letters 66, 504 (1991).
9.   M. Gokhale and D. L. Mills, Phys. Rev. Letters (to be published).

SPIN-POLARIZED EELS ON ULTRATHIN FCC CO LAYERS ON CU(100)

K.-P. KAMPER*, D.L. ABRAHAM**, AND H. HOPSTER
Department of Physics and Institute for Surface and Interface Science,
University of California, Irvine, CA 92717

ABSTRACT

The magnetism and the electronic structure of fcc Co films epitaxially
grown on Cu(100) was investigated by spin polarized electron energy loss
spectroscopy. Films above 2 atomic layers thickness show ferromagnetic
order above room temperature with the magnetization in the plane. An
exchange splitting of 0.8 eV and a Stoner gap of 300 meV is found. Films
thinner than 1.6 layers do not show remanent magnetization above 80 K. No
evidence for enhanced moments in monolayer films is found.

INTRODUCTION

Spin polarized electron energy loss spectroscopy (SPEELS) is a valuable
technique to study the magnetism and the electronic structure of 3d
ferromagnetic surfaces. SPEELS is sensitive to the magnetization of the
first few atomic layers due to the shortness of the electron mean free path.
Exchange scattering is a significant contribution to the total inelastic
scattering at low electron energies if the experiment is performed in off-
specular geometry in order to suppress dipolar contributions [1]. Although
SPEELS cannot provide a direct picture of the band structure like spin
polarized angle resolved photoemission, it has been demonstrated that the
average exchange splitting can be determined from the maximum in the
spin flip scattering rate (Stoner excitations) [1-4]. The surface sensitivity
makes SPEELS a very useful tool for the study of magnetic ultrathin films.
SPEELS is sensitive to the long-range ferromagnetic order, which leads to
spin asymmetries of the scattered intensity upon reversal of the primary
beam polarization. But even in a state with no long-range magnetic order
the "complete" SPEELS experiments, i.e polarized beam combined with
polarization analysis, is sensitive to the presence of local magnetic
moments. In this case, exchange scattering leads to a depolarization. This
has been demonstrated e.g. for Ni above the Curie temperature [5] and for a
disordered antiferromagnetic compound (Cr_2O_3) [6]. This capability of
SPEELS is very interesting in the case of ultrathin films for thicknesses
below the limit of long-range ferromagnetic order.

EXPERIMENT

The experiments were performed in a UHV system designed for various
spin polarized electron spectroscopies. A transversely polarized $(P_0=26\%)$
electron beam, derived from a GaAs photocathode, is scattered off the
surface. The scattered electrons are energy analyzed by a hemispherical
electrostatic analyzer and the spin polarization is measured in a high-
energy Mott detector. Spectra were taken at 20° off the specular direction in
order to suppress the contribution from direct dipole scattering. The
primary beam energy used was 25 eV. The total energy resolution was 300
meV. Co films were deposited from a high purity Co rod, which was heated
by electron bombardment. The substrate was a Cu(100) single crystal which

was mechanically polished and cleaned in situ by Ne ion sputtering and annealing cycles. Evaporation rates were typically 1 layer per minute. The Cu substrate was held at room temperature during deposition. The pressure during evaporation remained in the low 10^{-10} Torr range. Clean Co films with contamination on the percent level, as measured by Auger electron spectroscopy, were obtained. A sharp 1x1 LEED pattern was observed. The thickness of the films was determined from the normalized Co/(Co+Cu) Auger peak-to-peak ratio, which was calibrated against a quartz microbalance[7]. The films were magnetized by a current pulse through a magnetizing coil. The magnetic field is in the plane of the film.

RESULTS AND DISCUSSION

Our observation of a sharp 1x1 LEED structure confirms previous studies on the Co/Cu(100) system [8-13] and indicates that the Co is growing in the fcc structure. Figure 1 shows the SPEELS results for a thick Co layer (20 ML). At this thickness the spectra represent the surface of bulk fcc Co. The top panel shows the asymmetry spectrum, i.e. the normalized difference of the scattering intensity for incoming beam polarization parallel or antiparallel to the majority spin direction in the sample. Large negative asymmetries -- i.e. higher scattering intensities for incoming spin-down electrons--are typical for the ferromagnetic 3d metals and have been observed for Ni and Fe, the absolute value in the present case (40%) being between the Fe (30%) and Ni (50%) values. From the spin analysis of the scattered electrons one obtains the flip and non-flip intensities directly. These are shown in the center and lower panel of Fig.1. The flip-down intensity (i.e. incoming electron spin-down outgoing electron spin-up) is by a factor of five larger than the flip-up channel, very close to the observed ratio in Ni. In addition, the non-flip-down intensity is somewhat higher than the corresponding non-flip-up intensity, again very similar to the case in Ni. Both of these differences contribute to the asymmetry, with the difference in the flip rates playing the dominating role. As in Fe and Ni the
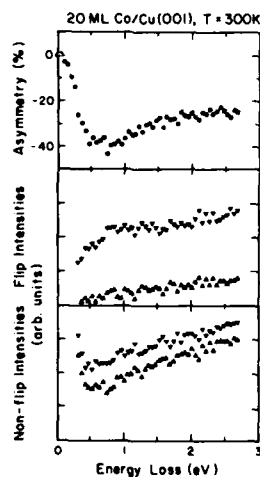
Fig. 1. Intensive asymmetry and flip non-flip intensities for a thick (20 ML) fcc Co film

20 ML Co/Cu(001), T = 300K
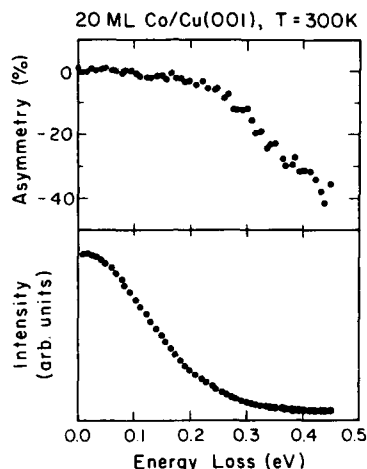
Fig. 2. Asymmetry spectrum and intensity at small energy
losses for a 20 ML fcc Co film

flip-down spectrum consists of a smoothly rising "background" and a
hump with a maximum at the position of the exchange splitting, in the
present case around 0.8 eV energy loss. We therefore identify this energy
with the exchange splitting of fcc Co. This value is in agreement with
photoemission spectroscopy on hcp and fcc Co [14,15], but much smaller
than theoretical values [16,17]. Besides the exchange splitting, a
fundamental quantity is the Stoner gap, i.e. for a saturated ferromagnet the
position of the top of the majority-spin band. Band structure calculations
predict fcc Co to be a saturated ferromagnet with a Stoner gap of about 300
meV [16,17]. This gap should show up as a threshold for Stoner excitations
in the flip-down intensity and also the asymmetry should show a threshold
at the value of the Stoner gap, as was shown in Ni[3]. Figure 2 shows an
asymmetry spectrum over a narrow energy range. The emergence of the
asymmetry is due in part to the superposition of the elastic and inelastic
contributions. However, the strongest rise of the asymmetry occurs where
the elastic intensity is already by a factor of four smaller than the inelastic
one, i.e. at about 320 meV. At 280 meV, where the elastic and inelastic
intensities are equal, the asymmetry has reached only -10%, inconsistent
with a mere superposition of elastic (with zero asymmetry) and inelastic
intensity with -40% asymmetry. We therefore conclude that a threshold
exists. We identify this threshold with the steepest rise of the asymmetry
spectrum around 300 meV. A Stoner gap of 300 meV is therefore
consistent with the data. Decreasing the Co film thickness does not change
the SPEELS spectra until about 4 ML are reached where the absolute
asymmetries start to decrease and the difference between the up and down
intensities become smaller. This can be attributed to scattering
contributions from the Cu substrate. The question of the electronic
structure of monolayer films and the possible increase of the magnetic
moment[18] for atoms with reduced coordination number can be studied for
these oligatomic films. Figure 3 shows SPEELS spectra on a 2 ML film. At
room temperature films below 2 ML did not show remanent magnetizations
because of the Curie temperature. At 80 K films with a thickness down to
1.6 ML showed remanent magnetization. As seen in Fig. 3 the absolute
values of the asymmetry and the difference between up and down

2 ML Co/Cu(001), T = 80K

Asymmetry (%)

Flip Intensities (arb. units)

Non-flip Intensities

Energy Loss (eV)
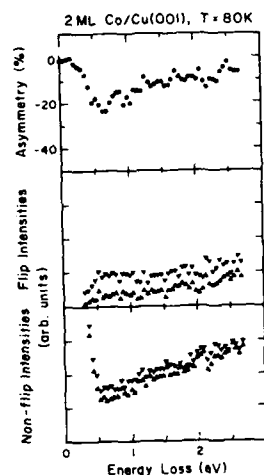
Fig. 3. SPEELS spectra for a 2 ML Co film at 80 K

intensity are smaller than the 20 ML data but the film clearly shows ferromagnetic long range order. The most interesting quantity is the value of the exchange splitting. The flip-down intensity shows the characteristic hump due to the Stoner excitations. If the moments in this 2 ML film were increased a shift to higher energies would be expected. Comparing this spectrum to the 20 ML film clearly does not show any indication of a shift. In films of one monolayer the ferromagnetic long range order is lost (at least at 80 K) but as mentioned above SPEELS can still give valuable information in this case. The asymmetry vanishes and the up and down intensities become equal, however spin-flip and non-flip can still be distinguished. Spin-flip scattering leads to a depolarization. In Figure 4 we

0.9 ML Co

Cu(001)

P_s/P_0

Flip   Non-flip

Flip   Non-flip

Intensities (arb. units)

Energy Loss (eV)

Energy Loss (eV)
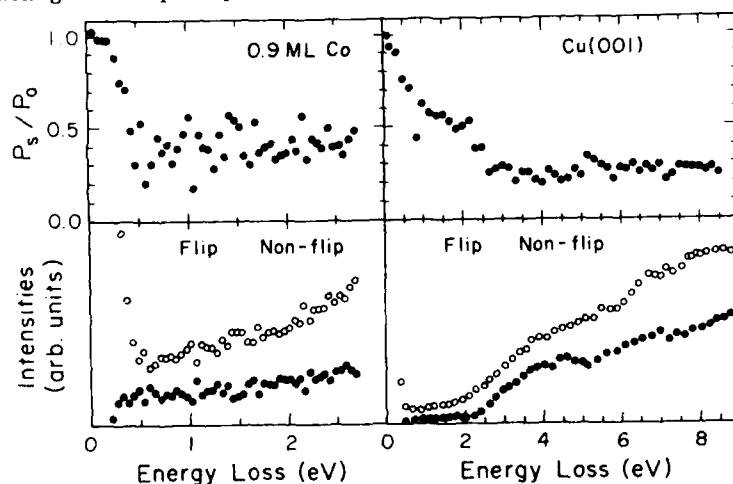
Fig. 4. SPEELS spectra from Cu(100) and 0.9 ML Co

compare SPEELS data from on a 0.9 ML Co film to the bare Cu substrate. Shown are the depolarization spectra, i.e. Ps/Po and the flip and non-flip intensities. For the bare Cu surface the depolarization sets in very gradually with increasing energy loss. There is a threshold at about 2 eV loss, which corresponds to the onset of spin-flip excitations involving Cu 3d electrons. With the 0.9 ML Co, on the other hand, very strong depolarization sets in already at very small energy losses. Even at this submonolayer coverage the flip intensity shows already the typical hump. Again the energetic position of this hump can be identified with the (in this case local) exchange splitting. No shift to higher energy is apparent. Therefore there is no evidence for enhanced moments even in these submonolayer films.

SUMMARY

Spin polarized electron energy loss spectroscopy measurements on epitaxial fcc Co films on Cu(100) reveal an exchange splitting of 0.8 eV independent of thickness. Films below 1.6 ML do not show a remanent magnetization above 100 K. Strong exchange scattering is also found on monolayer films. indicating the existence of local magnetic moments. No evidence is found for enhanced magnetic moments in monolayer films.

*II Physikal. Institut,. RWTH Aachen, Germany
**Department of Solid State Physics, University of Nijmegen, The Netherlands

References

1.   H. Hopster and D.L. Abraham, Phys. Rev. B40, 7054 (1989)
2.   D. Venus and J. Kirschner, Phys Rev. B37, 2199 (1988)
3.   D.L. Abraham and H. Hopster, Phys. Rev. Lett. 62, 1157 (1989)
4.   Th. Dodt, Ph.D. Thesis, University of Dusseldorf (1988)
5.   D.L. Abraham, Ph.D. Thesis, Univ. of California, Irvine (1989)
6.   H. Hopster, Phys. Rev. B42, 2540 (1990)
7.   K.-P. Kamper, D.L. Abraham, and H. Hopster, in preparation
8.   L. Gonzales, R. Miranda, M. Salmeron, J.A. Verges, F. Yndurain, Phys. Rev. B24, 3248 (1981)
9.   A. Clarke, G. Jennings, R.F. Willis, P.J. Rous, and J.B. Pendry, Surf. Sci. 187, 327 (1987)
10.   C.M. Schneider, P. Bressler, P. Schuster, J. Kirschner, J.J. Miguel, and R. Miranda, Phys. Rev. Lett. 64, 1059 (1990)
11.   D. Pescia, G. Zampiere, M. Stampanoni, G.L. Bona, R.F Willis, and F. Meier, Phys. Rev. Lett. 58, 933 (1987)
12.   Hong Li and B.P. Tonner, Surf. Sci. 237, 141 (1990)
13.   J.J. Miguel, A. Cebollada, J.M. Gallego, S. Ferrer, R. Miranda, C.M. Schneider, P. Bressler, J. Garbe, K. Bethke, and J. Kirschner, Surf. Sci. 211/212, 723 (1989)
14.   F.J. Himpsel and D.E. Eastman, Phys. Rev. B21, 3207 (1980)
15.   C.M. Scneider et al., J. Appl. Phys. (1991); in press
16.   D. Bagayoko, A. Ziegler, and J. Callaway, Phys. Rev. B27, 7046 (1983)
17.   V.L. Moruzzi, J.F. Janak, and A.R. Williams, Calculated Electronic Properties of Metals (Pergamon, New York, 1978)
18.   A.J. Freeman and C.L. Fu, J. Appl. Phys. 61, 3356 (1987)

Spin Polarization of Pt in Pt/Co Multilayers Studied by X-Ray Absorption

G. Schütz, H. Ebert[†], P. Fischer, S. Rüegg and W. B. Zeper[††]

Fak. f. Physik, Techn. Univ. München, D-8046 Garching, Federal Republic of Germany,
[†]Siemens AG ZFE ME TPH 11, D-8520 Erlangen, Federal Republic of Germany,
[††]Philips Res. Lab., 5600 JA Eindhoven, The Netherlands

Abstract

Local d-magnetic moments of the Pt interlayer in Pt/Co multilayered structures (4 ÅCo + X ÅPt, X=9,19,23,30,40) have been investigated theoretically and experimentally by circular magnetic x-ray dichroism studies.

It has been found that a significant Pt polarization is induced, which contributes by about 13% to the total magnetization. The experimental findings of the average Pt moments agree well with the theoretical expectations indicating the existence of a long-range exchange coupling through the Pt layer.

Introduction

The spin-dependent absorption or MXD (Magnetic X-ray Dichroism) for circularly polarized photons at inner-shell absorption edges supplies a direct experimental element-selective probe for local magnetic properties [1]-[23]. The spin-dependent absorption spectra, i.e. the energy-dependent difference for the absorption of circularly polarized photons in matter, magnetized parallel and antiparallel with respect to the photon spin, is correlated to the spin structure of electronic states at the Fermi level. In case of 5d impurities in a ferromagnetic iron host it has been verified that a simple correlation between the MXD signal and the local magnetic d-moment exists [14, 24]. The local 5d moments deduced from the spin-dependent absorption signal provide the first reliable confirmation of the theoretical predicted coupling mechanism [19, 25]. Furthermore the MXD of these systems are well understood in the framework of fully relativistic theories based on a single particle band-structure picture and allows a parameter-free description of the observed spectra [5]-[8],[10],[12]-[15], [18, 24, 32]. We have applied this new method to study Pt/Co multilayer systems, which are interesting new candidates for magneto-optical recording. Besides the technical importance the understanding of their magnetic properties is of scientific interest and has stimulated extensive studies of these artificial magnetic materials by a variety of methods. One of the problems addressed is the role of the – in the pure metal non-magnetic – Pt interlayer. The enhanced Kerr rotation at shorter wavelengths and larger effective magnetization, the larger magnetization and high energy Kerr rotation ($E \geq 4keV$) compared to pure Co is expected to result from an induced Pt moment.

Here we report the theoretical and experimental studies of the magnetic Pt moments and MXD of circularly polarized x-rays at the L_3-edge of $Pt_{50}Co_{50}$ and X Pt/ 2 Co multilayered structures with various numbers X of Pt monolayers (X = 4,7,10,13,17).

THEORETICAL APPROACH

To support the interpretation of our experimental MXD-investigations, calculations of the electronic structure of Pt/Co multilayer systems have been performed. For this purpose a three dimensional periodicity of these layered systems has been assumed, allowing to use a conventional LMTO (linear muffin tin orbital) band structure program package. The (111)-textured structure of the multilayers (see below) has been represented by a corresponding hexagonal unit cell. As an example the atomic arrangement corresponding to 4Pt/2Co is shown in Fig. 1.
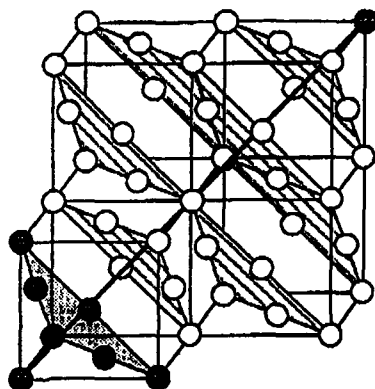
Figure 1: Atomic arrangement in the hexagonal unit cell used to represent the multilayered structure 4Pt/2Co.

Our spin-polarized calculations gave us a detailed information on the magnetic properties of the Pt/Co multilayered systems. This is demonstrated by Fig. 2, where the resulting magnetization profiles for the Pt-interlayers of some of the studied systems are shown (the Co-moments turned out to be around 1.9 μ_B in all cases). As one can see, the Pt-atoms at the Pt/Co-interface are strongly spin-polarized due to hybridisation with the d-states of the neighboring Co-atoms resulting in a magnetic moment of around 0.2 μ_B. This mechanism leads also to a polarisation of the inner Pt-layers, however with a resulting moment decreasing rapidly with the distance from the interface. Surprisingly, for rather thick Pt-interlayers, negative moments have been found in the middle of the Pt-interlayers. This behavior, also found by other authors for Pd/Co, however does not imply an antiferromagnetic coupling of the Co-layers. As will be shown below, in spite of the small negative moments in the middle of the thicker Pt-interlayers, the average Pt moment was found to be positive in all cases studied.

In addition to the investigation on the multilayers, band structure calculations for the disordered alloy $Pt_{50}Co_{50}$ have been performed. This has been done using the spin-polarized relativistic version of the KKR-CPA (Korringa-Kohn-Rostoker Coherent Potential Approximation) method. By accounting this way for spin-polarisation and spin-orbit

coupling, we were able to get a first principle description of the MXD, observed in this interesting reference system. The corresponding L_2- and L_3-spectra of Pt in $Pt_{50}Co_{50}$ have been calculated using a formalism derived earlier. Within the adopted approach, which is based on a spin-polarized relativistic version of multiple scattering theory, the absorption coefficient is given by

$$\mu_{L_\alpha} \propto \sum_i \int \int d^3r \, d^3r' \; \Phi_i^\times(\vec{r}) X_{\vec{q}\lambda}(\vec{r}) \, Im \, G^+(\vec{r}, \vec{r}', E)$$
$$X_{\vec{q}\lambda}^\times(\vec{r}') \, \Phi_i(\vec{r}') \, \Theta(E - E_F) \tag{1}$$

with $E = E_i + \hbar\omega$ and $\alpha = 2,3$. Here one sums over the relevant initial core states Φ_i, i.e. $2p_{1/2}$- and $2p_{3/2}$-states for the L_2- and the L_3-spectra, respectively. These tightly bound core states have been calculated taking spin-polarization of the system and all relativistic effects rigorously into account. However it turned out that the admixture of $2p_{3/2}$- ($2p_{1/2}$-) character to the $2p_{1/2}$- ($2p_{3/2}$-) states is completely negligible. This is also true for the energetic splitting of the μ-sublevels. The electron-photon interaction is treated in a relativistic correct form by the operator

$$X_{\vec{q}\lambda}(\vec{r}) = -e\vec{\alpha} \cdot \vec{A}_{\vec{q}\lambda}(\vec{r}). \tag{2}$$

Here the electron current operator is represented by means of the Dirac matrix vector $\vec{\alpha}$ and the vector potential $\vec{A}_{\vec{q}\lambda}(\vec{r})$ contains all information on the wave vector $\vec{q}$ and polarization λ of the X-ray radiation. Finally, the Greens function $G^+(\vec{r}, \vec{r}', E)$ represents the possible final states above the Fermi level E_F and is expressed with the help of the spin-polarized relativistic version of multiple scattering theory:

$$Im \, G^+(\vec{r}, \vec{r}', E) = \sum_{\Lambda, \Lambda'} Z_\Lambda(\vec{r}, E) \, Im \, \tau_{\Lambda, \Lambda'}^{nn}(E) \, Z_{\Lambda'}^\times(\vec{r}, E). \tag{3}$$

Here the index Λ represents the set of relativistic quantum numbers (κ, μ) and the functions $Z_\Lambda(\vec{r}, E)$ are the scattering solutions to the single site Dirac equation for a spin-dependent potential.

For a comparison with experiment, the spectra obtained from eq.(1) still have to be broadened appropriately to take finite lifetime effects and apparative broadening into account.
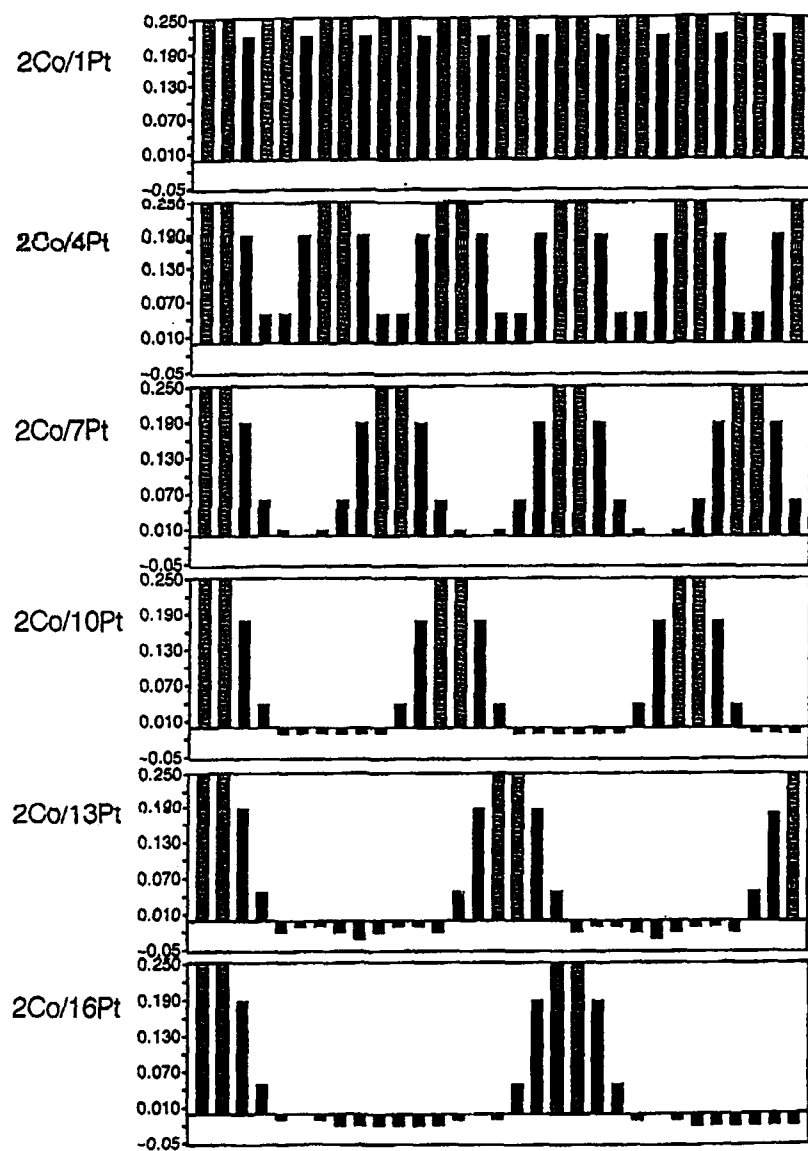
Figure 2: Magnetization profiles (in μ_B) of the Pt-interlayers in 2Co/nPt (n=1, 4, 7, 10, 13, 16) as obtained from LMTO band structure calculations.

EXPERIMENTAL ASPECTS

The experiments have been performed at the Hamburger Synchrotron Laboratory using circularly poralized x-radiation emitted from a bending magnet at small vertical angles with respect to the plane of the electron orbit. This "inclined view method" provides x-rays in the energy range of $5-30 keV$ with a high degree of circular polarization in the order of $P_c \sim \pm 80\%$.
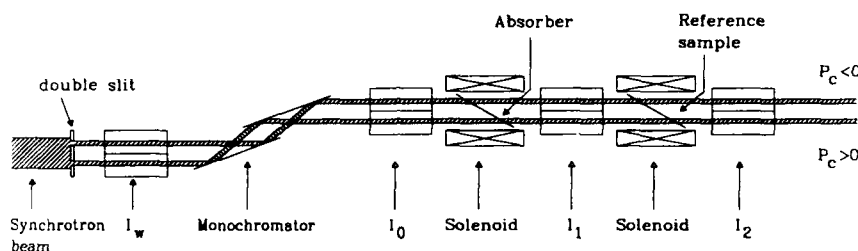
Figure 3: Experimental arrangement for spin-dependent absorption measurements using Pt Fe as reference sample.

The experimental arrangement, which is shown in Fig.3, allows a detection of the spin-dependent absorption profile with high accuracy and a significant reduction of systematic errors by using the "two beam" transmission mode: By a vertically adjustable double slit arrangement two beams emitted above and below the plane of the electron orbit with opposite sign of circular polarization are formed and their intensities are monitored by the double ionization chamber I_w. The photon beams are monochromatized by a Si(111) or Si(311) double crystal monochromator with an energy resolution of typically $1 - 3 eV$. The absorption spectra of the two beams in the energy range of $11.2 keV \leq E \leq 11.6 keV$ corresponding to the Pt L_3 energy of $11.56 keV$ are measured simultaneously and independently by two identical double ionization chambers in front (I_0) and behind (I_1) the sample. The intensity, which is transferred through the Pt/Co samples, was used as incident radiation for an on-line comparison with the spin-dependent absorption effects of a well-known PtFe reference target [5]-[10],[12, 14, 15, 24, 32] by a third double ionization chamber (I_2). The magnetic targets are mounted inside identical solenoids, the magnetic field direction $(|B_{max}| \sim 200 mT)$ being reversed every second. So two sets of absorption spectra, i.e. the absorption coefficient $\mu^{\pm} \cdot x = P_c \cdot \ln(I_{0,1}/I_{1,2})^{\pm}$ as function of energy, for each beam and each sample for antiparallel($+$) and parallel orientation ($-$) of the target magnetization and the photon spin direction were recorded. The spin-dependent absorption profile

$$\mu_c/\mu_0 = (\mu^+ - \mu^-)/(\mu^+ + \mu^-) \cdot (1/P_c) \cdot (M_s/M')$$

is given by the relative difference of the absorption coefficents $\mu^+(E)$ and $\mu^-(E)$. The factors $1/P_c$, which is measured simultaneously in the MXD signal of the PtFe sample and (M_s/M') take into account the incomplete degree of circular polarization and the magnetization of the sample M' $(M(B_{ext} = 0.18T, T = 300K))$ to the saturation magnetization, respectively. The Pt/Co layers $(30 \times [4\text{Å}Co + X\text{Å}Pt]$, X = 9,16,23,30,40) were prepared at room temperature by electron beam evaporation from separate Pt and Co sources onto $12 \mu m$ Upilex foils. These samples could be shown to have the pronounced

(111) texture [29]. Careful magnetization measurements were performed to determine the ratio M_s/M'. The optimum total thickness for the x-ray transmission measurement of 4–6 μm was achieved by stacking 80–120 foils. The PtCo alloy was prepared as a film by iron beam sputtering. Due to the high saturation field of the $Pt_{50}Co_{50}$ a not exact measurable effective magnetization of about $6 \pm 2\%$ was achieved in the relative small applied field.

RESULTS AND DISCUSSION

Measured and calculated MXD spectra

The normal Pt L_3 absorption spectra and the spin-dependent absorption profile $[\mu_c/\mu_0](E)$ of the $Pt_{50}Co_{50}$ alloy and the corresponding reference signal of PtFe are shown in Fig.4. The calculated profiles $\mu(E)$ and μ_c/μ_0 in case of PtFe indicate that the theory based on the single-particle approximation provides a parameter-free description of the experimental spectra. Because of the poor accuracy of the corresponding rescaling factor M' a quantitative comparison of theoretical and experimental data of the $Pt_{50}Co_{50}$ alloy was not exactly possible, but shows a nearly identical shape.
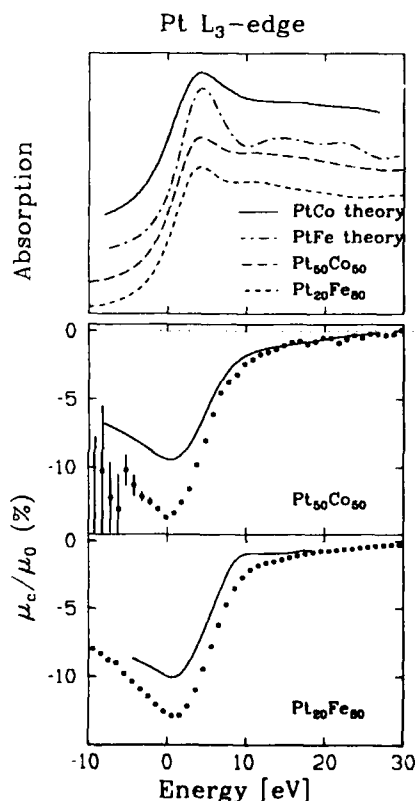
Figure 4: Normal (upper part) and spin-dependent Pt L_3-absorption signals μ_c/μ_0(lower part) of the reference sample PtFe and $Pt_{50}Co_{50}$ in comparison with the theoretical calculations (solid lines).

The corresponding Pt absorption profiles and MXD spectra of the Pt/Co multilayers are presented in Fig.5. The normal absorption profile of the thickest Pt layer is nearly identical compared to pure Pt. By lowering the Pt layer numbers the white line amplitudes decrease indicating a filling of the empty 5d states. Up to 17 ML Pt significant spin-dependent absorption profiles with identical shape have been observed, which decrease in amplitude with increasing Pt thickness. It shows directly that a significant Pt spin polarization is induced reflecting unambiguously a nonvanishing average Pt moment in all multilayer samples studied.
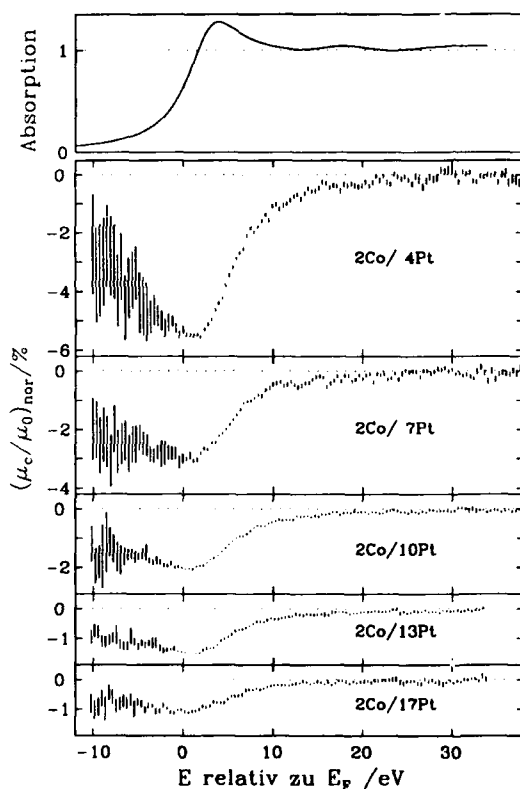
Figure 5: Normal (upper-part) and spin-dependent Pt L_3-absorption profiles and μ_c/μ_0 (lower part) of the Pt/Co multilayers (4 ÅCo and X ÅPt, X=9, 16, 23, 30, 40).

The magnetic Pt moments in Pt/Co multilayers

In a very simplified "two step" model the MXD originates from the phenomenon, that in the absorption process of a circularly polarized photon in an unpolarized inner shell the photoelectron is ejected with a partial spin polarization in the photon propagation direction. This "Fano effect" is a consequence of angular momentum conservation and spin-orbit interaction of the initial and final states [26]. For L_2- and L_3-absorption in the $2p_{1/2}$- and $2p_{3/2}$-state the photoelectron Polarization P_e ($P_e(L_2)$= -1/2 d $P_e(L_3)$=+1/4 calculated for free atoms) is very large due to the large initial state spin-orbit splitting of more than $1keV$ for 5d elements. In case of a spin-band ferromagnet the possible final unoccupied states at the Fermi level can also be spin polarized. Thus the (relative)

difference of the absorption coefficients for circularly polarized photons

$$[\mu_c/\mu_0](E) = P_e \cdot [\Delta\rho/\rho](E) \tag{4}$$

will exist and depends on the spin density $(\Delta\rho/\rho) = (\rho^+ - \rho^-)/(\rho^+ + \rho^-)$ of the final states, where ρ^+ (ρ^-) are majority (minority) unoccupied bands. The parameter P_e corresponds to the effective spin polarization of the photoelectron, which is calculated to amount to $P_e \sim 0.3$ at the Pt L_3-edge nearly independent of energy.
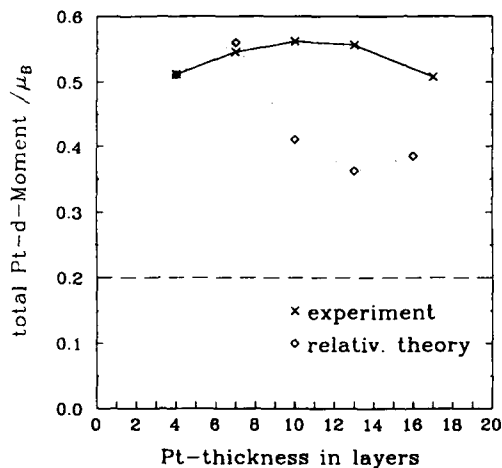
Figure 6: Theoretical values ($\Diamond$) of total Pt d-moments as a function of the Pt thickness in comparison with the experimental values ($\times$) deduced from the spin dependent absorption spectra in Fig. 5. The dashed line gives the moment for a pure interface-layer polarization (cf. text).

The validity of eq. (4) has been experimentally proven for nearly all 5d impurities in Fe. The d-band at the Fermi level of Pt or Pt impurities in 3d-hosts is located in an energy region of about $20eV$. In the latter case the Pt atom carries a d-moment given by the difference of the number of spin-up and spin-down d-bands in the occupied part, which has the same amplitude but opposite sign as the moment of the unoccupied d-hole $m_d = -m_d^{hole} = -\mu_B \cdot \int \Delta\rho(E)dE$. Thus in the simplified picture described above the magnetic d-moment

$$m_d = -\mu_B(1/P_e) \int [\mu_c/\mu_0](E)\rho(E)dE$$

can be directly deduced from the CMXD signal by integrating the spin-dependent absorption profile multiplied by the total density of the unoccupied states, which can be taken from theory or the measured white line areas [27, 28]. Very good agreement of the magnetic moments of 5d impurities in iron with the calculations have been found. It indicates that the spin-dependent absorption measurement can provide a fast and direct determination of the sign and qualitatively also the amplitude of local magnetic moments. In Fig.6a,b the average magnetic Pt moments m_d (a) and the total moments (b) as function of the Pt layer number N in comparison with the corresponding theoretical results are presented. The accuracy of the relative Pt moments is estimated to be $\Delta m_B/m_B \leq 4\%$. In case of the N=4 and N=7 sample a perfect agreement between the experimental and theoretical value has been found confirming that not only the first Pt layer at the interface is significantly polarized, but also the inner layers, but with a strongly reduced magnetic moment.

That a long-range Pt polarization should exist, is furthermore indicated by the absolute values of the experimental and calculated Pt moments. A magnetic Pt moment for a pure interface-layer polarization, caused by a short-range interaction (smaller than one layer thickness), estimated from the Pt moment in a very dilute Pt$\underline{Co}$ alloy (m_{Pt}(Pt$\underline{Co}$) $\sim 0.4 - 0.5\mu_B$) using coordination number arguments is marked by the dashed lines.

For the thicker Pt layers the experimental values are somewhat larger showing a nearly constant value of the total moment as function of N. The fact, that the experimental values for $N \geq 10$ do not follow the decrease of the calculated ones might be a hint, that an antiferromagnetic contribution of the inner Pt layer is not as large as expected from theory. However our recent calculations of the corresponding Pt moments for a (100) texture, which show no perpendicular magnetic anisotropy, predict a much larger antiferromagnetic coupling trend changing the sign of the total or average moment for $N \geq 6$. We hope, that the planned experimental MXD studies on the corresponding samples will give more detailed experimental information on the change from ferro- to anti-ferromagnetic coupling of the Pt interlayers, a coupling mechanism which has been observed and predicted for other systems as for example Co/Cu and Pd/Co [30, 31].

REFERENCES

[1] G. Schütz, W. Wagner, W. Wilhelm, P. Kienle, R.Zeller, R. Frahm and G. Materlik, Phys. Rev. Lett. 58(7), 737 (1987)

[2] G. Schütz, M. Knülle, R. Wienke, W. Wilhelm, W. Wagner, P. Kienle, and R. Frahm, Z. Phys. B73, 67 (1988)

[3] H. Ebert, P. Strange, and B.L. Gyorffy, J. Appl. Phys. 63, 3055 (1988).

[4] H. Ebert, P. Strange, and B.L. Gyorffy, Z. Phys. B73, 77 (1988).

[5] G. Schütz, R. Wienke, W. Wilhelm, W. Wagner, P. Kienle, R. Zeller, and R. Frahm, Z. Phys. B75, 495 (1989)

[6] G. Schütz and R. Wienke, Hyp. Int. 50, 457 (1989)

[7] G. Schütz, Physica Scripta, T29, 172 (1989)

[8] G. Schütz, R. Wienke, W. Wilhelm, W. Wagner, P. Kienle, R. Zeller, and R. Frahm, Physica B158, 284(1989)

[9] G. Schütz, R. Frahm, R. Wienke, W. Wilhelm, W. Wagner, and P. Kienle, Rev. Sci. Instr. 60, 1661 (1989)

[10] H. Ebert, B. Drittler, R. Zeller, and G. Schütz, Sol. Stat. Comm. 69(5), 485 (1989)

[11] S.P. Collins, M.J. Cooper, A. Brahmia, D. Laundy, and T. Pitkanen, J. Phys. Cond. Mat. 1, 323(1989)

[12] G. Schütz, R. Wienke, W. Wilhelm, W. B. Zeper, H. Ebert, and K. Spörl, J. Appl. Phys. 67(9), 4456 (1990)

[13] G. Schütz, P. Fischer, H. Ebert, R. Wienke, and W. Wilhelm, Conf. Proc. Vol. 25 "2nd European Conf. on Progress in X-ray Synchrotron Radiation Research", edited by A.Balerna, E. Bernieri and S. Mobilio (SIF, Bologna 1990), p. 229

[14] G. Schütz, Physikalische Blätter 46(12), 475 (1990)

[15] H. Ebert, R. Wienke, G. Schütz, and R. Zeller, J. Appl. Phys. 67(9), 4923 (1990)

[16] H. Ebert and R. Zeller, Phys. Rev B42, 2744 (1990)

[17] H. Ebert, G. Schütz, W. M. Temmerman, Solid State Comm. 76(4), 475 (1990)

[18] H. Ebert, R. Wienke, G. Schütz, and W.M. Temmermann, Physica A, in press

[19] H. Ebert, R. Zeller, B. Drittler, and P.H. Dederichs, J. Appl. Phys. 67, 4576 (1990)

[20] C.T. Chen, F. Sette, Y. Ma, and S. Modesti, Phys. Rev. B42, 7262 (1990)

[21] F. Baudelet, E. Dartyge, G. Krill, J.P. Kappler, C. Brouder, M.Piechuch, and A. Fontaine, Phys. Rev. B43, 5857 (1991)

[22] F. Baudelet, C. Brouder, E.Dartyge, A.Fontaine, J.P. Kappler, and G. Krill, Eur. Phys. Lett. 13, 751 (1990)

[23] F. Sette, C. T. Chen, Y. Ma, S. Modesti, and N.V. Smith, Conf. Proceedings "6th Int. Conf. on X-ray Absorption Fine Structure", edited by S. Samar Hasnain (Ellis Horwood Ltd., 1991), p.96

[24] R. Wienke, G. Schütz, and H. Ebert, J. Appl. Phys., in press

[25] H. Akai, Hyp. Int. 43, 255 (1989)

[26] Fano, U., Phys. Rev. 178, 131 (1969).

[27] J. A. Horsley, J. Chem. Phys. 79, 1451 (1982)

[28] T. K. Sham, Solid State Comm. 64, 1103 (1987)

[29] W. B. Zeper, F. J. A. M. Greidanus, P.F. Carcia, and C. R. Fincher, J. Appl. Phys. 61, 4971 (1989)

[30] D. Pescia, D. Kerkmann, F. Schumann, and W. Gudat, Z. Phys. B78, 475 (1990)

[31] R. H. Victoria, and J.M. MacLaren, J. Appl.Phys., in press

[32] G. Schütz, Conf. Proceedings "6th Int. Conf. on X-ray Absorption Fine Structure", edited by S. Samar Hasnain (Ellis Horwood Ltd., 1991), p.87

INVESTIGATION OF SURFACE MAGNETISM BY DETECTION OF POLARIZED LIGHT EMITTED AFTER LOW ENERGY He+ SCATTERING OFF A Fe(110) SURFACE

M. SCHLEBERGER*, A. NÄRMANN*, W. HEILAND*, C. HUBER** AND J. KIRSCHNER**
*Universität Osnabrück, Fachbereich Physik, W-4500 Osnabrück, Germany
**Freie Universität Berlin, Institut für Atom- und Festkörperphysik, W-1000 Berlin, Germany

ABSTRACT

We present data from low-energy He+ ion scattering off a magnetized Fe(110) surface where we monitored the circular polarization of the light emitted from particles neutralized into excited states. We investigated the dependence on incident energy, incident angle and magnetization for a singlet and a triplet transition. As expected, there is no dependence on magnetization for the singlet state, but for the triplet transition we observed a difference in the circular polarization of as high as 32% when changing the direction of the magnetization.

INTRODUCTION

Experiments detecting the circular polarization in surface scattering have been performed since the seventies [1,2,3].

The degree of circular polarization in the light emitted by atoms after being neutralized into excited states at a magnetic surface in a scattering event contains information about the spin of the captured electron. The spin $<S>$ can be extracted out of the circular polarization (S/I) data, if the directions of the magnetization M at the surface and the orbital angular momentum $<L>$ are known. The direction of M is simply given by the direction of the current used to magnetize the sample, whereas the orbital angular momentum is determined by the geometry of the experiment.

We determined S/I of the He 2^1P—3^1D and 2^3P—3^3D lines after He+ had been scattered off a magnetized Fe(110) surface at different incident angles varying from 5° to 25° and with different incident energies in the range of 3 to 12 keV.

EXPERIMENTAL

The experiments were performed in an UHV-chamber described in detail in Refs. 4 and 5, with a base pressure of 2×10^{-10} mbar. The ion beam was produced in an ion gun, accelerated thru some deflection plates and apertures towards a magnet which mass-selects the beam before it hit the target.

Below 3keV incident energy the photon yield was too small to give a reasonable statistics within an acceptable time.

The sample was carefully prepared by grazing incidence ion sputtering and annealing cycles. The details of the preparation procedure are given in Ref. 6. After that no signal but Fe was seen with Auger-electron spectroscopy.

The sample was mounted on a manipulator which allows for rotation (incident angle) and x-y-z translation. The crystal was oriented in a way that the incoming ions were scattered along $[\bar{1}10]$ direction.

The magnetization of the target was performed by a current pulse thru a coil around a magnet yoke of toroidal shape made of soft iron. The sample remained magnetized due to the remanence magnetization. The magnetization was reversed by changing the direction of the current thru the coil. A de-magnetization on a macroscopic scale was achieved by applying an ac current which was gradually decreased to some ten μA.

The optical unit to determine S/I consisted of a quarter-wave-plate rotated by a stepping motor, a linear polarization filter, an interference filter matching the wavelength of the transition under consideration and a photomultiplier cooled by a Peltier device down to -25°C. Countrates for the photon yield were typically $100 - 500$ cps for $3 - 12$ keV incident energy. The wavelengths used in this work are 667.9 nm (2^1P—3^1D transition) and 587.6 nm (2^3P—3^3D).

The sample was positioned inside UHV in a way that the photomultiplier collected the light emitted by atoms leaving the surface in about specular direction. We did not put an aperture in the outgoing beam, hence we cannot relate our results to any trajectory dependencies. An aperture would have reduced the already low countrate even more. This implies that our data represent an average over a certain range of scattering angles. This range is determined by the area (2.25×0.75 mm^2) from which light is collected by the cathode and the distance of that area from the point of impact of the ion beam on the surface. A rough estimate shows that we collected a range of $\pm 5°$ around specular reflection direction.

For data aquisition the quarter-wave-plate was rotated in steps of 22.5°, each time integrating the countrate over a predefined time. From these numbers the circular polarization S/I was determined. The numbers shown in the figures are an average of at least 5 different runs under the same conditions. The standard deviation is in all cases less than 4%. Systematical errors due to e.g. optical elements are much smaller.

RESULTS AND DISCUSSION

In the following we use the optical convention, i.e. positive S/I numbers correspond to clockwise circularly polarized light when observed against the positive z-direction. A sketch of the setup is given in Fig.1.
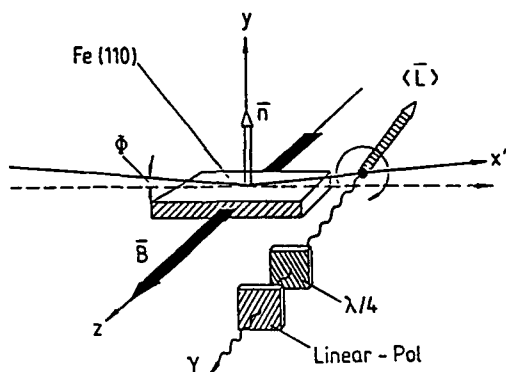
Fig.1. Sketch of the experimental setup.

In all figures shown, full circles (•) are used for measurements with the magnetization M parallel to the direction of the orbital angular momentum $<L>$, open circles (o) for M antiparallel to $<L>$, and crosses (x) for a macroscopical de-magnetized surface. The corresponding values for the circular polarization will be referred to in the following as $S/I_\uparrow$, $S/I_\downarrow$ and S/I_0, respectively. The difference between the S/I numbers for different magnetization is then $\Delta S/I = |S/I_\uparrow - S/I_\downarrow|$.

In Fig.2 we show that for the singlet transition S/I is independent of the magnetization.
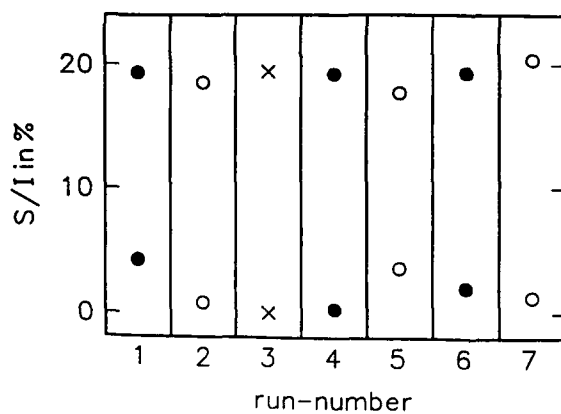
Fig.2. Dependence of S/I for the singlet transition 2^1P-3^1D on the magnetization of the surface for two incident angles (5°, top and 20°, bottom). Incident energy was 8 keV.

90

This is expected since there is no electronic spin polarization for a singlet transition. This is different for a triplet transition; Fig.3 displays a typical cycle of successive runs where the magnetization was changed before each run.
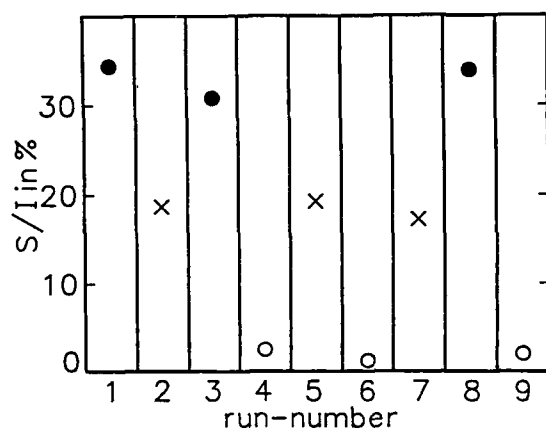
Fig.3. Dependence of S/I for the triplet transition 2^3P-3^3D on the magnetization of the surface for 5° incident angle. Incident energy was 8 keV.

First, a magnetization $\vec{M}$ antiparallel to the orbital angular momentum $<\vec{L}>$ was applied, yielding $S/I_{\downarrow} = 31\%$. Then the sample was de-magnetized giving $S/I_0 = 20\%$. Going back to the former magnetization recovered the corresponding S/I. Reversing M in the fourth run decreased the degree of circular polarization to $S/I_{\uparrow} = 3\%$. The following measurements demonstrate the reproducibility of the data. On average $\Delta S/I = 32 \pm 4\%$ was obtained.

The dependence of S/I on the angle of incidence is presented in Fig.4. The important thing to note is, that the difference between the upper and lower curve is constant over the whole range.
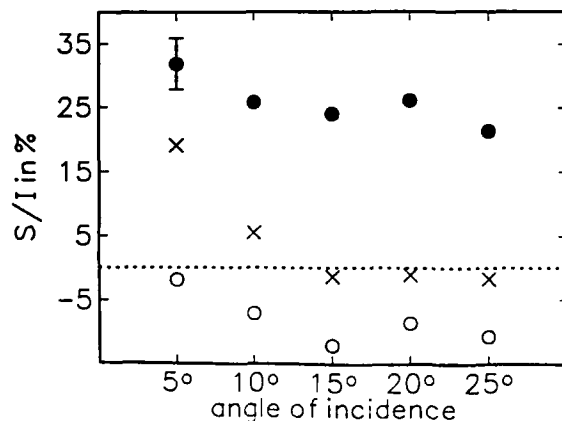
Fig.4. Dependence of S/I for the triplet transition 2^3P-3^3D on the incident angle. Incident energy was 8 keV.

The change of S/I with incident energy is shown in Fig.5. $S/I_\uparrow$ as well as $S/I_\downarrow$ increase with increasing energy and again $\Delta S/I$ stays constant.
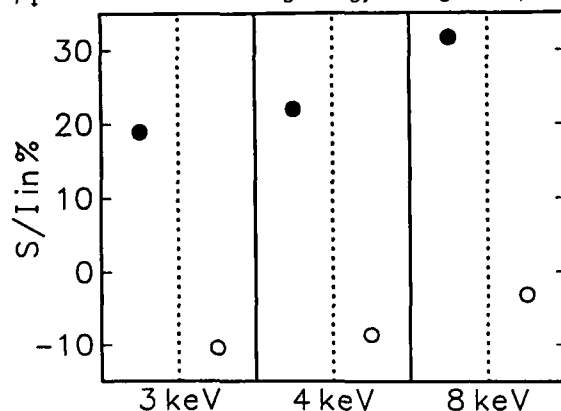
Fig.5. Dependence of S/I for the triplet transition 2^3P-3^3D on the incident energy. Incident angle was 5°.

For small incident angle one would expect from the density-gradient model[7] a positive sign for S/I_0, what is what we find after de-magnetizing the surface. A magnetization M antiparallel to $<L>$ increases the degree of polarization compared to the de-magnetized case. Reversing the magnetization leads to a decrease in S/I. In both cases obviously electrons with a spin $<S>$ antiparallel to M are captured, i.e. majority electrons.

These results are easily explained in terms of a sum of angular momenta. Since the degree of circular polarization is connected to the total angular momentum[8] $<J> = <L> + <S>$, a magnetization parallel to $<L>$ forces the captured electron to have a spin antiparallel to $<L>$ and hence yields a reduction of the modulus of $<J>$ which is detected as a decrease in the S/I value.

The data show that the difference $\Delta S/I$ is independent of the incident angle and incident energy. Since $\Delta S/I$ results from the capture of electrons with reversed spin orientations, the contributions of $<L>$ and M to the degree of circular polarization can be separated via this angle dependence.

Winter et al. have performed similar experiments for higher incident energies (20–200 keV) and more grazing incidence (0.8°) with otherwise about same conditions, see Refs. 9 and 10. They reported a much smaller $\Delta S/I$ in Refs. 9 and 10. But in the meantime they repeated the experiments and obtained similar numbers to ours [11,12].

References

1. H. J. Andrä. Phys. Lett. 54A, 315(1975).

2. N. H. Tolk. J. C. Tully. J. S. Kraus. W. Heiland, and S. H. Neff. Phys. Rev. Lett. 41, 643(1978).

92

3. N. H. Tolk, J. C. Tully, J. S. Kraus, W. Heiland, and S. H. Neff, Phys. Rev. Lett.,42,1475(1979).

4. W. Hetterich, Master's thesis, Universität Osnabrück, 1987.

5. J. Möller, PhD thesis, Universität Osnabrück, 1986.

6. A. Närmann, M. Schleberger, W. Heiland, C. Huber, and J. Kirschner in Proceedings of ECOSS-XI, (Salamanca, 1990), to be published in Surface Science,1991.

7. H. Schröder and E. Kupfer, Z. Phys. A, 279,13(1976).

8. E. Kupfer, H. Gabriel, and H. Schröder, Z. Phys. A, 283 ,321(1977).

9. H. Winter, H. Hagedorn, R. Zimny, H. Nienhaus, and J. Kirschner, Phys. Rev. Lett.,62,296(1989).

10. R. Zimny, H. Hagedorn, H. Winter, and J. Kirschner, Appl. Phys. A, 47,77(1988).

11. J. Kirschner, private communication.

12. C. Huber, ongoing work.

Rare-Earth Thin Films
and Multilayers

EPITAXIAL RARE-EARTH SUPERLATTICES AND FILMS

M.B. SALAMON*, R.S. BEACH*, J.A. BORCHERS**, R. W. ERWIN**, C.P. FLYNN*, A. MATHENY*, J.J. RHYNE[+], AND F. TSUI*

*Department of Physics, University of Illinois, Urbana, IL 61801
**National Institute of Standards and Technology, Gaithersburg, MD 20899
[+]Missouri University Research Reactor, Columbia MO 65211

ABSTRACT

Epitaxial growth of rare-earth superlattices is demonstrated to have opened important new areas of research on magnetic materials. The propagation magnetic order through non-magnetic elements, including its range and anisotropy, has been studied. The importance of magnetostriction in determining the phase diagram is demonstrated by the changes induced by epitaxial clamping. The crystallinity of epitaxial superlattices provides the opportunity to study interfacial magnetism by conventional x-ray and neutron scattering methods.

INTRODUCTION

A new direction in magnetism has been opened by the development of molecular beam methods for epitaxial growth of metal crystals. The key to this field was provided by Durbin and Flynn [1], who discovered methods to grow niobium single crystal films on sapphire in the desired orientation. Kwo, et al. [2] extended this work to the preparation of hexagonal yttrium (0001) on Nb(110). Subsequently, films and superlattices of Dy [3,4], Er [5], Ho [6], and Gd [7] have been grown on Y, with intervening layers of Y, Y-Dy [8] alloys, and Y-Sc-Y sandwiches. Quite recently, the growth of lutetium on Nb(110) has been perfected, [9] permitting epitaxial deposition of Dy and Er thin films on Lu(0001), and of Dy/Lu superlattices. All of the above systems are grown with the crystallographic c-axis along the growth direction. In a related development, Du, Tsui and Flynn [10] developed methods to grow rare-earth superlattices along either the b- or a-axis. Yttrium-dysprosium [11, 12] and yttrium-gadolinium superlattices have been grown in these orientations.

The growth techniques have been described previously and will only be mentioned here [13]. To prepare the c-axis samples a Nb(110) layer is first formed on semiconductor-grade sapphire (1120), followed by a 1000 Å yttrium buffer layer, both to separate the reactive rare earths from the sapphire, and to provide an epitaxial substrate for the rare-earth film or superlattice. Rare-earth films and superlattices are then deposited; their x-ray patterns commonly have Bragg peaks of order 0.1° wide and rocking curve widths of ~0.3°. With the growing sample held at ~600K, good layer by layer growth (ledge growth) can be achieved at a rate of approximately 1 Å/s. To grow superlattices along other crystallographic directions, thin, oriented yttrium single crystals are first subjected to a sputter-anneal sequence, followed by regrowth of yttrium on the surface [10]. Subsequent alternation of rare earth and yttrium layers results in superlattices that have the same coherence as the underlying bulk crystal. Fig. 1 shows x-ray scans of both c-axis and b-axis Dy/Y multilayers.
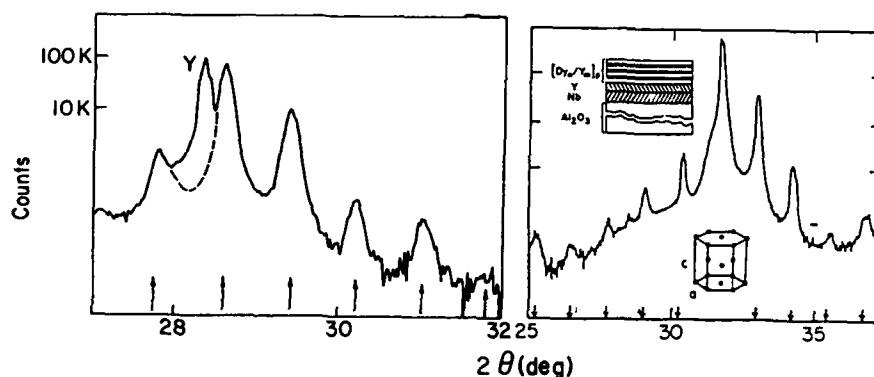
Fig. 1. X-ray diffraction at (00·2) positions for a b-axis |Dy$_{26}$|Y$_9$| sample (left) and a c-axis {Dy$_{16}$|Y$_9$| samples (right). The arrows indicate the structural satellites.

Structure of Superlattice Samples

Although yttrium and the rare earths are electronically and structurally similar, there are significant differences in their lattice parameters, so that epitaxial growth can only result in strained or dislocated samples. In Table I we summarize the room temperature basal plane lattice parameters of the rare earths and their mismatch with yttrium and lutetium. Thin layers grow in registry with the substrate, but can be expected to become unstable to the formation of misfit dislocations once the thickness exceeds a critical value. In the rare-earth-yttrium superlattices studied we find that the growth plane lattice constant takes on a value intermediate between that of the constituent elements generally in proportion to their relative thickness; both constituents are strained. This is shown in Fig. 2, where we plot the quantity $(c_Y \text{-} c_{SL})/(c_Y \text{-} c_{RE})$ versus the relative thicknesses of
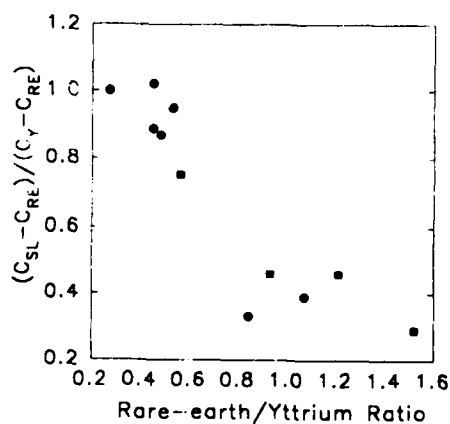
Fig. 2. C-axis strain of Er/Y (squares) and Dy/Y (circles) superlattices versus relative volume fraction of rare earth to yttrium.

the components. The c-axis strains follow the basal plane strains through Poisson's ratio. An x-ray line due to the Y buffer layer is not observed, indicating that the superlattice and buffer layer are elastically coupled to give a single set of lattice parameters. This suggests that plastic deformation at either the Y-Nb or Nb-sapphire interface or both occurs during superlattice growth, so that the superlattice strains during the growth process to achieve the observed structures. At room temperature and below, the growth-plane lattice parameters tend to remain locked to the substrate and do not show the normal thermal expansion or magnetostrictive behavior of the constituents.

The structure of the superlattice along the modulation direction can be readily obtained from the x-ray data of Fig. 1. Owing to the new periodicity Λ of the superlattice. Bragg reflections are observed at intervals of $\Delta Q = 2\pi/\Lambda$, for scattering wavevector Q along the growth axis. The amplitude of these reflections is determined by an envelope function that peaks near, but not at, the average lattice spacing. The attendant asymmetry reflects lattice-constant variation along the growth axis.

Table 1 Basal-plane lattice parameters of selected rare earths and their mismatch with yttrium and lutetium [14]

	Gd	Tb	Dy	Ho	Er
a-axis (Å)	3.634	3.604	3.593	3.578	3.560
Y mismatch	-0.4%	-1.2%	-1.6%	-2.0%	-2.5%
Lu mismatch	+3.7%	+2.8%	+2.5%	+2.1%	+1.6%

In order to account for deviations from abrupt modulation, Erwin et al. [3] introduced a damped square wave model, in which the lattice parameter and concentration vary smoothly between the square-wave ideal and an alloy. For example, the lattice parameter at atomic plane n is written as

$$c_n(\beta) = \frac{\Lambda}{N} + \frac{(c_A - c_B)}{\pi} \sum_{m=1}^{\infty} e^{-\beta m^2} \frac{1}{m} [\sin(\frac{2\pi mn}{N}) - \sin(\frac{2\pi m(n - N_A)}{N})] \qquad (1)$$

where N is the total number of atomic planes in a superlattice period, N_A is the number of A-atom planes in that period and β, the damping factor. Clearly $\beta = 0$ is the square-wave case and, in the limit of large β, the lattice spacing becomes that of an AB alloy. A similar equation can be written for the concentration of A and B atoms. Figure 3 shows an example of such an analysis for an Er/Y superlattice of 23.5 Er planes and 19 Y planes, repeated 100 times. We write this as $[Er_{23.5}|Y_{19}]_{100}$. For this superlattice, the composition changes abruptly within two atomic planes on each side of the interface, while the lattice spacing is modulated gradually. A significant difference between strain and composition profiles suggests that some degree of plastic deformation exists in the superlattice. In the analysis of magnetic data a damped wave model is used to determine the lattice parameter, composition, and the phase of the magnetic wave at each layer of the superlattice
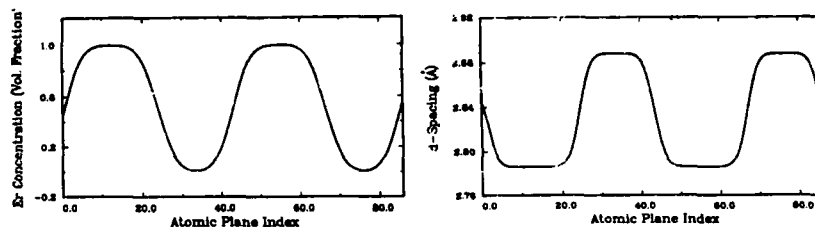
Fig. 3. Er concentration profile and d-spacing for $\{Er_{23.5}|Y_{19}\}$ from x-ray data.

Modification of Magnetic Phases due to Epitaxy

Both Dy and Er are ferromagnetic at low temperatures, Dy below 85 K and Er below 19 K [15]. In Dy, the magnetic moments are confined to the a-b (hexagonal) plane, forming a spiral at high temperatures that transforms into a ferromagnetic state with the magnetization along the easy a-axis. The transition is accompanied by a substantial orthorhombic distortion of approximately 0.5%. This distortion arises primarily from single-ion terms in the magnetoelastic energy [16] that come into play only in the ferromagnetic state; these are generally agreed to drive the first-order transition at 85 K. In Er, the high temperature phase is c-axis modulated (CAM), sinusoidal between 85 K and 50 K, and square-wave below 50 K. The ferromagnetic phase is conical. A basal-plane spiral, persisting to low temperature, appears along with the squaring up of the CAM structure. In Er, two-ion terms in the magnetoelastic energy dominate [17,18]. No ferromagnetic phase of either element is observed in films or superlattices grown epitaxially on Y, regardless of the orientation of the growth plane.

Unless the superlattice sample or thin film undergoes plastic deformation, it is not possible for the basal plane to distort. An epitaxial Dy sample cannot thereby gain the approximately 3 K per atom of magnetoelastic energy at 85 K that in the bulk overcomes the exchange energy of the spiral phase [16]. To calculate the effect of epitaxy, we force the basal plane distortion to be zero (completely clamped case) or allow the possibility of mobile dislocations at the Nb-Y interface by elastically coupling the Dy portion of the sample to the Y. This is accomplished by writing [8,19] the elastic contributions to the magnetoelastic energy in the form

$$\frac{1}{2}c_{11}\{(e_{xx}^2+e_{yy}^2)+r_z[(e_{xx}-e_o)^2+(e_{yy}-e_o)^2]\}$$ (2)

When the parameter r_z is large, the strain ϵ_{xx} is "clamped" at ϵ_o. For Dy at 10 K, the magnetoelastic energy gain in the clamped case is reduced from 4 K/atom to 2 K/atom, insufficient to produce spontaneous ferromagnetism. However, a field B = $k_B(2K)/10\mu_B$ = 3 kG, applied along the easy axis, provides the missing energy, and drives the superlattice ferromagnetic. The c-axis is unconstrained in these superlattices, and may contract. The c-axis magnetostriction does occur as the sample is magnetized, and the magnetoelastic strain persists when the field is removed; the ferromagnetic state is metastable. The fully clamped model predicts a c-axis distortion of 6×10^{-4}, in good agreement with the 9×10^{-4} observed.

Because the two-ion terms are more important in Er, the epitaxial constraint plays a different role. The two-ion terms depend on the relative orientation of spins on

different atomic planes and lead to a difference in the magnetoelastic energy between the CAM (AF) phase and cone (F) phase given by [5]

$$E_f - E_{af} = K_o + \frac{(K^a - K^f)}{2c_{13}}(K_z^a - c_{33}\bar{e}_{zz}^a),$$ (3)

where $\bar{e}_{zz}^a$ is the strain of the superlattice or film relative to the c-axis lattice parameter of the CAM phase, extrapolated to low temperatures, and K_o and $\hat{K}$ are related to the magnetoelastic coupling constants K_x, K_y, and K_z and the elastic constants c_{13} and c_{33}. The exchange barrier is, in this case, 1.01 J/cm^3 (2.25 K/atom) which must be overcome by the critical field for ferromagnetism, H_c. Using bulk Er parameters in Eq. (3), we find predict that the critical field in the strongly clamped limit is given by $\Delta\mu H_c$ = (1.5 + 460 ϵ_{zz}^a) J/cm^3, where $\Delta\mu$ is the difference between the saturation magnetic moment and that in the CAM structure. In Fig. 4 we plot the measured H_c vs the measured c-axis strain for Er superlattices and films grown on Y. Even films as thick as 960 nm are clamped at values of the strain too small to permit the spontaneous appearance of ferromagnetism in zero field.
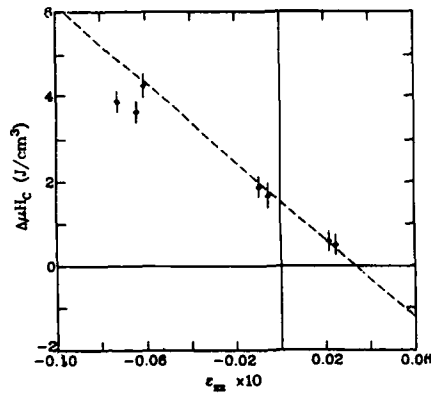
Fig. 4. Measured magnetic energy between c-axis modulated state and ferromagnetic state versus measured c-axis strain for Er superlattices and films. Dashed line is the result of the magnetoelastic calculation. (From Ref. 5)

A related analysis was carried out for b-axis grown Dy films and Dy/Y superlattices by Tsui, et al.[12]. The observed temperature dependence of the spiral angle from neutron scattering (see below) was used to estimate the exchange barrier as a function of temperature. When combined with the strong-clamping magnetoelastic model, good agreement between observed and calculated critical fields is obtained.

The results in Fig. 4 and data in Table I motivate the use of Lu as buffer layer for film growth and as interlayer for superlattices. Preliminary results show that Er films grown on Lu are strained only for thicknesses less than 800 Å. The thinner films show spontaneous ferromagnetism at or slightly above 20 K, comparable to bulk values, while T_C for thicker samples follows the trend of the Er/Y data when plotted on Fig. 4. Superlattices of Dy/Lu have much different properties than either the bulk or other superlattices, and will be discussed below.

Propagation of Order in Superlattices

It is now well established that magnetic order in superlattice structures can propagate even across non-magnetic metals such as Cu. This is generally explained in terms of the indirect exchange interaction in which the conduction electrons of the non-magnetic metal are polarized by the magnetization of the adjacent material [20]. For simple metals, the polarization oscillates with a period $\lambda_{RKKY} \sim 1/2k_F$, where $2k_F$ is the Fermi sphere diameter, and decays as $(\lambda_{RKKY}/r)^3$. These are commonly known as Rudermann-Kittel-Kasuya-Yoshida (RKKY) oscillations. In metals with more complex band structures, particularly regions in which electron and hole surfaces are nearly parallel, the oscillations can be of large amplitude, decay slowly, and have characteristic wavelengths that are considerable larger than λ_{RKKY}. This is related to incipient spin density wave (SDW) behavior. Yttrium and lutetium, with the band structures [21] of the heavy rare earths but no 4f moments, fall into this latter category. The oscillating spin polarization of the conduction electrons of the intervening material provides the coupling between magnetic layers. Recently, hybridization effects have been argued to play an important role in the long-period effects observed in Fe-Cu multilayers [22].

This simple picture must be modified for rare-earth/yttrium and lutetium superlattices. The spiral and CAM phases of the rare earth persist in the superlattices, and for c-axis structures propagate over as many as 13 bilayers. This can be readily seen in neutron scattering spectra. A simple spiral magnetic structure, in Dy for example, results in the appearance of magnetic satellites $Q_{002} \pm q_{mag}$, where Q_{002} is the reciprocal lattice vector of the (002) nuclear Bragg peak and q_{mag} is the wavevector of the spiral, parallel to the c* axis. In the superlattice structure, the Bragg peaks develop satellites spaced by $2\pi/\Lambda$ around the main Bragg peak, and each of these has a pair of magnetic satellites. An example is shown in Fig. 5 for a Dy/Y superlattice. The
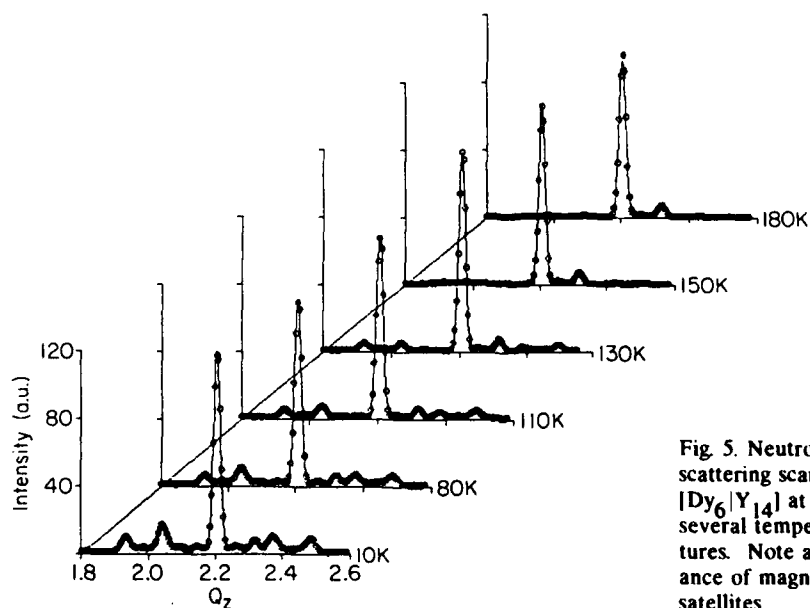
Fig. 5. Neutron scattering scans for $[Dy_6|Y_{14}]$ at several temperatures. Note appearance of magnetic satellites

asymmetry of the intensity arises because the magnetic intensity is almost entirely due to the Dy layer. The actual positions of the magnetic peaks determine the total phase advance in each bilayer while the peak in the envelope of the intensity is fixed by the phase advance in the Dy layer alone. From data such as these, we can deduce the phase advance (turn angle) for each component of the superlattice.

The analysis of phase advance for the various superlattices leads to the following conclusions: i) The turn angle per atomic layer for Y is always $51 \pm 1°$; ii) the temperature dependence of the turn angle for both Dy and Er superlattices is weaker than in the bulk, with the turn angle at a given temperature always larger in the superlattice; iii) the turn angle in Dy is larger for b-axis samples, both films and superlattices, than for c-axis samples of the same thickness. This is summarized in Fig. 6 for several superlattices; a c-axis $[Dy_{16}|Y_9]$ superlattice has a turn angle of $30°$ /atomic layer at low temperatures.
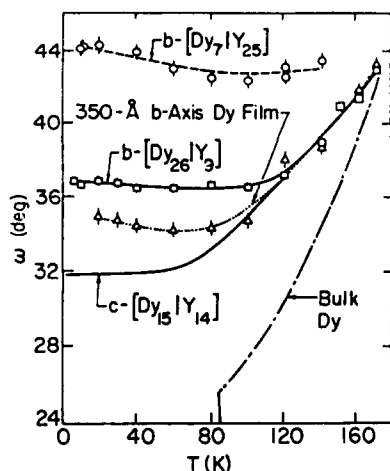
Fig. 6. Temperature dependence of the spiral turn angle per atomic layer for various c-axis-grown and b-axis grown Dy structures. Data for bulk Dy are shown for comparisons. (From Ref. 12)

The $51°$/plane turn angle in Y reflects a nesting feature in the yttrium band structure. Indeed, a variety of rare-earth/yttrium alloys order as spiral phases with this turn angle at low temperatures. However, the appearance of the long-range spiral and CAM order occurs at temperatures only slightly below the bulk ordering temperature, as may be seen in Fig. 5. While the ordering temperature does not decrease substantially as the thickness of the intervening Y increases, the coherence length is reduced. This length, deduced from the sharpness of the magnetic neutron scattering peaks, is shown in Fig. 7 for a number of Dy/Y and Er/Y superlattices. For the c-axis samples, the coherence decreases roughly inversely with the Y-layer thickness. That the ordering temperature is unchanged suggests that as order is developed within each rare-earth layer, magnetic polarization through the Y brings successive layers into coherence, both in terms of the phase of the magnetization wave and, in the case of spiral order, its handedness. As this coupling is reduced by increasing the Y thickness, order must be more fully developed in each RE layer to provide the same effective coupling. Accompanying that increased order is an increase in anisotropy energy, providing energy barriers to the alignment of successive RE layers that ultimately interrupt the spiral or CAM structure.

The nesting features of the yttrium Fermi surface produce a response function that is strongly anisotropic [21]. A magnetic moment embedded in Y gives rise to a

slowly decaying oscillation in the magnetic polarization along the c-axis, but a rapid, monotonic decay in the basal plane [10]. This strong anisotropy is evident in Fig. 7, where the b-axis multilayers (squares) are seen to have much shorter coherence lengths than their c-axis counterparts. In fact, the coherence in these samples is limited to the thickness of a single Dy layer. Similar results have recently been obtained on b-axis Gd/Y superlattices. The alternation of ferromagnetic and antiferromagnetic layers is observed as in the c-axis samples. However, the fields required to magnetize the antiferromagnetic samples are very small ($\approx$ 100 Oe), comparable with those expected for magnetic dipole interactions between successive Gd layers. Superlattices layers in the b-axis growth geometry are completely decoupled.
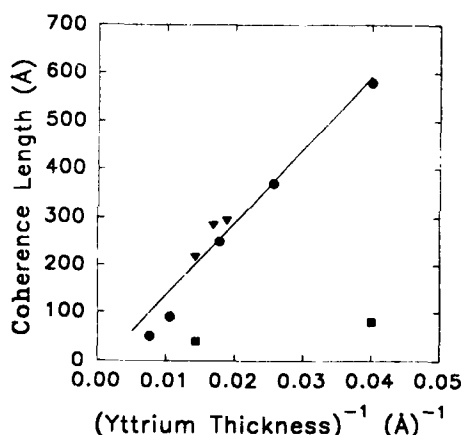
Fig. 7. Magnetic coherence length of the spiral in c-axis Dy (circles), c-axis Er (triangles) and b-axis Dy (squares) superlattices vs the inverse of the intervening Y layer thickness.

As noted above, the lattice mismatch between yttrium and the heavy rare earths compresses the basal plane and thereby suppresses the ferromagnetic transition. This motivates the use of Lu as base and intervening element. Indeed, Er films grown on Lu show a small enhancement of T_C when grown as strained layers. However, a dramatic change occurs for Dy/Lu superlattices. The spiral phase appears just below the bulk Neèl temperature. However, at temperatures as high as twice the bulk Curie temperature, the Dy layers become ferromagnetic, with successive layers either ferromagnetically or antiferromagnetically aligned. Fig. 8 shows a comparison of the high temperature and low temperature structure of $[Dy_x|Lu_y]$ in the spiral and antiferromagnetic phases. The appearance of superlattice lines between the structural satellites is the signature of oppositely aligned ferromagnetic Dy layers. The antiferromagnetic state is accompanied by a rhombohedral distortion at low temperature with no sign of plastic deformation. The dependence of the alignment on the Lu layer thickness and the nature of the rhombohedral distortion are currently under investigation.

Effect of Magnetic Fields

Because superlattice samples do not become ferromagnetic at low temperatures, it is possible to study the various intermediate magnetic states that appear in applied fields. Er/Y superlattices have been studied in some detail, and compared with unpublished magnetization data on bulk Er [23]. The magnetic field favors commensurate states with net moments. We follow the notation used by Gibbs, et al.
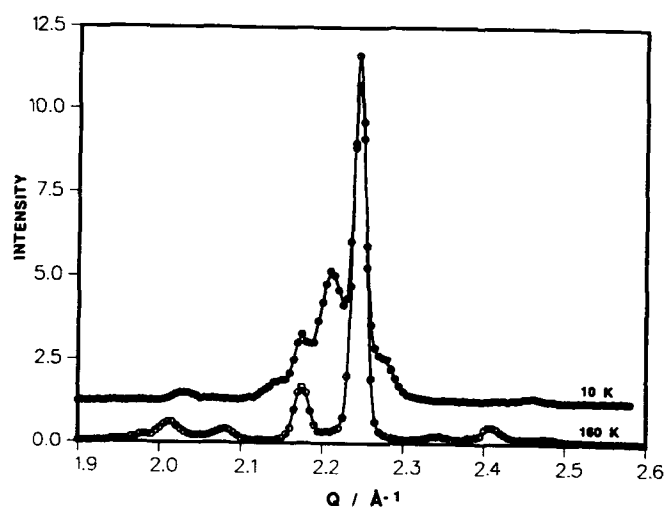
Fig. 8. Neutron diffraction results on a Dy/Lu superlattice at 160 K, just below the onset of the spiral phase and at 10 K, where the Dy blocks have become ferromagnetic, but are arranged antiferromagnetically along the growth axis, evidenced by new peaks between each structural satellite. A residual spiral peak persists at 10 K.
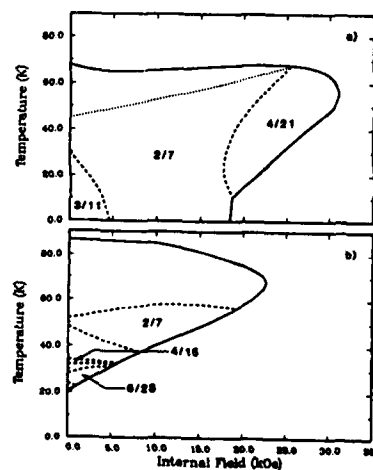
Fig. 9 Phase diagram an Er-Y superlattice (a) and of bulk Er (b) as deduced from magnetization data [23], magnetic x-ray scattering [24], and neutron scattering data in applied fields.

104
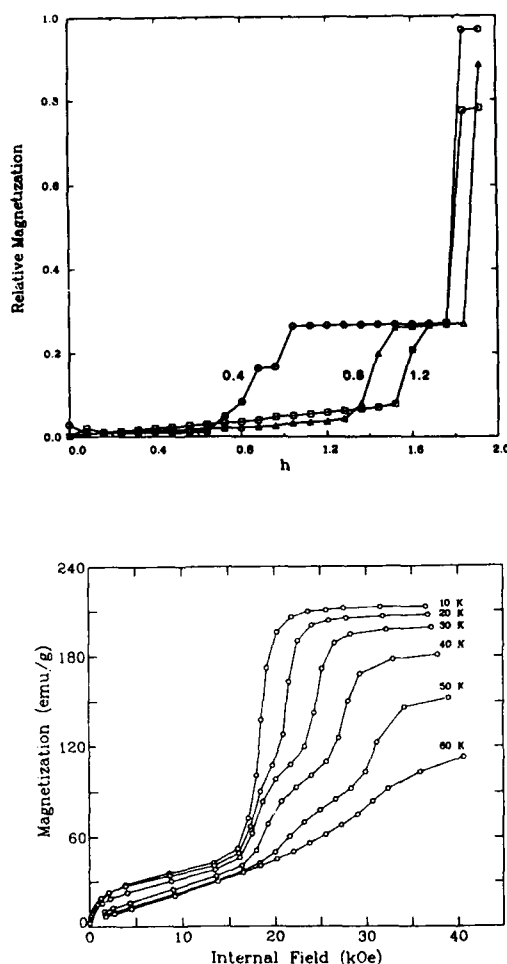
Fig. 10. a) ANNNI model simulation of the magnetization for $p = 1.5$. b) Magnetization of an $|Er_{23.5}|Y_{25}|$ superlattice.

[24], in which the states are labeled by twice the number of π phase changes in a magnetic unit cell. Hence, the 2/7 state has one phase reversal in a seven-plane cell, or four up spins and three down spins per magnetic cell. Clearly, this state has a net moment of 1/7 the saturation value. Similarly, the 1/4 state has a single phase reversal in an 8-plane cell and no net moment. Fig. 9 shows the phase diagram of $|Er_{13.5}|Y_{25}|$ in applied fields as compared with the phase diagram for bulk Er deduced from zero field x-ray scattering and magnetization data.

An intriguing aspect of the magnetic data is in the approach to saturation. The magnetization curves of epitaxial Er/Y superlattices and films with the field normal to the growth plane show a break at a critical field. Assuming that the demagnetizing factor $4\pi N$ has the value $N = 1$ expected for thin samples, we find that the magnetization is double valued. Single valuedness requires that the demagnetization factor be reduced for more strained samples. For the most strained samples, N approaches the value for spherical samples. One explanation is that the sample is magnetically separated into columns whose width decreases as the lattice strain increases. No such reduction in transverse magnetic coherence is observed in neutron scattering.

Alternatively, surface anisotropy might favor ferromagnetic alignment over the squared CAM structure, thereby reducing the effective demagnetization factor. This issue remains poorly understood.

As described above, the magnetoelastic model for the suppression of the ferromagnetism agrees quantitatively with experiment. Can it also explain reduced temperature dependence of the turn angle? We have explored this in the case of Er superlattices and films in the context of the antiferromagnetic next-nearest-neighbor Ising (ANNNI) model in a field [25]. This is the Ising analog of the usual three-plane model [26] in which the wavevector dependent exchange energy is written as

$$J(Q) = 4J_o + 2J_1\cos(qd) + 2J_2\cos(2qd), \tag{4}$$

where J_o, J_1, and J_2 are the same-plane, neighboring-plane, and next-neighbor plane exchange constants, respectively; d is the lattice constant. By including the dependence of the magnetoelastic energy on turn angle $\omega \equiv qd$, the interplanar exchange energies become temperature dependent. This causes the ratio $p = -J_2/J_1$, which determines the states of the system, to vary with temperature. This simple approach actually predicts an increase in the turn angle from its value at T_N for Er films and superlattices [27].

The ANNNI model has also been useful in understanding the sequence of field-induced phase transitions. An iterative calculation was carried out to minimize the total magnetic energy of a system of 264 layers as a function of temperature and magnetic field. Fig. 10a gives the magnetization curve of the ANNNI model for $p = 1.5$ at various $t = k_B T/J_1$ as a function of $h = \mu H/J_1$. For comparison, the magnetization of $|Er_{13.5}|Y_{25}|$ plotted in a similar form in Fig. 10b.

Discussion and Acknowledgements

Epitaxially grown superlattices and films have vastly increased the variety of magnetic systems that can be prepared. It makes possible "exchange spectroscopy," by which the strength and anisotropy of the exchange interaction can be measured by varying the separation of magnetic layers, the composition of the intervening material, and the growth orientation. This is not possible through alloying. The regularly occurring interfaces can be readily characterized by scattering techniques, and promise new insights into the magnetic scattering and the sources of coercivity. Epitaxial constraints point up sharply the importance of magnetostrictive effects in the rare-earths, and give us new tools to control magnetic phases. In short, epitaxy opens a new era in magnetism in which magnetic materials can be tailored on the atomic scale to permit detailed study of magnetic properties and, eventually, to produce technically useful new magnetic materials.

References

1. S.M. Durbin, J.E. Cunningham, M.E. Mochel and C.P. Flynn, J. Phys. F 11, L223 (1981).
2. J. Kwo, D.B. McWhan, M. Hong, E.M. Gyorgy, L.C. Feldman, and J.E. Cunningham, in Layered Structures, Epitaxy, and Intefaces, edited by J.H. Gibson and L.R. Dawson, (Mater. Res. Soc., Pittsburgh, 1985) p. 509.
3. M.B. Salamon, S. Sinha, J.J. Rhyne, J.E. Cunningham, R.W. Erwin, J. Borchers, and C.P. Flynn, Phys. Rev. Lett. 56, 259 (1986).
4. M. Hong, R.M. Fleming, J. Kwo, L.F. Schneemeyer, J.V. Wasczak, C.F. Majkrzak, D. Gibbs, and J. Bohr, J. Appl. 61, 4052 (1987).
5. J.A. Borchers, M.B. Salamon, R. W. Erwin, J.J. Rhyne, R. R. Du, and C.P. Flynn, Phys. Rev. 43, 3123 (1991).
6. J. Bohr, D. Gibbs, J.D. Axe, D.E. Moncton, K.L. D'amico, C.F. Majkrzak, J. Kwo, M. Hong, C.L. Chien, and J. Jensen, Physica B 159, 93 (1989).
7. J. Kwo, E.M. Gyorgy, D.B. McWhan, M. Hong, F.J. di Salvo, C. Vettier, and J.E. Bower, Phys. Rev. Lett. 55, 1402 (1985); C.F. Majkrzak, J. Kwo, M. Hong, J.W.

106

Cable, D.B. McWhan, Y. Yafet, J.V. Waszczak, and C. Vettier, Phys. Rev. Lett. **56**, 2700 (1986).

8. R. W. Erwin, J.J. Rhyne, M. B. Salamon, J. A. Borchers, S. Sinha, R. R. Du, J.E. Cunningham, and C.P. Flynn, Phys. Rev. B **35**, 6808 (1987).

9. R.S. Beach, J.A. Borchers, R.W. Erwin, A. Matheny, C.P. Flynn, J.J. Rhyne, M. B. Salamon, J. Appl. Phys. (in press).

10. R. R. Du, F. Tsui, and C.P. Flynn, Phys. Rev. B **38**, 2941 (1988).

11. C.P. Flynn, F. Tsui, M. B. Salamon, R.W. Erwin, J.J. Rhyne, J. Phys.:Condens. Matter **1**, 5997 (1989); C.P. Flynn, F. Tsui, M. B. Salamon, R.W. Erwin, J.J. Rhyne, *Magnetic Properties of Low-Dimensional Systems II*, edit by L. M. Falicov, F. Mejía-Lira, and J.L. Morán-López (Springer Verlag, Berlin, 1990) p. 128.

12. F. Tsui, C.P. Flynn, M. B. Salamon, R.W. Erwin, J.A. Borchers, J.J. Rhyne, Phys. Rev. B (in press).

13. C.P. Flynn, et al. (to be published)

14. *Magnetic Properties of Rare-Earth Metals*, edited by R.J. Elliott (Plenum, London, 1972) p. 5

15. W. C. Koehler in Ref. 14, Ch. 3

16. B.R. Cooper, Phys. Rev. **169**, 281 (1968); W.E. Evenson and S.H. Liu, Phys. Rev. **178**, 783 (1969).

17. M. Rosen, D. Kalir, and H. Klimker, Phys. Rev. **8**, 4399 (1973).

18. J. Jensen, J. PHys. F **6**, 1145 (1976).

19. R.W. Erwin, J. J. Rhyne, J. Borchers, M. B. Salamon, R. Du, and C.P. Flynn, MRS Symp. Proc. **166**, 133 (1990).

20. Y. Yafet, J. Kwo, M. Hong, C.F. Majkrzak, and T. O'Brien, J. Appl. Phys. **63**, 3453, (1988).

21. S.H. Liu, R.P. Gupta, and S.K. Sinha, Phys. Rev. B **4**, 1100 (1971).

22. Y. Wang, P.M. Levy, and J.L. Fry, Phys. Rev. Lett. **65**, 2732 (1990).

23. W.J. Gray and R.H. Spedding, Iowa State Report, IS(2044), 1988, (unpublished).

24. D. Gibbs, J. Bohr, J.D. Axe, D.E. Moncton, and K.L. D'Amico, Phys. Rev. B **34**, 8182 (1986).

25. C.S.O. Yokoi, M.D. Continho-Filho, and S.R. Salinas, Phys. Rev. B **24**, 4047 (1981).

26. B. R. Cooper in Ref. 14, Ch. 2

27. J.A. Borchers, M. B. Salamon, R.W. Erwin, J. J. Rhyne, G.J. Nieuwenhuys, R.R. Du, C.P. Flynn, R.S. Beach, (preprint, 1991).

MULTIPLET FINE STRUCTURE OF THE Gd AND Tb 5P LEVELS

Dongqi Li and P.A.Dowben
Department of Physics, Syracuse University, Syracuse, NY 13244-1130
M.Onellion
Department of Physics, University of Wisconsin, Madison, WI 53706

ABSTRACT

Fine structure is observed in the photoemission of Gd and Tb 5p levels as a result of multiplet splitting. These splittings are the consequence of different J final states that occur as a result of interactions with partly filled 4f and/or 5d levels.

INTRODUCTION

Photoemission from shallow core levels has been employed to probe magnetic ordering[1-7]. Recently we have investigated the rare earth 5p levels in different photoemission geometries to study rare earth thin film magnetism[3,4]. A model for the photoemission shallow core level fine structure is important to the understanding of this measure of magnetic ordering, the p-level anisotropy[3].

Rare earth metals are well known for exhibiting pronounced multiplet splittings of the 4d levels[8-11], 4f levels[10, 12-15] and 4s and 5s levels[10, 16-17]. Here we report, for the first time, the multiplet splittings of the Gd and Tb 5p levels and provide an explanation for their origin. As expected, the 5p photoemission fine structure due to multiplet splittings is a result of the unfilled 4f and 5d levels. We have undertaken our preliminary analysis by considering $4f^7$ only for convenience. Contributions from the 5d levels would not be expected to affect the number of multiplets, though this may seriously affect the multiplet oscillator strengths.

EXPERIMENTAL

The angle resolved photoemission experiments were carried out on a system described elsewhere[2] on a 6m toroidal grating monochrometer at the Synchrotron Radiation Center in Stoughton, Wisconsin. The photoelectrons were collected normal to the surface. The incident light of 37 or 70 degrees off normal was used to provide larger portion of light with its vector potential parallel to or perpendicular to the thin film (s- or p- polarization respectively). The combined energy resolution for photoemission was 0.25 eV.

Gd and Tb were deposited at room temperature onto W(110) and Ni(111) substrates respectively. The methods for preparing clean rare earth films have been described previously[1,2]. For Gd/W(110), the base pressure was normally 7×10^{-11} torr and the maximum during the deposition was 2×10^{-10} torr, while for Tb/Ni(111), the pressure was less than 5×10^{-10} torr during the evaporation. The thickness was determined by a quartz crystal oscillator. The relative thickness has small error of <2% while the absolute value can only be taken as nominal thickness. 1-3 monolayer Gd films on W(110) show sharp LEED pattern indicating the epitaxial growth with (0001) orientation of the hexagonal Gd overlayer. Tb/Ni(111) films were not well-ordered.

108

RESULTS

Photoemission spectra of the Gd 5p features were taken at 50eV and 60 eV for Gd
films on W(110) of different thicknesses. Fig. 1a is one of the typical spectra which include
two main features with binding energies of about 21 and 28 eV below the Fermi energy.
For the films thicker than one monolayer, 21 eV photoemission feature exhibits fine
structure as shown in Fig. 1a. The envelope can be fitted well with four Gaussian peaks
with binding energies of 20.3±0.1 eV, 20.9±0.1 eV, 22.0±0.2 eV, and 23.4±0.3 eV(Fig.2a).
Gd valence band spectra (not shown here and discussed in detail elsewhere[18]) shows 5d
bands at 0.2±0.1 eV and 1.3±0.1 eV. The 4f levels are observed at 8.6±0.1 eV. It should
be noted that the FWHM of the 4f is 1 eV and that of 5d about 0.5 eV.

The 5p levels of Tb/Ni(111) are shown in Fig. 1b. There are two main features with
binding energies of 22 and 28 eV respectively. As with Gd, the lower binding energy
feature contains several peaks. The binding energies of these fine structures are 20.7 eV,
21.6 eV, 22.7 eV, and 23.7 eV, as seen in Fig. 2b.
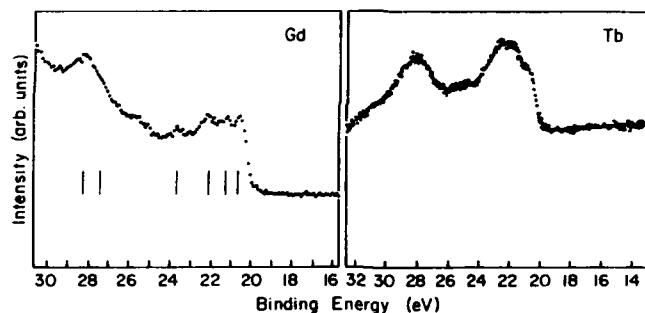
Fig. 1. (a) A typical Gd 5p level photoemission spectrum with photon energy of
50 ev. (b) Tb 5p level photoemission spectrum with the photon energy of 60 ev.
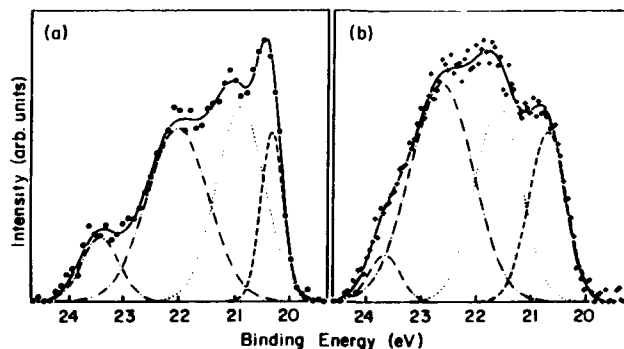
Fig. 2. The lower binding energy envelopes in Fig. 1. are fitted with four Gaussian
functions after the linear background subtraction. The solid lines are the fitting
result while the other lines showing the individual Gaussian function.

DISCUSSION

The large energy separation (~7eV) of the two main features has been observed
and is considered a result of spin-orbit coupling[10,19]. This value for the spin-orbit Gd

5p coupling is larger than the calculated result of 4.0 eV for atomic Gd[20]. Spin-orbit coupling only predicts two features, i.e. $5p_{1/2}$ and $5p_{3/2}$, without any further detailed structure.

Since rare earth atoms have unpaired 4f and 5d electrons, multiplet structures, caused by the interaction between the core level photohole and those partly filled subshell, can have a strong influence on the core level spectra. Multiplet structures can be understood as a final state effect in photoemission. After one 5p electron is excited, the hole left over will have an electrostatic interaction (direct, i.e. Coulomb interaction and indirect, i.e. exchange interaction) with the electrons in unfilled subshells to form different final states. This effect has been well studied on filled s and p core levels of some transition metals and rare earth 4s, 5s, and 4f levels[15-17, 21-23]. Most of multiplet studies have only considered the exchange interaction between the unpaired spins which results in two main features characterized by the hole spin parallel or anti-parallel to that of the unpaired electrons. Configuration interactions were proven to be an important addition to this simple picture[23-24] and may cause further splitting in photoemission spectra. For s-levels, there is no spin-orbit interaction since they have no orbital momentum($l=0$). For p-levels($l=1$), spin-orbit interaction can be ignored only when it is much weaker than the exchange interaction between the hole and other electrons, that is, in L-S coupling limit.

With L-S coupling scheme, we can work out the possible multiplets for Gd. The ground state configuration of Gd atom is $4f^7 5s^2 5p^6 5d^1$. Since $5d^1$ is mainly polarized by 4f electrons, here we only write down the coupling of 5p hole and $4f(^8S_{7/2})$ electrons for convenience. The existence of $5d^1$ electrons should not affect the basic result of the following discussion as indicated later in this paper. Photoemission of one 5p electron leaves an ion in $5p^5 4f^7$ configuration, which is complementary to $5p^1 4f^7$ (one 5p hole and seven 4f electrons). Since $l=1$, $s=1/2$ for ^2P and $L'=0$, $S'=7/2$ for ^8S, L-S coupling of $5p^1(^2P)$ and $4f^7(^8S)$ results in $^7P_{4,3,2}$ and $^9P_{3,4,5}$ final states with $L=L'+l$, $L'+l-1$, ... , $|L'-l|$, $S=S'+s$, $S'+s-1$, ... , $|S'-s|$ and $J=L+S$, $L+S-1$, ... , $|L-S|$. Without considering spin-orbit coupling, the two main features should be assigned as ^7P and ^9P with the later one at the lower binding energy. If weak spin-orbit coupling exists, the degeneracy of different J values should be lifted and 21 eV feature should split to three features of $^9P_3$, $^9P_4$, $^9P_5$. Experimentally, we observe a four-fold splitting. Configuration interaction can cause further splitting of the photoemission features. Since ^9P term can only come from one configuration with all the spins of 5p hole and 4f electrons parallel, ^9P cannot further split and cannot exhibit fine structure beyond the three basic features. Since L-S theory predicts only three features and we observe four in our experiments(Fig.2), configuration interaction combined with L-S coupling scheme cannot be used to explain the observed data.

Alternatively, j-J coupling can also result in multiplet splitting. Gupta and Sen[25] considered spin-orbit coupling in their multiplet calculations of Mn^{2+} 2p and 3p levels and realized that spin-orbit coupling can be ignored for the Mn 3p levels but it is the major factor in determining the photoemission structure of the 2p levels. Their calculations are qualitatively confirmed by experiment[23]. In rare earth 5p levels, spin-orbit coupling is strong and is larger for the heavier rare earths than the light rare earths. With strong spin-orbit coupling, the two main features should be assigned as $5p_{1/2}$- and $5p_{3/2}$-based levels with the latter one at lower binding energy. The relatively weaker exchange interaction of 5p hole with 4f and 5d electrons will lift the J-degeneracy. The $j=3/2$ term couples with $^8S_{7/2}$ to form four terms of $(3/2, 7/2)_5$, $(3/2, 7/2)_4$, $(3/2, 7/2)_3$, and $(3/2, 7/2)_2$ since $J=J'+j$, $J'+j-1$, ... , $|J'-j|$. This is consistent with the four-fold splitting observed by

experiment. Since L-S coupling and j-J coupling should give out the same J-state energy order[26], we can assign the features with J quantum numbers as shown in Fig. 3. As Kowalczyk et al.[23] pointed out for Mn 2p levels, this splitting will result in an increase in the spin-orbit splitting, which could explain the increase of the splitting between the $5p_{1/2}$ and $5p_{3/2}$ levels (7 ev) compared with theoretical spin-orbit splitting calculation (4 ev).
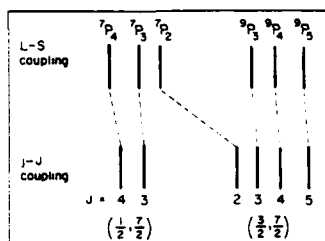
Fig. 3. The order of different J-terms in L-S and j-J coupling schemes

Whether L-S coupling or j-J coupling occurs is totally dependent on the strength of different interactions. It is not surprising that most s-level multiplets fit L-S coupling multiplet theory very well. For p-levels($l=1$), Mn 2p levels are better explained by j-J coupling while the 3p levels, with weaker spin-orbit coupling, agrees with L-S coupling qualitatively[23, 25]. Considering the magnititude of the two energy splittings caused by the two kinds of interaction (about 7eV and 1eV in our experiment), it is likely that a coupling intermediate between L-S and j-J occurs in the case of Gd 5p multiplets.

Several other effects may also considered as the possible origin of the 5p fine structure. Possible chemical shift, multiple valences, shake up or shake off effects can cause splittings in valence bands as well as in core levels. The necessary kinds of splittings are not observed, however, for the valence band[18] excluding these effects as the source of the shallow 5p core level fine structure in photoemission. Surface to bulk core level shifts have been observed in Gd 4f level of 0.5 eV[12]. We can expect a similar magnitude of shift for the 5p levels. This effect cannot explain the energy separation of at least 0.7 eV between 5p fine structure features and the observation of four, instead of two features in the $5p_{3/2}$ photoemission envelope.

The existence of magnetic field can also cause the lifting of degeneracy in $5p_{3/2}$ and also forms four features with $m_j = 3/2$, 1/2, -1/2, -3/2. This is, however, not likely to occur with a splitting as large as observed by experiment, nor can it explain the observed photoemission fine structure. This kind of magnetic field induced splitting should result in equal energy separations of $\Delta E = g\mu_B H$. This is not observed in the experimental results. Estimating the magnetic field necessary to produce an energy splitting shown in the experiments (~ 1 eV) with $\Delta E \sim \mu_B H$, we find $H \sim 10^8$ Gs. This is inconsistent with any reasonable external field produced by the rare earth film. If the field is produced by a magnetic dipole, the mean distance between the dipole and 5p electron should be about 10^{-10} cm. This is much smaller than the average distance between 4f and 5p or 5d and 5p electrons. Thus the local magnetic field produced by 4f and 5d magnetic moments cannot result in the observed photoemission fine structure of the rare earth 5p levels.

Possible crystal field effects has also been considered. Since Gd films show hexagonal structure, we treat $5p_{1/2}$ and $5p_{3/2}$ levels with a crystal double group based on D_6 point group(D_6') (Table I) similar to those derived by Tinkham[27] for cubic crystal. Comparing the character values of $p_{1/2}$ and $p_{3/2}$ levels with D_6' character table, we get
$$p_{1/2} \longrightarrow E_3$$

$$p_{3/2} \longrightarrow E_3 + E_5$$

This means that $5p_{1/2}$ should not split while $5p_{3/2}$ should split to two features. This effect itself cannot explain the four-fold splitting. Furthermore, since crystal field effect is basically electrostatic interaction caused by a periodically distributed charge density, it should be stronger for the outer levels. However, Gd 5d feature has only FWHM of 0.5 eV at normal emission. We conclude that crystal field effects do not play an important role in determining rare earth 5p fine structure, although we cannot eliminate crystal field contribution completely.

Table I. The character table of the crystal double group D'_6 (the first 9 lines) and the corresponding characters of the rotation groups D_J with $J=1/2$ and $J=3/2$ (the last 2 lines).

D'_6		E	R	C_2+RC_2	$2C_3$	$2RC_3$	$2C_6$	$2RC_6$	$3C'_2+3RC'_2$	$3C''_2+3RC''_2$
	A_1	1	1	1	1	1	1	1	1	1
	A_2	1	1	1	1	1	1	1	-1	-1
	B_1	1	1	-1	1	1	-1	-1	1	1
	B_2	1	1	-1	1	1	-1	-1	-1	-1
	E_1	2	2	-2	-1	-1	1	1	0	0
	E_2	2	2	2	-1	-1	-1	-1	0	0
	E_3	2	-2	0	1	-1	$\sqrt{3}$	$-\sqrt{3}$	0	0
	E_4	2	-2	0	1	-1	$-\sqrt{3}$	$\sqrt{3}$	0	0
	E_5	2	-2	0	-2	2	0	0	0	0
$j=1/2$		2	-2	0	1	-1	$\sqrt{3}$	$-\sqrt{3}$	0	0
$j=3/2$		4	-4	0	-1	1	$\sqrt{3}$	$-\sqrt{3}$	0	0

(left margin, rotated: irreducible representations of D'_6)

It should be noted that although we did not consider $5d^1$ electron in our multiplet analysis while writing out the final state terms, it is likely that 5d electrons have large contribution to 5p multiplets since they have the same principle quantum number. The j-J coupling of $5d^1(^2D_{5/2})$ and $5p^1(^2P_{3/2})$ results in four terms of J=4, 3, 2, and 1, which is also correspond to a four-fold splitting as we consider the coupling with 4f only. Further experiments and detailed calculations are needed to determine the portion of 5d contribution.

Tb has ground state configuration of $4f^8 5s^2 5p^6 5d^1$. This is similar to that of Gd though Tb has only six unpaired 4f electrons instead of seven in Gd. Most of the above discussion is valid for Tb. The fine structure can again be explained as multiplets under j-J coupling or intermediate coupling scheme.

CONCLUSION

We have observed the photoemission fine structure splitting the 5p levels for Gd and Tb. Our analysis suggests that multiplet structures arise as result of j-J coupling or intermediate coupling scheme. Since j-J coupling is more complicated than L-S coupling, more theoretical calculations considering spin-orbit coupling, exchange interaction, configuration interaction, and crystal field effects are necessary to fully understand this effect. Since the fine structure is caused by exchange interaction of the unpaired electrons, it has the potential to be used to study rare earth 4f and 5d unpaired spins and may give us some insights to many interesting problems such as local spin and mixed valence.

112

ACKNOWLEDGEMENTS

REFERENCES

1. D.LaGraffe, P.A.Dowben, and M.Onellion, Phys. Rev. B40, 970 (1989).
2. P.A.Dowben, D.LaGraffe, and M.Onellion. J. Phys. Cond. Matt., 1, 6751 (1989).
3. D.LaGraffe, P.A.Dowben, and M.Onellion, Phys. Lett. A147, 240 (1990).
4. P.A.Dowben, D.LaGraffe, Dongqi Li, A.Miller, Ling Zhang, L.Dottl, and M.Onellion, Phys. Rev. B43, 3171 (1991).
5. C.S.Fadley, in *Magnetic Properties of Low Dimensional Systems II*, Springer Proceeding in Physics, vol.50, Edited by L.M.Falicov, F.Mejia-Lira, and J.L.Moran-lopez, (Springer-Verlag, Berlin, 1990), p.36; Physica Scripta T17, 39 (1987).
6. B.Sinkovic and C.S.Fadley, Phys. Rev. B31, 4665 (1985).
7. B.Sinkovic, B.Hermsmeier and C.S.Fadley, Phys. Rev. Lett., 55, 1227 (1985).
8. C.S.Fadley and D.A.Shirley, Phys. Rev. A2, 1109 (1970).
9. S.P.Kowalczyk, N.Edelstein, F.R.McFeely, L.Ley and D.A.Shirley, Chem. Phys. Lett., 29, 491 (1974).
10. B.D.Padalia, W.C.Lang, P.R.Norris, L.M.Watson, and D.J.Fabian, Proc. R. Soc. Lond., 354, 269 (1977).
11. J.L.Dehmer, A.F.Starace, U.Fano, J.Sugar, and J.W.Cooper, Phys. Rev. Lett., 26, 1521 (1971).
12. R.Kammerer, J.Barth, F.Gerken, A.Flodström and L.I.Johansson, Solid State Commun., 41, 435 (1982).
13. Y.Baer and G.Busch, J. Electron. Spectrosc. Rel. Phenom., 5, 611 (1974).
14. J.K.Lang, Y.Baer and P.A.Cox, J. Phys. F11, 121 (1981).
15. P.A.Cox, J.K.Lang and Y.Baer, J. Phys. F11, 113 (1981).
16. R.L.Cohen, G.K.Wertheim, A.Rosenewaig and H.J.Guggenheim, Phys. Rev. B5, 1037 (1972).
17. F.R.McFeely, S.P.Kowalczyk, L.Ley and D.A.Shirley, Phys. Lett. 49A, 301 (1974).
18. Dongqi Li, C.Hutchings, P.A.Dowben, Rong-Tzong Wu, C.Hwang, M.Onellion, B.Andrews and J.L.Erskine, in preparation.
19. G.K.Wertheim, R.L.Cohen, A.Rosenewaig, H.J.Guggenheim, in *Electron Spectroscopy*, Edited by D.A.Shirley (Amsterdan: North Holland, 1972). p.813.
20. F.Herman and S.Skillman, *Atomic Calculations*, (Prentice-Hall, Englewood Cliffs, N.J., 1963).
21. C.S.Fadley, D.A.Shirley, A.J.Freeman, P.S.Bagus, J.V.Mallow, Phys. Rev. Lett., 23, 1397 (1969).
22. B.Hermsmeier, C.S.Fadley, M.O.Krause, J.Jimenez-Mier, P.Gerard, S.T.Manson, Phys. Rev. Lett., 61, 2592 (1988).
23. S.P.Kowalczyk, L.Ley, F.R.McFeely and D.A.Shirley, Phys. Rev. B11, 1721 (1975).
24. P.S.Bagus, A.J.Freeman and F.Sasaki, Phys. Rev. Lett., 30, 850 (1973).
25. R.P.Gupta and S.K.Sen, Phys. Rev. B10, 71 (1974); Phys. Rev. B12, 15 (1975).
26. H.E.White, *Introduction to Atomic Spectra*, (McGraw-Hill Book Company, 1934).
27. M.Tinkham, *Group Theory and Quantum Mechanics*, (McGraw-Hill Publishing Company, 1964), p.77.

REFLECTIVITY AND GRAZING ANGLE DIFFRACTION OF POLARIZED NEUTRONS

J.F. ANKNER*, C.F. MAJKRZAK*, D.A. NEUMANN*, A. MATHENY**, AND C.P. FLYNN**
*Materials Science and Engineering Laboratory, National Institute of Standards and Technology, Gaithersburg, MD 20899
**Department of Physics and Materials Research Laboratory, University of Illinois at Urbana-Champaign, Urbana, IL 61801

ABSTRACT

Using polarized-neutron reflectivity, one can determine the layer-averaged magnetic structure of films and multilayers with exquisite precision. By employing the closely related phenomenon of grazing-angle diffraction, it is possible to obtain information about the in-plane structure in interfacial layers some tens of Ångstroms thick. We have used polarized-beam methods to study the Y/Gd interface using both reflectivity and grazing-angle diffraction and discuss the status of these experiments.

INTRODUCTION

In response to intense fundamental and technological interest in surface and interfacial magnetism, there have evolved a number of techniques for studying the magnetic structure of films and multilayers. By employing the appropriate scattering geometry, neutrons can be used to investigate these interfacial structures. Due to the dipole-dipole interaction of the neutron magnetic moment with any moments present in a sample, neutron diffraction has long been essential in the study of magnetism. Neutrons possess several unique advantages vis-à-vis such specifically surface-sensitive probes as spin-polarized low-energy electron diffraction (SPLEED) or spin-polarized photoemission—specifically, the capability of extracting quantitative information easily from the observed scattering and the ability to probe below the surface several surface layers and thereby to study buried layers. These same advantages to a certain extent also characterize the resonant magnetic interaction of x rays with matter, with the important exception that this interaction is considerably more complicated and as yet not fully characterized.

Since first being proposed as a magnetic interfacial probe,[1] neutron reflectivity and its instrumentation have undergone a gradual process of refinement and in recent years an explosive growth, due largely to the demands of researchers studying polymers. Not all of these instruments possess polarized-beam capability and the application of neutron reflectivity methods to the study of interfacial magnetism remains consequently rather undeveloped. In this paper, we would like first to review the principles of neutron reflectivity, then derive from these principles the theory of grazing-angle diffraction, and finally to discuss our latest results on the development of the technique and our view of future applicability. We hope by this to stimulate interest in these measurements and to bring to the attention of the magnetic thin-film community the utility of neutron methods.

REFLECTIVITY

Neutron reflectometry has for some years been employed in the study of magnetic thin films and multilayers.[2,3] The interaction of the neutron magnetic moment with magnetic materials is well characterized and a number of papers describe the details of this

114

interaction for the reflection geometry.[4-7] For specular reflectivity, the scattering problem can be solved using the one-dimensional Schrödinger equation (one-beam approximation of dynamical diffraction theory[8]) for the two spinor components of the neutron,

$$\frac{\partial^2 \psi^+(z)}{\partial z^2} + \left(\frac{Q^2}{4} - 4\pi\rho_{11}\right)\psi^+(z) - 4\pi\rho_{12}\psi^-(z) = 0, \tag{1}$$

$$\frac{\partial^2 \psi^-(z)}{\partial z^2} + \left(\frac{Q^2}{4} - 4\pi\rho_{22}\right)\psi^-(z) - 4\pi\rho_{21}\psi^+(z) = 0, \tag{2}$$

where $\psi^\pm$ are the wavefunctions for the two neutron spin states, $Q = |\vec{k}_{0s} - \vec{k}_0| = 2k_{0z}$ (the z components of $\vec{k}$ and $\vec{k}_s$ are equal in magnitude and opposite in direction for specular reflectivity, see Figure 1a), and ρ_{ij} are functions of the magnetic and nuclear scattering densities[9] of the sample. For the case of a ferromagnetically ordered sample and an incident neutron beam polarized parallel or anti-parallel to the sample moment,

$$\rho_{12} = \rho_{21} = 0, \tag{3}$$

$$\rho_{11} = N(b+p) = N[b_R + ib_I + \frac{\gamma}{2}r_0 g\langle J\rangle f(Q)], \tag{4}$$

$$\rho_{22} = N(b-p), \tag{5}$$

where N is the number density of scatterers, b is the neutron-nuclear scattering amplitude, composed of a real part b_R and an imaginary part (related to the length absorption coefficient: $b_I = \mu/2\lambda N$), both of which are constant for most elements at thermal neutron wavelengths. The magnetic scattering length p is proportional to the gyromagnetic ratio γ, classical electron radius r_0, Landé g factor, expectation value of angular momentum per atom $\langle J\rangle$, and the neutron magnetic form factor f.[10] The determination of nuclear and magnetic depth profiles for ferromagnets follows in a straightforward fashion from the considerations outlined above.

For the magnetic structure we have postulated, the Schrödinger equations (1) and (2) decouple and we can solve for the two spin states independently, subject to the

(a)   (b)
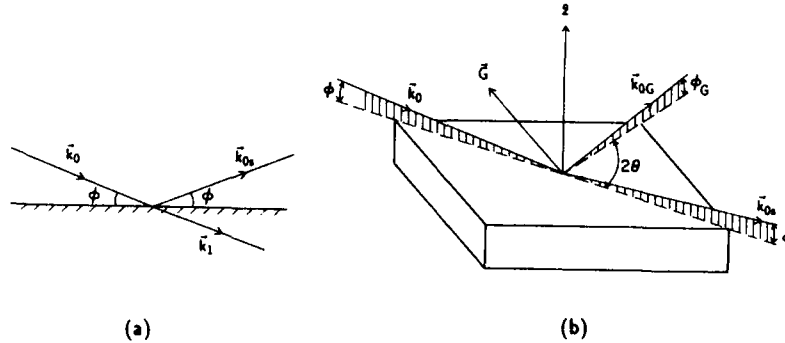
Figure 1. (a) Specular reflection geometry. A neutron beam of wavevector $\vec{k}_0$ strikes the sample at angle ϕ, exciting a specularly reflected $\vec{k}_{0s}$ and a refracted $\vec{k}_1$ beam. (b) Grazing-angle diffraction geometry. Simultaneously with the specular reflectivity process, the sample is oriented such that the components of $\vec{k}_0$ and $\vec{k}_{0G}$ in the plane of the sample surface satisfy the Bragg condition with reciprocal lattice vector $\vec{G}$.

continuity of $\psi^{\pm}(z)$ and $\partial\psi^{\pm}(z)/\partial z$ as boundary conditions. For the case of the single interface depicted in Figure 1a, the neutron wavefields consist of incident and reflected waves in vacuum and a transmitted wave in the reflecting medium,

$$\psi^{\pm}(z) = \begin{cases} e^{ik_0 z} + r_0^{\pm} e^{-ik_0 z} & z > 0 \\ t_1^{\pm} e^{ik_1^{\pm} z} & z \leq 0, \end{cases} \tag{6}$$

where, in the interests of optometry, we have omitted the z subscripts on the wavevectors. In the scattering process, only these components normal to the surface change, as described by Snell's Law,

$$k_1^{\pm} = \sqrt{k_0^2 - 4\pi N_1 (b_1 \pm p_1)}. \tag{7}$$

Using the two boundary condition equations, we can solve for $r_0^{\pm}$ to obtain the Fresnel reflectivity,[11]

$$r_0^{\pm} = \frac{k_0 - k_1^{\pm}}{k_0 + k_1^{\pm}}. \tag{8}$$

This formalism can be generalized to an arbitrary number of reflecting layers (using, for example, the Parratt recursion relation[12]). Simply insert the layers between vacuum (k_0) and substrate ($k_1 \Rightarrow k_N$) while obeying the boundary conditions at each successive interface. In this way, it is possible to construct a density profile of arbitrary complexity and calculate its specular reflectivity analytically.

We have developed a number of programs for modeling specular reflectivity. In order to demonstrate the first stages of this modeling process, consider the reflectivity data shown in Figure 2. The sample consists of an approximately 200 Å-thick (0001) yttrium film atop 5000 Å of (0001) gadolinium, both of which were grown by molecular-beam epitaxy on yttrium and niobium buffer layers on a 7.5 cm. (3 in.) sapphire substrate by A. Matheny and C.P. Flynn. The solid circles show the reflectivity of a neutron beam
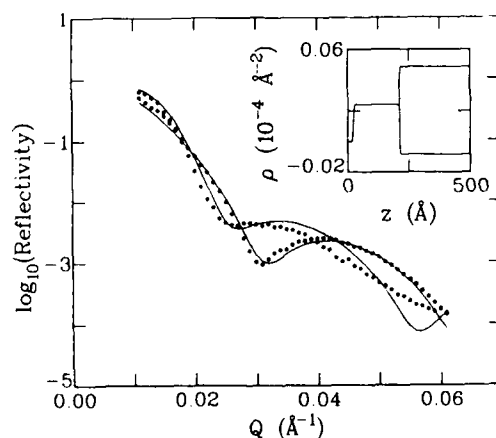
Figure 2. Polarized neutron reflectivity from Y/Gd. Solid circles represent data taken with neutrons polarized parallel to the sample moment, while the open circles are from anti-parallel neutrons. The inset shows the scattering density values for the two fits (solid lines): the first layer is vacuum ($\rho_0 = 0$), followed by 190 Å Y ($\rho_Y = 2.4 \times 10^{-6}$) and an effectively sem.-infinite Gd layer with $\rho_{Gd}^{+} = 4.8 \times 10^{-6}$ and $\rho_{Gd}^{-} = -0.8 \times 10^{-6}$.

polarized parallel to a 70 gauss field applied in the plane of the film; the open circles represent the reflectivity of the anti-parallel beam. We have described the experimental arrangement in an earlier work,[13] where we also observed that the magnetization profile in the Gd layer does not appear to be uniform up to the Y/Gd interface. However, for the purposes of the present discussion, let us attempt to fit the reflectivity data to such a uniform magnetization model. The solid lines in Figure 2 are fits calculated for the two polarization states, varying the thickness of the Y layer and the scattering density ρ of the Gd layer [recall equations (3), (4), and (5)]. The curves exhibit qualitative agreement with the data, but obviously the details need some work. Even from such a crude model, we can derive useful quantitative information, namely that the thickness of the yttrium layer is 190 ± 2 Å. One can also determine a value for the magnetic moment of the Gd bulk of 3.5 ± 0.8 μ_B $[p = (0.2695 \times 10^{-4} \text{ Å}/\mu_B)|\vec{\mu}|]$, but this value is highly model dependent and, given the rather poor fit, should not be given much weight. Indeed, the very fact that the agreement is so unsatisfactory indicates that a more complex model of the interface is required—we are currently constructing such a model.

GRAZING-ANGLE DIFFRACTION

Grazing-angle diffraction is a technique whereby one can observe in-plane order (as opposed to the z scanning of reflectometry) from near-surface and interfacial layers. The phenomenon of grazing-angle diffraction depends intimately on the total external reflection of neutrons (or x rays). The theory of this diffraction geometry, the distorted-wave approximation, has been worked out in a number of papers.[14-16] In this geometry, one uses the amplitude of the evanescent transmitted wave of the specular reflection process as the illuminating field for Bragg diffraction. In Figure 1b, the incident beam $\vec{k}_0$ strikes the sample surface near the total reflectivity threshold and excites a specularly reflected beam $\vec{k}_{0s}$, with the sample being oriented such that an in-plane reciprocal lattice vector $\vec{G}$ satisfies the Bragg condition with the in-plane components of wavevectors $\vec{k}_0$ and $\vec{k}_{0G}$: $(\vec{k}_{0G} - \vec{k}_0)_{\parallel} = \vec{G}$. The out-of-plane components control the depth of illumination,

$$Q_1^{\pm} = \sqrt{k_{0G}^2 - 4\pi N_1(b_1 \pm p_1)} + \sqrt{k_0^2 - 4\pi N_1(b_1 \pm p_1)}, \tag{9}$$

where, as in the reflectivity section, we have omitted the z subscripts on the wavevectors and are considering the case of a ferromagnetic layer with incident neutron moment oriented parallel or anti-parallel to an applied saturating field. The characteristic penetration depth is simply given by the inverse of the imaginary part of $Q_1^{\pm}$ and typically is of order 50-100 Å at the lowest angles of incidence and exit. Taking into account these refractive corrections, one proceeds with the calculation of the diffracted intensity according to conventional kinematical diffraction theory.[17] The resulting grazing-angle diffracted intensity is

$$I_{\pm}(\vec{Q}) = I_0 \left|t_1^{\pm}(k_0)\right|^2 \left|t_1^{\pm}(k_{0G})\right|^2 \left|F_1^{\pm}(\vec{Q}_{\parallel})\right|^2 \left|\frac{e^{iQ_1^{\pm}M_1 a_1} - 1}{e^{iQ_1^{\pm}a_1} - 1}\right|^2 \delta(\vec{Q}_{\parallel} - \vec{G}), \tag{10}$$

where the exponential terms result from the summation in the z direction, with M_1 being the number of atomic layers and a_1 their lattice spacing. The delta function expresses the Bragg condition with the in-plane wavevector components and $F^{\pm}$ is the structure factor for the crystal layer. The transmitted amplitudes $t^{\pm}$ are obtained in the same way as the reflectivity coefficient (8),

$$t_1^{\pm}(k) = \frac{2k}{k + [k^2 - 4\pi N_1(b_1 \pm p_1)]^{1/2}}. \tag{11}$$

Just as is the case for reflectivity, the above formulae can be derived for an arbitrary number of diffracting layers. In an earlier work[18] we carried out these calculations (note that the expression derived for the transmittivity factors t in that paper is incorrect—the correct prescription is to work out the analogue of the Parratt[12] relation for these terms).

We have used the same Y/Gd film as in the reflectivity measurements to demonstrate the use of polarized neutrons in grazing-angle diffraction. In previous papers, we described the apparatus used to carry out these measurements[18-20]. Figure 3 shows the grazing-angle intensity for spin parallel (solid) and anti-parallel (open) to the applied field at the sample. We have not as yet implemented a satisfactory fit program to analyze these data, but would like to show them merely to demonstrate the improving capability for performing grazing-angle measurements.

STATUS REPORT

We have attempted, in this report, to present the current status of neutron interfacial diffraction methods and to give some indication of current and future possibilities. For reflectivity, the instruments exist, an exact theory describes the data, and relatively sophisticated fitting routines are coming into use—all that is required are interesting problems and samples. Grazing-angle diffraction is a little farther from useful realization, both in hardware and software. The use of position-sensitive detectors[21] and the development of adequate data analysis tools in the near future should produce some nice experiments.
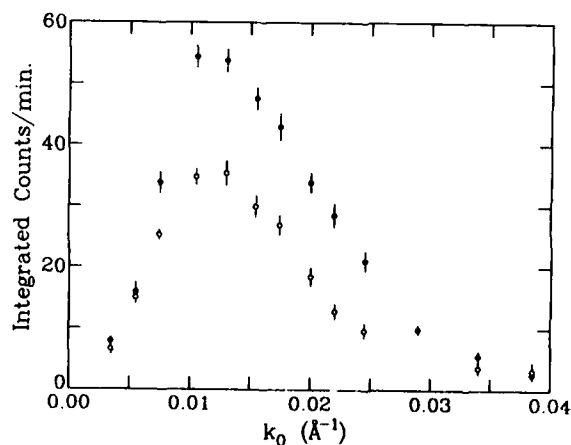
Figure 3. Polarized neutron grazing-angle diffraction from Y/Gd. The solid circles were measured with parallel-polarized neutrons and the open circles anti-parallel. The points represent values for fixed incident k_0, integrated over a broad range in k_{0G} and over a 2.2° width in diffraction angle θ (see ref. 18).

REFERENCES

1. G.P. Felcher, Phys. Rev. B 24, 1595 (1981).

2. C.F. Majkrzak and G.P. Felcher, Mater. Res. Bull. 15 (11), 65–72 (1990).

3. J. Penfold and R.K. Thomas, J. Phys. C 2, 1369 (1990).

4. P.J. Sivardiere, Acta Crystallogr. Sect. A 31, 340 (1975).

5. V.A. Belyakov and R.Ch. Bokun, Fiz. Tverd. Tela (Leningrad) 18, 2399 (1976) [Sov. Phys. Solid State 18, 1399 (1976)].

6. S.K. Mendiratta and M. Blume, Phys. Rev. B 14, 144 (1976).

7. G.P. Felcher, R.O. Hilleke, R.K. Crawford, J. Haumann, R. Kleb, and G. Ostrowski, Rev. Sci. Instrum. 58, 609 (1987).

8. H. Rauch and D. Petraschek, in Neutron Diffraction, edited by H. Dachs, Topics in Current Physics, Vol. 6 (Springer-Verlag, New York, 1978).

9. G.E. Bacon, Neutron Diffraction, 3rd ed. (Clarendon Press, Oxford, 1975.

10. G.L. Squires, Thermal Neutron Scattering (Cambridge University Press, 1978).

11. M. Born and E. Wolf, Principles of Optics, 6th ed. (Pergamon Press, Oxford, 1980).

12. L.G. Parratt, Phys. Rev. 95, 359 (1954).

13. J.F. Ankner, H. Zabel, D.A. Neumann, C.F. Majkrzak, A. Matheny, J.A. Dura, and C.P. Flynn, in Neutron Scattering for Materials Science, edited by S.M. Shapiro, S.C. Moss, and J.D. Jorgensen (Mater. Res. Soc. Proc. 166, Pittsburgh, PA, 1990), pp. 109-13.

14. G.H. Vineyard, Phys. Rev. B 26, 4146 (1982).

15. H. Dosch, B.W. Batterman, and D.C. Wack, Phys. Rev. Lett. 56, 1144 (1986).

16. H. Dosch, Phys. Rev. B 35, 2137 (1987).

17. B.E. Warren, X-ray Diffraction (Dover, New York, 1990).

18. J.F. Ankner, C.F. Majkrzak, D.A. Neumann, A. Matheny, and C.P. Flynn, Physica B, in press.

19. J.F. Ankner, H. Zabel, D.A. Neumann, C.F. Majkrzak, Phys. Rev. B 40, 792 (1989).

20. J.F. Ankner, H. Zabel, D.A. Neumann, C.F. Majkrzak, J.A. Dura, and C.P. Flynn, J. Phys. (Paris) 50 (7), 189-95 (1990).

21. K. Al Usta, H. Dosch, A. Lied, and J. Peisl, Physica B, in press.

STRUCTURAL AND MAGNETIC X-RAY SCATTERING MEASUREMENTS OF EPITAXIAL DY THIN FILMS

Michael F. Toney, David G. Wiesler, Brent D. Hermsmeier, and Robin F. Farrow.

IBM Research Division, Almaden Research Center, 650 Harry Road, San Jose, California 95120-6099.

ABSTRACT

We report structural and magnetic X-ray scattering measurements of a 2000Å thick Dy film, sandwiched by LaF_3 films on a GaAs(1̄1̄1̄) substrate. The structure was grown by molecular beam epitaxy with the c-axis of the Dy parallel to the LaF_3 c-axis and GaAs[1̄1̄1̄] axis. For the magnetic X-ray scattering, we used a polarization analyzer and an X-ray energy near the Dy L_{III} absorption edge. At this energy there is a resonant enhancement in the magnetic scattering intensity, and we obtained $\simeq 50$ counts per second in the magnetic diffraction peaks.

Between 85 and 179K, bulk Dy forms a helical antiferromagnetic structure, and below 85K, it transforms into a ferromagnet. We find that the c-axis lattice constant of the Dy film has a similar temperature dependence to bulk Dy from room temperature to about 110K, but below this, the film behaves differently from bulk and is strained. The temperature dependence of the turn-angle in the helical antiferromagnetic state is similar to bulk, although a weaker dependence is observed below $\sim 110K$ due to magnetoelastic effects. Surprisingly, the magnetic coherence length ($\simeq 310Å$) is significantly shorter than the structural coherence length ($\simeq 730Å$). The transition to ferromagnetic ordering at 86K exhibits temperature hysteresis as is evident in the structural and magnetic X-ray data and in SQUID magnetometry data. We believe this hysteresis arises from a combination of the strain-energy barrier accompanying the transition and magnetic inhomogeneities in the film.

INTRODUCTION

Modern growth techniques such as molecular beam epitaxy (MBE) permit the growth of high quality thin films and superlattices, which can be used to investigate a wide range of magnetic phenomena [1-6]. Thin films and superlattices of rare earth metals have proven to be a particularly rich field, and in previous papers, we have reported the growth and characterization of rare earth films sandwiched by epitaxial LaF_3 films [4-7]. Two key features of these structures are i) the magnetization versus temperature behavior is similar to that of bulk crystals and ii) at room temperature there is no coherency strain in the rare earth film, despite lattice misfit at the rare-earth LaF_3 interface. We have continued to investigate these films, and in this paper, we report lattice and magnetic X-ray diffraction studies of Dy films sandwiched by LaF_3 and determine the temperature dependence of the lattice and magnetic structure. We show the feasibility of magnetic X-ray diffraction measurements on these thin films and compare their behavior with bulk crystals and strained Dy films.

Between 85 and 179K, bulk Dy crystals have a hexagonal-close packed (hcp) lattice and form a helically ordered antiferromagnetic structure. Below 85K, bulk Dy undergoes a first order phase transition into a ferromagnet with an orthorhombic lattice. In the antiferromagnetic phase, the magnetic moments lie in the basal plane and form a helical structure about the c-axis with the moments in successive planes rotating by the turn angle ω; in this phase the helical period is incommensurate with the Dy lattice. This structure leads to magnetic diffraction in the (001) direction at wavevectors $2Lc^* \pm \tau$, where c^* is the reciprocal lattice vector from the Dy lattice and L is an integer. The magnetic wavevector is $\tau = 2\pi/d$, where d is the helical period ($d = (2\pi/\omega)(c/2)$).

EXPERIMENTAL TECHNIQUES

The epitaxial structure described in this paper was prepared by MBE as described earlier [4, 5]. It contained an initial layer of 2500Å thick, epitaxial LaF_3 on GaAs ($\overline{1}\overline{1}\overline{1}$) followed by a 2000Å film of Dy. To prevent oxidation the structure was capped with an epitaxial film of 250Å thick LaF_3. The Dy and LaF_3 c-axes are oriented perpendicular to the sample surface.

X-ray data were obtained at the National Synchrotron Light Source (NSLS) beam line X20A [8]. Approximately 4 milliradians (mrad) of X-ray radiation were collected from a bending magnet and focused onto the sample with a grazing incidence, torodial mirror. At the sample, this produced vertical and horizontal full-widths at half-maximum (FWHM) of 0.8mm and 0.7mm, respectively. The incident beam intensity was monitored by a NaI scintillation detector viewing a Kapton foil and the incident flux was $\simeq 10^{11}$/sec. For measurements of the lattice structure, the diffracted beam was analyzed with a Ge(111) analyzer crystal with a resulting resolution of 0.002Å^{-1}. Slits defined the acceptance of the diffracted beam out of the scattering plane (approximately 20 mrad).

A Ge(111) double monochromator was used to select an X-ray energy of 7790 eV (1.592 Å). We chose this energy, because it provided the maximum resonant enhancement [9, 10] of the magnetic X-ray scattering from our Dy thin film. Although the scattering of X rays from magnetic moments is usually much weaker ($\sim 10^{-6}$) than from electric charges (i.e., the usual Thompson scattering), by tuning the X-ray energy close to the Dy L_{III} absorption edge (at 7792eV), the magnetic scattering is greatly enhanced [9, 10]. We observed a resonant enhancement of the magnetic scattering by a factor of greater than 20 and found that the integrated intensity of magnetic diffraction at $(00\ 2+\tau)$ was about 10^{-5} of the Dy(002) integrated intensity.

For the magnetic X-ray scattering, a polarization analyzer [10, 11] was used to greatly reduce the background (non-magnetic) scattering compared to the magnetic signal. In this analyzer a pyrolytic graphite crystal was set to diffract the (006) planes at $2\theta = 90.8°$. The graphite crystal was aligned so the X rays were diffracted perpendicular to the scattering plane (the plane containing the incident and diffracted X rays). Thus, the analyzer diffracted X rays with a polarization in the scattering plane, but suppressed X rays with a polarization perpendicular to the scattering plane. This reduces the background scattering compared to the magnetic signal for two reasons: First, the synchrotron radiation is predominantly polarized perpendicular to the (vertical) scattering plane and the polarization is not changed in the usual (Thompson) scattering of X rays from electronic charge; the analyzer suppresses this background scattering. Second, the magnetic X-ray scattering from helical magnetic structures results in a change in the X-ray polarization, and thus, the analyzer diffracts these X rays. In the magnetic scattering experiments, the direction of the diffracted beam was defined with slits that had a collimation of about 6 mrad; the resulting resolution was 0.013 Å^{-1}.

RESULTS AND DISCUSSION

Figure 1 shows the temperature dependence of the c-axis lattice constant as the sample was cooled and then heated over the temperature range 300-10K. The data for the film (points) are qualitatively similar to that of bulk single crystal Dy (line) [12]; however, we observe differences for temperatures less than about 110K; the Dy film is strained. The c-axis lattice parameter exhibits the expected change from contraction to expansion at the Néel temperature (180K) as the magnetoelastic interactions compete with thermal contraction [12, 13]. On cooling below 80K, the transition to ferromagnetic ordering is accompanied by a gradual increase in lattice constant which appears complete by about 60K. On warming, the transition is much sharper and centered at about 88K. This hysteretic behavior is indicative of a strain energy barrier to ferromagnetic ordering and is similar to the hysteresis observed in magnetometry studies [7].
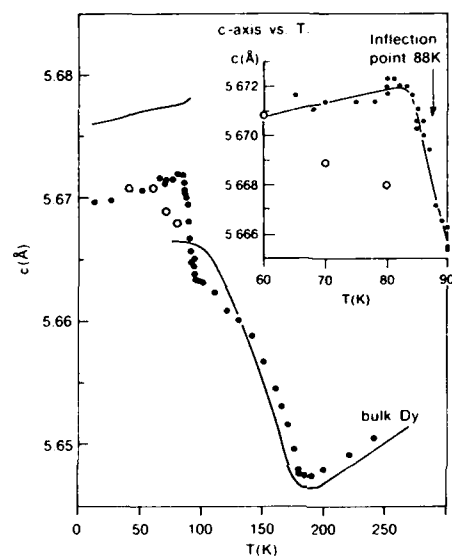
Figure 1. Dependence of the c-axis lattice parameter on temperature. The filled and open circles are from the Dy thin film (warming and cooling, respectively), and the line is for bulk Dy. [12]. The errors bars are approximately the size of the data points.
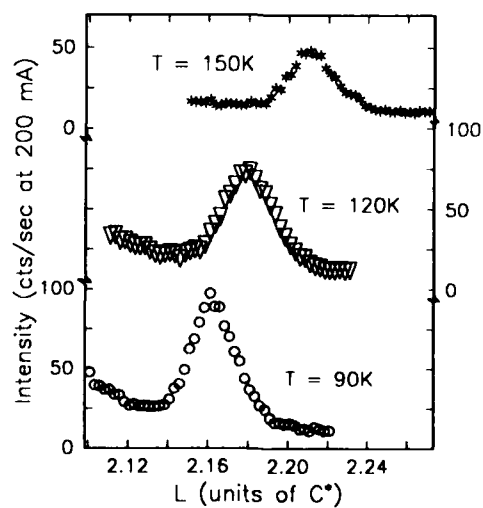
Figure 2. Magnetic X-ray scattering scans at three different temperatures. The ordinate is the scattering vector (in units of c*), while the abscissa is the intensity normalized to a storage ring current of 200 mA.
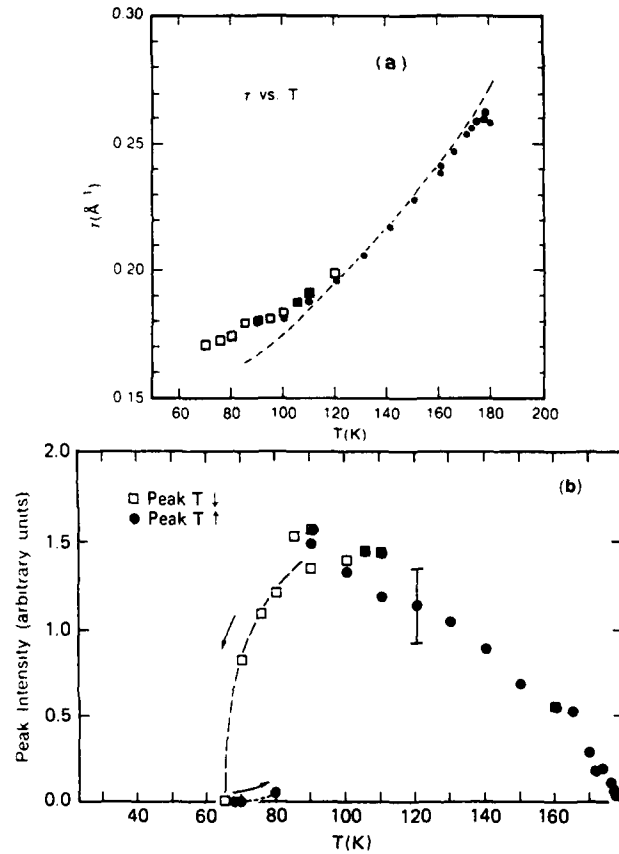
Figure 3. Temperature dependence of the magnetic diffraction in the helical antiferromagnetic phase. The filled circles and open squares are from the Dy thin film (warming and cooling, respectively), whereas the line is for bulk Dy [14]. (a) Position of the magnetic peak τ. The errors bars are approximately the size of the data points. (b) Peak intensity of the magnetic X-ray scattering. A typical error bar is shown.

Figure 2 shows typical scans of the magnetic X-ray scattering in the helically ordered antiferromagnetic phase of the Dy film. For this 2000Å thick film, we obtain count rates of about 50 counts per second (cps) in the magnetic diffraction peak at (00 2+τ) with a non-magnetic background of ≃20 cps. This peak count rate is comparable to that expected in neutron diffraction experiments, although the background is higher. The high background probably results because the incident beam has a small polarization parallel to the scattering plane, and when these X rays are (Thompson) scattered by the sample, they are not suppressed by the polarization analyzer. From the width of the magnetic coherence length is ≃310Å. This is substantially less than the structural coherence length of ~730Å, which we estimate from the Dy (002) peak width. This difference is surprising, since the structural and magnetic coherence lengths are essentially the same in bulk Dy and Dy·Y multilayers [1]; the cause of this difference is unclear.

Figure 2 shows that the magnetic peak position (τ) increases and the intensity decreases at higher temperatures, although the peak width (and hence the magnetic coherence length) are independent of temperature. The temperature dependence of the peak position and intensity are quantified in Fig. 3 for both warming and cooling. As the ferromagnetic transition is approached on cooling, the peak intensity continuously increases (Fig. 3b). On cooling, the ferromagnetic transition is not sharp (as expected for a first order transition), but occurs gradually over the range 90-65K. On warming, however, the transition is sharper and centered at $\simeq 85$K, in good agreement with the lattice expansion measurements (Fig. 1); this behavior is also indicative of a strain energy barrier to ferromagnetic ordering.

Figure 3a shows the temperature dependence of the magnetic wave vector τ (points), which is qualitatively similar to bulk single crystals (line) [14], although a weaker dependence is observed above ~ 170K and below ~ 110K. Since below about 110K the c-axis lattice constant is also different from bulk (Fig. 1), this suggests that the weaker temperature dependence below 110K is caused by magnetoelastic effects. We find no evidence for suppression of the ferromagnetic transition temperature (T_c) in this and thinner films of Dy, in marked contrast to the complete suppression of T_c observed in Dy/Y superlattices [1, 2]. In the superlattices coherency strain is observed at all temperatures [1, 2], but in our LaF$_3$/Dy/LaF$_3$ sandwich structure, coherency strain is found only below $\simeq 110$K. Since the suppression of T_c is due to lattice clamping of the Dy, we suggest that the clamping in the superlattices is more effective than in the sandwich structures and this causes the different behavior in the ferromagnetic transition of the superlattices and sandwiches. We do not understand the weaker temperature dependence observed in the sandwich structures above 170K. Finally, we note that Fig. 3b shows that there is hysteretic behavior near 120K; τ is larger on cooling than on warming. Although this has not been reported in bulk Dy before, it is not clear if this is a bulk or thin film effect.

SUMMARY AND CONCLUSIONS

We have shown that good magnetic X-ray scattering signals can be obtained from a 2000Å Dy film with the use of resonant enhancement and polarization analysis. The observed count rates are roughly comparable to neutron diffraction measurements, although the background is significantly larger. Despite this, magnetic X-ray scattering can be element specific, which will be useful in studies of superlattices and other heterogeneous materials. To use the technique for investigations of superlattices and much thinner films, a reduction in the background X-ray scattering will likely be required.

We find that for the present Dy film the lattice and magnetic structures have a temperature dependence that is similar to bulk Dy from room temperature to about 110K. Below this, the film behaves differently from bulk: it is strained and the temperature dependence of the turn-angle is weaker than in bulk. This suggests that the different magnetic behavior is due to magnetoelastic effects. The transition to ferromagnetic ordering at 86K exhibits temperature hysteresis and we speculate that this arises from a combination of the strain-energy barrier accompanying the transition and magnetic inhomogeneities in the film [7].

ACKNOWLEDGMENTS

124

REFERENCES

1. R.W. Erwin, J.J. Rhyne, M.B. Salamon, J. Borchers, S. Sinha, R. Du, J.E. Cunningham, and C.P. Flynn, Phys. Rev. B **35**, 6808 (1987).
2. J.J. Rhyne, R.W. Erwin, J. Borchers, M.B. Salamon, R. Du, and C.P. Flynn, Physica B **159**, 111 (1989).
3. J. Kwo, in *Thin Film Growth Techniques for Low Dimensional Structures*, edited by R.F.C. Farrow, S.S.P. Parkin, P.J. Dobson, and J.H. Neave (Plenum, New York, 1989), p. 337.
4. R.F.C. Farrow, S.S.P. Parkin, M. Lang, and K.P. Roche, Mat. Res. Soc. Symp. **103**, 205 (1988).
5. R.F.C. Farrow, S.S.P. Parkin, and V.S. Speriosu, J. Appl. Phys. **64**, 5315 (1988).
6. R.F.C. Farrow, S.S.P. Parkin, V.S. Speriosu, A. Bezinge, and A.P. Segmuller, Mat. Res. Soc. Symp. **151**, 203 (1989).
7. R.C.F. Farrow, M.F. Toney, B.D. Hermsmeier, S.S.P. Parkin, and D.G. Wiesler, J. Appl. Phys., in press (1991).
8. E.D. Specht, A. Mak, C. Peters, M. Sutton, R.J. Birgeneau, K.L. D'Amico, D.E. Moncton, S.E. Nagler, and P.M. Horn, Z. Phys. B **69**, 347 (1987).
9. E.D. Isaacs, D.B. McWhan, D.P. Siddons, J.B. Hastings, and D. Gibbs, Phys. Rev. B **40**, 9336 (1989).
10. D.B. Gibbs, D.R. Harshman, E.D. Isaacs, D.B. McWhan, D. Mills, and C. Vettier, Phys. Rev. Lett. **61**, 1241 (1988).
11. D.B. Gibbs, Physica B **159**, 145 (1989).
12. F.J. Darnell, Phys. Rev. **130**, 1825 (1963).
13. A.E. Clark, B.F. DeSavage, and R. Bozorth, Phys. Rev. **138**, A216 (1965).
14. M. Hong, R.M. Fleming, J. Kwo, L.F. Schneemeyer, J.V. Waszczak, J.P. Mannaerts, C.F. Majkrzak, D.B. Gibbs, and J. Bohr, J. Appl. Phys. **61**, 4052 (1987).

FERRIMAGNETIC BEHAVIOR AND MAGNETORESISTANCE
OF Fe/Gd DOUBLE STRUCTURED MULTILAYER FILMS

H. FUJIMORI, Y. KAMIGUCHI, Y. HAYAKAWA, AND K. TAKANASHI
Institute for Materials Research, Tohoku University, Katahira,
Aoba-ku, Sendai 980, Japan

ABSTRACT

We prepared Fe/Gd double structured multilayer films
(DSMLF's). The Fe/Gd DSMLF has a longer period λ_1, and it is
composed of alternate stacking of two types of Fe/Gd submulti-
layers with a shorter period λ_s.   One type of Fe/Gd submulti-
layers has dominant Fe layer magnetization, and the other,
dominant Gd layer magnetization. λ_s was varied in the range
from 12 to 100Å, keeping λ_1 to about 250Å. The magnetization
of Fe/Gd DSMLF's with $\lambda_s \leq 36$Å shows a spin-flop in magnetic
fields lower than 1kOe at room temperature. The compensation
temperature T_{comp} was found to decrease with increasing λ_s.
T_{comp} crosses room temperature at $\lambda_s = 24$Å, and then the spin-
flop field H_{sf} at room temperature takes a minimum value of the
order of a few tens oersteds.   Thus, we show that H_{sf} at room
temperature can easily be tuned to a desired value by varying
λ_s. Longitudinal (ρ_1) and transverse (ρ_t) magnetoresistances
show a crossover, depending on the angle between directions of
the electric current and of the Fe layer magnetization.

INTRODUCTION

We reported previously[1] that Fe/Gd multilayer films
behave as 'giant' ferrimagnets, that is, the magnetizations in
Fe and Gd layers are aligned in antiparallel due to the anti-
ferromagnetic exchange interaction between Fe and Gd magnetic
moments at the interface.   Consequently, a spin-flop at low
fields and compensation behavior of magnetization was observed.
A remarkable result we obatained is that longitudinal (ρ_1) and
transverse (ρ_t) magnetoresistances revealed a crossover around
the spin-flop field (H_{sf}).   The magnetization in Fe and Gd
layers begins rotating at H_{sf}. Anomalous magnetoresistance
depends on the angle between directions of the electric current
and of the magnetization.   Therefore, the crossover of ρ_1 and
ρ_t is considered to be due to the change in the angle between
directions of the electric current and of the magnetization ac-
companied with the spin-flop.
    The crossover of ρ_1 and ρ_t in Fe/Gd multilayer films sug-
gests the possibility of their application to magnetoresistance
devices. From the viewpoint of application, however, it is
important to obtain the spin-flop of magnetization and/or the
crossover of ρ_1 and ρ_t at room temperature (RT). The Gd layer
magnetization in Fe/Gd MLF's almost disappears at RT in the
case of large multilayer periods, because the Curie temperature
of Gd is close to RT. In the case of small multilayer periods,
on the other hand, the Gd layer magnetization remains alive
even at RT, due to the molecular field from the Fe layer magne-
tization. However, H_{sf} is considerably larger because H_{sf} in-
creases rapidly with decreasing the multilayer period.[2] Thus,
it is difficult to tune H_{sf} at RT to an appropriate value for
application. As one approach for this problem, we proposed a

126

new type of design of MLF's, that
is, an Fe/Gd double structured
multilayer film (DSMLF) as is
shown in Fig. 1.[3,4]   The Fe/Gd
DSMLF is an MLF having a longer
period λ_l, which is composed of
two types of Fe/Gd submultilayers
having a shorter period λ_s.   One
type of Fe/Gd submultilayers   has
dominant Fe layer magnetization,
and the other,   dominant Gd layer
magnetization.   The   former   is
called the Fe-rich submultilayer,
and the latter,   the Gd-rich sub-
multilayer, hereafter.   It is con-
sidered in Fe/Gd DSMLF's that the
Gd layer   magnetization   is alive
even at RT   when λ_s is small, and
that H_sf is sufficiently low when
λ_l is large.   As described in the
previous paper,[3] we observed the
spin-flop of magnetization and the
crossover of ρ_l and ρ_t at RT in
Fe/Gd DSMLF's. H_sf was found to
decrease with increasing λ_l.[4]

In this paper, we investigate
the λ_s dependence of H_sf, and
indicates that H_sf at RT is easily
controllable by changing λ_s.   The
behavior of magnetoresistance is
also investigated in Fe/Gd DSMLF's
with various λ_s's.
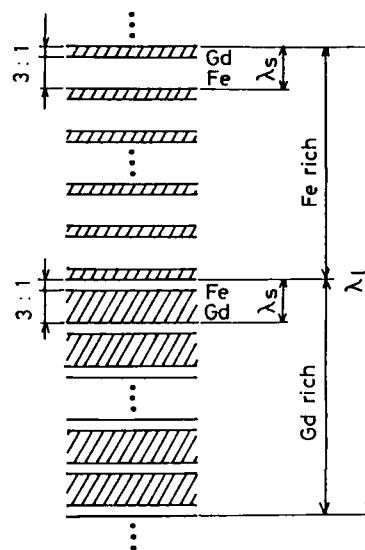
Fig. 1. The structure of
Fe/Gd DSMLF.

EXPERIMENTAL

Fe/Gd DSMLF's were prepared   by a dual-type rf sputtering.
The details of the sample preparation were described in the pre-
vious papers.[1,4] λ_s was varied   in the range from 4 to 100Å,
keeping λ_l to 250Å.   The ratios   of the Fe layer thickness to
the Gd layer thickness in submultilayers with dominant Fe layer
magnetization and with dominant Gd layer magnetization were 3:1
and 1:3, respectively.   The total thickness of Fe/Gd DSMLF's
was about 3000Å.   A standard X-ray diffraction measurement with
θ-2θ scanning was made for structure analysis.   The measurement
of magnetization was made using a vibrating sample magnetometer
in the temperature range from 4.2 to 500K.   A conventional four
terminals method was used to measure magnetoresistances at 4.2K,
77K and RT.

RESULTS AND DISCUSSION

Structure

Figure 2 (a)   shows an X-ray diffraction pattern in a low
angle region for the Fe/Gd DSMLF with λ_s=20Å.   Bragg peaks cor-
responding to λ_l are observed   up to high orders.   Odd-order
peaks are more intense than even-order ones,   because the thick-

nesses of Fe-rich and Gd-rich submultilayers are almost equal to each other. The Bragg diffraction corresponding to λ_S leads to the enhancement of intensities of the eleventh to thirteenth order of peaks. The calculated pattern based on a step model, where the composition is assumed to modulate completely stepwise, is shown in Fig. 2 (b). The calculation reproduces the experimental result fairly well. Therefore, we consider that the double structure as is shown in Fig.1 is successfully present in our samples.

Magnetization

The spin-flop behavior of magnetization was definitely observed at 4.2K and 77K in all the prepared samples. At RT, however, the spin-flop behavior was observed only for the samples with $\lambda_S \leq 36\text{Å}$. For example, the magnetic field dependences of magnetization (M-H curves) at RT in the samples with $\lambda_S = 12$, 36 and 56Å are shown in Fig. 3. In the cases of $\lambda_S = 12$ and 36Å, the M-H curves show a pattern characteristic of the spin-flop, while the case of $\lambda_S = 56\text{Å}$ shows a simple pattern as is often observed for ordinary ferromagnets. The effective molecular field in Gd layers from Fe layers is smaller as λ_S is larger, and consequently, the Gd layer magnetization is almost dead at RT in the case of large λ_S's. Therefore, the spin-flop disappears at RT in the samples with $\lambda_S > 36\text{Å}$.

Figure 4 shows the temperature dependences of magnetization in the samples with various λ_S's, which were measured at the applied field lower than H_{sf}. The compensation temperature T_{comp}, where the sum of Gd layer magnetization is equal to the sum of Fe
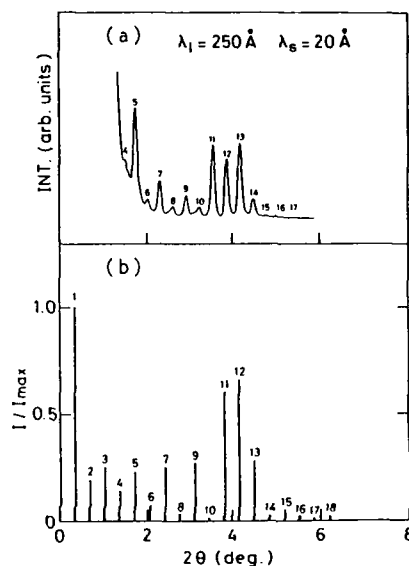
Fig. 2. (a) The X-ray diffraction pattern in a low angle region for the Fe/Gd DSMLF with $\lambda_S = 20\text{Å}$.
(b) The calculated pattern based on a step model.
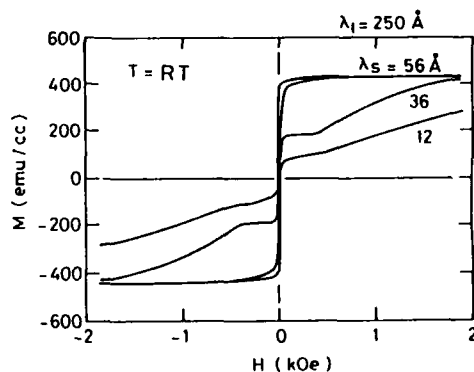
Fig. 3. Magnetization (M) vs. magnetic field (H) curves at room temperature for Fe/Gd DSMLF's with $\lambda_S = 12\text{Å}$, 36Å, 56Å.

layer magnetization, is found to increase with decreasing λ_S. The reason for this is considered to be as follows. In the case of smaller λ_S, the Gd layer magnetization remains alive even at higher temperatures due to the larger effective molecular field from Fe layers. Furthermore, the Curie temperature of the Fe layer magnetization becomes lower due to structural disorder and/or alloying with Gd. Consequently, T_{comp} is enhanced when λ_S is small.

The λ_S dependences of T_{comp} and H_{sf} at 4.2K, 77K and RT are shown in Fig. 5. H_{sf} at each temperature takes a minimum value, when T_{comp} crosses the corresponding temperature. This result is reasonable, because the colinear spin structure has no gain of Zeeman energy at T_{comp}, and hence the canted spin structure is stable in an infinitesimal applied field. Figure 5 reveals that H_{sf} is controllable by changing the λ_S at any temperatures. Particularly, it is noted that H_{sf} at RT is always lower than 1kOe in the case of $\lambda_S \leq 36\text{Å}$, and has a very small value of the order of a few tens oersteds* in the case of $\lambda_S = 24\text{Å}$, where T_{comp} is close to RT.

Magnetoresistance

The magnetic field dependences of ρ_l and ρ_t for the samples with $\lambda_S = 12$, 36 and 56Å are shown in Figs. 6 (a), (b) and (c), respectively, where the M-H curves are also shown for comparison. In the case of $\lambda_S = 12$Å, the two crossovers of ρ_l and ρ_t are definitely observed. In the case of $\lambda_S = 36$Å, ρ_t (ρ_l) shows an up and down (down
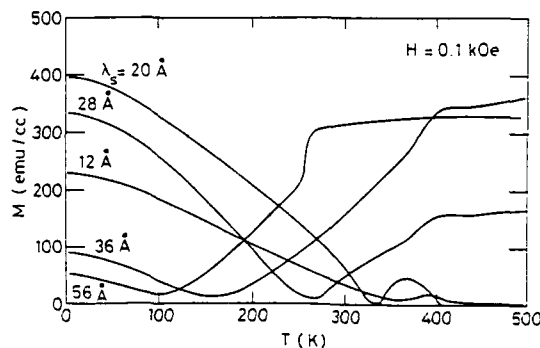
Fig. 4. Magnetization (M) vs. temperature (T) curves for Fe/Gd DSMLF's with various λ_S.
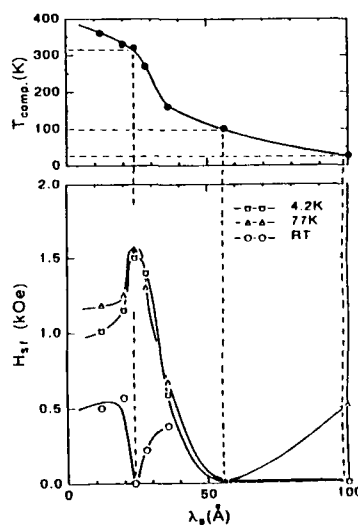
Fig. 5. The λ_S dependences of compensation temperature (T_{comp}) and spin-flop field (H_{sf}) at 4.2K, 77K and room temperature for Fe/Gd DSMLF's.

---

* In this case, H_{sf} is camparable to the coercive force. That is, the spin-flop occurs simultaneously with the motion of domain walls. Therefore, the exact value of H_{sf} cannot be extracted from the M-H curve.

and up) change accompanied with the spin-flop, however, they never cross. In the case of $\lambda_s = 56\text{Å}$, ρ_l and ρ_t show simple anisotropic magnetoresistance as is seen in pure Fe. The behavior of magnetoresistance in the three typical cases can be explained as follows. The electrical resistivity of Fe is two orders of magnitude smaller than that of Gd. This means that in Fe/Gd DSMLF's most of the electric current flows in Fe layers. Therefore, the magnetoresistance of Fe/Gd DSMLF's depends mostly on the angle between the directions of the electric current and of the Fe layer magnetization. In the case of $\lambda_s = 12\text{Å}$, T_{comp} is higher than RT, that is, the Gd layer magnetization points to the direction of the applied field (H_{appl}) lower than H_{sf}. When H_{appl} reaches H_{sf}, the Fe layer magnetization begins rotating. In larger H_{appl}, the Fe layer magnetization continues rotating, and finally points to the direction of H_{appl}. In this process, the angle between the directions of the electric current and of the Fe layer magnetization changes by 180°, leading to the two crossovers of ρ_l and ρ_t. In the case of $\lambda_s = 36\text{Å}$, on the other hand, T_{comp} is lower than RT, that is, the Fe layer magnetization points to the direction of H_{appl} lower than H_{sf} at RT. Therefore, the Gd layer magnetization rotates in H_{appl} larger than H_{sf} at RT. The Fe
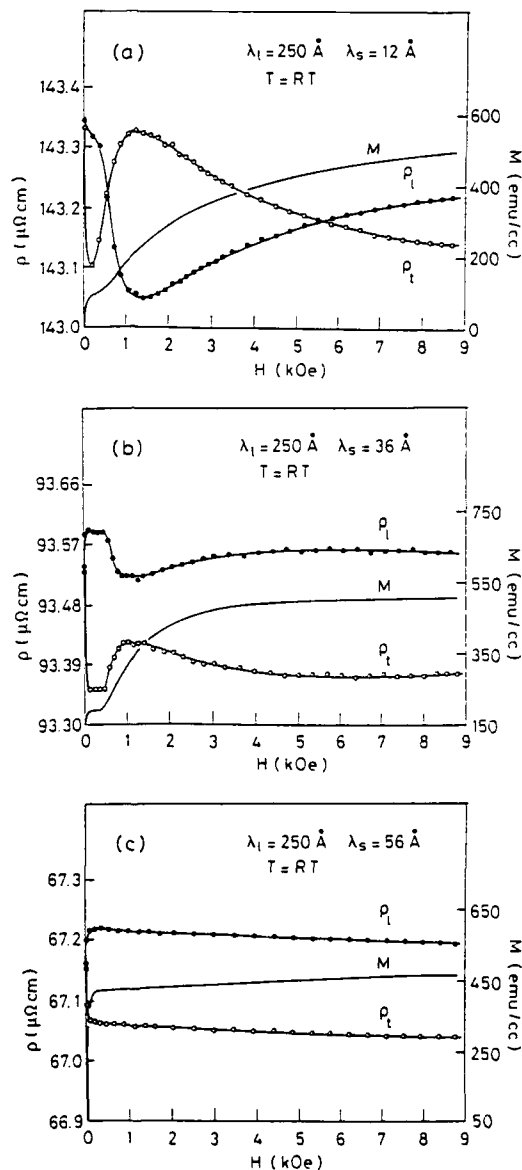
Fig. 6. Longitudinal (ρ_l) and transeverse (ρ_t) magnetoresistances vs. magnetic field (H) curves at room temperature for Fe/Gd DSMLF's with $\lambda_s = 12\text{Å}$ (a), 36Å(b), 56Å(c), compared with the magnetization (M).

layer magnetization is also canted from the direction of H_{appl} due to the interaction with the Gd layer magnetization. However, the canting angle is small, so that the angle between the directions of the electric current and of the Fe layer magnetization does not change very much.   Consequently, ρ_l and ρ_t do not show a so big change as they cross.   In the case of $\lambda_s=$ 56Å, the Gd layer magnetization disapears   at RT.   Therefore, the spin-flop does not occur, leading to no particular change in ρ_l and ρ_t.

SUMMARY AND CONCLUSION

Fe/Gd DSMLF's composed of Fe-rich and Gd rich submultilayers were prepared by an rf sputtering. λ_s was varied in the range from 12 to 100Å, keeping λ_l to 250Å. The magetization of Fe/Gd DSMLF's with $\lambda_s \leq 36$Å shows a spin-flop in magnetic fields lower than 1kOe at RT. T_{comp} was found to decrease with increasing λ_s. The λ_s dependences of T_{comp} and H_{sf} indicate that H_{sf} at a certain temperature takes a minimum value at λ_s where T_{comp} coincides with the temperature.   Particularly, H_{sf} at RT takes a small value of the order of a few tens oersteds in the case of $\lambda_s=24$Å. Thus, it has been shown that not only changing λ_l but also changing λ_s is an effective method for tuning H_{sf} at RT to a desired value. ρ_l and ρ_t at RT show the two crossovers with increasing the applied field in the cases of λ_s's where T_{comp} is higher than RT.   The behavior of ρ_l and ρ_t in Fe/Gd DSMLF's can be explained by considering that the magnetoresistance depends on the angle between the directions of the electric current and of the Fe layer magnetization.

Acknowdgment

References

1. Y. Kamiguchi, Y. Hayakawa and H. Fujimori, Appl. Phys. Lett. 55, 1918 (1989).
2. R. E. Camley and D. R. Tilley, Phys. Rev. B, 37 3413 (1988).
3. H. Fujimori, Y. Kamiguchi and Y. Hayakawa, J. Appl. Phys. 67, 5716 (1990).
4. Y. Kamiguchi, H. Fujimori, Y. Hayakawa and K. Takanashi, J. Magn. Soc. Jpn. 14, 355 (1990) [in Japanese].

Interlayer Exchange Coupling—
Experiment

OSCILLATION IN THE INTERLAYER COUPLING OF Fe FILMS ACROSS Cr FILMS MEASURED BY MEANS OF LIGHT SCATTERING FROM SPIN WAVES AND M(H)-CURVES.

S.DEMOKRITOV*, J.A.WOLF, P.GRÜNBERG, W.ZINN.

Forschungszentrum Jülich, IFF, Postfach 1913, D-5170 Jülich, Federal Republic of Germany.

* permanent address: P.L.Kapitsa Institute for Physical Problems, Moscow, USSR.

ABSTRACT

By means of light scattering from spin waves and magnetooptical Kerr measurements we investigated the exchange interaction of two Fe films across a Cr film as a function of the Cr thickness d_{Cr} .

Using good quality epitaxial samples with a special wedge geometry of the interspacer we observed up to four full periods of the long range oscillations of the exchange, including its ferromagnetic parts. At room temperatures the damping of the oscillations does not follow the d_{Cr}^{-2}-dependence predicted by zero-temperature RKKY-type theory.

After a special e-beam treatment of the samples a short-range oscillation with a period around a lattice constant of Cr are discovered. The value of coupling in the maximum in this case shows considerable temperature dependence .

The analysis of domain patterns and M(H) curves reveals the existence of a non-collinear interaction, which causes a configuration where the magnetizations of two Fe films are perpendicular to each other.

INTRODUCTION

It is now well established [1-4] that layered Fe/Cr structures display antiferromagnetic (AF) type interlayer coupling of the Fe films across the Cr interlayers. The effect is also of interest because of the remarkable increase in the electrical resistivity of such samples due to the antiparallel magnetization alignment of adjacent Fe films [2,4,5], which has a clear application potential. Recently Parkin et al. [4] have reported damped oscillations of the coupling as a function of the Cr interlayer thickness d_{Cr} . These results were obtained from the investigation of M(H) curves of multilayered, polycrystalline Fe/Cr samples and occur also in Co/Ru and Co/Cr. The normal M(H) method has the advantage of high sensitivity towards AF type interlayer coupling. It is however disadvantageous insofar that the evaluation of the M(H) curves does not give any information about ferromagnetic (FM) type interlayer coupling. Therefore the nature of the coupling for ranges of d_{Cr} between the regions of AF coupling found in the oscillations remained unclear. For a better theoretical understanding [6-10] of these interesting phenomena on the other hand it is important to have a more complete picture based on experimental data.

SAMPLES AND EXPERIMENTAL SETUP

Samples

In order to achieve high quality samples the preparation was performed in UHV (better than $2 \cdot 10^{-8}$ Pa) by means of molecular beam epitaxy (MBE). All samples were prepared on (100)-GaAs substrates. Based on well known recipes [11] a 1 nm Fe seed film was deposited on the substrate so as to maintain the (100) orientation throughout the layers. Following this a 150 nm Ag buffer layer was evaporated, onto which the Fe/Cr/Fe double layer was deposited. The samples were covered by a 50 nm protective overlayer of ZnS.

The UHV-chamber incorporates an Auger-Electron-Spectrometer (AES) and a

Spot-Profile-Analysis-Low-Energy-Electron-Diffraction (SPA-LEED)-system. With these methods an *in situ* check of the quality of the samples was possible. The evaluation of the spot profile data gives a sensitive method to check the single-crystal-quality of a given surface. By monitoring the layers using the SPA-LEED we were able to ascertain the high epitaxial quality of our samples. The surface of a typical (100)-Ag buffer-layer e.g. has a mean step width of 20 nm and therefore is a good base for the growth of the following layers. The SPA-LEED also allows a quick check of the epitaxy by comparing given spot profiles with previously exactly investigated surfaces. On account of this the reproducible high quality of our samples could be documented. In addition to this the samples were investigated with AES. The contamination of the different layers with e.g. oxygen was found to be negligible. No diffusion of Ga or As through the Ag buffer-layer into the Fe double layer could be detected.

Characterization of the Fe/Cr/Fe double layers can be performed using the magnetooptical Kerr-effect (MOKE). The aquisition of a hysteresis curve always includes the measurement of the coercive force of the magnetic layers. This coercive force is characteristic of the epitaxial structure of the ferromagnetic layer and is smaller the better this structure is. Fe-whiskers being ferromagnets with an ideal structure have a typical coercive force of 0.8 Oe. In our samples the coercive force was between 4 and 5 Oe, which to our knowledge is the smallest value ever obtained in a film.

The investigation of the coupling characteristics of the Fe/Cr-system was performed on samples with a special geometry. The Cr-interlayer was deposited in form of a wedge, having the advantage that a large range of Cr-thicknesses is available on one sample. The substrates for these wedge-samples were 16 mm long, while the height-difference of the interlayer was at the most 5-6 nm. This wedge-geometry does not influence the magnetic property of the system as the steepest grade of incline was 1 monolayer of Cr on approximately 0.4 mm. The measurements were also counterchecked with results of samples with a defined Cr-thickness and no difference was found.

In order to prepare a wedge-formed Cr-layer the sample was moved behind a mask during the evaporation. A change of the speed of this movement and of the rate of evaporation allows the preparation of wedges with different inclination. The results were never found to be dependent on the steepness of a wedge. As the movement of the sample and the evaporation rate were constant the thickness of the Cr-interlayer can be calculated for every position on the sample. This allows measurements dependent on the Cr-thickness in extremely small steps with a high precision.

In comparison with samples with a defined Cr-thickness the wedge-samples have a much higher accuracy. This is due to the preparation conditions which are exactly the same for all interlayer thicknesses. With multiple samples of defined interlayer thickness even the most careful preparation cannot eliminate differences due to e.g. slightly differing anisotropy fields or Fe-thicknesses. Therefore the error with multiple samples is higher and the correlation between the samples is more problematic.

Experimental

In our experiments the information about the interlayer coupling is obtained from the behaviour of the low lying spin wave modes in sandwich type structures as well as from $M(H)$ curves, measured by scanning magnetooptical Kerr effect (MOKE). The spin waves are detected by means of inelastic Brillouin light scattering (BLS). The latter method has the advantage that it also allows a determination of FM-type interlayer coupling. To investigate the different d_{Cr} we scanned the probing laser beam across the sample. The local $M(H)$ curves are obtained via the MOKE and the spin waves are examined by a frequency analysis of the inelastically scattered light. For both methods we confirmed by comparison with results obtained from single samples with fixed d_{Cr}, that the wedge geometry does not modify the magnetic behaviour of the films. It should be noted that in our case the MOKE-method is more sensitive than the BLS-method. On the other hand we used different lasers for the two kinds of experiments and the spot size of the focused laser beam was smaller in the case of the BLS measurements (BLS-spotsize $\approx 50\mu m$, MOKE-spotsize $\approx 300\mu m$). Therefore in the ranges with rapid changes of the coupling strength the BLS-method results in a higher resolution while the MOKE-method is more sensitive

in the ranges with a gradual change of the coupling strength.

For a quantitative evaluation of the exchange interaction of ferromagnetic films across an interface the interface exchange energy is written in the form [12]

$$E_s = -2A_{12} \cdot \frac{\vec{M}_1 \cdot \vec{M}_2}{|\vec{M}_1| \cdot |\vec{M}_2|} \tag{1}$$

Here $\vec{M}_1$ and $\vec{M}_2$ are the magnetizations of the two films and E_s denotes the energy per surface unit of interface. Instead of A_{12} often another parameter J is used, where $J = 2A_{12}$. The parameter A_{12} defined by Eq.(1) can be deduced from M(H) curves by measuring the field B_s where the sample saturates parallel to the external field, against the torque due to AF coupling. Therefore by this method, as previously stated, only negative A_{12} (AF coupling) can be determined, for positive A_{12} there is no equivalent torque. We should note that there is a method with auxiliary layers which makes it possible to determine FM -type coupling, using magnetometry [13]. However this method is quite complicated and not very sensitive. The expression for A_{12} from B_s depends upon the field orientation. In the case of $B_s \gg B_a$ (anisotropy field of Fe B_a =480 Oe) one can obtain:

$$A_{12} = -(B_s \pm B_a) \cdot \frac{Md}{4} \tag{2}$$

where M and d are respectively the magnetization and the thickness of the ferromagnetic films and $\pm B_a$ corresponds to the field orientation along the hard and easy axis. For multilayers the factor of 4 on the right-hand side of Eq.(2) has to be replaced by 8. For the situation when B_s is on the order of the value or smaller than B_a, which is the case for $d_{Cr} > 2$nm, it is difficult to derive an analytical expression similar to Eq.(2). For this reason we used the direct computation of the energy minimum to calculate A_{12} (d_{Cr}).

The other method to obtain quantitative information on the interlayer exchange is via the observation of spin wave modes. So far this method is restricted to double layers because of the complexity of the mode spectra in multilayers. A detailed description of the method has been given elsewhere [14]. In double layers we detect two spin-wave modes. The first is the Damon-Eschbach (DE) mode. Its frequency is independent of the interlayer exchange and can be used to test the magnetic homogeneity of the wedge samples. In our experiments the DE mode frequency was constant with an accuracy of 0.3%. The other mode is sensitive to the interlayer exchange and is called optical mode. From its frequency using a fitting procedure we calculate the A_{12} (d_{Cr}) dependence. Although for the M(H) measurements we applied the magnetic field along the easy axis, in the BLS experiments the orientation of the field along the hard axis has been used as well. It permits a dramatic decrease of the fitting freedom and an increase of the reliability of the fit. The spectral width of the peaks corresponding to the light scattering from both modes is around 1 GHz. However, using the method of the selfcorrelating transformation it is possible to find the position of the peak center with an accuracy better than the width of the peak, namely 0.1 - 0.2 GHz. In this approach the correlator $h(\nu)$ is calculated:

$$h(\nu) = \int f(\nu') \cdot f_0(\nu' - \nu) \, d\nu' \tag{3}$$

where $f(\nu)$ is the measured peak and $f_0(\nu)$ is the known apparatus function. Unlike $f(\nu)$ the correlator $h(\nu)$ is a smooth, symmetrical function. Its maximum shows us the center of the measured peak. The accuracy and the reliability of this method was tested with comparison of the data obtained for stokes and antistokes peaks of BLS from phonons and magnons in single films.

Domains were observed magnetooptically in reflection using a digital contrast enhancement scheme [15]. In addition to the Kerr effect the linear magnetic birefringence (the Voigt effect) and the recently discovered magnetooptic gradient effect [16]) were employed to analyse complicated patterns. Both a mercury arc lamp selecting the green and yellow spectrum lines and an argon laser illumination system were used. Due to opaque GaAs substrates, only the top side of the multilayer system could be investigated. The magnetooptical contrast thus is mainly determined by the top Fe layer, but the bottom

136

layer contributes for thin, transparent iron layers to some extent to the contrast. In-plane fields could be applied during domain observations along all directions. It was large enough to saturate the sample along the hard [110] direction.

EXPERIMENTAL RESULTS

Long – period oscillations

Figure 1 shows the oscillating A_{12} (d_{C_r}) dependence as derived from our BLS and scanning MOKE measurements. The results of both methods coincide very well. In addition to the well known first AF region around 0.6 nm the data reveal two other AF regions separated by FM regions. An important feature of the curve in Fig.1 is that even at large d_{C_r} in addition to the oscillatory term there is a monotonically decreasing AF type contribution which becomes compatible to the coercive force only for $d_{C_r} > 5$ nm . We will discuss this point below in connection with observation of some kind of noncollinear interaction, causing a 90° configuration.
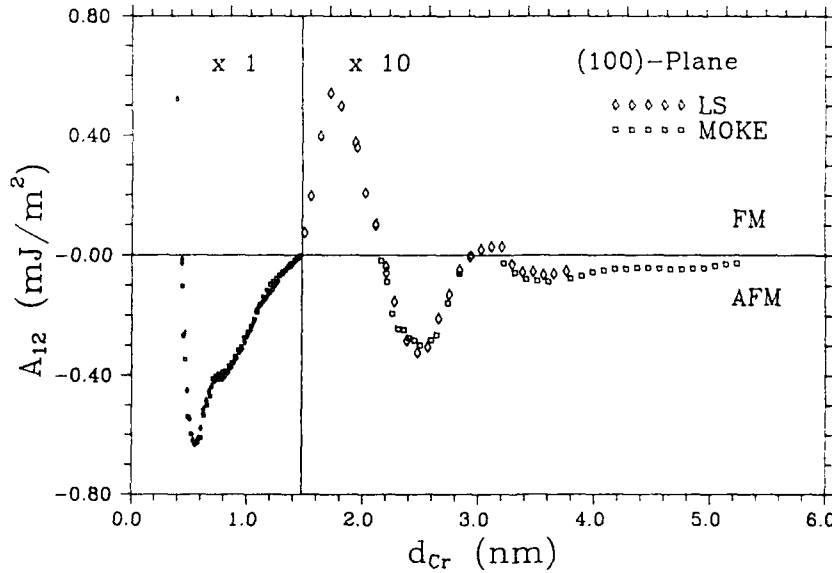
Fig.1. Interlayer exchange constant A_{12} as a function of d_{C_r} at room temperature, obtained from BLS-measurements ($\Diamond$) and scanning MOKE measurements ($\square$). The size of the token shows the experimental error. Note the factor of 10 difference in the scaling of the ordinate for the two parts of the graph. FM/AFM denote the ferromagnetic/antiferromagnetic type of the coupling. For $d_{C_r} > 3.8$ nm the BLS data are in agreement with the MOKE data, but were omitted for reasons of clarity.

In comparison with the data from [4] the damping of the oscillation is much stronger in our case. We observe the first maximum of AF type coupling at d_{C_r} =0.6 nm with the value of A_{12} =-0.65·$10^{-3}J/m^2$. For the second maximum around d_{C_r} =2.5 nm we obtain A_{12} =-0.03·$10^{-3}J/m^2$. Hence between the first and second maximum $|A_{12}|$ decreases by a factor of 22. In the data reported in [4] there is only a decrease by a factor of 7. In Fig.2 we plotted the amplitude dependence on d_{C_r} (the monotonic contribution is subtracted).
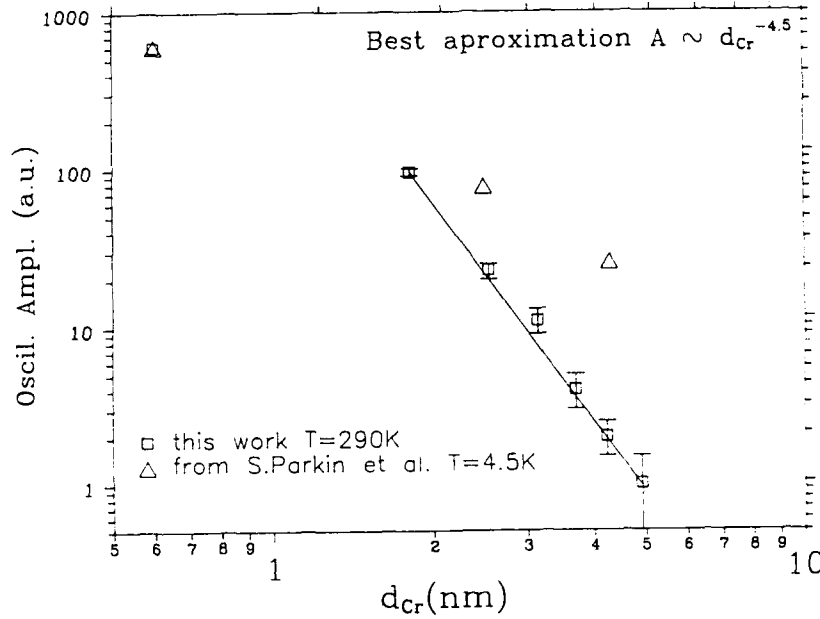
Fig.2 Amplitude of A_{12} -oscillations versus d_{Cr} . The ($\square$) token pertains to the data in this paper and the ($\triangle$) tokens are based on the data from [4]. The solid line presents the best power fit which corresponds to a $d_{Cr}^{-4.5}$-law.

It is obvious that the damping of the oscillations obeys rather a d_{Cr}^{-4}- or d_{Cr}^{-5}-law than a d_{Cr}^{-2}-law as predicted by the classical zero-temperature RKKY-theory. To understand this divergence we investigated the temperature dependence of the value of A_{12} for the first and the second maxima. The Fig.3 shows the measured temperature dependence. It is clear that the decrease of the A_{12} value with temperature for the second maximum (d_{Cr} =2.5 nm) is much large than that for the first maximum. From T=5K to T=290K the former drops by a factor of 2.5, while the latter changes its value by only 20%. If one takes into account this fact it is possible to explain the disagreement between results of the present work (data were obtained at T=290K) and [4], where measurements were performed at T=4.5K.

Short - period oscillation

The A_{12} (d_{Cr})-curve in Fig.1 also displays a fine structure in the first AF region around d_{Cr} =0.9 nm. At this point one should recall that the BLS-method is more sensitive for rapid changes of A_{12} whereas the scanning MOKE-method is more sensitive for gradual changes and small values of A_{12} . For this reason the fine structure is more pronounced in the BLS data. We pay this fine structure here so much attention because it indicates the existence of further maxima of AF type coupling within that range. From the theory such maxima are expected [6,7] to occur with a periodicity of the lattice constant a_0 = 0.288 nm of Cr. The shoulder at 0.9 nm indeed is just around 0.3 nm away from the main maximum at 0.6 nm.

A special treatment of the Cr wedge gave us the possibility to reveal this short-period oscillation. After deposition of the first Fe layer and Cr wedge the sample was exposed to an electron beam. After that the second Fe layer as well as covering Ag and ZnS layers were deposited in the usual way.
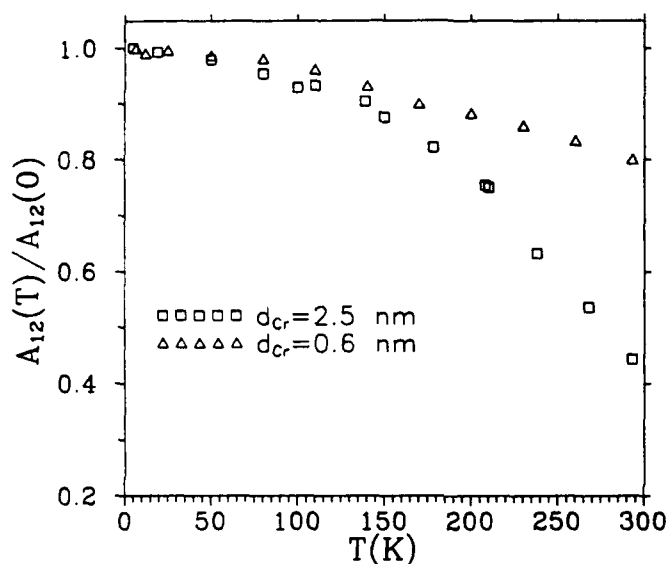
Fig.3. Temperature dependence of the A_{12} values for the first ($\triangle$, d_{Cr} = 0.6 nm) and the second ($\square$, d_{Cr} =2.5 nm) AF regions.

The A_{12} (d_{Cr})-curve measured on such specially prepared samples is shown in Fig.4. The short-period oscillation which was visible in Fig.1 as a hardly resolved fine structure became obvious. It is possible to measure the period of this oscillation with a good accuracy. It is equal to 0.25±.03 nm. The second difference of the curve in Fig.4 from the one in Fig.1 is the value of A_{12} , which is approximately three times smaller. Apparently e-beam treatment reveals the short-period oscillation, but quenches the long-period one.

For better understanding of the processes involved we have measured the temperature dependence of A_{12} in these e-beam treated samples. The results are shown in Fig.5. A_{12} at the point of the first short-period maximum (d_{Cr} = 0.6 nm) unlike the normal sample depends dramatically on the temperature. It has a maximum around T=20K and at this temperature the values of A_{12} for normal and e-beam treated samples are practically the same. At the point of the second short-period maximum (d_{Cr} = 0.9 nm) the temperature dependence is not so considerable. And it has a very smooth and wide maximum around 200 K.

From the comparison of the data presented here it is clear that the e-beam treatment changes the properties of the Cr wedge. What might be the reasons of these changes? The first reason which has been investigated is the heating of the sample by the e-beam. A small piese of In attached to the sample shows that the sample temperature never exceeded 430 K (157 °C). We have produced samples which were annealed without e-beam treatment at 430 K and 370 K . The magnetic properties of both samples are similar to the properties of normal samples.
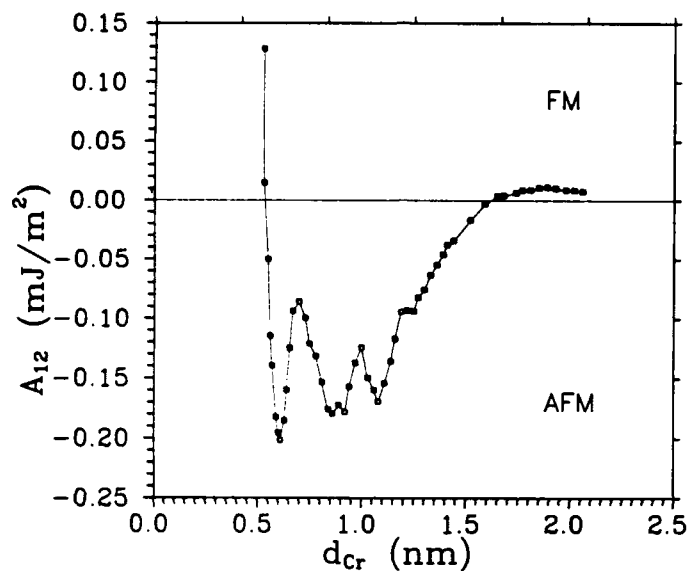
Fig.4. Interlayer exchange constant A_{12} as a function of d_{Cr} at room temperature, obtained from BLS measurements on the e-beam treated samples. As before FM/AFM denote the ferromagnetic/antiferromagnetic type of coupling.
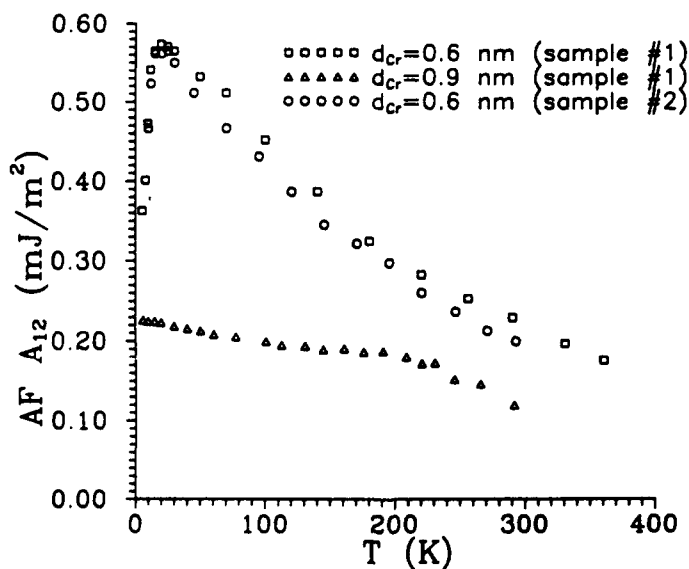

Fig.5. The A_{12} value versus temperature for the e-beam treated samples. Values of d_{Cr} =0.6 nm and d_{Cr} =0.9 nm correspond to the first and the second maxima of the short-period oscillation.

The second reason which can cause the change of the sample properties is an influence of the ions created in the residual gas by the e-beam. This possibility was checked experimentally. Next to the deposited Cr wedge a 6 mm wide area of Fe film was kept free. The e-beam was focused on this free Fe surface instead of sweeping along the Cr wedge. As to the creation of ions in the residual gas this experiment duplicates the normal e-beam treatment. The only difference consists in the lack of the direct interaction between the e-beam and the Cr wedge. After such modified treatment the sample shows the normal behaviour with $A_{12} = 0.7\ mJ/m^2$ in the first AF region at room temperature and without any pronounced short-period oscillation.

All these experiments together with the theoretical considerations [6] lead us to the conclusion that the interaction of the e-beam with Cr wedge changes the structure of the material (let us say the surface roughness and/or the internal stress become smaller). This is in agreement with the dramatic change of the temperature dependencies of A_{12} in the e-beam treated samples. investigations.

Domain observation. 90° configuration

Magnetooptical observations [15] reveal a unique way to demonstrate the oscillation of the interlayer exchange. During the magnetization reversal those parts of the wedge sample with FM-type coupling are characterized by saturation fields which are the same as in single Fe films. For external fields along the easy axis the coercive force is around 5 Oe. In contrast to this sample sections with AF type coupling show much larger saturation fields which increase together with the strength of the coupling. For external fields in between the saturation fields of FM and AF type ranges such samples therefore display zebra like patterns as shown in Fig.6.
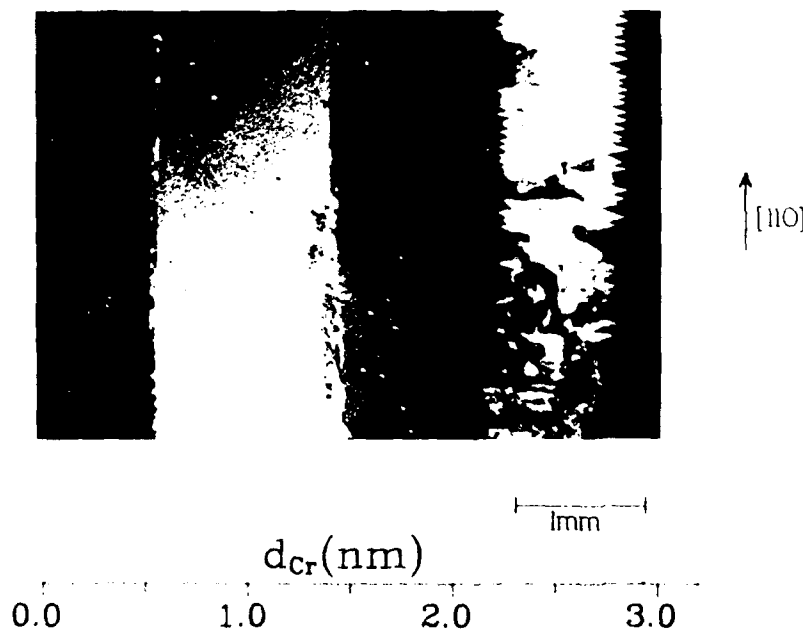

$d_{Cr}(nm)$

| 0.0 | 1.0 | 2.0 | 3.0 |

Fig.6. Zebra structure observed by Kerr microscope on the wedge sample.

Here the dark areas are already saturated FM type ranges whereas the brighter areas are the not yet saturated areas with AF type coupling. More details are revealed after application of a large magnification. Whereas ranges with FM type coupling behave essentially in the same way as single uncoupled Fe films, the ranges with AF type coupling show small irregularly shaped domains. This can be understood on the basis of the requirement for fluxclosure. In the case of FM type coupling as in single Fe films with fourfold inplane anisotropy it leads to 180° or 90° straight walls, oriented along the easy or hard axis of such films. For AF coupled films of the same thickness on the other hand due to antiparallel alignment the net moment cancels out. Therefore the requirement for fluxclosure disappears. The domain walls now have irregularly curved shapes due to local variations in the pinning fields.

Of particular interest are the transition zones between ranges of FM and AF type coupling. We should consider here the so-called exchange length, i.e. the distance in which spin correlate to each other due to inplane exchange in Fe. This is roughly identical with the domain wall width and for Fe it is smaller than 100 nm. This is far below the optical resolution of Kerr microscopy and therefore different parts of the domain patterns observed can be considered as having no mutual intraplane exchange interaction. We turn now to the transition zones between FM and AF type interlayer exchange. A domain pattern which can typically be observed in that range is illustrated in Fig.7. On the left side one can see the domain pattern visible with the Kerr setting (the Voigt setting picture is not shown). The arrow in the middle picture indicates the place of observation in the zebra structure. The picture on the righthand side shows the schematic of the observed domains, including the magnetization directions. In the single films the magnetization directions are again along the easy axis but for the two films they are orthogonal with respect to each other. Because of the limited space we can not go into details, they are published elsewhere [15]. We can only note that all details of this figure can easily be rationalized except for the fact that the magnetization directions in the lower and upper film are always perpendicular. In order to account for this observation we have to assume that an interaction is present which produces this orientation.
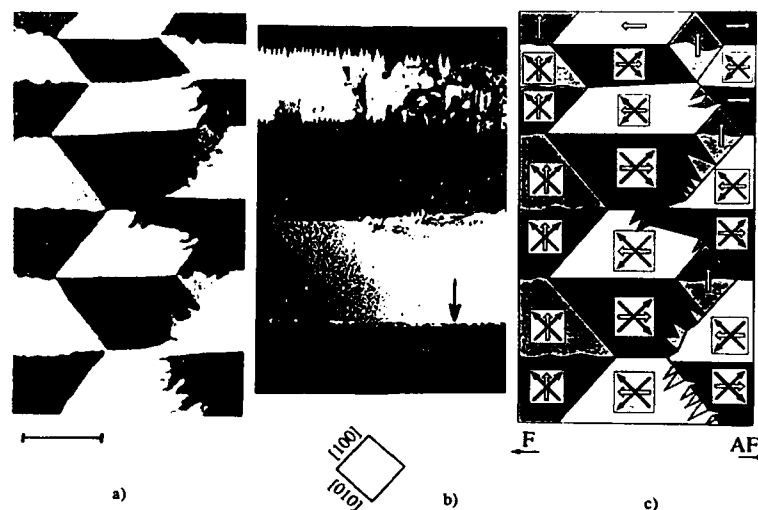

Fig.7. Analysis of a domain pattern of the transition zone. a) - pattern observed using the Kerr setting, the shown scale bar corresponds to 20 μm. b) - zebra structure with the indication of the investigated place. c)- interpretation consistent with pictures observed by means of Kerr and Voigt setting.
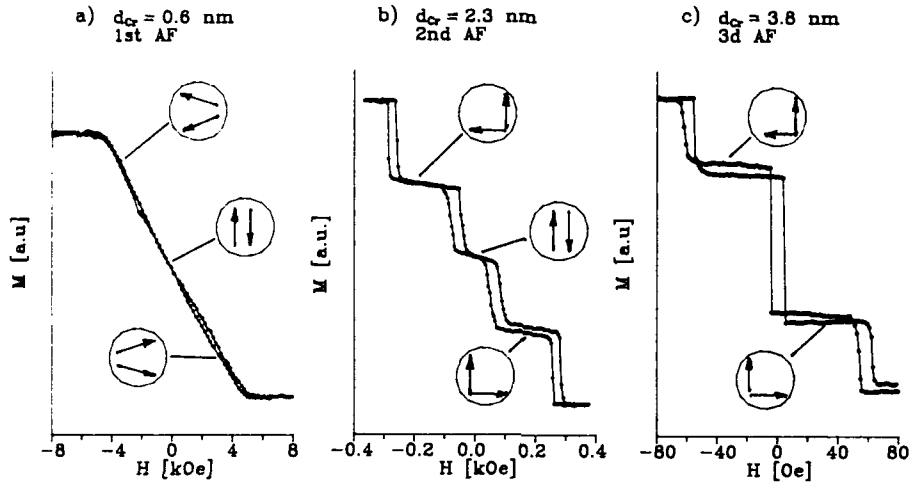
a) $d_{Cr} = 0.6$ nm
1st AF

b) $d_{Cr} = 2.3$ nm
2nd AF

c) $d_{Cr} = 3.8$ nm
3d AF

Fig.8. Magnetization curves, measured by scanning MOKE on the wedge sample for different d_{Cr} and different AF regions. Magnetic field is applied along the easy axis. Note different scales for H-axis.

Such interaction, if it exists, should be revealed in the M(H) curves. The examples of curves obtained by scanning magnetooptical Kerr measurements are shown in Fig.8. As we mentioned, in Fe films there exists the crystallographic fourfold anisotropy. The presented dependencies correspond to the situation when the magnetic field is applied along the easy axis. Note the different field scales in these pictures. The form of these pictures was reproducible for different samples. In one sample the curves obtained for both easy axes were identical. The curves b and c in Fig.8 demonstrate the existence of some phase with the total magnetization of $1/2M_s$. For the curve b this phase exists in the field region from 100 Oe to 270 Oe and for the curve c from 0 to 60 Oe. In both cases these intervals are much larger than the coercive force (5 Oe). It means that this phase has a real stable origin and can not present some metastable alignment.

The observed domain pattern and M(H) curves can be understood if we introduce in the energy expression some noncollinear interaction. This interaction might be either bilinear exchange with the contribution in (1) like

$$B_{12} \cdot \frac{(\vec{M_1} \cdot \vec{M_2})^2}{|\vec{M_1}| \cdot |\vec{M_2}|} \tag{4}$$

or an interaction of the Dzyaloshinskii type

$$B_{12} \cdot \frac{(\vec{n}_D \cdot (\vec{M_1} \times \vec{M_2}))^2}{|\vec{M_1}| \cdot |\vec{M_2}|} \tag{4a}$$

where $\vec{n}_D$ is a unit vector, perpendicular to the film plane. At the corresponding sign and value of the constant B_{12} the observed 90″ configuration becomes energetically preferable. We note here that the classic Dzyaloshinskii interaction like the following $\vec{n}_D \cdot (\vec{M_1} \times \vec{M_2})$ is symmetrically forbidden because of the inversion which exchanges the equivalent Fe films. For the same reason $\vec{n}_D$ is not a real vector , but it is what in liquid crystal physics is called a director. It yields the axis only, but the two directions of this axis are equivalent. The expressions (4) and (4a) correspond to the interactions with different

origin (exchange and spin-orbital coupling), but at the condition of in-plane magnetization the dependence of the energy on the magnetization directions of the films in both cases are the same. Thus, from the described experiments it is impossible to choose between these two interactions. One can do it if the in-plane magnetization will be destroyed, but it requires a high field (20-25 kG) and is a subject of further investigations. The analysis of the energy expression including the term (4) shows that the behavior of the system depends on the relation between A_{12} and B_{12}. When $A_{12} > B_{12}$, the system consistently passed the antiparallel, 90° and parallel configurations (Fig.8b). The 90° configuration corresponds to the energy minimum and is stable in some region of the applied field. But when $A_{12} < B_{12}$ the situation changes. Even in zero field the 90° configuration is stable and the system never has antiparallel configuration, as we can see in the experiment (Fig.8c). Bearing in mind the existence of such noncollinear interaction we should note that Fig.1 presents in fact the sum of A_{12} and B_{12}.

From this consideration it is possible to understand the origin of the peculiar domain patterns, observed in the transition zones. In these zones around points, where $A_{12}(d_{Cr})$ changes the sign, its value is smaller than the value of B_{12} and the 90° orientation become stable in small fields.

The values of A_{12} and B_{12} were measured for samples with different d_{Fe}. It was found that both values are roughly proportional to $1/d_{Fe}$. That fact confirms the surface origin of these interactions.

References

[1]   Grünberg P., Schreiber R., Pang Y., Brodsky M.B. and Sowers H., Phys. Rev. Lett.,57, 2442 (1986).
[2]   Baibich M.N., Broto J.M., Fert A., Nguyen Van Dau F., Petroff F., Etienne P., Creuzet G., Friederich A. and Chazelas J., Phys. Rev. Lett.,61,2472 (1988).
[3]   Krebs J.J., Lubitz P., Chaiken A., Prinz G.A., Phys. Rev. Lett., 63,1645 (1989).
[4]   Parkin S.S.P., More N., Roche K.P., Phys. Rev. Lett., 64,2304 (1990).
[5]   Binasch G., Grünberg P., Saurenbach F., Zinn W., Phys. Rev., B39,482 (1989).
[6]   Wang Y., Levy P.M., Frey J.L., Proc. of the E-MRS conference, Strasbourg, June 1990.
[7]   Stoeffler D., Ounadjela K., Gautier F., Proc. of the E-MRS conference, Strasbourg, June 1990.
[8]   Edwards D.M., Mathon J., Proc. of the E-MRS conference, Strasbourg, June 1990.
[9]   Hasegawa H., Phys. Rev., B42,2368 (1990).
[10] Lacroix L., Dieny B., Gavian J.P., Givord D., Thin Solids Films, 193/194, 887 (1990).
[11] Etienne P., Massies J., Nguen Van Dau F., Barthelemy A., Fert A., Appl. Phys. Lett.,55,2239 (1989), and references therein.
[12] Hoffmann F., Stankoff A., Pascard H., J. Appl. Phys., 41,1022 (1970).
[13] Parkin S.S.P. (private communication).
[14] Barnas J., Grünberg P., J. Magn. Magn. Mat, 82, 186 (1989), and Grünberg P. , Light scattering in solids V , edited by M.Cardona and G.Güntherodt, Topics in Applied Physics , (Springer 1989),vol 66, Chap.8.
[15] Rührig M., Schäfer R., Hubert A., Mosler R., Wolf J.A., Demokritov S., Grünberg P., Phys. Stat. Sol (a), 125, (1991) to be published.
[16] Schäfer R., Hubert A., Phys. Stat. Sol (a), 118, 271 (1990).

OSCILLATORY INTERLAYER EXCHANGE COUPLING THROUGH CU AND VARIOUS TRANSITION METALS

S.S.P. PARKIN
IBM Research Division, Almaden Research Center, 650 Harry Road, San Jose CA 95120-6099.

Abstract

We show that oscillatory interlayer exchange coupling of thin magnetic layers through metals is a general phenomenon present in almost all the transition and noble metals. Surprisingly the period of the oscillations is approximately the same, about 10Å, in all these metals with the sole exception of Cr for which the period is significantly longer. The strength of the coupling varies systematically throughout the 3d, 4d and 5d transition metals increasing exponentially along each of the transition metal periods and increasing from the 5d to 4d to 3d periods. These results appear to be inconsistent with simple Ruderman-Kittel-Kasuya-Yosida (RKKY) based models.

Introduction

The discovery of long-period oscillations in the magnetic interlayer coupling of thin Fe and Co layers separated by thin Cr or Ru layers in sputtered multilayers[1] has prompted much work on the origin of the magnetic coupling[2-11]. Whilst early experiments on single crystal Fe/Cr multilayers and sandwiches showed no evidence for oscillations in the interlayer magnetic coupling, later work on single crystal Fe/Cr/Fe wedges has not only confirmed the existence of long period oscillations but has shown the presence of additional short period oscillations with oscillation periods of just 2 Cr monolayers[12-14]. Whilst early speculations on the origin of the antiferromagnetic coupling in Fe/Cr multilayers and sandwiches were based on the unique magnetic character of Cr the discovery of similar and stronger antiferromagnetic coupling in Co/Ru ruled out such models[1]. More recently antiferromagnetic coupling and oscillations in the coupling have been found in numerous transition metals[15] as well as a number of noble metals including Cu[16-20].

Sample preparation

The samples described in this paper were deposited by standard dc magnetron sputtering methods in a computer controlled sputtering system. The base pressure of the system was $\simeq 1 \times 10^{-9}$. The multilayers were grown close to room temperature at deposition rates of 2Å/sec in 3.25 mTorr Ar. An important advantage of such a system compared to MBE (molecular beam epitaxy) techniques is its great speed and versatility. Series of up to 20 related structures can be grown in a matter of a few hours. Although the absolute accuracy of individual layer thicknesses is no more than ~5% very high relative accuracy of layer thicknesses from one structure to another in the same series is obtained. The resulting structures are polycrystalline, although usually textured along a particular crystallographic direction. Impurity levels of for example, oxygen and carbon are low, and typically below that of the auger sensitivity for these species (~1 atomic%). Moreover structures with flat contiguous layers can be grown for a wide variety of magnetic and non-magnetic spacer layer combinations. Figure
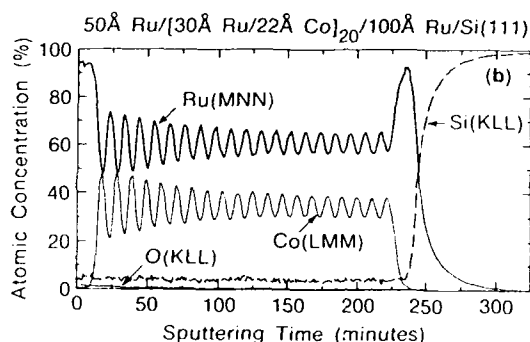
$$50\text{Å Ru/[30Å Ru/22Å Co]}_{20}\text{/100Å Ru/Si(111)}$$

Figure 1 Auger sputter depth profile of a Co/Ru multilayer of the form $Si(111)/Ru(100\text{Å})/[Co(22\text{Å})/Ru(30\text{Å})]_{20}/Ru(50\text{Å})$.

1 shows a typical auger sputter depth profile of a Co/Ru multilayered structure. These data were taken with rotation of the sample (Zalar rotation) during the sputtering process to improve depth resolution. The data are consistent with the growth of a multilayer with flat well defined multilayers, although the depth resolution of such a technique is limited to $\simeq 10\text{Å}$. The data shows no evidence for oxygen contamination above the background. Note that the silicon auger signal within the multilayer is not significant.

Results and Discussion

Typical in-plane magnetic hysteresis loops and transverse in-plane magnetoresistance data for two antiferromagnetically coupled Co/Cr multilayers are shown in Figure 2. The magnetic hysteresis loops show approximately zero moment in zero field consistent with antiferromagnetic alignment of successive Co layers in the structure. In contrast to similarly grown Fe/Cr multilayers[1, 21] the hysteresis loop shows a pronounced double S-shaped loop. Such a loop is consistent with some sort of effective spin-flop field where the Co moments arrange themselves approximately perpendicular to the applied field. Since the Co layers have much higher magnetic anisotropy than equivalent Fe layers a higher effective spin-flop field is expected. The antiferromagnetic coupling strength, as deduced from the field required to align the individual magnetic moments of the Co layers, is lower by about a factor of 2-3 than in comparable Fe/Cr multilayers. In contrast the magnitude of the saturation magnetoresistance is more than 20 times smaller.

Figure 2 shows evidence for oscillations in the antiferromagnetic interlayer exchange coupling in a series of Co/Cr multilayers as a function of Cr spacer layer thickness. Parallel oscillations in the saturation magnetoresistance are also observed. The period of the oscillations is similar to that found in Fe/Cr multilayers although the phase of the oscillations is shifted towards reduced Cr layer thicknesses.

The temperature dependence of the interlayer exchange coupling depends sensitively on the magnetic and non-magnetic layer materials. Figure 4 shows typical in-plane magnetic hysteresis loops at 6.5 K and 400 K for representative antiferromagnetically coupled Fe/Cr and Co/Ru samples. The coupling is much larger in the latter sample
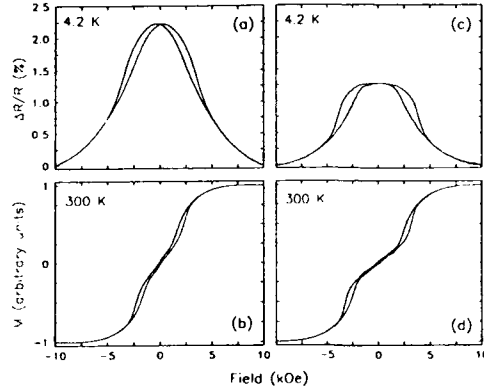
Figure 2: Magnetoresistance versus field curves (4.2 K) and magnetic hysteresis loops (300 K) for two Co/Cr multilayered structures, Si(111)/Cr(90Å)/[Co(12Å)/Cr(t)]$_{30}$/Cr(40Å), for Cr spacer layer thicknesses of (a) and (b), 3.5Å and (c) and (d), 7.0Å.
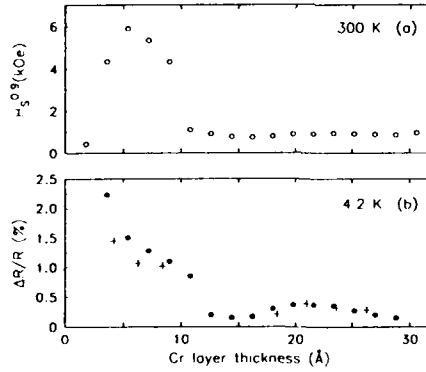
Figure 3: Dependence of (a) saturation field (300 K) and (b) saturation magnetoresistance (4.2 K) on Cr layer thickness, t, for Co/Cr multilayers of the form (○, ●) Si(111)/Cr(90Å)/[Co(12Å)/Cr(t)]$_{30}$/Cr(40Å) and (+) Si(111)/Cr(105Å)/[Co(17Å)/Cr(t)]$_{20}$/Cr(53Å). The saturation field, $H_s^{0.9}$, is the field at which the magnetization attains 90% of the saturation value.

as represented by the higher saturation field. The data also shows a stronger dependence of the coupling strength on temperature in the Co/Ru sample compared to Fe/Cr. Figure 5 shows the detailed dependence of the coupling strength on temperature for temperatures in the range 6.5 to 620 K. The coupling strength is proportional to the saturation field, $H_{sat}^{0.8}$, which we define as the field at which the magnetic moment is 80% of the saturation moment averaged over the four quadrants of the magnetic hysteresis loop. The error bars in the figure represent the variation in the individual saturation fields for the four quadrants. For temperatures below 400 K the data were measured in a squid magnetometer but for higher temperatures a vibrating sample magnetometer, which has lower sensitivity, was used. The coupling strength decreases with increasing temperature. For the range of temperature shown in Figure
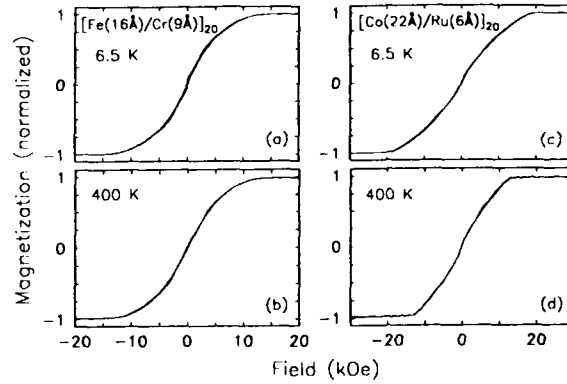
Figure 4: Magnetization versus in plane field loops at 6.5 and 400 K for multilayers of (a) and (b). Si(111)/Cr(110Å)/[Fe(16Å)/Cr(9Å)]/Cr(55Å) and (c) and (d). Si(111)/Ru(100Å)/[Co(22Å)/Ru(6Å)]/Ru(50Å).
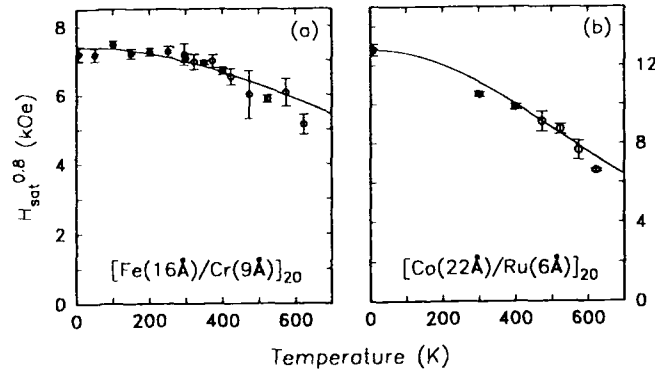
Figure 5: Dependence of saturation field, $H_{sat}^{0.8}$ on temperature for multilayers, (a) Si(111)/Cr(110Å)/[Fe(16Å)/Cr(9Å)]/Cr(55Å) and (b) Si(111)/Ru(100Å)/[Co(22Å)/Ru(6Å)]/Ru(50Å).

5 the data are reproducible on cycling up and down in temperature. However for both Fe/Cr and Co/Ru cycling to higher temperatures results in irreversible reductions in coupling strength presumably as a result of interdiffusion of the individual layers. The temperature dependence of the coupling strength is much larger for the Co/Ru sample compared to the Fe/Cr sample. Within RKKY based models the temperature dependence of the coupling strength is determined by thermal smearing of the Fermi surface as described by the Fermi-Dirac function. Such models predict that the exchange coupling strength will vary with temperature, T, as $(T/t)/\sinh(T/t)$ where t depends on the details of the Fermi surface topology[4, 11]. Such a functional form well describes the data in Fig. 5. The smooth lines drawn through the data in Figure 5 are fits to the data of this functional form (normalized to the measured values of $H_{sat}^{0.8}$ at low temperatures). Values of t are $500 \pm 25 K$ for the Fe/Cr sample and $320 \pm 10 K$ for the Co/Ru sample. The temperature dependence of the coupling

Ti ◯	V ⊛	Cr ⊛	Mn♠	Fe ⊛	Co ◯	Ni ▣	Cu ▣	
No Coupling	9	3	7	7		Ferro-Magnet	Ferro-Magnet	Ferro-Magnet	8	3
	0.1	9	.24	18					0.3	10
2.89	2.62	2.50	2.24	2.48	2.50	2.49	2.56	

Zr ◯	Nb ⊛	Mo ⊛	Tc ◯	Ru ◯	Rh ▣	Pd ▣	Ag ▣	
No Coupling	9.5	2.5	5.2	3		3	3	7.9	3	No Coupling	No Coupling
	.02	*	.12	11		5	11	1.6	9		
3.17	2.86	2.72	2.71	2.65	2.69	2.75	2.89	

Hf ◯	Ta ⊛	W ⊛	Re ◯	Os ◯	Ir ▣	Pt ▣	Au ▣	
No Coupling	7	2	5.5	3	4.2	3.5		4	3	No Coupling	No Coupling
	.01	*	.03	*	.41	10		1.85	9		
3.13	2.86	2.74	2.74	2.68	2.71	2.77	2.88	

Element
A_1	ΔA_1
(Å)	(Å)
J_1	P
	(Å)
r_{w-s}	
(Å)	

⊛ fcc   ⊛ bcc   ◯ hcp   ♠ complex cubic

Table 1: Periodic Table of A_1(Å), the spacer-layer thickness corresponding to the position of the first peak in antiferromagnetic exchange coupling strength as the spacer layer thickness is increased; J_1(erg/cm²), the magnitude of the antiferromagnetic exchange coupling strength at this first peak; ΔA_1(Å), the approximate range of spacer layer thickness of the first antiferromagnetic region; and P(Å), the oscillation period. The most stable crystal structure of the various elements are included for reference, as well as values of the Wigner-Seitz radii (r_{w-s}(Å)). Note that no dependence of the coupling strength on crystal structure nor any correlation with electron density ($\propto r_{w-s}^3$) is found.

* As discussed in the text for the elements Nb, Ta and W, only one AF coupled spacer-layer thickness region was observed, so it was not possible to directly determine P.
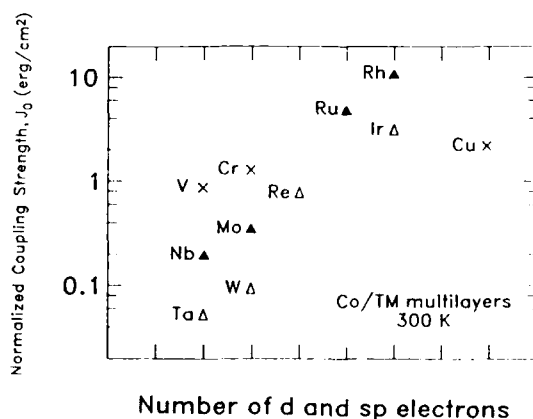

Figure 6 Dependence of normalized exchange coupling constant on the 3d, 4d and 5d transition metals in Co/TM multilayers.

strength is obviously unrelated to the Curie temperature, T_C, of the magnetic layer since T_C is considerably higher for Co than Fe. Indeed for the temperature range included in Fig. 5 the variation in the magnetization of the samples is only a few percent. However, for the Fe/Cr sample, taking into account this variation would indicate an even smaller temperature dependence of the interlayer exchange coupling.

Finally characteristics of the interlayer coupling for a variety of transition metals in Co based multilayers are summarized in Table 1. This table is described in more detail elsewhere[15]. We have similar although less extensive data for multilayers based on Fe, Ni and Ni based alloys. These data show that antiferromagnetic coupling and oscillations in the magnetic coupling is not limited to a small subset of magnetic multilayers but rather that this is the usual behaviour of most metals. The table shows that the period of the oscillations is similar for most metals with the particular exception of Cr for which the period is significantly longer. In no case have we found any evidence for a significant dependence of the oscillation period on the magnetic material although the phase of the oscillation is extremely sensitive to the magnetic material[1, 15, 22]. The phase of the oscillation also varies from element to element for the same magnetic material (see Table 1). Since the coupling strength falls off rapidly with increasing spacer layer thickness[1, 14-16, 22] coupling strengths must be compared for the same equivalent spacer layer thickness. By assuming that the coupling strength falls off as $1/t^2$ where t is the spacer layer thickness, values of the interlayer coupling strengths for the same t can be calculated. These values (for t = 3 Å) are plotted versus number of d electrons in Figure 6. Figure 6 shows that the coupling strength systematically varies throughout the periodic table from small values towards the bottom left hand side of the table to larger values towards the top right hand side. In some cases we observe no coupling. For Ti, Zr and Hf we find no evidence for significant magnetic interlayer coupling but for these elements the trends in coupling strength displayed in Fig. 6 would suggest very weak coupling. In other cases - Pd, Pt, Ag and Au - the presence of antiferromagnetic coupling, particularly if it is weak, may be obscured by structural defects such as pin-holes through the spacer layers.

Within RKKY and related models the oscillation period is related to the inverse length of wave-vectors which span or nest the Fermi surface according to appropriate rules[4, 11]. Since the topology of the Fermi surfaces of the elements shown in Table 1 which display oscillatory coupling are very different one would conclude that the period of the oscillations should vary widely from element to element. Indeed these elements have different crystal structures and moreover these films are polycrystalline with different orientations of the structures along the film growth axis. In a particular film structure the crystallites are oriented in a variety of directions, although usually there is some preferential orientation. Thus the universal oscillation period which we find for most of the elements, excluding Cr, is quite surprising. Again the strength of the coupling should depend, within RKKY like models, on the details of the Fermi surface topology. Thus it is surprising that the strength of the interlayer exchange coupling varies so systematically throughout the periodic table.

Conclusions

Oscillatory interlayer exchange coupling is shown to be a general property of almost all the transition and noble metals. The oscillation period appears to be approximately the same for all metals at about 10Å, with the exception of Cr for which the period is

about twice as long. Oscillatory interlayer coupling is found in multilayers comprised of all the 3d transition metal ferromagnets, Ni, Co and Fe as well as various alloys of these metals. Surprisingly the strength of the coupling varies systematically throughout the periodic table increasing rapidly along each of the 3d, 4d and 5d periods and from the 5d to 4d to 3d periods. These results appear to be at odds with simple RKKY or RKKY related models.

Acknowledgements

References

[1] S.S.P. Parkin, N. More and K.P. Roche, Phys. Rev. Lett. **64**, 2304 (1990).
[2] H. Hasegawa, Phys. Rev. B **42**, 2368 (1990).
[3] Y. Wang, P.M. Levy and J.L. Fry, Phys. Rev. Lett. **65**, 2732 (1990).
[4] D.M. Edwards, J. Mathon, R.B. Muniz and M.S. Phan, Phys. Rev. Lett. **67**, 493 (1991).
[5] D.M. Edwards, J. Mathon, R.B. Muniz and M.S. Phan, J. Phys.: Cond. Mat. **3**, 4941 (1991).
[6] J. Mathon, Contemp. Phys. **32**, 143 (1991).
[7] J.L. Fry, E.C. Ethridge, P.M. Levy and Y. Wang, J. Appl. Phys. **69**, 4780 (1991).
[8] C. Chappert and J.P. Renard, Europhys. Lett. **15**, 553 (1991).
[9] D.M. Deaven, D.S. Rokhsar and M. Johnson, Phys. Rev. B **44**, 5977 (1991).
[10] R. Coehoorn, (unpublished).
[11] P. Bruno and C. Chappert, Phys. Rev. Lett. **67**, 1602 (1991).
[12] J. Unguris, R.J. Celotta and D.T. Pierce, Phys. Rev. Lett. **67**, 140 (1991).
[13] S.T. Purcell, Phys. Rev. Lett. **67**, 903 (1991).
[14] S. Demokritov, J.A. Wolf and P. Grunberg, Euro. Phys. Lett. **15**, 881 (1991).
[15] S.S.P. Parkin, Phys. Rev. Lett. (to be published).
[16] S.S.P. Parkin, R. Bhadra and K.P. Roche, Phys. Rev. Lett. **66**, 2152 (1991).
[17] S.S.P. Parkin, Z.G. Li and D. Smith, Appl. Phys. Lett. **58**, 2710 (1991).
[18] W.R. Bennett, W. Schwarzacher and W.F. Egelhoff, Phys. Rev. Lett. **65**, 3169 (1990).
[19] A. Cebollada, R. Miranda, C.M. Schneider, P. Schuster and J. Kirschner, J. Mag. Mag. Mat. **102**, (1991).
[20] B. Heinrich, Z. Celinski, J.F. Cochran, W.B. Muir, J. Rudd, Q.M. Zhong, A.S. Arrott, K. Myrtle, and J. Kirschner, Phys. Rev. Lett. **64**, 673 (1990).
[21] S.S.P. Parkin, A. Mansour and G.P. Felcher, Appl. Phys. Lett. **58**, 1473 (1991).
[22] S.S.P. Parkin and D. Mauri, Phys. Rev. B. Rapid Comm. **44**, 7131 (1991).

CEMS INTERFACE STUDY OF (Fe/M)–MULTILAYERS (M=Cr,Gd)

CH. SAUER, J. LANDES AND W. ZINN
Institut für Festkörperforschung, Forschungszentrum Jülich, D–5170 Jülich, Germany

H. EBERT
Siemens AG, Central Research Labs, ZFE ME TPH 11, D–8520 Erlangen, Germany

ABSTRACT

The temperature dependence of the magnetic hyperfine (hf.) fields near the interfaces in epitaxial Fe/Cr and partly epitaxial Fe/Gd bilayers were measured using ^{57}Fe Conversion Electron Mössbauer Spectroscopy (CEMS). It was found that the Fe–Cr magnetic interaction extends only up to the second Fe–neighbor at the Fe/Cr interface, whereas the interaction range at the Fe/Gd interface is four times larger. For comparison the hf. fields and magnetic moments for Fe/Cr multilayers were obtained performing LMTO (Linear Muffin Tin Orbital) band structure calculations. The Néel temperature of a thin Cr–interlayer in a Fe/Cr/Fe sandwich structure was determined in dependence of the Cr–layer thickness.

Introduction

Recently, the study of the magnetic properties of thin layered structures with antiferromagnetic (AF) interlayer coupling [1] has gained wide interest.This is mainly due to the large magnetoresistance effect which was detected first in an Fe/Cr/Fe sandwich structure [2,3]. Because the possible mechanisms of the AF interlayer coupling are still a matter of discussion we have investigated the local magnetic interactions near the interfaces in Fe/Cr and Fe/Gd film systems with monolayer (ML) resolution by means of ^{57}Fe Conversion Electron Mössbauer Spectroscopy (CEMS). Such experiments are also highly attractive with respect to the recent progress of band structure calculations providing now magnetic moments and hyperfine (hf.) fields at interfaces and surfaces [4–6] in thin film structures. This work concentrates mainly on our results of the Fe/Cr system. It extends the measurements at T=300K presented in ref. [7] to lower temperatures and provides information on the range of the magnetic interaction at the Fe/Cr interface. In addition, we performed LMTO (Linear Muffin Tin Orbital) band structure calculations of Fe/Cr multilayers in order to determine theoretically the hf. fields and magnetic moments at the Fe/Cr interface.

Experimental

The in–situ CEMS experiments were performed in an ultrahigh vacuum (UHV) system [8] combining a film preparation chamber and a CEMS chamber. Thin film structures were prepared by evaporation in UHV with the following composition: GaAs(110)/30nm ^{56}Fe/2 ML ^{57}Fe/d ML ^{56}Fe/4nm Cr and GaAs(110)/15nm ^{56}Fe/2 ML ^{57}Fe/d ML ^{56}Fe/3nm Gd. By varying the thickness d of the interlayer of the non–Mössbauer effect (ME) isotope ^{56}Fe one can shift the ^{57}Fe probe layer from the interface. The Fe/Cr films grow with an epitaxial structure as has been proven by Rutherford backscattering (channelling) analysis. In the Fe/Gd system only the Fe–film grows epitaxially, whereas the Gd–film is amorphous. Nevertheless, in both cases the interfaces are sharply defined (1–2 ML) without interdiffusion. Details of the sample preparation are given in ref [7]. The ME–source was (^{57}Co)Rh.

Results and discussion

As described in ref. [7] all ME–spectra of the Fe/Cr interface region as measured using the [57]Fe probe layer technique could be decomposed into 4 subspectra with hf. field values of $B_{hf} = -33.4, -30.6, -26.4$ and -22.0 T at T=300K. From an analysis of Fe–Cr alloys the transferred hf. field contributions $\Delta B_1 = 3.19$ T and $\Delta B_2 = 2.15$ T caused by one Cr–atom in the next and second nearest neighbor shell around an Fe–atom are known [9]. Based on these data the four subspectra could be attributed [7] to a bulk–like Fe–site (– 33.4 T) and Fe atoms at flat regions (–22.0 T) and step positions (–30.6, –26.4 T) directly at the Fe/Cr interface. Correspondingly, on moving the [57]Fe probe layer further than 2 ML from the interface the three interface sub-spectra disappear and only the bulk–like spectrum remains. This reflects the sharpness of the interface.

As a function of temperature all four subspectra fulfil a Bloch spin wave law $\Delta B/B(0) = b \cdot T^{3/2}$ as it is usually observed for thin magnetic films. By extrapolation of the B_{hf} data of the bulk–like subspectrum to $T = 0$ K we obtained the saturation hf. fields. These values are plotted in Fig. 1 as a function of the distance d from the Fe/Cr interface. Similar to the results at $T = 300$ K [7] the hf. field is strongly reduced to –23.7 T in the first Fe–ML at the interface compared with the bulk value B_{hf} (bulk) = –34.3 T (at $T = 0$ K). However, in the 2nd and 3rd Fe–ML B_{hf} is slightly enhanced by about 2% and approaches the bulk value already in the 4th Fe–ML.

So far, theoretical calculations are available only for the magnetic moments at the Fe/Cr interface [4,10]. In order to gain also theoretical data of the corresponding hf. fields we performed LMTO calculations of the bandstructure of (100) oriented Fe/Cr multilayers with 3Fe/3Cr, 7Fe/3Cr, 11Fe/5Cr and 13Fe/7Cr sequences. Scalar relativistic effects are taken into account in the calculations which improves (increases) the absolut B_{hf} values by about 5% for 3d–elements (Fe,Cr) compared with a non–relativistic treatment. The results of the magnetic moments, the hf. fields and the contributions of core polarization and conduction electron polarization are shown in Fig. 2 for the 13Fe/7Cr multilayer sequence. The magnetic moments are slightly reduced in the first and enhanced in the second Fe–ML in agreement with ref. [10].
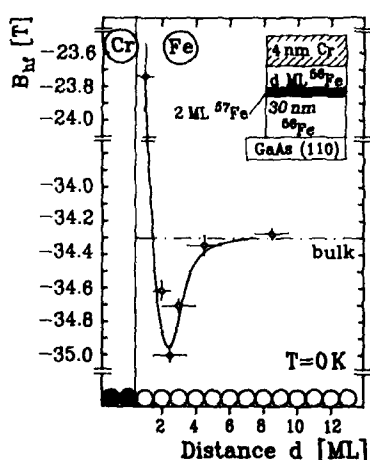

Fig.1: Magnetic hf. fields B_{hf} extra-polated to T=0K within the Fe film versus the distance d from the Fe/Cr interface. Dashed dotted line =B_{hf}(Fe–bulk).
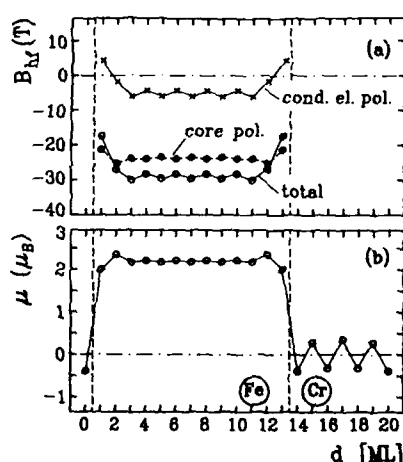
Fig.2: Results of the LMTO band structure calculations of the hf. field B_{hf} (a) and the magnetic moment (b) of a 13 ML Fe/7 ML Cr multilayer (100) struc-ture

While the absolute values of B_{hf} are too small, as it is also found for pure Fe, their distance dependence with respect to the interface agrees very well with the experimental data of Fig. 1.

As mentioned before, the hf. field data of the individual ME–subspectra related to interface effects follow a Bloch $T^{3/2}$ spin wave law. This is shown in Fig. 3 for the B_{hf} data attributed to flat (ideal) interface regions. The film structure was GaAs(110)/^{56}Fe/d ML Cr/^{56}Fe with varying Cr–interlayer thickness. This corresponds exactly to the Fe/Cr structure revealing the AF interlayer coupling [1]. At both interfaces a thin (2 ML) ^{57}Fe probe layer was intercalated. Despite the scattering of the data points a discontinuity in the $T^{3/2}$ behavior can be seen which shifts to lower temperatures with increasing Cr–interlayer thickness d. Because the sample with the largest thickness d(Cr) = 20 ML exhibits this discontinuity near the Néel temperature of bulk–Cr (T_N= 311 K) it is supposed that this effect may reflect the onset of magnetic order (Neel temperature) of the Cr–interlayer. The ^{57}Fe probe layer at the interface is expected to sense the transition from paramagnetic to the antiferromagnetic state of the Cr–layer via the transferred hf. fields. In Fig. 4 we have plotted the different temperatures T_D where the discontinuity is occuring versus the thickness d of the Cr–interlayer. The result is a smooth curve which can be fitted by the power law $(T_D(\infty) - T_D(d)) / T_D(\infty) = c \cdot d^{-\lambda}$ with c = 1.65 $\mp$ 0.6 and λ = 1.0$\mp$0.2. For T_D (∞) we have used T_N(bulk–Cr) = 311 K. We believe that the smooth variation of T_D with d supports our interpretation that T_D is equivalent to the Néel temperature T_N of the Cr–interlayer.
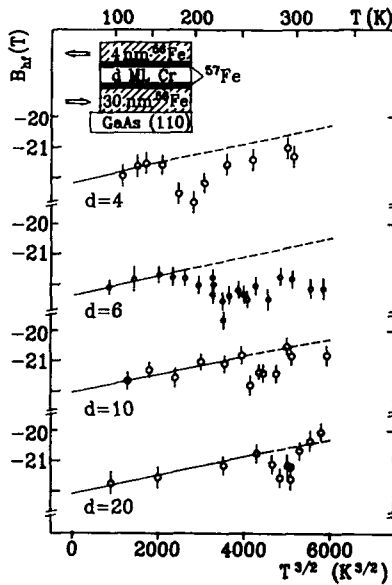

Fig.3: $T^{3/2}$ temperature dependence of the hf. fields B_{hf} measured directly at the Fe/Cr interface for Fe/d ML Cr/Fe sandwich structures (see text).
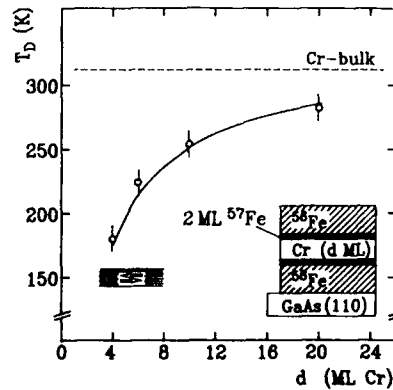
Fig.4: Temperature T_D as obtained from the data of Fig.3 versus the Cr interlayer thickness d (see text).

Such a power law is usually used to describe the thickness dependence of the Curie temperature of thin ferromagnetic films [11,12]. The constant c ranges from 1 to 10 in various experiments, while the shift exponent λ is predicted to vary between 1.0 and 2.0, depending on whether free—surface or periodic boundary conditions are assumed [11,14]. For the so far most often investigated Ni—films experimental values of $\lambda = 1.42 - 1.44$ are found recently [13,14]. Because our system contains an antiferromagnetic film bordered by two ferromagnetic films it seems to be not surprising that our result of $\lambda = 1.0$ deviates from the Ni—data. Furthermore, our T_D may be somewhat shifted with respect to the true T_N(Cr—interlayer) by local Fe—Cr alloying effects at the interface. This possibility might be deduced from the magnetic Fe—Cr phase diagram [15] which reveals a strong influence of Fe impurities on T_N(Cr).

The essential consequence of the data of Fig. 4 is, that T_N(Cr—interlayer) amounts to $180 - 230$ K for interlayer thicknesses of $d = 4 - 8$ ML, i.e. for the thickness range where the AF coupling of the Fe—layers is observed. Because the AF coupling occurs even at 300 K, apparently, it can be mediated via a paramagnetic Cr—interlayer. This finding is in agreement with the recent theoretical model of Wang et al. [16] which explains the AF coupling by a RKKY—like interaction through a paramagnetic Cr film.

The other useful information one can obtain from the $T^{3/2}$ temperature dependence of the hf. fields is the spin wave parameter b. This b—parameter is approximately related to the magnetic exchange parameter J by $b \propto J^{-3/2}$. According to Mathon [17] J should represent at interfaces and surfaces essentially the inter—plane exchange interaction between two neighboring Fe—MLs perpendicular to the film plane. In order to analyze the range of the magnetic Cr—Fe interaction we measured the spin wave parameter b as a function of the distance d from the Fe/Cr interface. As shown in Fig. 5 the b—parameter is strongly enhanced at the interface, i.e. the inter—plane exchange is reduced. The data can be fitted by an exponential law $b(d) = b(\text{bulk}) + 14.0 \cdot \exp(-d/\delta)$, where d is given in Fe—ML and the interaction length amounts to $\delta = 0.7$ ML. b (bulk) is determined to be $5.5 \cdot 10^{-6}$ K$^{-3/2}$. Consequently, the Fe—Cr interaction is of short range and extends up to the second Fe neighbor only. As a mechanism for this interaction we suggest a direct exchange interaction by the overlap of the 3d—orbitals of Fe and Cr. Any polarization of conduction electrons should play a minor role.

For comparison, we have investigated in the same way the distance dependence of the ^{57}Fe hf. fields and of the spin wave parameter b for the Fe/Gd interface. It is
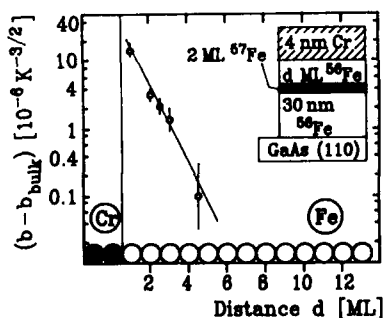

Fig.5: Deviation of the spin wave parameter b from the Fe—bulk value as a function of the distance d from the Fe/Cr interface.
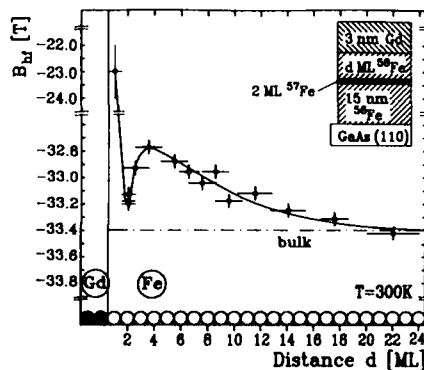
Fig.6: Distance dependence with respect to the Fe/Gd interface of the ^{57}Fe hf. field at T=300K. Dashed dotted line = B_{hf} (Fe—bulk).

known [18] that the magnetic interaction between Gd and Fe atoms is also antiferro-magnetic. The experiments, especially the measurements of the temperature depend-ences are not yet fully completed. Therefore, a detailed analysis of the Fe/Gd interface will be given elsewhere [19]. Fig. 6 shows the magnetic hf. field at 300 K within the Fe film as a function of the distance d from the Gd/Fe interface. Again we found a strong reduction of B_{hf} in the first Fe–ML and a peak–like enhancement in the following few MLs. But in contrast to the Fe/Cr system B_{hf} remains below the bulk value up to about 16 Fe–ML suggesting a much longer interaction range for the Gd/Fe interface. This explanation is supported by preliminary data of the spin wave parameter b. Also for the Fe/Gd system the b–parameter seems to follow an exponential distance law $b(d) = b(\text{bulk}) + 26.1 \cdot \exp(-d/\delta)$. But here the interaction length is found to be $\delta = 2.7$ ML which is about four times larger compared with Fe/Cr. Possible reasons for such a long interaction range may be (I) a pronounced conduction electron polarization within the Fe film induced by the large Gd spin moment $(7\mu_B)$ and/or (II) a stronger

hybridization of the Gd $-$ 5d wavefunction with the Fe $-$ (3d,4s) orbitals compared with the Cr $-$ 3d orbitals.

Conclusion

The band structure calculations of the Fe/Cr interface reveal the essential fea-tures of the hf. fields near the interface very well. The peak–like enhancement of B_{hf} in the second and third Fe–ML at the interface which is observed for both the Fe/Cr and Fe/Gd structures is mainly due to the modification of the conduction electron polari-zation at the interface. For a detailed understanding of the observed long range of the Gd–Fe interaction band structure calculations of the Fe/Gd interface are needed.

References

[1] P. Grünberg, R. Schreiber, Y. Pang, M.B. Brodsky and H. Sowers, Phys. Rev. Lett. 57, 2442 (1986).
[2] M.N. Baibich, J.M. Broto, A. Fert, F. Nguyen van Dau, F. Petroff, P. Etienne, G. Creuzet, A. Friedrich and J. Chazelas, Phys Rev. Lett. 61, 2471 (1988).
[3] G. Binasch, P. Grünberg, F. Saurenbach and W. Zinn, Phys. Rev. B39, 4828 (1989).
[4] J.H. Xu, A.J. Freeman and T. Oguchi, J. Mag. Magn. Mat. 86, 26 (1990).
[5] A.J. Freeman, C.L. Fu, M. Weinert and S. Onishi, Hyperf. Interact. 33, 53 (1987).
[6] H. Ebert, S. Ruegg, G. Schütz, R. Wienke and W.B. Zeper, Proc. of E–MRS Spring Meeting, Strasbourg, France, May 29 – June 1, 1990, in press.
[7] J. Landes, Ch. Sauer, R.A. Brand, W. Zinn, S. Mantl and Zs. Kajcsos, J. Mag. Magn. Mat. 86, 71 (1990).
[8] Ch. Sauer, A. Holzwarth, Zs. Kajcsos and W. Zinn, Nucl. Instr. Meth. B34, 377 (1988).
[9] S.M. Dubiel and J. Zukrowski, J. Mag. Magn. Mat. 23, 214 (1981).
[10] C.L. Fu and A.J. Freeman, J. Mag. Magn. Mat. 54–57, 777 (1986).
[11] G.A.T. Allen, Phys. Rev. B1, 352 (1970).
[12] C. Domb, J. Phys. A6, 1296 (1973).
[13] Yi Li, M. Farle and K. Baberschke, Phys. Rev. B41, 9596 (1990).
[14] C.A. Ballentine, R.L. Fink, J. Araya–Pochet and J.L. Erskine, Phys. Rev. B41, 2631 (1990).
[15] S.K. Burke, R. Cywinski, J.R. Davis and B.D. Rainford, J. Phys. F: Met. Phys., 13, 451 (9183)
[16] Y. Wang, P.M. Levy and J.L. Fry, Phys. Rev. Lett. 65, 2732 (1990).
[17] J. Mathon, Physica B149, 31 (1988).
[18] M. Taborelli, R. Allenspach, G. Boffa and M. Landolt, Phys. Rev. Lett. 56, 2869 (1986).
[19] J. Landes, Ch. Sauer and W. Zinn, J. Mag. Magn. Mat., to be published

INTERLAYER MAGNETIC COUPLING IN SPUTTERED Ag/Ni SUPERLATTICES

CARLOS A. DOS SANTOS[*] AND BERNARD RODMACQ[**]
Service de Physique des Matériaux et Microstructures, Département de
Recherche Fondamentale sur la Matière Condensée, Centre d'Etudes Nucléaires
de Grenoble, 85X, 38041 Grenoble Cédex, France
[*]Laboratoire de Magnétisme et Diffraction par Interactions Hyperfines.
On leave from Departamento de Fisica - UFRN, 59072 Natal (RN), Brasil
[**]Laboratoire de Métallurgie Physique

ABSTRACT

We report results of X-ray diffractometry and magnetic measurements
performed on Ag/Ni superlattices prepared by triode dc-sputtering. The
X-ray results suggest structural coherence and interface sharpness whatever
the thickness of the elemental layers with (111) textures for both Ag and
Ni. Magnetization measurements confirm the existence of sharp interfaces.
They also indicate that the magnetic moments preferentially lie in the
plane of the layers whatever the Ag or Ni thicknesses. We also present
evidence of the oscillatory character of the magnetic coupling of the Ni
layers through the non-magnetic Ag layers, which correlates with both
magnetoresistance and low-angle neutron diffraction experiments.

INTRODUCTION

Since the observation of oscillatory magnetic coupling in Gd/Y
superlattices [1], and the possible correlation between magnetization and
resistivity behaviors in Fe/Cr superlattices [2], interest in multilayered
materials has increased considerably. Antiferromagnetic coupling between
ferromagnetic layers separated by non-magnetic or antiferromagnetic ones
has been observed in different types of multilayers [2-4]. Furthermore,
oscillatory magnetic coupling has been also observed in Co/Cu [5,6], Co/Ru,
Co/Cr and Fe/Cr [7] superlattices, and Fe/Cu/Fe [8] sandwich structures.
All these results are related to the existence of exchange-dominated
collective spin-wave excitations indicated by Brillouin light scattering
experiments in multilayered systems [9-11].

In this paper we report recent results on the Ag/Ni multilayered
system. The choice of this system was motivated by the fact that non-
miscible Ag and Ni elements could produce sharp interfaces in superlattice
samples, and also because it is the first Ni-based system investigated up
to now from the point of view of possible interlayer magnetic coupling.

EXPERIMENTAL DETAILS

Layers of Ag and Ni were alternately deposited on glass substrates, at
100 K, by dc-sputtering, in order to prepare Ag_xNi_y samples -referred to
later on as (x,y)- where x and y are layer thicknesses, with x ranging from
about 5 to 40 Å and y ranging from about 2 to 20 Å. As described elsewhere
[12], the samples were grown with deposition rates of 0.98 Å/sec for Ag and
0.85 Å/sec for Ni. Total thicknesses were usually of the order of 5 μm.
X-ray scattering experiments were carried out using the Co Kα radiation
(λ = 1.7903 Å) in both reflection and transmission geometries. Magnetiza-
tion measurements were performed with a SQUID magnetometer at temperatures
between 5 and 300 K.
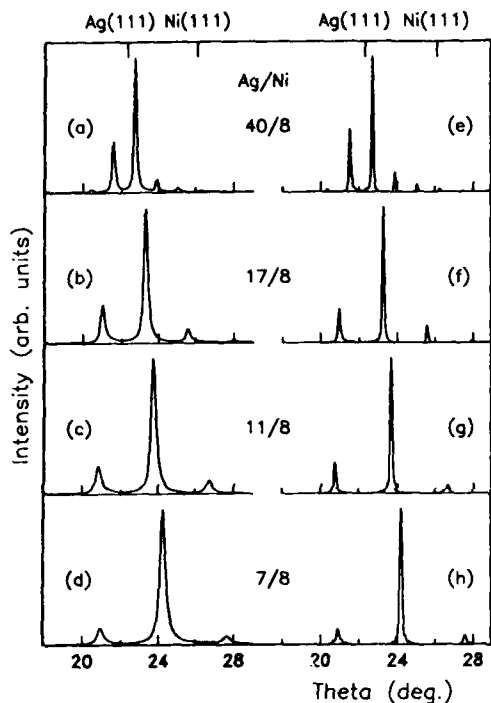
Ag(111) Ni(111)   Ag(111) Ni(111)

Fig. 1: Experimental (a to d) and simulated (e to h) X-ray diffraction spectra of Ag/Ni superlattices. The numbers give the thickness in Å of the elemental layers.

RESULTS AND DISCUSSION

Figs. 1(a) to 1(d) show typical large-angle diffraction spectra in reflection geometry. The spectra are characteristic of coherent superlattices with (111) Ag and Ni textures. Figs. 1(e) to 1(h) present the corresponding simulated spectra, obtained by assuming a rectangular composition profile (no chemical mixing) and constant Ag and Ni (111) interplanar distances (no relaxation) [12]. One sees that the relative intensities of the superlattice peaks agree quite well with the experimental ones, even for the smallest periods studied.

Further support to this model is given by the magnetization results. Interfacial phenomena in magnetic multilayers (like for example interdiffusion or lattice deformation) are usually related to the so called "dead layer" by simple models supposing that the magnetic atoms at the interface carry no magnetic moment [15]. Under this assumption, the variation of the magnetization with the thickness of the magnetic layer can be written as:

$$M_s \, t = M_m (t - 2 \, t_{nm})$$

where M_s is the multilayer saturation magnetization (in Bohr magnetons per magnetic atom), M_m is the magnetization of the "live" magnetic layer, t is the total thickness of the magnetic element layer, and t_{nm} is the "dead layer" thickness at each interface. We have performed a systematic study of this effect at 5 K for samples (t_{Ag}, t_{Ni}) with $t_{Ag} = 8$, 14 and 18 Å. As can be seen in Fig. 2, a linear variation of $M_s \, t_{Ni}$ vs t_{Ni} is obtained, and a linear regression through the three sets of data points leads to the values
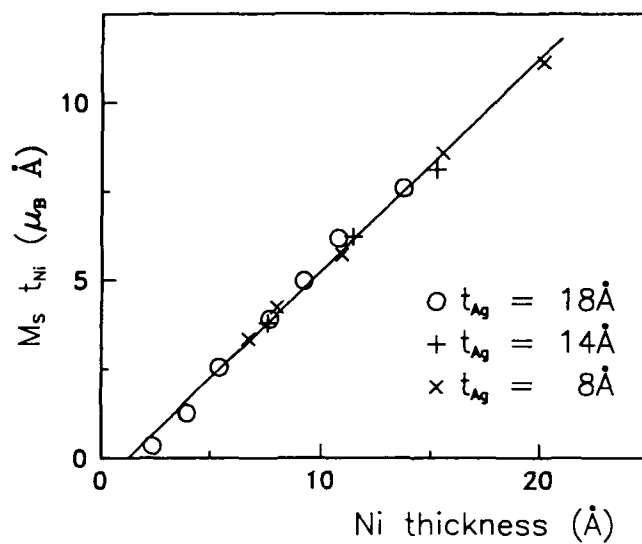
Fig. 2: Variation of $M_s \, t_{Ni}$ versus t_{Ni} at 5 K for three sets of samples with different Ag thicknesses.
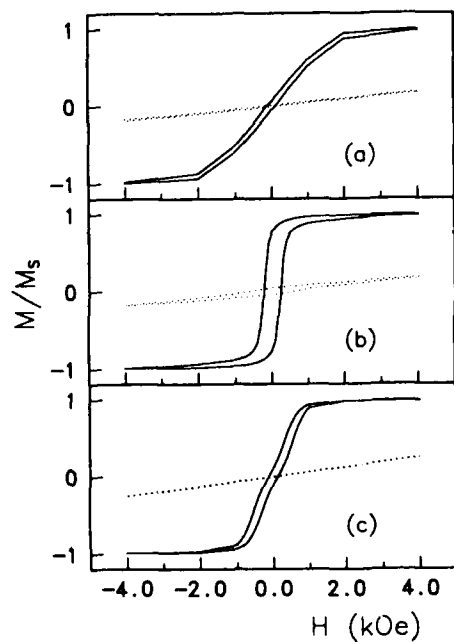

Fig. 3: Hysteresis curves at 5 K with in-plane (solid line) and perpendicular (dotted line) applied field for samples (a) (11,8); (b) (40,8); (c) (11,17).

$t_{nm} \cong 0.62$ Å and $M_{Ni} \cong 0.598$ μ_B (practically identical to the bulk value for Ni $\cong 0.60$ μ_B). The uncertainty on the value of t_{nm} is estimated at about 0.32 Å (from the scatter of the data points in Fig. 2 and keeping constant the above value of M_{Ni}). These results are thus in agreement with the X-ray results, which also suggest sharp interfaces.

Fig. 3 shows normalized hysteresis curves obtained at 5 K with in-plane and perpendicular applied magnetic fields for (11,8), (40,8) and (11,17) samples. In all cases the easy magnetization axis lies in the plane of the layers, but the shape of the hysteresis curves seems to depend mainly on the Ag layer thickness. It is possible to classify the samples in two groups, those samples with a high saturation field and low remanence on the one hand , and those with a low saturation field and high remanence on the other hand. This difference can be interpreted as a result of oscillations in the interlayer magnetic coupling. For samples with Ag thicknesses between 10 Å and 15 Å the Ni layers are coupled antiferromagnetically; for the other samples with Ag thicknesses below 10 Å or above 15 Å the antiferromagnetic coupling is weaker, or the interlayer magnetic coupling is ferromagnetic, or the Ni layers are decoupled. From our measurements it is not possible to distinguish between these possibilities.

The differences between these samples can be characterized by the variation of the saturation field H_{sat}, defined as the difference between the coercive field and that at the intercept of the low-field and high-field slopes. Fig. 4 shows the variation of H_{sat} with the Ag layer thickness, at a measurement temperature of 5 K. It presents a maximum at an Ag thickness of between 11 and 12 Å, and then decreases very rapidly at larger thicknesses. A very weak second maximum can be observed at about 30 Å Ag. A similar behavior is also observed for samples with different Ni layer thicknesses (10 Å and 16 Å). This indicates that the antiferromagnetic coupling is mostly dependent on the Ag thickness whatever the thickness of the Ni layer.
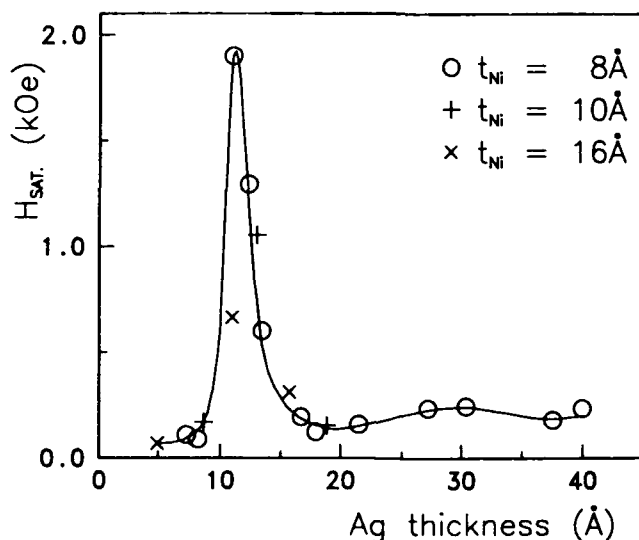

Fig. 4: Saturation field at 5 K versus Ag layer thickness for three sets of samples with different Ni thicknesses.

The present results are in agreement with those published recently for different superlattice structures. For example, the thickness of the non-magnetic spacer for which the saturation field is maximum is about 8 Å for Cr [7] and Cu [5,6], and about 11 Å for Ag. A major difference between our results and those obtained by Kwo et al [1], Mosca et al [6] and Parkin et al [7] is related to the number of observed periods of oscillation. These authors have observed several periods, while in Fig. 4 the second oscillation is hardly observable.

In addition, magnetoresistance measurements [14] on the same samples show a variation of the magnetoresistive effect very close to the one of the saturation field, with a maximum effect of 25 % at 4.2 K for the same Ag thickness of 11 Å. Finally, recent low-angle neutron experiments on similar samples [15] indicate a doubling of the chemical period, thus confirming the antiparallel arrangement of the magnetic moments in successive Ni layers

CONCLUSION

In conclusion, the results presented in this paper give indication of an oscillatory magnetic coupling in Ag/Ni superlattices prepared by dc-sputtering. The coupling is maximum for an Ag layer thickness of about 11 Å and is highly damped for larger thicknesses. Such an effect has been observed for series with different Ni thicknesses (8, 10 and 16 Å), and seems to be confirmed by neutron scattering experiments. Preliminary results also indicate a similar dependence of the magnetoresistive effect on the thickness of the nonmagnetic spacer.

REFERENCES

1. J. Kwo, M. Hong, F.J. DiSalvo, J.V. Waszczak and C.F. Majkrzak, Phys. Rev. B35, 7295 (1987).

2. M.N. Baibich, J.M. Broto, A. Fert, F. Nguyen Van Dau, F. Petroff, P. Etienne, G. Creuzet, A. Friederich and J. Chazelas, Phys. Rev. Lett. 61, 2472 (1988).

3. P. Grünberg, R. Schreiber, Y. Pang, M.B. Brodsky and H. Sowers, Phys. Rev. Lett. 57, 2442(1986).

4. A. Cebollada, J.L. Martinez, J.M. Gallego, J.J. de Miguel, R. Miranda, S. Ferrer, F. Batallan, G. Fillion and J.P. Rebouillat, Phys. Rev. B39, 9726 (1989).

5. D. Pescia, D. Kerkmann, F. Schumann and W. Gudat, Z. Phys B 78, 475 (1990).

6. D.H. Mosca, F. Petroff, A. Fert, P.A. Schroeder, W.P. Pratt, Jr. and R. Laloee, J. Magn. Magn. Mat. 94, L1 (1991).

7. S.S.P. Parkin, N. More and K.P. Roche, Phys. Rev. Lett. 64, 2304 (1990)

8. W.R. Bennett, W. Schwarzacher and W.F. Egelhoff, Jr., Phys. Rev. Lett. 65, 3169 (1990).

164

9. I.K. Schuller and M. Grimsditch, J. Appl. Phys. $\underline{55}$, 2491 (1984).

10. M. Vohl, J. Barnas and P. Grünberg, Phys. Rev. B$\underline{39}$, 12003 (1989).

11. B. Hillebrands, J.V. Harzer, G. Güntherodt, C.D. England and C.M. Falco, Phys. Rev. B$\underline{42}$, 6839 (1990).

12. B. Rodmacq, submitted to J. Appl. Phys.

13. N. Sato, J. Appl. Phys. $\underline{63}$, 3476 (1988).

14. C.A. dos Santos, B. Rodmacq, M. Vaezzadeh and B. George, submitted to Appl. Phys. Lett.

15. B. Rodmacq, Ph. Mangin and Chr. Vettier, submitted to Europhys. Lett.

INFLUENCE OF LAYER STRUCTURE ON ANTIFERROMAGNETIC
EXCHANGE COUPLING OF IRON FILMS THROUGH CHROMIUM INTERLAYERS

A.P. Payne, H. Kataoka, M. Farle, B.M. Clemens
Department of Materials Science and Engineering, Stanford University, Stanford CA, 94305-2205

ABSTRACT

The effect of layer structure perturbations on antiferromagnetic coupling in Fe-Cr-Fe trilayer systems is investigated. By varying the sputtering pressure, the layer structure of Fe-Cr-Fe trilayers is systematically altered, as indicated by changes in the low angle superlattice spectra of multilayers fabricated under identical conditions. The effect of topographic roughness is investigated by fabricating identical trilayers on Cr buffer layers of different thickness. Scanning tunneling microscopy is used to measure surface roughness. In each case the saturation field is measured as a function of Cr interlayer thickness by means of tapered Cr interlayer structures in which the thickness of the spacer varies linearly from 0 to 28 Å upon a single substrate. Antiferromagnetic coupling is measured locally by means of the magneto-optic Kerr effect. Results show that although the coupling is diminished by structural perturbations, it is a remarkably robust effect which persists even in instances of poor layer structure.

INTRODUCTION

There is much current interest in the exchange coupling of ferromagnetic thin films through non-magnetic interlayers. In selected systems it has been found that ferromagnetic layers couple antiferromagnetically through a non-magnetic spacer of appropriate thickness [1,2,3]. It has since been discovered that the antiferromagnetic coupling (AFC) is a oscillatory function of interlayer thickness such that subsequent antiferromagnetic excursions appear at even larger interlayer thicknesses [4]. The antiparallel orientation of moments in the ferromagnetic layers is accompanied by a dramatic increase in magnetoresistance (giant magnetoresistance) [5,6], endowing the phenomenon with a practical significance for sensor applications. The Fe-Cr system is the most studied system exhibiting this effect, an it has been demonstrated in Fe-Cr films produced by a variety of processes. For purposes of comparison, the Fe-Cr system was selected in this experiment as well. The objective of this study was to examine the effect of layer structure on the phenomenon, with the expectation that this will aid in its eventual understanding.

BACKGROUND

It has long been known that sputtering pressure plays an important role in determining the the physical properties and morphology of sputter deposited films [7]. By a process known as thermalization, the initial energy of the sputtered atom is diminished through collisions with the sputtering gas atoms [8], and the fraction of initial energy lost increases exponentially with sputtering pressure [9]. Adatoms arriving with higher energy are more able to seek out low energy attachment locations than are the less energetic adatoms, and since the bulk structure of a vapor deposited film is determined largely by behavior at the growing interface, this has important consequences to the final structure of the film. We have found sputtering pressure to have dramatic effects on the layer structure of Fe-Cr-Fe multilayer films. Rapid degradation of ideal layer structure occurs as pressure is increased from 1 to 10 mT. This was used in the present study to examine the influence of layer structure on antiferromagnetic exchange coupling. The effects of topographic roughness were also investigated by fabricating Fe-Cr-Fe trilayers on chromium buffer layers of various thickness.

Because both the sign and magnitude of the coupling are strong functions of interlayer thickness[10], comparative studies are complicated by the difficulty of fabricating two individual multilayer systems with identical coupling. In this study the problem was approached by fabricating an entire range of Fe-Cr-Fe trilayer films and then locating the thickness at which the AFC is strongest. Coupling strengths were then compared relative to this point. To circumvent the need to fabricate many individual samples, we varied the Cr interlayer thickness systematically on a single substrate and used a localized magnetic probe (the magneto-optic Kerr effect, MOKE) to study the exchange coupling.

EXPERIMENTAL

Deposition System and Film Preparation

All multilayers and tapered trilayers were prepared by sputter deposition in a compact UHV system with a base pressure of $4 \cdot 10^{-9}$ Torr. Three individually shuttered magnetron sources face the substrate at a distance of 6". All films were sputter-deposited on polished, vapor degreased polycrystalline quartz disks. The sputtering pressure was varied between 1.4 and 10 mT argon using a precision needle valve capable of maintaining the desired sputtering pressure to within .01 mT of the desired value for the duration of the run. Sputtering pressure was monitored throughout the deposition by means of a capacitance manometer. In all cases the deposition rate was held constant at 1.0 Å/s with .05 Å/s maximum uncertainty. Rates were monitored both by profilometry and by linear regression analysis of the low angle superlattice peaks.

Tapered Fe-Cr-Fe trilayer films with Cr buffer and cap (Quartz/XÅCr/25Fe/0-28Cr/25Fe/10Cr) were fabricated by partially masking the substrate while rotating it at constant angular velocity during deposition of the Cr interlayer. The 0-28Å thickness regime brackets the first antiferromagnetic excursion of the Fe-Cr-Fe system. This is the strongest excursion [4] and is most easily recognized from hysteresis loops. The 25Å Fe layer thickness was selected because it is thick enough to allow well developed bulk ferromagnetism yet thin enough to insure that the difference in integrated laser intensity reflected by each Fe layer is less than 20%. The 10Å Cr buffer was used to mitigate substrate effects on the lower Fe layer, while the 10Å Cr cap was used to prevent oxidation of the upper Fe layer. Two sets of films were fabricated in order to investigate the influence of layer roughness and topographic roughness respectively. In the first case tapered trilayers were fabricated at argon pressures of 1.4, 3.0, 5.0 and 10.0 mT. Under identical conditions, multilayer films were deposited for structural analysis. In the second set of films, identical trilayers were fabricated but with Cr buffer layer thickness of 10, 100, 500, and 1000Å .

Magnetic Characterization and Structural Analysis

A conventional Kerr magnetometry system with phase sensitive detection was employed [11,12]. Following the laser beam, the train of optical components is as follows: He-Ne laser, photoelastic modulator, 250 mm converging lens, aperture, sample, Glan-Thomson polarizer, photodiode. The size of the laser spot at the substrate was less than 0.5 mm, and the angle of incidence was fixed at 55° with respect to the sample normal. The maximum applied field of the electromagnet was ± 2.53 kG. Low-angle x-ray diffraction was used to characterize the layer roughness of the multilayer films sputtered at different argon pressures. This was performed in a standard powder diffractometer at two-theta angles ranging from 0.5 to 10°. For the trilayers deposited on the various Cr buffer layers, the STM was used to determine the average roughness of the film surfaces. The analysis was carried out immediately after deposition.

RESULTS AND DISCUSSION

Effect of Sputtering Pressure on Layer Roughness

Figure 1 shows a series of Fe-Cr low angle superlattice spectra from identical structures (20•[25ÅFe/30Cr]) sputtered at a variety of pressures. With increasing sputtering pressure, the higher order harmonics are attenuated with increasing severity. In addition, the peaks systematically broaden with increasing two-theta. The 10 mT structure shows only a single, broad superlattice peak. These effects are caused both by thickness fluctuations within each layer comprising the film and alloying between the two constituents at interfaces.
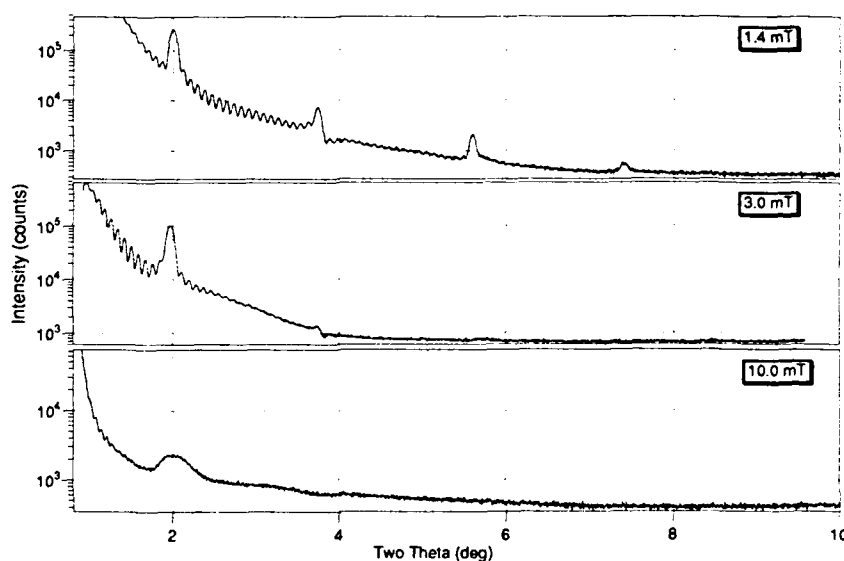

Fig. 1: Low angle XRD spectra from 20•(25ÅFe/30Cr) multilayers sputtered at several argon pressures.

Buffer Layer Thickness and Topographic Roughness

For each tapered trilayer prepared on Cr buffer of different thickness, a square area of approximately 3000Å was imaged using a scanning tunneling microscope. Figure 2 shows two images, one from the bare quartz substrate (coated with 10Å chromium to facilitate tunneling) and another from an identical substrate with a 100Å Cr buffer and Fe-Cr-Fe trilayer. In the latter, a distinct topography has evolved consisting of hill-like features approximately 300Å in lateral dimension. Image analysis allows the calculation of average roughness for each surface. This is defined as the full width at half maximum of the surface height histogram. The bare substrate showed an average roughness of less than 4Å while that of the buffer+ trilayer was nearly 20Å. Figure 3 is a compilation of roughness values for all of the buffer+trilayer systems. The trend indicates that by varying the buffer layer thickness, the topography of the superimposed trilayer is also modified.
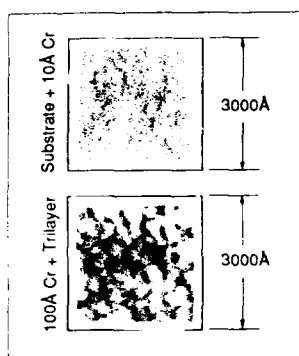
Fig. 2: STM images of bare substrate and
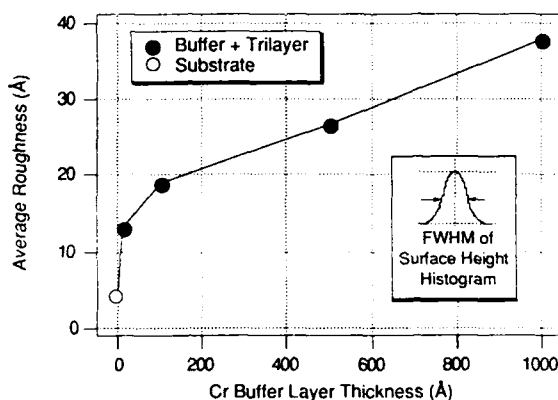substrate + 100ÅCr + Fe-Cr trilayer

Fig. 3: Surface roughness of Fe-Cr-Fe trilayer deposited on
Cr buffer layers of various thickness

Characteristic Shape and Trend of Hysteresis Loops

Fig. 4 shows the typical hysteresis behavior observed in all of the tapered trilayers we studied. Coupling is initially ferromagnetic with square loops. At approximately 5-9 Å Cr, some degree of antiferromagnetic coupling becomes evident as manifested by an increase in the saturation field (H_S) and a reduction of the area enclosed in by the loop. H_S is directly related to the exchange energy for antiferromagnetically coupled systems and is used here as a measure of its strength [10,13]. H_S increases rapidly (over 5-9Å) to values beyond 2.5 kG. It then decreases gradually with increasing chromium thickness until at approximately 28 Å at which point ferromagnetic coupling is once again observed. The shape of the loops was isotropic with respect to in-plane orientation of the applied magnetic field. In is interesting to note that the shape of the loops is not symmetric about the thickness at which maximum antiferromagnetic coupling occurs ($t^* = 11.5$Å) . For thinner chromium interlayers (9.5Å) a weak but squarish open loop is observed at low fields. This may be due to residual ferromagnetic coupling through pinholes in the thin chromium interlayer. At Cr interlayers beyond t^*, a wasp-waist loop is routinely observed, similar to that observed along the hard axis of epitaxial prepared Fe-Cr-Fe trilayer structures prepared by Grünberg et. al.[6]. This behavior was common to all of the tapered trilayer structures we examined.

Effect of Layer Roughness and Topography on Antiferromagnetic Coupling

Figs. 5 and 6 respectively show the low angle superlattice spectra and saturation field values (H_S) obtained from multilayers and tapered trilayers sputtered at a variety of pressures. It is evident that the location of both the onset and the maximum excursion in AFC (t^*) is relatively insensitive to sputtering pressure over most of the range studied. Further work is needed to confirm the slight shift exhibited by the 10 mT trilayer. Since we are unable to access fields higher than 2.5 kG, it is not possible to determine how the maximum antiferromagnetic coupling is affected in the first two cases (asterisks denote instances in which we were unable to saturate the films). However, the 3.0, 5.0 and 10.0 mT samples show a systematic decrease in coupling strength indicating that perturbations to the layer structure degrade antiferromagnetic coupling. It is worth noting that shape of the H_S curve is asymmetric about t^*. As it is approached from smaller interlayer thicknesses the coupling increases rapidly. Beyond t^*, the coupling decreases again, but more gradually. This tendency is also reflected in the raw loops shown in Fig. 4, and may result from the same effects mentioned there. Perhaps the most

interesting aspect of the data is the tenacity of the coupling with respect to severe perturbations to the layering. In light of the poor layer quality reflected in the 10.0 mT multilayer, it is indeed amazing that antiferromagnetic coupling is present at all. Kerr magnetometry was also carried out on the trilayers deposited on the different buffer layers, and the results are presented in Fig. 7. Here a dramatic decrease in AFC is observed, while the location of t* appears to remain largely unchanged. The results indicated that topographic roughness of the underlayer has a strong bearing on the magnitude of the antiferromagnetic coupling between the iron layers.
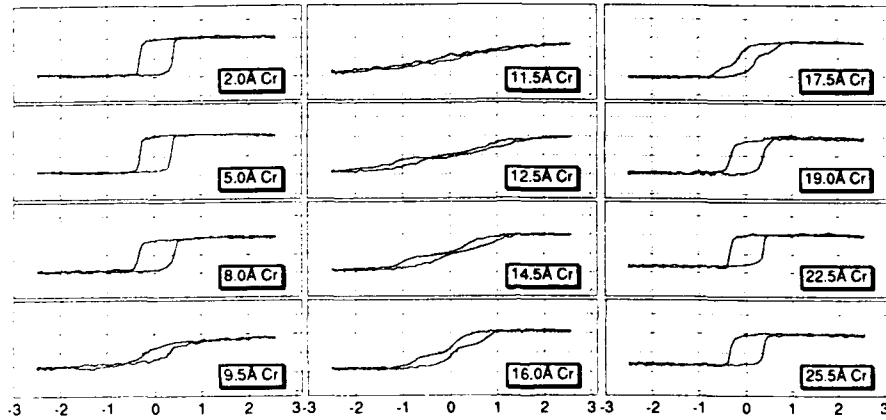

Fig. 4: Hysteresis loops for Quartz/100ÅCr/25Fe/0-28Cr/25Fe/10Cr multilayer. Cr interlayer thickness labeled. X-axis is in units of kiloGauss, Y-axis is photodiode voltage (1V/div.)
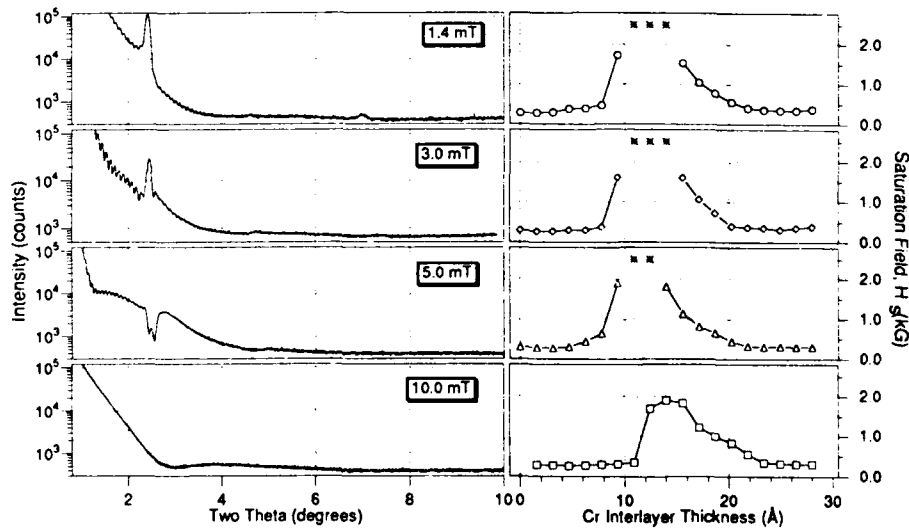

Fig. 5: 25•(20Cr/25Fe)+ 10Cr superlattices sputtered at several pressures. Note decay of harmonics.

Fig. 6: Hs for corresponding tapered trilayer films. Maximum Hs decreases with argon pressure.

170

CONCLUSIONS

It appears that the antiferromagnetic exchange in Fe-Cr-Fe trilayers is a robust phenomenon with respect to perturbations to ideal layer structure. Though diminished in strength, the effect is observed even in instances where no evidence of layer structure is observed in the low angle x-ray diffraction spectra from identically prepared multilayer films. The strength of the antiferromagnetic exchange of the trilayer system is also affected by the surface topography on which it is deposited. Topographically rougher surfaces decrease the maximum observed exchange interaction. The chromium interlayer thickness at which the antiferromagnetic exchange is maximum (t*) does not appear to be as strong function of either layer roughness or topographic roughness, though more precise thickness measurements are required to confirm this. In all cases, the peak in saturation field as a function of Cr interlayer thickness was found to be asymmetric about t*. For thinner Cr interlayers it rises sharply toward its maximum value. For thicker interlayers it decreases again, but more gradually. This appears to be related to similar asymmetries in the shape of the hysteresis loops for chromium interlayers below and above t*.

Fig. 7: Effect of surface topography on Hs

ACKNOWLEDGEMENTS

REFERENCES

[1]   P. Grünberg, R. Schreiber, Y.Pang, M.B. Brodsky, H. Sowers, Phys Rev Lett. 57 (19) , (1986).

[2]   C. Carbone, S.F. Alvarado, Phys. Rev. B. 36 (4), (1987).

[3]   F. Saurenbach, U. Walz, L. Hinchey, P. Grünberg, W. Zinn, J. Appl. Phys. 63 (8), (1988).

[4]   S.S.P. Parkin, N. More, K.P. Roche, Phys. Rev. Lett. 64 (19), (1990).

[5]   M.N. Baibich, J.M. Broto, A. Fert, F. Nguyen Van Dau, F. Petroff, P. Eitenne, G. Creuzet, A. Friederich, J, Chazelas, Phys. Rev. Lett. 61 (21), (1988).

[6]   G. Binasch, P. Grünberg, F. Saurenbach, W. Zinn, Phys. Rev. B. 39 (7),(1989).

[7]   J.A. Thornton and D.W. Hoffman, J. Vac. Sci. Technol. 14 , (1977).

[8]   H. Oecheuer, Appl. Phys. 8, 185, (1975).

[9]   K. Meyer, I.K. Shuller, C.M. Falco, J. Appl. Phys. 52 (9), (1981).

[10] P. Grünberg, J. Barnas, A. Fuß, M. Vohl, J.A. Wolf, presented at the 1990 E-MRS Meeting, Strasbourg, France (1990),(unpublished).

[11] K. Baberschke, M. Zomak, M. Farle in Magnetic Properties of Low-Dimensional Systems, edited by L.M. Falicov. and Y.L. Moran-Lopez, Springer Proc. in Physics 14 (84)(Springer, Berlin, 1986)

[12] Yi Li, M. Farle, and K. Baberschke, Phys Rev. B. 41(956) (1990).

[13] P. Grünberg, S. Demokritov, A. Fuß, M. Vohl, J.A. Wolf, presented at the 1990 Conference on Magnetism and Magnetic Materials, San Diego, CA. (unpublished).
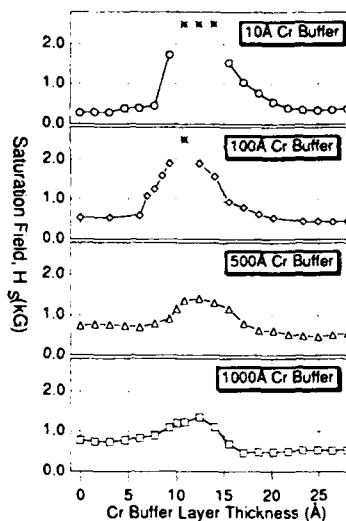
Magnetic Exchange Interaction between Fe(110) Layers across a Ag(111) Intervening Layer

Z. Q. Qiu[1], C. J. Gutierrez[2], H. Tang, S. H. Mayer, and J. C. Walker
The Henry A. Rowland Department of Physics and Astronomy, Johns Hopkins University, Baltimore, MD

[1] Presently at Argonne National Laboratory
[2] Presently at the Naval Research Laboratory

Abstract

We have grown a series of Fe(110)/Ag(111)/Fe(110) sandwich structures using a PHI 430B MBE system and analyzed their magnetic properties using transmission Mössbauer spectroscopy. The heterostructures consisted of two 30-monolayer (ML) ^{56}Fe(110) slabs separated by an intervening Ag(111) layer 2 to 35 ML thick, with a 2 ML ^{57}Fe Mössbauer probe layer placed at one of the Fe/Ag interfaces. We found that temperature dependence of the hyperfine field in the probe layer and the saturation hyperfine field value as well stronly depend on the Ag interlayer thickness. This result demonstrates that there exists an interlayer magnetic exchange interaction between the Fe layers across Ag. In addition, preliminary evidence suggests that this is probably an RKKY interaction.

In recent years, great effort, both experimental and theoretical, has been made to study the magnetic exchange interaction between magnetic layers across a nonmagnetic or magnetic intervening layer. In rare earth superlattices, this magnetic coupling leads to coherent magnetic structure and can be explained by RKKY interaction between localized 4f elctrons mediated by conduction electrons in the intervening layer[1,2]. In 3d transition metal heterostures, similar magnetic coupling has also been observed across Cr or Cu spacer layers[3-6]. However, as the 3d electrons are not completely localized, the nature of the magnetic coupling is less well understood. In order to better understand the magnetic coupling in 3d transition metal heterostructures, we carried out an investigation on the Fe(110)/Ag(111)/Fe(110) sandwich system. We found conclusive evidence for magnetic coupling between the Fe layers across the Ag(111) layer less than about 20 ML thick and less conclusive evidence for an oscillatory behavior as the thickness of the Ag(110) interlayer is varied.

Fe and Ag are chosen as the heterostructure connstituents for the following resons. First, Fe and Ag are mutually immiscible and can be epitaxially grown on each other. Thus, sharp and flat interfaces may be formed. Secondly, since there is very little d-band overlap between Fe and Ag, the magnetic property of Fe is only minimally affected by Ag. The Fe(110)/Ag(111)/Fe(110) heterostructure samples were made using a PHI 430B MBE system equiped with RHEED and residual gas analysis. The detailed growth procedures are as follows: A Ag(111) base of about 2000 Å thick was first grown on a synthetic Fe-free mica substrate held at 180 °C. The substrate was then cooled to 100 °C, and 30 ML of ^{56}Fe and 2 ML of ^{57}Fe, both of (110) orientation, were subsequently deposited. Then, a thin Ag(111) interlayer of 2 to 35 ML thick was deposited followed by the growth of another 30 ML of ^{56}Fe. Finally, 1000 Å of Ag was deposited to protect the film from

oxidation for ex-situ magnetic and structural analysis. The lowered substrate temperature during the heterostructure growth was a measure to prevent possible interdiffusion between ^{56}Fe and ^{57}Fe. A total of six samples were made with the Ag(111) interlayer being 2, 5, 8, 12, 20, and 35 ML thick. In-situ RHEED and ex-situ X-ray measurements indicated that high quality, single crystalline Fe(110)/Ag(111)/Fe(110) heterostructures have been fabricated.

The 2 ML ^{57}Fe was used as a probe for Mössbauer measurements, which can very accurately measure the magnetic hyperfine field. This probe layer is deliberately placed at the Fe/Ag interface so that any magnetic exchange interaction between the the two Fe layers across the Ag interlayer can be most sensitively detected. The temperature dependence of the hyperfine field for Fe, $H(T)$, is known[7] to be proportional to the temperature dependence of the magnetization, $M(T)$. At the Fe(110)/Ag(111) interface, the hyperfine field has been found to follow a bulk-like Bloch $T^{3/2}$ law:

$$H_S(T)/H_S(0) = 1 - B_S \times T^{3/2} \tag{1}$$

with B_S significantly enhaced and $H_S(0)$ slightly enhanced over the bulk values[8,9]. Theoretically, the enhancement of the factor B_S has been predicted by Rado[10] and by Mills et al[11] for a free standing surface, and is also expected for an Fe/Ag interface. This enhancement is mainly caused by the weakened magnetic exchange interactions among the Fe atoms at the surface (or interface) owing to the reduced coordination number. The enhancement of $H_S(0)$ is related to the enhanced magnetic moment at the surface or interface[12]. In essence, therefore, the enhancement of both B_S and $H_S(0)$ is simply a surface effect. Our heterosture samples have such a form that any magnetic exchange interaction between the separated Fe layers will be most sensitively detected by the ^{57}Fe probe layer. If such a magnetic exchange interaction indeed exists for certain Ag interlayer thicknesses, then, both B_S and $H_S(0)$ should decrease from the values in the Fe/Ag interface case and approach their bulk values. These changes are expected because the interlayer coupling serves to partially restore the bulk character (or equivalently, reduce the surface effect) at the Fe surface (inteeface) where the ^{57}Fe probe is placed. A simple model calculation on such a heterostructure by Qiu et al qualitatively predicted such a trend[13].

Transmission Mössbauer spectroscopy measurements were performed for all of the samples in the temperature range from 4.2 K to 300 K with the incident γ-ray direction perpendicular to the film plane. The Mössbauer spectra of the six samples are shown in Fig. 1(a). All of them show a 3:4:1 ratio for the intensities of the outer, middle, and inner lines. For our experimental arrangement, such a line intensity ratio indicates that the magnetic moment of Fe in the probe layer lie in the film plane. This is expected because the large shape anisotropy favors an in-plane orientation for the magnetization. The relatively narrow linewidths, about 0.4 mm/s at half maximum, suggest that a flat and sharp Fe(110)/Ag(111) interface has been formed. Otherwise, a rough interface would have resulted in much broadened absorption lines. The spectra obtained at higher temperatures all show similar narrow linewidths. Fig. 1(b) shows the Mössbauer spectra at 300 K. The complete absence of central features further attests to the high quality of these films.

From these excellent Mössbauer spectra, we have accurately determined the hyperfine field values for all of the films at various temperatures. For each film, the temperature dependence of the hyperfine field follows the expected Bloch $T^{3/2}$ law: $H_S(T) = H_S(0)(1 - B_S T^{3/2})$. The magnitudes of $H_S(0)$ and B_S are determined from

Fig. 1: Mössbauer spectra of the Fe(110)/Ag(111)/Fe(110) heterostructures at (a) 300 K and (b) 4.2 K. The thickness of the Ag interlayer is shown to the right of each spectrum.
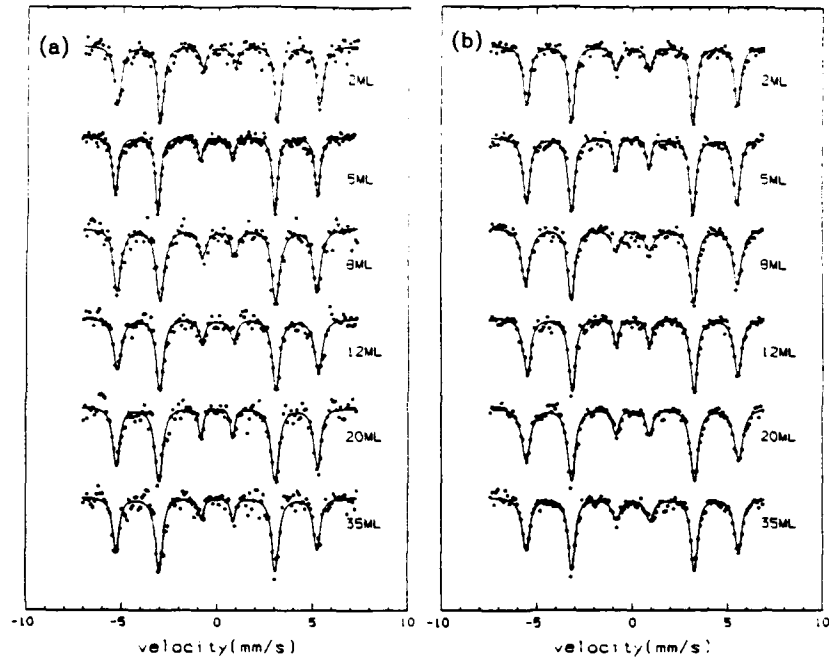

Table 1: Values of $H_S(0)$ and B_S for all of the six films. The bulk values for α Fe are also included for comparison.

Ag Thickness (ML)	$H_S(0)$ (kOe)	B_S (10^{-6} K$^{-3/2}$)
0	340.0	6.20
2	344.9	8.62
5	344.3	7.70
8	345.4	9.27
12	344.4	9.18
20	347.0	10.67
35	347.0	11.32

least squares fits, and are summerized in Table 1 for all of the six films. To be more illustrative, we also plotted in Fig. 2 the results of $H_S(0)$ and B_S against the Ag interlayer thickness.
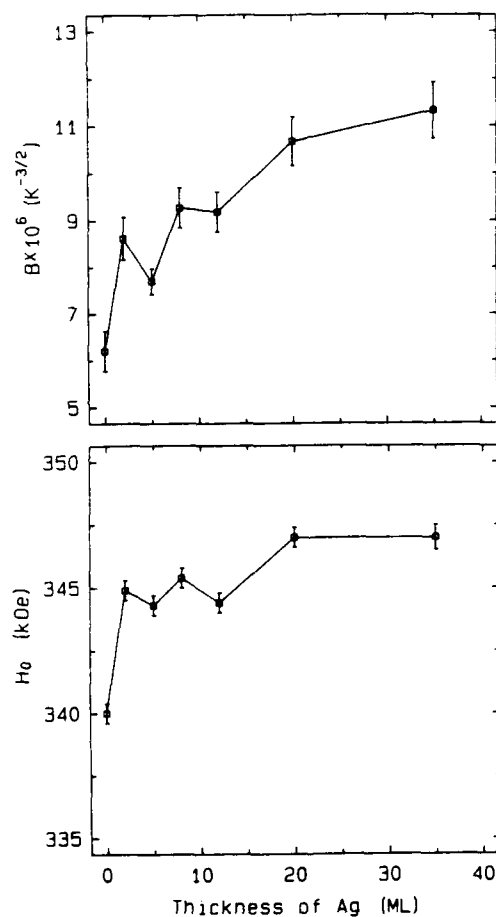
It is clear that the values of $H_S(0)$ and B_S for all films are greater than bulk Fe values, which we took as those obtained from our thick α Fe calibration foil. When the thickness of the Ag interlayer exceeds 20 ML, $H_S(0)$ and B_S are roughly stabilized at 347 kOe and 11×10^{-6} $K^{-3/2}$, respectively, which are close to the values of 348 kOe and 12×10^{-6} $K^{-3/2}$ reported for Fe interfaceed with Ag[8]. As the thickness of the Ag interlayer is reduced, $H_S(0)$ and B_S become smaller. The most interesting feature in Fig. 3 is the indication of an oscillatory behavior for $H_S(0)$ and B_S as the Ag interlayer thickness is varied. Since the oscillation amplitude almost falls within the uncertainties of the data points, however, we are not absolutely sure of its reality.

The above results demonstrate that there exists magnetic interaction between the two Fe layers through the Ag interlayer. We believe that this interaction is not due to pin holes in the Ag interlayer which would allow for the formation of Fe magnetic bridges connecting the two otherwise separated Fe layers. The reasons are as follows: (1) From surface energy arguments, Ag is expected to wet Fe very well, hence continuous and full coverage of Ag on Fe is possible. Recent growth characterization of Ag(111) on Fe(110) with Auger spectroscopy revealed breaks or kinks in the Auger signal[14], indicating the growth proceeds in a layer-by-layer manner and therefore should be pin-hole free. (2) If there are pin holes in the Ag interlayer, the interaction between the two Fe layers separated by 2 ML of Ag ought to be larger than by 5 ML of Ag. This would make $H_S(0)$ and B_S smaller, or more bulk-like, for the 2 ML (Ag) sample than those for the 5 ML (Ag) sample. Thus, we can conclude that the interaction is not caused by the pin holes. The remaining quastion is whether the interaction between the Fe layers across the Ag interlayer is an RKKY interaction. The typical signature of an RKKY interaction is the oscillatory characteristcs in both the strength and the sign of the interaction as the separation between the two magnetic moments is varied. Our results indeed seem to indicate the presence of such oscillations in both $H_S(0)$ and B_S. But as we pointed out, the oscillation amplitude is too small to be absolutely sure of its reality, though we would like to believe it.

In rare earth superlattices, the RKKY interaction can lead to an anit-domain structure, in which the neighboring ferromagnetic layers are antiferromagnetically coupled. In this case, the in-plane saturation field will be enhanced compared with the ferromagnetically coupled case. We measured the in-plane saturation field at 5 K for all six samples with a SQUID magnetometer, and found no sizable variations. Several possibilities may explain this inconclusive result. In the Fe/Ag/Fe system, the RKKY interaction is due to the exchange interaction between the less localized 3d magnetic moment of Fe and the s-p electrons of Ag and may be significantly weaker than the rare earth case. This would make it harder to observe the variations in the saturation field in our samples. Also, our samples are in a sandwich form instead of a superlattice and the thickness of the Fe layers are relatively large (30 ML). Thus, the enhancement of the saturation field is probably overwhelmed by the bulk behavior of Fe. Of course, other mechanisms may be responsible for the interaction between the Fe layers. Further investigations are planned in order to clarify this important issue.

In conclusion, we have made a series of Fe(110)/Ag(111)/Fe(110) heterostructures and studied the magnetic exchange interaction through the Ag interlayer. By using Mössbauer spectrscopy, the temperature dependence of the hyperfine field in the 2ML of

Fig. 2: B_S and $H_S(0)$ versus the Ag interlayer thickness. The solid line is a guide for the eye.

References

1. C. F. Majkrzak, J. W. Cable, J. Kwo, M. Hong, D. B. Mcwhan, Y. Yafet, J. Waszczak, and C. Vettier, Phys. Rev. Lett. **56**, 270u (1986).

2. J. J. Rhyne, R. W. Erwin, J. Borchers, S. Sinha, M. B. Salomon, R. Du, and C. P. Flynn, J. Appl. Phys. **61**, 4043 (1987).

3. S. S. P. Parkin, N. More, and K. P. Roche, Phys. Rev. Lett. **64**, 2304 (1990).

4. P. Grunberg and F. Saurenbach, in *Proceedings of the MRS International Meeting on Advanced Materials, Tokyo, Japan 1988*, Vol. 10, p. 255.

5. W. R. Bennet, W. Schwarzacher, and W. F. Egelhoff, Jr., Phys. Rev. Lett. **65**, 3169 (1990).

6. S. S. P. Parkin, R. Bhadra, and K. P. Koche, Phys. Rev. Lett. **66**, 2152 (1991).

7. G. Lugert and G. Bayreuther, Phys. Rev. B **38**, 11068 (1988).

8. J. C. Walker, R. Droste, G. Stern, and J. Tyson, J. Appl. Phys. **55**, 2500 (1984).

9. J. Tyson, A. W. Owens, and J. C. Walker, J. Magn. Magn. Mat. **35**, 126 (1983).

10. G. T. Rado, Bull. Am. Phys. Soc. II **2**, 127 (1957).

11. D. L. Mills and A. A. Maradudin, J. Phys. Chem. Solids **28**, 1855 (1967).

12. M. Weinert, A. J. Freeman, S. Ohnishi, and J. W. Davenport, J. Appl. Phys. **57** (1), 3641 (1985).

13. Z. Q. Qiu and J. C. Walker, J. Appl. Phys. **67**, 5643 (1990).

14. Z. Q. Qiu and S. D. Bader, to be published.

Interlayer Exchange Coupling—Theory

THEORY OF OSCILLATORY EXCHANGE BETWEEN MAGNETIC LAYERS THROUGH A NONMAGNETIC TRANSITION-METAL SPACER

J. MATHON
Dept. of Mathematics, City University, London EC1V OHB, UK

ABSTRACT

A general theory of oscillations in the exchange coupling between two transition metal ferromagnets separated by a nonmagnetic transition metal spacer is developed. A close analogy between oscillations in the exchange coupling and de Haas-van Alphen oscillations is established and exploited to show that the period, asymptotic decay, and temperature dependence of the oscillations are determined by properties of the d band Fermi surface in the spacer layer. The theory accounts qualitatively and even semiquantitatively for all the salient experimental features of the oscillations in the exchange coupling observed recently in Co/Ru, Co/Cr, and Fe/Cr superlattices.

Antiferromagnetic coupling between the iron layers in Fe/Cr/Fe sandwiches and superlattices has been observed by several experimental techniques [1], [2], and [3]. Recently, Parkin et al. [4] reported oscillations in the exchange coupling and magnetoresistance as a function of the thickness of the nonmagnetic spacer layer in Co/Ru, Co/Cr and Fe/Cr superlattices.

To explain the observed oscillations in the exchange coupling, we proposed a new mechanism for the exchange coupling through a nonmagnetic transition metal spacer and evaluated the coupling for a sandwich with a simple cubic tight-binding band structure [5]. In this paper we describe a more general theory of the exchange coupling in the asymptotic limit of a large thickness of the spacer layer which is valid for an arbitrary tight-binding band, arbitrary orientations of the layers, and finite temperatures. It is shown that such a tight-binding model can produce the following experimental features of the oscillations in the exchange coupling: (i) long oscillation period of the order of 10 interatomic distances; (ii) variable sign of the coupling for small thicknesses of the spacer layer; (iii) large overall amplitude of the coupling and an asymptotic decrease proportional to the inverse square of the spacer thickness; (iv) strong temperature dependence of the exchange coupling on a scale ≅100K.

It is also shown that there is a close analogy between oscillations in the exchange coupling as a function of the spacer thickness and oscillations of the magnetisation as a function of the applied field in the de Haas-van Alphen effect. As in the de Haas-van Alphen effect, the period, asymptotic decay, and temperature dependence of the oscillations in the exchange coupling are shown to be determined by properties of the d band Fermi surface in the spacer layer.

To obtain the exchange coupling we calculate the difference in energy between parallel and antiparallel orientations of the magnetic moments of two infinitely thick magnetic layers separated by a nonmagnetic spacer containing N-1 at. planes. The ferromagnetic metal is assumed to have a full majority spin d band and a partially occupied minority spin d band. The nonmagnetic metal has equal numbers of holes in each spin sub-band. The

densities of states in the spin sub-bands in the ferromagnetic and nonmagnetic spacer layers, together with the spatial variation of the hole densities $\rho_\uparrow$, $\rho_\downarrow$ are shown schematically in Figs. 1a and b for the parallel
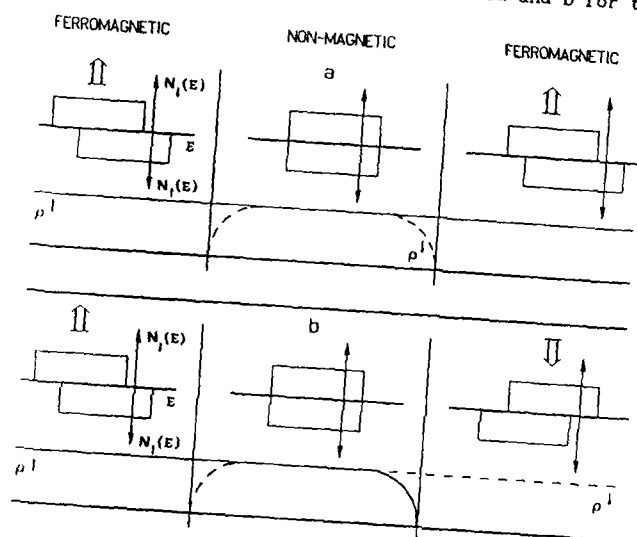

Fig.1. Schematic representation of the densities of states in the d band and of the densities of holes ρ^σ in a sandwich for ferromagnetic (a) and antiferromagnetic (b) alignements of the magnetic layers.

and antiparallel orientations of the layer moments. For simplicity we assume that the number of d holes per atom of each spin in the bulk nonmagnetic metal is equal to the number of holes in the bulk ferromagnetic metal, which is a reasonable approximation to the actual situation in Co/Ru, Co/Cr and Fe/Cr systems. It is also assumed that the exchange splitting in the ferromagnetic layers is so large that holes of the wrong spin are completely excluded. It follows that the intra-atomic Coulomb interaction between holes of opposite spin plays no role; holes of opposite spin completely avoid each other except in the spacer layer where we assume no interaction. The total energies of the two configurations may, therefore, be calculated as sums of one-electron energies.

It is clear from Fig.1 that in the ferromagnetic configuration there are no available states for down spin holes in the two ferromagnets and, therefore, they become trapped in the spacer layer. Up spin holes, on the other hand, can move freely across both interfaces.

In the antiferromagnetic configuration, up spin holes can cross the left interface but encounter a high potential barrier at the right interface which causes their density to go to zero in the right ferromagnet. Similarly, the density of down spin holes goes to zero at the left interface. It is, therefore, clear that in either configuration, deviations from bulk hole densities occur in the spacer layer near the interfaces with the ferromagnetic layers. For the ferromagnetic configuration, Fig. 1a, both interface effects occur in the down-spin hole density and, therefore,

interfere with each other. In the antiferromagnetic configuration, Fig. 1b, the interface effects at each end of the spacer layer occur in opposite spin densities and no interference takes place. The exchange coupling between the ferromagnetic layers, which is given by the difference in energy between the two configurations, is therefore determined entirely by the interference effect in the down-spin band of the spacer layer. It is then clear that the energy difference $\Delta E(N-1)=E_{\uparrow\uparrow}-E_{\uparrow\downarrow}$ is given by

$$\Delta E(N-1) = E(N-1) - E(\infty) \tag{1}$$

where $E(N-1)$ is the kinetic energy of the down-spin holes trapped in the spacer layer of a sandwich with ferromagnetically aligned magnetic layers measured relative to a $N-1$ plane reference state with bulk density. The term $E(\infty)$ is subtracted in Eq. (1) to eliminate the two independent interface effects, present in both configurations, and thus isolate the required net interference effect.

To conserve the number of particles we must consider instead of the total energy of holes in the spacer layer their thermodynamic potential

$$\Omega(N-1) = E(N-1)-E_F n(N-1) \tag{2}$$

where E_F is the Fermi energy and $n(N-1)$ is the number of holes in the spacer measured again relative to the bulk reference state. The change in energy between the two configurations conserving the number of particles is, therefore, given by

$$\Delta\Omega(N-1) = \Omega(N-1) - \Omega(\infty) . \tag{3}$$

Following Parkin et al. [4] we finally define an exchange coupling constant per unit area for a spacer layer of $N-1$ at. planes by

$$J(N-1) = \Delta\Omega(N-1)/A . \tag{4}$$

At finite temperatures the total thermodynamic potential $\Omega_{tot}=\Omega+\Omega_{ref}$ is clearly given by

$$\Omega_{tot}= - T \sum_{k,r} \ln[1+\exp\frac{\mu-E(k,r)}{T}] \tag{5}$$

where μ is the chemical potential, $E(k,r)$ is the hole energy, k is the wavevector parallel to the sandwich and r labels the discrete energy levels of holes $(k_B=1)$.

Since the exchange potentials are equivalent in our model to two infinitely high potential barriers, we simply require the dependence of the thermodynamic potential Ω of size-quantised holes in a layer of $N-1$ at. planes on the thickness of the layer $d=Na$. This is a familiar problem in the theory of de Haas-van Alphen effect where two-dimensional quantisation of the carrier energy in a magnetic field takes place in a plane perpendicular to the field. In the present problem, we have one-dimensional quantisation in the direction perpendicular to the sandwich induced by the exchange

potential. We can, therefore, adapt the conventional theory of the de Haas-van Alphen effect [6] to determine the thermodynamic potential Ω.

To evaluate the discrete sum over r in Eq.(5), we apply the Poisson summation formula

$$\sum_{r=1}^{\infty} \Phi(r) = 2\text{Re} \sum_{s=1}^{\infty} \int_{0}^{\infty} \Phi(\zeta)\, e^{2\pi i s\zeta} d\zeta + \text{nonoscillatory term} \tag{6}$$

where the discrete quantum number r is replaced by a continuous variable ζ.

It is easy to show that the oscillatory term in the Poisson formula picks from Ω_{tot} precisely the required interference contribution $\Delta\Omega$. The exchange coupling J is, therefore, given by

$$J = -2T\frac{1}{(2\pi)^2} \text{Re} \sum_{s=1}^{\infty} \iint_{BZ} dk_x dk_y \int_{0}^{N-1} d\zeta \ln\{1+\exp[(\mu-E(k_x,k_y,\zeta))/T]\exp(2\pi i s\zeta) \tag{7}$$

where the integral with respect to k_x, k_y is over the two-dimensional Brillouin zone in the sandwich plane which is assumed to be parallel to the x,y plane.

To proceed further, we have to make some assumption about the size quantisation of the carrier energy. In [5] we modelled the spacer layer by a simple cubic tight-binding band

$$\varepsilon(k_x,k_y,k_z) = - [\cos(k_x a) + \cos(k_y a) + \cos(k_z a)] \tag{8}$$

where the energy is measured in units of the hopping $2|t|$. For such a band and a sandwich parallel to the x,y plane, the quantisation of k_z is given by

$$k_z = \frac{r\pi}{Na} , \qquad r = 1, 2, \ldots, N-1 \tag{9}$$

where a is the distance between neighboring planes. One can easily show that the same quantisation is obtained for any single band and any orientation of the sandwich. Hence $E(k_x,k_y,\zeta)=\varepsilon(k_x,k_y,\zeta\pi/Na)$.

Assuming the quantisation (9), integrating in Eq.(7) by parts with respect to ζ and then passing from integration over ζ to integration over the energy ε, we obtain

$$J = - \frac{1}{(2\pi)^2} \text{Re} \sum_{s=1}^{\infty} \frac{1}{s\pi i} \int_{0}^{N-1} d\varepsilon \{1+\exp[(\varepsilon-\mu)/T]\}^{-1} \iint_{BZ} dk_x dk_y \exp(2isNak_z) \tag{10}$$

For large N, the factor $\exp(2isNak_z)$ oscillates rapidly and only the regions in the k_x,k_y plane where $k_z(\varepsilon,k_x,k_y)$ is stationary with respect to k_x,k_y contribute to the Brillouin zone integral. We can, therefore, use the method of stationary phase to approximate the integral for large N. The remaining energy integral is evaluated as in the conventional theory of de Haas-van Alphen effect [6], i.e only the contribution from the vicinity of $\varepsilon=\mu$ is included. This leads to the following general asymptotic formula:

$$J(N-1) = \frac{1}{4\pi Na} \, \mathrm{Re} \sum_{s=1}^{\infty} \frac{\sigma}{s^2} \left| \frac{\partial k_z^2}{\partial k_x^2} \cdot \frac{\partial k_z^2}{\partial k_y^2} \right|^{-1/2} \frac{\exp[2isNak_z^0(\mu)]}{T^{-1}\sinh[2\pi sNaT\frac{\partial k_z}{\partial \varepsilon}]}$$

$\sigma = i,$ both 2nd derivatives >0

$\sigma = -i,$ both derivatives <0

$\sigma = 1,$ one derivative >0 , the other <0 (11)

Here, $k_z^0(\mu)$ is an extremal radius of the Fermi surface in the direction perpendicular to the layers and all the derivatives in Eq.(11) are taken at the stationary point $k_z^0 \equiv k_z^0(\mu,k_x^0(\mu),k_y^0(\mu))$.

The consequences of the general asymptotic formula for J(N) are:

(i)   The exchange coupling J oscillates with a period $N_p = \pi/ak_z^0(\mu)$ determined by the calliper measurement of the Fermi surface;

(ii)   the amplitude contains a factor determined by the curvature of the Fermi surface at its extremal points;

(iii)   the temperature dependence of the oscillations is governed by the velocity of carriers at the extremal points;

(iv)   the asymptotic decay at T=0 is proportional to $1/N^2$.

To illustrate the properties (i)-(iv) of the general formula (11) we applied it to a sandwich with the simple cubic band structure (8) and with the layers parallel to the x,y-plane. Oscillations in J are determined by the extrema of the bulk Fermi surface in the spacer layer in the direction perpendicular to the layers. These can be seen in the cross section of the Fermi surface by a plane perpendicular to the x,y-plane and passing through the origin. Such cross sections are shown in Fig.2 for three different
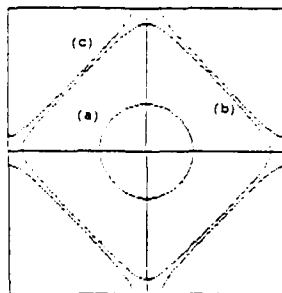

Fig.2.   Cross sections of the Fermi surface in the spacer layer by a plane perpendicular to the layers and passing through the origin for three fillings of the band: $E_F=-2.5$ (a), -1.05 (b) (b) and -0.95 (c).

184

fillings of the band (8): E_F=-2.5 (a), -1.05 (b) and -0.95 (c) (the band edges are at ±3.0 in our energy units).

Long period oscillations of J with a period N_p of about ten interatomic distances are obtained for E_F=-1.05. They are due to a simple maximum of the Fermi surface at k_x=k_y=0. The long period oscillations are shown in Fig.3 together with the corresponding calliper measurement of the Fermi surface (the inset).

We found in [5] by direct evaluation of $\Delta\Omega$ that the strength of J for N=2 is J≅1erg.cm^{-2}. This is in qualitative agreement with the largest value of exchange J≅6erg.cm^{-2} observed for Co/Ru. The period and the initial sign (antiferromagnetic) of the oscillations are also as observed for Co/Ru.

For E_F=-0.95 the Fermi surface develops four necks of a small diameter at $(0,\pm\pi/a)$ and $(\pm\pi/a,0)$. The necks on the opposite faces of the Brillouin zone combine into two saddle points which lead again to long period oscillations. These are shown also in Fig.3. It is interesting to note that the initial sign of the oscillations for E_F=-0.95 is ferromagnetic. This comes about because the factor σ in Eq.(11) has value σ=1 for a saddle point, which leads to a phase shift in the oscillations.
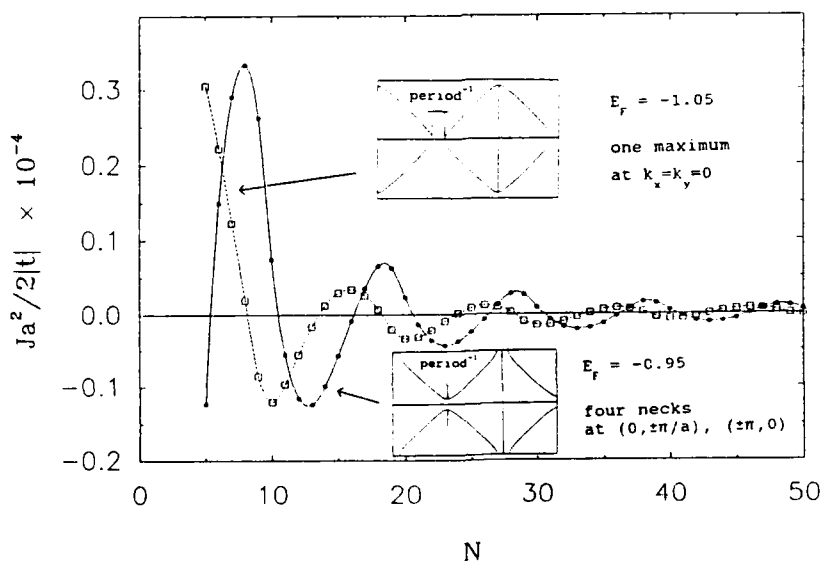

Fig.3. Long period oscillations of the exchange for E_F=-1.05 and -0.95.

The dependence of the amplitude of oscillations in J on the curvature of the Fermi surface is shown in Fig.4 where the oscillations for E_F=-1.05 (case b in Fig.2) are compared with the oscillations for E_F=-2.5 (case a in

Fig.2). In the case of $E_F=-2.5$ the Fermi surface is almost spherical, its curvature is small and, therefore, the oscillation amplitude is much larger than for the long period oscillations at $E_F=-1.05$.
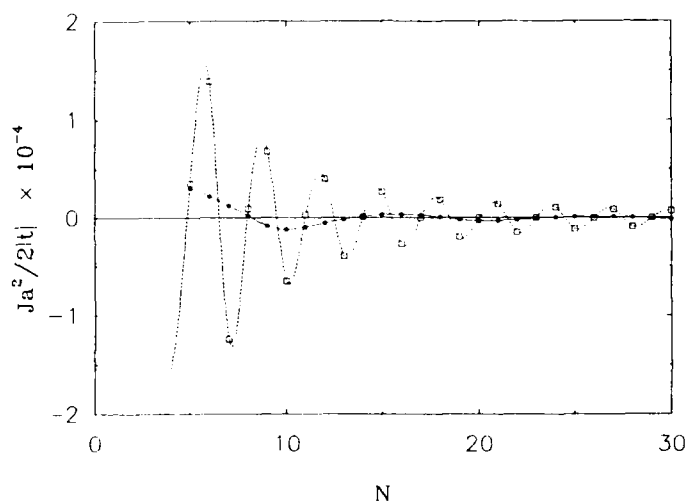

Fig. 4. Comparison of the amplitudes and periods of oscillations in the exchange coupling for two different fillings of the band: $E_F=-1.05$ (circles) and $E_F=-2.5$ (squares)

The temperature dependence of the oscillations in J is controlled in our theory by the sinh factor in Eq.(11) which has exactly the same form as in the de Haas-van Alphen effect provided the following correspondence is made:

$$N \frac{\partial k_z a}{\partial \varepsilon} \longrightarrow \frac{1}{\hbar \omega_c} \qquad (12)$$

where ω_c is an effective "cyclotron" frequency. Substituting in Eq.(12) typical values of E_F, it is easy to see that the effective cyclotron frequency in the present problem is $\hbar\omega_c \approx 10^3 K$ for small N. The dominant temperature dependent factor in Eq.(11) is $T/\sinh(2\pi T/\hbar\omega_c)$ and hence the temperature dependence of the exchange coupling is on the scale $\approx 100K$, as observed by Parkin et al. [4]. The calculated temperature dependence of J is shown in Fig.5 for $E_F=-1.05$.
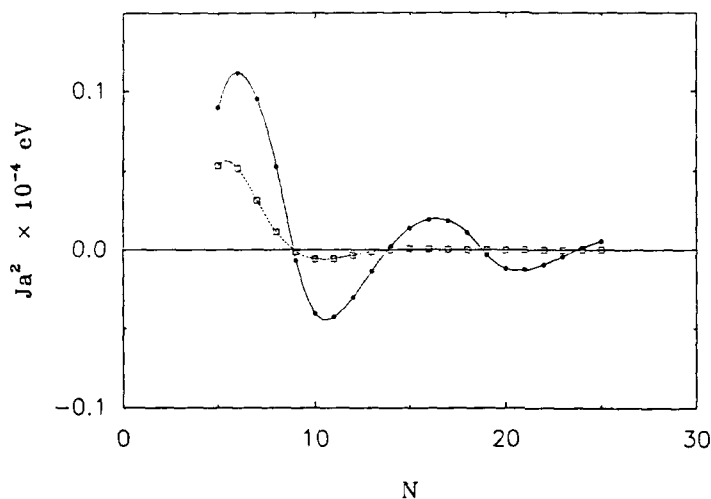
Fig.5. Oscillations in J for E_F=-1.05 at T=0K (circles) and at

   T=50K (squares).

The calculated temperature dependence of J is stronger than observed. This is not surprising since the simple tight-binding model underestimates the strength of the coupling by a factor of about six. For this particular Fermi surface, the same factor appears in the the sinh function which controls the temperature dependence but this time it leads to an enhancement of the effect of temperature.

   Our exact asymptotic formula (11) also allows us to assess the feasibility of direct numerical calculations of J. Every such calculation is either for a slab [7, 8] or for a cluster of atoms [9]. In slab calculations, Brillouin zone summations over a two-dimensional zone have to be done numerically and it turns out that these summations are the main factor that limits the accuracy of such calculations.

   In our approach, "brute-force" calculation of J means direct evaluation of the thermodynamic potential $\Delta\Omega$ of magnetic carriers trapped in the spacer layer. This involves a two-dimensional BZ sum over k_x, k_y. Any discrete summation means that the wave vectors k_x, k_y effectively become quantized as if periodic (or other) boundary conditions were imposed over a region with transverese dimension L. It is clear that to obtain reliable results for a layer structure, the length L must be much larger than the thickness of the structure d. Taking $L/d \approx 100$ and the number of atomic planes in the spacer $N \approx 50$, which is needed to see long period oscillations, the number of k points in the two-dimensional zone is $\approx 2.5 \times 10^7$. However, even using this huge number of ordinary k-space points the computed results for J amount to more or less random noise. The situation improves somewhat when one uses special Cunnigham points [10] and the results are shown in Fig. 6 for 16 640 and 1 050 624 Cunningham points in the two-dimensional BZ.
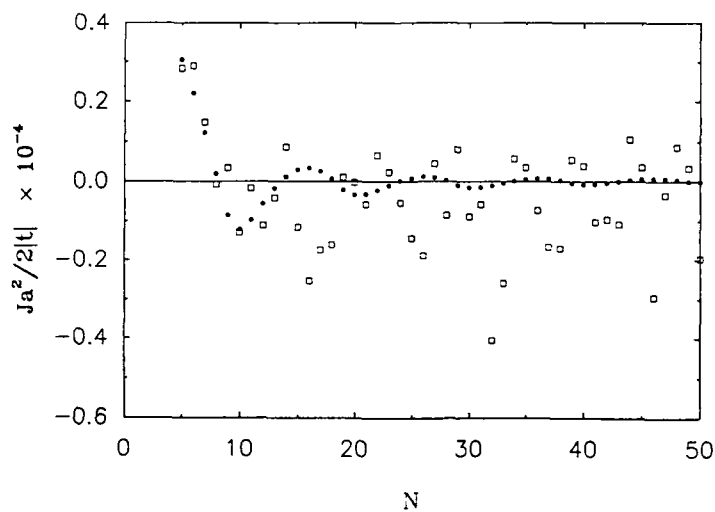
Fig.6. Direct evaluation of the energy differenece $\Delta\Omega$ for $E_F=-1.05$ using 16 640 (squares) and 1 050 624 (circles) points in the 2D Brillouin zone.

It is clear that well-defined oscillations are obtained only for $\cong 10^6$ k points and this number is several orders of magnitude larger than the number of k points used in conventional first-principle band calculations. We believe that this is the most likely reason why the first-principle calculations have so far failed to reproduce the observed long period oscillations in J.

Finally, we wish to mention a connection between the oscillations of J obtained in our theory and RKKY. Our asymptotic results obtained for a one-band model concerning the period, rate of decay, and even the temperature dependence of J are directly comparable with the asymptotic RKKY results obtained by Roth et al. [11] for a general shape of the Fermi surface. It is only necessary to transpose their results to the appropriate planar geometry. However, the overall amplitude of the exchange coupling, its initial sign and behavior at short distances are all model dependent features and cannot be predicted from the conventional RKKY theory.

Even more importantly, the exchange coupling in our theory is directly related to the size and shape of the d band Fermi surafce which is not the same as the observed Fermi surface. It is, therefore, essential to extend the calculations to include the sp band. It is expected that hybridization effects will modify the the simple direct relationship to the observed Fermi surface.

188

REFERENCES
1. P. Grünberg, R. Schreiber, Y. Pang, M.N. Brodsky and H. Sowers, Phys. Rev. Lett. 57, 2442 (1986).
2. C. Carbone and S.F. Alvarado, Phys. Rev. B 36, 2433 (1987).
3. M.N. Baibich, J.M. Broto, A. Fert, F. Nguyen Van Dau, F. Petroff, P. Etienne, G. Creuzet, A. Friederch and J. Chazelas, Phys. Rev. Lett. 61, 2472 (1988).
4. S.S.P. Parkin, N. More and K.P. Roche, Phys. Rev. Lett. 64, 2304 (1990).
5. D.M. Edwards and J. Mathon, J. Magn. Magn. Mater. (in press).
6. A.A. Abrikosov, Introduction to the Theory of Normal Metals, Academic Press, New York (1972).
7. H. Hasegawa (preprint).
8. P.M. Levy, K. Ounadjela, S. Zhang, Y. Wang, C.B. Sommers, and A. Fert, J. Appl. Phys. (in press).
9. D. Stoeffler, K. Ounadjela, and F. Gautier, J. Magn. Magn. Mater. (in press).
10. S.L. Cunningham, Phys. Rev. B 10, 4988 (1974).
11. L.M. Roth, H.J. Zeiger, and T.A. Kaplan, Phys. Rev. 149, 519 (1966).

INTERLAYER MAGNETIC COUPLING
IN TRANSITION-METAL MULTILAYERED STRUCTURES

Peter M. Levy,* J.L. Fry** and E.C. Ethridge**
*Department of Physics, New York University, 4 Washington Place, New York, NY 10003.
**Department of Physics, The University of Texas at Arlington, Arlington, TX 76019.

ABSTRACT

Recent experiments have confirmed the main features of the interlayer coupling we calculated for Fe/Cr multilayers. We discuss the origins of these features and present new results on the interlayer coupling for Fe/Mo(100) multilayered structures. We find they share many of the features seen in Fe/Cr structures; in particular the rapid oscillations of the coupling which are suppressed by the roughness of the interfaces in sputtered superlattices.

IRON-CHROMIUM

Recent experiments using SEMPA [1], BLS and MOKE [2] have borne out four key features of the interlayer magnetic coupling we calculated for Fe/Cr multilayers [3]: 1) short wavelength oscillations are present; they are associated with the Fermi surface nesting features that give rise to the spin-density-wave instability in chromium, 2) long wavelength oscillations also exist, 3) it is the roughness of the interfaces between iron and chromium layers that filters out or attenuates the short wavelength oscillations, and leaves the residual long wavelength oscillations seen in *sputtered* Fe/Cr superlattices, and 4) for very thin thicknesses of chromium the coupling is antiferromagnetic irrespective of the sharpness of the interface.

In Fig. 1 we reproduce our calculated interlayer coupling in Fe/Cr which shows these three features.
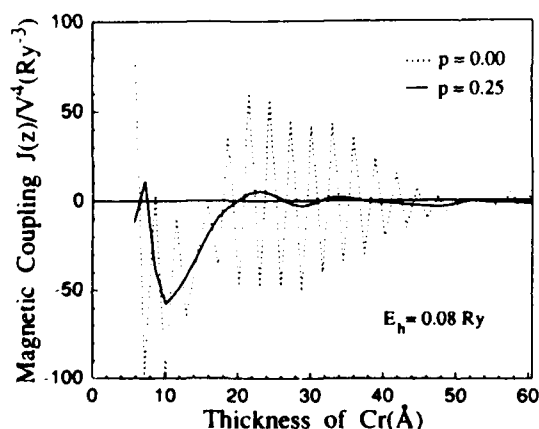

Fig. 1.The interlayer coupling $J(z)$ of Fe/Cr(100) calculated with $E_h = 0.08$Ry, and $p = 0$ (dotted line) for smooth interfaces and $p = 0.25$ (solid line) for rough interfaces. The units of J are rydbergs where V is expressed in rydbergs. Positive J represents ferromagnetic coupling.

The details of the calculations are given in Ref. 1. For perfectly smooth interfaces p=0 (see Eq. (1) below), we see the rapid oscillations with a wavelength λ-3Å. These come from the Fermi surface nesting features that also produce the spin-density-wave instability in paramagnetic chromium. The rapid oscillations are *amplitude modulated* with a period of λ-33Å, due to their interference with another oscillation with q~1.05×2π/a, see the insert to Fig. 1 of Wang et al., Ref. 3. In addition the rapid oscillations ride on a slowly varying background with a much longer period, see Fig. 1 p=0.25. In fact the coupling is aperiodic and can not be characterized by one period; it does not have *one* simple origin. Rather the long wavelength oscillations come from a *competition* between the two terms which contribute to the coupling. The first one has its main contributions coming from *about* the Fermi surface; it is predominantly ferromagnetic and has been dubbed a RKKY-like term [4]. The long wavelength oscillation in this term with λ-15Å can be traced back to the relatively sharp feature in the coupling $j_1(q)$ at q~0.2×2π/a, see insert to Fig. 1 of Wang et al., Ref. 3. The second term has contributions far away from the Fermi surface; it provides antiferromagnetic coupling and is called the superexchange term [4].

For perfectly smooth interfaces p=0, it is difficult to discern the long wavelength oscillations on which the higher frequencies ride. However, the effect of roughness of the interfaces on the interlayer coupling is to *attenuate* the high frequency (short period) oscillations, and thereby bare the long wavelength oscillations. We have taken account of interface roughness by introducing a structure form factor [3],

$$f(q_z) = (1-2p) + 2p \cos (q_z a/2).$$ (1)

We note that for p=0 it is one and does not affect the coupling; however for rough interfaces with p=1/4

$$f(q_z)\big|_{p=1/4} = \frac{1}{2} \{1 + \cos (q_z a/2)\}.$$ (2)

This has the propertry that it vanishes for $q_z = 2\pi/a$. As the short wavelength oscillations come from the nesting feature on the Fermi surface, q_{SDW}~0.95×2π/a, we can easily see why this factor, which represents interface roughness, effectively removes these high frequency oscillations and leaves only the slowly varying background which is characterized by much smaller wave vectors.

That the coupling is antiferromagnetic for very thin chromium layers, in the range 8-17Å, see Fig. 1, is a consequence of (a) the strong antiferromagnetic background coupling which persists even for p=1/4, and b) a *node* in the rapid oscillations at t_{cr}~14Å because of the beat phenomenon mentioned before. This phenomenon is even clearer at t_{cr}~52Å; there the "background" coupling (p=1/4) is nearly zero so that a node in the rapid oscillations produces a zero in the coupling. The beat phenomenon is quite striking, and there is another no' 86Å, see Fry et al., Ref. 3.

Finally, the oscillations in the coupling seen in sputtered Fe/Cr superlattices (rough interfaces) are determined by the competition between the two terms entering

the coupling [3]. They are controlled, in our simplified model of the coupling, by the position E_h of the local d state of iron in chromium. While the rapid oscillations are *not* adjustable (they come from a nesting feature in the Fermi surface of chromium), the *nodes* where our coupling goes through zero can be adjusted by choosing E_h; see Fig. 2 of Wang et al., Ref. 3.

IRON-MOLYBENUM

Sputtered Fe/Mo superlattices were recently grown and characterized by large angle x-ray diffraction profiles, Kerr-rotation, and magnetoresistance measurements [5]. The diffraction profiles and the low magnetoresistance indicate an enhanced structural order and perhaps sharper interfaces in these superlattices compared to Fe/Cr superlattices. We have calculated the coupling of iron layers across molybdenum (100) spacer layers by using the same model as for Fe/Cr[3], but with the band structure for bulk paramagnetic molybdenum [6].

Molybdenum and chromium have similar susceptibilities [7]; there is a feature at $q_0 \sim 0.95 \times 2\pi/a$ which produces rapid oscillations in the coupling with a wavelength $\lambda \sim 3.3$Å. These are amplitude modulated by neighboring peaks in the coupling $j_1(q)$; while similar to the structure shown in the insert of Fig. 1 of Wang et al., Ref. 3, the peaks in Mo are less pronounced, broader and of different amplitudes. Therefore the beat phenomena in Mo, see Figs. 2 and 3, are not as pronounced as for Cr, see Fig. 1.
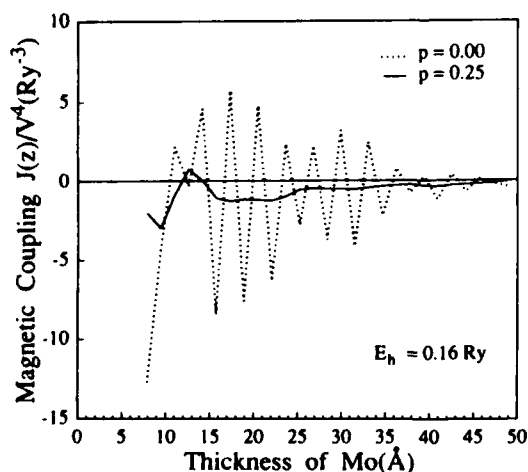

Fig. 2. The interlayer coupling J(z) for Fe/Mo(100) calculated with $E_h = 0.16$Ry, and for p=0 (dotted line) and p=0.25 (solid line). The units of J are rydbergs when V is expressed in rydbergs.

The structure form factor Eq. (1) plays the same role in Mo as for Cr, and effectively filters out the rapid oscillations coming from q_0 when the interfaces are rough (p=1/4). However as noted above it is thought that the sputtered Fe/Mo superlattices [5] have a higher degree of order, and smoother interfaces than Fe/Cr superlattices; therefore a lower value of p is more appropriate for these structures and vestiges of the rapid oscillations *may* be seen in these sputtered superlattices, see Fig. 3.
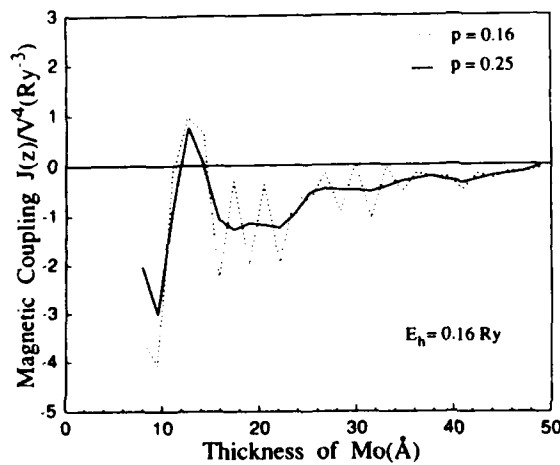
192

Fig. 3. The interlayer coupling $J(z)$ for Fe/Mo(100) calculated with $E_h = 0.16$Ry, and for $p = 0.16$ (dotted line) for moderately rough interface and $p = 0.25$ (solid line) for a rough interface. The units of J are rydbergs when V is expressed in rydbergs. Note the expanded scale for the coupling strength, as compared to the one in Fig. 2.

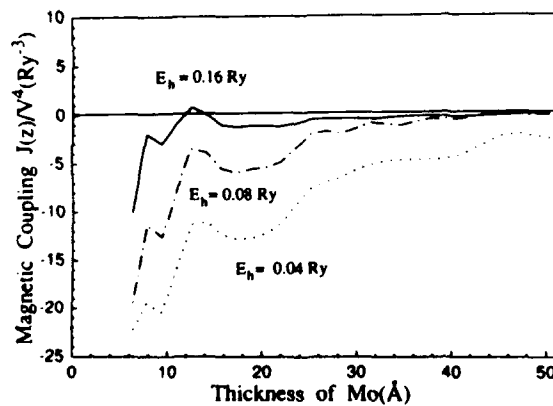In Fig. 4 we show the interlayer coupling for Fe/Mo(100) for three values of E_h.

Fig. 4. The interlayer coupling $J(z)$ for Fe/Mo(100) calculated for $E_h = 0.04$Ry (dotted line), 0.08Ry (chain line) and 0.16Ry (solid line). The units of J are rydbergs when V is expressed in rydbergs. To accommodate the curves on the same figure the scale for $E_h = 0.08$Ry has been multiplied by 0.5, and that for $E_h = 0.04$Ry by 0.10.

We have used $p = 0.25$, which is perhaps too large for the sputtered Fe/Mo superlattices [5], to remove the rapid oscillations so that the background coupling is more evident. Only for $E_h = 0.16$Ry is there some ferromagnetic coupling. From Fig.

3 we see that $E_h = 0.16Ry$ and $p \sim 0.16$ bears a resemblance to the oscillations between ferro and antiferromagnetic interlayer coupling as a function of t_{Mo} that can be *inferred* from the data on Kerr-rotations for $Fe(25\text{Å})/Mo(t_{Mo})$, see Figs. 2 and 4 in Ref. 5. However it should be cautioned that we have calculated the interlayer coupling for Fe/Mo(100), whereas the existing data is for sputtered films with a (110) texture grown on sapphire [5].

SUMMARY

Our model calculation of the interlayer coupling in transition-metal multilayered structures has been able to reproduce the salient features observed in Fe/Cr. The rapid oscillations, induced by the spin-density-wave instability, seen in epitaxially grown sandwich structures are attenuated by the roughness of the interfaces in sputtered superlattices. Our preliminary results for Fe/Mo(100) bear a reasonable resemblance to recent data on sputtered Fe/Mo superlattices with a (110) texture.

REFERENCES
1. J. Unguris, R.J. Celotta, and D.T. Pierce, submitted for publication.
2. S. Demokritov, J.A. Wolf, P. Grunberg, and W. Zinn, presented at this conference, paper S8.1.
3. Y. Wang, P.M. Levy and J.L. Fry, Phys. Rev. Lett. 65, 2732 (1990); J.L. Fry, E.C. Ethridge, P.M. Levy, and Y. Wang, J. Appl. Phys. 69, 4780 (1991).
4. C.E.T. Goncalves da Silva and L.M. Falicov, J. Phys. C5, 63 (1972).
5. Mary E. Brubaker, J.E. Mattson, C.H. Sowers, and S.D. Bader, App. Phys. Lett. 58, to appear in May 27, 1991 issue.
6. D.A. Papaconstantopolous, Handbook of the Band Structure of Elemental Solids (Plenum, New York, 1986), p. 141.
7. K. Schwartzman, J.L. Fry and Y.Z. Zhao Phys. Rev. B40, 454 (1989).

LONG AND SHORT RANGE OSCILLATORY EXCHANGE COUPLING
IN Fe/Cu AND Co/Cu MAGNETIC MULTILAYERS

F. HERMAN*, J. STICHT**, and M. VAN SCHILFGAARDE+
* IBM Almaden Research Center San Jose, CA 95120-6099 USA
** Technische Hochschule, D-6100 Darmstadt, Germany
+ SRI International, Menlo Park, CA 94025 USA

ABSTRACT

By carrying out accurate first-principles superlattice calculations, we determined the exchange coupling in bcc Fe/Cu and fcc Co/Cu multilayers as a function of the Cu spacer thickness. The fact that we can obtain long-range oscillatory coupling directly from first principles suggests that our theoretical model includes the underlying physical mechanism, and that such coupling is indeed a band structure effect. The exchange coupling depends on the interfacial orientation as well as on the Cu spacer thickness. In bcc [001] Fe/Cu, fcc [001] Co/Cu, and fcc [110] Co/Cu, the coupling has both long and short-range oscillatory components, while in fcc [111] Co/Cu, the long-range component dominates. Using a simplified model for the Fermi surface of the Cu spacer, we can relate the short-range oscillations to electronic transitions across the Fermi sphere, and the long-range oscillations to electronic transitions between spheres in adjacent zones in extended k-space, i.e., to interzonal transitions.

INTRODUCTION

The discovery of long-range oscillatory exchange coupling in transition metal multilayers [1] has stimulated considerable theoretical and experimental interest. The present symposium expresses this. Here we summarize the results of our recent first-principles band structure calculations which demonstrate that long as well as short-range oscillatory coupling can be obtained from such calculations provided they are carried out with sufficiently high accuracy. To our knowledge, these are the first multilayer calculations leading to long-range oscillatory coupling which do not rely on empirical parameters or adjustments of theory to experiment. The only input parameters are the crystal structure, lattice constant, and chemical composition.

THEORETICAL APPROACH AND RESULTS

Our first-principles self-consistent spin-polarized ASW/ASA band structure calculations are based on local spin density functional theory [2]. We consider idealized superlattices all of whose atoms lie on a common bcc or fcc lattice. (We use the terms superlattice and multilayer interchangeably.) All interfaces are atomically abrupt. All atoms in each plane parallel to the interfaces are magnetically equivalent: they have the same spin (up or down). We calculate the total energies of corresponding pairs of Co/Cu multilayers, $Co(m)Cu(n)Co(m)Cu(n)$ and $Co(m)Cu(n)Co'(m)Cu(n)$, where m and n are the number of Co and Cu monolayers in half the unit cell, and the two Co slabs $Co(m)$ and $Co'(m)$ in the full unit cell are constrained to be ferromagnetically or antiferromagnetically coupled. By comparing the total energies of corresponding partners, we are able to determine the favored structure (lower total energy) and the interaction energy

(total energy difference). These calculations are then repeated for a range of Co and Cu spacer thicknesses, as well as for progressively finer k-space sampling meshes to check the convergence of the solutions. For the fcc Co/Cu system we also examined different interfacial orientiations.

Our previous ASW/ASA studies of bcc Fe/Cr and bcc Fe/Cu multilayers [3] did not at first lead to long-range oscillatory coupling. After convincing ourselves that the difficulty was not due to geometrical idealizations, for example, using body-centered cubic rather than more realistic body-centered tetragonal structures, we decided to improve the numerical accuracy of our ASW/ASA computer codes by tightening up some of the algorithms. After doing so, we were able to obtain short-range oscillatory coupling as well as the beginning of the first long-range oscillation in bcc [001] Fe/Cu, as can be seen in Fig. 1(a). If there were no long-
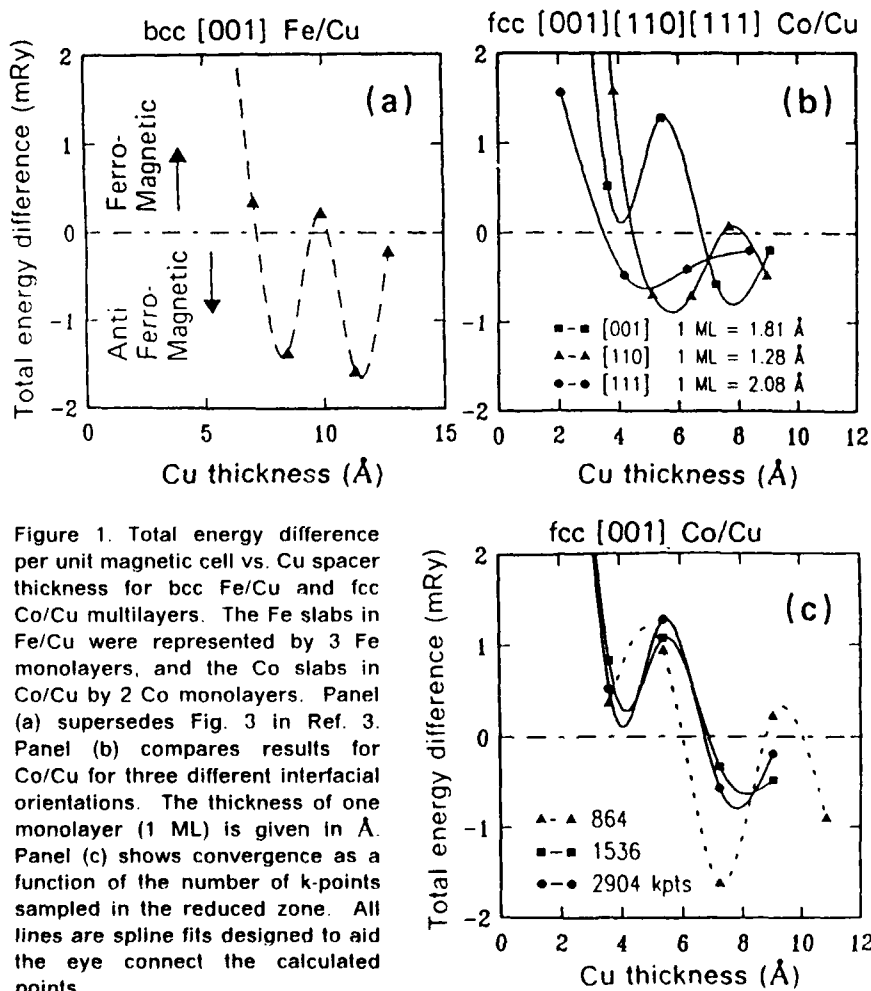

Figure 1. Total energy difference per unit magnetic cell vs. Cu spacer thickness for bcc Fe/Cu and fcc Co/Cu multilayers. The Fe slabs in Fe/Cu were represented by 3 Fe monolayers, and the Co slabs in Co/Cu by 2 Co monolayers. Panel (a) supersedes Fig. 3 in Ref. 3. Panel (b) compares results for Co/Cu for three different interfacial orientations. The thickness of one monolayer (1 ML) is given in Å. Panel (c) shows convergence as a function of the number of k-points sampled in the reduced zone. All lines are spline fits designed to aid the eye connect the calculated points.

range oscillatory component, but only a short-range component, the calculated points would oscillate more or less symmetrically about the zero of energy as a function of Cu thickness. Even with the small number of calculated points shown in Fig. 1(a), it is clear that the short-range oscillation is with respect to a moving average which represents the beginning of the long-range oscillation.

In experimental samples, the short-range oscillations are suppressed by interfacial roughness. We can simulate interfacial roughness by averaging adjacent solutions [Co(m)Cu(n), Co(m)Cu(n + 1)]. This is equivalent to using the moving average of the calculated points just mentioned. Note that the long-range component shifts from ferromagnetic to antiferromagnetic coupling at several Å, in agreement with experiment [4].

In Fig. 1(b) we compare our calculated results for three different interfacial orientations for fcc Co/Cu. The [001] and [110] solutions contain short as well as long-range components, while the [111] solution contains principally a long-range component. Note that the short-range components for [001] and [110] are out of phase with one another. It is difficult to estimate the half-period of the long-range component from the limited number of points available, but rough estimates are consistent with 5 ± 1 Å, the value observed in polycrystalline samples [5].

CONVERGENCE STUDIES

To illustrate the convergence of our solutions as a function of the number of k-points sampled in the reduced zone, in Fig. 1(c) we compare solutions for fcc [001] Co/Cu based on 864, 1536, and 2904 k-points. Although detailed features such as phase and amplitude change at first, there are clear indications that the solutions are indeed converging as the number of k-points is increased, and that long and short-range oscillatory behavior are stable features.

The results shown in Fig. 1 for bcc [001] Fe/Cu and fcc [111] Co/Cu are based on 864 k-points, while those for fcc [110] Co/Cu are based on 1944 k-points. Our convergence studies indicate that these solutions are sufficiently stable to reveal the essential features of the coupling energy vs spacer thickness, particularly the presence of short and/or long-range oscillatory components.

We have checked many of these ASW/ASA results for Co/Cu using entirely different computer programs and calculational methods (LMTO/ASA). The ASW/ASA studies reported here are based on direct k-point sampling in the reduced zone, while our LMTO/ASA calculations utilize the tetrahedron k-space integration scheme, which is more accurate. For fcc [111] Co/Cu, both approaches yield similar results, though the coupling obtained with the LMTO/ASA method is weaker than that given by the ASW/ASA method. A detailed account of our LMTO/ASA studies will be reported elsewhere [6].

THEORETICAL MODELS

With a view to understanding the physical origin of long-range exchange coupling, we consider various generalizations of RKKY theory. In 1968 Cullen et al [7] showed that the indirect exchange interaction in many-valley magnetic semiconductors can exhibit new and interesting features due to intervalley transitions. The inclusion of these transitions among the intermediate states of RKKY perturbation theory gives rise to additional oscillations or beats having a period $1/K_o$, where K_o is the separation of the centers of the valleys in the reduced zone. Clearly, long-range oscillations can occur if the valleys (or analogous Fermi

surface segments) lie close together in the reduced zone. Since such band structures can be generated in multilayers by superzone folding, Ref. 7 provides a clue as to possible mechanisms.

As is well known from earlier work on magnetically ordered rare earth metals [8,9], the Fermi surface of a multilayer can be generated by folding the Fermi surface of the bulk solid in extended k-space into the reduced zone of the multilayer. The folding is actually accomplished by translating the contents of adjacent zones into the central zone by reciprocal lattice vectors. This construction is illustrated in Fig. 2, where we begin with the Fermi surface of bulk fcc Cu [10], and fold or translate it into the reduced zones of "multilayers" of pure Cu containing two and four Cu atoms per unit cell, Cu(2) and Cu(4). Note that the dogbone orbit originally part of extended k-space of bulk Cu is fully enclosed by the reduced zone of the Cu(4) "multilayer." In this way, closely spaced extremal [11] Fermi surface segments in adjacent zones in the extended k-space of the spacer can become closely spaced segments within the reduced zone of the "multilayer" itself, possibly giving rise to long-range exchange coupling.
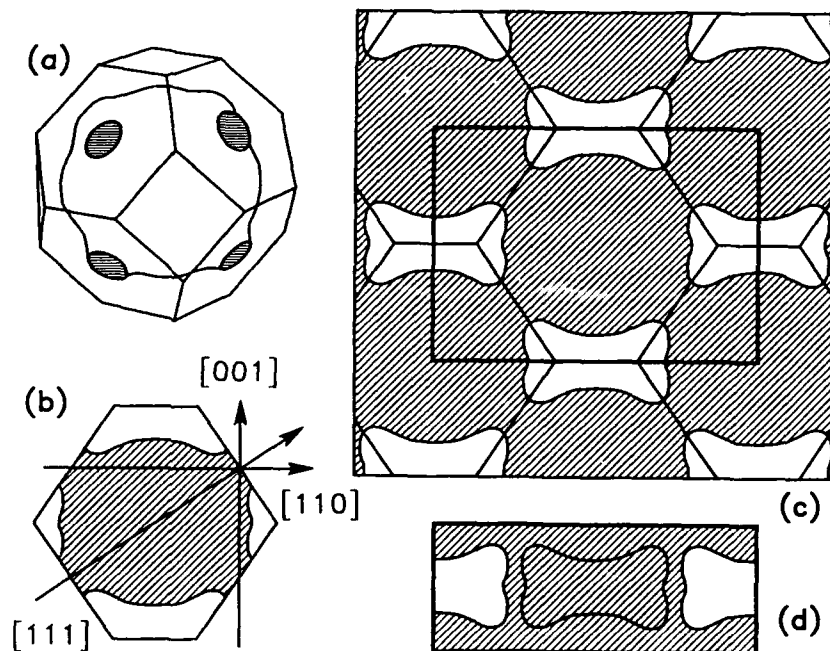

Figure 2. Band structure of fcc Cu. (a) Fermi surface enclosed by reduced zone. (b) Cross-section passing through necks. Arrows denote directions in reciprocal space. (c) Corresponding cross-section in extended k-space showing formation of dogbone contours. The reduced zone of the fcc [001] "multilayer" containing two Cu atoms per unit cell is defined by the second Brillouin zone of fcc Cu. Its cross-section is denoted here by the interior rectangle. (d) Reduced zone of fcc [001] "multilayer" containing four Cu atoms per unit cell. The central dogbone orbit has been superimposed by zone folding.

As the number of Co and Cu monolayers in the multilayer supercell increases, the size and location of the superzone boundaries will change. Nevertheless, multilayers with progressively larger supercells will have common features in their respective reduced zones for a given interfacial orientation. Since long-range oscillatory coupling is a feature of a series of multilayers having progressively thicker spacers, the physical mechanism must involve features common to each of the members of such a series. Moreover, the same mechanism must apply to sandwich geometries. The common feature, of course, is the translation of adjacent zones into the central zone by reciprocal lattice vectors. In this way we arrive at the idea that interzonal transitions are involved.

Recent RKKY-type perturbation calculations [12,13] have demonstrated that long-range exchange coupling can be produced when the band structure is favorable. For the model band structure of Ref. 12, the essential requirement is close approach of the Fermi surface to the zone boundaries. For a realistic band model of bcc Fe/Cr [13], the electronic transitions responsible for the long-range coupling have not yet been identified, owing to the complexity of the Cr band structure. In a number of recent papers [14-17], it has been suggested or implied [18] that interzonal transitions having short spanning vectors are responsible for long-range exchange coupling. None of these papers provides a satisfactory theoretical justification for this idea.

Independently, we have been drawn to the interzonal transition mechanism by the analogy [19] with Ref. 7. In effect, we are suggesting that interzonal transitions that might not play an important role in bulk solids could be activated or enhanced by the broken symmetry induced by multilayer (or sandwich) geometries. After the present work was completed, Schrieffer pointed out in a private communication that interzonal transitions can in principle contribute to the RKKY interaction in bulk solids as well as in multilayers in various ways. In a subsequent joint paper [20] we will present and illustrate a generalized RKKY perturbation theory which provides a theoretical basis for the interzonal transition mechanism in bulk solids and multilayers.

THEORETICAL INTERPRETATION

Our detailed ASW/ASA (and LMTO/ASA) band calculations indicate that the Fermi surfaces of Co/Cu multilayers are considerably more complicated than the simple pictures shown in Fig. 2. Multilayer Fermi surfaces reflect the presence of Co as well as Cu slabs. There are different Fermi surfaces for spin up and spin down electrons. In addition to Co/Cu hybridization at the interfaces, there are discontinuities at the zone boundaries induced by the broken symmetry (superzone folding). Moreover, the differences between the magnetic moments of the Co atoms in corresponding ferromagnetically and antiferromagnetically coupled Co/Cu multilayers are comparable to the differences in the induced Cu atom moments. Thus, long-range exchange coupling may well involve changes in the magnetic structure of the Co slabs as well as in the Cu spacers as a function of spacer thickness. We will discuss these complications in a subsequent paper [6].

For the purposes of discussion, we will confine our attention here to the induced spin polarization in the Cu spacers, as given by RKKY perturbation theory. It is remarkable that many of our calculated results describing the orientation dependence of the long and short-range oscillatory components (cf. Fig. 1) can be interpreted in terms of the Fermi surface for bulk Cu shown in Fig. 2. As will be seen, it is essential to take interzonal as well as intrazonal transitions into account.

fcc [001] Co/Cu: The short-range oscillations are undoubtedly due to across-the-sphere transitions in the reduced zone. These are the normal RKKY oscillations. We attribute the long-range oscillatory component to interzonal transitions parallel to the minor axis of the dogbone, both in the midsection and near the corners. The spanning vectors for these intrasphere and intersphere transitions are consistent with the estimated periods of the short and long-range oscillations, respectively. Similar remarks apply to bcc [001] Fe/Cu.

fcc [110] Co/Cu: We attribute the long-range oscillatory component to transitions *across each of four necks whose axes are perpendicular* to the [110] direction, namely, the $[1\bar{1}1]$, $[1\bar{1}\bar{1}]$, $[\bar{1}11]$, and $[\bar{1}1\bar{1}]$ axes. The four necks shown in Figs. 2(b) and 2(c) do not play a role since they are oriented along axes that are not perpendicular to the [110] direction. We attribute the short-range oscillations to across-the-sphere (normal RKKY) transitions as well as to intersphere transitions *parallel to the major axis of the dogbone*. As already noted, the [001] and [110] short-range oscillations are out of phase with one another. If the intersphere transitions are more important than the intrasphere transitions for [110], then the crucial comparison involves the intersphere transitions for [110] and the normal (across-the sphere) transitions for [001]. Since the former connect concave Fermi surface sections, and the latter convex sections, these two sets of transitions would have opposite phases [11], thus providing a possible explanation.

fcc [111] Co/Cu: We have not found significant short-range oscillations for this orientation in the present studies. The absence (or near-absence) of short-range oscillations implies the suppression of normal (across-the-sphere) transitions. According to our simple model, such transitions cannot take place since the extremal sections are absent, having been replaced by the empty neck interiors. The long-range oscillatory component is most probably due to transitions across the waists of the dogbones. Since these transitions are not parallel to the interface normal, as for the other two orientations, the coupling strength is reduced by the cosine of the angle between the transition vector and the interface normal.

To recapitulate, we have shown that many of our calculated results for fcc Co/Cu multilayers can be interpreted in terms of simplified pictures which take interzonal as well as intrazonal transitions into account. We have not actually proved that such interpretations are correct, but the fact that we can explain so many features of our results this way should not be dismissed lightly. In spite of their apparent success, simplified models such as those shown in Fig. 2 above and treated in Refs. 14 to 17 should be treated with caution since they neglect matrix element effects, zone boundary discontinuities, and the effects of Co/Cu hybridation at the interfaces [6].

DISCUSSION

In comparing theoretical and experimental results, it is important to bear in mind that our idealized interfaces can differ considerably from experimental interfaces at the atomic level. Moreover, experimental interfaces are known to be sensitive to growth conditions. For example, long-range oscillations *are not* observed in [111] Co/Cu multilayers grown by molecular beam epitaxy [21], but such oscillations are observed in sputter-deposited Co/Cu samples having a preferred [111] texture [1,5]. According to de Jonge [22], NMR measurements indicate that interfaces are slightly sharper for evaporated polycrystalline Co/Cu multilayers compared with sputtered Co/Cu multilayers, but the interfaces may be flatter for the latter. We tend to believe that the interfaces in the MBE-grown

samples are more nearly like our idealized interface models than are the sputter-deposited samples, but this remains to be seen.

Experimental estimates of exchange coupling strengths [1] yield values that are roughly one order of magnitude smaller than the strengths we obtain from ASW/ASA first-principles calculations. A substantial fraction of this discrepancy disappears when the calculations are carried out using more sophisticated k-space integration schemes, such as the tetrahedron method employed in our LMTO/ASA studies [6]. As for the remainder, in our view the most likely explanation is that a significant fraction of the coupling strength is lost due to structural imperfections at or near the interface. Similar differences between theoretical and experimental coupling strengths were noted earlier in studies of permalloy/MnFe ferromagnetic / antiferromagnetic interfaces [23]. Another factor that could play a role in polycrystalline materials is partial cancellation between different grains having different crystallographic orientations and opposite exchange coupling phases. Since theoretical coupling strengths are larger than their experimental counterparts, there is hope that experimental strengths can be enhanced by improving the structural (and hence magnetic) match across interfaces.

CONCLUSIONS

We have demonstrated for the first time that long and short-range oscillatory coupling can be obtained directly from first-principles band calculations, and that this coupling depends on interfacial orientation. These calculations are based on local spin density functional theory, assuming collinear magnetism (spin up or spin down). It is significant that we did not have to introduce spin-orbit coupling, non-collinear spin arrangements, or electron correlation effects beyond those already included in local spin density functional theory.

We have also demonstrated that many of our calculated results can be interpreted in terms of simplified Fermi surface models, with specific and identifiable interzonal and intrazonal transitions playing key roles. It is important to understand why such simplified models work as well as they do, given the complexity of actual Co/Cu multilayer band structures [6]. It is also important to put the interzonal transition mechanism and interpretations based on this mechanism on a firm theoretical basis [20]. Finally, it is important to test the universality of such interpretations by examining other multilayer spacer materials having more complicated Fermi surfaces than fcc Cu. We are currently investigating other types of magnetic multilayers with this in mind.

We encourage experimentalists to test our predictions, particularly the orientation dependence of the short-range coupling, by using more structurally perfect samples than are presently available [1,4,5].

ACKNOWLEDGEMENTS

202

REFERENCES

[1] S. S. P. Parkin, N. More, and K. P. Roche, Phys. Rev. Lett. **64**, 2304 (1990). For more recent results for a large number of systems and extensive references to work by others, see S. S. P. Parkin, Phys. Rev. Lett., to be published.

[2] A. R. Williams, J. Kuebler, and C. D. Gelatt, Jr., Phys. Rev. B **19**, 6094 (1979).

[3] F. Herman, J. Sticht, and M. Van Schilfgaarde, J. Appl. Phys. **69**, 4783 (1991).

[4] B. Heinrich et al, Phys. Rev. Lett. **64**, 673 (1990).

[5] S. S. P. Parkin, R. Bhadra, and K. P. Roche, Phys. Rev. Lett. **66**, 2152 (1991).

[6] F. Herman, J. Sticht, and M. Van Schilfgaarde, to be published.

[7] J. R. Cullen, E. Callen, and A. H. Luther, J. Appl. Phys. **39**, 1105 (1968); C. Kittel, Solid State Phys. **22**, 1 (1968), Appendix C.

[8] B. Coqblin, *The Electronic Structure of Rare-Earth Metals and Alloys: the Magnetic Heavy Rare-Earths.* (Academic Press, London, 1977).

[9] Y. Yafet, J. Kwo, M. Hong, C. F. Majkrzak, and T. O'Brien, J. Appl. Phys. **63**, 3453 (1988).

[10] D. Shoenberg, *Magnetic Oscillations in Metals.* (Cambridge Univ. Press, 1984).

[11] L. M. Roth, H. J. Zeiger, and T. A. Kaplan, Phys. Rev. **149**, 519 (1966).

[12] D. M. Edwards, J. Mathon, R. B. Muniz, and M. S. Phan, J. Magn. Magn. Mater., **93**, 85 (1991); Phys. Rev. Lett. **67**, 493 (1991).

[13] Y. Wang, P. M. Levy, and J. L. Fry, Phys. Rev. Lett. **65**, 2732 (1990); J. L. Fry, E. C. Ethridge, P. M. Levy, and Y. Wang, J. Appl. Phys. **69**, 4780 (1991). In bcc Fe/Cr these authors find that the short-range oscillations are due to transitions within the reduced zone between nested Fermi surface segments. These transitions are also responsible for the incommensurate spin density waves in bulk Cr.

[14] R. Coehoorn, submitted to Phys. Rev. B.

[15] C. Chappert and J. P. Renard, Europhys. Lett. **15**, 553 (1991).

[16] D. M. Deaven, D. Rokhsar, and M. Johnson, Phys. Rev. B **44**, 5977 (1991).

[17] P. Bruno and C. Chappert, Phys. Rev. Lett. **67**, 1602 (1991).

[18] These papers describe long-range oscillatory coupling as an aliasing phenomenon produced by sampling very short-range oscillations at the uniformly spaced atomic planes of the multilayer. These latter oscillations are presumably related to interzonal transitions between closely spaced extremal Fermi surface segments.

[19] This analogy must be treated with caution, however. From the standpoint of RKKY perturbation theory, the transitions giving rise to additional oscillations in Ref. 7 are intervalley (intrazonal) transitions, while in multilayers they are ultimately transitions between adjacent zones in the extended zone scheme of the spacer, i.e., interzonal transitions involving reciprocal lattice vectors.

[20] F. Herman and J. R Schrieffer, to be published.

[21] R. F. Marks et al, in *Heteroepitaxy of Dissimilar Materials*, eds. R. F. C. Farrow, J. P. Harbison, P. S. Peercy, and A. Zangwill (MRS, Pittsburgh, 1991), Vol. 221 of the MRS Symposium Proceedings Series.

[22] W. J. M. de Jonge et al, in *Magnetic Thin Films, Multilayers, and Surfaces,* ed. S. S. P. Parkin (MRS, Pittsburgh, 1991), Vol. 231 of the MRS Symposium Proceedings Series.

[23] A. P. Malozemoff, Phys. Rev. B **35**, 3679 (1987).

MAGNETISM IN 4d TRANSITION METAL–Ag(001) SANDWICHES

DENNIS P. CLOUGHERTY* M. E. McHENRY† AND J. M. MacLAREN‡
* Department of Physics, University of California, Santa Barbara, CA 93106
† Department of Metallurgical Engineering and Materials Science, Carnegie Mellon University, Pittsburgh, PA 15213
‡ Department of Physics, Tulane University, New Orleans, LA 70018

ABSTRACT

Using *ab-initio* spin-polarized layer Korringa–Kohn–Rostoker (LKKR) band structure calculations, we investigated the possibility of having a stable ferromagnetic ground state in 4d transition metal (TM)–Ag(001) sandwiches (TM = Tc, Ru, Rh, and Pd). In contrast to recent calculations performed on systems with TM overlayers on Ag (001), we find that the TM sandwich configuration gives a paramagnetic ground state. While excellent agreement in general is obtained for the layer-projected densities of states (LDOS), the sandwich configuration lowers the densities of states at the Fermi energy (E_F) in the case of Rh and Ru by a small amount which seemingly prevents the marginal ferromagnetic instability predicted by Eriksson *et. al.* (Phys. Rev. Lett. **66**, 1350 (1991)) from occurring.

INTRODUCTION

Recent theoretical calculations by Eriksson *et. al.* [1] have predicted ferromagnetism and metamagnetism in systems where certain 4d transition metal (TM) monolayers are chemisorbed on a Ag(001) surface. Rh overlayers on Ag(001) were predicted to be ferromagnetic with a moment of $1.32\mu_B$ per unit cell, while Ru overlayers were predicted to have a low spin ($0.29\mu_B$ per unit cell) ferromagnetic ground state and two higher spin ($0.77\mu_B$ and $3.42\mu_B$ per unit cell) metamagnetic states. The Ru/Ag ferromagnetic state was found to be tenuously stabilized below the paramagnetic state by less than $1mRy$ per atom, and the Rh/Ag ferromagnetic state was stabilized by $2.4mRy$ per atom. In contrast, neighboring TMs, Tc and Pd, were found to have paramagnetic ground states. Calculations of Zhu *et al.* [2] also predict that Pd overlayers on Ag(001) are paramagnetic. It was our intent to investigate whether the layered ferromagnetic states remain stabilized and/or the paramagnetic overlayers become ferromagnetic when in a sandwich configuration.

CALCULATIONAL DETAILS

Using *ab-initio* spin-polarized layer Korringa–Kohn–Rostoker (LKKR) band structure calculations, the electronic structure of TM sandwiches (TM = Tc, Ru, Rh, and Pd) consisting of a single TM layer sandwiched between two semi-infinite spaces of Ag(001) planes has been determined. The LKKR technique [3] is ideally suited for studies of systems which have such a layered topology, since the technique only requires two dimensional periodicity. Schematically the LKKR method self-consistently solves for the one-electron Green's function of the system, dividing the wavefunction scattering paths into interlayer and intralayer scattering. The potential is approximated to be of the muffin-tin form, while exchange-correlation effects are treated within the local spin density approximation. Semi-relativistic effects [4] are taken into account.

With the one-electron Green's function, $G_\sigma(r, r', \vec{k}; E)$, the layer–projected densities of states (LDOS) are found from

$$N_\sigma(r; E) = -\frac{1}{\pi} \; Im \int d\vec{k} \; G_\sigma(r, r, \vec{k}; E) \tag{1}$$

where σ denotes the spin species considered. The k integrations are performed using 10 special k-points in the irreducible wedge in the two dimensional Brillouin zone.

In the case of the sandwich calculations, a two–dimensional square lattice is formed within the layers. The TM layer lattice spacing was taken to be equal to the lattice spacing of the Ag(001) layers. Spacing between the layers was found by requiring tangent muffin–tin spheres. The Fermi energy (E_F) was taken to be equal to that of the bulk host, Ag. The possibility of two-dimensional antiferromagnetism was not investigated here.

RESULTS

LDOS for the four sandwiches considered are presented in Figs. 1 and 2. For a given sandwich, the TM LDOS and the succeeding two Ag LDOS, denoted by Ag(TM)(I) and Ag(TM)(I-1), are shown. A certain trend in the bandwidth is immediately apparent for the TM LDOS: the bandwidth decreases monotonically across the series from Tc to Pd, with the Pd bandwidth being approximately 25% smaller than the Tc bandwidth. While the lower band edge remains at approximately the same energy with respect to E_F, it is the lowering in energy of states in the upper edge which is responsible for the narrowing. These states are found to have primarily TM-d antibonding character with respect to both the adjacent Ag layer and within the TM layer. In the case of Pd, the band is practically completely below E_F, with a very tiny LDOS at E_F. Ru has the highest LDOS at E_F in the series considered; consequently it is not too surprising that the overlayer calculations of Eriksson et. al. found a ferromagnetic ground state. Both Rh and Tc also have substantial LDOS at E_F, with Rh having the smaller bandwidth.

The successive Ag LDOS also show systematic trends in the series. The center of gravity of the Ag band in the interface layer moves up slightly in energy as one traverses the series from Tc to Pd. This indicates a greater amount of hybridization in the end of the series. In the Ag layer below the interface layer, all four LDOS look very similar indicating that TM hybridization with the second Ag layer is small and that these systems really are quasi-two-dimensional.

While similar trends can be found in the overlayer calculations, there are two important, subtle differences: (1) the position of the Ag interface band is a little closer to E_F for all TM sandwich configurations, and (2) the magnitude of the LDOS at E_F in the cases of Ru and Rh is a little smaller in the sandwich configuration. The first difference indicates that the Ag interface hybridization is seemingly more important in the sandwich configuration, while the second difference (which may well be a consequence of the first) indicates that the sandwich configuration will have less propensity to formation of a ferromagnetic state. In fact we have found that in contrast to the overlayer configuration, all TM sandwiches investigated were paramagnetic.

It has been demonstrated in the case of bulk Fe [5] that different forms for exchange and correlation effects can alter the ground state ordering. To test this possibility in the case of the TM sandwiches, results using both the Vosko–Wilk–Nusair [6] and the Janak–Moruzzi–Williams [7] forms were found to agree.
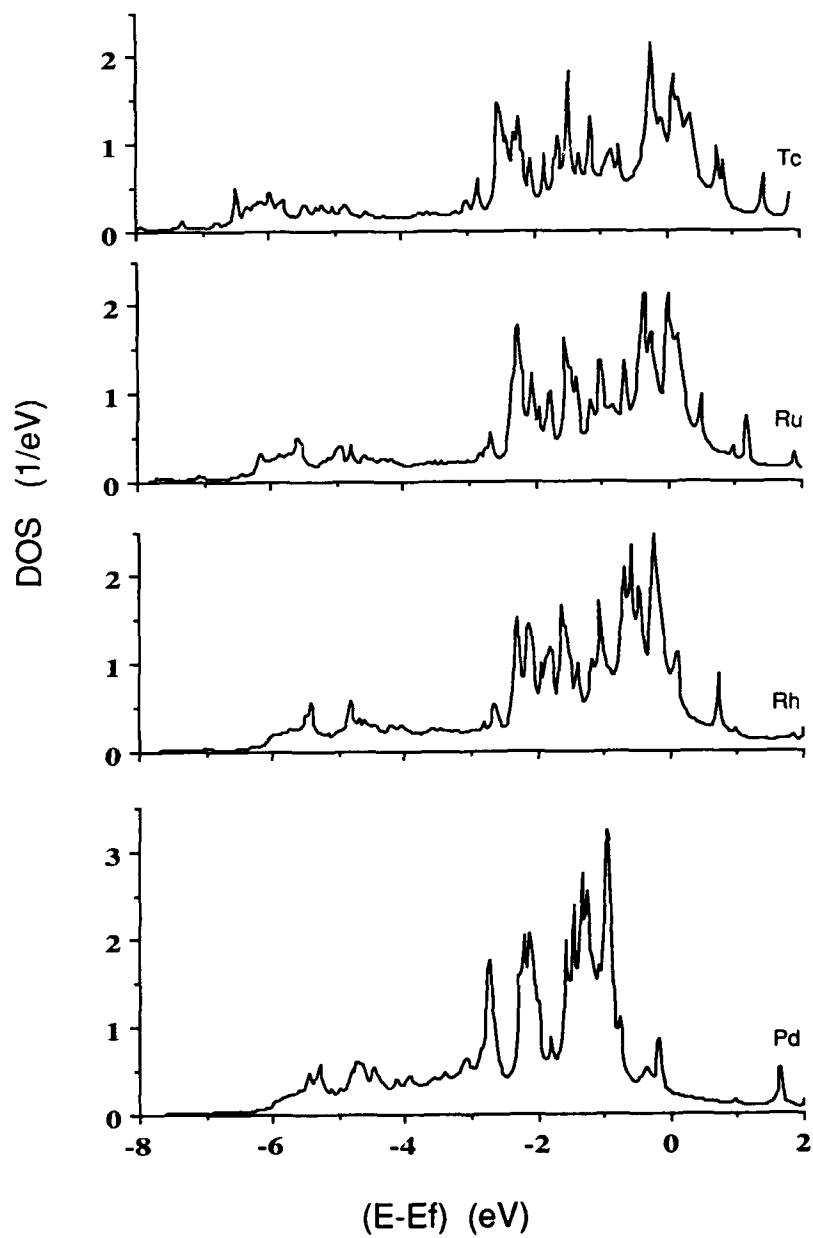
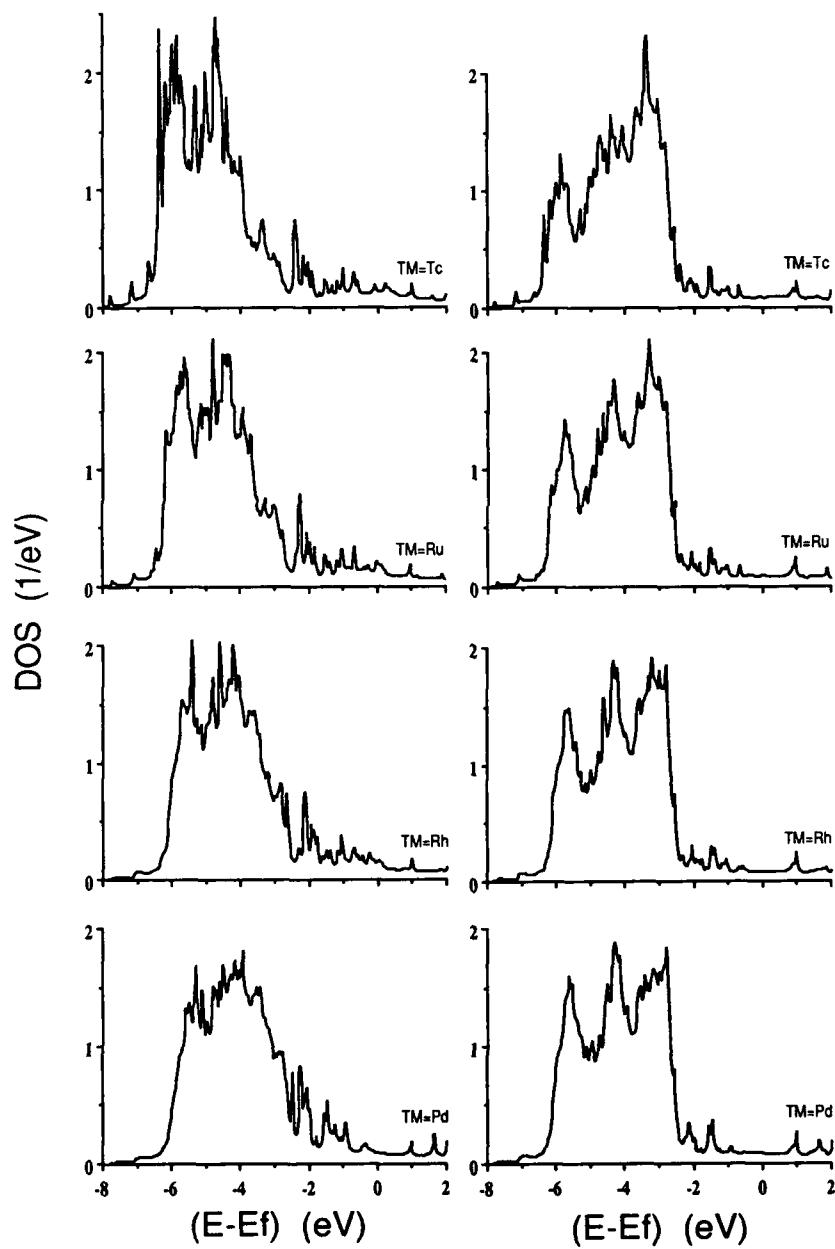Figure 1. Densities of states (per spin) for TM layers.

Figure 2. Densities of states (per spin) for Ag(TM)(I) layers (on left),
and Ag(TM)(I-1) layers.

DISCUSSION

Pd initially seemed to be a promising system for developing two-dimensional ferromagnetism because bulk Pd has a rather large paramagnetic susceptibility enhancement [8]. There is also recent experimental evidence suggesting that the Pd layer in an overlayer configuration relaxes outward [9] further encouraging ferromagnetism, but because the Pd band is shifted below E_F, the tiny value of the LDOS at E_F lowers the Stoner product to below the threshold of ferromagnetic instability,

$$N(E_F)I < 1 \qquad (2)$$

where I is the exchange-correlation integral [8]. This finding is corroborated by similar theoretical results in overlayer configurations obtained by Eriksson *et. al.* and Zhu *et al.*, and Fink *et al.* [10] have found paramagnetism for Pd overlayers experimentally.

In agreement with the overlayer calculations of Eriksson *et. al.*, we found a qualitatively similar shape for the LDOS in Rh, Ru, and Tc sandwiches; however we found a higher spectral weight at low energies $(3 - 4eV$ below $E_F)$ with an accompanying reduction in weight in the central peak just below E_F. The marginal ferromagnetism in Rh and Ru in the case of overlayers does not occur in the sandwiches. It would seem that the slight reduction in LDOS at E_F causes the Stoner product to fall just below one. For the Tc sandwich, the large bandwidth of Tc spread the spectral weight over a larger energy range and further suppressed $N(E_F)$.

The fundamental difference between the overlayer and sandwich configurations is the reduced coordination of the TM layer. It is possible that this effect, which slightly increases the tendency toward ferromagnetism by narrowing the bandwidth of the TM layer, is sufficient to push the TM layer into a ferromagnetic state. However it should also be noted that the two configurations used very different models for the substrate–TM interaction. The overlayer calculation of Eriksson *et. al.* ignored surface–relaxation effects, and the Ag lattice constant was used for all the spacings. It is thought that a surface layer of Ru will contract when deposited on Ag [2] and certainly the layer spacing determined by tangent muffin-tin spheres will yield a smaller layer spacing from bulk Ag since the muffin-tin radii of the TM is smaller than that of Ag. The differences in spectral weight at low energies for the TM LDOS might well be attributable to the decrease in TM–Ag layer spacing which would tend to increase interlayer hybridization and shift spectral weight to energies closer to the Ag band. This shift in spectral weight would lower $N(E_F)$ and tend to inhibit ferromagnetism.

ACKNOWLEDGMENTS

REFERENCES

1. O. Eriksson, R.C. Albers, and A.M. Boring, Phys. Rev. Lett. **66**, 1350 (1991).
2. M.J. Zhu, D.M. Bylander, and L. Kleinman, Phys. Rev. B **42**, 2874 (1990).
3. J.M. MacLaren, S. Crampin, D.D. Vvedensky, and J.B. Pendry, Phys. Rev. B **40**, 12164 (1989).
4. D.D. Koelling and B.N. Harmon, J. Phys. C **10**, 3107 (1977).
5. J. M. MacLaren, D. P. Clougherty, and R. C. Albers, Phys. Rev. B **42**, 3206 (1990).
6. S.H. Vosko, L. Wilk, and M. Nusair, Can. J. Phys. **58**, 1200 (1980).
7. J.F. Janak, V.L. Moruzzi, and A.R. Williams, Phys. Rev. B **12**, 1257 (1975).
8. J.F. Janak, Phys. Rev. B **16**, 255 (1977).
9. R.F. Liu, Y.S. Li, J. Quinn, D. Tian, F. Jona, and P.M. Marcus, Bull. Am. Phys. Soc. **35**, 384 (1990).
10. R.L. Fink, C.A. Ballentine, J.L. Erskine, and J.A. Araya-Pochet, Phys. Rev. B **41**, 10175 (1990).

Copper Based Multilayers

GIANT MAGNETORESISTANCE AND OSCILLATORY INTERLAYER EXCHANGE COUPLING IN COPPER BASED MULTILAYERS

S.S.P. PARKIN
IBM Research Division, Almaden Research Center, 650 Harry Road, San Jose CA
95120-6099.

Abstract

Giant magnetoresistance values exceeding 65% at room temperature are reported in antiferromagnetically coupled Co/Cu multilayers grown on Fe buffer layers using magnetron sputter deposition. For such samples the saturation fields exceed 10 kOe. However by taking advantage of the rapid decrease of the Co interlayer magnetic exchange coupling with increasing Cu spacer layer thickness, large magnetoresistance values exceeding 35% can be obtained at room temperature for saturation fields of just a few hundred oersted.

Introduction

The transport properties of metal multilayers and sandwiches has become an area of great interest following the discovery of dramatic enhancements of the magnetoresistance of multilayered films containing thin magnetic layers sandwiched about thin metal layers[1-4]. The giant magnetoresistance (GMR) phenomenon has been found in a variety of systems. Very large effects are found in Fe/Cr multilayers, both in single crystal multilayers prepared by molecular beam epitaxy[2, 3] and in polycrystalline multilayers prepared by sputter deposition techniques[4]. At room temperature saturation magnetoresistance values of about 15% are found in such structures. However by far the highest values of magnetoresistance have been reported in Co/Cu multilayers grown by magnetron sputter deposition[5-7]. Using such growth techniques high quality multilayered structures containing thin copper layers can be readily obtained[7].

Sample preparation

Sample preparation was carried out using conventional dc magnetron sputtering in a high vacuum deposition system with a base pressure of $\simeq 1 \times 10^{-9}$ Torr. The samples were prepared in an argon atmosphere of 3.25 mTorr at deposition rates of $\simeq 2$Å/sec at a deposition temperatures of $\simeq 40°C$. Families of up to 20 multilayered structures were prepared sequentially via computer control of the substrate platform and shutters placed between the platform and each magnetron source. A substrate is placed under a source and the shutter opened for a controlled length of time. The same substrate is successively placed under the appropriate sources until the programmed structure for that substrate is completed. The structures obtained are polycrystalline but the level of contaminants is low and comparable to that typically obtained in molecular beam epitaxy growth of single crystal material. Auger sputter depth profiles of a number of samples gave no evidence for oxygen or carbon concentrations above the auger sensitivity for these species ($\simeq 1$ at%).
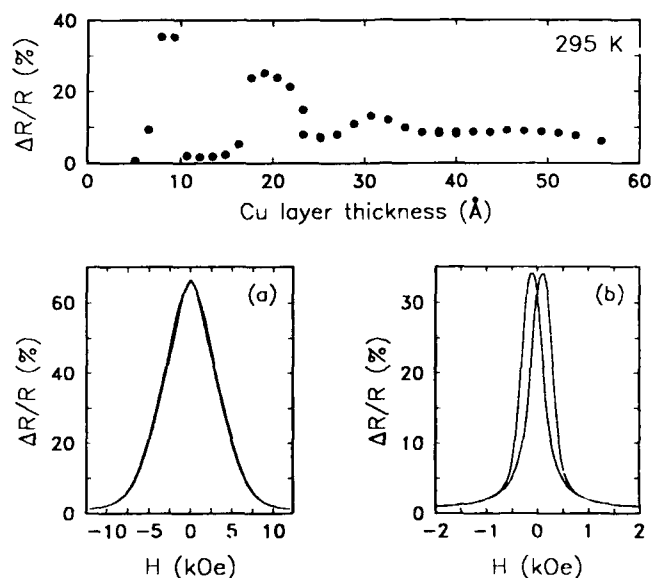
Figure 1: The upper part of the figure shows the dependence of the room temperature saturation transverse magnetoresistance on Cu spacer layer thickness, t_Cu, for a series of samples of the form Si(100)/Fe(45Å)/[Co(10Å)/Cu(t_Cu)]₁₆/Cu(55 − t_Cu Å). The lower part of the figure shows room temperature resistance versus field curves for structures optimized to have very large magnetoresistance. The structures are (a) Si(100)/Fe(50Å)/[Co(8Å)/Cu(8.3Å)]₆₀/Cu(50Å) and (b) Si(100)/Fe(50Å)/[Co(9Å)/Cu(20Å)]₅₀/Fe(25Å). The resistivities of the films in zero field are 29.0 μΩcm and 18.0 μΩcm respectively.

Results and Discussion

Figure 1 show magnetoresistance data for Co/Cu samples grown on thin Fe buffer layers. The saturation magnetoresistance (the increase in resistance in low fields divided by the high field resistance) oscillates as a function of Cu spacer layer thickness with a period of about 10Å[6]. The oscillations parallel oscillations in the magnetic coupling from ferromagnetic to antiferromagnetic of the Co layers via the Cu spacer layers. These data are similar to those previously reported for the Fe/Cr and Co/Ru systems[4]. In the latter systems the antiferromagnetic arrangement of the magnetic Fe and Co layers for certain Cr and Ru layer thicknesses has been established by polarized neutron reflectivity studies[8, 9]. Antiferromagnetic coupling in Co/Cu single crystalline superlattices was originally reported by Cebollada et al[10] who have recently found evidence for oscillatory coupling in single crystalline (100) Co/Cu/Co sandwiches[11] with a similar period to that we find in polycrystalline Co/Cu multilayers. We also find evidence for indirect antiferromagnetic exchange coupling via Cu spacer layers sandwiched between Ni₈₁Fe₁₉ layers[12], Co and Fe layers[5], and Co and Ni layers[5]. In each case the magnetic coupling oscillates as a function of Cu layer thickness with a period of approximately 10 angstrom with parallel oscillations in saturation magnetoresistance. The phase of the oscillations is similar in each of these cases.
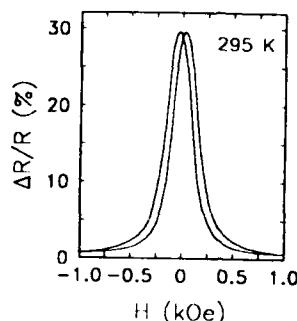
Figure 2. Resistance versus transverse field curve for a sample of the form Si(100)/Ru(50Å)/[Co(10Å)/Cu(17Å)]₂₀/Ru(15Å). The resistivity in zero field is 16.5 μΩcm.

For well defined layered structures the largest magnetoresistance values are found for multilayers containing thin Co and Cu layers ≈8Å thick. This results from the dominant role of interfacial scattering causing the GMR effect. Figure 1(a) shows a saturation magnetoresistance value of more than 65% in such a sample. For such thin Cu layers the Co layers are strongly antiferromagnetically coupled and thus the saturation field is very large. The magnetic coupling strength decays rapidly with increasing Cu thickness whereas the saturation magnetoresistance decays much more slowly as approximately the inverse Cu layer thickness. Thus in structures with Cu layer thicknesses corresponding to the second antiferromagnetic oscillation, saturation magnetoresistance values of about half that at the first antiferromagnetic oscillation are found for saturation fields more than 20 times smaller as shown in Figure 1(b). The saturation field at the second oscillation can be further reduced by growing structures on Ru buffer layers as shown in Figure 2.

The magnetic and transport properties of the Co Cu multilayers are surprisingly reproducible for the same growth conditions. However, varying these conditions can substantially alter the properties. In particular, for growth on silicon substrates, the buffer layer onto which the multilayered structure is grown is very important[7]. Figure 3 shows a comparison of two identical Co Cu multilayers grown on 50Å thick Cu and Fe buffer layers with respectively 50Å thick Fe and Cu capping layers. The capping layers were chosen such that the structures have the same total layer thicknesses of Cu and Fe as well as Co. This is important in order to compare the magnetoresistance of these samples since Cu is much more conducting than Fe and thus shunts the sensing current away from the multilayer more than Fe. For the samples in Fig. 3 the magnetoresistance of the multilayer grown on Fe is ≈ 60% higher than that grown on Cu. The magnetic data in Fig. 3 show that the sample grown on Fe has a moment in zero field corresponding to that of the Fe buffer layer. This is consistent with an almost perfect antiferromagnetic arrangement of the Co layers. In contrast the multilayer grown on Cu has a zero field moment considerably larger than that of the Fe moment in this structure suggesting incomplete antiferromagnetic alignment. Both auger sputter depth profiles and cross section transmission electron micrographs show that the Co and Cu layers are more regularly layered when grown on Fe buffer layers[7]. These conclusions are also consistent with x-ray diffraction studies. Figure 4 shows both low and high angle x-ray diffraction patterns taken with
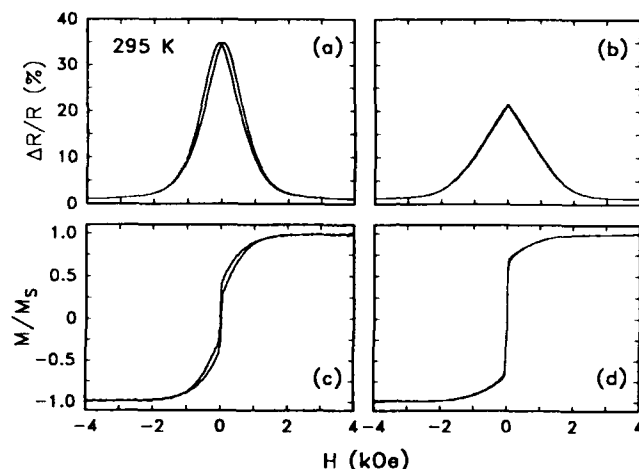
Figure 3: Resistance and magnetization versus field curves for two samples of the form Si(100)/bufferlayer/[Co(10Å)/Cu(9Å)]₁₆/cappinglayer. (a) and (c) correspond to a sample grown on a 50Å thick Fe layer with a 50Å capping layer, whereas (c) and (d) are for a sample grown on 50ÅCu with a 50ÅFe cap. The resistivities of the films in zero field are 19.5 μΩcm and 22.0 μΩcm respectively.

a Cu x-ray source for the same two samples of Fig.3. The multilayer grown on Cu shows only a weak first order reflection whereas that for the sample grown on Fe is well defined. In the latter case the peak position corresponds to a period of ≃22Å somewhat larger than the nominal multilayer period of 19Å. The latter is inferred from the measured thicknesses of ≃1000Å thick calibration films made at the same time as the multilayers. We ascribe this difference to a reduced density in the multilayer films. The high angle x-ray data shown in Fig. 4(b) shows for both samples a strong (111) reflection with a much weaker (200) reflection. The relative intensities of these reflections is about 5 times larger than expected for completely randomly oriented crystallites. Thus the films are (111) textured.

Finally Figure 5 shows a comparison of the dependence of the saturation magnetoresistance on Cu layer thickness for Co/Cu multilayers grown on Fe and Cu buffer layers. These data were measured at 4.2 K. Again, for thin Cu spacer layers, these data show diminished magnetoresistance values for growth on Cu buffer layers compared to growth on Fe buffer layers. However for thicker Cu spacer layers the two series of samples show very similar values of saturation magnetoresistance. These data are thus consistent with partial direct magnetic coupling of the Co layers for thin Cu layers for structures grown on Cu, perhaps resulting from the poor layered morphology. With thicker Cu layers this presumably becomes less important. Figure 5 shows that the period of the oscillation is similar for both sets of samples but that there is a significant shift in the phase of the oscillations towards thicker Cu layers for the structures grown on Cu. This again is presumably simply a result of the poorer structural integrity of these samples.
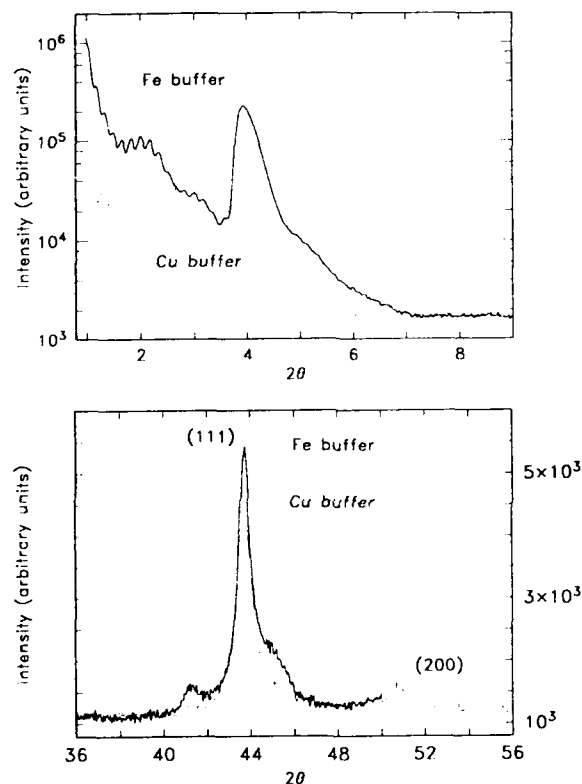
Figure 4: Low and high angle x-ray diffraction patterns for two Co Cu multilayer samples of the form Si(100)/Fe(50Å)/[Co(10Å)/Cu(9Å)]₁₆/Cu(50Å). and Si(100)/Cu(50Å)/[Co(10Å)/Cu(9Å)]₁₆/Fe(50Å).

Conclusions

Very large magnetoresistance values are found in Co Cu multilayers grown by magnetron sputter deposition. The saturation magnetoresistance oscillates with increasing Cu spacer layer thickness as a consequence of oscillations in the magnetic coupling via Cu from ferromagnetic to antiferromagnetic. For Cu layer thicknesses corresponding to the first antiferromagnetic oscillation saturation magnetoresistance values exceeding 65% at room temperature are found with saturation fields of about 10 kOe. At the second antiferromagnetic oscillation magnetoresistance values of more than 35% are found for saturation fields 20 times smaller. The use of Fe buffer layers was shown to give rise to more perfect layered structures with higher magnetoresistance values than similar structures grown on Cu for thin Cu spacer layers. For thicker Cu layers there is little difference in the magnitude of the magnetoresistance. For structures grown on Cu or Fe buffer layers the period of oscillations in magnetoresistance is the same but the phase of the oscillations is shifted towards thicker Cu layers for structures grown on Cu.
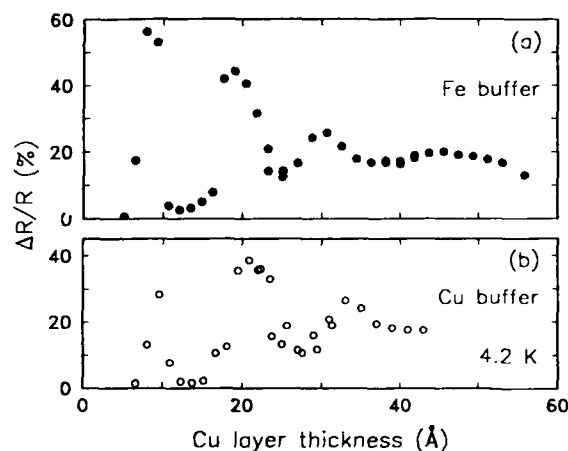
216

Figure 5: Dependence of saturation transverse magnetoresistance on Cu spacer layer thickness for two families of similar samples grown on (a) Fe buffer layers and (b) Cu buffer layers. The structures are (a) Si(100)/Fe(45Å)/[Co(10Å)/Cu(t_{cu})]₁₆/Cu(55 − t_{cu}Å). and (b) Si(100)/Cu(50Å)/[Co(9Å)/Cu(t_{cu})]₂₀/Cu(65 − t_{cu}Å).

Acknowledgements

References

[1] E. Velu, C. Dupas, D. Renard, J.P. Renard and J. Seiden, Phys. Rev. B 37, 668 (1988).

[2] G. Binasch, P. Grunberg, F. Saurenbach and W. Zinn, Phys. Rev. B 39, 4828 (1989).

[3] M.N. Baibich, J.M. Broto, A. Fert, F. Nguyen van Dau, F. Petroff, P. Etienne, G. Creuzet, A. Friederich, and J. Chazelas, Phys. Rev. Lett. 61, 2472 (1988).

[4] S.S.P. Parkin, N. More and K.P. Roche, Phys. Rev. Lett. 64, 2304 (1990).

[5] S.S.P. Parkin, Bull. Amer. Phys. Soc. 36, 843 (1991).

[6] S.S.P. Parkin, R. Bhadra and K.P. Roche, Phys. Rev. Lett. 66, 2152 (1991).

[7] S.S.P. Parkin, Z.G. Li and D. Smith, Appl. Phys. Lett. 58, 2710 (1991).

[8] S.S.P. Parkin, A. Mansour and G.P. Felcher, Appl. Phys. Lett. 58, 1473 (1991).

[9] Y.Y. Huang, G.P. Felcher and S.S.P. Parkin, J. Mag. Mag. Mat. 99, L31 (1991).

[10] A. Cebollada, J.L. Martinez, J.M. Gallego, J.J. de Miguel, R. Miranda, S. Ferrer, F. Batallan, G. Fillion, and J.P. Rebouillat, Phys. Rev. B 39, 9726 (1989).

[11] A. Cebollada, R. Miranda, C.M. Schneider, P. Schuster and J. Kirschner, J. Mag. Mag. Mat. 102, (1991).

[12] S.S.P. Parkin, Appl. Phys. Lett. (to be published).

MAGNETISM AND MAGNETORESISTANCE OF MULTILAYERS WITH TWO MAGNETIC COMPONENTS.
I. Cu-BASED FILMS

H. YAMAMOTO* , T. OKUYAMA** , H. DOHNOMAE*** and T. SHINJO
Institute for Chemical Research, Kyoto University, Uji, Kyoto-fu 611, Japan

ABSTRACT

Magnetoresistance (MR) properties were studied in $Cu/Co/Cu/Ni_{80}Fe_{20}$ system, and a large MR ratio was observed in weak external fields. In the course of field sweeping, these two magnetic components (Co and Ni(Fe)) are oriented antiparallel, because of the difference of coercive forces, and then the resistivity is greatly enhanced. The MR ratio was observed to be 10% at 300K, and 32% at 20K, respectively, in a multilayer $[Cu(55Å)/Co(25Å)/Cu(55Å)/Ni_{80}Fe_{20}(25Å)] \times 15$.

INTRODUCTION

Recently, a large magnetoresistance (MR) effect has been a topic in the foundamental and applied physics. Baibich et al. found that the reduction of resistance in an Fe/Cr multilayers reaches about 50% at 4.2K in 20 kOe[1]. More recently, two groups reported that the Co/Cu multilayers show more larger MR changes[2,3]. The MR ratio in a Co/Cu multilayer reaches 50% at room temperature (RT), and up to 120% at 4.2K, respectively. In Fe/Cr and Co/Cu systems, the magnetizations of adjacent magnetic layers couple antiparallel in weak external fields, due to an antiferromagnetic interlayer interaction across a non magnetic layer if the thickness is a proper value. At this situation, the resistivity of these samples is high. In higher external fields enough for the ferromagnetic orientation, the spin-dependent scattering mechanism does not work and the resistivity decreases. The origin of the giant magnetoresistance (GMR) effect is believed to be the scattering of the conduction electrons by the magnetic spins of d-electrons.

Firstly, Grünberg et al.[4] found that in Fe/Cr/Fe sandwiches the adjacent Fe layers coupled antiferromagnetically across Cr layer. Hosoito et al.[5] and Barthelemy et al.[6] studied the magnetic structure in Fe/Cr multilayers by means of neutron diffraction and confirmed that the antiparallel orientation of adjacent Fe layers is realized in weak external fields.

The authors found that a Cu/Co/Cu/Ni(Fe) multilayer shows a large MR at weak fields[7]. This system realizes an antiparallel magnetic orientation by a different cause from Fe/Cr or Co/Cu systems. In the Cu/Co/Cu/Ni(Fe) system, the magnetic layers are well separated by intervening nonmagnetic Cu layers. The exchange coupling between the magnetic layers is negligible.

Permanent addresses:
*Functional Devices Research Labs. NEC Corporation 4-1-1 Miyazaki, Miyamae-ku, Kawasaki 213.
**TOYOBO Research Inst., TOYOBO Corp., 2-1-1 Katata, Ohtsu Shiga 520-02.
*** R & D Labs.I, Nippon Steel Corp., 1618 Ida, Nakahara-ku, Kawasaki 211.

Thus a "giant ferrimagnetic state" is induced in the magnetization process because of the different coercive fields. The resistivity increases sharply due to the spin-dependent scattering when the magnetizations are antiparallel. It is a great merit for technical applications that a weak field can induce a large MR change.

EXPERIMENTAL

Multilayers consisting of two magnetic components were prepared by successively depositing Cu, Co, Cu and Ni(Fe) alloy layers on glass substrates using alternate vapor deposition technique by E-guns in ultrahigh vacuum. Residual gas pressure was in the range of 10^{-10} torr. Ni(80wt%)-Fe(20wt%) alloy, Co and Cu metals were used as the evaporation sources. The composition of deposited Ni(Fe) alloy layer is believed to be almost the same as that of evaporation source. The deposition rate was in the range $0.2 \sim 0.5$ Å/s on the substrates at RT. The multilayers were analyzed by X-ray diffractometory. The dimension of the samples for the MR measurements was 0.3×10 mm^2. The resistance was measured using the conventional four-terminal method. The direction of the current was in-plane. The external fields applied in an in-plane direction at the right angles with that of the current. The MH curve was obtained by a vibrating sample magnetometer (VSM) and a superconducting quantum interference device (SQUID). Most of the MR curves and the MH curves were measured between ±500 Oe. MR ratio was defined as $\Delta\rho/\rho_0 \times 100$ %, where ρ_0 is the resistivity at the ferromagnetically saturated state.

RESULT AND DISCUSSION

Magnetization and Resistance

If the Cu layer is enough thick to separate the magnetic layers, the magnetizations of two magnetic components turn over almost independently. Since the effective anisotropies of Co and Ni(Fe) layers are different, the magnetizations of two magnetic layers turn over at different magnetic fields. That is to say, the magnetization of the soft component reverses in the low external field region ($|H| \leq 50$ Oe), while the hard components reverse at $|H| \geq 50$ Oe. The resistance is increasing abruptly with reversing the Ni(Fe) magnetization. The maximum resistance was obtained at the external field where the directions of two magnetic components are oriented antiparallel with each other (Fig.1). We have
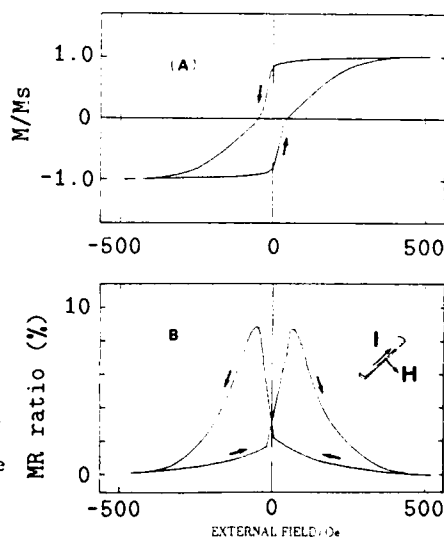

Fig.1 Magnetic hysteresis loop (A) and magnetoresistance (B), at RT of a multilayer [Cu(50Å)/Co(30Å)/ Cu(50Å)/Ni(Fe)(30Å)]×15.

observed MR ratio $\Delta\rho/\rho_0$ (H=3 kOe) of 10% at RT and 33% at OK, respectively, in a multilayer [Cu(50Å)/Co(30Å)/ Cu(50Å)/Ni(Fe)(30Å)] × 15.

Figure 2 shows the MR effect as a function of temperature, which is the peak value against the resistance at H=3 kOe. The base resistivity ρ_0 (H=3 kOe) decrease with the decrease of temperature. Above 100K, the ρ_0 decrease linearly. While below 100K, gradually the differential value of ρ_0 becomes smaller. Figure 3 shows the absolute change as a function of temperature. The absolute resistivity change $\Delta\rho$ increases monotoniously, with the decrease of temperature. The $\Delta\rho$ at 20K ($\simeq 1.3\mu\Omega\cdot cm$) proved to be nearly twice the value at 300K ($\simeq 0.6\mu\Omega\cdot cm$). This result shows that the magnetic contribution in the spin-dependent scattering at 20K is 2 times larger than that at 300K. On the other hand, the bulk magnetization is almost equal in the range of OK ~ 300K in a multilayer [Cu(55Å)/Co(25Å)/Cu(55Å)/ Ni(Fe)(25Å)] × 15, because the Curie temperatures of both components are much higher than RT (Fig.3). It is an important clue for the understanding of the MR effect.
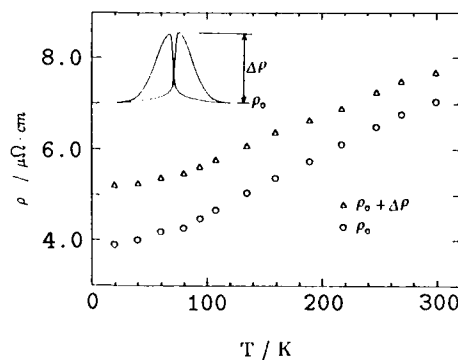

Fig.2 Specific resistivities of the Cu/Co/Cu/Ni(Fe) sample at the peaks(△) and at H=3 kOe (O), respectively, as a function of temperature.

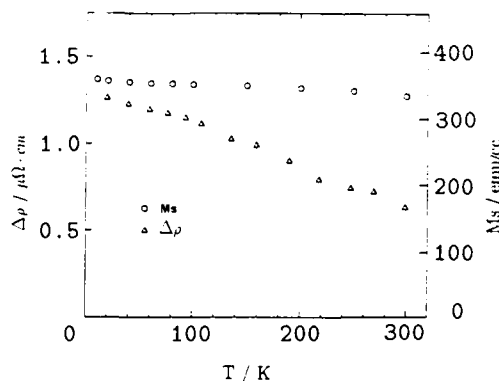

Fig.3 Magnetization at H=3 kOe, Ms, and the magnetic contribution to the resistivity, $\Delta\rho$, as a function of temperature in a multilayer [Cu(55Å)/ Co(25Å)/Cu(55Å)/Ni(Fe)(25Å)] × 15.

Dependence of MR on Annealing Temperatures

Petroff et al. studied the dependence of MR on annealing temperatures in the Fe/Cr multilayers[8].

In Fe/Cr system, the MR change increases with annealing temperatures. They concluded a mixing at Fe/Cr interfaces to a certain extent is favorite to enhance the spin-dependent scattering. In order to know the influence of an annealing on Cu/Co/ Cu/Ni(Fe) system, a heat treatment experiment was carried out. Figure 4 shows the MR ratio for various annealing temperatures in a multilayer [Cu(55Å)/Co(25Å)/ Cu(55Å)/Ni(Fe)(25Å)]×15. The samples were annealed for 1 hour in a ultrahigh vacuum at 50°C ~ 300°C.
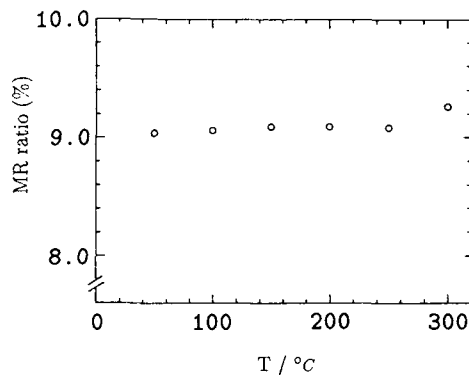
Fig.4 Dependence of MR on annealing temperatures.

The MR ratio does not increase as a result of annealing in this system. The difference of MR ratio of each sample was in the range of experimental errors. Because Cu-Ni(Fe) and Cu-Co are not the combinations to make solubility compounds, heat treatments at moderate temperatures do not induce a significant change. On the other hand, for a technical use, multilayers of this system have a good heatproof characteristic below 300°C.
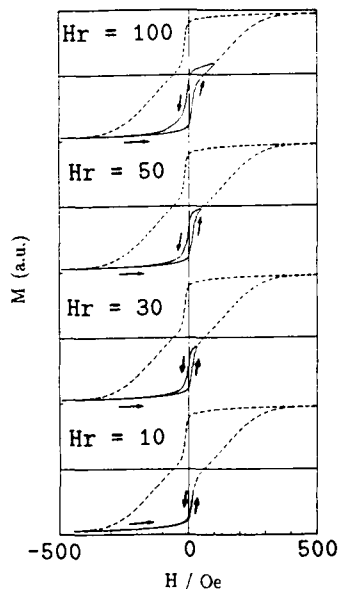
Fig.5 Magnetic minor loops of [Cu(55Å)/Co(25Å)/Cu(55Å)/ Ni(Fe)(25Å)]×15 ; for various Hr.
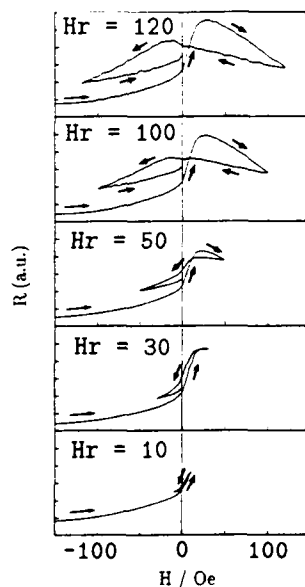
Fig.6 MR minor loops of [Cu(55Å)/Co(25Å)/Cu(55Å)/ Ni(Fe)(25Å)]×15 ; for various Hr.

Minor Loops

The dependence of MR on the magnetic structure has been studied by changing appled fields in the range of a few Oe. The minor loops of MH and MR in a multilayer [Cu(55Å)/Co(25Å)/Cu(55Å)/Ni(Fe)(25Å)]×15, are respectively shown in Figs. 5 and 6. The field was swept between ± Hr after applying −200 Oe, where Hr is the reverse point of the external field. Because the rotation of the hard component (Co layer) needs a higher field, the magnetization and the resistance change reversibly for |Hr|≤30 Oe. Then, the MR ratio increases sharply. Especialy in the range |Hr|≤20 Oe, the field dependence of resistance is almost linear. This is an important result for technical applications. As Hr is increased above 30 Oe, the hard component rotates gradually. Because the reversals of soft component and hard one occur in different ranges of field, the MH curves become hysteretic. The area of MH hysteresis loop increases gradually with Hr. The resistance decreases with rotating Co magnetization and the MR curves become hysteretic with sweeping between ±Hr (>50 Oe),too. The MR loops have two peak values at ±50 Oe where giant ferrimagnetic state is realized, respectively. As +Hr is below 50 Oe, the MR loop does not have the peak value at −50 Oe. With incresing of +Hr, the peak value at −50 Oe becomes high. At +Hr=500 Oe, the two peak values are almost equal, since the Co magnetization is saturated (Fig.1).

Dependence of MR on the Cu layer thickness

The dependence of MR on the thickness of the Cu layer was studied in [Cu(d)/NiFe(25Å)/Cu(d)/Co(25Å)]×5 (Fig.7). The magnetization process and MR curve change dramatically with the Cu layer thickness, d(Cu). This result suggests that there is a ferromagnetic type interlayer coupling between two magnetic layers. As d(Cu) is thin, there is a strong interlayer coupling, then the MH curves show single ferromagnetic hysteresis loops because of the magnetizations of Ni(Fe) and Co layers rotate almost at the same field.

Fig.7 MR ratio and resistivity at RT as a function of Cu layer thickness (d(Cu)) in a multilayer [Cu(d)/Co(25Å)/Cu(d)/Ni(Fe)(25Å)]×5 ; H=500 Oe.

As d(Cu)≥55Å, the antiparallel orientation is realized because the magnetizations of two magnetic layers turn over at different fields. It is interesting to note that the curvature of MH curve for d(Cu)=72Å is

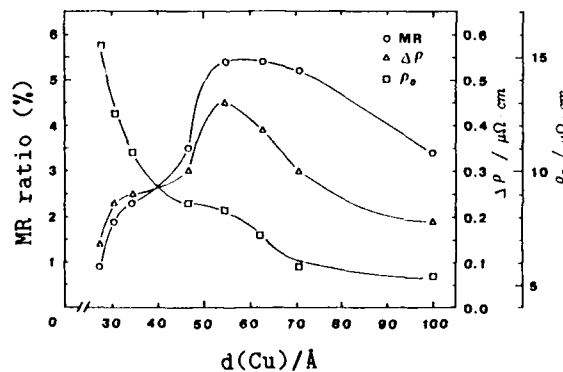slightly different from that for d(Cu)=55Å, which means a weak interlayer coupling between two magnetic layers exists even above d(Cu)=55Å. Parkin et al. studied the dependence of MR on the Cr or Ru layer thicknesses in Fe/Cr or Co/Ru systems[9]. The MR changes were found to depend oscillatorily on the nonmagnetic layer thickness. They argued that the origin of the oscillations is a Ruderman-Kittel-Kasuya-Yosida (RKKY) type interaction. In the present work, the dependence of MR in the region where d(Cu) is smaller than 50Å, is necessary to examine in more detail.

SUMMARY

Because of the difference of coercive fields in the two magnetic components, "giant ferrimagnetic states" is realized at weak fields in the system Cu/Co/Cu/Ni(Fe) and the resistance is increasing by the spin-dependent scattering. With varing layer thicknesses or layer number, the magnetization process and the MR change are controlled. These results show that a large MR effect in this system is useful for technical applications.

ACKNOWLEDGMENTS

References

[1] M.N.Baibich, J.M.Broto, A.Fert, F.Nguyen Van Dau, F.Petroff, P.Etienne, G.Creuzet, A.Friederich and J.Chazelas: Phys.Rev.Lett. 61 (1988) 2472.
[2] D.H.Mosca, F.Petroff, A.Fert, P.A.Schroeder, W.P.Pratt Jr.   and R.Laloee : J.Magn.& Magn.Mater. 94(1991) L1.
[3] S.S.P.Parkin, Z.G.Li and David J.Smith : preprint
[4] G.Binasch, P. Grünberg, F.Saurenbach and W.Zinn: Phys.Rev. B39 (1989) 4828.
[5] N.Hosoito, S.Araki, K.Mibu and T.Shinjo, J.Phys.Soc.Jpn.   59(1989) 1925.
[6] A.Barthelemy, A.Fert, M.N.Baibich, S.Hadjouji, F.Petroff, P.Etienne, R.Cabanel, S.Lequien, F.Nguyen Van Dau and G.Creuzet, J.Appl.Phys. 67(1990) 5908.
[7] T.Shinjo and H.Yamamoto, J.Phys.Soc.Jpn. 59 (1990) 3061.
[8] F.Petroff, A.Barthelemy, A.Hamzic, A.Fert, P.Etienne, S.Lequien and G.Creuzet, J.Magn.& Magn.Mater. in press.
[9] S.S.P.Parkin, N.More and K.P.Roche, Phys.Rev.Lett. 64 (1990) 2304.

MAGNETISM AND MAGNETORESISTANCE OF MULTILAYERS WITH TWO MAGNETIC COMPONENTS. II. Au-BASED FILMS

T.OKUYAMA[*],H.DOHNOMAE[**],H.YAMAMOTO[***] and T.SHINJO
*Institute for Chemical Research,Kyoto University,
Uji,Kyoto-fu 611, Japan*

ABSTRACT

Magnetoresistance(MR) properties of Au-based multilayers including two magnetic components, i.e.[Au/Co/Au/Ni(Fe)]×n, were investigated and compared with those of Cu-based films. The interlayer coupling between Co and Ni(Fe) through Au layer was found to be strongly antiferromagnetic if the thickness is less than 35Å. Antiparallel alignment of magnetizations caused by the difference in the coercive fields of Co and Ni(Fe) layers is realized when the Au layer thickness is larger than 50Å. Then, the resistance is enhanced by the spin-dependent scattering but the observed MR ratio is smaller than the case of Cu-based multilayers.

INTRODUCTION

In the preceding paper[1], MR properties of Cu-based multilayers including two magnetic components, Co and Ni(Fe) (permalloy), were described. If the spacing Cu layers are thick enough, each magnetic layer is isolated and in the course of external field sweeping, the magnetizations of Co and Ni(Fe) layers are oriented antiparallel to each other, in a certain field region, because the coercive fields are different. Then, a large enhancement of resistance occurred due to the spin-dependent scattering. In order to study the mechanism of the spin-dependent scattering and also to look for the condition to realize larger MR changes, it is of significant importance to examine the MR properties of other systems, with replacing the Cu layers by some other non-magnetic metal. In this paper, experimental results on Au-based multilayers are introduced and compared with the Cu-based ones. Some results of other systems will be mentioned very briefly.

EXPERIMENTAL

Samples were prepared by succeedingly depositing Au, Co, Au and permalloy($Ni_{80}Fe_{20}$) in ultrahigh vacuum, onto glass substrates at room temperature. The base vacuum was in 10^{-10} Torr range and in 10^{-9} Torr during the deposition. Typical deposition rate was 0.3Å/sec. The magnetic layer thicknesses were always 25Å and the Au layer thickness was varied from 15Å to 100Å. The deposition of the four-layers-unit was repeated up to 15 times. The artificial periodic structures were confirmed by X-ray diffraction. Cross-sections of some samples were observed by transmission electron microscope (TEM). Four-terminal resistivity measurements were

applied to the samples with the size of 0.3×10mm. The
direction of the external field was in the film plane,
perpendicularly to the electric current($1×10^{-4}$ A). The MR ratio is
expressed as the difference from the resistance at H=3kOe, which
is taken as the standard resistance at the full saturation.

RESULTS

An example of X-ray diffraction pattern for a Au/Co/Au/
Ni(Fe) multilayer is shown in Fig.1. Observed peaks are rather
sharp since the densities of Au and 3d metals are different. Such
X-ray patterns indicate that the artificial periodic structure has
been established as designed and each interface is sufficiently
sharp. The structure is regarded as texture with
Au(111)/Ni(Fe)(111)/Co(001) epitaxy. The coherence length
estimated from the X-ray line broadening is about 250Å. It is more
than twice of the artificial period (the four layers' thickness)
and suggests that the crystallographic quality of the sample is
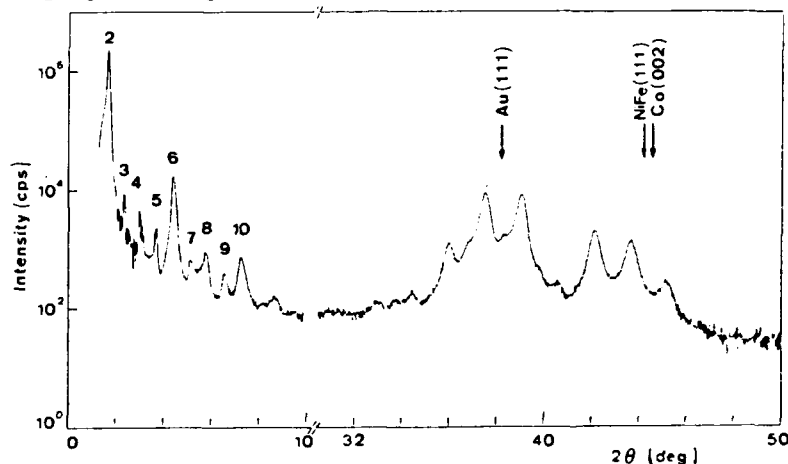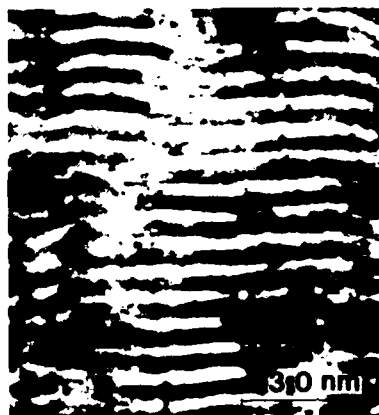fairly good. Figure 2 is an example of the cross-sectional

Fig.1.X-ray diffraction patern
for [Au(30Å)/Co(25Å)/Au(30Å)/
$Ni_{80}Fe_{20}(25Å)$]×15.

Fig.2.Cross-section of the
same sample as Fig.1 by TEM
observation.
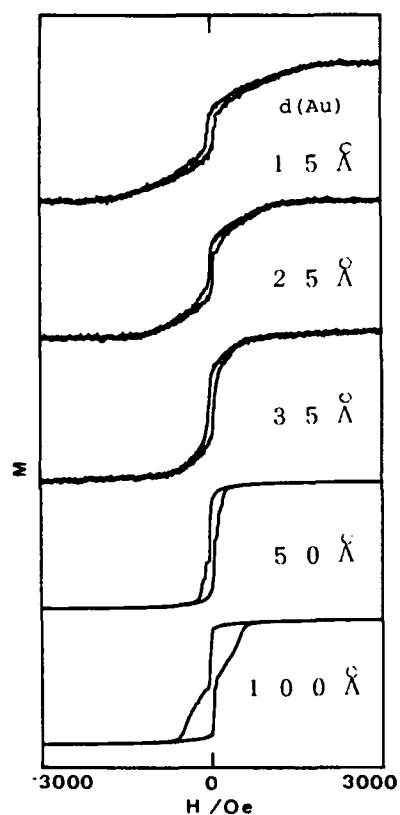
Fig.3.Magnetic   hysteresis
curves   for   the   sample
[Au(d)/Co(25Å)/Au(d)/Ni(Fe)
(25Å)]×15,   as a function of
the Au layer thickness, d(Au).
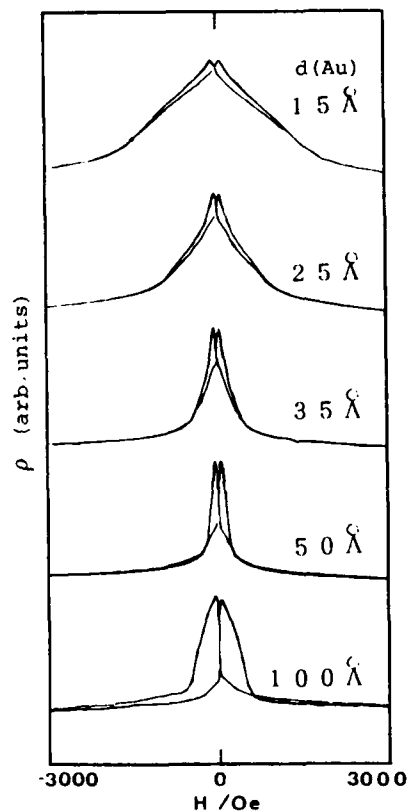
Fig.4.MR curves for the same
samples as Fig.3.

observation by TEM, which also indicates the establishment of
artificial periodicity.

     Magnetic hysteresis curves for the [Au/Co/Au/Ni(Fe)] samples
are shown in Fig. 3. The Au layer thickness,d(Au), was varied from
15 to 100Å, while the magnetic layer thicknesses, d(Co) and
d(Ni(Fe)), were constantly 25Å. When d(Au) is less than 50Å, two
magnetic components are not independent with each other but
coupled antiferromagnetically. The saturation field corresponds
to the strength of antiferromagnetic coupling and becomes larger
if d(Au) is smaller. The magnetic structure is therefore
determined   by   the   competition   between   the   interlayer
antiferromagnetic coupling and the external field. In this case,

an antiparallel alignment of magnetizations is caused by the interlayer coupling and therefore realized in the vicinity of zero field.

Figure 4 shows an example of resistance enhancement caused by the interlayer antiferromagnetic coupling. The peaks are observed at small fields and the hysteresis (the difference between field increasing and decreasing) is rather small. The interlayer coupling, Co-Au-Ni(Fe) is indeed a very interesting problem. However, the main subject of this paper is the region where the interlayer coupling is very small. A further discussion on the interlayer magnetic coupling will be given in a forthcoming paper[2]. If d(Au) is larger than 50Å, the interlayer coupling becomes negligible and two magnetic components behave independently. In the couse of field sweeping, an antiparallel alignment is realized becuase of the difference of coercive fields. Then, as also shown in Fig.4, the resistance is enhanced by the spin-dependent scattering as was already demonstrated in the Cu-based multilayers[1]. As long as the non-magnetic spacing layer, Cu or Au, is thick enough, the MR properties of Au-based films are qualitatively the same as those of Cu-based ones.

The observed MR ratio at room temperature of Au-based films is shown in Fig.5a as a function of d(Au). As mentioned already, there are two causes for the antiparallel alignment. The interlayer coupling is dominant in smaller d(Au) region, while the difference of coercive fields is the dominant reason for antiparallel magnetizations in larger d(Au) region. As is shown in the figure, the resultant MR ratio changes gradually and the values at d(Au)=50,80 and 100A are nearly the same. The two regions cannot be clearly separated but two mechanisms are superposing at the boundary. The maximum value at room temperature does not exceed 5%, which is smaller than that in Cu-based multilayers. In Fig.5b, the specific resistance values of ρ_0 and $\Delta\rho$ are expressed as a function of d(Au). ρ_0 is the base resistance and $\Delta\rho$ the MR change (peak height), respectively. It is to be noted that the absolute magnetic contribution does not change greatly. The increase of resistance with the decrease of d(Au) is due to the change of 3d/Au ratio and crystallographic reasons.

COMPARISON WITH OTHER SYSTEMS

The $\Delta\rho$ value at d(Au)=50Å is about 0.5$\mu\Omega$cm. This is comparable to the largest value in the Cu-based samples, which was about 0.6$\mu\Omega$cm. Therefore it is likely that the spin dependent scattering at Au/3d itself is not smaller than that at Cu/3d interfaces. Because the base resistance ρ_0 in Au layer is higher than that in Cu, eventually the observed MR ratio turns out to be smaller in Au-based films.

Several Al-based samples were also prepared with the same procedure. An example of hysteresis curve is shown in Fig.6, which indicates that the magnetic layers are well separated and an antiparallel alignment is certainly established. Nevertheless, the MR curve shows no peak at all. The resistivity of the Al-based multilayers is one order larger than that of Cu-ones. Therefore, an MR ratio should be one order smaller even if there works a similar spin-dependent scattering at the interface between Al and 3d metals. However it is certain that the magnetic contribution is less than 0.1$\mu\Omega$cm. Therefore the spin-dependent scattering at Al/3d seems to be much less effective than that at Cu/3d or Au/3d.

A systematic investigation on other systems is in progress.
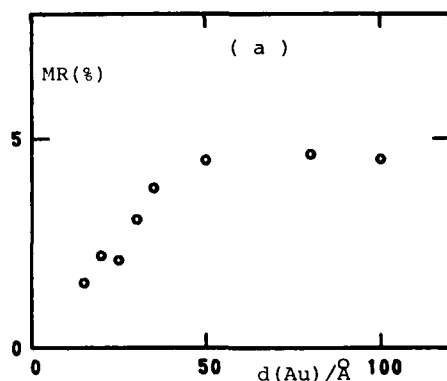
Fig.5a. MR ratio at RT of
Au/Co/Au/Ni(Fe) as a function
of the Au layer thickness,
d(Au).
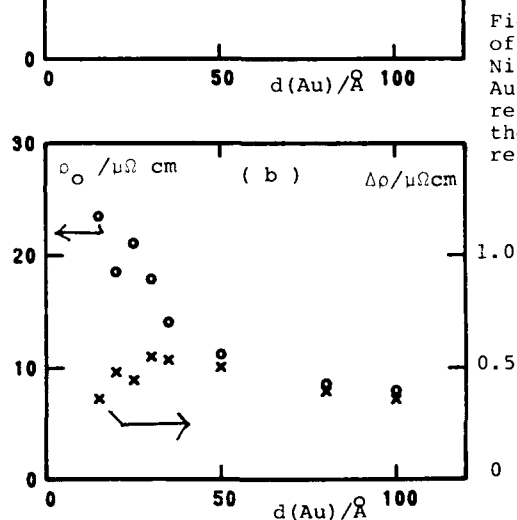
Fig.5b. Specific resistance
of ρ_O and Δr for Au/Co/Au/
Ni(Fe) as a function of the
Au layer thickness. ρ_O is the
resistance at H=3kOe and $\Delta\rho$,
the maximum increase of
resistance by the MR effect.
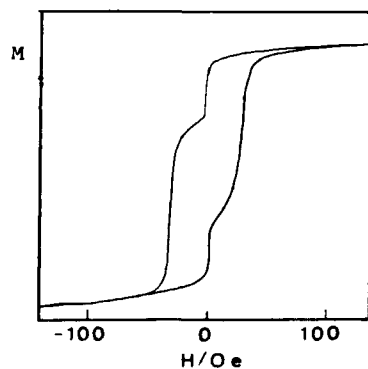
Fig.6.Magnetic   hyesteresis
curve   of   [Al(35Å)/Co(25Å)/
Al(35Å)/$Ni_{80}Fe_{20}$(25Å)]×15.

REFERENCES
[1] T. Shinjo and H. Yamamoto, J. Phys. Soc. Jpn. Jpn.59(1990)3061
    H.Yamamoto,H.Dohnomae,T.Okuyama and T.Shinjo,
    the preceding paper in this volume.
[2] H.Dohnomae,T.Okuyama,H.Yamamoto and T.Shinjo,in preparation.

NMR study on the nanostructure of Co/X multilayers

W. J. M. DE JONGE, H. A. M. DE GRONCKEL and K. KOPINGA,
Department of Physics, Eindhoven University of Technology (EUT),
5600 MB Eindhoven, The Netherlands,

P. PANISSOD,
IPCMS, 4 rue Blaise Pascal, 67070 Strasbourg, France,

F. J. A. DEN BROEDER,
Philips Research Laboratories, 5600 JA Eindhoven, The Netherlands.

The nanostructure and local strain of [111] FCC Co/Cu and Co/Ni multilayers is studied by means of nuclear magnetic resonance. The atomic topology of the interface can be deduced from the NMR spectrum, the local strains from the shift in the hyperfine fields. The results show that the Co/Cu interface is a mixed monolayer and that the Co layers, including the interface, have uniform (tensile) strain inversely proportional to the Co thickness (within experimental error) with the proportionality constant depending on the Cu thickness. In Co/Ni the interface consists of two mixed layers and the Co layers have uniform compressive strain inversely proportional to the Co thickness.

The new phenomena observed in thin films and magnetic multilayers -e.g., change in preferential direction of the magnetic moment [1], giant magnetoresistance [2], dimensionality effects [3], etc.- are strongly determined by structural and interfacial perfection of the films and the presence of strains [4]. In multilayers information on these vital parameters is generally hard to obtain. For surfaces, detailed information on the topology can be obtained by many experimental techniques from surface physics. For interfaces and individual layers embedded in the multilayer structure such information is much more difficult to obtain. In principle techniques such as nuclear magnetic resonance (NMR) and Mössbauer spectroscopy provide the possibility to probe the multilayers and the interfaces on a nanoscopic scale.

In this contribution we will demonstrate the potential power of nuclear magnetic resonance (NMR) for the research of the nanostructure of multilayered materials. We will show that a clear distinction can be made between interface and bulk atoms and that detailed information on the topology of the interface and the strain within the layer can be obtained. To this purpose the interface structure and local strains of various Co/X (X = Ni, Cu, Pd, Ir, Au) multilayers have been studied with NMR. We will emphasize the results on [111] FCC Co/Cu and Co/Ni. Preliminary results on the former system have been published elsewhere [5].

The Co/Cu multilayers were prepared at the Philips Research Laboratories by e-beam evaporation in HV on oxidized silicon substrates ($12 \times 4 \times 0.4$ mm^3) at room temperature. The deposition was started with a base layer of 200 Å Cu, the deposition rate was in the order of a few Å/s and the total thickness of the multilayers was about 2000 Å. Chemical analysis was used to check the amount of Co. Values of the layer thicknesses quoted below are accurate to about 5%. X-ray diffractometry at high and low scattering angles confirmed the [111] FCC texture and the superlattice modulation. The Co/Ni multilayers were prepared by MBE on oxidized silicon substrates using a base layer of 300 Å Au which was annealed at 150 °C for 20 minutes prior to the multilayer deposition. The deposition rate was about 0.5 Å/s.

NMR experiments were performed with and without a magnetic field. The in-field spectra were recorded in fields (up to 5 T) applied parallel to the film plane at a tempera
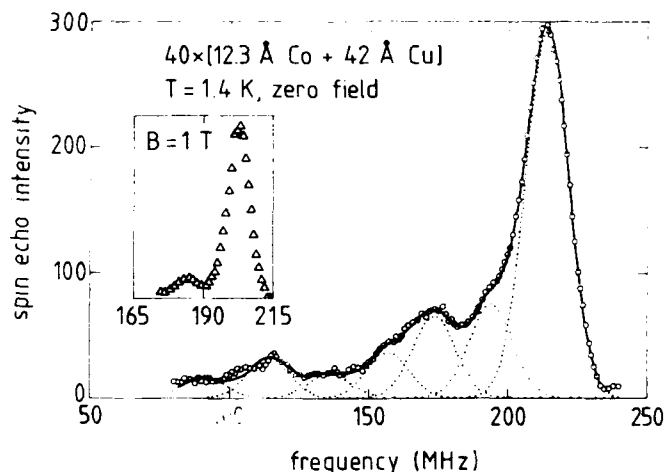
Figure 1. *NMR spin echo intensity as function of resonance frequency for a 40×(12 Å Co + 42 Å Cu) [111] multilayer in zero field as recorded. The solid line represents the result of a fit with seven Gaussians. Each Gaussian (denoted by the dotted lines) corresponds to Co atoms in a specific environment. The dependence of the spin echo intensity on the square of the frequency has been incorporated in the fitting program. The inset shows that application of a magnetic field reduces the line broadening due to inhomogeneous magnetization, thereby clearly resolving the first satellite from the main line.*

ture of 1.4 K with the incoherent spin echo spectrometer at EUT. The zero field spectra were recorded at constant r.f. field strength with the automated coherent spin echo spectrometer at the IPCMS. The sensitivity of both installations amounts to roughly 10^{16} Co spins at 1.4 K.

Fig. 1 and 2 show typical examples of a NMR spectrum. Fig. 1 shows the spin echo intensity for a 40×(12.3 Å Co + 42 Å Cu) multilayer versus frequency in zero field. Fig. 2 shows the spin echo intensity for a 50×(12.3 Å Co + 42 Å Ni) multilayer as function of the hyperfine field, expressed in terms of the zero field resonance frequencies, in a magnetic field applied parallel to the film plane. Spectra for different thicknesses of Co (or Cu,
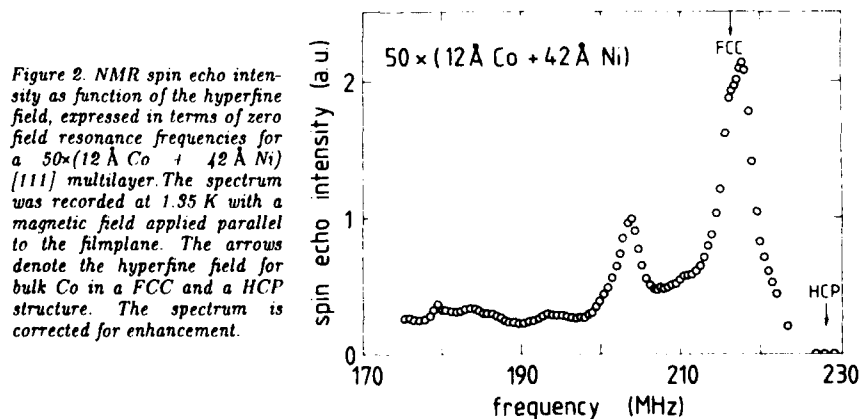

Figure 2. *NMR spin echo intensity as function of the hyperfine field, expressed in terms of zero field resonance frequencies for a 50×(12 Å Co + 42 Å Ni) [111] multilayer. The spectrum was recorded at 1.35 K with a magnetic field applied parallel to the filmplane. The arrows denote the hyperfine field for bulk Co in a FCC and a HCP structure. The spectrum is corrected for enhancement.*
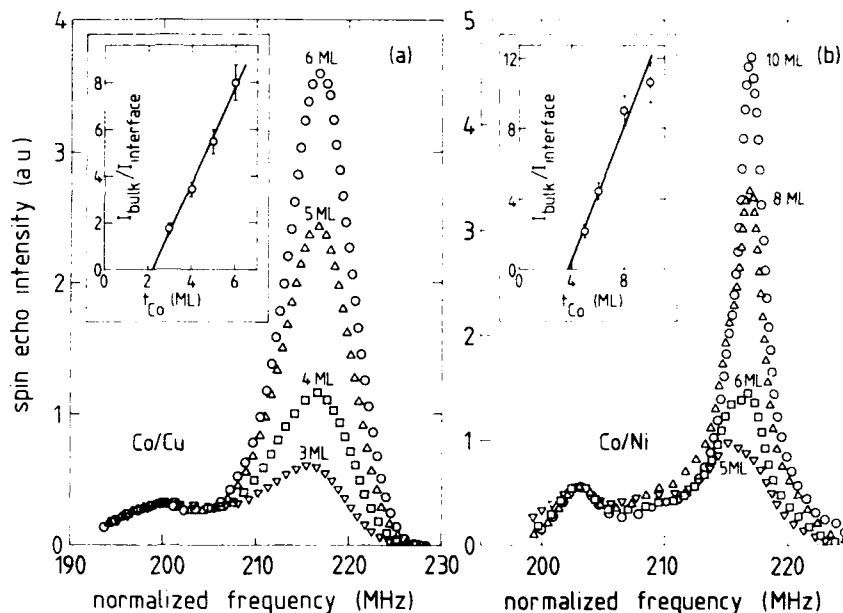
Figure 3. In field spectra of Co_xCu_{21} multilayers (Fig 3a, left part of the figure) and of Co_xNi_{42} multilayers (Fig. 3b, right part of the figure) showing the systematic increase in intensity ratio between the main line and the most intense satellite as function of the Co thickness t_{Co} (expressed in monolayers). For easy comparison the spectra have been normalized to the most intense satellite (in intensity as well as in frequency). The insets show the ratio of intensity of bulk to interface as function of Co thickness.

respectively, Ni) are qualitatively similar, but shifted in frequency. The main line in the spectrum appears close to the value of FCC surrounded bulk Co (217 MHz). The shift of this line with respect to the bulk value is caused by strain in the Co layer, as we will argue in detail later. At the high frequency side there is practically no intensity, indicating that in our samples the amount of HCP Co and the number of stacking faults is very small. This is in marked contrast with measurements on Co/Pd, Co/Ir and Co/Au [6]as well as recent X-ray and NMR experiments on some Co/Cu multilayers [7] where stacking faults and fractions of HCP Co up to 40% are reported. Since the intensity ratio between the main line and the lower frequency part of the spectrum increases systematically with t_{Co} as shown in Fig. 3, the part of the spectrum below the main line is assigned to Co atoms at the interfaces where one or more nearest neighbor Co atoms are replaced by Cu, respectively, Ni. This assignment is supported by the observation that the spin-spin relaxation time T_2 for the satellites is typically twice the value measured for the main (bulk) peak, evidencing a different origin of the signals. From the inset of Fig. 3a it appears that for Co/Cu the intensity ratio between the main line and most intense satellite varies as $n_{Co}-2$, indicating unambiguously that the mixed layer is only one layer thick.

To analyse the interface spectrum of Co/Cu (Fig. 1) more quantitatively we fitted the intensity by Gaussian lines. Since the spectrum originates from Co atoms with one or more Cu atoms in their nearest neighbor shell, it should consist of a number of absorption lines shifted with respect to the bulk FCC line by approximately 18 MHz per substituted Cu atom as deduced from experiments in diluted alloys [8]. The solid line in Fig. 1 shows that the structure of the spectrum is indeed well fitted by (seven) approximately equally spaced Gaussians (denoted by the dotted lines) with an average spacing of 19 ± 3 MHz.

All parameters in the fit were free except for the linewidth, which was constrained to have the same value for all lines. We stress that the fit was insensitive to changes of the starting parameters and always converged to the same positions and intensities for the lines. Attempts to reduce the number of lines gave evident misfit whereas attempts to introduce more than seven lines resulted in a merging of the supplementary lines into one of the seven within less than 1 MHz. We are thus very confident that the reconstructed spectrum with seven lines represents the actual hyperfine field distribution to a fair degree of correctness.

Given this result the various lines can thus be assigned to Co nuclei having 12 Co neighbors ("bulk" atoms) and nuclei having 11 to 6 Co neighbors ("interface atoms"). The existence of Co sites with an environment different from 12 Co neighbors ("bulk" atoms) or 9 Co neighbors (sites in perfectly flat interface layers have 9 Co neighbors for the [111] oriented growth) is obviously related to interface roughness.

In order to substantiate this conclusion somewhat more we have compared the experimental intensity of the satellite spectrum with a complete random distribution as well as a more structured model. The latter model, which is schematically shown in Fig. 4, contains monoatomic steps with an average width equal to the average distance d between them. Since the edges of a step are not necessarily perfectly straight an average length l of its straight sections is also introduced. Angles between the straight sections are symmetry determined, i. e., 120^0 (Cu rich angle) and 240^0 (Co rich angle), and assumed to be equally probable. The relative occurrences of the various neighborhoods in the two tentative models determines the intensity. A surprizing agreement (within 10%) between the step model (with d and l in the order of two atomic distances) and the experimental data was obtained. These values for d and l show that in the interface monolayer atomic steps are quite numerous. However, it must be stressed that the observed distribution of neighborhoods clearly differs from the limiting case of a random distribution of 50% Co and 50% Cu in a flat but diffused interface layer. This means that in the mixed interface layer the Co atoms prefer to be surrounded by Co and the Cu atoms by Cu, which is not unlikely.
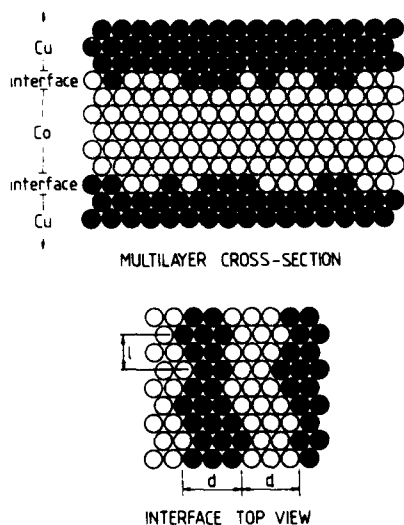
MULTILAYER CROSS-SECTION

INTERFACE TOP VIEW

Figure 4. Schematic view of a Co/Cu multilayer with atomic step defects in the interface monolayer. The steps have an average length d equal to the average distance between them. The average length of the straight parts of the edges of the steps is denoted by l.

In the case of Co/Ni the fact that there is more than one satellite visible (Fig. 2) also directly indicates that the interfaces are rather thoroughly mixed. From the inset of Fig. 3b it appears that the intensity ratio between the main line and most intense satellite varies as n_{Co}-4, indicating that, in contrast to Co/Cu, there are at least two mixed layers at each interface. This makes the interpretation in terms of a specific interface structure model much more complicated. Preliminary analysis, however, seems to indicate that the interface may not be completely randomly diffused but contain numerous mono-atomic and bi-atomic steps.

We will now focus on the dependence of the spectra on the Co thickness (t_{Co}). NMR spectra have been recorded by field-sweeps at constant r.f. frequencies for multilayer samples having a Cu layer thickness of 21 Å and 42 Å, respectively, a Ni layer thickness of 42 Å, and a Co layer thickness ranging from 6 Å to 40 Å. The observed positions of the
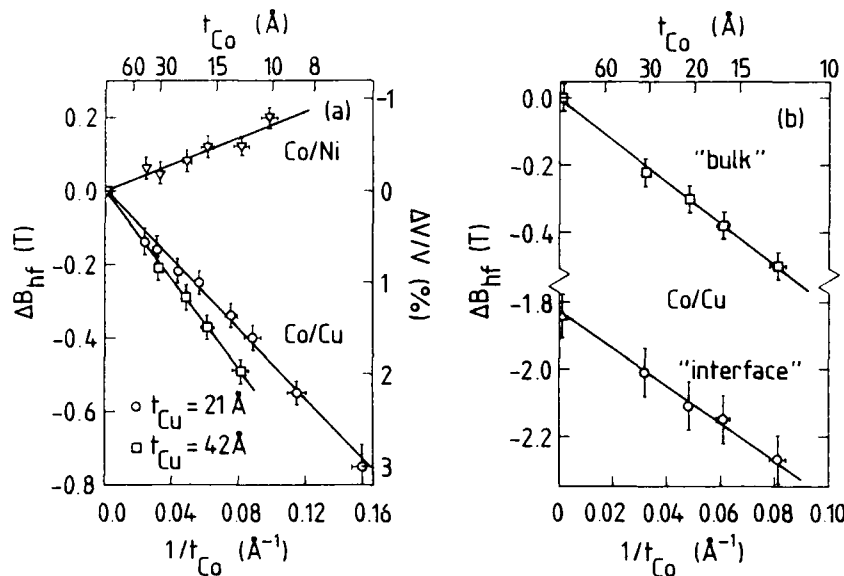
Figure 5. a) Hyperfine field B_{hf} derived from in-field spectra as function of inverse Co thickness $1/t_{Co}$ for [111] FCC Co/Cu and Co/Ni multilayers. The solid lines represent least squares fits of a straight line to the data.

b) Hyperfine field B_{hf} derived from in-field spectra as function of inverse Co thickness $1/t_{Co}$ for [111] FCC Co/Cu multilayers with a Cu thickness of 42 Å. The squares represent the hyperfine field of Co atoms with 12 Co atoms as nearest neighbor ("bulk" atoms). The triangle (data taken from ref. 8) and circles represent the hyperfine field of Co atoms with 11 Co nearest neighbors and 1 Cu nearest neigbor (atoms at the interface).

main line are plotted in Fig. 5a as ΔB_{hf} against $1/t_{Co}$. The hyperfine field B_{hf} was obtained from the resonance field B_0 and the frequency f by the relation $f = \gamma(B_{hf}-B_0)$, where $\gamma = 10.054$ MHz/T is the ^{59}Co nuclear gyromagnetic ratio. The "bulk" value $B_{hf} = 21.54$ T observed for a 1000 Å thick Co layer is used as reference value. It is obvious that in the multilayers B_{hf} is shifted from the bulk value by an amount ΔB_{hf} depending on t_{Co}. From pressure experiments as well as theoretical calculations it is known that the magnitude of the hyperfine field is related to the atomic volume (V) or, alternatively, the strain [9]. Using the proportionality of $\Delta B_{hf}/B_{hf}$ to $\Delta V/V$ ($\Delta_{hf}/B_{hf} \approx$ -1.16 $\Delta V/V$ for isotropic pressure) the data indicate that the strain in the Co layers as probed by the bulk atoms seems to be inversely proportional to the Co thickness for Co thicknesses from 6 Å up to bulk. The sign and magnitude of the strain, however, clearly depend on the chemical composition of the multilayer (Fig. 5a). For Co/Ni the strain in the Co layers is compressive while for Co/Cu the strain is tensile (and depends on t_{Cu}). Since the lattice mismatch between Co and Ni is about +0.6% and between Co and Cu about -2.0% this strongly suggests that the strain in the Co layers is related to the lattice mismatch. If we compare the magnitude of the strain in Co/Cu for $t_{Cu} = 42$ Å with the magnitude of the strain in Co/Ni ($t_{Ni} = 42$ Å) we even find a perfect agreement between the ratio of the strains and the ratio of the mismatches.

For the interface atoms the same analysis can be performed to probe the strain at the interface. This provides us with the unique opportunity to probe the *variation of strain in the whole Co layer*. Figure 5b reveals that for Co/Cu (the results for Co/Ni are not shown but are analogous), within experimental accuracy, the relative shift $\Delta B_{hf}/B_{hf}$ of the hyperfine field of the "interface" atoms is equal to the relative shift of the "bulk" atoms. This strongly indicates that the atomic distances within the Co layers are equal on a

EPITAXIAL Co-Cu SUPERLATTICES

ELIZABETH SCHULER*, SEZAI ELAGOZ*, WILLIAM VAVRA*, FRANK LAMELAS**, HUI DAVID HE***, AND ROY CLARKE*
* University of Michigan, Dept. of Physics, Ann Arbor MI 48109
** AT&T Bell Laboratories, 600 Mountain Ave., Murray Hill NJ 07974
***University of Minnesota, Dept. of Electrical Engineering, Minneapolis MN 55455

ABSTRACT

We describe measurements on the magnetic properties of Co-Cu superlattices in which the Co layer thickness was fixed at 20 Å and the Cu thickness was varied from 4 Å to 24 Å. The samples were grown on Ge-buffered (110) GaAs by molecular beam epitaxy. X-ray scattering and in-situ RHEED indicate that the multilayers are oriented in the (111) direction with the Co layers stacked in an fcc arrangement. Our interest in this series of samples lies in their unusual hysteresis curves which show distinct transitions. We have found that the appearance of these transitions is directly related to the Cu thickness, indicating the presence of complex spin configurations as a consequence of competing interactions. The results are not consistent with a simple RKKY antiferromagnetic coupling.

INTRODUCTION

Co-Cu multilayers have received attention recently due to their unusual magnetic properties.[1] The motivation behind the work described here stems from our previous studies in which the Co thickness was varied while keeping the Cu layer fixed at 20 Å.[2] For this superlattice configuration, the samples exhibited a cross-over from the magnetic easy axis lying in the film plane to an easy axis perpendicular to the film plane when the Co layer thickness is $\leqslant$ 10 Å (see Figure 1).
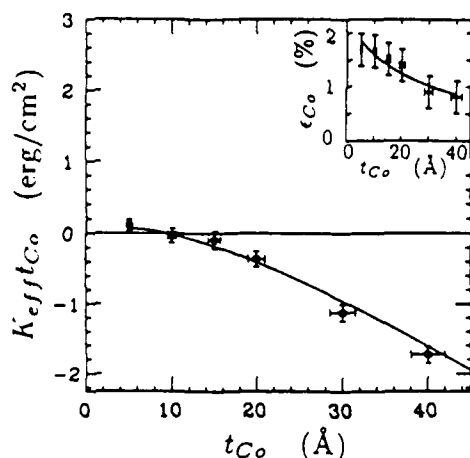

Figure 1:
Magnetic anisotropy of Co-Cu superlattices with 20Å Cu layers, as a function of Co layer thickness. Inset: parallel epitaxial strain of cobalt layers. From Ref.[2]. T = 300 K

The experimental values for the effective anisotropy, K_{eff}, agree with the theoretical values (solid curve) which were calculated[2] from an energy equation containing three contributions; shape, magnetocrystalline, and magnetostriction[3] anisotropy. The values for the magnetostriction anisotropy were based on x-ray measurements of the epitaxial strain.

Thus the samples with fixed non-magnetic layer thickness and variable Co thickness have effective anisotropy values which are relatively well understood. In this paper we are interested in investigating the magnetic properties of samples composed of fixed Co thickness and variable Cu thickness, in the context of interlayer magnetic coupling[4].

EXPERIMENTAL DETAILS

The superlattices were grown under UHV conditions on GaAs(110) substrates held at 50°C in a Vacuum Generators V-80M MBE system. The substrates were annealed at 600°C for 15 minutes prior to the deposition of a 500 Å buffer layer of epitaxial Ge(110). Two additional buffer layers of Co(110) and Cu(111) were required to assure the proper orientation of the multilayers. The multilayers were grown with alternating layers of 20 Å Co(111) and x Å of Cu(111), where x varied from 4 Å to 24 Å for each sample. The Co layers grow with fcc stacking.

The Co was deposited from an electron beam hearth at a rate of 0.3 Å/sec and Cu was deposited from an effusion cell at 0.5 Å/sec. The total superlattice thickness was ~3000 Å for all samples. Epitaxial quality and crystallographic orientation were characterized by *in-situ* reflection high energy electron diffraction (RHEED). Magnetization measurements were performed using a Quantum Design SQUID magnetometer.

RESULTS AND DISCUSSION

Our current research is based on five samples in which the Co layer thickness was fixed at 20 Å and the Cu layer thicknesses were 4, 12, 16, 20 and 24 Å. Representative data from the sample composed of 20 Å Co/ 16 Å Cu superlattice layers are shown in Figure 2.
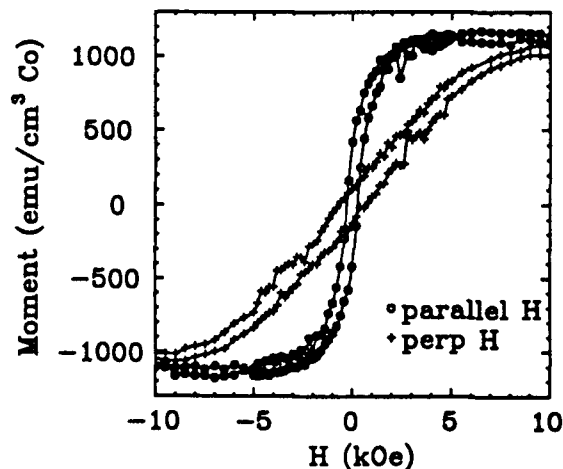

Figure 2:
Parallel and perpendicular hysteresis loops for 20 Å Co - 16 Å Cu superlattices.
T= 5 K

The hysteresis curves were recorded at a temperature of 5K for magnetic fields parallel and perpendicular to the film plane. Since the effective anisotropy is defined as the difference in area between the parallel and perpendicular field hysteresis curves, it is evident that the magnetic easy axis lies in the plane of the film. This is expected since the Co thickness (20 Å) is larger than the cross-over thickness of 10 Å.[2]

We illustrate how the magnetic properties of the samples change as a function of the non-magnetic layer thickness by examining a plot of the effective anisotropy versus Cu layer thickness (Figure 3).
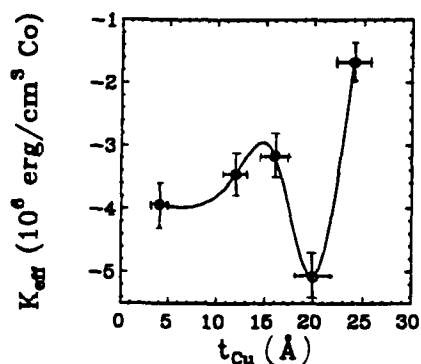

Figure 3:
Magnetic anisotropy of Co-Cu superlattices with 20 Å Co layers as a function of Cu layer thickness. T = 5 K.
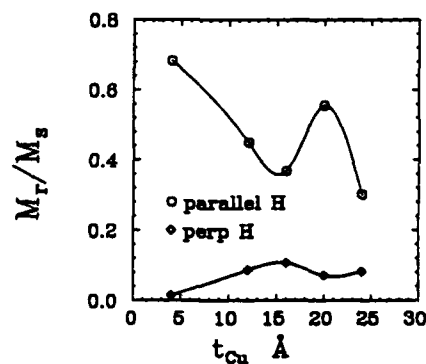
Figure 4:
Remnant magnetization as a function of Cu layer thickness for applied magnetic field parallel and perpendicular to film plane. T= 5 K.

We first notice that K_{eff} is negative and thus the magnetic easy axis of all five samples lies in the plane of the film, as expected. However, the value of K_{eff} depends on the Cu thickness in a complicated manner. There appear to be marked variations on a length scale (> 10 Å) similar to that reported recently in sputtered Co-Cu superlattices[4]. For example the maximum value of the anisotropy here occurs at t_{Cu} ~ 20 Å and this coincides with a peak in the transverse magnetoresistance.

We also observe a non-monotonic Cu-thickness dependence in the remnant magnetization for an applied magnetic field perpendicular and parallel to the film plane. (Figure 4) It is interesting that the parallel remnant magnetization, M_r, is quite large in our samples, which is not consistent with the antiferromagnetic exchange

coupling mechanism suggested recently for these materials[4]. In fact we observe a *peak* in M_r at a Cu thickness where there is supposed to be antiferromagnetic coupling. Note that the interfaces in our samples are very sharp[5] so that one cannot ascribe the behavior of M_r to interface roughening [4] in this case.

An important clue to the nature of the interlayer coupling mechanism can be seen in the low-field hysteresis loops. A recent calculation[6] for ferromagnetic multilayers with antiferromagnetic coupling showed the presence of sub-loops in the parallel field hysteresis. We did not observe such features in the parallel orientation; however, for *perpendicular* fields (see Fig 5) there are distinct transistions in the hysteresis curves prior to saturation. This suggests that the interlayer coupling may be considerably more complex than the RKKY mechanism suggested previously[4]. The multiple low-field transitions suggest a complex series of spin configurations akin to those appearing in ANNNI models[7]; these are normally the result of *competing interactions* in the system.
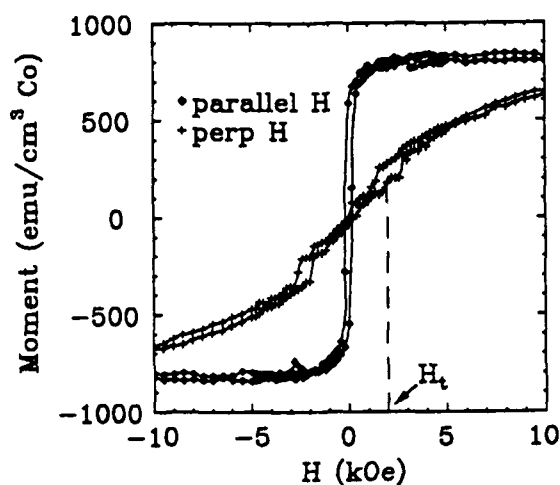
Figure 5:
Parallel and perpendicular hysteresis loops for 20 Å Co - 4 Å Cu superlattices at T= 5K.

The sub-loops or transitions were observed in the perpendicular field hysteresis curves for three of the five samples. Table I summarizes the relationship between the appearance of the sub-loops, the Cu thickness, and the position of the sub-loops with respect to the applied magnetic field. One can see that the value of the applied field where the transitions occur is strongly dependent on the Cu thickness.

SAMPLE #	Cu THICKNESS(Å)	$H_t(Oe)$
248	4	2000
247	12	4000
250	16	-
246	20	4000
251	24	-

Table I: Approximate transition field (H_t) as a function of Cu layer thickness.

CONCLUSIONS

We have grown epitaxial Co-Cu (111) superlattices exhibiting unusual magnetic properties. Both the effective anisotropy energy and the remnant magnetization show non-monotonic behavior as a function of Cu thickness. This strong dependence on the thickness of the non-magnetic spacing layer indicates the presence of an interlayer coupling mechanism, perhaps resulting from competing interactions. We also find evidence for a series of complex spin configurations indicated by abrupt transitions in the perpendicular field hysteresis curves. The appearance of these transitions is dependent on the Cu layer thickness.

ACKNOWLEDGMENTS

REFERENCES

1.   A. Cebollada, J.L. Martinez, J.M. Gallego, J.J. de Miguel, R. Miranda, S. Ferrer, F. Batallan, G. Fillion and J.P. Rebouillat, Phys. Rev. B 39, 9726 (1989); D. Pescia, D. Kerkmann, F. Schumann, and W. Gudat, Z. Phys. B 78, 475 (1990).

2.   C.H. Lee, Hui He, F.J. Lamelas, W. Vavra, C. Uher, and R. Clarke, Phys. Rev. B 42, 1066 (1990).

3.   C. Chappert and P. Bruno, J. Appl Phys. 64, 5736 (1988).

4.   S.S.P. Parkin, R. Bhadra, and K.P. Roche, Phys. Rev. Lett 66, 2152 (1991).

5.   K. Le Dang, P. Veillet, H. He, F.J. Lamelas, C.H. Lee and R. Clarke, Phys Rev. B 41, 12902 (1990).

6.   B. Dieny, J.P. Gavigan, J.P. Rebouillat, Materials Research Society Proceedings, 151, 35 (MRS, Pittsburgh, 1989).

7.   W. Selke and P.M. Duxbury, Z. Phys. B 57, 49 (1984).

Giant Magnetoresistance In
Fe/Cr Superlattices

MAGNETIC AND TRANSPORT PROPERTIES OF ION BEAM SPUTTERED FE/CR MULTILAYERS

K.INOMATA.S.N.OKUNO S.HASHIMOTO and K.Yusu
 Toshiba Corporation,Research and Development Center,1,Komukai Toshiba
-cho,Saiwai-ku,Kawasaki 210,Japan

ABSTRACT

    Fe/Cr/Fe sandwiches and $(Fe/Cr)_n$ multilayers were prepared by ion
beam sputtering on MgO(100) substrates by changing acceleration volta-
ges.Lower acceleration voltage was crucial to obtain multilayers with
high quality interfaces.Single crystalline Fe/Cr/Fe sandwiches were
prepared with ambient substrate temperature having a relation of Fe(1
00)<110>//MgO(100)<100>.On the substrates with elevated temperature
above 150°C,however,polycrystalline films were grown.Magnetic coupling
between Fe-layers through intervening Cr layers was investigated by
FMR using 9.4GHz,in which three resonance lines were observed for sin-
gle crystalline Fe/Cr/Fe sandwiches and $(Fe/Cr)_n$ multilayers with ant-
iferromagnetic Fe-layer interactions,while a single resonance line
was observed for the polycrystalline films.Magnetoresistance measured
on $(20AFe/12ACr)_{15}$ single crystalline multilayers showed anisotropy in
saturation fields Hs which are about 2 times lower in the applied fie-
ld parallel to Fe<100> than to Fe<110>,which is consistent with the
magnetization process for the films.It was found that the shapes of
the magnetoresistance curve vs magnetic field differ for H//Fe<100>
and H//Fe<110>.

INTRODUCTION

    Recently,multilayer films consisting of ferromagnetic layers sep-
arated by non-magnetic layers have been shown to have a variety of in-
teresting magnetic and electron transport properties.Several multilay-
er structures with layer thicknesses below 100A have been observed to
exhibit unusual coupling,in which the successive ferromagnetic layers
are antiparallel in low fields and can be made parallel by application
of an external field;large changes in the resistivity are observed in
some cases,as the magnetizations in successive layers are made parall-
el.
    Such behavier has been observed in Fe/Cr multilayers which is or-
iginated from antiferromagnetic Fe-layer interactions through interve-
ning Cr layers.The giant magnetoresistance(GMR)in the Fe/Cr multilaye-
rs,however,has been observed only in the multilayer films prepared by
ultra high vacuum(UHV)systems,such as MBE[1]-[3] or UHV sputtering[4].The me-
chanisms for the unusual MR and coupling properties are not understood.
    This paper reports results of investigations on Fe/Cr multilayers
prepared by ion beam sputtering with a base pressure of 2×10^{-7} Torr to
test the processing influence on magnetic and MR properties.The MR,ma-
gnetization and FMR were measured as a function of substrate temperat-
ures.Fe/Cr/Fe sandwich films were also investigated.

EXPERIMENT

Fe/Cr/Fe sandwiches and (Fe/Cr)$_n$ multilayer thin films with different Cr thicknesses were prepared by ion beam sputtering from Fe and Cr targets on MgO(100) substrates in a cryo-pumped vacuum system with a base pressure of $2x10^{-7}$ Torr. Sputtering was carried out using $2x10^{-4}$ Torr Ar ions.Acceleration voltage for the sputtering was changed from 300V to 1kV.Substrate temperature was varied between room temperature (RT)and 500°C.The film structure was determined by X-ray diffraction and transmission electron microscopy.Thicknesses were determined from rates measured using thick samples made in separate depositions.Magnetic properties were measured by VSM and FMR with 9.4GHz frequency,in which magnetic fields were applied in the film plane.MR was measured using a conventional four point probe method as a function of applied magnetic field at room temperature and at 77K.Resistivity was observed to vary little with the angle between the applied field and the current.

RESULTS AND DISCUSSION

Lower accelaration voltage was crucial to obtain multilayers with high quality interfaces.Figure.1 shows magnetization curves at RT for low and high magnetic field for (13ACr/40AFe)$_5$ on MgO(100) substrate prepared using 300,500 and 1k volts as accelaration voltages.The magnetic field was applied paralell to the MgO(100)<100>.Each magnetization curve exhibits a hysteresis with multi-steps,which will be associated with the antiferromagnetic(AF) interlayer couplings between the Fe layers across the Cr layers.The numbers of steps are the fewest and saturation field is the lowest for films prepared by 300V,which suggests that higher interface quality may be prepared by lowering the accelaration voltage.This is consistent with the small angle X-ray diffraction results with more diffraction lines as lower acceleration voltage. Hereafter,all the films were prepared by 300V.
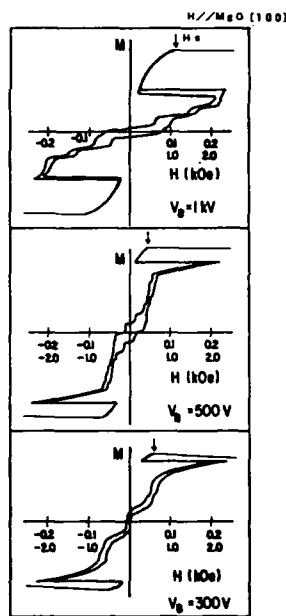
Fig.1.Magnetization curves at RT of (13ACr/40AFe)$_5$ multilayers on MgO (100) substrates for various acceleration voltages.

Fe/Cr/Fe Sandwiches

Figure.2(a) shows hysteresis curves for 40AFe/nACr/40AFe sandwiches with n=5,13 and 30 with an applied field parallel to MgO(100)<100>.The hysteresis curves for n=5 and 30 show saturation for small fields and are typical for ferromagnetism. The films with n=13,however,exhibit stepwise hysteresis,which is also shown for larger fields in Fig.2(b).The magnetization is linear to H in the small field, and shows a sudden jump at H=60 Oe,followed by a slow approach to saturation above Hs=625 Oe. This is a typical magnetization process for the applied field parallel to Fe(100)<110>[5], which means that the sandwiches are single crystals with a relation of

MgO(100)<100>//Fe(100)<110>.

FMR data measured on Fe/Cr/Fe sandwich films with different Cr thicknesses on RT substrates revealed one,three and two resonance lines for 5A,10A and 30ACr thicknesses,respectively as shown in Fig.3,in which the magnetic field was applied for Fe(100)<110>.The film with 10 A Cr thickness exhibits a pattern typical for antiferromagnetic Fe-layer alignment .The single FMR line for the 5A Cr thick films suggests the strong interactions between Cr intervening Fe-layers.The two resonance lines for the 30A Cr sandwiches imply that the Fe-layer interactions are weak and that the Fe magnetic anisotropies are little different in the two Fe layers.Rresonance field H_{res},resonance line width ΔH and crystalline magnetic anisotropy K_1 were estimated as shown in Table 1 using the following relation:$(\omega/\gamma)^2 = (H_{res}+4\pi Ms+K_1/Ms)(H_{res}-K_1/Ms)$.Ms was used as the values by VSM measurements.K_1 is comparable to the bulk Fe value ($4.72 \times 10^5 erg/cm^3$) for 5A Cr films and decreases with increasing Cr thickness.Figure.4 shows FMR patterns for 30AFe/10ACr/30 AFe prepared with different substrate temperatures.Three resonance lines,observed for the RT substrate film,are changed to one resonance line for both the films with 150℃ and 300℃ substrate temperatures.This means that Fe/Cr single crystalline multilayer films will not grow at elevated temperatures above 150℃ on MgO(100)susbstrate.

(Fe/Cr) multilayers

Figure.5 shows an FMR pattern for (13ACr/40AFe)₁₅ on the RT MgO(100) substrate.This pattern also shows AF single crystalline like behavior,as suggested from the comparison in Fig.3(b),although it has fine structures around magnetic field of about 500 Oe.The single crystalline like nature in this film was also confirmed by TED,observed with spot type patterns.
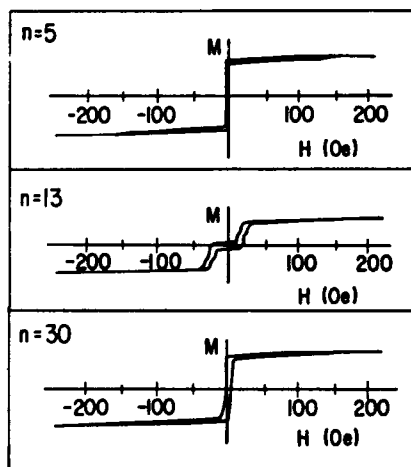

Fig.2(b).A hysteresis curve for 40AFe/13ACr/40AFe.

Fig.2(a).Hysteresis curves for 40AFe/nACr/40AFe sandwiches with n=5,13 and 30 with applied field parallel to MgO(100)<100>.

246
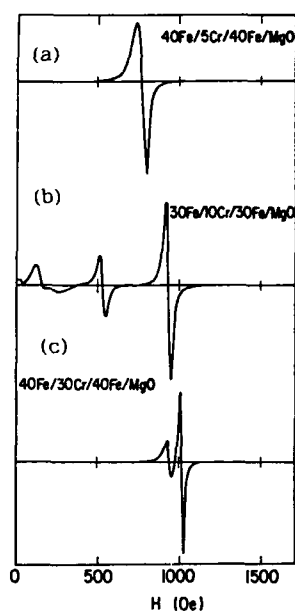
Fig.3.FMR for sandwiches on MgO
(100)substrates.Magnetic field
is applied parallel to Fe(100)<110>.
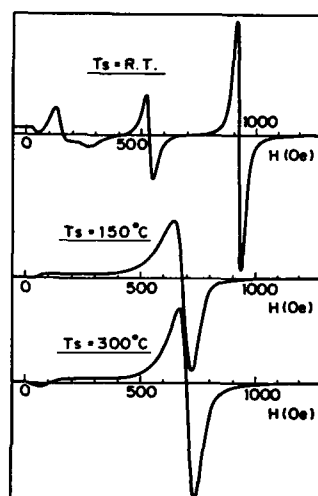
Fig.4.FMR for 30AFe/10ACr/30AFe
sandwiches for three substrate
temperatures.

Table 1.Resonance fields(H_{res}),resonance line width(ΔH) and crystalline
magnetic anisotropy(K_1) obtained by FMR.Saturation magnetization(Ms)
was measured by VSM.

	Hres (Oe)	ΔH (Oe)	Ms (emu/cc)	K_1 (erg/cc)
40Fe/5Cr/40Fe	760	50	1680	4.1×10^5
30Fe/10Cr/30Fe	160	83	1670	3.4×10^5
	530	33		
	925	33		
40Fe/30Cr/40Fe	955	35	1570	3.1×10^5
	1030	20		

The MR value depends on Fe layer thickness as well as Cu thickne-ss.It was quite small with 0.5 % for the films in Fig.5.Figure 6 shows MR curves for $(20AFe/12ACr)_{15}$ multilayers as a function of magnetic fi-elds at RT with different applied field direction of H//Fe<110> and H//Fe<100>.The current was applied parallel or perpendicular to the field in the film plane.The MR values were little different between both current directions.It is noticed that saturation field Hs is ani-sotropic for the field direction applied,and is about 2 times lower for H//Fe<100> than for H//Fe<110>.This can be understood by consider-ing the easy magnetization axis of Fe<100>.Also attention should be paid to the shapes of the MR curvature in Fig.7 differing between H//Fe<100> and H//Fe<110>.The latter shows a conventional curve similar to that for Fe/ Cr superlattices grown on GaAs substrates[i],measured with a field parallel to Fe<110>.The former hanging bell type, however, has not been observed for Fe/Cr multilayers.

The magnetization curves are shown in Fig.7 for the multilayers shown in Fig.6.The magnetization is almost linear to the field,up to saturation for H//Fe<100>,which is understood by easy axis magnetizat-ion process of single crystalline Fe multilayers with large antiferro-magnetic layer coupling[b].Such magnetization curve has also been found for Fe/Cr/Fr sandwiches on GaAs(110) substrate via the magneto-optic Kerr effect with magnetic field parallel to Fe<100>[7].The magnetization curve for H//Fe<110> having a small loop around the origin and satura-ting with a curvature can be compared with the magnetization curve for sandwiches in Fig.2(b).

The maximum MR value was 2.4% at RT (6.2% at 77K) in the present investigation,which is quite small compared with the that for multila-yers grown on MgO substrates by MBE exhibiting 12.5% at RT[9].The reason for this is not clear,but it might be due to the differece between base pressure and interface structure.
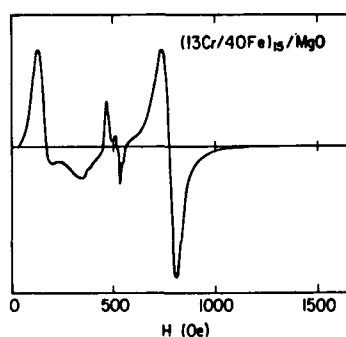
Fig.5.FMR for $(13ACr/40AFe)_{15}$ multilayers with ambient subst-rate temperature.
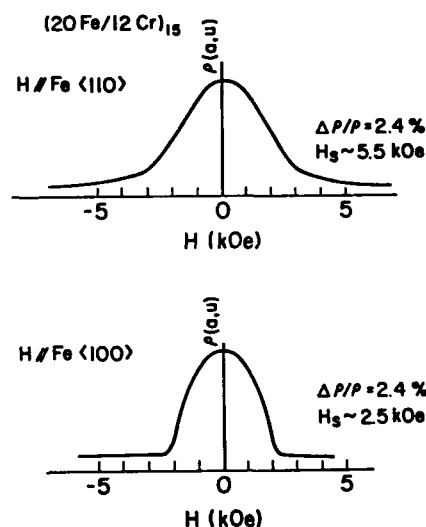
Fig.6.Magnetoresistance curves for $(20AFe/12ACr)_{15}$.
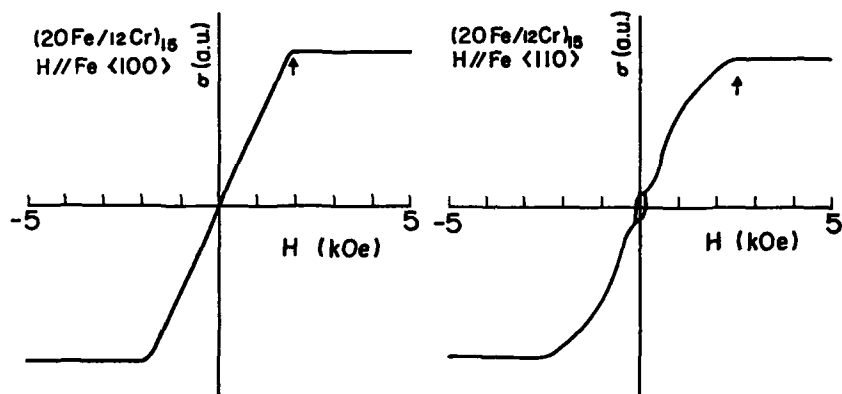
Fig.7.Magnetization curves for
(20AFe/12ACr)₁₅ with applied fields
parallel to Fe<110> and Fe<100>.

1)M.N.Baibich,J.M.Broto,A.Fert,F.Nguyen van Dau,F.Petroff,P.Etienne,G.
  Creuzet,A.Friedderrich and J.Chazelas:Phys.Rev.Lett.61,2472(1988).
2)G.Binasch,P.Grunberg,F.Sauerenbach and W.Zinn:Phys.Rev.B39,4828(1989)
3)S.Araki and T.Sinjo:J.Mag.Soc.Japan 14,351(1990).
4)S.S.P.Parkin,N.More and K.P.Roche:Phys.Rev.Lett.64,2304(1990).
5)J.J.Krebs,P.Lubitz,A.Chaikien and G.A.Prinz:Phys.Rev.Lett.63,1645(19
  89).
6)W.Schmidt:J.Mag.Mag.Mater.84,119(1990)
7)F.Saurenbach,U.Walz,L.Hinchey,P.Grunberg and W.Zinn:J.Appl.Phys.63,
  3473(1988)

MAGNETISM AND MAGNETORESISTANCE OF Fe/Cr COMPOSITE MULTILAYERS.

SATORU ARAKI, YOSHIKAZU NARUMIYA and TERUYA SHINJO*.
R&D Center, TDK Corporation, 15-7 Higashi Owada 2, Ichikawa, Chiba 272, Japan.
*Institute for Chemical Research, Kyoto University, Uji, Kyoto 611, Japan.

ABSTRACT

Fe/Cr multilayers with composite layered structures were prepared onto MgO (100) and glass substrates by alternate deposition in ultrahigh vacuum. A multilayer with two thicknesses of Fe layers shows a larger MR change, 6.2 % at RT and 13.5 % at 77 K, than a simple type ones with the applied field upto 3 kOe. This is due to the ferrimagnetically coupled Fe layers. For the multilayers of Cr-composite type, the MR ratio could be enhanced, 12.9 % at RT with the field of 2 T.

INTRODUCTION

In recent years, many studies have been concentrated on large magnetoresistance (MR) of multilayers having antiferromagnetic coupling between adjacent magnetic layers. This phenomenon is of considerable interest also from technical viewpoints. The giant magnetoresistance can be arisen by several mechanisms [1]-[7]. Grünberg et al. have reported for sandwiched Fe/Cr/Fe [1] and found the antiferromagnetic interlayer coupling between Fe layers across a Cr intervending layer [2]. Baibich et al. have reported that the decrease of resistance in an Fe/Cr multilayer by applying 20 kOe was 46 % at 4.2 K [3]. The reason is attributed to the interlayer antiferromagnetic coupling between Fe layers through Cr. In weak fields, magnetizations of adjacent Fe layers are antiparallel and the resistivity is high because of the spin dependent scattering. If an applied field is sufficiently high for saturation, all magnetizations are aligned parallel to the applied field, so that the spin dependent scattering does not occur. This antiferromagnetic alignment of magnetization in Fe/Cr multilayers was directly confirmed by using neutron diffraction technique by Hosoito et al.[8] and by Barthelemy et al.[9]. The results of ferromagnetic resonance also showed the exsistence of the antiferromagnetic coupling modes in Fe layers [10][11]. Very recently, many theoretical papers have been reported to discuss the mechanism of spin dependent scattering [12]-[14].

In this paper we report about Fe/Cr multilayers with composite layered structures in order to study the giant magnetoresistance phenomena in

Fig.1: Schematic drawing of composite layered structures of F/Cr multilayers. Cr layer thickness is fixed 15 Å for Fe-composite types, and Fe is fixed 30 Å for Cr-composite ones.
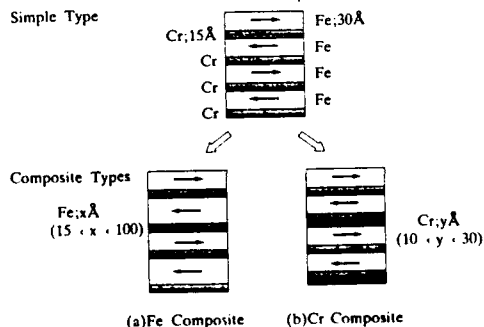
relation with the magnetic structures. The schematic drawing of these composite multilayers is shown in Fig.1. We present the following two types of composite structures: (a)Fe-composite type, (Cr-thickness is fixed), and (b)Cr-composite type, (Fe-thickness is fixed). Namely either Fe or Cr layers consist of two thicknesses to modify the magnetic structures.

EXPERIMENTAL

Fe/Cr multilayers were prepared onto glass and MgO(100) single crystal substrates, using electron-beam evaporation in Molecular Beam Epitaxy system. Achieved initial pressure was typically 6×10^{-11} Torr. The background pressure during deposition was maintained in the early range of 10^{-9} Torr. The typical deposition rate was controlled at around 0.5 A/sec for both materials. The substrate temperature (Ts) was changed in the range from room temperature (RT) to 450 °C. Each layer thickness was monitored during deposition with a quartz oscillator. The deposition was always started from Fe, and finished with Cr layer. The surface was not covered by any protecting layer. The number of Fe/Cr bilayers in each sample was changed from 15 to 50.

The artificial periodicities structures and crystal structures were checked by X-ray diffraction (XRD). Grain sizes of the multilayers were estimated from scanning electron microscope (SEM) observation of the film surfaces. Magnetic hysteresis curves were measured by vibrating sample magnetometer (VSM) with the fields applied upto 15 kOe at RT. The magnetoresistance (MR) properties were measured with magnetic fields upto 20 kOe at RT, and 7kOe at 77K, respectively, using conventional dc 4-terminal method. The samples for MR measurements were stripes, 0.3×10 mm^2. The measuring dc current was between 14 to 80 µA and the direction in in-plane and perpendicularly to the external field.
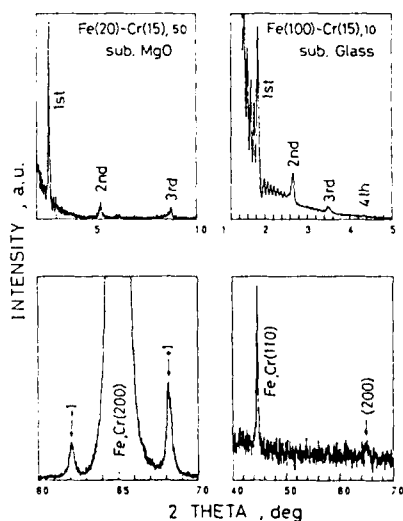

Fig.2: X-ray diffraction patterns of the simple type multilayers. Arrows indicate satellite peaks.
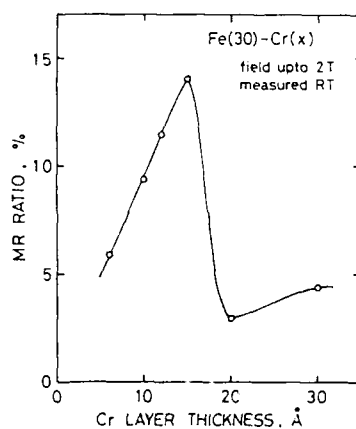
Fig.3: Magnetoresistance ratio as a function of Cr layer thickness. The data was measured with the field upto 2 T and at RT.

RESULTS AND DISCUSSION

Simple Type Multilayers

For typical examples of XRD pattern, results on two kinds of the multilayers are shown in Fig.2. For the multilayer with 20 A of Fe and 15 A of Cr, up to 5th Bragg reflections were observed. It is reasonable that the 2nd reflection is weak, because the thickness ratio of Fe and Cr layers is close to 1:1. For the multilayer with 100 A of Fe and 15 A of Cr, ripple peaks are observed around the 1st Bragg reflection. These ripple peaks are derived from the total reflection of the film's thickness. It is thus believed that the superstructure is realized satisfactorily as designed. As for the crystal structure of the samples deposited onto MgO(100) single crystal substrates XRD results indicate that crystallographic (100) plane is orientated in the plane. The full width at half maximum (FWHM) of the Fe and Cr (200) rocking peaks decreased below 1.0 deg when Ts increased above 120 °C, (that of the substrate was 0.2 deg) [15]. It is certain that Fe and Cr are epitaxially grown onto the MgO substrates. The samples formed on glass substrates showed typical polycrystalline patternss with sharp interfaces. From a SEM photograph of the film surface, the grain size of the sample on glass substrate was estimated to be about 500 A, whereas the sample on MgO substrate has almost continuous surfaces. These results agree quantitatively with the XRD results.

The remanent magnetization (Mr), of the sample on glass substrates took the minimum for Ts of around 180 °C, whereas Mr of the sample on MgO substrate was about 0.1 of the saturation value, Ms, in all cases. So the growth temperature was chosen as 200 °C. A further discussion on crystallographic aspects will appear elsewhere [16].

The change of the MR ratio, $\Delta \rho / \rho$ (H=0), is conventionally expressed as follows:

$$\Delta \rho / \rho \ (H=0) = [\rho \ (H=0) - \rho \ (H_{max})] / \rho \ (H=0), \qquad (1)$$

where H_{max} is 20kOe at RT and 7kOe at 77K. Figure 3 shows the MR ratio as a function of Cr layer thicknesses. The MR ratio takes the maximum for the sample with Cr layer thickness, t(Cr), of 15 A, and decreases rapidly at t(Cr) of 20 A. Quantitatively these data are consistent with other works [17][18].
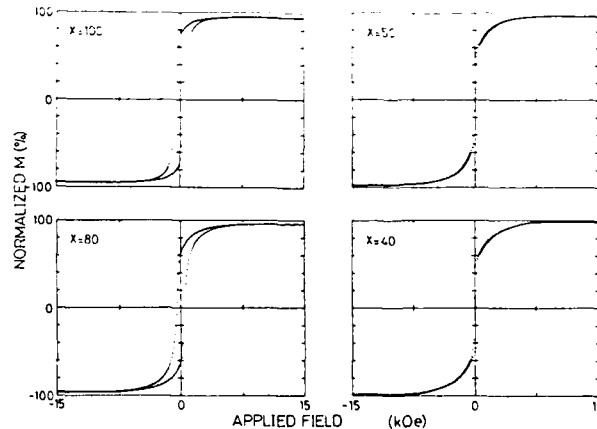

Fig.4: Magnetization curves for Fe-composite type multilayers with various Fe layer thicknesses, x, of [Fe(30)-Cr(15)-Fe(x)-Cr(15)].

252

Multilayers with two Fe layer thicknesses

In the Fe-composite series, the Cr layer thickness was fixed to be 15 A. For Fe layer thicknesses: one is fixed to be 30 A, the other, x, is chosen from 15 A to 100 A. This composition is expressed as [Fe(30)-Cr(15)-Fe(x)-Cr(15)]. For the composite type samples it is hard to judge the superstructures from small angle XRD patterns because the wavelength of the compositional modulation is not unique. However, as discussed before, rather sharp interfaces were confirmed for the two samples of simple type, i.e. (Fe,Cr)=(30,15) and (x,15), so that the structure of the composite type samples was suggested to be well performed.

Magnetization curves of composite samples are shown in Fig.4. The remanent magnetization, Mr, of Fe-composite samples becomes larger with increasing x. A simple model is assumed here: at weak fields the moment of the thicker Fe was aligned parallel to the field, and that of thinner Fe was aligned antiparallel to the field. Accordingly, the magnetization at zero field is expressed as the difference between the magnetization of thicker Fe and that of thinner layers. The calculated Mr are shown in Fig.5 as the solid line. Here the Mr of simple samples have always limited values of about 0.1. The Mr of simple type samples is caused from the imperfectness of the antiferromagnetic compensation. The calculated data fit the measured one if we assume that the imperfectness of the antiferromagnetic compensation in composite samples is comparable to that of the simple type.

The profiles of magnetoresistance at RT with the fields applied upto 7kOe are shown in Fig.6. It is clear that the composite multilayer with x=20 A has larger MR change at weak fields than that of the simple type multilayer, (i.e. x=30 A). The MR ratio of this composite sample is 6.2% at RT and 13.5 % at 77K with the field of 3kOe. For our knowledge this is a relatively large value among the valus for Fe/Cr multilayers with the field of 3kOe.

The main reason is the perfectness of the antiparallel orientation of magnetizations. For the composite type, magnetizations of thicker Fe layers are oriented to the field uniformly, and those of thinner Fe layers are oriented antiparallel to the magnetization of thicker Fe, (i.e. ferrimagnetic orientation). Thus a perfectly oriented ferrimagnetic state is rather easily established. On the other hand, in the case of simple type multilayers with antiferromagnetic coupling, the nucleation of antiferromagnetic domains occur randomly and accordingly many antiphase boundaries are formed, which decrease the effect of spin dependent
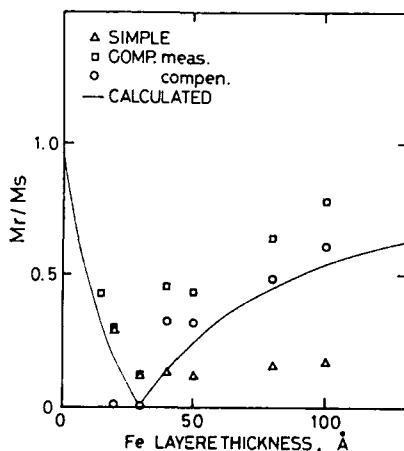

Fig.5: Remanent magnetization for the simple and composite multilayers. Rectangulars were measured data for composite types, and circles were the difference between rectangulars and triangles. Solid line was calculated from the model that the Fe moment was aligned antiparallel to the applied field.

scattering. Compared with simple and Fe-composite types, ferrimagnetic orientation of Fe-composite structure is more suitable to obtain a perfect antiparallel alignment.

Magnetization process of ferrimagnetic Fe-composite type would differ from that of antiferromagnetic simple type. In the former case, the magnetization of thicker Fe is almost pinned to the field direction and that of thin Fe rotates rather easily. The experimental results support this hypothesis, that is, the saturation field for Fe-compsite sample of x=20 A was smaller than the simple one. And it is likely that ferrimagnetic structures of Fe-composite multilayers exhibit large MR ratios at weak fields by choosing moderate Fe layer thicknesses. For a further discussion, a theoretical calculation of magnetization process is required.

In addition, there is some contribition of the decrease of non-magnetic resistance. The zero field specific resistances for composite samples of x<30 A are about 20 % smaller than that of Fe(30)-Cr(15) simple sample. As the results MR ratio of the composite types of x<30 A is larger than that of simple type. These differences of non-magnetic resistances would be derived from the difference of microscopic structures.

Multilayers with two Cr layer thicknesses

In this series Fe layer thickness was fixed to be 30 A, one Cr layer thickness was fixed to be 10 A, and the other was varied from 15 A to 30 A, which is namely expressed as [Fe(30)-Cr(10)-Fe(30)-Cr(y)].

The MR profiles for two simple types and a composite type of multilayers are shown in Fig.7, which is an example that the MR effect is enhanced by fabricating the Cr-composite layers. For the simple types, because the sample with d(Cr)=10 A has a stronger antiferromagnetic coupling energy than the sample with d(Cr)=20 A, the former has a larger MR ratio than the latter, and MR ratios are 9.3 % of d(Cr)=10 A and 2.9 % of d(Cr)=20 A, respectively. The MR ratio of the composite sample of y=20 A, 12.9 %, is much larger than the two simple ones. However, the other Cr composite types, y=15 A and y=30 A, did not enhance the MR ratio.

The saturation field is reduced with the increase of y from 15 A. If the
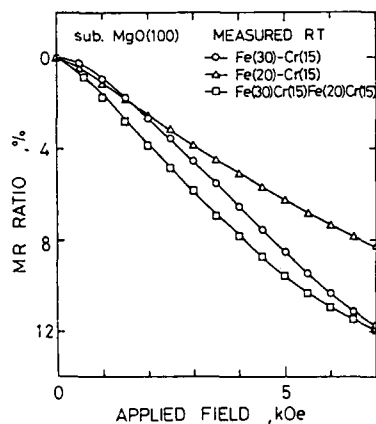

Fig.6: MR profiles for simple and Fe composite types of multilayers. Composite type indicates larger MR change below 7kOe than the simple ones.
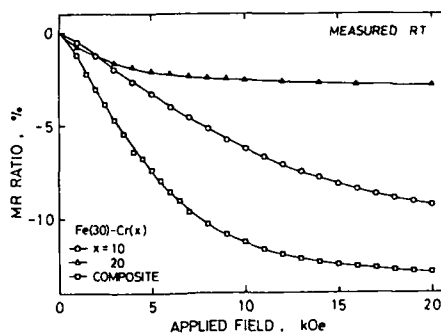
Fig.7: MR profiles for simple and Cr composite types of multilayers. Cr composite type shows larger change than the simple ones.

interlayer interaction is strongly antiferromagnetic, the saturation field becomes very large. On the other hand, if it is weak, magnetizatons at zero field are not oriented perfectly antiparallel. In order to choose an appropriate Cr layer thickness, there is a dilemma concerning the strength of interaction. A practical solution might be a composite type multilayers. By choosing two Cr thicknesses; one is strong, while the other is weakly antiferromagnetic, it may be possible that antiparallel orientation is well established at weak fields but can be reoriented rather easily by moderate fields.

SUMMARY

Molecular Beam Epitaxy grown Fe/Cr composite multilayers with two kinds of Fe or Cr layer thicknesses exhibit enhanced MR ratios for the field applied upto 7kOe. This is due to the change of magnetization process: from antiferromagnetic to ferrimagnetic spin flopping. Cr composite multilayers with Cr layer thicknesses of 10 A and 20 A have a larger saturated MR ratio than the simple type multilayer.

ACKNOWLEDGEMENT

REFFERENCES

1. P.Grünberg, R.Schreiber, and Y.Pang, Phys.Rev.Lett. 57,2442 (1986): P.Grünberg, R.Schreiber, Y.Pang, U.Waltz, M.B.Brodsky and H.Sowers, J.Appl.Phys. 61,3750 (1987)
2. G.Binasch, P.Grünberg, F.Saurenbach and W.Zinn, Phys.Rev.B 39,4828 (1989)
3. M.N.Baibich, J.M.Broto, A.Fert, F.Nguyen Van Dau, F.Petroff, P.Etienne, G.Creuzet, A.Friegrich and J.Chazelas, Phys.Rev.Lett. 61,2472 (1988)
4. T.Shinjo and H.Yamamoto, J.Phys.Soc.Jpn, 59,3061 (1990)
5. H.Yamamoto, T.Okuyama, H.Dohnomae and T.Shinjo, permitted for publication in J.Mag.Mag.Mater.(1991)
6. B.Dieny, V.S.Speriosu, S.S.P.Parkin, B.A.Gurney, D.R.Wilholt and D.Mauri, Phys.Rev B, 43,1297 (1991)
7. C.Dupas, P.Beauvillain, C.Chappert, J.P.Renard, F.Trigui, P.Veillet, E.Velu and D.Renard, J.Appl.Phys., 67,5680 (1990)
8. N.Hosoito, S.Araki, K.Mibu and T.Shinjo, J.Phys.Soc.Jpn., 59,1925 (1989)
9. A.Barthelemy, A.Fert, M.N.Baibich, S.Hadjouji, F.Petroff, P.Etienne, R.Cabanel, S.Lequien, F.Nguyen Van Dau, and G.Creuzet, J.Appl.Phys. 67,5908 (1990)
10. J.J.Krebs, P.Lubitz, A.Chaiken and G.A.Prinz, Phys.Rev.Lett. 63,1645 (1989)
11. O.Kohmoto, Alexander Jr and S.Araki, to be presented at MMM-INTERMAG Conf., June, 1991, Pittsberg.
12. P.M.Levy, K.Ounadjela, S.Zhang, Y.Wang, C.B.Sommers and A.Fert, J.Appl.Phys. 67,5914 (1990)
13. H.Hasegawa, Phys.Rev. B 42,2368 (1990)
14. J.Inoue, A.Oguri and S.Maekawa, submitted to J.Phys.Soc.Jpn.
15. S.Araki and T.Shinjo, Jpn.J.Appl.Phys. 29,L621 (1990)
16. S.Araki, Y.Narumiya and T.Shinjo, in preparation.
17. S.S.P.Parkin, N.More and K.P.Roche, Phys.Rev.Lett. 64,2304 (1990)
18. D.H.Mosca, F.Petroff, A.Fert, P.A.Schroeder, W.P.Pratt Jr, and R.Laloee, J.Mag.Mag.Mater., 94,L1 (1991)

MAGNETORESISTANCE OF MAGNETICALLY UNCOUPLED MULTILAYERED STRUCTURES

SHUFENG ZHANG* AND PETER M. LEVY**

*Department of Physics, UCSD, La Jolla, CA 92093

**Department of Physics, New York University, New York, NY 10003

ABSTRACT

The magnetoresistive effect first observed in Fe/Cr and other antiferromagnetically coupled metallic multilayered structure, has also been observed, albeit somewhat attenuated, in structures where the magnetic layers are not coupled. We explain the magnetoresistive effect in these systems that are nominally uncoupled, and we provide a new interpretation for the magnetoresistance of Co/Cu, Fe/Cr and Co/Ru by considering these multilayered structures to consist of, not only ferro and antiferromagnetically aligned layers, but also mixtures of the two which have zero magnetization.

PRESENT UNDERSTANDING

Our present understanding of the "giant" magnetoresistance (MR) for currents in the plane of the layers (CIP) of multilayered structure (MS) was developed in Ref.[1]. The large negative MR comes from the spin-dependent scattering of conduction electrons. We write the scattering potential as

$$V(\sigma)=v+j\hat{\sigma}\cdot\hat{M},$$

and

$$p=j/v=\frac{\sqrt{\alpha}-1}{\sqrt{\alpha}+1}, \tag{1}$$

where

$$\alpha=\rho^-/\rho^+.$$

All the symbols are defined in Ref.1. The origin of the scattering for transition metal MS is the s-d mixing or hybridization term rather than the Coulomb exchange interaction which is dominant in rare-earth strutures.

At T=0K the potential in Eq(1) reduces to

$$V(\sigma)=v\pm j\sigma \tag{2}$$

where the ± refers to magnetizations of the layers pointing either up or down. In Fig.1 we show this spin-dependent scattering potential for the H=0 antiferromagnetic (AF) state, and for the $H>H_s$ (saturation field) ferromagnetically (F) aligned state. In the AF state the scattering is the same in
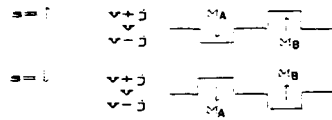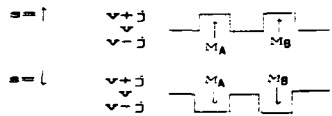
Fig.1 Spin-dependent scattering potentials in a MS. a) for two adjacent magnetic layers AF aligned with an intervening non-magnetic layer. b) same as part a except layers are F aligned.

each spin channel. In the F state the scattering is weaker in the spin-down channel, therefore the mean free path (mfp) $\lambda \uparrow > \lambda \downarrow$. As the spin channels carry the current "in-parallel", i.e., $\sigma = \Sigma_s \sigma(s)$, most of the current will be carried by the path of least resistance. This produces a "short-circuit" effect, so that

$$\rho(H_s) < \rho(H=0);$$ (3)

this is the origin of the negative magnetoresistance in MS. However beware there are exceptions to this negative MR, see Ref.1

The role of the external field is solely to reorient the AF aligned layers for H=0, so they are parallel for $H \geq H_s$. We do not consider the usual effect of the field on the trajectory of the conduction electrons (the Lorentz force); for MS the MR we described above dwarfs this effect. The field needed to align the layers H_s is proportional to the strength of the coupling between layers J, however the MR is not proportional to J.

For flux-sensing applications a figure of merit is the ratio of the magnetoresistance to the saturation field. As H_s goes very roughly as $1/t_{nm}^2$, where t_{nm} is the thickness of a non-magnetic spacer between magnetic layers, one should choose large t_{nm} to lower the field H_s. This is counter-manded by the attenuation of the MR effect due to the effect of the mfp, i.e., conduction electrons contribute a MR effect only as long as they can distinguish between the scattering potentials V_{AF} and V_F, see Fig.1, within the distance λ that they remain in a state with momentum $\vec{k}$. Thus, for a given mfp if the distance between magnetic layers t_{nm} increases the MR decreases, and an optimum t_{nm} keeps MR as large as possible, while minimizing H_s.
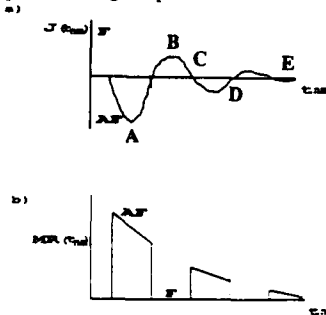

Fig.2 a) A sketch of the interlayer coupling in MS as a function of the thickness of the non-magnetic layers t_{nm}. b) What one expects for the MR of the same MS.
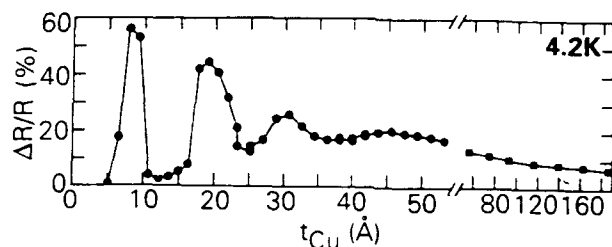
Fig.3. The MR for $Co(10\text{Å})/Cu(t_{Cu})$ taken from S. S. P. Parkin, R. Bhadra and K. P. Roche, Phys. Rev. Lett. **66**, 2152(1991).

FERRO, ANTIFERRO AND NO COUPLING

If $J(t_{nm})$ oscillates between F and AF coupling as shown in Fig.2a, one *expects* this reflects itself in the MR in the manner shown in Fig.2b. We stress that the decay in the MR with t_{nm} is due to the effect of mfp, and *not* that J is decreasing with t_{nm}. Up till now, the conventional interpretation has been that peaks in the MR represent MS with layers that are AF aligned, and troughs represent F aligned layers. However, this is *not what has been seen*. As shown in Fig.3 for Co/Cu the troughs do not go to zero as they should for F aligned MS, *and* as we will show the peaks are not as high as they would be if the layers were AF aligned.

Our explanation for this unexpected behavior is as follows. In regions A and B the coupling is sufficiently strong to overcome random coercive or pinning forces that oppose realignment within the magnetic layers, so that the MS is purely AF aligned in region A and F aligned in B. However for larger t_{nm} the coupling is no longer strong enough compared to the pinning forces to uniquely define the magnetic configuration of the multilayers. This occurs in region E where the layers are completely uncoupled and in regions C and D near the nodes where the coupling goes through zero.

While the state with zero magnetization M=0 is *unique* for AF coupled MS, it is *ill-defined* where there is no coupling. For example for four spins all six configurations in Fig.4 have M=0 and the *same* energy. However the resistivities of these configurations are different,

$$\rho_\alpha = \rho_{AF} > \rho_\beta > \rho_\gamma. \tag{4}$$

In a MS with no coupling the CIP-conductivity is

$$\sigma_{//} = \frac{1}{N} \sum_{config} \sigma_i \tag{5}$$
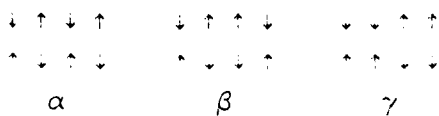
Fig.4. Illustration using four spins of the different configurations which have M=0 and the same energy when the layers are not magnetically coupled. Note that configurations α have three pairs of AF aligned layers, β has two, and γ has one pair of AF aligned layers.

As some configurations have adjacent layers that are ferromagnetically aligned, σ_i is closer to $\sigma_{Ferro} > \sigma_{AF}$, see Eq(3). It follows that when one averages over all configurations for a MS with no coupling (UN) that

$$\sigma_{//}^{UN}(M=0) > \sigma_{//}^{AF}(M=0) \tag{6}$$

or

$$\rho_{//}^{UN}(M=0) < \rho_{//}^{AF}(M=0).$$

The MR ratio is defined as

$$R \equiv \frac{\rho(H_c) - \rho(H_s)}{\rho(H_s)}. \tag{7}$$

As $\rho(H_s)$ is the same for UN and AF coupled MS, we find by using our result Eq(6) that for the CIP-MR

$$R_{//}^{UN} < R_{//}^{AF}. \tag{8}$$

We conclude that for MS with weakly coupled regions C and D or uncoupled regions E, the CIP-MR is *attenuated* with respect to the value one expects on the basis of AF coupled layers.
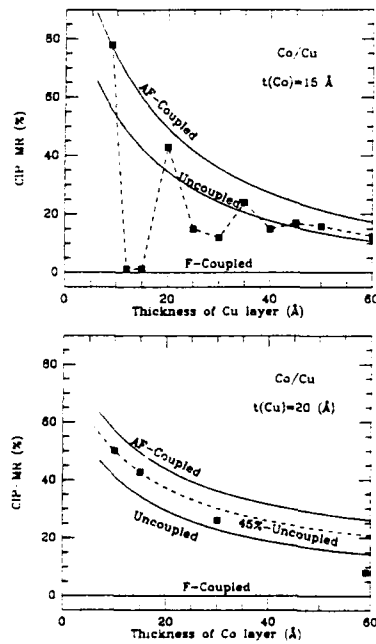
Fig.5 a) The CIP-MR for $Co(15\mathring{A})/Cu(t)$ as estimated by taking the layers F, AF aligned, and mixtures of the two with M=0. The latter is labelled as "uncoupled". The squares represent data at T=4.2K from Ref.2, and A. Fert, private communication. b) The CIP-MR for $Co(t)/Cu(20\mathring{A})$ by assuming F, AF, "uncoupled", and the dashed curve which represents the MS as 55% AF and 45% "uncoupled". The latter is obtained by fitting the data in part a. The data represented by squares come from A. Fert et al., private communication. The parameters we use in the fits are $\lambda_{Co}=40\mathring{A}$, $\lambda_{Cu}=75\mathring{A}$, $w_s=0.3$ $p_{Co}=0.2$ and $p_s=0.52$. That the datum at $t_{Co}=60\mathring{A}$ falls far below our predicted value may be due to a change in the cobalt layer structure at larger thicknesses; S. S. P. Parkin, private communication.

Fig.6 The CIP-MR for $Fe\,(20\text{Å})/Cr\,(t)$ as estimated by taking the layers F, AF, and "uncoupled". The squares represent data from Ref.3 at T=4.5K. The parameters used in the fits are $\lambda_{Fe}=\lambda_{Cr}=40\text{Å}$, $w_s=0.3$, $p_{Fe}=0.23$ and $p_s=0.42$.

We have analyzed the CIP-MR data on Co/Cu, Fe/Cr and Co/Ru. Except for the first AF peak and F points, e.g., at $t_{Cu}=9\text{Å}$ and $t_{Cu}=12\text{Å}$ and 15Å for Co/Cu, the MS are neither *completely* AF nor F aligned, therefore we do *not* attempt to fit our AF-coupled curves in Figs. 5 thru 7 to go through the subsequent peaks in the CIP-MR. Rather we fit the "uncoupled" curve, calculated by using Eq(5) and (7), to fit the CIP-MR in the region where the oscillations die out, e.g., for $t_{Cu}\geq50\text{Å}$ in Co/Cu, see Fig.3. With this interpretation we are able to fit the data as shown in Figs.5 thru 7, with mfp's that are able to nearly reproduce the resistivities $\rho_{//}(H_s)$ that have been observed. For example, with the parameters (mfp's) used to fit Co/Cu, see Fig.5, we find $\rho_{//}(H_s)=20\mu\Omega cm$ for $Co\,(15\text{Å})/Cu(9\text{Å})$, while the experimental value is $17.1\mu\Omega cm$[2]. If we fit the AF coupled curve so it goes through all the peaks in the CIP-MR we would find smaller mfp's $\lambda_{Co}=19\text{Å}$ and $\lambda_{Cu}=30\text{Å}$, and an unreasonably large $p_s=0.65$ which corresponds to $\alpha=22$, see Eq(1). With these parameters the fit to the data in Fig.5b would not be as good, and the resistivities would be much too large, e.g., for $Co\,(15\text{Å})/Cu\,(9\text{Å})$ $\rho_{//}(H_s)=37\mu\Omega cm$.

Another example of our interpretation that MS have mixtures of F and AF regions is given in Fig.6 where we have fit the data on sputtered samples of Fe/Cr[3]. Here it is clear that the oscillation in the MR asymptotically approach the uncoupled curve, and that only the first peak represent a MS
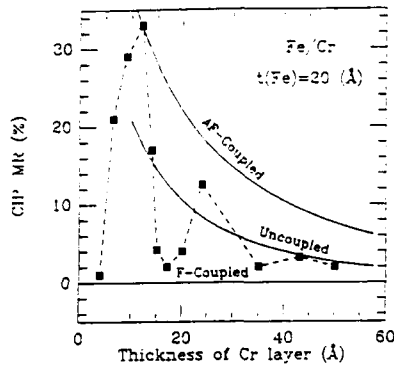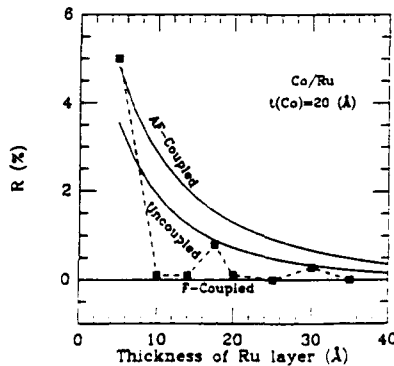

Fig.7. The CIP-MR for $Co\,(20\text{Å})/Ru\,(t)$ as estimated by taking the layers F, AF and "uncoupled". The squares represent data from Ref.3 at T=4.5K. The parameters used in the fits are $\lambda_{Co}=40\text{Å}$, $\lambda_{Ru}=30\text{Å}$, $w_s=0.25$, $p_{Co}=0.08$ and $p_s=0.2$.

in which all layers are AF aligned. If we assumed all peaks represented MS in which all layers are AF aligned we find $\lambda_{Fe}=\lambda_{Cr}=19\text{Å}$ which is unreasonably small; these parameters yield for Fe (20Å)/Cr (9Å) $\rho_{//}(H_s)=46\mu\Omega cm$, while we find $26\mu\Omega cm$ by using the parameters quoted for Fig.6. Finally in Fig.7 we present an analysis of the CIP-MR for Co/Ru. For these MS all peaks other than the first seem to represent mixtures of F and AF alignments with M=0; the troughs seem to represent structures which are ferromagnetically aligned, and the oscillations in the MR approach the F coupled line. These results are at variance with those on Co/Cu and Fe/Cr, and are not understood.

In summary we have provided a new interpretation of the CIP-MR for MS as mixtures of F and AF aligned layers. With this interpretation we find parameters that are much closer to fitting other data, e.g., resistivities, than if we interpret the peaks in the MR as corresponding to MS with *only* AF aligned layers.

REFERENCES

1. P. M. Levy, S. Zhang and A. Fert, Phys. Rev. Lett. **65**, 1643(1990); S. Zhang, P. M. Levy and A. Fert, submitted for publication.

2. D. Mosca, F. Petroff, A. Fert, P. A. Schroeder, W. P. Pratt Jr., R. Loloee and S. Lequien, J. Mag. Mag. Mat., **94**, L1(1991).

3. S. S. P. Parkin, N. More and K. P. Roche, Phys. Rev. Lett. **64**, 2304(1990).

THE EFFECT OF SPIN DEPENDENT SCATTERING FROM IMPURITIES ON GIANT
MAGNETORESISTANCE AND THERMAL CONDUCTIVITY IN Fe/Cr MULTILAYERS

B.L. Johnson[*] and R.E. Camley[**]
*Dept. of Physics, University of Colorado, Boulder, Colorado 80309-0390
**Dept. of Physics, University of Colorado, Colorado Springs, Colorado 80933-7150

ABSTRACT

Recent experiments have tested the assumption that a spin-dependent asymmetry in scattering is
responsible for the giant magnetoresistance (GMR) in Fe/Cr multilayers by introducing
additional impurities (with different spin-dependent scattering asymmetries) at the interfaces.
This paper presents a theoretical calculation based on a Boltzmann transport equation approach
which is appropriate for these new experiments. We find that when impurities (Mn, V) are
introduced which have a spin-dependent scattering asymmetry similar to that of Cr in Fe the
GMR is not substantially changed. When impurities (Al, Ir) with a spin-dependent scattering
asymmetry opposite to that of Cr in Fe are introduced there is a rapid degradation of the GMR.
Our results are compared with experiment and good agreement is found provided that the
magnitude of the scattering asymmetry in Al is reduced somewhat from low-temperature
published values. It is argued that thermal effects could indeed provide such a reduction. We
also point out that the thermal conductivity should undergo changes with magnetic field in these
structures, since the thermal conductivity also depends upon electron mobility.

INTRODUCTION

Recent experiments[1,2] have demonstrated that Fe/Cr multilayer structures with
antiferromagnetic coupling between the Fe layers can exhibit giant magnetoresistance (GMR)
effects, i.e, the resistivity of the structure changes markedly when an applied magnetic field is
used to overcome the antiferromagnetic coupling, leaving the structure in a state where all the
Fe spins are aligned. At low temperatures, the resistivity can change by 30%-50%, and at
room temperature changes of 10% have been measured.
Theoretical investigations of GMR have focused upon the effects of spin-dependent
scattering at the interfaces and in the bulk Fe[3-5]. We can understand the basic idea behind
these models by looking at the following simple picture. First, we note that in Fe with Cr
impurities, spin-down electrons experience less scattering than spin-up electrons. We can then
imagine that as a given electron passes from one Fe layer to the next, the amount of scattering
that it will encounter depends upon the directions of the magnetizations in the Fe layers. For
example, if all the Fe layers have their magnetizations in the same direction, a spin-down
electron passes relatively easily through the entire structure, while a spin-up electron scatters
strongly at each interface and in the bulk Fe. On the other hand, if the Fe layers are aligned
anti-parallel, then spin-down electrons leaving one layer will be strongly scattered at the next
Fe layer, since their spins are now aligned with the magnetization (i.e. they are now locally
spin up). The spin-up electrons are still strongly scatterd in the bulk Fe and at the interfaces.
Therefore, the resistivity of the structure should be greater in the anti-aligned state, since there
is more overall scattering.
Recent experiments by Baumgart, et. al.[6], demonstate the effects of spin-dependent
scattering on the GMR in Fe/Cr multilayers by introducing impurities at the Fe/Cr interfaces.
These impurities, when alloyed with Fe, exhibit known asymmetries for scattering spin-up and
spin-down electrons. The results of the experiments show that when the impurites have
spin-dependent bulk scattering asymmetry (N_b) similar to that of Cr in Fe, there is little effect
on the GMR, but when the asymmetry is inverse ($1/N_b$) to that of Cr in Fe, the GMR is
rapidly degraded. Furthermore, these results are roughly independent of whether the impurity
is added at only one Fe/Cr interface/unit cell, or whether the impurity is present at both Fe/Cr
interfaces/unit cell. This supports the idea that it is the number (and type) of scattering centers

which is the principal parameter influencing the GMR.

The purpose of the present paper is to account theoretically for the results of Baumgart, et. al. by extending the calculation of ref. [4] to include the following. 1) Rather than assuming a sharp interface at the Fe/Cr boundaries as has been used previously, we assume that there are thin regions where the Fe and Cr are mixed. We examine the effect of diffusion of Fe into Cr, although other combinations are possible. Given a region where the Fe and Cr are mixed we assume that there is bulk asymmetric scattering in the mixing region, rather than asymmetric scattering at the interfaces. The transmission coefficients at the interfaces are assumed to be spin-independent. 2) It is assumed that the introduction of the impurity scatterers changes the composition of the mixing region, principally the (net) bulk scattering asymmetry and mean free path.

In addition, we demonstrate that the thermal conductivity of the Fe/Cr superlattice structure might undergo large changes with applied field, since the calculation utilized to find the electrical resistivity differs only slightly from the heat flow calculation.

THEORY

In this section we present the theory for calculating the resistivity and thermal conductivity of a magnetic multilayer structure. We consider a unit cell composed of two films of Fe separated by a film of Cr, with thin regions of overlap at the interfaces. The geometry of a single period structure is shown in figure 1. Physically, the mixing region, m, represents a layer in which Fe has penetrated into the Cr (or vice-versa), creating a layer of mixed Fe and Cr. The addition of impurities at the interfaces then simply introduces a third material into the mixing region, provided the layer of added impuritiy is thin. We assume that a static electric field is applied along the z-axis, parallel to the interfaces, as shown. A magnetic field will also be applied along the x-axis, in order to overcome the antiferromagnetic coupling between the Fe layers. In the absense of a magnetic field and for anitiferromagnetically-coupled Fe layers, the Fe magnetizations lie parallel or antiparallel to the x-axis.
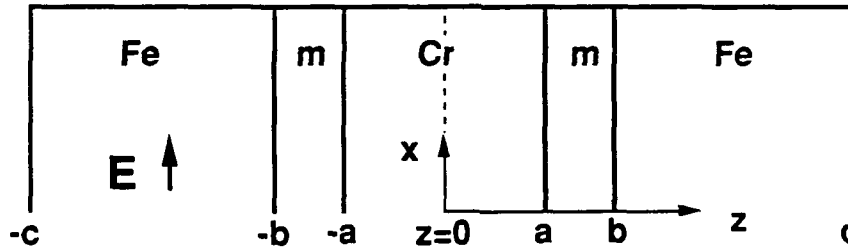
Figure 1. The geometry of a single period of the Fe(15Å)/m/Cr(12Å)/m/Fe(15Å) structure. The center of the structure is at z=0, and the boundaries of the mixing region are at z=±a and z=±b. An electric field is applied along the x-axis, as shown.

Following ref. [4], we assume that the electron transport through the structure is governed by the Boltzman equaton, and that the electron distribution function f may be thought of as the Fermi-Dirac distribution plus corrections due to the interfaces and the electric field:

$$f^{\uparrow(\downarrow)}(z,v) = f_0^{\uparrow(\downarrow)}(v) + g^{\uparrow(\downarrow)}(z,v)$$

$$(1)$$

where the arrows refer to the distributions for spin-up (spin-down) electrons, f_0 is the Fermi-Dirac distribution, and g is the correction term. For brevity, we will suppress writing the functional dependance of g on z and v from now on. Substituting (1) into the Boltzman equation and keeping only linear terms yields

$$\frac{\partial g^{\uparrow(\downarrow)}}{\partial z} + \frac{g^{\uparrow(\downarrow)}}{\tau^{\uparrow(\downarrow)} v_z} = \frac{eE}{mv_z} \frac{\partial f_0}{\partial v_x}$$

(2)

where e is the electron charge, E is the applied electric field, τ is the spin-dependent relaxation time, and m is the electron effective mass in each region. As usual, we assume that we may separate g into two parts, g_+ for electrons with positive v_z and g_- for electrons with negative v_z. The general solution to (2) may then be written

$$g_\pm^{\uparrow(\downarrow)} = \frac{eE\tau^{\uparrow(\downarrow)}}{m} \frac{\partial f_0}{\partial v_x} \left[1 + F_\pm^{\uparrow(\downarrow)} \exp\left(\frac{-z}{\tau^{\uparrow(\downarrow)} v_z} \right) \right]$$

(3)

where F is an arbitrary function of v, which is determined by the boundary conditions.

The solutions (3) may be written in each layer, which gives a set of functions F to be determined. We therefore construct enough boundary conditions to determine these and solve the resulting coupled set of equations numerically. Once the F's are known, and thus the g's, the current density in each region may be written

$$J_x(z) = -2e\left(\frac{m}{h} \right)^3 \int v_x f(v_z, z) \, d^3v$$

(4)

where m is the effective mass in each region. The current in the whole structure may be easily calculated by integrating the current density over z, and thus the effective resistivity for the entire structure may easily be found.

We may also examine the heat flux in the presence of a thermal gradient within an Fe/Cr structure in order to calculate the thermal conductivity. The Boltzman equation in the absence of electric or magnetic fields may be written in the relaxation time approximation as

$$v \cdot \nabla f^{\uparrow(\downarrow)} = -\frac{f^{\uparrow(\downarrow)} - f_0}{\tau}$$

(5)

If we now impose a thermal gradient parallel to the interfaces (along z), then we note that f_0 becomes a function of z through T(z). Insertion of equation (1) into (5) gives, after some rearrangement

$$\frac{\partial g^{\uparrow(\downarrow)}}{\partial z} + \frac{g^{\uparrow(\downarrow)}}{v_z \tau} = \frac{\mathcal{E} - \mu}{v_z T} \frac{\partial f_0}{\partial \mathcal{E}} \left(\frac{\partial T}{\partial z} \right)$$

(6)

where $\mathcal{E}$ is the electron energy, μ is the chemical potential, and the term in parenthesis is the thermal gradient. The solutions to (6) are easily written down:

$$g^{\uparrow(\downarrow)} = \frac{(\mathcal{E} - \mu)\tau^{\uparrow(\downarrow)}}{T} \frac{\partial f_0}{\partial \mathcal{E}} \left(\frac{\partial T}{\partial z} \right) \left[1 + F^{\uparrow(\downarrow)} e^{\frac{-z}{\tau^{\uparrow(\downarrow)} v_z}} \right]$$

(7)

Note that this expression differs from (3) only in the multiplying factors in front. Therefore,

264

for a given electron energy, the same boundary conditions will apply, and the functions F may be easily determined in manner analogous to that above. The heat flux equation

$$Q_x = 2\left(\frac{m}{h}\right)^3 \int v_x f(v,z)[\epsilon - \mu] d^3 v$$

(8)

is then solved to find the thermal conductivity. Although we do not give explicit numerical examples of the thermal conductivity analysis in the next section, we have shown that the calculation proceeds in a similar fashion, and thus one should expect to obtain changes of up to 50% in the thermal conductivity as a function of applied field

RESULTS

In this section, we present the results of numerical calculations for the resistivity of Fe/Cr multilayers. In order to compare with experimental results, we study the addition of Al and Mn to the interfaces of an Fe(15 Å)/Cr(12Å) multilayer structure. We note that the scattering asymmetry for Mn in Fe is similar to that for Cr in Fe, and the asymmetry of Al in Fe is roughly the inverse of that for Cr in Fe, as discussed the introduction.

The input parameters for the problem are: 1) λ_{Fe}, the arithmetic mean of the mean free paths for spin up and spin down electrons in the Fe; 2) N_{bFe}, the bulk scattering asymmetry (= $\rho^\uparrow / \rho^\downarrow$) in Fe; 3) λ_m, the arithmetic mean of the mean free paths in the mixing region; 4) N_{bm}, the bulk scattering asymmetry in the mixing region; and 5) λ_{Cr}, the mean free path (spin-independent) in Cr. The individual mean free paths for spin up and spin down electrons in the Fe and mixing layers may be calculated from the arithmetic mean of the mean free paths and the bulk scattering asymmetries. The other parameters are the thickness of the mixing region (t=b-a in figure 1), and the individual thicknesses of the Fe and Cr layers. A bit of algebra allows us to write the resistivity of the structure calculated in the theory section entirely in terms of the above parameters.

As we pointed out earlier, in the absense of impurities there is a region of thickness t at the interfaces where the Fe and Cr are mixed. When the impurities are added, we assume that i) they affect the mean free path and the scattering asymmetry in the mixing layer, ii) the distance between Fe layers is increased by the thickness per period of added impurity, and iii) that the thickness t=b-a of the mixing layer is constant. To arrive at the bulk scattering asymmetry and mean free path in the mixing region as a function of impurity thickness, we use the following averaging scheme. The net individual resistivities for spin up ($\rho^\uparrow$) and spin down ($\rho^\downarrow$) electrons in the mixing layer may be calculated from Matthiessen's rule (neglecting spin mixing), weighted by the thickness of impurity, and the asymmetry is then the ratio of the new resistivities $N_{bm} = \rho^\uparrow / \rho^\downarrow$. Explicitly,

$$N_{bm} = \frac{g_m \rho_m^\uparrow + g_{Cr} \rho_{Cr}^\uparrow}{g_m \rho_m^\downarrow + g_{Cr} \rho_{Cr}^\downarrow} = \frac{g_m N_m}{g_m + g_{Cr} K} + \frac{g_{Cr} N_{Cr}}{g_{Cr} + g_m (1/K)}$$

where N_m is the bulk asymetry of the impurity in Fe, N_{Cr} is the bulk asymmetry of Cr in Fe, $K = \rho_{Cr}^\downarrow / \rho_{m}^\downarrow$, and g_m and g_{Cr} are the geometric weighting factors given by

$$g_m = \frac{M}{2}, \quad g_{Cr} = t - \frac{M}{2}$$

where M is the thickness/period of impurity (recall that the mixing layer is present at both interfaces in the unit cell and thus half the total thickness resides at each interface).The mean free path in the mixing region is also affected by the inclusion of impurities as follows:

$$\lambda_m = \frac{\rho_m^o}{\rho_m} \lambda_m^o$$

where

$$\frac{\rho_m^o}{\rho_m} = \frac{g_{Cr}(\rho_{Cr}^{\uparrow} + \rho_{Cr}^{\downarrow})}{g_{Cr}(\rho_{Cr}^{\uparrow} + \rho_{Cr}^{\downarrow}) + g_m(\rho_m^{\uparrow} + \rho_m^{\downarrow})}$$

is the ratio of the arithmetic means of the resistances in the mixing region with (numerator) and without (denominator) impurities, and λ_m^o is the mean free path in the mixing layer without impurities. Note that the subscripts Cr and m on the resistivities refer to the value of the resistivities of these elements when mixed with Fe.

In figure 2, we plot the % change in the resistivity of the structure from the Fe-aligned state to the Fe-antiparallel state, ($\rho^{\uparrow\uparrow} - \rho^{\uparrow\downarrow})/\rho^{\uparrow\uparrow}$, as a function of the thickness per period of added impurity. The added impurities shown in figure 2 are Al and Mn, and the experimental points are shown as heavy dots (Al), and heavy squares (Mn). At zero added impurity (mixing region of Fe-Cr only), we achieve a fit assuming that the mean free path and bulk scattering asymmetry in Fe are $\lambda_{Fe}=38$ Å and $N_{bFe}=2$, respectively, the mean free path and asymmetry in the mixing layer are $\lambda_m = 18$ Å and $N_{Cr}=4.4$, respectively, the thickness of the mixing layer is $t=4$ Å, and the mean free path in Cr is $\lambda_{Cr} =20$ Å. We have set the transmission probability T=1 since the effective interface scattering is taken into account in the thin mixing region. The plots for Mn agree quite well with experiment using the averaging scheme outlined above and the two published [7] values for the bulk asymmetry of Mn in Fe, $N_m = 4$ (solid line) and $N_m = 6.5$ (dashed line).
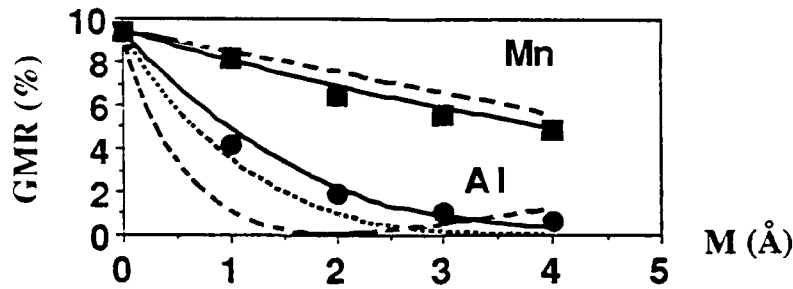

Figure 2. The percent change in the magnetoresistance as a function of thickness per period of added impurity. The upper set of curves is for Mn impurities, and the lower set is for Al impurities. The heavy squares are the experimental data for Mn, while the heavy dots are the experimental data for Al, both taken from ref (6). For Mn, the solid curve is calculated using the value for bulk scattering asymmetry $N_m=4$, while the dashed curved is calculated using $N_m=6.5$. For Al, the dashed line is obtained for $N_m=0.117$, the dotted line for $N_m=.281$, and the solid line for $N_m=.468$. Note that .468 is a smaller asymmetry than .117, as explained in the text.

Theoretical curves for the addition of Al impurity are also shown in figure 2 for different values of bulk asymmetry. Here the dashed curve is obtained using the published value ($N_m = .117$), the dotted curve is for $2.4N_m$, and the solid curve is for $4N_m$. For self-consistency, we note that the multiplying factors must also act on the parameter K above, i.e. we use K, 0.42K and 0.25K, respectively. The effect of the multiplying factor is to reduce the net bulk asymmetry of Al in the Fe-Cr mixing layer; i.e. 0.117 is a rather large asymmetry (compare the magnitude $1/0.117 = 8.5$ to the value 4.4 for Cr), whereas 4 times 0.117 is a rather small asymmetry ($1/0.468 = 2$). We note that since the latter produces the best

fit, the experiment seems to show that the scattering asymmetry of Al in an Fe-Cr background is smaller than that for Al in Fe. We note that the values of α (=1/N_b) and ρ are taken from low temperature data. The large impurity concentration of Cr in Fe near the interfaces probably means that the values for Cr in Fe are still reasonable. However, at room temp, spin independent scattering due to phonons and other mechanisms will reduce the asymmetry of lower concentration impurities. Therefore, it is not unreasonable to expect a smaller asymmetry in the case of Al impurities, as the experiment seems to show.

We note that for some values of parameters our calculations show that the GMR reaches a minimum and then begins to get larger as more impurity is added (see the dotted and dashed curves in Fig. 2. The reason for this is as follows. In the present model the GMR depends upon the **magnitude** of the bulk scattering asymmetry, and therefore as M gets larger, the magnitude of the asymmetry in the mixing region reaches a minimum when the asymmetries for the Cr and Al "cancel" one another, and then gets larger as the Al asymmetry begins to dominate. This upturn is not seen experimentally. One reason for the difference between experiment and theory is that our model neglects any changes in the antiferromagnetic coupling as M increases. Experiments have shown that the antiferromagnetic coupling between the Fe layers depends upon the thickness of the Cr layers [8], ie. the antiferromagnetic coupling dissapears by the time d_{Cr}=19Å, and the present theoretical model does not account for the decay of the antiferromagnetic coupling [9].

In addition, we note that the value of t =4Å we chose for figure 2 is fixed by fitting the experimental values along with reasonable choices for the other parameters, such as mean free paths. It is not the only possibility. We point out that the effect of larger t is to increase the GMR due to the increased number of scatterers, and therefore to fit the data we would need to reduce the bulk asymmetry. For instance, if we let t=5Å , then to fit the data we would need N_{Cr} = 3.25 (all other parameters the same) instead of 4.4. We could also adjust the mean free paths (increase the distance between scattering events to compensate for the increase in the number of scatterers), but since the effect of changing the mean free paths on the GMR is much smaller than the effect of the asymmetries, we get quickly out of the range of reasonable mean free paths at room temperature. For example, if t=5Å and N_{Cr}=4.4, then to match the data we need to let l_m=70Å, which is very long for room temperature. The reason for the relative insensitivity of the GMR to mean free path comes from the bulk asymmetry in the Fe (N_{bFe}=2), which by itself accounts for roughly 35% of the GMR, i.e. if we let N_{bFe}=1, so that there is no bulk asymmetry in the Fe, then with all other parameters the same, we find the GMR drops from 9.4% to 5.9%.

When larger values of t are used in the calculation, with the corresponding lower values for the asymmetries, the major features seen in figure 2 are the same. The value of t=4Å is a reasonable minimum, since we would expect that the penetration of one material into another ought to be around one atomic diameter in ultra-thin films.

REFERENCES

1. M.N. Baibich, J.M. Broto, A. Fert, F. Nguyen Van Dau, F. Petroff, P. Eitenne, G. Creuzet, A. Friederich, and J. Chazelas, Phys. Rev. Lett. **61**, 2472 (1988)
2. G. Binasch, P. Grunberg, F. Suarenbach, and W. Zinn, Phys. Rev. B **39**, 4828 (1989) and J. Krebs, P. Lubitz, A. Chaiken, G.A. Prinz, Phys. Rev. Lett. **63**, 1645 (1989)
3. R.E. Camley and J. Barnas, Phys. Rev. Lett. **63**, 664 (1989)
4. J. Barnas, A. Fuss, R.E. Camley, P. Grunberg, and W. Zinn, Phys. Rev. B **42**, 8110 (1990)
5. P.M. Levy, S. Zhang, and A. Fert, Phys. Rev. Lett. **65**, 1643 (1990)
6. P. Baumgart, B. Gurney, D. Wilhoit, T. Nguyen, B. Dieny, V. Speriosu, presented at MMM 1990 (BC-08), to appear in J. of Appl. Phys.
7. I.A. Campbell and A. Fert in *Ferromagnetic Materials*, ed. by E.P. Wohlfarth, North Holland (1982), Vol. 3, p. 747
8. S.S.P. Parkin, N. More, K.P Roche, Phys. Rev. Lett. **64**, 2304 (1990)
9. Y. Wang, P.M. Levy, J.L. Fry, Phys. Rev. Lett. **65**, 2732 (1990)

Thin Film Growth

MORPHOLOGIES OF SOLID SURFACES PRODUCED FAR FROM EQUILIBRIUM

R. Stanley Williams*, Robijn Bruinsma** and Joseph Rudnick**
*Department of Chemistry and Biochemistry
University of California Los Angeles
Los Angeles, CA 90024-1569
**Department of Physics
University of California Los Angeles
Los Angeles, CA 90024-1547

ABSTRACT

We present the first quantitative experimental study of the morphology of amorphous solid surfaces formed by non-equilibrium processes and compare the results with theories developed to explain the formation of such surfaces.

I. INTRODUCTION

The preparation of surfaces and the growth of thin films are areas of great technological importance, with applications including such diverse fields as optics, chemical analyses, fabrication of microelectronic and recording devices, containment vessels for fusion reactors and manufacture of composite materials. A feature common to all these applications is that the surface preparation processes used are far from chemical equilibrium. Many of the processes involve an energetic ion beam, plasma or gas that is used to modify a surface, either by etching or depositing material. The electrical, optical and mechanical properties of the resulting systems depend strongly on the new surface morphology, which in turn depends on the kinetics of the processes that modify the surface. There have been many experimental studies of the morphology of surfaces created far from equilibrium, but so far most of these studies have been more descriptive than quantitative. With the introduction of scanning tunneling microscopy (STM) and atomic force microscopy (AFM), it is now possible to obtain a detailed three dimensional topograph of a surface h(r), which is the height of the surface at position r, with atomic scale resolution. One can compare the surface topographs for different processing conditions to empirically optimize the morphology of the desired surface and, as we shall demonstrate below, also understand the details of the kinetic processes that produce the observed morphology.

On the theoretical side there has been in recent years considerable progress in our understanding of the morphology of surfaces growing far from equilibrium as well as an enlarged capability for numerical simulation of film-growth under realistic conditions. On the experimental side, the STM presents us with a tool with unprecedented possibilities for quantitative characterization of surfaces over length scales ranging from 1Å up to 10^4Å. In particular, we can measure the topographical profile of the height of the surface h(r) with a lateral resolution of 1-2Å and a vertical resolution better than 1Å for a rough surface. From h(r), we can calculate the height-correlation function in reciprocal space, $<|h(q)|^2>$, which has become the focus for the theoretical descriptions referred to above. Thus, the STM allows us to obtain "real-space" and "momentum-space" representations of a surface on a side by side basis, whereas most electron or photon scattering techniques can only be used to obtain $<|h(q)|^2>$, because of the loss of phase information.

A) Sputtering

Sputtering is the most commonly used technique for the preparation of technologically relevant thin films.[1-3] The sputter process deposits fairly energetic atoms or ions on a growing surface. The incoming particles move along ballistic trajectories predominantly along the normal to the substrate surface. Once they reach the surface, the atoms move around by surface diffusion or by evaporation/recondensation until they reach a site where the binding energy is particularly high. At very low deposition rates, this process can preserve the crystallinity and facetting, by stepflow and island growth, as for instance described by the classical model of Burton, Cabrera and Frank.[4,5] However, for lower temperatures and economically reasonable deposition rates, the

atoms coalesce into microcrystallites and the film will be amorphous. It has been known since 1870 (!) that such films develop fascinating morphologies. The nature of the morphology depends on a variety of factors such as temperature, deposition rate and incidence angle of the beam, but the observed morphologies are commonly classified by the structure zone model (SZM) proposed by Movchan and Demchishin[7]and expanded by Thornton.[8] Our primary interest is "Zone I" with $T/T_{(melting)}$ less then 0.3 or so, where there exists a columnar fine-grained micro-structure. The boundaries between the columns are of low adatom density and they play a significant role in determining the mechanical and transport properties of the film as well as its durability and stability. Columnar structures were first observed[9] using small angle electron scattering for sputtered Pd films. Since then, there have been many reports of columnar microstructure in studies by fractography, TEM, small angle electron scattering and X-ray scattering.[10] This columnar structure has strong effects on the magnetic, optical and mechanical properties of a film.[10]

The large-scale, macroscopic morphology has been investigated in the materials-science literature since the early 1950's. Konig and Hellwig[17] first pointed out the geometrical "shadowing" effect. Protruding parts of a surface shield deeper lying sections. In particular for uncollimated incoming beams, this leads to enhancement of the surface roughness.[8] This mechanism for roughening competes with a variety of annealing mechanisms first discussed by Herring[18] At modest temperatures when the vapor pressure of the substrate is low, the dominant annealing mechanism is surface diffusion. As the vapor pressure rises, evaporation-recondensation starts to play a role. Shadowing and surface diffusion have been invoked[8]to explain the "universal" classification of thin-film microstructure: the shadowing should lead to Zone I micro-structure of low-density tapered columns with domed tops. Increased temperature increases the surface diffusion constant leading to wider, smoother columnar grains.[8] Shadowing and surface diffusion are also believed [9]to be the important factors in the evolution of rough "cone-like" surface topologies observed during sputter erosion of surfaces.[20]

There have been extensive numerical investigations of surface growth close to equilibrium.[21] Much of the earlier work was based on the solid-on-solid (SOS) model as pioneered by Gilmer[22] More recently, the growth morphology of chemical vapor deposition[23] (CVD) and molecular beam epitaxy[24] (MBE) have been investigated. Numerical studies of surfaces far from equilibrium were stimulated by observations of the microstructures of amorphous thin films. The first numerical studies of roughening due to shadowing were based on the "ballistic aggregation model" of Vold.[25] Sticky spheres were constrained to approach a substrate on straight-line ballistic trajectories. Leamy and Gilmer[26] showed that shadowing on an atomic scale produces the "tangent-rule" for the growth direction. Very large-scale simulations[27,28] of this ballistic aggregation model revealed deposits consisting of quasi-fracta[29] tree-like structure riddled with holes but obeying the tangent rule.

Real coatings, though, are smooth over distances of 100 - 1000 Å, which is the result of various annealing mechanisms. Surface diffusion can be included to some extent in computer simulations[30,31] and it indeed produces a more compact deposit. The ballistic aggregation model with surface diffusion included is thus believed to contain the basic physical mechanisms to understand the columnar structure. Because of computational limitations, at present it is difficult to perform numerical simulations on a system with more than 100 x 100 lattice constants. Thus, it is not practical to use atomic-scale simulations to study the macroscopic evolution of real columnar structures for length-scales exceeding 1000 Å and time-scales exceeding nanoseconds.

Numerical simulation of macroscopic evolution is possible if we do not attempt to describe the surface down to atomic lenghts as illustrated by the work of Srolovitz[32] and Ling and Anderson.[33] Continuum theories are thus aimed at understanding the macroscopic evolution and should be complementary to numerical studies. To model the macroscopic properties of amorphous thin-film growth, a number of continuum models have been used in the materials science literature, in particular in the context of electron-beam etching of masks for micro-electronics applications: Carter[34] reviewed a very elegant approach based on the construction of an eikonal equation for the evolution of the surface of a growing film ("Huyghens Construction") and applied it to sputter erosion. Macroscopic evolution based on shadowing was also used extensively in simulations[35] of sputter deposition onto patterned substrates. The success of these methods suggested that they could also be used for understanding the macroscopic evolution of the columnar microstructure. Continuum models have also been used for understanding the early stages of thin film evolution.[36,37]

C) Scaling Theories

Apart from the effort to model the structure of sputtered films, there has been an explosion of interest in the general features of non-equilibrium surfaces.[38] This work has centered on local growth contiuum SOS models but with atomicity included through shot-noise in the incoming current. A scaling description[39-41] was proposed for this class of models in terms of the evolution of the surface roughness. Let h(r,t) be the time dependent height profile of the film. Then the height correlation function

$$C(q,t) = <|h(q,t)|^2 > \tag{1a}$$

$$= \int \frac{d^2r}{(2\pi)^2} e^{iq \cdot r} \langle (h(0) - h(r))^2 \rangle_t / Area \tag{1b}$$

with $\langle \cdots \rangle_t$ indicating a sample average after exposure time t. This correlation function should have the general form

$$C(q,t) \propto q^{-v} F(t\,q^z) \tag{2}$$

would predict a power law decrease proportional to q^{-v} in $C(q,t)$ for $q \geq t^{-1/z}$ and $C(q,t) \sim t^{v/z}$ for $q \leq t^{-1/z}$. Under conditions of rotational invariance, $z = 2 - \alpha$ with $2\alpha = v-2$, so there is only one free exponent (say α). This scaling law has been verified for a wide variety of local growth models.[38] Particularly influential was the KPZ model[42] where

$$\partial h/\partial t = \gamma \nabla^2 h + J + J/2\,(\nabla h)^2 + \eta(r,t) \tag{3}$$

with γ a measure of the surface annealing, J the average deposition current and $\eta(r,t)$ the shot-noise fluctuations around the average current. In "1+1" dimensions (d=1 substrate), scaling is obeyed [42] for the KPZ model with $\alpha=0.5$. Many models have been investigated[43-56] and it has been found that in "2 + 1" dimensions (i.e. physical substrates) α depends on the degree of non-linearity. For very weak non-linearity (Edwards-Wilkenson Model)[57] $\alpha \to 0$ while $\alpha \to 4.0$ for strong coupling. As a function of the non-linearity there appears to be a phase-transition for discrete but not for continuum models. The connection of the KPZ model with sputtered films is that the Huyghens construction, mentioned above, can be approximated for smooth surfaces by Eq. 3 with $\gamma = \eta = 0$. Moreover, if we define an "active" surface for deposition by ballistic aggregation and fit this surface with an h(r,t), then the results appear to agree with the scaling predictions. There have, however, been few studies that investigated the experimental relevance of the scaling approach for thin film growth.[58]

II) MACROSCOPIC THEORY OF THIN-FILM GROWTH

In this section we discuss the analytical and numerical work done at UCLA aimed at investigating for the concrete case of sputtered films whether the scaling ansatz in general and the KPZ model in particular provide a viable description. The *a priori* questions were as follows:

(i) The shadow-mechanism is only local when applied to individual atoms. For a non-flat surface, shadowing is a non-local roughening mechanism. For non-local growth models (e.g. DLA) there is no reason to assume that Eq. 3 correctly gives the asymptotic (i.e. large length and time scale) properties. In particular the SOS description is invalid for DLA because the surface develops "overhangs".

(ii) Sputtered films anneal at lower temperatures by surface diffusion. This is described by a $\nabla^4 h$ term[18] rather than a $\nabla^2 h$ term, which is more appropriate for an evaporation-recondensation mechanism.[59] How does this affect the conclusions?

(iii) The surfaces of Zone I thin films look very different from those created by numerical simulation of the KPZ model. In the latter case the characteristic "domed top" and cauliflower structure of Zone I are missing. This question is related to the subsurface groove/void network. In general, SOS models cannot be expected to account for the d=3 internal structure of a film, yet the groove structure is of crucial importance for the physical properties of thin films. Of course, ballistic deposition does create an internal structure but, as we have seen, it is computationally difficult to allow annealing to proceed sufficiently to create >1000Å scale structures.

A) Column/Groove Microstructure

To answer these questions we have developed[60] a "shadow model" for the growth of the groove microstructure, based on the macroscopic description for sputtered films used in the microelectronics applications[35]. We extended these descriptions to the submicron regime by including shot-noise and surface diffusion. In this model, the local growth rate v_n is controlled by the flux $RJ(\theta)$, with $J(\theta)$ a dimensionless vector, and by surface diffusion:

$$v_n = D \, d^2\kappa/ds^2 + R \int_{\theta-(s)}^{\theta+(s)} J(\theta) \cdot n(s) \, d\theta + \eta(r,t) \tag{4}$$

with D proportional to the surface diffusion constant. Next, κ is the local curvature, s the arclength (in 1+1 dimension), $n(s)$ the local surface normal, and $\theta^{\pm}(s)$, which determine the limits of integration in Eq. 4, are the exposure angles at point s on the surface (Fig.1a). For D=η=0, this model has been very successful in describing the macroscopic morphology of sputtered films. (Eq. 4 is actually a generalization, due to Bales and Zangwill,[63] of our model which used the SOS approximation).

For D=0, we succeeded[60] in solving Eq. 4 analytically in the SOS approximation producing a self-similar mountain landscape. However, the columnar structure was controlled by the substrate roughness rather then by the shot-noise. Numerical simulation of Eq. 4 for η=0 by Bales and Zangwill[63] beyond the SOS approximation revealed a columnar/groove structure. The groove structure showed amazing similarity with experimental results[62] (see Fig.1b). The initial characteristic length scale of the columnar structure was again found to be set by the substrate roughness. The columnar structure appeared to coarsen with h, as noted by Messier and Yehoda, but the process could not be followed long enough because of computer limitation. The column/groove structure of Zone 1 is thus determined by the substrate surface roughness and not by the shot noise (as had been frequently assumed on the basis of ballistic deposition simulations). We established[62] a criterion for the initial substrate roughness to be small enough so film-quality would not be affected by column/groove microstructure. Quantitative comparisons between theory and experiment (STM studies) were found to be feasible to some extent.[62]
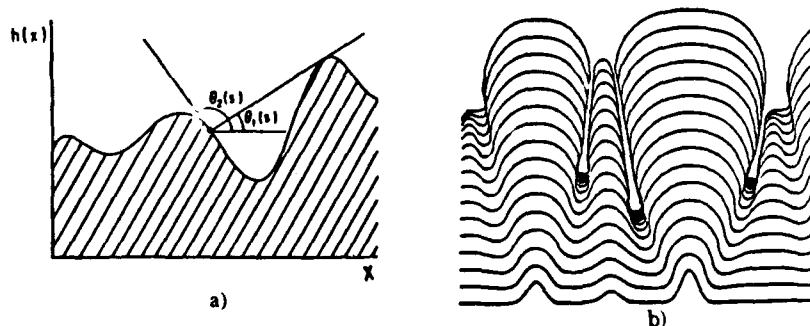

Fig. 1 a)   Surface profile h(x). Incident particles can reach the surface from all directions within the cone defined by the angles $\theta_+(s)$ and $\theta_-(s)$.

    b)   Growth of a surface, with no shot noise, according to Eq. 4. (from ref. 62)

B) Coarsening and Scaling

The non-local algorithm for columnar growth revealed the origin of the groove structure and their connection to the initial roughness. However, the algorithm was very computer intensive and could not be used to obtain the long-time evolution of the groove structure as for instance seen in the sputter deposition of amorphous graphite films by Messier and Yehoda[12-14] To that purpose, we investigated[64] the connection between our non-local growth algorithm, and the Huyghens Construction, which is much less computer intensive. Via numerical simulation of Eq. 4 we found[64] that the Huyghens Construction actually produces mathematical singularities ("cusps") at exactly the location where the much more accurate "equation of motion" Eq. 4 produced grooves. The evolution of cusps in the Huyghens construction in the presence of noise leads to scaling for the "coarsening length" $\xi_c(h)$ (the mean distance between grooves) with exponents which agree well with experiment[12-14] In the KPZ model annealing erases the cusp

C) Surface Diffusion

We thus have found that for sputtered thin films a reasonably realistic non-local growth law (Eq. 4) can be approximated by the local Huyghens Construction. The Huyghens Construction is apparently a very powerful tool which can be used also at shorter length scales - provided the cusp singularity structure is tracked. If, with the above mentioned proviso, we can use the Huyghens Construction, does the KPZ model describe the surface structure of sputtered films correctly on length scales less than the coarsening length? Recall that on length scales less than $\xi_c(h)$, the surface of Zone I columns is (sometimes) self-similar[13]

This issue was investigated by Golubovic and Bruinsma. Surface diffusion would contribute a "$\nabla^4 h$" term and evaporation-recondensation[55] a "$\nabla^2 h$" term to the KPZ model:

$$\partial h/\partial t = D\nabla^4 h + \gamma\nabla^2 h + J + J/2 \ (\nabla h)^2 + \eta(r,t). \tag{5}$$

A renormalization group treatment demonstrated that the KPZ description for non-conservative noise[67] is valid provided γ is sufficiently positive. For pure surface diffusion, $\gamma = 0$, the surface becomes unstable towards a new fixed point because of breakdown of the SOS condition. In practice this means that KPZ can be used but only for growth problems with substantial evaporation-recondensation and for length scales less than the coarsening length $\xi_c(h)$.

Golubovic and Karunasiri[68] then investigated both analytically and numerically what will happen for pure surface diffusion, i.e. sputtering at low temperatures. They concluded that the surface will undergo a form of spinodal decomposition into a mountain landscape with cones that have a characteristic length scale that increases with time. This form of coarsening is fundamentally different from that associated with the Huyghens Construction as it is not controlled by the substrate roughness.

We thus can briefly summarize the results of the past theoretical effort as follows:

1. The column/groove microstructure is essentially a "deterministic" effect resulting from reproduction and coarsening of the initial substrate roughness through the shadowing effect.

2. If surface diffusion is the dominant annealing mechanism then the surface evolves via a spinodal decomposition mechanism leading to a coarsening mountain structure. If there is substantial annealing by evaporation/recondensation, then the scaling theories should apply.

III. EXPERIMENTAL STUDIES

This section will present the status of experimental studies. First, we will briefly review the techniques that have been used in the past to characterize deposited films and rough surfaces. Then, a substantial portion of this section will present the results and analyses of our studies of sputter etching of graphite surfaces. The discussion will demonstrate the general data collection and analysis tools that we have developed and will continue to follow in our future work, since they are substantially different from anything that has been done previously. Sputter etching and rapid film growth share the same surface annealing characteristics, so the analyses are valid for

both cases. It will also show the value of having a joint theoretical/experimental effort, since the two sides of the project have reinforced each other greatly.

A)   Review of Analyses of Rough Surfaces

As mentioned previously,[9,10] the only method used in the past to obtain information about $C(q)$ for the surfaces of sputtered films was low-angle scattering of electrons or x-rays[69-71] Historically, these experiments were very important for determining the structural properties of rough surfaces, but it is not possible to reconstruct $h(r)$ from $C(q)$ because the phase information is lost in the scattering process. Thus, scattering experiments must be supplemented if one is to obtain a real-space picture of the rough surface.

A great deal of experimental work involving rough surfaces has been performed with different forms of microscopy,[12-14] especially scanning electron microscopy (SEM) and transmission electron microscopy (TEM). An advantage of electron microscope techniques is that they can be used to obtain valuable information about the cross section and internal structure of a film, as long as the sectioning process does not damage the film too heavily. This is especially useful in characterizing intergranular voids and grooves. However, most researchers do not obtain a quantitative height profile of the surfaces they investigate, but rather analyze the lateral inhomogeneities of the surface by examining the variation in the gray scale of their micrographs. One of the major results from this work is the near universality of the cauliflower morphology that is observed on films of essentially anything grown under the proper conditions by a vapor deposition process.[12-14]

Rasigni et.al.[72,73] have developed a method to obtain quantitative height profiles of rough surfaces. They use a microdensitometer to digitize the gray scale of a TEM image of a carbon replica of the surface, and then assign a height scale to the digitized image based on various calibrations they can make. They have been primarily concerned with calculating various moments that characterize the surface, such as the autocovariance function (or real-space height-height correlation function), defined by

$$G(|r_2 - r_1|) = \langle h(r_2)h(r_1) \rangle - \langle h(r)^2 \rangle. \tag{6}$$

This function, which is the Fourier transform of $C(q)$ from Eq. 1 above, is used by Rasigni et al.[72,73] primarily to characterize the degree of roughness of the surface, the length scale over which correlation of surface structure appears and to model the scattering of light from their rough surfaces. They have not related $G(r)$ to any theories of film growth, although they could simply Fourier transform it to find $C(q)$ and follow the prescriptions outlined above. The problems with this TEM technique are that it is very labor intensive, forming the carbon replicas can damage the surfaces on which they are made, and the resolution is no better that 100Å.

Most of the film growth studies performed with STM have involved relatively smooth surfaces produced by evaporation of films onto flat substrates.[74,75] Denley has emphasized the study of rough surfaces with STM.[76] He showed that the roughness of an evaporated Au film, defined as the average peak-to-peak height of the surface over an area imaged in a STM topograph, depended strongly on the temperature of the substrate during the deposition. He observed that the surface roughness was minimized for a substrate temperature of 300°C, which demonstrates the importance of kinetic processes even for evaporated films. He has also used STM topographs to determine the fractal dimension of rough surfaces, in an attempt to characterize different roughening processes.

Schönenberger et al.[77] have used STM to study conducting films of Fe_3O_4 deposited onto Si (100) substrates by sputtering. The surfaces of the deposited material were characterized by the now familiar domelike terminations of columnar grains of oxide with lateral dimensions in the 200-500 Å range. The mean diameter of the grains and the surface corrugation increased significantly with increasing substrate temperature, with the rms corrugation always 10% of the grain diameter. The domes were smooth and featureless. The results that were obtained depended strongly on the tips that were used, with etched Au and PtIr thermocouple wire tips producing the smallest tip artifacts in the images. The authors did not have a theoretical model to explain the morphology of their surfaces.

Poirier and White[78] have examined the effects of ion bombardment and annealing on TiO$_2$ (001) surfaces, and then examined the growth of Rh films on the rutile surface. They have observed that bombarded surfaces roughen, and that the rough surfaces become smoother with the initial stages of annealing. However, after annealing for 2 hours at 510°C, the surface roughens again to expose (011) and (114) facets. When Rh is evaporated onto an unfaceted surface, it forms a cauliflower pattern on the rutile. The STM topographs of these various surfaces are qualitatively similar to those collected in our laboratory from graphite surfaces sputtered etched at the higher ion doses. This is an indication of the universality of the processes that occur for etching and deposition of material from the vapor.

The recent work of Mitchell and Bonnell[79] on the analysis of sputter-deposited films and rough fracture surfaces by STM is the closest to ours in terms of the manner in which the data are represented. These researchers accumulate single STM line scans of their surfaces with 1000-2000 data points in the scan. Each scan is then Fourier transformed to yield a high quality power spectrum, and several of the power spectra are averaged to further improve the signal to noise ratio. If a substantial portion of the plot of the logarithm of the power spectrum versus the logarithm of the wavenumber is linear, then the surface displays a fractal character over the corresponding length scales and the fractal dimension is related to the slope of the line segment. At the present time, these characterizations have not been extended to the understanding of the mechanisms that give rise to the particular fractal dimensionality that is observed.

There have been several STM studies of sputtered surfaces,[80-89] but most of them have emphasized the very low ion dose limit so that they could examine the damage created by a single ion impact with the surface[80-87] or examine surface morphology after the removal of a single monolayer of material[88,89] For the case of ion bombardment of graphite with 50 keV Ar$^+$ ions, the surface is characterized by hillocks rather than depressions at the ion-impact sites.[85-87] These hillocks, which are roughly 10Å in radius and 1Å high, are presumed to be the result of interplanar stresses caused by the collision cascade that leads to a local volume expansion of the graphite.[87] The atomic order of the surface in the area around the hillocks is also severely distorted. Michely and Comsa[88,89]have examined the initial stages of ion etching of single crystal metal surfaces such as Pt(111) with keV energy He$^+$ and Ar$^+$ ions. With the heavier projectile, which has a sputter yield > 1, the surfaces are characterized by hexagonal vacancy islands. For He$^+$, which has a sputter yield << 1, the surfaces exhibit a variety of hillocks, adatom islands, and dislocations that intersect the surface. In all of these studies, the surfaces were still dominated by the structures of the underlying substrate material.

B)   STM Analysis of Sputter-Etched Graphite

In contrast to the above sputtering studies, we have examined surfaces bombarded with intermediate ion doses designed to remove between 10 and 1000 atomic layers from the substrate. The surface chosen for our initial investigations was the cleaved (0001) face of highly oriented pyrolytic graphite (HOPG). This surface is inert in air and is easily imaged with the STM[83-86] Graphite also has a rigid lattice, with a melting temperature of ~3800°C. This indicates that surface diffusion should be minimal at room temperature and thus bombardment induced topography is "frozen in" and can be observed with the STM long after sputtering has occurred. Aside from experimental convenience, sputtering of graphite is intrinsically interesting to many different communities of researchers. Besides its basic theoretical interest, this work has relevance to the investigation of plasma-surface interactions at the limiters in tokamac reactors,[90] the mechanisms of diamond film growth,[91] and erosion of surfaces of composit materials in low earth orbit.[92]

Freshly cleaved graphite samples were examined with the STM before sputter etching. The STM was operated at atmospheric pressure in the constant current mode, with a tunnel current of 0.5 nA and a sample to tip bias of -100 mV. The tips used were either made from Au or PtIr wire. Low magnification topographs (2400 Å x 2400 Å image size) showed atomically flat areas over many thousands of square Angstroms, while at higher magnifications (25 Å x 25 Å) the atomic scale features of clean graphite were easily observed.

After stable images of clean graphite were obtained, the samples were transferred to the sample treatment chamber of a KRATOS XSAM-800 surface analytical system. The graphite surfaces were sputter etched with a beam of 5 keV Ar$^+$ ions, rastered over a 9 mm^2 area on the sample and incident at an angle of 60° to the surface normal. The beam flux incident on the sample was determined by using an electrometer to measure the ion beam current. A small positive bias

(45 volts) was applied to the sample to suppress secondary electron emission. The experimental parameters that have been varied so far were the flux J incident on the sample, the total ion fluence $Q = Jt$ for a given exposure time t, and the substrate temperature T.

The graphite samples were re-examined with the STM after etching using identical operating parameters and, if possible, the same tunneling tip used prior to sputtering. The results shown here were reproducible from sample to sample and even with different tunneling tips. The surfaces were stable for several days, but after prolonged exposure to the air tip noise dominated the images. The images used for the data analysis were usually collected within a couple of hours of the first removal of the sample from the vacuum chamber.

The study of rough surfaces with an STM presents special problems associated with the tip and various imaging artifacts that may arise. Asymmetric tips produce artificial anisotropy in the images and blunt tips will fail to resolve closely spaced features.[93] Surfaces with very sharp protrusions will yield images of the sides of the tunneling tip instead of the surface features.[94] We have been very careful to characterize and understand these artifacts. First, we always scan a cleaved graphite surface with the tips that are used to image a rough surface to ensure that the tip is capable of producing atomic-resolution images that are free of distortion. Second, we collect dozens of images from each sample to make certain that features are reproducible and that the features scale properly as the image area is changed. Finally, we analyze the images to determine the average and maximum slopes of the features that are imaged. In all the sputtered sample work on which we have reported, the surface structures never form an angle greater than 35° with respect to the horizontal plane of the sample. We do observe structures that can be attributed to tip imaging artifacts, but images with such features are never included in our data analysis.

So far we have analyzed over 1,000 STM topographs collected from more than 15 bombarded samples. The three different incident ion fluxes reported here were $J_1 = 6.9 \times 10^{13}$, $J_2 = 3.5 \times 10^{14}$ and $J_3 = 6.9 \times 10^{14}$ ions/cm^2 sec. By varying the time of exposure to the ion beam, the total fluences obtained were $Q_1 = 10^{16}$, $Q_2 = 10^{17}$ and $Q_3 = 10^{18}$ ions/cm^2, which correspond to removing 10, 100 and 1000 monolayers of carbon, respectively, assuming a sputter yield of one atom per ion.[95,96] A matrix of STM topographs collected for the three fluxes and three fluences is shown in Fig. 2, with the lateral scale of 2400Å for all the images. In addition to the ambient temperature experiments, etching was also performed at substrate temperatures of approximately 600K and 900K for the J_2 flux and Q_2 fluence, with the corresponding topographs shown in Fig. 3. The surface roughness has been greatly exaggerated in the topographs because of the expanded z-axis scale. One feature of the data presented in Fig. 2 that surprises many people is the strong dependence of the surface morphology on the ion flux. Based on the results of the theoretical work at UCLA described above, we anticipated that the flux would be important and therefore intentionally performed experiments to character the flux dependence.

The primary new feature that we have brought to this research area is the analysis of the data, which is assisted greatly by the coupling between the theoretical and experimental groups. The calculation of the auto-covariance function G(r) with Eq. 6 provided a quantitative determination in real space of the surface roughness and the short range lateral correlation.[72,73] Selected plots of G(r) vs. r are shown in Fig. 4. For a totally random surface, G(r) resembles a delta function; G(0) is the variance of the surface height h(r) (or the square of the interface width δ)[72,73] and G(r>>0)=0. The fact that the peaks in the G(r) plots of Fig. 4 have a finite autocovariance length λ means that the surfaces have some type of correlation in their structure, which is not often visible in the STM topograph. Higher fluxes produce more disordered surfaces (smaller λ), whereas higher fluences produce more correlated surfaces (larger λ).

Selected correlation functions C(q) calculated with Eq. 1 from the height profiles of Figs. 2 and 3 are shown in Fig. 5.
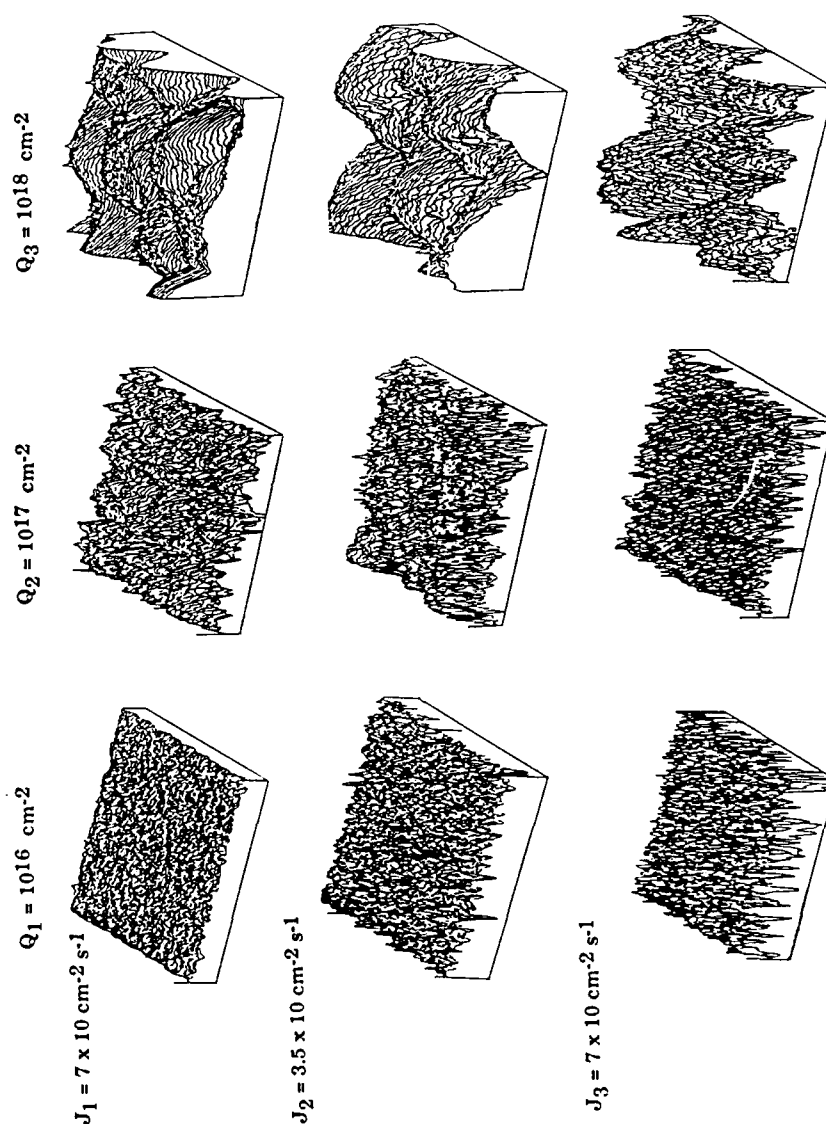
Fig. 2 Matrix of STM topographs of graphite surfaces sputtered with 5 keV Ar ions. The columns and rows of the matrix are labeled with the fluences and fluxes that caused the roughening for each surface imaged. The images all represent 2400 x 2400Å regions of the surfaces, and the scale perpendicular to the surface varies from image to image. The surface roughness is greatly exagerated so that the different surface features can be emphasized.
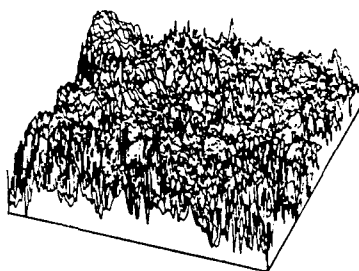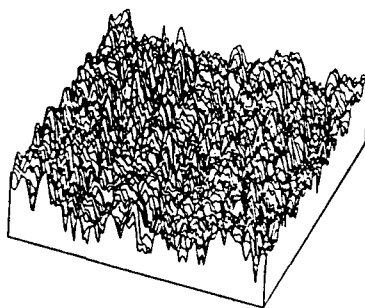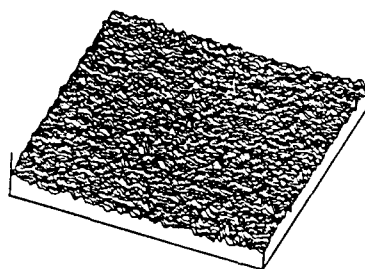
278

$T_1 = 300 \, K$

$T_2 = 600 \, K$

$T_3 = 900 \, K$

$(\, Q_2 = 10^{17} \, cm^{-2}, \quad J_2 = 3.5 \times 10 \, cm^{-2} \, s^{-1} \,)$

Fig. 3 STM topographs for surfaces sputtered with flux J_2 and fluence Q_2. The surfaces were held at approximately 300, 600 and 900K during the sputtering process. Elevated temperatures result in surfaces that are much smoother.
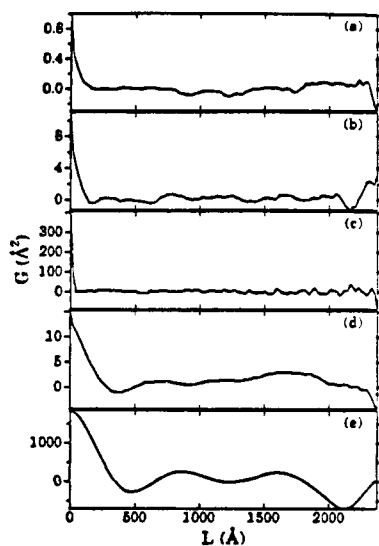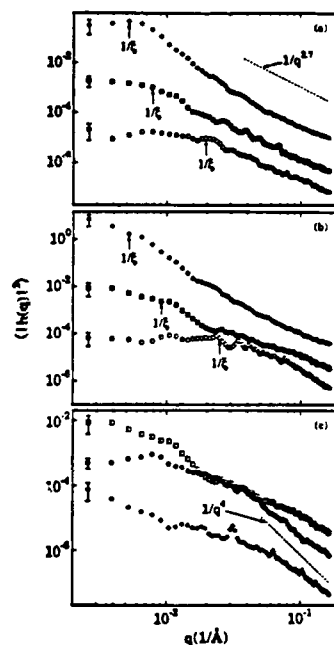
Fig. 4 Plots of the autocovariance function G as a function of length for selected surfaces imaged in Fig. 2. The interface width δ is the square root of G(0), and the autocovariance length λ is indicated on each of the plots. The conditions for the plots are as follows: (a) J_1, Q_1; (b) J_2, Q_1; (c) J_3, Q_1; (d) J_1, Q_2; and (e) J_1, Q_3.

Fig. 5 Height correlation functions:

(a) $\langle |h(q)|^2 \rangle$ for the data in Fig. 2, with $Q = 10^{16}$ ions/cm^2 (O), 10^{17} ions/cm^2 (■), and 10^{18} ions/cm^2 (◇). The crossover wavevector $q_0 = 1/\xi$ is indicated for each curve and a $1/q^{2.7}$ dependence is shown for comparison in the large q regime.

(b) $\langle |h(q)|^2 \rangle$ for topographs with the same parameters as in Fig. 5a, except that the flux is higher: $J = 3.5 \times 10^{14}$ ions/cm^2 sec. Note that there is a significant flux dependence, with $\langle |h(q)|^2 \rangle$ larger (the surfaces are rougher) for the higher flux.

(c) Temperature dependence of $\langle |h(q)|^2 \rangle$ from Fig. 3, with J_2, Q_2 and the temperature of the substrate $T = 300K$ (J), $T = 600K$ (●) and $T = 900K$ (♦). A $1/q^4$ dependence is shown for comparison in the large q regime. Note that $\langle |h(q)|^2 \rangle$ decreases (the surfaces are smoother) with increasing T.

The average $\langle |h(q)|^2 \rangle$ was obtained for each sample by summing the two-dimensional power spectrum, $|h(q)|^2$, over the azimuthal angle at increments of $1°$ for each value of q. The variance of C(q) was also calculated to provide the error bars in Fig. 5 for the correlation function of each sample. If the surface is random, C(q) will be a constant for all values of q, but if correlation is present in the surface features C(q) will have some functional dependence on q. Examining the behavior of the correlation function allowed us to determine the scaling behavior of the surfaces as a function of the wavevector q and to make comparisons to the theories of sputter erosion morphology.[97,98] Because of the absence of phase information in the height correlation function, however, it is less sensitive to uncorrelated -- but prominent -- surface features, which are much more easily visible in the real-space STM topographs. Thus, having both types of data available for exactly the same region of the surface helps greatly in understanding the structure of the surface.

The creation of correlated structures by particle radiation, which is a stochastic process that might be expected to form a totally random surface, at first seems counter-intuitive. However, the theoretical analyses of the previous section showed that the correlation arises from the various surface healing mechanisms, such as surface diffusion and evaporation-recondensation. We examined a linear version of Eq. 5 above and tested its predictions by comparing the asymptotic limits to our experimental data.[97,98] In the linear response approximation

$$\partial h(q,t)/\partial t = - w(q) h(q,t) + \eta(q,t) , \qquad (7)$$

where $w(q)$ is the q-dependent healing rate of a surface modulation of wavevector q and $\eta(q,t)$ is the reciprocal-space shot noise term. For the case of isotropic radiation erosion, which was not strictly valid because the sample was etched by an ion beam, and including annealing by an evaporation/recondensation-like mechanism and surface diffusion, the healing rate is

$$w(q) \propto J|q| + \gamma |q|^2 + D|q|^4. \qquad (8)$$

with J the flux, γ the healing rate for redeposition, and D proportional to the surface diffusion constant. Equation 7 can be solved analytically to yield the correlation function :

$$C(q,t) \sim \frac{J}{w(q)} [1 - \exp(- 2w(q)t)] . \qquad (9)$$

By expanding the exponential in Eq. (9) one can see that for small q, C(q,t) is proportional to t and independent of q, while for large q, C(q,t) is proportional to $w(q)^{-1}$ and therefore must decrease with q. Thus, there are two distinct regions in plots of C(q,t) vs. q at any given value of t and Fig. 5 shows that this type of behavior is observed experimentally. The transition should occur at the crossover wavevector $q_0 = \xi^{-1}$, defined by $w(\xi^{-1})t = 1$, which predicts that the correlation length ξ at the knee in the C(q,t) vs. q curve is proportional to the fluence $Q = Jt$ (assuming $\xi \leq (D/J)^{1/3}$). From Fig. 5a, we see that ξ increases with Q, albeit more slowly than linearly. In Fig. 5b, we show C(q,t) for the same three fluences as for Fig. 5a, but with J increased by a factor of 5. Indeed, within the uncertainties of the experimental data, ξ does not appear to have changed significantly for surfaces sputtered with the higher flux, even though these surfaces were rougher, i.e. had larger values of C(q,t), for all values of q.

We also investigated the limiting behavior of C(q,t) for large values of q. At this limit, the healing function $w(q) \propto \gamma q^2 + D q^4$, so that C(q,t) should decrease at least as fast as q^{-2}, depending on the relative values of γ and D. The observed functional dependence for samples sputter etched at roughly 300K is $C(q,t) \propto q^{-2.7}$, so apparently two different mechanisms are involved in the healing process. Since the diffusion constant D is strongly temperature dependent, a q^{-4} tail should characterize C(q,t) for surfaces sputtered at elevated temperatures. In Fig. 5c, we show C(q,t) for graphite samples that were sputtered at temperatures $T = 300, 600,$ and $900K$. Above

600K. $C(q,t)$ drops more sharply with q and, for large q, has a tail with an approximately q^{-4} dependence. At the lower surface temperatures, the q^{-2} healing process is apparently more important. The substrate temperatures during sputter etching are much too low for the process responsible for the q^{-2} behavior of $C(q,t)$ to be evaporation/recondensation. However, the incident ions create a localized thermal spike when hitting the surface that can result in the formation of impact craters. Thus, the q^{-2} mechanism for healing the surface might be characterized as a "sputter/redeposition" process in which atoms move from one spot on the surface to another as flying debris from the impact of the ion.[14]

By expanding the exponential term in Eq.(9) for the limit $q \rightarrow 0$, we see that the interface width, $W = \langle |h(q\rightarrow 0)|^2 \rangle_t^{1/2}$, should be proportional to $(Jt)^{1/2} = Q^{1/2}$, a prediction which is *independent* of the healing rate function, $w(q)$, and consistent with the stochastic nature of particle radiation. For large Q (ie. long times) and $q > 0$, the exponential term is small and can be neglected, making $C(q,t)$ independent of the fluence, i.e. there should be a saturation value Q_s above which $C(q,t)$ does not change with increasing fluence (in real space the morphology would still evolve, but the moments characterizing the surface would not). From the experimental results in Figs. 5a and 5b, we see the surprising result that W increases more like Q than $Q^{1/2}$ and that $C(q,t)$ shows a significant dose dependence at large q. Thus, the linear response theory qualitatively accounts for the smoothening processes that lead to correlated structures on sputtered graphite surfaces, but it does not provide a quantitative description of our data because it fails to predict the Q dependence of the roughening.

We also compared the general scaling description described earlier (Eq. 2) to our experimenal data. In Fig. 5a, we see an approximate power law dependence in the correlation function at large q for the *lower* ion doses, with an associated exponent v of order -2.5 to -2.9, resulting in $z \sim 1.6 - 1.8$ and $v/z \sim 1.5$. This would mean that for small q, $C(q,t) \sim t^{v/z}$ should increase *faster* than linearly with increasing time (or fluence), while the correlation length at crossover, $\xi \sim t^{1/z}$, should increase *more slowly* than linearly. Both predictions are valid for the experimental data collected to date. The values of α obtained from our experiments are $\sim 0.2 - 0.4$, which corresponds to the regime of weak nonlinearity discussed in the previous section. The results embodied in Fig. 5 thus appear to be consistent with local growth models, at least at lower fluences, which illustrates the close relationship between sputter etching and film growth.

In summary, we obtained quantitative height profiles for the initial stages of sputter etching (removal of 10-1000 monolayers) of an initially smooth surface. Ion bombarded graphite surfaces evolve a rough morphology characterized by the divergence of the correlation length, as predicted by linear response theory. By examining the q-dependence of the height correlation function, we were able to determine that two healing mechanisms, sputter/redeposition and surface diffusion, were important for forming the correlated structures on the surface. However, the experimental height-height correlation function is not quantitatively consistent with a linear response model, because it does not predict the correct fluence dependence of the surface roughening, but does have features in common with the scaling theory for sputter growth. Our work is the first to relate quantitative experimental data on the morphology of solid surfaces formed by nonequilibrium processes to the theories that have been developed to explain their formation

REFERENCES

1. J. L. Vossen and W. Kern, *Thin-Film Processes* (Academic Press, New York, 1978).

2. C. R. M. Grovenor, H.T.Z. Hentzell and D.A. Smith, Acta Met. **32**, 773 (1984).

3. R. Messier, A. P Giri and R. A Roy, J. Vac. Sci. Technol. **A 2**, 500 (1984).

4. W. K. Burton, N. Cabrera and F. C. Frank, Phil. Trans. Roy. Soc. (London) **A 243**, 299 (1951).

5. W. K. Burton and N. Cabrera, Disc. Farad. Soc. **5** , 38,40 (1949).

6. I. J. Hodgkinson and P.W. Wilson, CRC Crit. Rev. Sol. State and Mat. Sci **15** 27 (1988).

7. B. A Movchan and A. V. Demchishin, Phys. Met. Metallogr. **28**, 83 (1969).

282

8. J. A Thornton, Ann. Rev. Mat. Sci. **7**, 239 (1977).

9. R. H. Wade and J Silcox, Appl. Phys. Lett. **8**, 7 (1966).

10. A. Dirks and H.J. Leamy, *Thin Solid Films* **47**, 219 (1977).

11. J.M. Nieuwenhuisen and H. B. Haanstra, Phillips Tech. Rev. **27**, 87 (1966).

12. R. Messier and J.E. Yehoda, J. Appl Phys. **58**, 3739 (1985).

13. J.E. Yehoda and R. Messier, Appl. Surf. Sci. **22/23**, 590 (1985).

14. R. Messier and R.C. Ross, J. Appl Phys. **53**, 6220 (1982).

15. S.C. Moss and J. F. Graczyk, Phys.Rev.Lett. **23**, 1167 (1969); M.H. Brodsky and R.S.Title, Phys.Rev.Lett. **23**, 581 (1969) and F.L. Galeener, Phys.Rev.Lett. **27**, 1716 (1971)

16. H.J. Leamy and A. G. Dirks, J. Appl Phys. **49 (6)**, 3430 (1978).

17. H. Konig and G. Helwig, Optik **6**, 111 (1950); L. Reimer, Optik **14**, 83 (1957).

18. C. Herring, J. Appl Phys. **21**, 301 (1950) and in *Structure and Properties of Solid Surfaces*, eds. R. Gomer and C.S. Smith (University of Chicago, Chicago, 1953), pp. 5-72, see discussion on pg. 64.

19. S.M. Rossnagel, in *Erosion and Growth of Solids Stimulated by Atom and Ion Beams*, G.Kiriakidis, G. Carter and J. L. Whitton, eds. (Martinus Nijhoff, Dordrect, 1986),pp. 181-199.

20. R.S. Williams, R.J. Nelson and A.R. Schlier, Appl. Phys. Lett. **36**, 827 (1980), for a review, D.D. Vvedensky, S. Clarke, K.J. Hugill, A.K. Myers-Beaghton and M.R. Nilly in *Kinetics of Ordering and Growth of Surfaces*, NATO, A S I Series. **239**, ed. M. Lagally (Plenum, New york, 1990).

21. G.H. Gilmer and K. A. Jackson, *Crystal Growth and Materials*, eds. E. Kaldis and H. J. Scheel, North Holland, Amsterdam, 1977).

22. B.J. Palmer and R. G. Gordon, *Thin Solid Films*, **158**, 313 (1988); G.S. Bales, A. C. Redfield and A. Zangwill, Phys.Rev.Lett. **62**, 776 (1989).

23. S.V. Ghaisas and A. Madhukar, J. Appl Phys. **65**, 1888 (1989), and references therein.

24. M. Rasigni, G. Rasigni, F. Varnier, C. Dussert, J. Palmari, and N. Mayani, "Statistical Analysis of Rough and Random Surfaces," in *Surface Measurement and Characterizatic*, J. M Bennett, ed., Proc. SPIE 1009, pp. 68-76 (1989).

25. M.J. Vold, J. Colloid Interface Sci. **14**, 168 (1959).

26. H.J. Leamy and G.H. Gilmer, *Current Topics in Materials Science*, **6**, E. Kaldis, ed. (North-Holland, Amsterdam, 1980), pp. 309 - 344.

27. P. Meakin, J. Colloid Interface Sci. **105**, 240 (1985); D. Bensimon, B. Shraiman and S.Liang, Phys. Lett., **A102**, 238 (1984).

28. P. Meakin, CRC Critical Reviews in *Solid State and Materials Science* **13**, 143 (1987).

29. R. C. Ball and T. Whitten, Phys. Rev. **A29**, 2966 (1984).

30. K.H. Muller, J. Appl. Phys. **58**, 2573 (1985).

31. F. Family, J. Phys. **A19**, (1986) L441.

32. D. J. Srolovitz, J. Vac. Sci. Technol. **A 4**, 2925 (1986).

33. S. Ling and M.P. Anderson, J. Electr. Mat. **17**, 459 (1988).

34. G. Carter, *Erosion and Growth of Solids Stimulated by Atom and Ion Beams*, G. Kiriakidis, G. Carter and J.L. Whitton, eds. (Martinus Nijhoff, Dordrect, 1986), pp. 70-97.

35. H.P. Bader and M. A Larden, J. Vac. Sci. Technol. **B4**, 833 (1986).

36. S. Lichter and J. Chen, Phys.Rev.Lett. **56**, 1396 (1986).

37. A. Mazor, D.J. Srolovitz, P.S. Hagen and B. G. Bukiet, Phys.Rev.Lett. **60**, 424 (1988).

38. For a recent review: F. Family, Physica A, **168**, 5 61 (1990).

39. F. Family and T. Vicsek, J. Phys. **A18**, L75 (1985).

40. F. Family, *Universalities in Condensed Matter Physics*, R. Jullien, L. Peliti, R. Rammal and N. Boccara, eds., (Springer Proc. Phys.Springer Berlin, 1988).

41. T. Vicsek, *Fractal Growth Phenomena* (World Scientific, Singapore, 1989)

42. M. Kardar, G. Parisi and Y.C. Zhang, Phys.Rev.Lett. **56**, 889, (1986).

43. P. Meakin and R. Jullien, J. Phys. (Paris) **48**, 1651 (1987).

44. R. Jullien and P. Meakin, Europhys. Lett. **4**, 1385 (1987).

45. M. Plischke, Z. Racz and D. Liu, Phys. Rev. **B35**, 3485 (1987).

46. D. Liu and M. Plischke, Phys. Rev. **B38**, 4781 (1988).

47. J. Krug and H. Spohn, Phys. Rev. **A38**, 4271 (1988).

48. R. Jullien and R. Botet, J. Phys. **A18**, 2279 (1985).

49. J. G. Zabolitzky and D. Stauffer, Phys. Rev. **A34**, 1523 (1986); Phys.Rev.Lett. **57**, 1809 (1986).

50. J. Kertesz and D. E. Wolf, J. Phys., **A21**, 747 (1988).

51. D. E. Wolf and J. Kertesz, Europhys. Lett. **4**, 651 (1987).

52. J. M. Kim and J. M. Kosterlitz, Phys.Rev.Lett. **62**, 2289 (1989).

53. D. E. Wolf and J. M. Kosterlitz, Phys.Rev.Lett. **62**, 2571 (1989).

54. J. Amar and F. Family, Phys.Rev.Lett. **64**, 543 (1990).

55. T. Sun, H. Guo and M. Grant, Phys. Rev. **A40**, 6763 (1989).

56. H. Yan, D. Kessler and L. M. Sander, preprint (1989).

57. S. F. Edwards and D. R. Wilkinson, Proc. R. Soc. London, **A381**, 17 (1982).

284

58. For experimental tests of the scaling theory see for instance; M. A. Rubio, C. A. EdwardsA. Dougherty and J. P. Gollub, Phys.Rev.Lett. **63**, 1685 (1985).

59. W. W. Mullins, J. Appl Phys. **28**, 333 (1957).

60. R. P. U. Karunasiri, R. Bruinsma and J. Rudnick, Phys.Rev.Lett. **62**, 788 (1989).

61. R. Bruinsma, R. P. U. Karunasiri and J. Rudnick, *Kinetics of Ordering and Growth at Surfaces*, NATO A S I, Series B, **239**, M. Lagally, ed. (Plenum, 1990).

62. G. S. Bales, R. Bruinsma, E. A. Eklund, R.P.U. Karunasiri, J. Rudnick and A. Zangwill, *Science* **249**, 264 (1990).

63. G. S. Bales and A. Zangwill, Phys.Rev.Lett. **63**, 692 (1989); J. Vac. Sci. Technol.(to be published).

64. C. Tang, R. Bruinsma and S. Alexander, Phys.Rev.Lett. **64**, 772 (1990).

65. E. Medina, T. Hwa, M. Kardar and Y. Zhang, Phys. Rev. **A39**, 3053 (1989).

66. L. Golubovic and R. Bruinsma, Phys.Rev.Lett. **66** , 321 (1991).

67. For conservative (thermal) noise, Eq. 5 was investigated in ref. 55.

68. L. Golubovic and R. P. U. Karunasiri, submitted to Phys.Rev.Lett.

69. N. G. Nakhodkin, A. I. Shaldervan, A. F. Baramid, and S. P. Chenakin, Thin Solid Films **34**, 21 (1976).

70. S. C. Moss and J. F. Graczyk, Phys. Rev. Lett. **23**, 1167 (1969).

71. G. S. Cargill, III, Phys. Rev. Lett. **28**, 1372 (1972).

72. G. Rasigni, M. Rasigni, F. Varnier, J. Palmari, J. P. Palmari and A. Llebaria, Surf. Sci. **162**, 985 (1985).

73. M. Rasigni, G. Rasigni, F. Varnier, C. Dussert, J. Palmari, N. Mayani and A. Llebaria, SPIE **1009** (Surface Measurement and Characterization), 68 (1988).

74. P. K. Hansma and J. Tersoff, J. Appl. Phys. **61** (2), R1 (1987).

75. H. Rohrer, in *Scanning Tunneling Microscopy and Related Methods*, R. J. Behm, N. Garcia, and H. Rohrer, eds. (Kluwer Acadedmic Publishers, Dordrecht: 1990), pp.1-26
76. D. R. Denley, J. Vac. Sci. Technol. **A 8** (1) 603 (1990).

77. C. Schönenberger, S. F. Alvarado, and C. Ortiz, J. Appl. Phys. **66** (9) 4258 (1989).

78. Poirier and J. M. White, private communication.

79. M. W. Mitchell and Dawn A. Bonnell, J. Mats. Res. **5**, 2244 (1990).

80. J. H. Wilson, N. J. Zheung, U. Knipping and I. S. T. Tsong,Phys. Rev. B **38**, 8444 (1988).

81. I. H. Wilson, N. J. Zheung, U. Knipping and I. S. T. Tsong, J. Vac. Sci. Technol. **A 7**, 2840 (1989).

82. I. H. Wilson, N. J. Zheung, U. Knipping and I. S. T. Tsong, Appl. Phys. Lett. **53**, 2039 (1988).

83. I. Kojima, N. Fukumoto, and M. Kurahashi, J. Electron Spectrosc. Relat. Phenom. **50**, c9 (1990).

84. T. C. Shen, R. T. Brockenbrough, J. S. Hubacek, J. R. Tecker, and J. W. Lyding, J. Vac. Sci. Technol. **B 9**, 1376 (1991).

85. L. Porte, M. Phaner, C. H. deVilleneuve, N. Moncoffre and J. Tousset, Nucl Instrum. Meth. Phys. Res. B **44**, 116 (1989).

86. R. Coratger, A. Claverie, F. Ajustron, and J. Beauvillain, Surf. Sci. **227**, 7 (1990).

87. L. Porte, C. H. deVilleneuve and M. Phaner, J. Vac. Sci. Technol. **B 9**, 1064 (1991).

88. Th. Michely, K. H. Besocke, and G. Comsa, Surf. Sci. Lett. **230**, L135 (1990).

89. Th. Michely and G. Comsa, J. Vac. Sci. Technol. **B 9**, 862 (1991).

90. Y. Hirooka, R. W. Conn, T. Sketchley, W. K. Leung, G. Chevalier, R. Doerner, J. Elverum, D. M. Goebel, G. Gunner, M. Khandagle, B. Labombard, R. Lehmer, P. Luong, Y. Ra, L. Schmiotz, and G. Tynan, J. Vac. Sci. Tech. **A8**, 1790 (1990).

91. J. W. Rabalais and S. Kasi, Science **239**, 623 (1988).

92. For example, Carbon Fibers, Filaments and Composites, J. L. Figueirdo, C. A. Bernardo, R. T. K. Baker and K. J. Huttinger, eds. (Kluwer Academic Publishers, Dordrecht: 1990), pp. 169-440.

93. E. J. Snyder, E. A. Eklund, and R. S. Williams, Surf. Sci. Lett. **239**, L487 (1990).

94. E. J. van Loenen, D. Dijkkamp, A. J. Hoeven, J. M. Lenssinck, and J. Dieleman, Appl. Phys. Lett. **56** (18) 1755 (1990).

95. J. F. Ziegler, J. P. Biersack, and U. Littmark, *The Stopping and Range of Ions in Solids*, (Pergammon Press, New York: 1985).

96. R. Kelly, in *Ion Bombardment Modification of Surfaces*, O. Auciello and R. Kelly, eds. (Elsevier, Amsterdam: 1984), pp. 53.

97. E. A. Eklund, R. Bruinsma, J. Rudnick and R. S. Williams, submitted to Phys. Rev. Lett.

98. E. A. Eklund, Ph.D. thesis, University of California, 1991.

Thin Film Magnetism

ANISOTROPY ENERGIES AND CRITICAL BEHAVIOR OF ULTRATHIN Ni(111) FILMS GROWN ON SMOOTH AND ROUGH W(110) (invited)

YI LI, K. BABERSCHKE
Institut für Experimentalphysik, Freie Universität Berlin, Arnimallee 14,
1000 Berlin 33, Federal Republic of Germany

ABSTRACT

6 to 80 Å thin Ni(111) films were prepared on smooth and rough W(110) substrates in UHV and characterized by LEED and Auger spectroscopies. The measurements of the magnetic properties were carried out in situ by ferromagnetic resonance at 9 GHz between 300 and 600 K. We found that the effective anisotropies, which consist of surface, crystal, and stress induced anisotropy, increase with decreasing film thickness and temperature. The roughness of the substrate results in the drastic decrease of the effective anisotropy. This is attributed to the change of the surface structure and the stress within the Ni films. Furthermore we found that the Curie temperature T_c and the critical exponent β of Ni films on the smooth and rough substrates show no change.

PACS numbers: 75.70.AK, 75.50.Cc

INTRODUCTION

Ultrathin magnetic films of few layers thickness only, are of great interest for technological applications. For "magnetic engineering" the determination of the Curie temperature T_c and anisotropy energy and its dependence on the film preparation are important. A question of choice would be how sensitive is T_c and the anisotropy energy on the growth modus and the substrate conditions. Recently our understanding of the magnetic properties in ferromagnetic thin films has advanced considerably through improved experimental techniques. Much work in this field has been concentrated on the determination of the magnetic anisotropy. Ferromagnetic resonance [1–5], the magneto–optic Kerr effect [6–9], and magnetometry [10] have also been widely used for such studies. The most fascinating features observed in the experiment are the dependence of the orientation of the easy direction of the magnetization as a function of the film thickness d and the growth conditions. In the present work we present a ferro– and paramagnetic resonance study (FMR and EPR) of ultrathin Ni(111) films in UHV. The resonance experiment is performed in the

identical UHV chamber directly after the film was deposited and characterized. Magnetic resonance has the advantage of supplying two independent informations at once: (i) the resonance field H_r yields local fields and magnetization and (ii) the line width gives information on relaxation, spin fluctuations and consequently T_c. Whereas (i) is well established (e.g.,[1, 2]), the latter (ii) became possible only very recently in particular for T_c^+ [11, 12].

The FMR resonance conditions for a thin film are [13] for H in the plane:

$$(\frac{\omega}{\gamma})^2 = H_r\ [H_r + 4\pi M - \frac{2K_{eff}}{M}]\ , \quad \text{for } H_r \geq \frac{2K_{eff}}{M} - 4\pi M \tag{1}$$

$$(\frac{\omega}{\gamma})^2 = [\frac{2K_{eff}}{M} - 4\pi M]^2 - H_r^2\ , \quad \text{for } H_r \leq \frac{2K_{eff}}{M} - 4\pi M \tag{2}$$

where $\omega/2\pi$ is the microwave frequency, H_r is the external resonance field, and K_{eff} the effective anisotropy energy. $K_{eff}<0$ means that the magnetization M favors lying in the film plane (planar anisotropy). $K_{eff}>0$ means that M favors lying perpendicular to the film plane (perpendicular anisotropy). From eqs. (1) and (2), K_{eff} may be determined if M is known.

EXPERIMENT

In order to study the influence of the substrate roughness on the magnetic anisotropy and critical behavior two sorts of W(110) substrates were prepared in UHV. The W(110) surface as substrate was cleaned by several cycles of Ar ion bombardment followed by annealing cycles.The result was a smooth surface with a sharp LEED pattern and low diffuse background. To get a rough W substrate we sputtered again gently for 3 to 5 minutes. This surface did still show the bcc (110) LEED pattern, but the diffuse background was increased considerably and the LEED spot size was also enlarged by a factor of $\simeq$ 3. No complete structural analysis in real space (STM) has been made so far, but we refer the two surfaces to be : " smooth" conventional flat over 100 Å or more; and "rough" showing in addition small craters one to two atomic layers deep and a mean separation of 20 to 50 Å [14]. The ratio depth(σ)/width(ξ) of the craters is probably of the order of 0.05 to 0.1. The 6 to 80Å Ni(111) films were prepared on both W substrates and characterized with Auger and LEED in UHV as described earlier [12]. The magnetic resonance at 9 GHz was performed in situ on freshly evaporated films with the external field in or perpendicular to the film plane. The temperature of the films was varied from 300 to 600 K. In the present communication we report only [15] on data for the external field lying in the film plane and oriented along the [001] direction of the bcc(110) substrate. This is identical
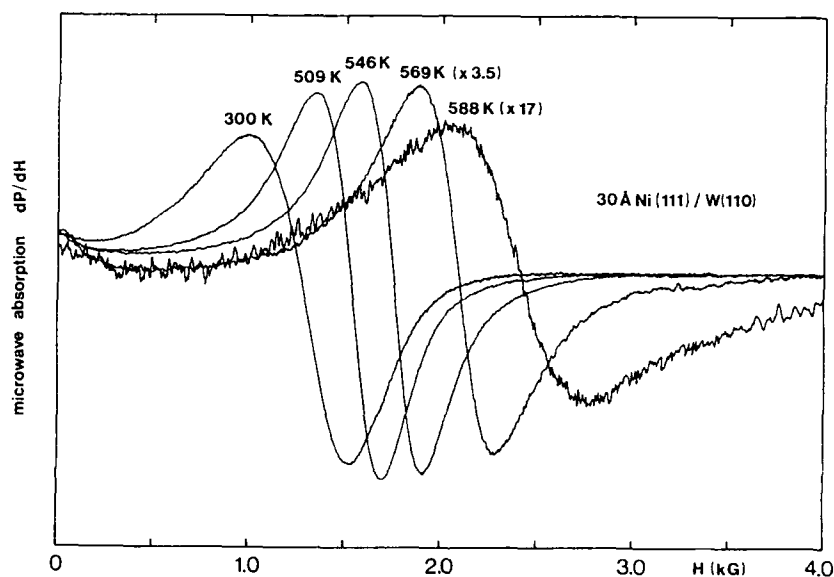
Fig.1 *FMR signal of a 30Å–rough Ni film. The signals at 300, 509, and 546K are taken with the same gain and a scan time of 4 minutes. The gain was increased by a factor of 3.5 and 17 respectively, for higher temperatures.*

to the [1̄10] direction of the fcc(111) Ni film. Along this direction the misfit beween Ni and W is about 3.6%. Fig.1 shows the experimental spectra for the 30Å rough film at various temperatures. The signal is the derivative with respect to the magnetic field of the microwave power absorption for a (standing) spin wave at a uniform mode. These signals are free of noise and can easily be detected. Only at 588K, 5K below T_c, the resonance gets broader and consequently looses in amplitude.

ANALYSIS

The resonance fields H_r obtained with the external field parallel to the film plane are plotted in Fig.2. It should be noted that the anisotropy and the magnetization in thin films are known to be strongly dependent upon the temperature [16]. In addition, the Curie temperatures in thin films are thickness dependent [12,16]. Therefore the analysis and comparison of the resonance field and the effective anisotropy for thin films should be performed for different thicknesses at the same
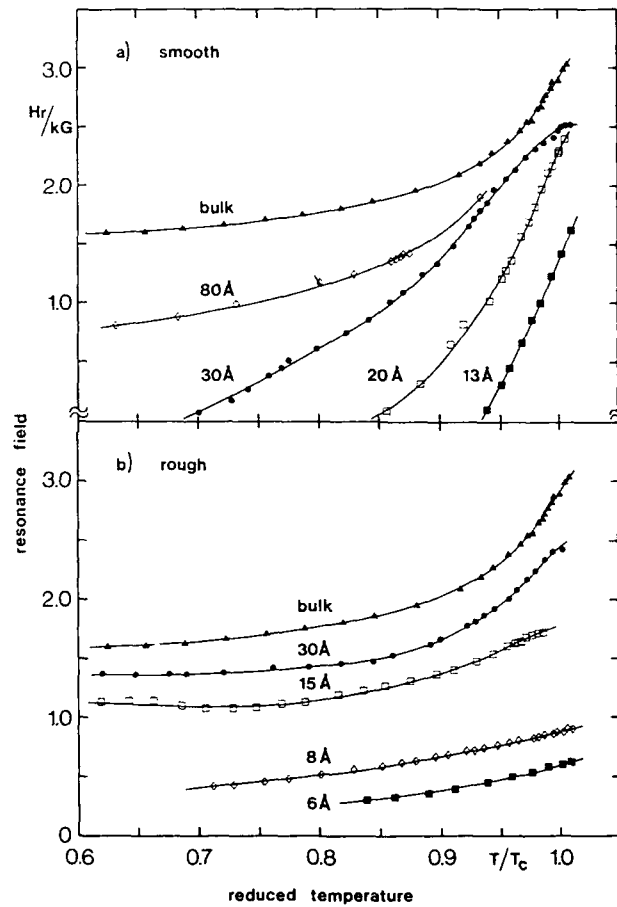
Fig. 2: *Field for resonance H_r as function of reduced temperature T/T_c. Note:Åa comparison of H_r between different films is meaningful only at the same reduced temperature. Fig.2a shows the results for 80 to 13Å films on a smooth substrate and Fig.2b for 30 to 6Å on a rough substrate. For comparison both figures show the same bulk data taken from a Ni single crystal with H_r in the (111) plane.*

reduced temperature, not at the same absolute temperature. To analyse the $H_r(T/T_c)$ we apply equation (1) (K_{eff} will be negative) and use for $M(t)$ the value from bulk Ni measurements[17] or the value given by Bergholz and Gradmann[16], both values agree to within a few percent. It is already clear from eye inspection in fig.2 that

TABLE I

Experimental results for Ni(111)/W(110); K_{eff} and H_{an} are calculated using eqs. (1)and (3). Magnetization data and thickness dependent Curie temperatures T_c are taken from refs. [12,16].

d (Å)	W(110) substrate	$T_c(d)$ (K)	$T/T_c(d)$	K_{eff} (10^5erg/cm^3)	H_{an} (kG)
6	rough	371	0.9	−27.2(8)	24.5(1)
8	"	435	0.9	−11.4(8)	12.1(1)
15	"	512	0.9	−0.67(9)	3.73(8)
30	"	593	0.9	−0.39(7)	3.50(6)
20	smooth	557	0.9	−17.09(9)	16.60(8)
30	"	592	0.9	−2.42(7)	5.10(6)
80	"	619	0.9	−0.74(7)	3.78(6)
bulk	—	630	0.9	1.30(6)	2.18(5)

$|K_{eff}|$ increases dramatically the thinner the film is. For $T/T_c \approx 0.7$, 0.85, and 0.94 corresponding to d = 30, 20, 13Å thick films H_r tends to zero applied field: the resonance vanishes. For similar Ni films on a "rough" substrate H_r shifts, in contrast, very little with respect to the bulk values and is detectable over a large temperature range. In particular for two films of the same mass deposition and an effective thickness of 30Å, K_{eff} differs by a factor of 6 at a reduced temperature of 90%. This is at T=533K (Table I). For thinner films this effect is even larger at $T/T_c = 0.95$. K_{eff} for a 13Å–smooth and a 15Å–rough film differs by a factor of 15. To compare these anisotropy energies with the ones found using other experimental techniques (e.g.,SMOKE) we list in the last column of Tab I the corresponding anisotropy fields:

$$H_{an} = 4\pi M - \frac{2K_{eff}}{M} \qquad (3)$$

We now turn to the analysis of line width ΔH_{pp}. As has been discussed previously [12] ΔH_{pp} shows a peak like broadening in the vicinity of the ferromagnetic phase transition. A broadening of the FMR line width at higher temperature has been

294
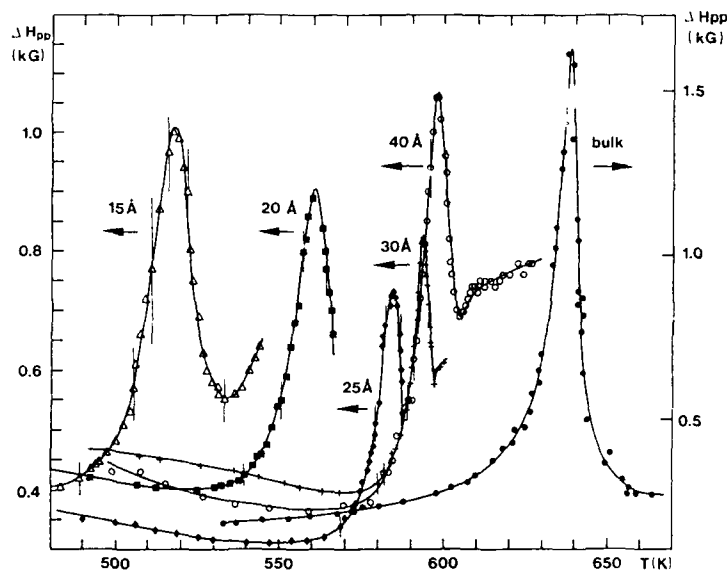
Fig.3: Peak to peak line width ΔH_{pp} as a function of temperature For 20, 25, 30, 40Å a smooth film and a 15Å rough film are shown.
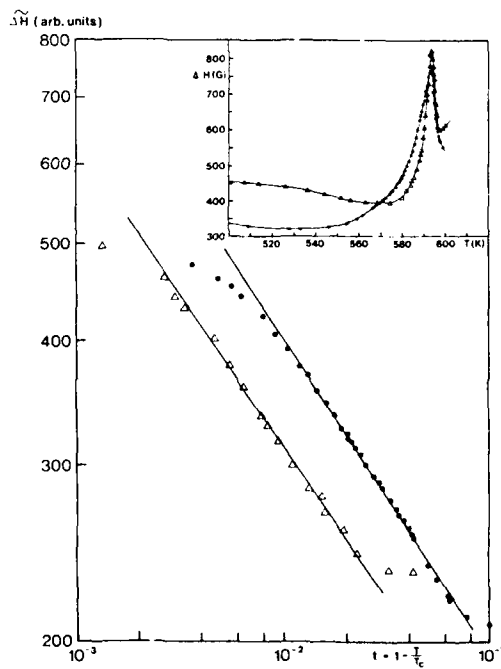
Fig.4: A log–log plot of the experimental peak to peak line widths $(\Delta H = \Delta H_{pp} - \Delta H_0)$ as a function of reduced temperature for both 30Å films. The same residual line widths $\Delta H_0 = 50G$ are subtracted. The insert shows the same data as Fig.3 for both films on an enlarged scale ($\triangle$:smooth, $\bullet$:rough)

Multilayers

reported frequently in the literature. Only very seldom one was able to pass through the phase trasition, coming from the low temperature side and follow the signal into the paramagnetic regime. In fig.3 this is shown for various films. As one can see from Tab.I : 15Å is a rough, 20Å a smooth film and for 30Å we show both rough and smooth films. T_c is a monotonic function of d and does not depend on the roughness or smoothness of the substrate. A quantitative fit for T_c (for details see [12]) yields the numbers given in the second column of Tab.I. For the two effective 30Å thick films both T_c's agree within 1K!

The $\bar{T_c}$ tail of the ΔH_{pp} peak can be fitted to a function proportional to M^{-1} [12]. This gives the possibility to determine the exponent β from $M \propto t^{-\beta}$. This is shown in Fig.4 for the two 30Å films. Both slopes are identical within the experimental error with $\beta = 0.33(4)$. The inset of Fig.4 shows the $\Delta H_{pp}(T)$ data on an enlarged scale. The maxima of the smooth(Δ) and rough films($\bullet$) coincide. The absolute values of ΔH_{pp} show a different temperature dependence, however the power law of ΔH has the same exponent.

DISCUSSION

Different approaches exist in the literature to analyze the anisotropy energy of thin films. A phenomenological treatment is:

$$K_{eff} = K_{cry} + K_{me} + 2K_s/d \qquad (4)$$

The effective anisotropy is decomposed into magnetocrystalline, magnetoelastic (stress induced), and surface contributions. As can be seen from our experimental data K_{eff} of the smooth and rough films increases dramatically with decreasing thickness. This can not be attributed to K_s only. K_{me} will also depend on the film thickness, as it does depend on the roughness of the substate. At $t = 0.9$ $K_{eff}(\text{rough})/K_{eff}(\text{smooth})$ is 0.17 for a 30Å film. There are two effects to be considered: (i) a change in K_s caused by the structure of the surface and (ii) a change in K_{me} caused by stress in the film. The first effect was discussed by Bruno et al. [18]. Roughness of the surfaces or interfaces reduces K_s. The relative change is given by

$$\Delta K_s/K_s = -2\sigma/\xi \qquad (5)$$

σ and ξ being the vertical (depth) and lateral (width) dimension of a rough structure, and $\Delta K_s = K_s(\text{rough}) - K_s(\text{smooth})$. From our discussions about the structure of the surface after sputtering we would get $\sigma/\xi \simeq 0.05$ to 0.1. After eq. (5) the reduction of K_s should be 10 to 20%. This is much smaller than the experimental values. From

Tab.I one gets for example for the 30Å film and for t = 0.9 a $\Delta K_s/K_s$ of 84% , assuming K_{cry} and K_{me} constant. The effect on K_{me} (ii) is known through the magnetostrictive effect. It is shown that the mismatch between the Ni layers and the W substrate is large and causes a large stress for smooth films[15]. Therefore it would be reasonable to expect that the larger stress in the smooth films results in a larger K_{me}. The quantitative calculation of this effect is complicated, because one needs to know the distribution of the stress in a film, as both effects (i) and (ii) are superimposed and cannot be separated easily from our experimental data.

With regard to the critical behavior, the important fact is that we found that the Curie temperature T_c and the critical exponent β of both 30Å films show no change. Thus there is no significant influence of the roughness of the substrate on T_c and β. In fact, only the finite size effect dominates the Curie temperature for our films.

In conclusion we have shown that the roughness of the substrate has a very strong influence on the magnetic anisotropy in a thin film. This fact should be of considerable help in interpreting the contradictory experimental results of the magnetic anisotropy in a thin film. In contrast to the anisotropy, the Curie temperature T_c and critical exponent β are not affected by the roughness of the substrate.

ACKNOWLEDGEMENT

REFERENCES

1.   B. Heinrich, K.B. Urquhart, A.S. Arrott, J.F. Cochran, K. Myrtle and S.T. Purcell, Phys. Rev. Lett. 59 (1987) 1756

2.   J.J. Krebs, F.J. Rachford, P. Lubitz, and G.A. Prinz, J. Appl. Phys. 53 (1982) 8058, G.A. Prinz. G.T. Rado, and J.J. Krebs, 53 (1982) 2087

3.   A. Berghaus, M. Farle, Yi Li, and K. Baberschke, in: Magnetic Properties of Low–Dimensional Systems II, eds. L.M. Falicov, F. Mejia–Lira, and Y.L. Moran–Lopez, Springer Proc. in Physics 50 (Springer, Berlin, 1990)

4.   P. Bruno, J. Phys. F18 (1988) 1291

5.   C. Chappert, K. Le Dang P. Beauvillain, H. Hurdequint D. Renard Phys. Rev. B34 (1986) 3192

6.   C. Liu and S.D. Bader, ref. [3]

7.   C.A. Ballentine, R.L. Fink, Y. Araya–Pochet and Y.L. Erskine, Appl. Phys. A49 (1989) 459

9.   J.W.D. Martens, W.L. Peeters, P.Q.J. Nederpel and M. Erman,
     J. Appl. Phys. 55 (1984) 1100
10. H.J. Elmers and U. Gradmann, Appl. Phys. A51 (1990) 255
11. M. Farle and K. Baberschke, Phys. Rev. Lett. 58. (1987) 511
12. Yi Li, M. Farle, and K. Baberschke, Phys. Rev. B41 (1990) 9596
13. S.V. Vonsovskii, ed., Ferromagnetic Resonance (Pergamon Press, Oxford, 1966)
14. E. Taglauer, Appl. Phys. A51 (1990) 238 and E. Bauer, private communication
15   for other results see: Yi Li, M. Farle, and K.Baberschke J. Mag. Mag. Mat.
     (1991) in press
16. R. Bergholz and U. Gradmann, J. Magn. Magn. Mat. 45 (1984) 389
17. H.P.J. Wijn. ed. Landolt–Börnstein, New Series, vol.19.sub a (Springer–Verlag)
18. P. Bruno and J.–P. Renard, Appl. Phys. A49 (1989) 499

MAGNETIZATION AND CURIE TEMPERATURE OF FERROMAGNETIC ULTRATHIN FILMS: THE INFLUENCE OF MAGNETIC ANISOTROPY AND DIPOLAR INTERACTIONS (invited)

P. BRUNO

Institut d'Electronique Fondamentale, Université Paris-Sud,
F-91405 Orsay CEDEX, France

and

Institut für Angewandte Physik, Universität Regensburg,
D-8400 Regensburg, Federal Republic of Germany

ABSTRACT

Theoretical investigations of the magnetization and Curie temperature of ferromagnetic ultrathin films in the presence of magnetic anisotropy and long-range dipolar interactions are presented. The Curie temperature of fcc (001) cobalt ultrathin films is calculated and compared with experimental results on Co/Cu (001) films. The influence of an external magnetic field, and the surface gradient of the magnetization are also discussed.

1 INTRODUCTION

For more than 60 years, the problem of two-dimensional ferromagnetism has been—and still is—a matter of controversy. It has been addressed for the first time in 1930 by F. Bloch [1], who pointed out that a two-dimensional Heisenberg spin system cannot be ferromagnetically ordered at finite temperature. Bloch's conjecture, based on a spin-wave argument, has been later rigorously proved by Mermin and Wagner [2], whose theorem states that a two-dimensional spin system cannot exhibit any long-range magnetic order (neither ferromagnetic, nor antiferromagnetic or other) at finite temperature, provided that

(i) the interaction is isotropic,

(ii) the interaction is short-ranged (more precisely, it must decrease more rapidly than $1/r^3$).

This theorem has stimulated a very important experimental activity, in order to check its prediction. In particular, the recent progress of preparation and characterization techniques under ultrahigh-vacuum conditions has enabled to prepare clean transition-metal single-crystal ultrathin films of high structural quality down to one atomic layer (AL) [3]. Such metallic monolayers are currently among the best experimental realizations of the theorists' concept of a two-dimensional system. Nethertheless, they unambiguously ferromagnetic order persiting down to 1 AL, with fairly high Curie temperatures (100 to 300 K) [3].

The apparent contradiction between theoretical predictions and experimental results can be removed if one remarks that none of the two basic hypotheses of the Mermin-Wagner theorem is actually fulfilled in a real system:

(i) According to Curie's symmetry principle [4], the properties of a physical system must reflect its underlying structural symmetry. A two-dimensional system is therefore intrinsically anisotropic: the axis normal to the plane is not equivalent to an axis lying in the plane. Indeed, ultrathin films have been found to exhibit strongly enhanced magnetic anisotropies [5].

(ii) The dipolar interactions, which are always present in a spin system, decrease like $1/r^3$.

The magnetic anisotropy and the dipolar interactions are several orders of magnitude weaker than the exchange interaction. In three-dimensional systems, they induce only small corrections to the pure Heisenberg behavior, and can therefore be neglected in a first approximation. The situation is completely different in the case of a two-dimensional system: as a matter of fact minute deviations from the ideal Heisenberg case discussed by Mermin and Wagner will drastically modify its qualitative behavior.

It is therefore necessary to take into account the magnetic anisotropy and the long-range dipolar interactions, in order to correctly interprete the experimental observations. In the past, many authors have discussed the thermodynamics of a two-dimensional spin system when either the magnetic anisotropy [6] or the long-range dipolar interactions [7] are considered.

In the present paper, the magnetic anisotropy and the dipolar interactions are *both* taken into account, on an equal footing. The study of this problem has been undertaken for the first time very recently [8]. For this purpose, we have used the Green-function theory of ferromagnetism, within the random-phase approximation [9].

It is found that the behavior of the system depends crucially on the effective anisotropy resulting from the competition between the magnetocrystalline anisotropy and the shape anisotropy (due to the dipolar interactions):

(i) When the effective anisotropy leads to an easy-magnetization axis perpendicular to the film plane, a gap occurs at the bottom of the spin-wave spectrum. As a consequence of this gap, long-range ferromagnetic order is allowed, with a non-zero Curie temperature. In this case the long range of the dipolar interactions produces only small corrections.

(ii) The situation is completely different when the effective anisotropy favors an easy-magnetization plane. Since the spins can be freely rotated within the plane, the spin-wave spectrum remains gapless. The effective anisotropy alone is therefore not able to stabilize the ferromagnetic order at non-zero temperature. In this case, the long range of the dipolar interactions turns out to play the decisive rôle in stabilizing the ferromagnetic order at non-zero temperature.

The Curie temperature T_c of ultrathin films has been calculated. For monolayers, approximated analytical expressions of T_c are given, allowing a physically transparent interpretation of the respective influence of exchange, anisotropy, and dipolar interactions. Numerical calculations of T_c have been performed for ultrathin films with thickness ranging between 1 and 20 AL, allowing quantitative comparison with experimental results. In particular, the case of fcc (001) cobalt films on (001) copper single-crystal substrates, which has been widely investigated experimentally [10, 11], will be discussed in detail.

The influence of an applied magnetic field has been also investigated. It is found that two-dimensional ferromagnets are much more sensitive to an external field than

three-dimensional ones, particularly in the easy-plane case. This can lead to very serious difficulties for the experimental determination of the dependence of the spontaneous magnetization versus temperature.

The depth-profile of the magnetization has been calculated. Important surface magnetization gradients are exhibited only by fairly thick films, whereas ultrathin films remain very homogeneously magnetized up to the Curie temperature.

2 MODEL

The ultrathin film is described by an array of localized spins S, and is assumed to have a fcc structure, with the (001) axis normal to the film plane. The exchange interaction is represented by a Heisenberg Hamiltonian

$$\mathcal{H}_{ex} = -\sum_{(i,j)} J \, \vec{S}_i \cdot \vec{S}_j \, , \tag{1}$$

where the indices i and j label the atomic sites, J is the exchange integral, and the notation (i,j) indicates that the sum is restricted to nearest neighbors pairs. The dipolar Hamiltonian is given by the usual expression

$$\mathcal{H}_{dip} = \frac{1}{2} \sum_{i \neq j} \frac{(2\mu_B)^2}{r_{ij}^3} \left[\vec{S}_i \cdot \vec{S}_j - 3 \left(\vec{S}_i \cdot \vec{u}_{ij} \right) \left(\vec{S}_j \cdot \vec{u}_{ij} \right) \right] . \tag{2}$$

The magnetocrystalline anisotropy is introduced as a pseudo-dipolar interaction between nearest neighbors,

$$\mathcal{H}_K = -\frac{K}{2} \sum_{(i,j)} \left[\vec{S}_i \cdot \vec{S}_j - 3 \left(\vec{S}_i \cdot \vec{u}_{ij} \right) \left(\vec{S}_j \cdot \vec{u}_{ij} \right) \right] . \tag{3}$$

One easily checks that in the bulk, the different terms cancel out and give no net anisotropy, whereas at the interfaces the missing neighbors give rise to the magnetic interface anisotropy. Actually, this is the form used originally by Néel to introduce the concept of interface anisotropy [12]. The sign convention contained in the above equation implies that positive (negative) values of K favor perpendicular (in plane) magnetization.

The strength of the different interactions is best expressed in field units; we therefore define the exchange field H_{ex}, the interface anisotropy field H_K^S, and the dipolar field H_a, given respectively by

$$2\mu_B H_{ex} = 2JS \, , \tag{4}$$

$$2\mu_B H_K^S = 2KS \, , \text{ and} \tag{5}$$

$$2\mu_B H_a = 4\pi M_0 . \tag{6}$$

The numerical calculations will be done for cobalt films, and we give to the parameters the bulk values, i.e $S = 0.86$, $4\pi M_0 = 18.2$ kOe, and $H_{ex} = 1870$ kOe. The interface anisotropy H_K^S is a variable parameter; values ranging between -50 and +50 kOe are representative for ultrathin films [5].

Since the dipolar interactions contribute to the total anisotropy field via the shape anisotropy, the direction spontaneously assumed by the magnetization is determined by the sign of the effective anisotropy field H_K^{ef}, given by

$$H_K^{ef} = \frac{2H_K^S}{N} - 4\pi M_0 \, . \tag{7}$$

where N is the number of atomic planes; for positive (negative) values of H_K^{sf}, the spontaneous magnetization lies perpendicular to the plane (in the plane).

3 GREEN-FUNCTION THEORY

The formalism of the Green-function theory of ferromagnetism will be briefly sketched below; the reader is refered to the original papers on this subject for more details [9]. Let us consider the double-time temperature-dependent Green-function

$$G_{i,j}^{\pm}(t - t', \alpha) = \langle\langle S_i^{\pm}(t); \exp(\alpha S_j^z(t'))S_j^-(t')\rangle\rangle , \tag{8}$$

where (A and B being operators in the Heisenberg representation)

$$\langle\langle A(t); B(t')\rangle\rangle \equiv -i\theta(t - t')\langle[A(t); B(t')]\rangle . \tag{9}$$

In the above equation the square brackets indicate the commutator, the angular brackets the thermodynamical average, and $\theta(t) = 0$ for $t < 0$ (respectively $\theta(t) = 1$ for $t > 0$). The energy dependent Green functions $\langle\langle A; B\rangle\rangle_E$ and $G_{i,j}^{\pm}(E, \alpha)$ are the Fourier transform with respect to the time of $\langle\langle A(t); B(t')\rangle\rangle$ and $G_{i,j}^{\pm}(t - t', \alpha)$, respectively. The former is related to the correlation function $\langle B(t')A(t)\rangle$ by the spectral theorem

$$\langle B(t')A(t)\rangle = \lim_{\epsilon \to +0} i \int_{-\infty}^{+\infty} \frac{\langle\langle A; B\rangle\rangle_{\hbar\omega+i\epsilon} - \langle\langle A; B\rangle\rangle_{\hbar\omega-i\epsilon}}{\exp(\hbar\omega/k_BT) - 1} e^{-i\omega(t-t')} d\omega . \tag{10}$$

With the help of this theorem, the knowledge of $G_{i,i}^{+}(E, \alpha)$ thus yields the correlation function $\langle\exp(\alpha S_i^z)S_i^- S_i^+\rangle$. The later can finally be related to $\langle S_i^z\rangle$ (i.e. to the magnetic moment at site i) by using the relation

$$S_i^- S_i^+ = S(S + 1) - S_i^z - (S_i^z)^2 . \tag{11}$$

The equation of motion of $G_{i,j}^{\pm}(E, \alpha)$ is

$$EG_{i,j}^{\pm}(E, \alpha) = \delta_{i,j}\frac{\Theta_i^{\pm}(\alpha)}{2\pi} + \langle\langle[S_i^{\pm}; \mathcal{H}]; \exp(\alpha S_j^z)S_j^-\rangle\rangle , \tag{12}$$

where

$$\Theta_i^{\pm}(\alpha) \equiv \langle[S_i^{\pm}; \exp(\alpha S_i^z)S_i^-]\rangle . \tag{13}$$

The second term on the right hand side of Eq. 12 is a higher order Green function, since it contains terms of the form $\langle\langle S_l^z S_i^{\pm}; \exp(\alpha S_j^z)S_j^-\rangle\rangle$. Eq. (12) can be linearized by the RPA decoupling procedure, which consists in performing the substitution

$$S_i^{\pm,z}S_l^{\pm,z} \quad \to \quad \langle S_i^{\pm,z}\rangle S_l^{\pm,z} + S_i^{\pm,z}\langle S_l^{\pm,z}\rangle - \langle S_i^{\pm,z}\rangle\langle S_l^{\pm,z}\rangle \tag{14}$$

in the commutator $[S_i^{\pm}; \mathcal{H}]$. One thus gets a set of linear equations that must be solved self-consistently, since it contains the thermodynamical averages $\langle S_i^z\rangle$. The problem is then equivalent to diagonalizing a spin-wave Hamiltonian with self-consistently renormalized interaction parameters. The physical interpretation of the RPA is that some correlations between the motions of spins located on different atoms are neglected. It is a good approximation at low temperature where the spins are almost frozen, and at high temperature where all motions are decorrelated. In these two extreme regimes it yields the results of the spin-wave theory and of the molecular field theory, respectively

In the intermediate regime, it provides a useful interpolation and, in particular, gives a good approximation of the Curie temperature.

Most complications arise for the lack of translational symmetry along the direction normal to the plane, and from the dipolar interactions, which couple the left (S_i^+) and right polarized (S_j^-) spin operators. As a consequence the polarization of the normal modes is no longer circular, but elliptical. The detailed formalism will be presented elsewhere [13].

In the case of a single atomic layer, the Curie temperature is given as a function of the spin-wave spectrum *at zero kelvin* by the simple expression

$$k_B T_c = \frac{S+1}{3} \left(\int \frac{N^{\text{eff}}(E)}{E} dE \right)^{-1} . \tag{15}$$

In the above equation, the effective density of states $N^{\text{eff}}(E)$ is the product of the usual density of states $N(E)$ and of a factor $D(E)$ which takes into account the ellipticity of the spin waves. The factor $D(E)$ measures the spin reduction due to the excitation of a spin wave of energy E; for a circularly polarized spin wave, $D(E) = 1$, but for an elliptically polarized spin wave, one has $D(E) > 1$, and $D(E)$ increases to infinity as the ellipticity increases [8].

4 CURIE TEMPERATURE OF A MONOATOMIC LAYER

It is clear from Eq. 15 that the Curie temperature a monoatomic film is governed by the effective density of states at the bottom of the spin-wave spectrum. For a pure two-dimensional Heisenberg system, the effective density of states is constant for $E \to 0^+$, and the integral diverges in Eq. 15, giving $T_c = 0$, in agreement with the Mermin-Wagner theorem.

If the magnetic anisotropy and the long-range dipolar interactions are taken into account, the spin-wave spectrum is strongly modified [8], and one obtains a non-zero Curie temperature.

(i) In the case of a perpendicular easy-axis ($H_K^{\text{eff}} > 0$), the effective anisotropy opens a gap of width

$$\Delta = 2\mu_B H_K^{\text{eff}} \tag{16}$$

at the bottom of the spin-wave spectrum, as shown on Fig. 1a. This gap prevents the divergence of the integral in Eq. 15, and leads to a non-zero Curie temperature

$$T_c \approx \frac{4\pi(S+1)}{3} \frac{2JS}{\ln(4\pi 2JS/\Delta)} . \tag{17}$$

In this case, the inclusion of the long range of the dipolar interactions gives only a negligible correction to the above result.

(ii) In the case of easy-plane anisotropy ($H_K^{\text{eff}} < 0$), one has a completely different situation. As can be seen on Fig. 1b, if only the effective anisotropy is taken into account, the effective density of states $N^{\text{eff}}(E)$ remains step-like at $E = 0$ (solid line), thus yielding $T_c = 0$. If also the long range of the dipolar interactions is considered (dashed line), a depletion (pseudo-gap) of width

$$\Delta' \approx 2\mu_B \frac{H_d}{8} \left(\frac{2\mu_B |H_K^{\text{eff}}|}{2JS} \right)^{1/2} \tag{18}$$
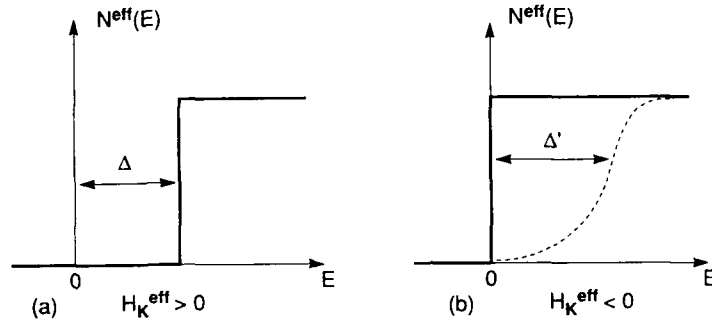
Figure 1: Sketch of $N^{eff}(E)$ as a function of E at the bottom of the spin-wave spectrum, when taking into account the effective anisotropy only (solid line), or both the long range of the dipolar interactions and the effective anisotropy (dashed line). (a): perpendicular easy axis ($H_K^{eff} > 0$). (b): easy-plane anisotropy ($H_K^{eff} < 0$).

appears at the bottom of the spin-wave spectrum. This *pseudo-gap* removes the divergence of the integral in Eq. 15, and one obtains for the Curie temperature

$$T_c \approx \frac{4\pi(S+1)}{3} \frac{2JS}{\ln(4\pi 2JS/\Delta')} .\qquad(19)$$

The concept of pseudo-gap has been already introduced in a previous publication [8].

It is quite remarkable that the Curie temperatures of monolayers with perpendicular easy axis and with easy-plane anisotropy are given by very similar formulae (Eqs. 17 and 19), although the mechanism of stabilization of the ferromagnetism is quite different in both cases. However, Δ' is generally expected to be about one order of magnitude smaller than Δ, because of the occurence of the very large exchange energy at the denominator in Eq. 18. Therefore, for similar systems, the Curie temperature should be higher in the case of perpendicular easy axis than in the case of easy-plane anisotropy.

If we consider the respective rôle of the different interactions, we see that the Curie temperature is proportional to the exchange energy, whereas the anisotropy and the dipolar interactions enter the expression of T_c only as a logarithm. Although the latter must be non-zero in order to stabilize the ferromagnetic order at non-zero temperature, the Curie temperature will not depend very sensitively on them. In this sense, they play merely the role of a *trigger* for the ferromagnetism. On the other hand, T_c is expected to be strongly influenced by the exchange energy and by the coordination number; thus larger T_c's should be observed for hcp (0001) or fcc (111) monolayers (coordination 6), than for fcc (001) monolayers (coordination 4).

5 CURIE TEMPERATURE OF FCC (001) COBALT FILMS

The Curie temperature of fcc (001) cobalt ultrathin films grown onto (001) single-crystal copper substrates has been experimentally investigated by different groups. It is a very interesting test-system for our calculations, since it has an easy-plane anisotropy, the case for which the long range of the dipolar interactions plays a decisive role. However, it has given rise to much controversy.

(i) The group of D. Pescia in Zürich and Jülich has found that the Curie temperature of one atomic layer of fcc (001) cobalt on (001) copper is *much higher than 450 K* [10]. Actually they found no significant variation of the magnetization up to 450 K, and did not measure at higher temperature in order to prevent any alteration of the samples.

(ii) On the other hand, a collaboration between the groups of J. Kirschner in Berlin and R. Miranda in Madrid has studied the same system, and finds that the Curie temperature of the monolayer is *lower than 50 K*.

This strong contradiction is puzzling. It is clear that at least in one case, the system under investigation is not the claimed clean monolayer. The most convincing structural information is given by the Berlin-Madrid group who used jointly the Auger-breaks method, the medium-energy electron-diffraction (MEED) intensity oscilations, and the thermal energy atomic scattering (TEAS) intensity oscillations for the thickness calibration, and very recently performed *in situ* scanning tunnelling microscopy (STM) investigations of the growth mode [11]. The Zürich-Jülich group relied mainly on the Auger-breaks method for the thickness calibration [10], which might be misleading [14].

In order to tentatively explain their surprisingly high monolayer Curie temperature, the Zürich-Jülich group suggested that such a high Curie temperature might be due the long-range dipolar interactions [10]. This interpretation is in contradiction with our numerical calculations (see below), which yield $T_c = 145$ K for one atomic layer; therefore, according to the present theoretical model, the dipolar interactions cannot explain the high monolayer Curie temperature reported by the Zürich-Jülich group. Moreover, if this interpretation were correct, the reported effect should be universal, since the dipolar interactions are present in every system; however, such a high monolayer Curie temperature has never been observed for any other system.

We have performed numerical calculations of the Curie temperature for ultra-thin fcc (001) cobalt films. Since the effective anisotropy is dominated by the shape anisotropy, we have set $H_K^S = 0$. The long range of the dipolar interaction is taken into account. The calculations have been performed by solving numerically the self-consistent RPA equations and sampling the first two-dimensional Brillouin zone. No other approximation than the RPA has been made. The results are displayed on Fig. 2 (solid circles), compared with the experimental data for Co/Cu (001) from the Berlin-Madrid group (open squares) [11]. One observes a fairly good agreement between the theoretical and experimental results, except for cobalt thicknesses smaller than 2 AL. However, this discrepancy can tentatively be explained as follows. The Berlin-Madrid group reports a significant drop of the Curie temperature under coating with copper, as shown on Fig. 2. This indicates that the contact between Co and Cu tends to reduce the Curie temperature, and this effect should be the stronger, the thinner the cobalt film. Thus the discrepancy at very low cobalt thickness can be ascribed to the influence of the copper substrate, which is not considered in the theoretical calculations.
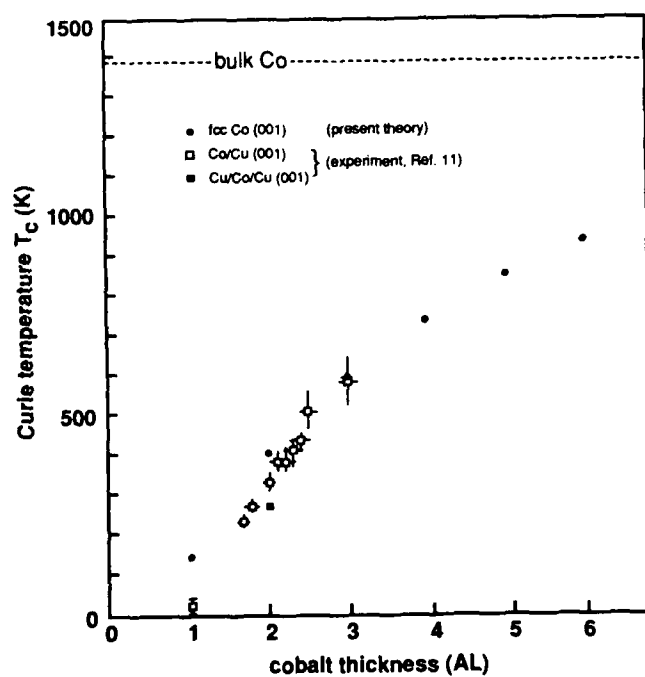
Figure 2: Curie temperature of ultrathin fcc (001) Co films: theoretical results (solid circles), and experimental data for Co/Cu (001) from [11] (open squares); the closed square indicates the effect of coating with Cu

Table I: Magnetization deviation $\Delta M(H) = M(H) - M(0)$ (normalized to the ground state magnetization M_0) induced by an external field H at $T_c/2$, calculated for bulk fcc Co and for Co monolayers with perpendicular easy axis ($H_K^{\text{ef}} > 0$) and easy plane anisotropy ($H_K^{\text{ef}} < 0$)

H (Oe)	$\Delta M(H)/M_0$ at $T_c/2$		
	bulk Co	Co monolayer	
		perpendicular	in plane
	$T_c = 1388$ K	$T_c = 235$ K	$T_c = 145$ K
1	$< 10^{-3}$	$< 10^{-3}$	0.7×10^{-2}
10	$< 10^{-3}$	$< 10^{-3}$	4.0×10^{-2}
10^2	$< 10^{-3}$	$< 10^{-3}$	9.1×10^{-2}
10^3	0.1×10^{-2}	0.5×10^{-2}	13.3×10^{-2}
10^4	0.2×10^{-2}	3.6×10^{-2}	18.1×10^{-2}
10^5	1.5×10^{-2}	12.2×10^{-2}	24.3×10^{-2}

6 FIELD DEPENDENCE OF THE MAGNETIZATION

The quantity of primary interest in a ferromagnet is the spontaneo·s magnetization (the order parameter). Because of the general tendency of magnetic bodies to break into domains, the magnetization measured in zero field (the remanent magnetization) is usually smaller than the spontaneous magnetization. The sample can be brought into technical saturation by applying an external field, but the magnetization is then modified by the field. Fortunately, in three-dimensional ferromagnets, the influence of an external field on the magnetization is very weak, at least at temperatures well below T_c, thus allowing the spontaneous magnetization to be measured to a good accuracy. It is not clear a priori that this holds also for two-dimensional ferromagnets.

We have calculated the magnetization deviation $\Delta M(H) = M(H) - M(0)$ induced by an external field H at $T_c/2$, for bulk cobalt, and for cobalt monolayers with perpendicular easy axis ($H_K^{\text{ef}} > 0$) and easy plane anisotropy ($H_K^{\text{ef}} < 0$). The field was applied along the easy axis (respectively in the easy plane). The results are displayed in Table I. As mentioned above, it is seen that the magnetization of a three-dimensional ferromagnet is very insensitive to an external field: a field of about 100 kOe is needed in order to induce a magnetization deviation of 1 percent. The sensibility to the external field appears to be much greater for two-dimensional ferromagnets, in particular in the case of easy-plane anisotropy. In the latter case, minute fields are sufficient to induce a sizable increase of the magnetization. Much care should be given to this problem when attempting to measure the temperature dependence of the spontaneous magnetization in ultrathin films, especially as the Curie temperature is approached.

7 MAGNETIZATION PROFILE

For the surface of a semi-infinite ferromagnet, the magnetization versus temperature is known to drop twice as fast as for the bulk [15]. This leads to a strong surface gradient of the magnetization. Much effort has been done to experimentally observe this surface magnetization gradient in ultrathin films [16] or at the surface of a bulk ferromagnet [17]. However, as discussed by Korecki et al. [18], it is not clear that
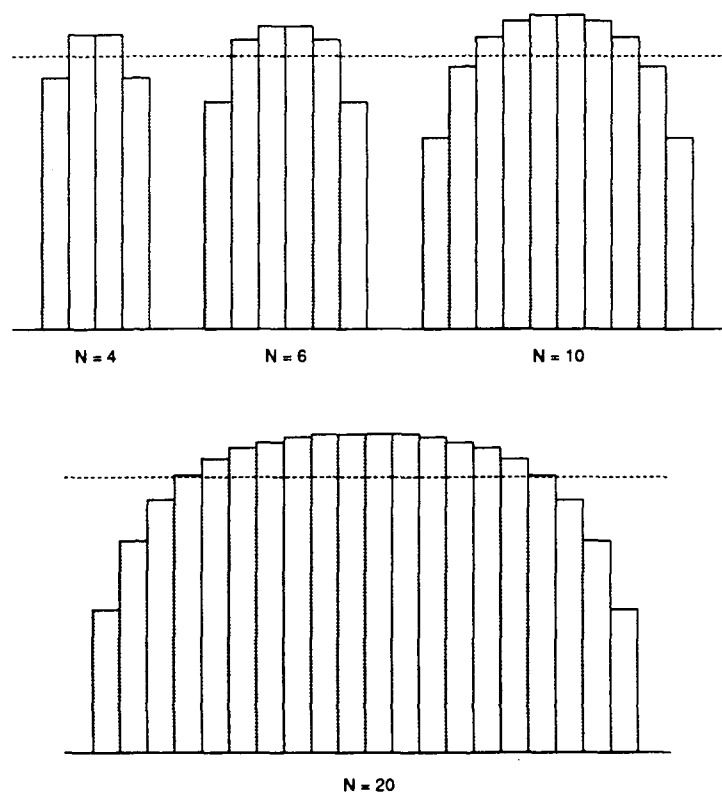
Figure 3: Reduced magnetization profile at T_c calculated for fcc (001) cobalt ultrathin films of various thicknesses

the same gradient is to be expected at the surface of an ultrathin film and of a bulk ferromagnet.

In order to study the magnetization profile we define the normalized layer-dependent magnetization $m(l,T)$ by

$$m(l,T) = \frac{N\,M(l,T)}{\sum\limits_{n=1}^{N} M(n,T)} \ , \quad (l = 1 \text{ to } N) \ , \tag{20}$$

where $M(l,T)$ is the magnetization of layer l at temperature T, and N the number of atomic layers. The normalization is done with respect to the average magnetization of the film. This allows the magnetization profile at T_c to be defined by

$$m(l,T_c) = \lim_{T \to T_c^-} m(l,T) \ . \tag{21}$$

The magnetization profile at T_c of various fcc (001) cobalt ultrathin films (with $H_K^S = 0$) has been calculated. The results are shown on Fig. 3. Since the surface magnetization gradient increases from zero whith increasing temperature, $m(l,T_c)$ represents an upper limit for the surface gradient. This figure clearly shows that for films consisting of only a few atomic layers, the magnetization remains very homogeneous up to the Curie temperature. Important magnetization gradients are exhibited only by fairly thick films. These conclusions are well supported by the experimental observations of Korecki et al. [18].

8 CONCLUSION

A random-phase approximation Green-function theory of two-dimensional ferromagnets with magnetic anisotropy and dipolar interactions has been presented. It yields a physically transparent interpretation of the respective rôle of the different interactions with respect to the stabilization of the long-range ferromagnetic order at non-zero in two-dimensional ferromagnets. Quantitative calculations of the Curie temperature of ultrathin fcc (001) cobalt films are in good agreement with experimental results of the Berlin-Madrid group [11] for Co/Cu (001) films; the very high monolayer Curie temperature reported for the same system by the Zürich-Jülich group [10] is inconsistent with the present theoretical investigations. It has been shown that unlike bulk materials, ultrathin films are very sensitive to an external magnetic film, especially in the case of easy-plane anisotropy. Finally, we have discussed the problem of the magnetization gradient at the surface of ultrathin films.

ACKNOWLEDGEMENTS

REFERENCES

[1] F. Bloch, Z. Phys. 61, 206 (1930)

310

[2] N.D. Mermin and H. Wagner, Phys. Rev. Lett. 17, 1133 (1966)

[3] W. Dürr, M. Taborelli, O. Paul, R. Germar, W. Gudat, D. Pescia, and M. Landolt, Phys. Rev. Lett. 62, 206 (1989); U. Gradmann, M. Przybylski, H.J. Elmers, and G. Liu, Appl. Phys. A 49, 563 (1989)

[4] P. Curie (1908), in Œuvres de Pierre Curie, Société Française de Physique, Paris; R.R. Birss, Selected Topics in Solid State Physics, vol. III: Symmetry and Magnetism, edited by E.P. Wolfarth, North-Holland, Amsterdam, 1964

[5] U. Gradmann, J. Magn. Magn. Mat. 54-57, 733 (1986); P. Bruno and J.P. Renard, Appl. Phys. A 49, 499 (1989)

[6] C. Herring and C. Kittel, Phys. Rev. 81, 869 (1951); W. Döring, Z. Naturforsch. 16a, 1008 (1961); W. Döring, Z. Naturforsch. 16a, 1146 (1961); A. Corciovei, Phys. Rev. 130, 2223 (1963); S.B. Khokhlachev, Sov. Phys.-JETP 43, 137 (1976); K. Binder and D.P. Landau, Phys. Rev. B 13, 1140 (1976); R.B. Stinchcombe, J. Phys. C: Solid State Phys. 14, 397 (1981); M. Bander and D.L. Mills, Phys. Rev. B 38, 12015 (1988); M.A. Continnentino and E.V. Lins de Mello, J. Phys.: Condens. Matter 2, 3131 (1990)

[7] S.V. Maleev, Sov. Phys.-JETP 43, 1240 (1976); V.L. Pokrovskiĭ and M.V. Feĭgel'man, Sov. Phys.-JETP 45, 291 (1977); M.V. Feĭgel'man, Sov. Phys.-JETP 49, 395 (1979); Y. Yafet, J. Kwo, and E.M. Gyorgy, Phys. Rev. B 33, 6519 (1986)

[8] P. Bruno, Phys. Rev. B 43, 6015 (1991); A. Rettori and M.G. Pini, preprint (1991)

[9] N.N. Bogolyubov and S.V. Tyablikov, Sov. Phys. Dokl. 4, 589 (1959); R.A. Tahir-Kheli and D. ter Haar, Phys. Rev. 127, 88 (1962); H.B. Callen, Phys. Rev. 130, 890 (1963)

[10] D. Pescia, G. Zampieri, M. Stampanoni, G.L. Bona, R.F. Willis, and F. Meier, Phys. Rev. Lett. 58, 933 (1987); M. Stampanoni, D. Pescia, G. Zampieri, G.L. Bona, A. Vaterlaus, and F. Meier, Surf. Sci. 198/190, 736 (1987); T. Beier, H. Jahrreiss, D. Pescia, T. Woike, and W. Gudat, Phys. Rev. Lett. 61, 1875 (1988); W. Dürr, T. Woike, T. Beier, and D. Pescia, J. Phys. (Paris) 49, C8-1615 (1988); D. Kerkmann, Appl. Phys. A 49, 523 (1989); D. Kerkmann, J.A. Wolf, D. Pescia, T. Woike, and P. Grünberg, Solid State Commun. 72, 963 (1989); L. Smardz, U. Koebler, D. Kerkmann, F. Schumann, D. Pescia, and W. Zinn, Z. Phys. B 80, 1 (1990)

[11] C.M. Schneider, J.J. de Miguel, P. Bressler, J. Garbe, S. Ferre, R. Miranda, and J. Kirschner, J. Phys. (Paris) 49, C8-1657 (1988); J.J. de Miguel, A. Cebollada, J.M. Gallego, S. Ferrer, R. Miranda, C.M. Schneider, P. Bressler, J. Garbe, K. Bethe, and J. Kirschner, Surf. Sci. 211/212, 732 (1989); C.M. Schneider, P. Bressler, P. Schuster, J. Kirschner, J.J. de Miguel, and R. Miranda, Phys. Rev. Lett. 64, 1059 (1990); J. Kirschner, communication at the First Kyoto-Duisburg Workshop on Ultrathin Magnetic Films and Multilayers, Duisburg, 1991

[12] L. Néel, C. R. Acad. Sci. 137, 1468 (1953); L.Néel, J. Phys. Radium 15, 376 (1954)

[13] P. Bruno, to be published (1991)

[14] C. Argile and G.E. Rhead, Surf. Sci. Reports 10, 277 (1989)

[15] G.T. Rado, Bull. Am. Phys. Soc. 2, 127 (1957)

[16] J. Tyson, A.H. Owens, J.C. Walker, and G. Bayreuther, J. Appl. Phys. 52, 2487 (1981)

[17] D.T. Pierce, R.J. Celotta, J. Unguris, and H.C. Siegmann, Phys. Rev. B 26, 2566 (1982)

[18] J. Korecki, M. Przybylski, and U. Gradmann, J. Magn. Magn. Mat. 89, 325 (1990)

MORPHOLOGY AND MAGNETIC PHASE TRANSITIONS
OF MONOLAYER-RANGE Fe FILMS ON Au(001)

Y.-F. LIEW AND G.-C. WANG
Rensselaer Polytechnic Institute, Department of Physics, Troy, NY 12180-3590

ABSTRACT

We have studied the morphology and magnetic phase transitions of monolayer-range Fe films on a reconstructed Au(001) surface using the combination of High-Resolution Low-Energy Electron Diffraction (HRLEED) and Surface Magneto-Optic Kerr Effect (SMOKE) techniques. Through the measurement of energy dependent angular profiles of the specularly diffracted beam, we discovered a simple method to determine not only the interfacial spacings (Fe-Au and Fe-Fe) but also to detect the build up of the second layer. For a one-level (2-D) Fe films with coverage of ~ 0.6 monolayer (ML) perpendicular magnetization was observed. For a 1 ML equivalent 3-D film both perpendicular and in-plane magnetization were observed. The magnetic phase transitions of these magnetic islands showed finite size broadening effect. The perpendicular saturation magnetization decreases with temperature above 100°C but never vanishes and the magnetization curve has no hysteresis loop above ~ 120°C. The implication of superparamagnetism is discussed.

INTRODUCTION

The study of magnetic properties of thin films, in particular the magnetic phase transition and magnetic anisotropy, has attracted considerable interest. Theoretical predictions on perpendicular magnetic anisotropy in ultrathin ferromagnetic films[1, 2] provide the impetus for researchers to study and engineer such a system. Both the properties mentioned, among others, are of great technological importance to the data storage industry. Despite the wealth of experimental data, many questions still awaits conclusive experimental confirmation and answers[1, 3]. One example is the magnetic phase transition of 2-D magnetic films. The strong coverage dependence of the magnetic phase transitions and magnetic anisotropy in films of submonolayer coverage remains unsolved. Many disagreements are attributed to the uncertain morphology of the films. The growth and characterization of such films is itself a challenging task. In particular the determination of the submonolayer coverage and morphology of ultrathin film demands a highly surface sensitive tool with a very good resolution. Among the advanced techniques that has been used are Auger electron spectroscopy, X-ray photoelectron forward scattering, Low-energy electron diffraction and Scanning tunneling microscopy[4-6]. We have used a High-Resolution Low-Energy Electron Diffractometer (HRLEED)[7] with angular intensity distribution analysis to monitor and study the growth, coverage and morphology of ultrathin Fe films grown on the reconstructed Au(001) surface.

In this paper we present the effect of morphology of monolayer-range Fe films/Au(001) on the magnetic phase transitions and magnetic anisotropy. We show that perpendicular magnetization is present in both 2-D and 3-D films even though we have incomplete covering of the substrate. Interestingly, for the case of a 1 ML equivalent 3-D Fe film, in-plane magnetization was also observed.

EXPERIMENTAL

The experiment is performed in a UHV chamber with a base pressure of about $1 - 2 \times 10^{-10}$ torr. It is equipped with a CMA Auger system, a sputter ion gun, and a High-Resolution Low-Energy Electron Diffractometer with a narrow instrumental width of $\sim 6 \times 10^{-3} Å^{-1}$ or a resolving power of better than 2000 Å[8]. It also has a rotatable electromagnet for Surface Magneto-Optic Kerr Effect (SMOKE) study[9]. The preparation and characterization of the Au(001) substrate has been described elsewhere[10].

The Fe source is a resistively heated high purity Fe wire enclosed in a tantulum-stainless steel housing. The Fe beam is constrained by a Ta spout of 10 mm in diameter and 25 mm long directed perpendicular to the substrate surface. The flux is easily changed by varying the current through the iron filament. The growth is monitored by both the HRLEED and AES. The exposure dependent angular profiles of the specular beam and superlattice beam were measured to determine the coverage and morphology of the films. The Auger Signal-Time (AST) plot shows clear break points for both the Au(69 eV) and Fe(701 eV) Auger signals. Each break point corresponds to the completion of a layer.

For the SMOKE experiment, the sample is rotated into the gap between the poles of the electromagnet. The magnet can be oriented to have the magnetic field, $\mathbf{B}$, in the plane of the sample or perpendicular to the sample. The B-field is changed periodically by ramping a saw-tooth current through the coil of the electromagnet. A polarized 5mW He-Ne laser beam is shined onto the sample and the reflected beam is passed through an analyzer and into a photocell detector. The variation in the intensity of the reflected beam at the detector is plotted against the periodic sawtooth voltage to give the surface magnetic hysteresis loop.

RESULTS AND DISCUSSION

The detail shape of the angular intensity distribution of a diffraction spot (angular profile) is very sensitive to defects, like steps, present on the surface of the sample. These small changes in the angular profile are easily detected by the HRLEED. In contrast, the broad instrument response function of most LEEDs ($\sim 10^{-2} Å^{-1}$) would have buried these small changes in the angular profile. The measured HRLEED angular profile can be fitted to a model function to yield information on the average size of the overlayer islands, domains or terraces and also their separation and size distributions. The width of the angular profile reflects the average size of the ordered region while the tail of the profile gives the size distribution of these ordered regions.

For a 2-D island growth mode in the monolayer-range, at the out-of-phase diffraction condition (to be discussed later), the full-width-at-half-maximum (FWHM) of the (00) beam broadens with increasing adlayer-substrate step density. The width peaks at half coverage, $\theta = 1/2$, where the step density is at its maximum and narrows down to its original value at $\theta = 1$ when the substrate is completely covered by one layer of adatoms[11]. Figure 1(a) illustrates this. The film was grown at a substrate temperature of 85°C. At the cummulative exposure time of about 3 min, which coresponds to $\theta = 1/2$, the FWHM measured at 21.5 eV is at a maximum. On further exposure to the Fe beam the FWHM narrows and at 6 ± 1 min when one layer of Fe has been deposited on the Au(001) surface, the FWHM is at its original value. The average island size is about 360 Å, which is as good as the substrate surface would allows. In addition we see that the FWHM of the $(0\frac{1}{5})$ superlattice beam broadens until the beam vanishes at about 4 min corresponding to a coverage of about one half. The $(0\frac{1}{5})$ beam reflects the super-

periodicity of the surface reconstruction present on the top most layer of the substrate and is thus very useful for monitoring the uncovered area (reconstruction domains) on the substrate. In the case of 3-D islanding where the film was grown at slower deposition rate and a substrate temperature of 105°C (see Fig. 1(b)) the width of the (00) beam does not return to its initial value indicating that the resultant islands are smaller than the ordered regions on the substrate. However, we still see the initial broadening due to the increasing Fe-Au step density and at about 11 ± 1 min the FWHM reaches a maximum. Similarly the width of the $(0\frac{1}{5})$ beam also broadens until the beam disappears at 9 ± 1 min corresponding to a coverage of about 1/2 ML. Additional Fe deposit does not increase the size of the first layer Fe islands appreciably, as shown by the nearly constant FWHM after 11 min, but results in the build up of the second Fe layer above the incomplete first layer (to be explained in the next paragraph). The narrowing of the profile due to the increase in the island size of the first layer is offset by the increase in the Fe-Fe step density resulting from the build up of the second Fe layer on top of the first. Therefore although 1 ML equivalent of material was deposited the Au surface is not completely covered by Fe.

We can determine the presence of the second Fe layer above the first more convincingly by measuring the FWHMs of the (00) beam angular profiles at different primary electron energies, E. By changing the energy of the electrons incident on a surface with step height, t, we can vary the path difference between electrons scattered from different terraces. If the path difference for a given step height t, is equal to an integral number of wavelength, $\lambda = \sqrt{150.4eV/E}$, we have constructive interference and the diffraction beam is at its narrowest. This is the in-phase condition. At the out-of-phase condition, the path difference between electrons scattered from different terraces is half-integral number of wavelength and thus we have destructive interference and the diffraction spot is at its broadest. Therefore the FWHM of the (00) beam from a stepped surface is expected to broaden and narrow with increasing electron energy as in Fig. 2 for the clean Au. The amplitude of this width oscillation depends on the step density on the surface. Using the out-of-phase condition and Eq. 1 the step height coresponding to the peaks in the FWHM vs Energy plot can be determined[12].

$$E_n(eV) = \frac{150.4}{4t^2 cos^2\theta} n^2,$$ (1)

where θ is the angle of incident of the electron and n may take on integral or half integral values corresponding to the in-phase and out-of-phase conditions, respectively.
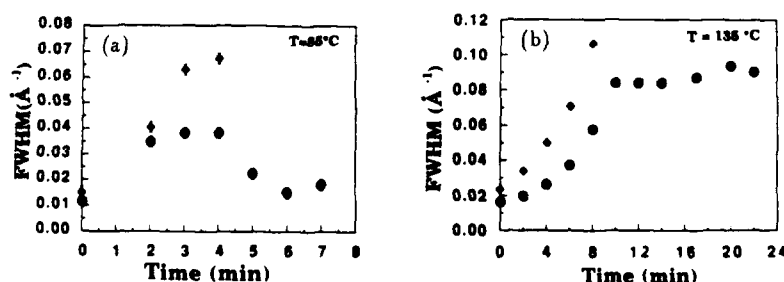
Figure 1: FWHM of the (00) beam, ●, and $(0\frac{1}{5})$ beam, ◆, as a function of deposition time for (a) one layer (2-D) island growth and (b) double layer (3-D) island growth.

314

This gives us a simple method to determine the presence of Fe-Fe steps and Fe-Au steps in addition to any Au-Au steps on the sample. In general, the analysis can be carried over to any heteroexpitaxial system for which the relative phase difference of the atomic scattering factor between the adlayer and the substrate is a slowly varying function of energy[13].

The FWHM vs Energy plot for a 2-D Fe layer is shown in Fig. 3(a) and that of a 3-D layer is shown in Fig. 3(b). In Fig. 3(a) we see a peak at 29 eV. Using Eq. 1 and $n = \frac{3}{2}$ we obtained a step height of 1.71 ± 0.03 Å. In Fig. 3(b) in addition to the 29 eV peak we also observed a peak at 45 eV. With $n = \frac{3}{2}$ this gives a step height of 1.37 ± 0.03 Åwhich we attribute to the presence of the second Fe layer above the first. If we use the bulk lattice constants, the average step height of Au (2.04 Å) and Fe (1.44 Å) comes out to be 1.74 Å. Therefore in the 2-D film we have a contraction of 2% between Fe and Au, and the 3-D film a contraction of 5% between Fe and Fe. These contractions are expected in metals surfaces where smoothing of surface electron charge densities[14] occur.

Longitudinal and polar Kerr measurements using the SMOKE technique were made on a 2-D 0.6 ML (one layer) and a 3-D 1 ML equivalent (double layer) Fe films. From the FWHM of the angular profiles, the average size of the 2-D islands and 3-D islands are estimated to be ~ 65 Å and ~ 75 Å. Even for these incompletely covering ultrathin Fe films, polar Kerr hysteresis loops were present in both types of films. In addition, square longitudinal Kerr hysteresis loop was also detected in the 3-D 1 ML equivalent film indicating a strong zero field magnetization in the plane of the film. The 2-D film has no in-plane magnetization but shows a strong perpendicular magnetic anisotropy with the magnetization normal to the surface. The spin-orbit coupling strength (which favors perpendicular spin orientation) in such film is thus greater than the magnetostatic dipole interaction (which favors in-plane magnetization)[2].

These films also exhibit magnetic phase transitions. The temperature dependent magnetization curves (see Figs. 4(a) and 4(b)) for both films show a drop that starts at about 100°C but in both cases the magnetizations never vanish. However, the magnetic hysteresis loops close up at ~ 120°C. This disappearance of hysteresis is consistent with the films going superparamagentic, analogous to the 3-D superparamagnetism observed in fine Fe particles of radius ~ 125 Å[15]. In the 2-D case the magnetic island each forms domain with definite magnetization direction. At low temperatures the ensemble of domains with large magnetic moments are aligned. At ~ 120°C these ensembles are randomized giving the film a paramagnetic characteristic. The susceptibilities of the closed loops are large (~ 50% of the original susceptibility).
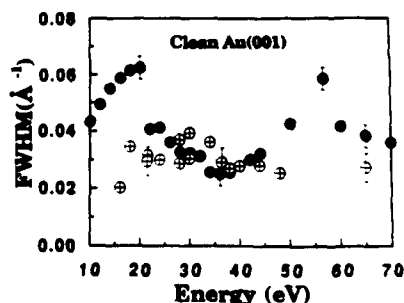
Figure 2: FWHM of the (00) beam vs energy for a clean Au(001) surface. ● are data taken from a stepped region and ⊕ from a region of relatively low step density.
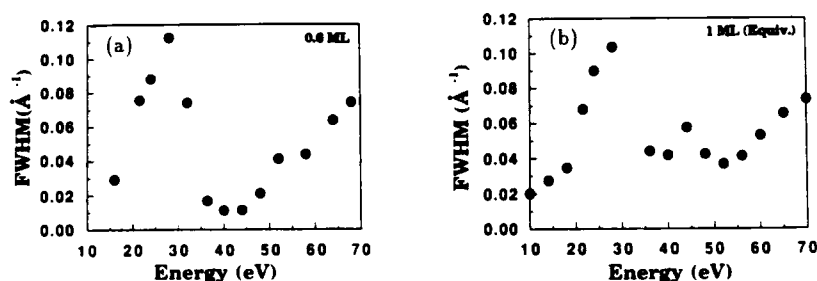
Figure 3: FWHM of the (00) beam vs energy for (a) a 0.6 ML one layer (2-D) Fe film and (b) a 1 ML equivalent double layer (3-D) Fe film.
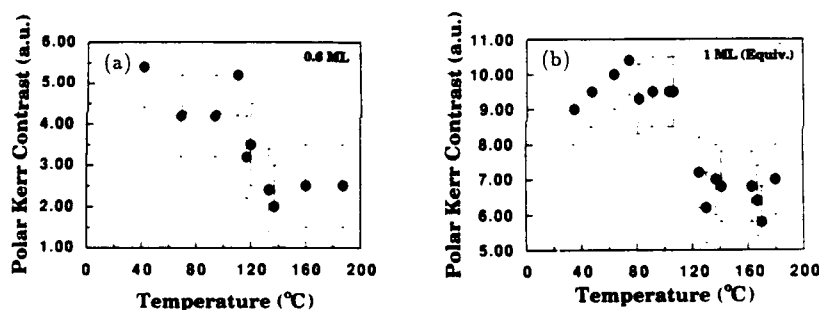
Figure 4: The temperature dependent polar Kerr contrast of the (a) 0.6 ML 2-D Fe film and (b) the 1 ML equivalent 3-D Fe film.

The magnetization curves are reversible. The width of the transition is broad ($\sim 20°$C to $30°$C), suggestive of a distribution of finite size magnetic islands. HRLEED angular profile measurement of the films as a function of film temperature shows that these Fe films are stable up to a temperature of $\sim 180°$C where slight interdiffusion of Fe into Au sets in. At this temperature the AES peak-to-peak signals are still unchanged. Therefore for thicker films with critical temperatures greater then $\sim 200°$C, the decrease in magnetization is due to the loss of Fe by diffusion in addition to that due to spin disordering.

CONCLUSION

The HRLEED with spot profile analysis is a powerful tool for in-situ monitoring of ultrathin film growth. We have used it to accurately determine the coverage and the morphology of ultrathin monolayer-range Fe films deposited on a Au(001) surface. The energy dependent angular profile together with a simple data analysis allows us to detect the build up of a second Fe layer on top of the first. The use of the $(0\frac{1}{2})$ superlattice beam on the reconstructed Au(001) substrate gives complementary information on the clean uncovered region of the Au(001) surface. Even for films that did not completely cover the surface, polar Kerr hysteresis loops were detected. The one layer 2-D 0.6 ML Fe films shows a strong perpendicular magnetic anisotropy. For the double layer 3-D

316

Fe film, square longitudinal Kerr hysteresis loop was also detected. The temperature dependent magnetic phase transition curves are reversible and the transition broadens due to finite size effect. Closed hysteresis loops at temperatures above ($\sim 120°C$) suggest that the films are superparamagnetic.

ACKNOWLEDGEMENTS

References

1. L.M. Falicov, Daniel T. Pierce, S.D. Bader, R. Gronsky, Kristl B. Hathaway, Herbert J. Hopster, David N. Lambeth, S.S.P. Parkin, Gary Prinz, Myron Salamon, Ivan K. Schuller, and R.H. Victora, J. Mater. Res. 5, 1299 (1990).

2. C.L. Fu, A.J. Freeman, and T. Oguchi, Phys. Rev. Lett. 54, 2700 (1985); J.G. Gay and R. Richter, Phys. Rev. Lett. 56, 2728 (1986); J. Appl. Phys. 61, 3362 (1987); Chun Li, A.J. Freeman, H.J.F. Jansen, and C.L. Fu, Phys. Rev. B 42, 5433 (1990).

3. S.D. Bader and C. Liu, J. Vac. Sci. Technol. A, to be published; W. Dürr, M. Taborelli, O. Paul, R. Germar, W. Gudat, D. Pescia, and M. Landolt, Phys. Rev. Lett. 62, 206 (1989); C.M. Schneider, P. Bressler, P. Schuster, and J. Kirschner, Phys. Rev. Lett. 64, 1059 (1990).

4. W.F. Egelhoff, Jr. in CRC Crit. Rev in Solid State and Mater. Sci. Vol. 16, 213 (1990); S.Y. Tong and C.H. Li, ibid., Vol. 10, 209 (1981).

5. The Structure of Surfaces II, Vol. 11 of Springer Series in Surface Sciences, edited by J.F. van der Veen and M.A. Van Hove (Springer, Berlin, 1988).

6. D.D. Chambliss, R.J. Wilson, and S. Chiang, J. Vac. Sci. Technol. B9, 933 (1991).

7. U. Scheithauer, G. Meyer, and M. Henzler, Surf. Sci. 178, 441 (1986).

8. T.-M. Lu and M.G. Lagally, Surf. Sci. 99, 695 (1980).

9. J.-P. Qian and G.-C. Wang, J. Vac. Sci. Technol. A8, 4117 (1990), and references therein.

10. Y.-F. Liew and G.-C. Wang, Surf. Sci. 227, 190 (1990).

11. J.M. Pimbley and T.-M. Lu, J. Appl. Phys. 57, 1121 (1985).

12. M. Henzler, Surf. Sci. 22, 12 (1970).

13. Y.-F. Liew, Y.-L. He, A. Chan, and G.-C. Wang, to be published.

14. M.W. Finnis and V. Heine, J. Phys. F: Metal Phys. 4, L37 (1974); P. Jiang, F. Jona, and P. Marcus, Phys. Rev. B. 35, 7952 (1987).

15. I.S. Jacob and C.P. Bean in Magnetism Vol. III, edited by G.T. Rado and H. Suhl (Academic Press, New York, 1963) pp. 275-280.

THICKNESS DEPENDENCE OF THE FERROMAGNETISM OF Pd FILMS

S. BOUARAB * , C. DEMANGEAT * , A. MOKRANI ** and H. DREYSSE ***
* IPCMS, Université Louis-Pasteur, 4, rue Blaise Pascal, 67070 Strasbourg, France
** Laboratoire de Physique du Solide, 2, rue de la Houssinière, 44072 Nantes
*** Laboratoire de Physique du Solide, BP239, 54506 Vandoeuvre-les Nancy

ABSTRACT

We report the electronic structure of Pd(001) films with various thicknesses, within a self-consistent real-space description of the Hubbard Hamiltonian. We point out that the onset of ferromagnetism in Pd films is not a surface effect, but is directly related to the thickness of the slab: when the lattice parameter increases, films of two or three planes become ferromagnetic. Films with increasing thicknesses (from five layers to the bulk size) need a greater increase of the lattice parameter. An important supplementary lattice expansion is necessary to obtain a free-standing ferromagnetic monolayer. The surprising experimental results of Pd films on Ag or Fe substrate, are well described within this framework.

INTRODUCTION

The Pd is a very intriging system. Due to this high paramagnetic susceptibility, Pd can be seen as a good candidate which needs only a small configuration variation to become ferromagnetic. A very simple description relates the onset of magnetism through the well-known Stoner criterion. Thus a reduction of the coordination number, as in the surface or more drastically in a monolayer, would increase the density of states at the Fermi level, leading to onset of ferromagnetism. Even if this model is extremely crude, it indicates a trend which seems to apply to 3d transition metal film or overlayer [1] or even in Rh film [2] . Of course detailed calculations are needed and the fine structure of the density of states plays a major role. Let us mention that ferromagnetic arrangement is surely the simplest one and usually more complex arrangements must be considered (antiferromagnetic coupling in a monolayer or between layers for instance). The richness of magnetic arrangements is very large, but, one can expect that, for Pd, ferromagnetic coupling is the most usual [3] (some antiferromagnetic coupling has been reported recently by Victoria and MacLaren in CoPd multilayers calculations [4]).

Using Electron Capture Spectroscopy, Rau and coworkers did not find evidence for magnetism on a Pd(001) surface but preliminary results of Pd thin films epitaxially grown on Ag(001) substrate, have shown existence of ferromagnetic arrangement at the topmost layer of Pd film [5] . Using the Surface Magneto-Optic Kerr Effect (SMOKE), Fink et al did not detect ferromagnetism in the case of a Pd monolayer on Ag semi-infinite crystal [6] . The experiments of Rau have been performed with the Pd film, thicker than 2 layers and thus the contradiction between Rau and Erskine groups [6] is only apparent: these results seem to indicate that, a Pd film with the Ag lattice spacing (at least in the plane parallel to the interface Pd/Ag) is experimentally not magnetic in the monolayer case and ferromagnetic for a higher number of Pd planes. This interpretation got more credit with the recent results of Celinski et al [7] : Pd films were grown on Fe(001), with an expanded lattice of 5%. For thickness up to four monolayers, ferromagnetic Pd is found but one additional layer of Pd destroys the ferromagnetism and only a small polarization at the Fe/Pd interface remains.

Theoretical calculations have shown that, without spin-orbit coupling, a 5-6% Pd lattice expansion, leads to onset of ferromagnetism (a higher value of 10% was reported if spin-orbit coupling is considered [8-10]). The case of Pd with the Fe or Ag lattice parameter is just near the critical bulk expansion value.

318

In this paper, we will investigate in details the electronic and magnetic structure of Pd films. We will show that a Pd monolayer needs an important increase of the lattice parameter to be ferromagnetic, contrary to thicker films and that a specific "film" effect occurs.

FORMALISM

A tight-binding Hubbard Hamiltonian, in the unrestricted Hartree-Fock approximation is used [11]. The spin polarized local densities of states are computed by using the recursion method [12] which allows a calculation in the real space. Thirteen levels of the continued fraction are used in order to reach good convergence of the Green's fonction matrix elements. In this calculation only "d" orbitals are considered. Hopping integrals are taken spin independent.

The main quantity in this problem is the diagonal part of the Hamiltonian, given by:

$$E_{i\sigma} = E_i^0 + U\Delta N_i - \sigma \frac{J}{2} \mu_i$$

where i is the index of the ith atomic plane (all the atoms in the same plane parallel to the surface are equivalent) and σ the spin. E_i^0 is the paramagnetic metallic d level and U is the intra-atomic Coulomb integrals which is known from the literature [13] .ΔN_i is the variation of charge as compared to bulk paramagnetic case. J is the exchange integral. Using LMTO framework, systematical values for J have been derived [14]. In our previous work [15], these values have been used.

In this work, we will investigate systematically the local magnetic moment versus the Pd exchange integral J. J is known to decrease, when the lattice parameter a increases, slower [8] as the band width which varies roughly as a r^{-5} law . Thus by scaling, the curve $\mu_i = \mu_i(J)$ is similar to the curve $\mu_i = \mu_i(a)$.

As we have shown for Fe and V films [11,16,17] canonical integrals [18] reproduce quite well the magnetic properties of transition metals and are used in this work. Finally let us mention that monolayer and bilayer are obviously neutral, and charge transfer is allowed between layers, requiring only global charge neutrality.

ELECTRONIC STRUCTURE OF Pd FILMS.

On figure 1, we report the magnetic moments versus J for different configurations. The critical value for onset of ferromagnetism of a Pd film with n layers is called J_{cr}^n

1.Bulk ferromagnetism

The electronic occupation has been taken 9.52 electrons. In this case, the bulk Fermi level falls near a peak of the local density of states (cf figure 2). The transition para-ferro is second-order but is very nearly a sharp transition. The critical value J_{cr}^{bulk} is directly given by the Stoner criterion (i.e $J_{Stoner}^{bulk} = 1 / n^{bulk}(E_F)$ when $n^{bulk}(E_F)$ is the local density of states of the paramagnetic band normalized to 5 electrons per spin). Good agreement with ab-initio calculation is found [8-10] .
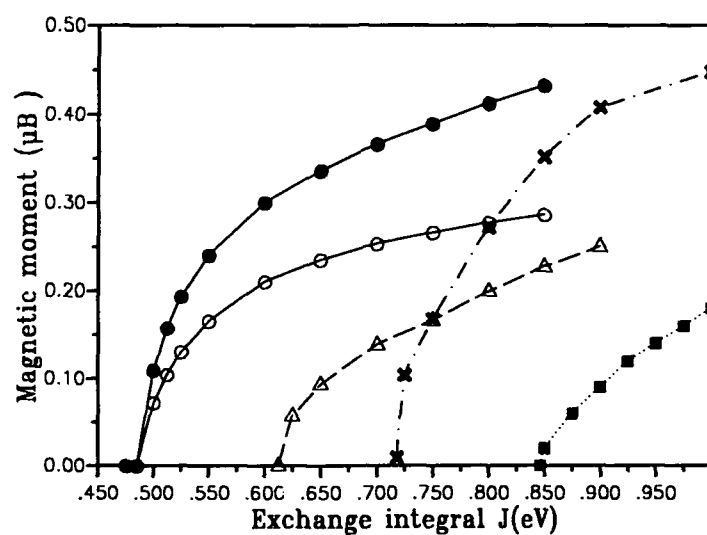
Figure 1. Magnetic moment per atom (μ_B) in Pd(001) in terms of the exchange integral J (eV): bulk (×), 1-layer (■), 2-layer (△), 3-layer (center(•), surface(O))
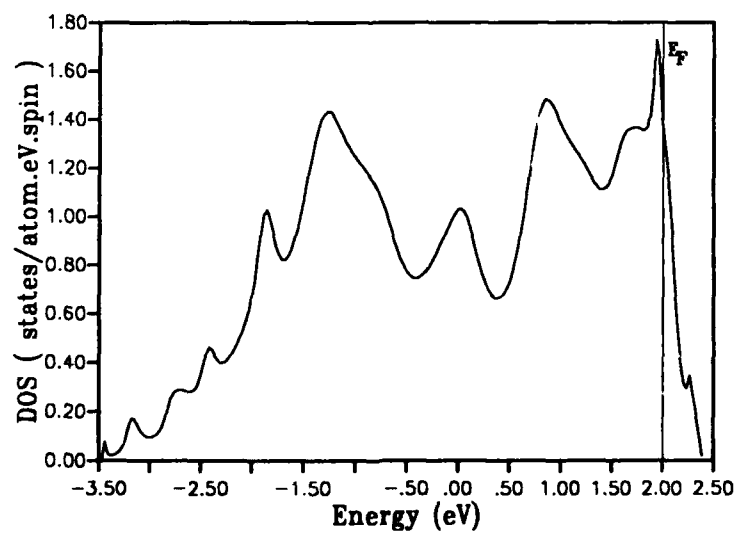
Figure 2. "d" density of states on paramagnetic Pd bulk. E_F is the Fermi level.
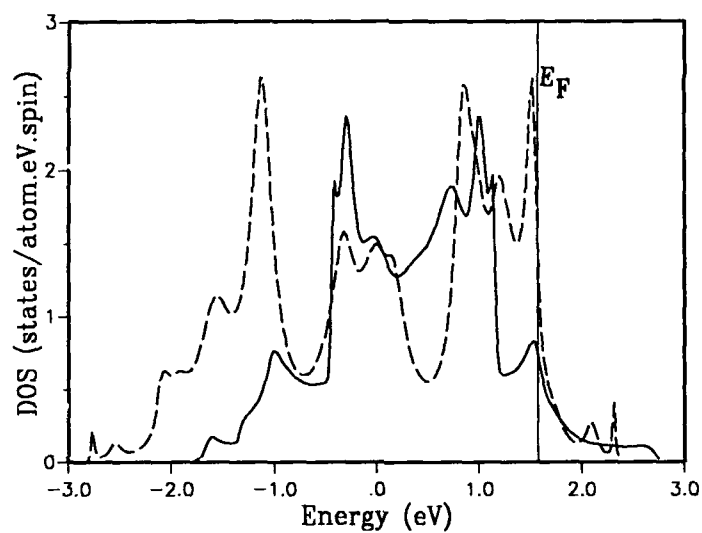
Figure 3. "d" density of states of paramagnetic Pd(001) monolayer (full curve) and bilayer (dotted curve). E_F is the Fermi level.
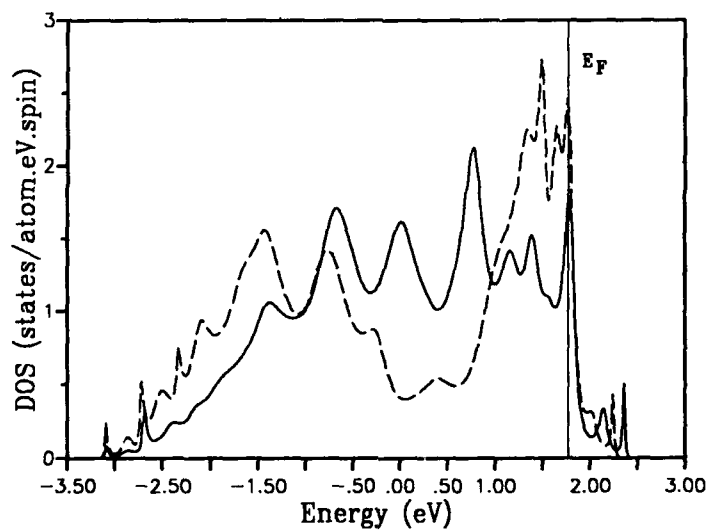
Figure 4. "d" density of states on paramagnetic Pd(001) 3-layer: center (dotted line), surface (full line). E_f is the Fermi level.

2. Monolayer

Onset of ferromagnetism occurs for a critical value J^1_{cr} larger than J^{bulk}_{cr} . The para-ferro transition is of second order and arises from the particular shape of the paramagnetic density of states of the monolayer at the top of the band (figure 3). We can conclude that the free standing Pd monolayer, when only "d" orbitals are considered, can be ferromagnetic only with an important lattice parameter expansion. This result is in disagreement with Zhu et al [19] who reported ferromagnetic state, and with Huang et al [20] who used the Fe lattice parameter. Very recently, a detailed study of Pd film by LMTO approach excludes clearly any possibility of ferromagnetism and a similar behavior of the paramagnetic density of states at the Fermi level has been reported [21] .

3. Beyond Pd monolayer

The behavior of two and three Pd layers is opposite to the monolayer behavior. For a value of $J^2_{cr} = 0.625$ eV, the bilayer becomes ferromagnetic. In this case the Fermi level is in a peak of the density of states (figure 3) and due to the fact that no important peaks are present till the top of the band, a second order transition occurs. In the case of the trilayer fully self-consistent calculation shows that the onset of magnetism is for a $J^3_{cr} < J^2_{cr}$ (the density of states is reported on figure 4). Let us insist on the fact that ferromagnetism appears from a unique value of J^3_{cr} : all the three planes are ferromagnetic or not. Also we notice that the magnetic moment is higher on the central plane as compared with the surface plane.

4. Ferromagnetism and lattice parameter.

Taking into account that a 5% lattice parameter expansion is mandatory to have onset of ferromagnetism in Pd bulk, a value of $J \sim 0.58eV$ for bulk equilibrium lattice parameter is reasonable. This value is slightly smaller than the LMTO value given by Christensen (0.65 eV) for Pd with bulk equilibrium lattice parameter [14] which has been used in our previous work [15] concerning Pd films.

The present work indicates clearly that it is not possible to describe ferromagnetism in free-standing Pd(001) films by simple coordination arguments. The main conclusions are:
- free-standing "d" monolayer would require an important increase of the lattice parameter to be ferromagnetic.
- the critical value of J^n_{cr} for n = 2 and 3 is smaller than J^{bulk}_{cr} .
- in all cases the most important magnetic moment is found in the most central atoms and smallest one on the surface planes.

5. Pd_n ⁄Ag(001)

The Pd_n ⁄Ag(001) system has been investigated with a value of J = 0.52 eV [16] which is below the value of 0.58 eV which is necessary to have onset of bulk Pd with the lattice parameter of Ag (epitaxial growth). Different thicknesses ranging from n = 1 to 11, have been considered and onset of ferromagnetism is found from n = 3 to 6 Pd layers grown on Ag(001), considering always "d" orbitals [16] . As for the Pd films, the highest magnetic moment is systematically found on the central layer Pd atoms, the smallest one on the surface planes. Also first order transition occurs and one finds that the critical values of J for $n \geq 7$ are greater than 0.52 eV.

We found that a 20% increase of J keep the monolayer of Pd on Ag substrate paramagnetic. This result is completly in agreement with the experimental results [6] and theoretical predictions [2,19] .

CONCLUSION

Hubbard tight-binding Hamiltonian provides an efficient way to perform systematic studies on transition metal magnetism [22] . Considering only "d" orbitals, for bulk equilibrium lattice parameter the free-standing monolayer is paramagnetic. Increasing the lattice parameter, thicker Pd films become progressively ferromagnetic. For Pd films on Ag(001), good agreement with experimental results is found. For Pd films on Fe(001), similar behavior is expected. As already shown for Fe/V interface [23] , the influence of the substrate-Pd hybridization would be important only on the two first Pd planes, which are in all cases polarized due to the presence of Fe ferromagnetic neighbor atoms. The main effect of the substrate is to expand the lattice parameter. This expansion is not enough to have bulk Pd ferromagnetism and similar behavior as with Ag substrate is expected: all planes are polarized for small Pd thicknesses. For greater thickness, only interface polarization remains. Calculations are now in progress.

References:

1. S. Blügel, B. Drittler, R. Zeller and P. H. Dederichs,
   Appl. Phys. A 49 , 547 (1989); and references there in.
2. O. Eriksson, R.C. Albers and A. M. Boring, Phys. Rev. Lett. 66 , 1350 (1991);
   A. Mokrani, H. Dreyssé and C. Demangeat, to appear in JMMM.
3. V. Heine and J.H. Samson, J. of Phys. F 13 , 2155 (1983).
4. R. H. Victora and J. M. McLaren, J. of Appl. Phys. 69 (1991).
5. C. Rau, private communication (1990).
6. R. L. Fink, C.A. Ballentine, J. L. Erskine and J. Araya-Pochet
   Phys. Rev. B, 41 , 10175 (1990); and references there in.
7. Z. Celinski, B. Heinrich, J. F. Cochran, W. B. Muir, A. S. Arrott
   and J. Kirschner, Phys. Rev. Lett. 65 , 1156 (1990).
8. L. Fritsche, J. Noffke and H. Eckardt, J. Phys. F. 17 (1987) 943. 17 , 943 (1987).
9. V. L Moruzzi and P. M. Marcus Phys. Rev. B, 39 , 471 (1989).
10. H. Chen, N. E. Brener and J. Callaway, Phys. Rev. B, 40 , 1443 (1989).
11. A. Mokrani, C. Demangeat and H. Dreyssé, Phys. Rev. B, 42 , 10139 (1990).
12. R. Haydock, V. Heine and M. J. Kelly, Solid State Phys. 35 , 215 (1980).
13. T. Bandyopadhyay and D. D.Sharma, Phys. Rev. B, 39 , 3517 (1989).
14. N. E. Christensen, O. Gunnarsson, O. Jepsen and O.K. Andersen,
    J. Physique, Paris, 49, C8 (1988) 17. 49 , C8-17 (1988).
15. S. Bouarab, C. Demangeat, A. Mokrani and H. Dreyssé,
    Phys. Lett. A, 151 , 103 (1990).
16. H. Dreyssé, A. Mokrani, S. Bouarab and C. Demangeat, Surf. Sci. (1991).
17. A. Mokrani, C. Demangeat and H. Dreyssé, J. Magn. Magn. Mater (1991).
18. D. G. Pettifor, Phys. Rev. B, 2 , 3031 (1970).
19. M. J. Zhu, D. M. Bylander and L. Kleinman, Phys. Rev. B, 42 , 2874 (1990).
20. H. Huang, J. Hermanson, J.S. Gay, R. Richter and J. R. Smith,
    Surf. Sci. 172 , 363 (1986).
21. M. A. Khan, to be published in Phys. Rev. B.
22. L. Falicov, in this issue.
23. A. Vega, A. Rubio, L. C. Balbas, J. Dorantes-Davila, S. Bouarab,
    C. Demangeat, A. Mokrani and H. Dreyssé, J. Appl. Phys. 69 (1991).

STEPPED Fe(100) AND V/Fe(100) MAGNETISM

A. VEGA [a], A. RUBIO [a], L.C. BALBAS [a], J. DORANTES-DAVILA [b],
C. DEMANGEAT [c], A. MOKRANI [d] and H. DREYSSE [e]
a Depto de Fisica Teorica, Universidad de Valladolid, 47011 Valladolid, Spain
b Instituto de Fisica, UASLP, Alvaro Obregon 64, 78000 San Luis Potosi, S. L. P.,
Mexico
c IPCMS, Université Louis-Pasteur, 4, rue Blaise Pascal, 67070 Strasbourg, France
d Laboratoire de Physique du Solide, 2, rue de la Houssinière, 44072 Nantes, France
e Laboratoire de Physique du Solide, BP239, 54506 Vandoeuvre-les Nancy, France

ABSTRACT

We have investigated the magnetic arrangment of 3d transition-metal stepped surface by using a self-consistent real-space tight-binding method. As expected, the presence of steps modifies locally the properties of a transition-metal surface. We emphasized the influence of atomic environment. We found for the (100)-Fe surface, an enhancement of the magnetic moments of the external edge of this step as compared to the flat surface. The results are not very sensitives to the step length. More striking is the case of the (100)-V stepped surface where atoms at the external edge display a large magnetic moment.

INTRODUCTION

The magnetic properties of transition-metal surfaces are of significant interest, due to their promising practical applications [1] . In the last years, the development of new experimental techniques [2] for investigating surface physics has led to considerable progress in the understanding of their geometrical structure and magnetic properties. Recently [3] , experiments of vacuum tunneling of spin-polarized electrons with scanning tunneling microscopy showed an antiferromagnetism between ferromagnetic terraces, separated by single steps, of the (100)-Cr surface. This was already conjectured theoretically by Blügel et al [4] . Most theoretical works consider ideally flat surfaces, but as confirmed by experiments, even for the well treated surfaces; remain steps which can modify locally the magnetic properties of a transition-metal surface or interface.

In this work we present results of the effect of stepped terraces on the magnetic properties of the (100)-Fe and preliminary results on (100)-V/Fe surfaces

We consider the Hubbard-like Hamiltonian for s, p and d electrons

$$H = H_0 + H_I \tag{1}$$

where H_0 is the single particle Hamiltonian which can be written in the usual no-tation as:

$$H_0 = \sum_{\substack{\alpha, \beta, \sigma \\ i \neq j}} t_{ij}^{\alpha\beta} c_{i\alpha\sigma}^{+} c_{j\beta\sigma} \tag{2}$$

where $c_{i\alpha\sigma}^{+}(c_{i\alpha\sigma})$ refers to the creation (annihilation) operator of an electron with spin σ at atomic site i in the orbital $\alpha(\alpha = s, p, d)$ and $t_{ij}^{\alpha\beta}$ to the hopping integral between sites i and j . The interaction Hamiltonian H_I in the unrestricted Hartree-Fock approximation is given by

$$H_I = \sum_{i\alpha\sigma} \varepsilon_{i\sigma}^{\alpha} \hat{n}_{i\sigma}^{\alpha} - E_{dc} \tag{3}$$

$$\varepsilon_{i\sigma}^{\alpha} = \varepsilon_i^{\alpha} + \sum_{\substack{\beta\sigma' \\ (\alpha, \sigma) \neq (\beta, \sigma')}} U_{\alpha\beta}^{\sigma\sigma'} < \hat{n}_{i\sigma'}^{\beta} > \tag{4}$$

Here, $E_{dc} = 1/2 \sum_{i\alpha\sigma} < \hat{n}_{i\sigma}^{\alpha} > (\varepsilon_{i\sigma}^{\alpha} - \varepsilon_i^{\alpha})$ refers to the correction due to double counting, and $\hat{n}_{i\sigma}^{\alpha}$ to the electron number operator. The intraatomic Coulomb interactions $U_{\alpha\beta}^{\sigma\sigma'}$ between electrons can be written in terms of the exchange and direct Coulomb integrals, $J_{\alpha\beta} = U_{\alpha\beta}^{-} - U_{\alpha\beta}^{+}$ and $U_{\alpha\beta} = (U_{\alpha\beta}^{-} + U_{\alpha\beta}^{+})/2$, respectively, where + (-) means $\uparrow\uparrow(\uparrow\downarrow)$.

The number of s, p and d electrons $n^{\alpha}(i), (\alpha = s, p, d)$, and the local magnetic moments $\mu^{\alpha}(i)$ at site i given by

$$\mu^{\alpha}(i) = < \hat{n}_{i\uparrow}^{\alpha} > - < \hat{n}_{i\downarrow}^{\alpha} >$$

$$\tag{5}$$

$$n^{\alpha}(i) = < \hat{n}_{i\uparrow}^{\alpha} > + < \hat{n}_{i\downarrow}^{\alpha} >$$

are determined self-consistently by requiring

$$< \hat{n}_{i\sigma}^{\alpha} > = \int_{-\infty}^{E_F} \rho_{i\sigma}^{\alpha}(\varepsilon) d\varepsilon \tag{6}$$

The local density of states $\rho_{i\sigma}^{\alpha}$ is calculated by using the recursion method [5]. For the parametrized Slater-Koster hopping integrals $t_{ij}^{\alpha\beta}$, we take the values chosen to fit the bulk band structure as reported by Papaconstantopoulos [6] .

RESULTS AND DISCUSSION

The exchange integral is considered only for d electrons i. e. $J_{\alpha\beta} = J$ and is fitted to the bulk magnetic moment μ_b for iron. For vanadium, because bulk is paramagnetic, we took the ratio J_V/J_{Fe} as in the LMTO calculations of Christensen et al. [7] . For the matrix elements between V and Fe we take the geometric mean of the respective V-V and Fe-Fe matrix elements. It is very difficult within the tight-binding approximation to treat charge transfer accuratly at non-symmetrical systems (e. g. clusters, surfaces). To avoid the problem, we impose local charge neutrality for each orbital component (i. e. $\Delta n_{sp} = \Delta n_d = 0$). Thus a supplementary term is introduced in equation 4 which is determined by the local neutrality criterion (let us notice that within such assumption, the knowledge of the exact value of U_{ii} is not needed). This restriction seems not to be very important for the values of the local magnetic moments for different layers, since a charge transfer of less than $0.1d$ electron is expected [8] . To check our approximation (local charge neutrality) we calculated the local magnetic moments for different layers of the (100)-Fe surface and we obtained the same results as reported in [8] .

Table I : Local magnetic moments $\mu(i)$ at different sites i of stepped (100)-Fe surface (S) and the corresponding sites of the layer under the step (S-1). The size of the step, in atomic sites, is 4. Results for a monolayer of vanadium (V) adsorbed on steps of iron is also given. Pure (100)-Fe surface corresponding to a step size of ∞ is also reported.

step size	layer	$\mu(1)$	$\mu(2)$	$\mu(3)$	$\mu(4)$
4	S	2.73	2.76	2.81	2.88
	S-1	2.41	2.33	2.35	2.46
	V	-1.17	-1.64	-1.77	-2.42
4	S	2.19	1.83	1.78	1.79
	S-1	2.22	2.23	2.36	2.39
∞	S	2.77			
	S-1	2.35			
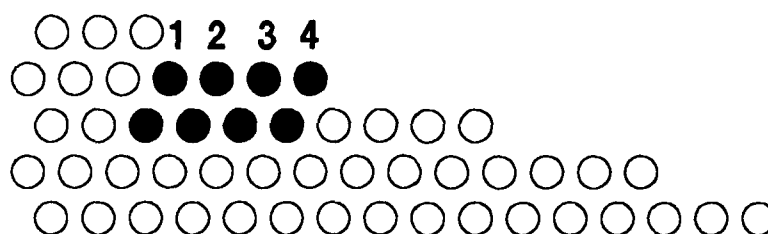
Figure 1. Geometry of the studied stepped surface. Projection in a (010) plane

In table I, we report the results obtained with six level of the continued fraction within the recursion method. The geometry is given in figure 1. Orientation of the surface planes is (100). The steps consist of four rows parallel to the direction (100), with a step height of one atomic plane: index 1 indicates the most internal atom. These steps can be considered as vicinal surface (1,0,7). For pure Fe-terraces we notice an increase of the local magnetic moment on the external edge (site 4), as compared to the flat surface. This can be understood by recalling that these atoms have a small coordination number and therefore the effective bandwith is smaller than in the flat surface. As shown elsewhere [9] , this simple picture has strong limitation and especially for d-metals at the end of the serie. Similar effect occurs for internal edge atom (site 1) in the opposite direction since these atoms have larger coordination number with respect to the surface. However, these atoms have as first neighbors the external edge atoms which have large local magnetic moment; this will tend to induce larger magnetic moment and thus to compensate the effect of the larger coordination number. At the surface, for atoms between the internal and external edge, magnetic moment is very similar to the value of the pure surface.

We report also in table I preliminary results of one V monolayer adsorbed on Fe(100) with four row steps. The value of the hopping integrals are those given by Papaconstantopoulos [6] , which correspond to bulk equilibrium V lattice parameter ($a_V = 5.71 a.u.$). For Fe, the similar length is $a_{Fe} = 5.41 a.u.$. Thus, one can consider that V hopping integrals have been underestimated, favorising an increase of the magnetic moment. An improvement of this calculation would be the use of hopping integrals with distance variation laws. Nevertheless, these results show clearly trends. We notice, as already found experimentally [10] and theoretically [11] for pure interface, an antiferromagetic coupling between V and Fe layers. Considerations made on the coordination number previously hold strongly in that case. The increase

of the magnetic moment from internal edge to external edge is very important. This behaviour is not surprising. Previous studies [12, 13] have found that the free standing V monolayer is strongly ferromagnetic. In our previous calculation of adsorbate interface, a magnetic moment of $-1.67\mu_B$ has been found for a V monolayer adsorbed on semi-infinite (100)-Fe. Let us mention also that we also varied the length of the step but magnetic moments are only very slightly affected.

For bcc V and Fe, the influence of the direct neighboring is clearly emphasized. The choice of the exchange integral J_V for V is crucial. Thus, a systematical study of the magnetic moments versus J_V has to be performed. Also, the number of levels of the continued fraction could be increased. Neverthless the controversial experimental results of the magnetic nature of (100)-V [14] can be understood considering steps. A such study is under progress.

References:
1. See for example the proceedings of this conference.
2. R. J. Celotta and D. T. Pierce, Science 234 , 334 (1986);
    M. Landolt, Appl. Phys. A 41 , 83 (1986);
    J. Kirchner, Polarized Electrons at Surfaces (Springer Verlag, Berlin, 1985);
    C. Rau, J. Magn. Magn. Mat. 30 , 141 (1982);
    R. Feder, J. Phys. C 14 , 2049 (1989).
3. R. Wiesendanger, H. J. Guntherodt, G. Guntherodt, R. J. Gambino and
    R. Rulf, Phys. Rev. Lett. 65 , 247 (1990).
4. S. Blügel, D. Pescia and P. H. Dederichs, Phys. Rev. B 39 , 1392 (1989).
5. R. Haydock, Solid State Physics (Academic, London, 1980) 35 , p215
6. D. A. Papaconstantopoulos, Handbook of The Band Structure of Elemental Solids
    (Plenum Press, New-York and London, 1986).
7. N. E. Christensen, O. Gunnarsson, O. Jepsen and O.K. Andersen,
    J. Physique, Paris, 49 , C8-17 (1988).
8. R. H. Victora and L. M. Falicov, Phys. Rev. B 31 , 7335 (1985);
    R. H. Victora, L. M. Falicov and S. Ishida, Phys. Rev. B 30 , 3896 (1984)
9. S. Bouarab, C. Demangeat, A. Mokrani and H. Dreyssé, this conference.
10. N. K. Jaggi and L. H. Schwartz, J. Phys. Soc. Jpn. 54 , 1652 (1985).
11. A. Vega, A. Rubio, L. C. Balbas, J. Dorantes-Davila, S. Bouarab,
    C. Demangeat, A. Mokrani and H. Dreyssé, J. Appl. Phys. 69 , 4544 (1991).
12. S. Ohnishi, C. L. Fu and A. J. Freeman, J. Magn. Magn. Mat. 50 , 161 (1985).
13. A. Mokrani, C. Demangeat and H. Dreyssé, Phys. Rev. B, 42 , 10139 (1990).
14. C. Rau, C. Liu, A. Schmalzbauer and G. Xing,
    Phys. Rev. Lett. 57 , 2311 (1986).

SUBSTRUCTURE-MAGNETIC PROPERTY CORRELATION
IN CO/AG COMPOSITE THIN FILMS

C.P REED**, R.J. DEANGELIS**, S.H. LIOU°*, S. NAFIS*, JOHN A. WOOLLAM*, K.W.
LEE*, R.J. JACOB^
*Mechanical Engineering Department, °Behlen Laboratory of Physics,
*Electrical Engineering Department,*Center for Materials Research and
Analysis, University of Nebraska-Lincoln, Lincoln, NE 68588; ^Nano Probe
Laboratory of the Markey Cancer Center and Department of Microbiology and
Immunology, University of Kentucky, Lexington, KY 40506

ABSTRACT

Three series of nanostructured, $2\mu m$ thick, Co/Ag composite thin films
(13, 39 and 61 volume % Co) were produced by dc magnetron sputtering at
various substrate temperatures (100-600°C) to determine their magnetic
properties and characterize the microstructure. The films were found to be
composed of finely dispersed Ag and Co particles. The film surfaces become
rougher as the substrate temperature was increased. The crystal lattice
structure of the Co was found to be fcc except at the lower substrate
temperatures (<300°C) in the 61 volume % films where it was found to be a
mixture of fcc and some hcp. The average diffracting particle size of both
the Co and Ag rich phases increase with substrate temperature. The magnetic
coercivity of the films reached a maximum value when the Co particle size
was between $100-150\text{Å}$.

INTRODUCTION

Fine dispersed magnetic particle systems are of interest because of
the opportunities they present for engineering materials with specific
magnetic properties. The structural characteristics of the films control
the magnetic properties of the material. For example, films containing
single domain sized magnetic particles show much enhanced magnetic
coercivity and may be useful as recording media.

Studies have been performed on a variety of small magnetic
particle/metal matrix systems including Fe in a Ag matrix [1] and Fe in a Cu
matrix [2]. In this study, Co and Ag were mixed to form nanostructured
composite materials. The average diffracting particle size of the Co and Ag
in these films can be controlled by varying the composition of the films and
the substrate temperature. The effects of substrate temperature on the
surface roughness, crystallite size, and crystal structure of the phases
present were determined. The relationships among the structural
characteristics and the magnetic properties of the films were investigated.

EXPERIMENTAL PROCEDURE

Co/Ag composite films, about $2\mu m$ thick, were prepared by dc magnetron
sputtering using a single target. The targets were made by sintering a
mixture of Co and Ag powders. The substrate temperature during deposition
was varied from 100-600°C. The sputtering gas was 4mtorr of Ar. The Co/Ag
films were prepared using conditions employed in producing Fe/Ag films [1].

330

The structural characteristics were investigated with a Philips x-ray diffractometer with a copper tube and a diffracted beam monochromater. Scanning electron microscope observations were made with a Hitachi S-900 SEM equipped with a Crew cold cathode FEG and operating in the SE-1 mode. Film compositions and compositional maps were determined using energy dispersive x-ray analysis. Magnetic properties of the films were determined with a commercial SQUID magnetometer.

RESULTS AND DISCUSSION

The films used in this study had compositions $Co_{19}Ag_{81}$, $Co_{50}Ag_{50}$ and $Co_{71}Ag_{29}$. The variation in composition for films prepared at different substrate temperatures was less than 5 atomic%.

The surface roughness of the films increased with substrate temperature. scanning electron micrographs of films produced at 100 and 400°C are shown in Figs. 1 and 2. At low substrate temperatures, the films were relatively flat, while the higher temperature films show large features which protrude from the surface of the film. These observations are in agreement with the surface structures predicted by the thin film growth model developed by Thornton [3].
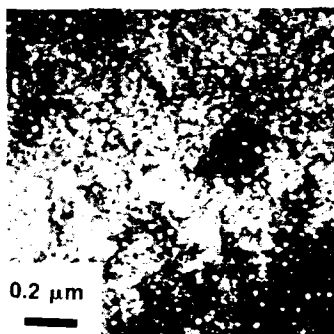
Figure 1   Scanning electron micrograph taken at 1.5 kV of $Co_{50}Ag_{50}$ film produced at 100°C substrate temperature.
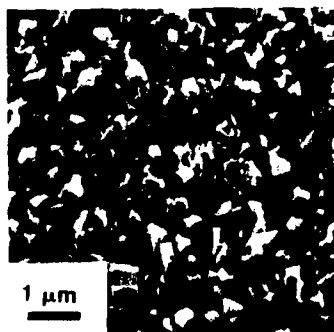
Figure 2   Scanning electron micrograph taken at 1.5 kV of $Co_{50}Ag_{50}$ film produced at 400°C substrate temperature.

The films were also shown to be composed of a fine, uniform dispersion of Ag and Co. The x-ray compositional maps shown in Figs. 3 and 4 show no observable segregation of individual components occurring during deposition at any substrate temperature.
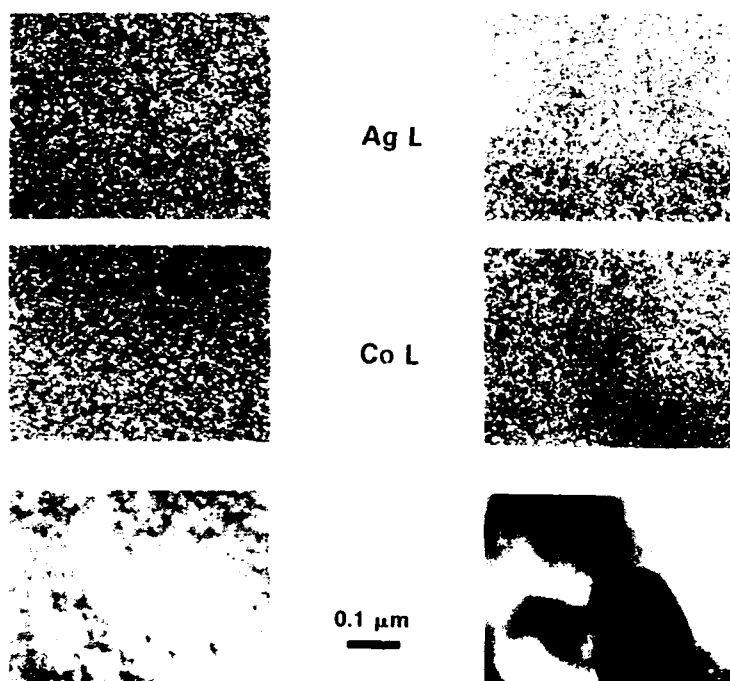
Figure 3

Figure 4

Figure 3   Fast x-ray maps for 100°C substrate temperature film. Maps made with 7 kV beam at 37° tilt. Imaging Ag and Co L radiation.

Figure 4   Fast x-ray maps for 400°C substrate temperature film. Maps made with 7 kV beam at 37° tilt imaging Ag and Co L radiation.

The x-ray diffraction profiles for the $Co_{50}Ag_{50}$ films obtained by varying the substrate temperatures from 100 to 500°C are shown in Fig. 5. As the substrate temperature was increased, the line widths of the diffraction peaks decreased. The position of the peaks was also dependent on the substrate temperature. The variations in d-spacing of the Ag(111) and Co(200) were very similar to the changes observed in Fe/Ag films produced at the same substrate temperatures [1].
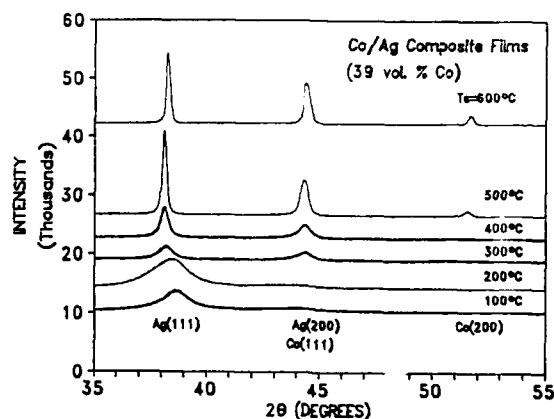
Figure 5   X-ray diffraction patterns for $Co_{60}Ag_{60}$ films.

The x-ray diffraction patterns show that the films were composed of fcc Ag and fcc Co. An exception to this was observed in the $Co_{71}Ag_{29}$ films at substrate temperatures less than 300°C. In these films, the Co was a mixture of fcc and hcp.

The broadening of the diffraction peaks as the substrate temperature decreases is due to decreasing crystallite size. The average crystallite sizes for the Ag and Co phases were determined by the Scherrer method [4]. LaB_6 was used to determine the broadening due to the instrument. The crystallite size increases with substrate temperature as shown in Figs. 6 and 7. As the substrate temperature was increased the Ag crystallite size increased from 61Å at 100°C to 700Å at 600°C and the Co crystallite size increased from 150Å at 400°C to 321Å at 600°C in the $Co_{60}Ag_{60}$ films. At substrate temperature of 400°C particle size starts to increase rapidly regardless of the film composition. This is the same temperature at which the d-spacing of the respective diffracting planes approaches the bulk value [1]. This indicates that all alloying which occurred during low temperatures deposition was eliminated by diffusion at substrate temperatures of 400°C and above and the structure consists of separate Ag and Co particles.

The magnetic coercivity of the films was measured at 6K parallel and perpendicular to the films. The coercivities obtained in the direction perpendicular to the film surface are shown in Fig. 8. The maximum value of coercivity in the $Co_{60}Ag_{60}$ film was found to be 522 Oe in the 400°C substrate temperature film. The coercivity maxima occur at different substrate temperatures as the film composition is varied. If the maximum coercivity points are compared to the corresponding Co particle sizes, it is seen that the maximum coercivity occurs when the Co particle size is between 100Å and 150Å. This size is in good agreement with the single domain size for Co reported by Luborsky [5].

The maximum coercivity values measured perpendicular to the films are higher than the maximum coercivity values measured parallel to the films. This anisotropy is due to the shape of the Co particles. This data indicates that the Co particles are longer in the dimension normal to the film surface than in the dimension parallel to the film surface. This is also in good agreement with the data obtained in the Fe/Ag films [1].
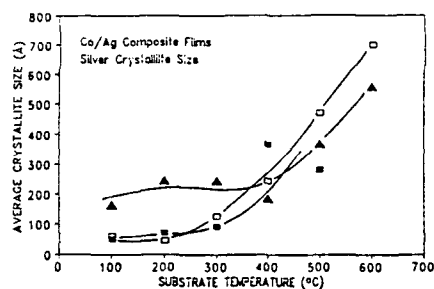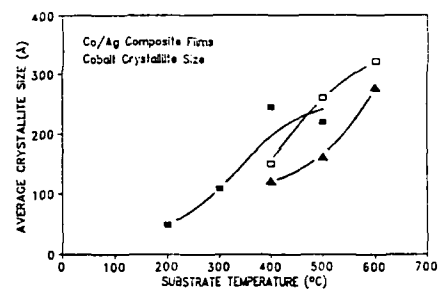
Figure 6   Figure 7

Figures 6 and 7   Average crystallite sizes of silver and cobalt vs.
substrate temperature.
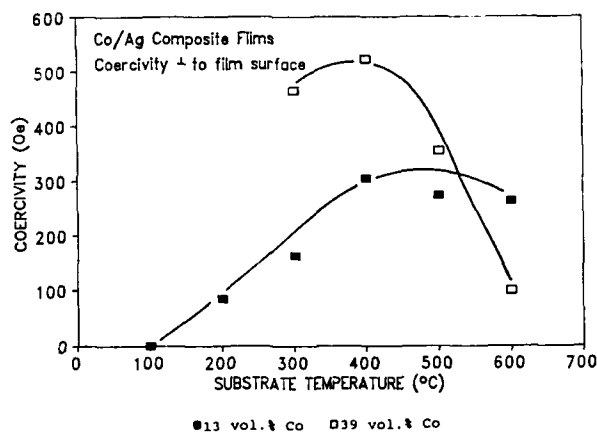
Figure 8   Coercivity measured perpendicular to film surface vs. substrate
temperature.

334

CONCLUSIONS

(1)   The surface roughness of the Co/Ag films increased with substrate
      temperature.

(2)   The films are composed of a fine, uniform dispersion of Co and Ag.

(3)   The Ag in the films is always fcc in structure. The Co in the films
      is fcc except at low substrate temperatures (<300°C) in the 61 vol. %
      Co films.

(4)   The crystallite size of both the Co and Ag phases increases with
      substrate temperature.

(5)   Maximum coercivity is found when the Co crystallite size is between
      100Å and 150Å.

REFERENCES

1. C.P Reed, R.J. DeAngelis, Y.X. Zhang, and S.H. Liou, Advances in X-Ray
   Analysis. 34, 557 (1990).

2. S.H. Liou, Y.Z. Zhang, and R.J. DeAngelis, Mat. Res. Soc. Symp. Proc.
   195, 451 (1990).

3. J.A. Thornton, J. Vac. Sci. Technol. 11, 666 (1974).

4. B.D. Cullity, Elements of X-Ray Diffraction, (Addison-Wesley Publishing
   Company, Inc., 1978) p.284.

5. F.E. Luborsky, J. Appl. Phys. 34, 171S (1961).

ACKNOWLEDGEMENT

SMALL d-SPACING AND INTERNAL STRESS OF Co-Cr FILMS DEPOSITED BY Kr ION SPUTTERING

S.AKIYAMA, S.NAKAGAWA AND M.NAOE
Department of Physical Electronics, Tokyo Institute of Technology,
2-12-1 O-okayama, Meguro-ku, Tokyo 152, Japan

ABSTRACT

It is important to control the internal stress of the deposited film because the magnetic tape is becoming thinner for attaining higher recording density per volume. Kr gas was used as the working gas in the facing targets sputtering (FTS) system for depositing Co-Cr films. Kr gas has the larger ionization cross section and atomic mass than those of Ar, Co and Cr, so that Kr gas could make stable discharge at lower pressure and the recoiling of Kr atoms on the surface of the Co-Cr target was more effectively suppressed. Therefore, Kr ions seem to be more advantageous as working gas than Ar ions which are the most common working gas. The FTS method with Kr ions could deposit the stress-free Co-Cr films with good crystallinity. Actually, $\Delta\theta_{50}$ and $(Mr/Ms)_{\parallel}$ of $Co_{79}Cr_{21}$ films deposited on Si wafer by Kr ion sputtering in the pressure range of $10^{-4} \sim 5\times10^{-3}$ Torr were as small as $4°$ and 0.1, respectively. The compressive stress of $1500Å$-thick $Co_{79}Cr_{21}$ films was as small as 10^{8} dyne/cm^{2}, of which the value was smaller than 10% of that by Ar ion sputtering. Therefore, the combination of the FTS method and Kr gas seems to be very convenient for solving the problem of the internal stress.

INTRODUCTION

In this study, the convenient technique of depositing Co-Cr films on polyethylene naphthalate (PEN) tape substrates has been developed by using the FTS method. Since tape substrates are becoming thinner for attaining higher recording density per volume, the internal stress of deposited films must be enough released. The FTS method has high ability of confining the γ-electrons and can maintain stable discharge even at low working gas pressure. Ar gas which is the most common sputtering gas could obtain stable discharge at pressure as low as 0.1 mTorr. However, Kr gas seems to be more advantageous as the sputtering gas than Ar gas. Since the Kr gas has larger ionization cross section, atomic mass and ion size than Ar gas, Kr gas can maintain stable discharge at lower gas pressure, increase the sputtering yields and promote the ejection of γ-electrons from the target surface. Moreover, the recoiling of Kr atoms on the target surface was suppressed because of the larger atomic mass, so that the bombardment of the recoiled Kr atoms to the depositing films may be prohibited. Therefore, the combination of the FTS method and Kr gas seems to be very convenient for solving the problem of the internal stress. In this study, the crystallinity and magnetic properties of Co-Cr films deposited by using Kr ions in the FTS equipment were compared with those of Co-Cr films deposited by using Ar ions.

EXPERIMENTAL

The FTS equipment used for preparing Co-Cr films in this study is shown in Fig. 1. [1][2] This system was composed of the facing targets sputtering source, the slit and the can roll. In the source, a pair of targets with composition of $Co_{79}Cr_{21}$ were located face to face and the permanent magnets were installed behind the targets to confine the plasma in the space between the two targets. The substrates were 12µm-thick PEN tape and Si
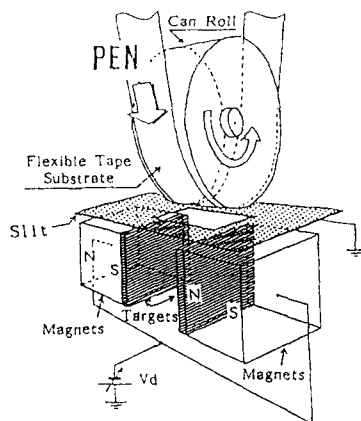
Fig.1 Schematic diagram

of facing targets sputtering

(FTS) equipment
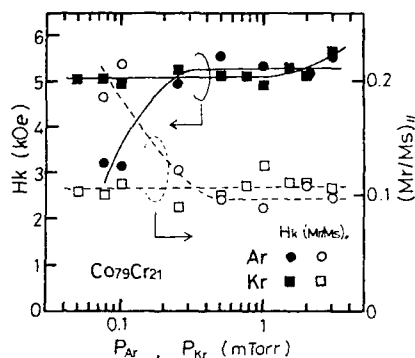
Fig.2 Dependence of Hk and (Mr/Ms)⊮

of Co₇₉Cr₂₁ films on P_{Ar} and P_{Kr}

wafer. The PEN tape was wound around the can roll which was located out of
the space between the two targets and perpendicular to the target plane.
The Si wafer was set on the can roll in the usual case and at the position
closer to the targets in the particular case. The substrate temperature T_s
was kept at room temperature and the sputtering gases were Ar and Kr.
Some films were deposited on the PEN tape substrate applied the DC bias
voltage, where the 100Å-thick $Co_{79}Cr_{21}$ underlayer was beforehand prepared on
it as the electrode. The crystallinity and magnetic properties of the
deposited films were examined by the X-ray diffractometry and the VSM,
respectively. The internal stress σ of the $Co_{79}Cr_{21}$ films deposited on
the PEN tape was calculated by the Stoney's equation based on the
deformation amount of the specimens measured by the cantilever method.

RESULTS AND DISCUSSION

Figure 2 shows the dependence of magnetic properties such as the
perpendicular anisotropic field Hk, the squareness (Mr/Ms)⊮ of the Co-Cr
films deposited on Si wafer at room temperature on the Ar and Kr gas
pressure P_{Ar} and P_{Kr}. Figure 3 shows the dependence of the crystallinity of
the Co-Cr films on P_{Ar} and P_{Kr}. While Hk, (Mr/Ms)⊮ and the dispersion angle
$\Delta\theta_{50}$ became worse at P_{Ar} below 0.1 mTorr, they were excellently good
even at P_{Kr} as low as 0.05~0.1 mTorr. Kr ions had the larger ionization
cross section than Ar ions, so that they could maintain stable discharge at
lower pressure, where the sputtered particles co. d obtain large kinetic
energy to become adatoms with higher migration potential on substrate planes
because of the longer mean free path. And Kr ions could transfer larger
momentum to the sputtered particles because of their larger mass.
Therefore, Kr ions were more advantageous as the working gas at lower
pressure than Ar ions, and the Co-Cr films deposited at lower P_{Kr} were
composed of well crystallized grains without inclusion of Kr and
impurities, and possessed high flexibility with densely packed micro
structure. As shown in Fig. 3, the interplanar spacing d of crystallites
in the films increased with decrease in P_{Ar} and P_{Kr}, where Kr ions gave
smaller d in Co-Cr films than Ar ions. This result may be attributed to more
remarkable suppression of the bombardment of recoiled Kr atoms to growing
films because of their larger atomic mass. The amount and direction in the
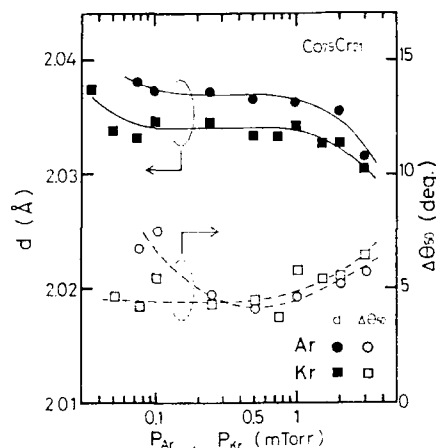
Fig.3 Dependence of d and $\Delta\theta_{50}$ of $Co_{79}Cr_{21}$ films on P_{Ar} and P_{Kr}

flux of recoiled atoms from the target surface depended on the elements of working gas and target. In general, the amount of recoiled atoms may depend apparently on the ratio of the atomic mass of working gas to that of the constituents of target. As the ratio increases in the range of one, the amount of recoiled atoms will decrease. When the ratio becomes more than two, the number of recoiled atoms will become negligible. [3] The atomic mass numbers of Ar, Cr, Co and Kr are 40, 52, 59 and 84, respectively. Since Kr ions have more two times larger atomic mass than Ar ones, the amount of Kr atoms recoiled from the surface of Co-Cr target were much smaller than that of Ar atoms. The Si wafer substrate was usually mounted on the surface of the can roll away 10 cm from the targets. In the special case, the Si wafer was moved to the position closer by 7 cm from the usual position to the targets. Figure 4 shows the dependence of d and $\Delta\theta_{50}$ on P_{Ar} and P_{Kr} in this special case. This figure indicates that the increase in d with decrease in the distance between substrate and targets decreased at lower P_{Ar} and P_{Kr}, though the recoiled amount of Kr ions was much smaller than that of Ar ions. This result could be attributed to the increase in the incident angle of the recoiled atoms to the substrate with movement of the substrate closer to the targets.
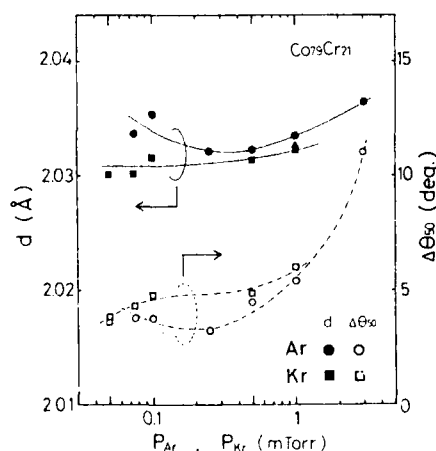
Fig.4 Dependence of d and $\Delta\theta_{50}$ of $Co_{79}Cr_{21}$ films deposited on substrate closer to targets on P_{Ar} and P_{Kr}

338

Figure 5 shows the dependence of the internal stress σ of the Co-Cr films deposited on the PEN tape substrate at room temperature on P_{Ar} and P_{Kr}, where the substrate was wound around the can roll . The subscripts MD and TD to parentheses of Ar and Kr in this figure denote the moving direction and the traverse direction of the tape, respectively. For both of
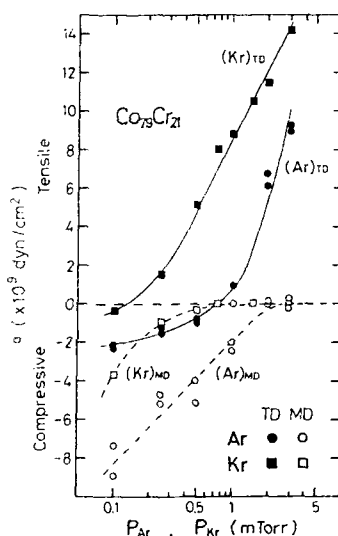
Fig.5 Dependence of internal stress σ

in $Co_{79}Cr_{21}$ films on P_{Ar} and P_{Kr}

the directions, σ was compressive and tensile at lower and higher P_{Ar} and P_{Kr}, respectively. Therefore, both of P_{Ar} and P_{Kr} had the optimum value for depositing the stress-free films and the optimum value of P_{Kr} was lower than that of P_{Ar}. Accordingly, Kr ions were more advantageous than Ar ions for depositing the stress-free Co-Cr films with good crystallinity. The compressive σ of the films deposited at lower P_{Kr} was smaller than that of the films at lower P_{Ar}. The strong correlation between d and σ was found, so that the difference in the compressive σ between the films deposited at lower P_{Ar} and P_{Kr} seemed to correspond to that in d. In order to confirm this assumption, 1500Å-thick $Co_{79}Cr_{21}$ films were deposited at lower P_{Ar} and P_{Kr} below 0.25 mTorr as the DC bias voltage was applied to the PEN tape substrate on which the 100Å-thick $Co_{79}Cr_{21}$ underlayer had been deposited in advance as the electrode. Figure 6 shows the dependence of d and $\Delta\theta_{50}$ on the DC bias voltage V_{sub}. This figure indicates that the bombardments of particles to the growing films increased the value of d. d of the films deposited in Ar gas at V_{sub} of 0 V was already lengthened so largely that it could not change so much even by applying the moderate bias voltage to the substrate. On the other hand, d of the films deposited in Kr gas at V_{sub} of 0 V was so short that it could increase very much by applying the bias voltage, since the accelerated Kr ions with large mass bombarded the depositing films. Figure 7 shows the dependence of σ at various P_{Ar} and P_{Kr} on V_{sub}. The compressive σ tended to change in correspondence to d. When the films deposited in Kr gas showed larger increase in d with the applied bias voltage than ones in Ar gas, the former films also showed the larger increase in σ than the latter ones. These results seems to support the assumption on the origin of the compressive stress.
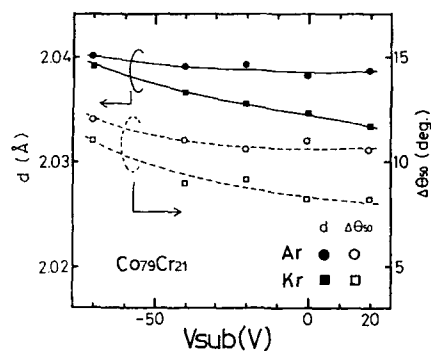
Fig.6 Dependence of d and $\Delta\theta_{50}$ of $Co_{79}Cr_{21}$ films on V_{sub}
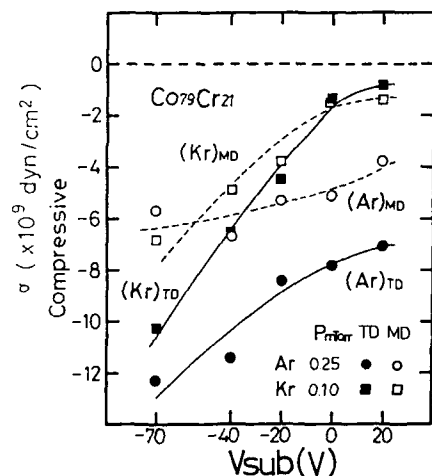
Fig.7 Dependence of σ in $Co_{79}Cr_{21}$ films on V_{sub} at P_{Ar} and P_{Kr} of 0.25 and 0.1 mTorr, respectively

Figure 8 shows the secondary electron images of surface appearance of the 1500Å-thick $Co_{79}Cr_{21}$ films deposited on the PEN tape at P_{Ar} and P_{Kr} of 0.25, 0.5, 1.0 and 3.0 mTorr. The surface appearance of the PEN tape looked rather uneven. All the specimen films revealed the stripe pattern very similar to that of the PEN tape. This result means that they were extremely homogeneous because the FTS method can carry out the plasma-free sputtering. However, there was the significant difference in the dependences of the surface appearance on P_{Ar} and P_{Kr} between the films deposited in Ar and Kr gases. While the films at P_{Ar} below 1 mTorr exhibited the compressive σ and the sparser stripes, the films at P_{Ar} above 1 mTorr exhibited the tensile σ and the crowded stripes. On the other hand, the films at P_{Kr} in the whole range from 0.25 to 3 mTorr exhibited the tensile σ and the crowded stripes. The films with the tensile stress deposited in both of Ar and Kr gases seemed to exhibit the the crowded stripe pattern. Therefore, the origin of tensile σ could be attributed to the morphological change in the deposited films.

340

$P_{Ar} \cdot P_{Kr}$ gas	0.25 mTorr	0.5 mTorr	1.0 mTorr	3.0 mTorr
Ar				
Kr				
ref.		12 μm-PEN 1 μm upper ⊢ lower ⊢		
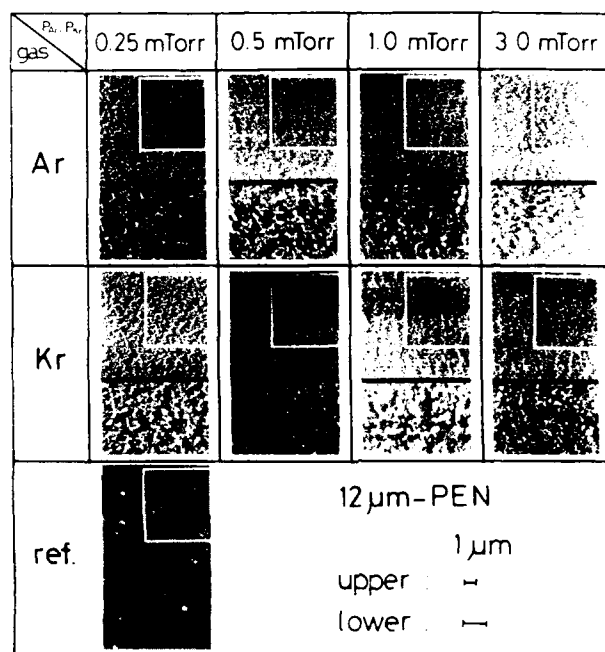
Fig.8 Secondary electron images of 1500Å-thick $Co_{79}Cr_{21}$ films

on PEN tape at P_{Ar} and P_{Kr} of 0.25, 0.5, 1.0 and 3.0 mTorr

CONCLUSION

$Co_{79}Cr_{21}$ films were deposited by using Kr ions in the FTS system. Since Kr atoms has larger ionization cross section and atomic mass than Ar gas which is the most common working gas. Kr gas could maintain stable discharge at lower pressure in the range of 10^{-5} Torr and deposit $Co_{79}Cr_{21}$ films with good crystallinity and sufficient perpendicular magnetic anisotropy. Since Kr gas could suppress the recoiling of Kr atoms on the target surface, the deposited films could avoid the increases in d-spacing and the compressive stress. Therefore, the FTS method with use of Kr ions should be very useful to the process for depositing the stress-free Co-Cr films with good crystallinity and flexibility for the perpendicular magnetic recording tape.

REFERENCES

[1]S.Akiyama,M.Sumide,S.Nakagawa and M.Naoe:
    IEEE Trans.Magn.,No5,25(1989),4189
[2]S.Akiyama,Y.Furuto,S.Nakagawa and M.Naoe:J.Appl.Phys.,No9,67(1990),5181
[3]G.K.Wehner,R.M.Warner,Jr.,P.D.Wang and Y.H.Kim:
    J.Appl.Phys.,No12,64(1988),6754

EPITAXIAL τMnAl/AlAs/GaAs HETEROSTRUCTURES WITH PERPENDICULAR MAGNETIZATION

T. SANDS, J.P. HARBISON, S.J. ALLEN, JR., M.L. LEADBEATER, T.L. CHEEKS, M.J.S.P. BRASIL, C.C. CHANG, R. RAMESH, L.T. FLOREZ, F. DEROSA AND V.G. KERAMIDAS, Bellcore, 331 Newman Springs Rd, Red Bank, NJ 07701-7040

ABSTRACT

Epitaxial films of ferromagnetic τMnAl with perpendicular magnetization have been grown on {100}AlAs/GaAs substrates by molecular beam epitaxy. A multistep growth procedure involving the formation of a template followed by codeposition and subsequent annealing yields thin epitaxial τMnAl films that exhibit the extraordinary Hall effect with nearly ideal hysteretic characteristics.

INTRODUCTION

Thin film magnetic recording media with magnetization perpendicular to the substrate surface offer the potential advantage of higher bit densities over conventional longitudinal recording media. Magnetic thin films with perpendicular magnetization are also desirable for magneto-optic recording utilizing the polar magneto-optic Kerr effect. Since the demagnetizing field in the thin film geometry favors in-plane magnetic moments, the attainment of perpendicular magnetization depends on the presence of structural anisotropy that establishes the film normal as the easy magnetization axis. Such anisotropy may be imposed by, for example, substrate-induced stress, artificial superlattices of alternating magnetic and nonmagnetic layers, surface anisotropy in ultrathin films, or crystallographic texture in a film of a material with uniaxial magnetocrystalline anisotropy. This latter method has been exploited in the present work to grow perpendicularly magnetized films of τMnAl on AlAs/GaAs substrates. In this paper, we discuss the relationships between growth conditions, microstructure, and magnetotransport properties in these heterostructures.

THE MnAl-AlAs MATERIALS SYSTEM

The only known ferromagnetic phase in the Mn-Al system is τMnAl, a metastable phase that is formed by quenching the high-temperature hexagonal ϵ phase, at a composition of 55 at% Mn, through the eutectoid point at 870°C (Fig. 1) [1]. The structure of the τ phase consists of alternating Al and Mn planes stacked along the c axis of the tetragonal unit cell. The Mn-Mn spacing in the basal plane is 0.277 nm (a_o) and the spacing between Mn planes along the c direction is 0.35-0.36 nm (c_o). The Mn moments on the Mn sublattice are ferromagnetically coupled and the c axis is the magnetically easy axis. This uniaxial magnetocrystalline anisotropy is strong, as indicated by the anisotropy field of 40kOe [2]. Excess Mn is incorporated onto Al sites and is antiferromagnetically coupled to the Mn sublattice [3]. The structure of τMnAl can also be visualized as a tetragonally distorted (c/a = 1.28) CsCl structure, the ordered cubic structure adopted by FeAl, CoAl, and NiAl. It is this similarity to the cubic transition metal aluminides (TM-Al), a class of intermetallics that may be grown as epitaxial films on III-V semiconductors, that initially attracted our attention. In our previous work with the cubic TM-Al phases, we demonstrated the epitaxial growth of III-V/TM-Al/III-V

342

heterostructures with electrically continuous TM-III films as thin as 1 nm [4]. The epitaxy is made possible by the close lattice match between $2a_o$ (TM-Al) and a_o(GaAs). Since $2a_o$ (τMnAl) is also within 2% of a_o(GaAs), we speculated that epitaxy of τMnAl on GaAs or AlAs with the basal plane of τMnAl parallel to the (100) substrate plane would be likely (see Fig. 2) [5]. Furthermore, we expected that the net decrease in free energy associated with epitaxy would favor the formation of the τ phase over the formation of ϵ, the high temperature hexagonal phase, or ζ (a rhombohedral Al-rich phase) + β Mn, the equilibrium two-phase mixture at low temperatures. All of the above phases have been identified in Mn-Al films deposited by sputtering onto glass slides [6].

Besides epitaxy, the nearly equiatomic TM-Al phases, including MnAl, exhibit a high degree of chemical stability on AlAs. The large mole fraction of Al in the TM-Al decreases or eliminates the thermodynamic driving forces for reaction with AlAs. Also, the nearly equiatomic TM-Al phases have relatively high melting points, further enhancing their stability in contact with AlAs, even at temperatures approaching III-V growth and device processing temperatures (400 - 600°C) [4].
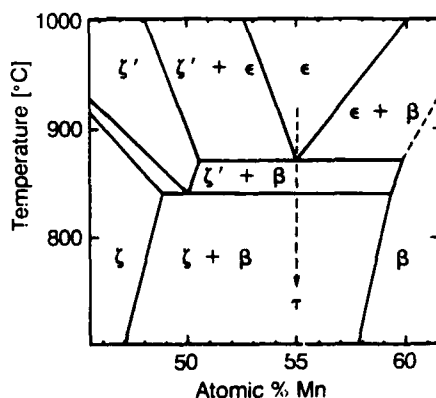
Figure 1. Portion of the Mn-Al phase diagram adapted from Ref. 1. The τ phase is formed by quenching the ϵ phase ($\sim$Mn$_{55}$Al$_{45}$) through the eutectoid point at 870°C.
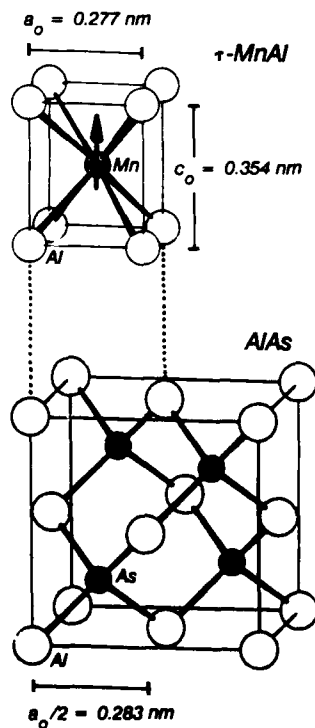
Figure 2. Correspondence of the AlAs and τMnAl structures. In this orientation, the Mn moments are aligned along the {100}AlAs substrate normal (from Ref. 5).

EPITAXIAL GROWTH

The epitaxial growth of MnAl/AlAs/GaAs heterostructures has been performed in a Riber 1000 MBE system equipped with effusion cell sources for Mn, Al, Ga, As and dopants. The details of the growth sequence have been described previously [5,7]. For the purposes of this paper, we can summarize the growth procedure as consisting of five consecutive steps; i) growth of the underlying III-V semiconductor heterostructure under conventional III-V growth conditions, ii) deposition of a thin (0.3 - 5 nm) amorphous Mn-Al template at about 20°C, iii) solid phase epitaxial growth of the τMnAl template initiating at the MnAl/AlAs interface during annealing at 100 - 300°C, iv) subsequent codeposition of Mn and Al at about 200°C, and v) annealing at about 400°C following growth.

MICROSTRUCTURE

The growth of τMnAl films on AlAs has been monitored *in situ* by reflection high-energy electron diffraction (RHEED). Our previously reported RHEED studies [5,7] have shown that the τ phase with the orientation relationship described by Fig. 2 is formed by solid phase epitaxial growth during the template annealing stage. During subsequent codeposition of Mn and Al, the epitaxial τ phase is in competition with the ε phase and, at low substrate temperatures, with an amorphous phase. These data have been confirmed by cross-sectional transmission electron microscopy (XTEM). The XTEM image in Fig. 3 shows a τMnAl film on AlAs. Note the horizontal lattice fringes of spacing 0.37 nm which corresponds to the spacing between (001) planes in the ordered
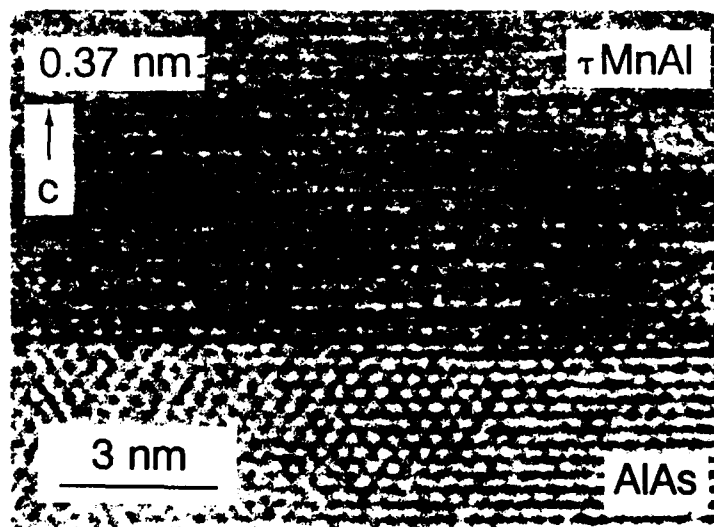
Figure 3. XTEM image of a τMnAl film on AlAs. The horizontal planes of spacing 0.37 nm are the (001) planes of τMnAl. AlAs appears in <011> zone-axis orientation.

344

tetragonal structure of τMnAl. A second phase, identified tentatively as the hexagonal ε phase (Fig. 4) has also been observed. Assuming hexagonal symmetry, we measure lattice parameters of a_o = 0.25 nm and c_o = 0.42 nm. The deviation in these values from the reported bulk lattice parameters of this phase, a_o = 0.2697 nm and c_o = 0.4356 nm [1], suggests a significant departure from the eutectoid composition of 55 at% Mn. It should be further noted that the ε phase is also epitaxial with {10$\bar{1}$1} planes of spacing 0.2 nm parallel to the vertical {022} AlAs planes of the same spacing. Because of the lower symmetry of ε, this orientation relationship has at least two, and possibly four, variants. We have found that the relative amounts of the ε and τ phases depend sensitively on the growth temperature and film thickness. RHEED studies indicate that the τ phase is only favored for very thin films (<10 nm) grown at temperatures of about 200°C. Moreover, films grown by direct codeposition without the template step consist primarily of the ε phase.
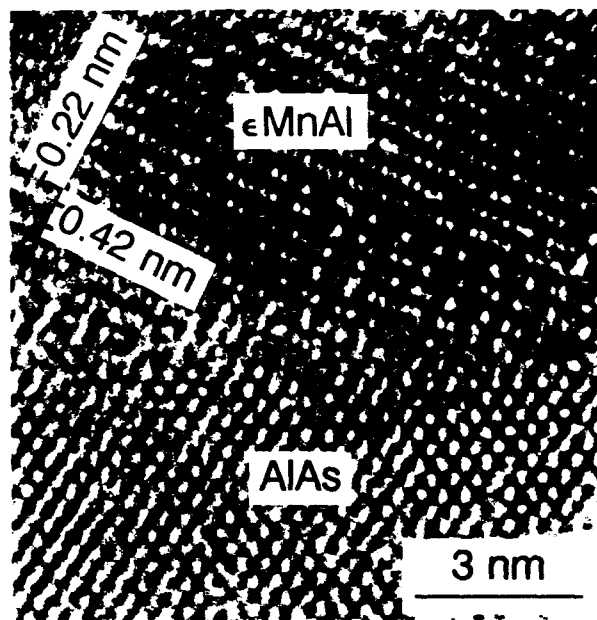
Figure 4. XTEM image of a grain of εMnAl in the predominantly τ-phase film imaged in Fig. 3. The εMnAl-AlAs orientation relationship is described in the text.

MAGNETOTRANSPORT: THE EXTRAORDINARY HALL EFFECT

It is well known that the Hall effect measured in a ferromagnetic film consists of an ordinary contribution and an "extraordinary" or "anomalous" contribution [8]. The extraordinary Hall effect (EHE), which is often much larger than the ordinary effect, arises from the asymmetric scattering of charged carriers off magnetic atoms. The transverse voltage that develops as a result of this asymmetry is proportional to the component of the magnetization that is normal to the film plane. In figure 5 we show a measurement of the Hall effect in a 5 nm film of τMnAl grown on an AlAs/GaAs substrate and patterned in a Hall bar geometry. The 100% remanence and the rectangular shape of the hysteresis loop are indicative of a very uniform ferromagnetic film with perpendicular magnetization. In essence, these Hall bars behave as nonvolatile binary memory elements. We are presently exploring reading and thermomagnetic writing processes in submicron Hall crosses fabricated from these films.

PROCESSING-MICROSTRUCTURE-PROPERTY RELATIONSHIPS

Considering the many variables associated with the Mn-Al system and the multistep epitaxial growth technique, it is an important, but complex, endeavor to establish the detailed processing-microstructure-property relationships. Our experience thus far is
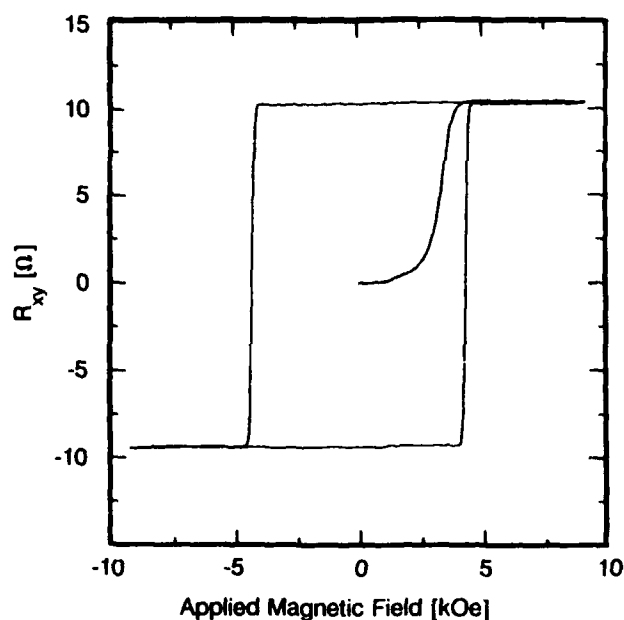
Figure 5. Extraordinary Hall effect measured in a 5 nm τMnAl film with the applied field normal to the film plane. The measurement was made at 295K. The resistivity and the extraordinary Hall resistivity of the film were found to be 130 $\mu\Omega$-cm and 5 $\mu\Omega$-cm, respectively.

346

limited, consisting only of about fifty growth runs. Nonetheless, we have observed several qualitative trends that have permitted some optimization of the growth process: i) The template step is necessary to obtain epitaxial τ-phase films; ii) Postgrowth annealing at about 400°C appears to be necessary to attain rectangular EHE characteristics with minimum coercive fields (3.5 - 5kOe at 300K). Samples that were not annealed generally exhibited "soft" EHE loops with large coercive fields (10 - 20kOe) [5,9]; iii) The most rectangular EHE characteristics are obtained with thin films (<20 nm) that have compositions near the bulk τMnAl composition of 55 at% Mn. Films of this composition also appear to be the most resistant to oxidation. We have observed accelerated deterioration of Mn-rich films in air, whereas thin films with nearly equiatomic composition have not degraded significantly during storage for months in the laboratory ambient. Auger electron spectroscopy (AES) depth profiles have revealed the formation of a thin (3-4 nm) protective oxide film that is primarily Al-O on these nearly equiatomic films. To avoid possible shifts in MnAl stoichiometry associated with oxide formation, we generally cap the MnAl film with amorphous GaAs prior to removal from the growth chamber.

SUMMARY AND CONCLUSIONS

In summary, we have demonstrated the epitaxial growth of perpendicularly magnetized τMnAl films on a GaAs substrate. These films exhibit rectangular EHE hysteresis loops indicating a high degree of uniformity in magnetic properties. We have further shown that these films can withstand typical III-V device processing temperatures by virtue of their intrinsic chemical stability in contact with AlAs. The compatibility of such magnetic films with III-V semiconductors provides a tantalizing building block for the fabrication of novel devices integrating magnetic, photonic and electronic effects.

ACKNOWLEDGEMENTS

We acknowledge useful conversations with A. Scherer, B. P. Vander Gaag, D. E. Aspnes, R. E. Nahory, H. L. Gilchrist and C.J. Palmstrøm. The assistance of D. Loretto and the staff of the National Center for Electron Microscopy, Lawrence Berkeley Laboratory, with the electron microscopy is appreciated.

REFERENCES

1. H. Kono, J. Phys. Soc. Japan 13, 1444 (1958).
2. A.J.J. Koch, P. Hokkeling, M.G.V.D. Steeg, and K.J. de Vos, J. Appl. Phys. 31 (Suppl.), 75S (1960).
3. P.B. Braun and J.A. Goedkoop, Acta Crystallogr. 16, 737 (1963).
4. See review: T. Sands, C.J. Palmstrøm, J.P. Harbison, V.G. Keramidas, N. Tabatabaie, T.L. Cheeks, R. Ramesh and Y. Silberberg, Mater. Sci. Reports 5, 99 (1990).
5. T. Sands, J.P. Harbison, M.L. Leadbeater, S.J. Allen, Jr., G.W. Hull, R. Ramesh and V.G. Keramidas, Appl. Phys. Lett. 57, 2609 (1990).
6. A. Morisako, M. Matsumoto and M. Naoe, J. Appl. Phys. 61, 4281 (1987).
7. J.P. Harbison, T. Sands, R. Ramesh, L.T. Florez, B.J. Wilkens and V.G. Keramidas, J. Crystal Growth (1991) in press.
8. See review: E.D. Dahlberg, K. Riggs and G.A. Prinz, J. Appl. Phys. 63, 4270 (1988).
9. M.L. Leadbeater, S.J. Allen, Jr., F. DeRosa, J.P. Harbison, T. Sands, R. Ramesh, L.T. Florez and V.G. Keramidas, J. Appl. Phys. (1991) in press.

ORDERING IN Zn$_{0.5}$Fe$_{0.5}$Se EPILAYERS GROWN ON InP SUBSTRATES BY MOLECULAR BEAM EPITAXY

L. SALAMANCA – RIBA*, K. PARK* AND B. T. JONKER**
* Department of Materials and Nuclear Engineering, University of Maryland, College Park, MD 20742-2115
** Naval Research Laboratory, Washington, DC 20375-5000

ABSTRACT

We have observed an ordered structure in Zn$_{0.5}$Fe$_{0.5}$Se epilayers grown on (001) InP substrates using transmission electron microscopy. The ordered structure of Zn$_{0.5}$Fe$_{0.5}$Se has Fe atoms occupying the (0,0,0) and ($\frac{1}{2},\frac{1}{2}$,0) sites and Zn atoms occupying the (0,$\frac{1}{2},\frac{1}{2}$) and ($\frac{1}{2}$,0,$\frac{1}{2}$) sites in the zinc-blende unit cell. Ordering is observed in both electron diffraction patterns and cross-sectional high-resolution lattice images along the $< 100 >$ and $< 110 >$ directions. This ordered structure consists of alternating ZnSe and FeSe monolayers along the $< 100 >$ and $< 110 >$ directions. Computer image simulations of the high-resolution images under various thicknesses, and defocusing conditions have been obtained and are compared with those obtained experimentally.

INTRODUCTION

Diluted Magnetic Semiconductors (DMS) - or semimagnetic semiconductors - are ternary or quaternary semiconducting compounds whose lattices are made up of partial substitution of magnetic ions [1]. DMS alloys are of considerable interest in the area of heterostructures and superlattices because the lattice parameter, energy gap, and effective mass can be "tuned" in a controlled fashion by varying the composition [2]. This tunability has recently been exploited in the fabrication of DMS superlattices. ZnSe, with a large direct band gap of 2.7 eV at room temperature, has potential applications for blue-light-emitting devices [3]. The magnetic ion, Fe, promotes the growth of the epilayer, and produces a more stable bonding configuration, and superior material stability compared to the Mn-based compounds [4]. Recently, ordered structures were observed in III − V, as well as, IV − VI semiconductors. The first ordered structure in a semiconductor III-V ternary alloy was observed in (AlGa)As alloy by Kuan et al. [5]. Since then, there have been numerous observations of ordered structures in several III-V ternary and quaternary alloys, such as, Ga(AsSb) [6, 7], (AlIn)As [8], Ga(AsP) [9], In(AsSb) [10], (GaIn)(AsP) [11, 12, 13]. Ordered structures have also been observed in IV − VI compounds, such as, (PbEu)Te [14]. To our knowledge, this is the first observation of an ordered structure in Zn$_{0.5}$Fe$_{0.5}$Se alloy.

EXPERIMENTAL DETAILS

A Zn$_{0.57}$Fe$_{0.43}$Se film of 525 Å thickness was grown on (001) InP substrates using a PHI Model 400 MBE system equipped with Auger electron spectroscopy (AES) and reflection high energy electron diffraction (RHEED). The detailed method of film growth has been published elsewhere [4]. Cross-section samples for transmission electron microscopy (TEM) were prepared by mechanical grinding and subsequent ion milling at liquid nitrogen temperature. The samples were ion-milled using 3 keV Ar$^+$ ions and 1 mA current to minimize the damage induced by ion milling. The structural studies were made using Philips EM 430, JEOL 2000FX-II, and JEOL 100CX transmission electron microscopes operated at 300 keV,

200 keV, and 100 keV, respectively.

To obtain more detailed information on the structure at the atomic level, computer simulations of the high-resolution lattice images were performed using the multislice method [15]. The simulated images were obtained for thicknesses in the range of 8 Å to 403 Å in steps of $\sim$ 8 Å with defocusing values in the range of -469 Å to -969 Å in steps of 100 Å.

RESULTS AND DISCUSSIONS

Figure 1 shows a (110) selected area diffraction (SAD) pattern from the interface between (ZnFe)Se film and (001) InP substrate. The strong spots in the SAD pattern originate from the overlap between the (110) planes of the film and the substrate because both have the same zinc-blende structure and relatively close lattice match. Double spots are observed in the SAD pattern far from the transmitted beam indicating that the film is relaxed. In addition to the allowed spots due to the zinc-blende structure, the SAD pattern shows the appearance of extra weak spots (marked by arrows) at the positions of the zinc-blende (001) and (110) reflections which suggests that $Zn_{0.5}Fe_{0.5}Se$ is an ordered alloy along the [001] and [110] directions. The shape of the extra weak spots is circular without any streaks or broadening. This suggests the near absence of antiphase boundaries [5, 11].

Dark field images were obtained under several two-beam conditions and showed the presence of misfit dislocations at the film-substrate interface. Some dislocations with Burgers vectors of $\frac{a}{2} < 110 >$ type lie on the (111) slip planes to make an angle of $\sim 54°$ with the (001) interfacial plane. Thus, the lattice mismatch of ~ 3.1 % between the substrate and the film is accommodated by the generation of misfit dislocations and by elastic strain. This suggests that the film thickness of 525 Å is larger than the critical thickness for the creation of misfit dislocations. The lattice constant of (ZnFe)Se alloy with 42.7 % Fe has been estimated and given by [16] :   a $= (5.666 \pm 0.001) + (0.051 \pm 0.01)x$. The calculated lattice constant of $Zn_{0.57}Fe_{0.43}Se$ alloy is 5.688 Å and the lattice constant of InP is 5.869 Å.

Figure 2 shows a model for the atomic configuration of an ordered compound of $Zn_{0.5}Fe_{0.5}Se$. The Fe atoms are placed at (000), $(\frac{1}{2}\frac{1}{2}0)$, the Zn atoms are placed at $(0\frac{1}{2}\frac{1}{2})$, and $(\frac{1}{2}0\frac{1}{2})$, and the Se atoms are placed at $(\frac{1}{4}\frac{1}{4}\frac{1}{4})$, $(\frac{1}{4}\frac{3}{4}\frac{3}{4})$, $(\frac{3}{4}\frac{1}{4}\frac{3}{4})$, and $(\frac{3}{4}\frac{3}{4}\frac{1}{4})$. This ordered
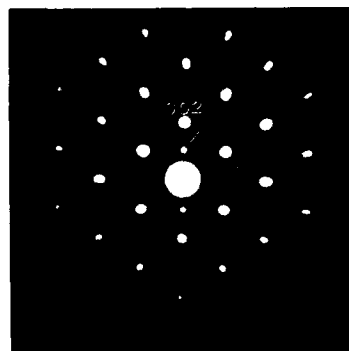
Fig. 1. (110) electron diffraction pattern from the interface between a (ZnFe)Se film and an InP substrate.
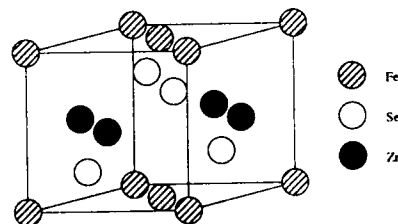
Fig. 2. Model for an ordered structure of $Zn_{0.5}Fe_{0.5}Se$ compound.

structure thus consists of alternating ZnSe and FeSe monolayers along both the [001] and the [110] directions. The calculated structure factors for extra diffraction spots originating from the ordered structure presented in this figure are: $F(001) = 2(f_{Fe} - f_{Zn})$ and $F(110) = 2(f_{Fe} - f_{Zn})$, where f_{Fe}, and f_{Zn} are the atomic form factors of Fe and Zn, respectively. This gives rise to (001) and (110) weak spots in the SAD pattern shown in Fig. 1. Generally, these weak spots have (hkl) indices such that h + k = even and k + l = odd, in other words, (hkl) are either (even,even,odd) or (odd,odd,even). This structure is identical to that reported for ordered $In_{0.5}Ga_{0.5}As$ observed by Kuan et al. [11].

Figures 3(a) and 3(b) are (110) high-resolution lattice images and their corresponding SAD patterns of the interface between the film and the substrate showing an ordered region and a disordered region, respectively. Eleven beams contributed to the lattice images in Fig. 3(a) and seven to Fig. 3(b). Figure 3(b) shows the typical image of a zinc-blende structure of a disordered alloy. The (111), (11$\bar{1}$) and (002) lattice fringes are observed. Occasionally, stacking faults and twins were observed on the (111) planes in some areas of the high-resolution lattice images. Examples of stacking faults are marked by arrows in Fig. 3(b). The interface between the film and the substrate is also marked by arrows.

Contrary to Fig. 3(b), contrast modulations with periodicities of 5.639 Å and 3.939 Å along the [001] and [110] directions, respectively, are observed in Fig. 3(a). The values of 5.639 Å and 3.939 Å were obtained from optical diffractograms taken from the negatives of the images and approximately correspond to the (100) and (110) interplanar spacings of (ZnFe)Se obtained from the SAD patterns, respectively. The radius of the objective aperture used to obtain the images shown in Fig. 3 was 0.337 Å^{-1}. This aperture is not large enough to include completely the (002) spots. Thus, the (001) and (110) fringes are clearly seen in Fig. 3(a) but the (002) fringes are weak. The alternate variations of contrast in the lattice images confirm the ordered structures along the [001] and [110] directions. An anti-phase boundary (APB) is shown on the right-hand side of Fig. 3(a), where a phase-shift of the
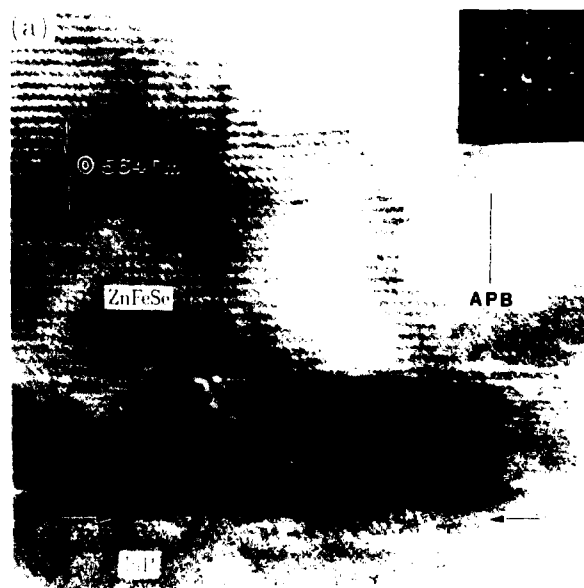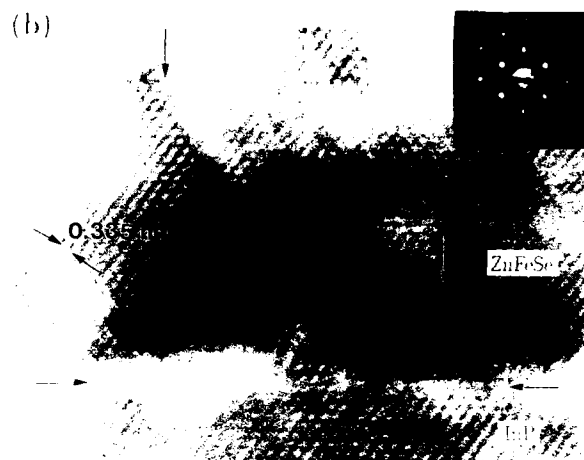
Fig. 3. (a) (110) lattice images showing an ordered structure in (ZnFe)Se alloy and (b) (110) lattice images showing a disordered structure in (ZnFe)Se alloy.

(001) fringes is observed. APB's have been observed by Ueda *et al.* [13] in high-resolution lattice images of ordered (InGa)P compounds. Figure 3(a) also shows an unidentified layer in the (ZnFe)Se film close to the interface. At this time we do not know the origin and composition of this layer. An interplanar distance of 3.398 Å in the layer was obtained from optical diffractograms taken from the negative of the image. We should note that the ordered structure was observed in areas with and without the unidentified layer. This indicates that the ordered phase is not related to the unidentified phase. We believe that the ordered structure forms at the surface of the film during epitaxial growth as it was previously suggested [6]. The formation of the ordered structure is believed to result from surface diffusion of Zn and Fe atoms during the high temperature growth. The diffusion coefficient in the solid at room temperature is too low to allow post-growth formation of ordered structure by solid state diffusion. The ordered structure is more stable than the disordered structure partially due to strain effects [17]. The ordering transition is strain driven and strain stabilized [18].

Computer image simulations using the multislice method [15] was performed for the model shown in Fig. 2 with compositional modulations along the [001] and [110] directions. The beam direction of [110] perpendicular to the modulation directions was used to obtain the simulated images. The contrast in these images is largely controlled by the sample thickness and microscope imaging conditions. Figure 4 shows pendollösung plots for (001), (002), (110), and (220) beams as a function of sample thickness. The thickness of the strongest contrast for the ordered structure is ~ 274 Å.

Simulated images for a sample thickness of 274 Å with defocusing values of $\Delta f = -169$ Å, -569 Å, -669 Å, -769 Å, -869 Å, and -969 Å are shown in Fig. 5. The best match between simulated and experimental images is obtained for a thickness of 274 Å with a defocusing value of -869 Å. Clear contrast due to the ordered structure was obtained for thicknesses in the range of 169 Å to 346 Å. However, when the sample thickness is less than 169 Å or greater than 346 Å, only weak compositional modulation contrast was obtained.

The simulated images in the calculation were obtained using 566 beams. The total intensity of all beams used in the calculation for a thickness of 403 Å is ~ 90 % of the incident intensity. The parameters used in the computation of the images are the operating voltage, $V = 200$ kV, the radius of the objective aperture, $r_s = 0.337$ Å^{-1}, spherical aberration, $C_s = 2.3$ mm, semi-angle of illumination, div $= 1.0$ mrad, half width of Gaussian spread of vibration, vib $= 0.0$ Å, and half width of Gaussian spread of defocus, del $= 50$ Å.
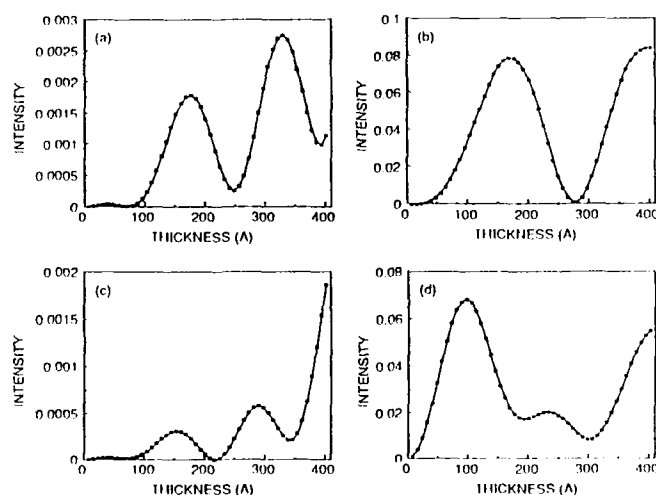
Fig. 4. Pendollösung plots for the beams which give rise to ordered structure. (a) (001), (b) (002), (c) (110), and (d) (220).
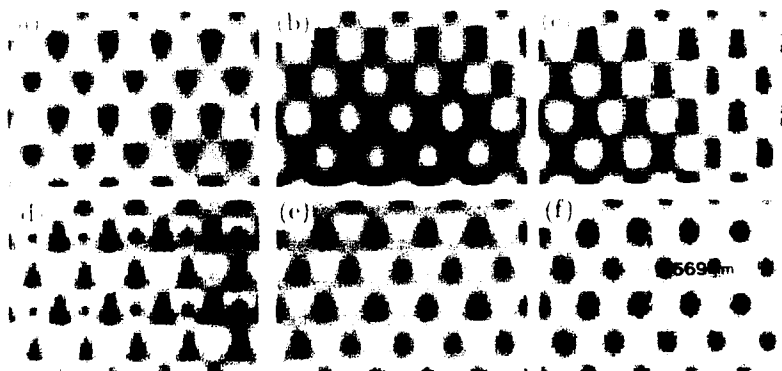
Fig. 5. (110) simulated images of a $Zn_{0.5}Fe_{0.5}Se$ alloy with 274 Å thickness for several defocusing values. (a) −469 Å, (b) −569 Å, (c) −669 Å, and (d) −769 Å, (e) −869 Å, and (f) −969 Å.

352

CONCLUSIONS

Ordered structures were observed for the first time along the [001] and [110] directions in electron diffraction patterns and high-resolution lattice images of a $Zn_{0.57}Fe_{0.43}Se$ film grown on (001) InP substrate by MBE. The ordered structure consists of a sequence of alternating ZnSe and FeSe layers along the [001] and [110] directions.

ACKNOWLEDGEMENTS

REFERENCES

[1] J. K. Furdyna, J. Vac. Sci. Technol. **A 4**, 2002 (1986).

[2] S. Datta, J. K. Furdyna. and R. L. Gunshor, Superlattices and Microstructures, **1**, 327 (1985).

[3] S. B. Sant, J. Kleiman, M. Melech, R. M. Park, G. C. Weatherly, R. W. Smith, and K. Rajan, in Inst. Phys. Conf. Ser. **87**, 129 (1987).

[4] B. T. Jonker, J. J. Krebs, S. B. Qadri, and G. A. Prinz, Appl. Phys. Lett. **50**, 848 (1987).

[5] T. S. Kuan, T. F. Kuech, W. I. Wang, and E. L. Wilkie, Phys. Rev. Lett. **54**, 201 (1985).

[6] H. R. Jen, M. J. Jou, Y. T. Cherng, and G. B. Stringfellow, J. Cryst. Growth **85**, 175 (1987).

[7] I. J. Murgatroyd, A. G. Norman, and G. R. Booker, J. Appl. Phys. **67**, 2310 (1990).

[8] A. G. Norman, R. E. Mallard, I. J. Murgatroyd, G. R. Booker, A. H. Moore, and M. D. Scott, in Inst. Phys. Conf. Ser. **87**, 77 (1987).

[9] H. R. Jen, D. S. Cao, and G. B. Stringfellow, Appl. Phys. Lett. **54**, 1890 (1989).

[10] H. R. Jen, K. Y. Ma, and G. B. Stringfellow, Appl. Phys. Lett. **54**, 1154 (1989).

[11] T. S. Kuan, W. I. Wang, and E. L. Wilkie, Appl. Phys. Lett. **51**, 51 (1987).

[12] M. A. Shahid, S. Mahajan, D. E. Laughlin, and H. M. Cox, Phys. Rev. Lett. **58**, 2567 (1987).

[13] O. Ueda, M. Takikawa, M. Takechi, J. Komeno, and I. Umebu, J. Cryst. Growth **93**, 418 (1988).

[14] L. Salamanca-Young, D. L. Partin, and J. Heremans, J. Appl. Phys. **63**, 1504 (1988).

[15] J. M. Cowley, and A. F. Moodie, Acta Cryst. **10**, 609 (1957); J. M. Cowley, and A. F. Moodie, Acta Cryst. **12**, 353 (1959); J. M. Cowley, and A. F. Moodie, Acta Cryst. **12**, 360 (1959).

[16] H. J. M. Swagten, A. Twardowski, W. J. M. de Jonge, and M. Demianiuk, Phys. Rev. **B 39**, 2568 (1989).

[17] G. P. Srivastava, J. L. Martins, and A. Zunger, Phys. Rev. **B 31**, 2561 (1985).

[18] A. Ourmazd, and J. C. Bean, Phys. Rev. Lett. **55**, 765 (1985).

HIGH-PRESSURE X-RAY DIFFRACTION STUDIES OF ELASTIC ANOMALIES IN SUPERLATTICE

Y. FUJII, Y. OHISHI[*], H. KONISHI[**], N. NAKAYAMA[+] AND T. SHINJO[++]
   Univ. of Tsukuba, Inst. of Mat. Sci., Tsukuba 305, Japan
 * Sumitomo Chem. Ind., Tsukuba 300-32, Japan
** Jpn. Atomic Energy Res. Inst., Tokai 319-11, Japan
 + Kyoto Univ., Dept. of Chem., Kyoto 606, Japan
++ Kyoto Univ., Inst. of Chem. Res., Uji 611, Japan

ABSTRACT

This paper has made an overview on elastic and structural aspects of three distinct superlattices under hydrostatic pressure up to about 8GPa, which were studied by our unique x-ray diffraction technique incorporated with a diamond-anvil cell. They are metallic fcc/fcc Au/Ni, bcc/fcc Mo/Ni, and semiconductive epitaxially-grown PbSe/SnSe superlattices. In their layer-stacking direction, both metallic superlattices show the supermodulus behavior while the semiconductive one doesn't. However, its pressure-driven cubic-to-orthorhombic phase transition, successively taking place in the SnSe and PbSe layers, has been found to significantly shift by stress due to its epitaxial growth.

INTRODUCTION

Koehler's early theoretical prediction of the "strong solid" in alternately-deposited layered materials[1] motivated experimental studies on elastic properties of various types of artificially-fabricated superlatices. Particularly since the anomalously large biaxial elastic modulus Y_B ("supermodulus effect") was reported in Au/Ni and Cu/Pd superlattices[2], the elastic property has extensively been studied as one of major subjects to explore novel solid state properties expected in superlattices. Some metallic superlattices have been known to show a significantly larger or smaller elastic modulus than that of either bulk of two consituent components. Elastic measurements are made by several methods such as a bulge-tester, a vibrating reed, and the Brillouin scattering[3], which probe the elastic response with the wavelength much longer than interatomic distances. Khan et al.[4] carried out both x-ray diffraction and Brillouin scattering on Mo/Ni superlattices. They found that the softening of surface acoustic wave velocity was remarkably enhanced near its superlattice period $\Lambda = 17A$ and it correlated well with the anomalous lattice-spacing expansion of the Ni layer. This was the first observation of the structural anomaly correlated with the elastic anomaly. However, only a small number of such structural examinations has been made so far. To obtain any clue to the microscopic mechanism of the elastic anomaly

taking place in superlattices, we previously developed a unique x-ray diffraction technique to detect both elastic and structural anomalies by applying hydrostatic pressure. We applied this technique for the first time to Mo/Ni superlattice and observed the supermodulus effect in its layer-stacking direction[5].

In this paper, we have briefly reported two other superlattices of Au/Ni and PbSe/SnSe similarly-examined, in conjunction with our previous data of Mo/Ni.

EXPERIMENTAL TECHNIQUES

Since this technique was previously reported[5], a brief description is given in this section. By applying hydrostatic pressure, we measure the peak position and intensity of Bragg reflections from a superlattice. The pressure dependence of lattice constants (a,b,c vs P) enables us to determine each elastic modulus along its three principal directions of the superlattice. A measure defined by $\kappa_a = -\partial(a/a_0)/\partial P$ is called a linear compression along the a axis where a_0 is a at atmospheric pressure. When it differs significantly from that of bulk, analyzing the intensity data makes it possible to examine any structural anomaly in the elastically-anomalous state.

Diamond-anvil cell

We used a diamond-anvil high-pressure cell(DAC) to apply hydrostatic pressure to a superlattice [5-7]. A sample specimen was removed from a substrate and placed on a thin kapton film($7\mu m$) to avoid any elastic influence Then it was trimmed as typically 0.3mm in diameter and mounted in a sample chamber of DAC, which was a hole (0.35mm in diameter and 0.05mm in thickness) drilled in a metal gasket sandwitched by two opposed diamond anvils (Fig.1). Hydrostatic pressure was assured up to about 10GPa by the use of an alcohol mixture (ethanol : methanol = 4 : 1 in volume) as pressure-transmitting fluid. Pressure was determined from the energy shift of fluorescence line from ruby chips enclosed with the sample[7].

Figure. 1

A superlattice specimen confined with a metal gasket compressed by two diamond anvils. Typical sizes used in the present experiment are given in mm. X-ray beam path is also shown.
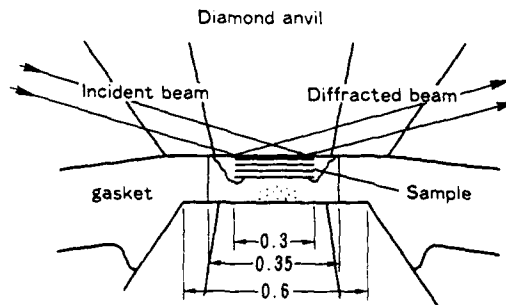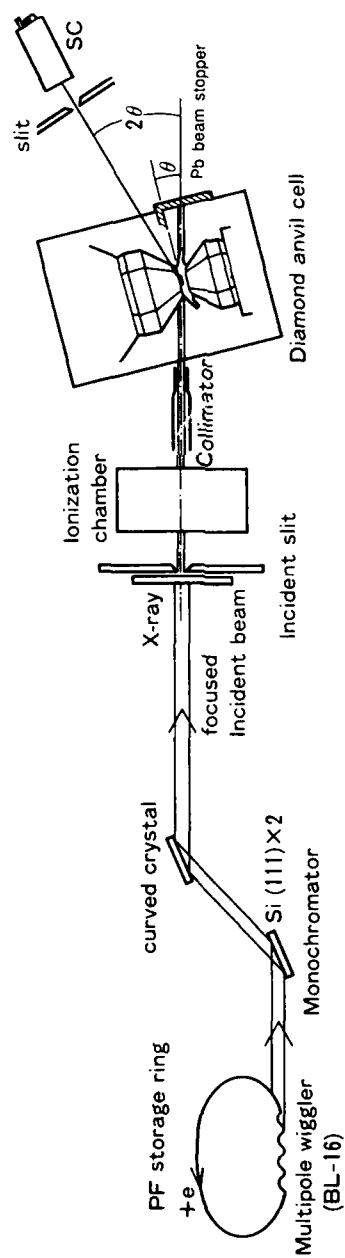
Figure 2.   A schematic drawing of a set-up of the present high-pressure experiments on a multi-pole wiggler beam line at Photon Factory.

X-ray diffraction

At an early stage of our experiments, we used a rotating-anode x-ray source(12kW, Mo target) incorporated with a position-sensitive detector to detect very weak signal from a small sample. Later synchrotron radiation x-rays(SRX) were employed at Photon Factory (positron storage ring, 2.5GeV/350mA) as schematically shown in Fig. 2. Either a conventional bending-magnet source(BL-4C, 6B) or a multipole wiggler souce(BL-16X) was used. Incident beams monochromatized by a sagitally-focussing double Si(111) monochromator ($\lambda = 1.0 -1.1$ A) were further collimated by a pin-hole collimater 0.15mm in diameter. Diffraction patterns were measured by a scintillation counter with a step-scanning mode of operation. All measurements were made at room temperature.

Figure 3 displays diffraction patterns around the (200) reflection along the layer-stacking direction of [PbSe(10A)/SnSe(10A)]50 superlattice measured on (a) the SR bending-magnet source and (b) the rotating-anode source[8]. One can clearly see remarkable improvement of intensity as well as momentum resolution by the use of SRX.
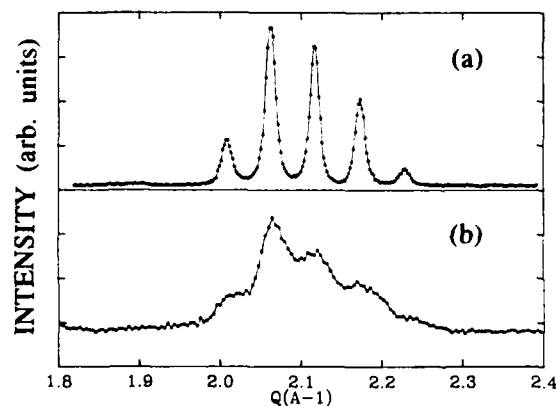
Figure 3.

Diffraction patterns around (200) in the layer-stacking direction of [PbSe(10A)/ SnSe(10A)]50 measured on (a) bending-magnet SR and (b) rotating-anode sources. Peak intensity of the strongest reflection is (a) 720 and (b) 1.2 cps.

METALLIC SUPERLATTICE

Au/Ni superlattice

This is the first superlattice in which in-plane biaxial elastic modulus $Y_B[111]$ was found to be significantly enhanced. The present specimens were prepared by a ultrahigh vacuum deposition technique on a kapton film(7μm) with a Au(111)fcc buffer layer(250A); therefore, both Au and
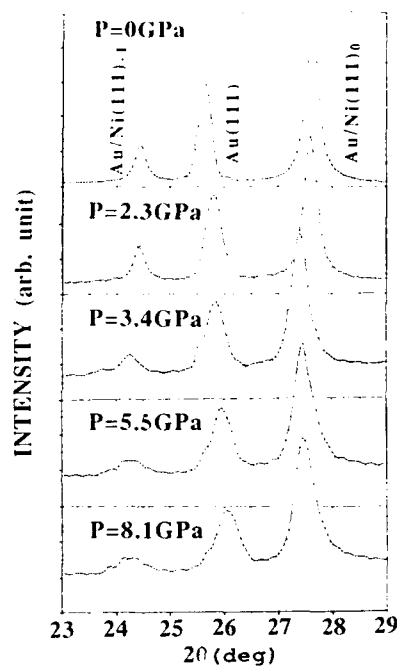
Figure 4

Diffraction patterns along the
layer-stacking direction of
$[Au(10A)/Ni(10A)]_{50}/Au(250)$
as a function of pressure.

Ni layers had the $(111)_{fcc}$ texture. Figure 4 shows the pressure dependence of medium-angle diffraction patterns around the (111) reflection along its layer-stacking direction observed on [Au(10A)/ Ni(10A)]$_{50}$/Au(250A) [9]. The central peak corresponds to the Au(111) Bragg reflection from the buffer layer while the right and left ones are the average (111) from the superlattice and the first order satellite in the lower-angle side, respectively. From the shift of peak positions, the relevant lattice spacings can be obtained as a function of pressure as plotted in Fig. 5. One can see that the superlattice is much less compressible than the buffer layer which is as compressible as bulk. Elastic moduli are calculated from the slope of lines drawn in Fig. 5 as follows:

Au/Ni superlattice		2,750 GPa
Au buffer layer		210
Reference	bulk Au	217
	bulk Ni	177 - 187.

An analysis of the intensity data is now being made to explore any structural anomaly correlated with such a supermodulus effect observed in this system.

360
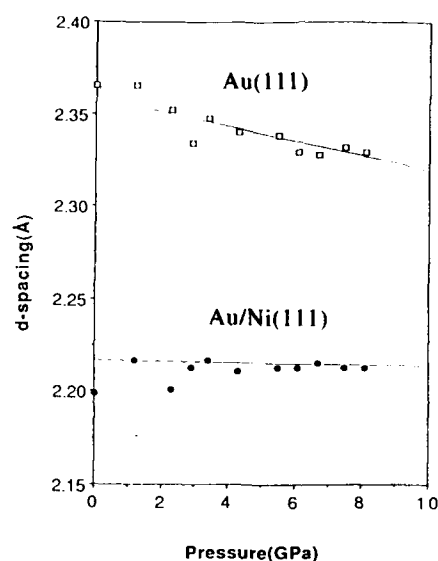
Figure 5.   Pressure dependence of lattice-spacings of
Au(111) of the buffer layer and the average
(111) of the superlattice. One can see that the
superlattice is much less compressible than the
buffer layer.

Mo/Ni superlattice

In this system, the softening of both shear elastic constant measured by Brillouin scattering[4] and perpendicular elastic stiffness by pico-reflectance[11]   was previously reported to critically enhance towards its critical superlattice period of about 20A.   In contrast to these results, we previously observed   that both [Mo(20A)/Ni(20A)]80 and [Mo(60A)/ Ni(60A)]40 prepared by an ion-beam sputtering showed the super-modulus effect along their layer-stacking direction Mo[110]bcc/Ni[111]fcc in a pressure range from atmospheric pressure to about 4GPa[5].   Beyond this point, they became as compressible as bulk metals.   According to our recent preliminary structure analysis of the latter superlattice by an extended step model[11] taking a variable interface thickness into account, the Mo layer is anomalously expanded (max. 2%) and the interface thickness is larger than the average of two bulk lattice-spacings in the pressure range where *the supermodulus effect is observed.*

SEMICONDUCTIVE SUPERLATTICE

PbSe/SnSe superlattice

Preliminary results were also reported previously[12]. A bulk of PbSe
and SnSe compounds has the cubic $B1(O_h^5)$ and orthorhombic $B16(D_{2h}^{16})$
structures stable at atmospheric pressure. respectively. The B16 lattice
can be realized as a denser structure by doubling one of principal <100>
axes of the B1 lattice [13]. In fact. PbSe undergoes the B1-to-B16 phase
transition at 4.3GPa while the B16 structure is stable in SnSe at lowest up
to 34GPa [14]. Hiroi et al.[15] successfully grew epitaxial superlattices of
PbSe/SnSe on a NaCl(100) substrate and found four types of structures
stabilized systematically depending upon the thickness of two layers.
They are [B1/B1], [B1/B16], [distorted B16/B16], and [B16/B16] for the
[PbSe/SnSe] layer structure. Figure 6 displays diffraction patterns around
the (400) reflection along the layer-stacking direction observed on
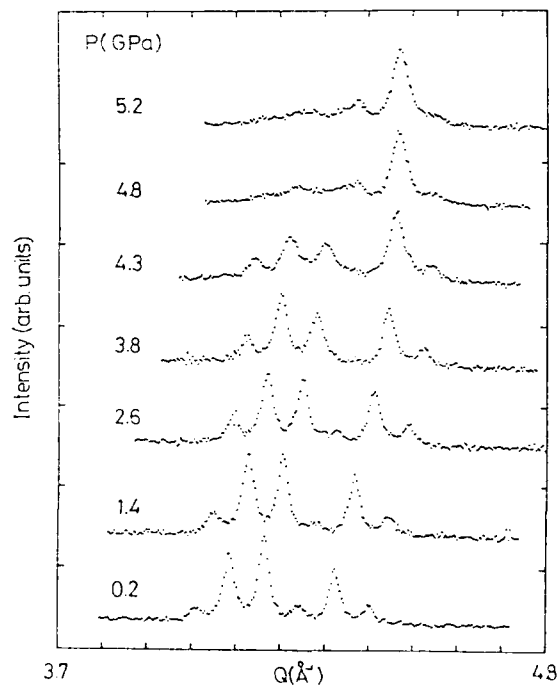
Figure 6.   Pressure dependence of diffraction patterns around
(400) along the layer-stacking direction observed on
[PbSe(40A)/SnSe(40A)]25. One can see a drastic change
between 4.3 and 4.8 GPa where the low-pressure
[B1/B16] structure transforms to [B16/B16].

[PbSe(40A)/SnSe(40A)]25 with the as-grown [B1/B16] structure. When we apply hydrostatic pressure, it contracts as compressible as bulk and then the PbSe layer undergoes the first-order B1-to-B16 transition at 4.3GPa. This fact can be directly evidenced by a remarkable change in diffraction pattern (Fig. 6) as well as in the linear compression curve obtained from the peak position (Fig. 7). The slope of the linear compression, i.e. compressibility, is nearly equal to that of a bulk of PbSe. Therefore no elastic anomaly was observed in this system. Figure 8 summarizes the B1-to-B16 transition pressure(P_C) of the PbSe layer as a function of the number of PbSe atomic planes deposited(m). The transition pressure of a bulk PbSe was measured to be 5.3GPa by the use of a similarly-deposited thin PbSe film (1000A). Our detailed intensity analysis of the observed patterns evidences normal compression of both PbSe and SnSe layers in contrast to the metallic superlattices[16]. We also succeeded in calculating the Pc vs m curve by a phenomenological theory taking the stress effect due to the epitaxial growth into account[17].
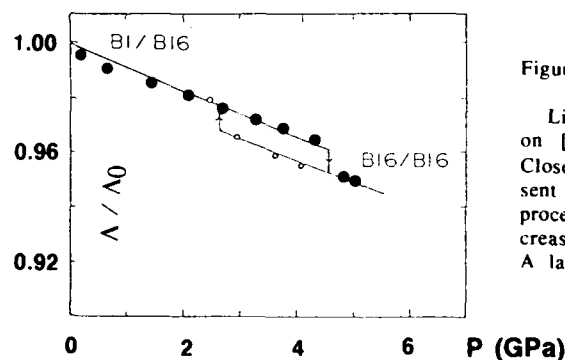
Figure 7

Linear compression measured on [PbSe(40A)/SnSe(40A)]25. Closed and open circles represent data points mesured in the process of increasing and decreasing pressure, respectively. A large hysteresis is observed.
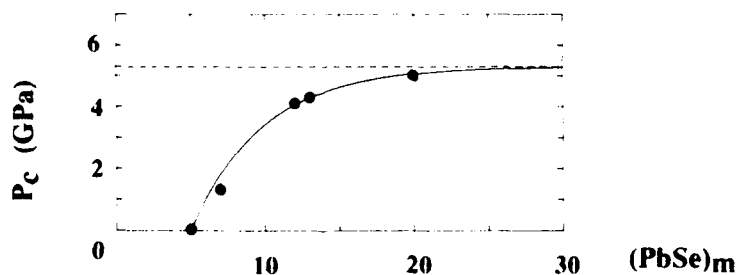
Figure 8   The B1-to-B16 transition pressure (P_C) versus number of atomic planes of PbSe layer(m). Closed circles represent data points while solid curve shows theoretical calculation expressed by $P_C=5.3[1-\exp\{-0.209(m-5)\}][17]$.

DISCUSSION

Our previous and present high-pressure x-ray diffraction studies show the anomalously large elastic modulus in two metallic superlattices Au/Ni and Mo/Ni and no anomaly in the semiconductive one PbSe/SnSe. This elastic modulus was measured as an inverse of the linear compression along the layer-stacking direction being an elastic response to hydrostatic pressure. However, this is not a conventional macroscopically-measured quantity because it was obtained from the pressure dependence of a microscopic superlattice period. Due to a geometrical restriction of our present DAC design, an in-plane elastic mudulus in the film plane has not been measured. There must be an anisotropy in elastic property. In fact our recent measurements of thermal expansion of the present Au/Ni sample between room temperature and 10K have evidenced a large anisotropic contraction with decreasing temperature as well as appreciable difference from the bulk nature[9].

Many theoretical and computational works have been reported about a microscopic origin of elastic anomalies[3]. However, most of them provided elastic moduli for an axial stress, not for hydrostatic pressure. Therefore, no calculated results are directly available to compare with our present experimental data. According to Imafuku et al.[18] who carried out molecular dynamics calculations of Young's modulus Y[111] along the layer-stacking direction of Au/Ni superlattice, a large enhancement by a factor of about five was obtained at $\Lambda = 20A$ which corresponds to our sample. In our case, an enhancement factor is about 12. About the origin of this hardening, they claimed the incoherent structure at interface. If this is the case, a superlattice with the longer Λ shows less anomaly because the volume of the interface relative to the bulk layer decreases. In the case of Mo/Ni superlattices, however, such a hardening was observed equally in both $\Lambda = 40A$ and $120A$ samples as we showed in the previous experiments[5].

As stated in the preceding section on Mo/Ni superlattice, the elastic stiffness measured by pico-reflectance[11] softened oppositely to our results[5]. Since both groups measured it along the layer-stacking direction, the experimental condition different between two experiments is that they measured an elastic response to the uniaxial stress dynamically-applied with pico-second duration(THz) while we measured that to hydrostatic pressure statically applied(0Hz). However, no probable explanation has not been made for this puzzling problem.

In the case of epitaxially grown semiconductive superlattice PbSe/SnSe, in addition to the present sample we have carried out similar measurements on several others with different layer thickness[16]. The linear compressibility of all specimens behaves normally in contrast to the metallic superlattices. It has not been clear that such an elastically normal state is due to its nonmetallic character or to its epitaxy without structural disorder at the interface.

We have planned further experiments not only to explore the in-plane elastic modulus of these three superlattices but also to systematically investigate elastic properties of other systems by using our unique technique. We also hope that our experimental works encourage theoretical calculations on elastic properties under hydrostatic pressure.

REFERENCES

1. J.S. Koehler, Phys. Rev. B$\underline{2}$, 547 (1970).
2. W.M.C. Yang, T. Tsakalakos, and J.E. Hilliard, J. Appl. Phys. $\underline{48}$, 876 (1977).
3. See, for example, I.K. Schuller, Physics, Fabrication and Application of Multilayered Structures, edited by P. Dhez and C. Weisbuch (Plenum Press, New York and London, 1988) p.139; I.K. Schuller, A. Fartash, and M. Grimsditch, MRS Bulletin (Oct. 1990) p.33.
4. M.R. Khan, C.S.L. Chun, G.P. Felcher, M. Grimsditch, A. Kueny, C.M. Falco, and I.K. Schuller, Phys. Rev. B$\underline{27}$, 7186 (1983).
5. Y. Ohishi, Y. Fujii, N. Nakayama, T. Shinjo, T. Matsushita, and J. Fujita, Multilayers (MRS Intn'l Meeting on Advanced Materials) $\underline{10}$, 569 (1990).
6. Y. Fujii, Y. Ohishi, M. Kowaka, N. Hamaya, K. Takemura, S. Hoshino, K. Tsuji, and S. Minomura, Physica $\underline{139\&140}$B, 907 (1986).
7. For example, A. Jayarahman, Rev. Mod. Phys. $\underline{55}$, 65 (1983); Rev. Sci. Instrum. $\underline{57}$, 1013 (1986).
8. Y. Ohishi, PhD. thesis ,Univ. of Tsukuba, 1991.
9. H. Konishi, Y. Fujii, Y. Ohishi, N. Hamaya, H. Kawada, N. Nakayama, R. Yu, H. Donomae, T. Shinjo, and T. Matsushita, to be presented at SRI-91 (Chester, U.K., July 1991).
10. B.M. Clemens and G.L. Eesley, Phys. Rev. Lett. $\underline{61}$, 2356 (1988).
11. Y. Fujii, T. Ohnishi, T. Ishihara, Y. Yamada, K. Kawaguchi, N. Nakayama, and T. Shinjo, J. Phys. Soc. Jpn. $\underline{55}$, 251 (1986).
12. Y. Ohishi, N. Shingaki, Y. Fujii, Z. Hiroi, N. Nakayama, Y. Bando, and T. Shinjo, High Pressure Research $\underline{4}$, 300 (1990).
13. Y. Fujii, K. Kitamura, A. Onodera, and Y. Yamada, Solid State Commun. $\underline{49}$, 135 (1984).

14. T. Chattopadhyay, A. Werner, H.G. Schnering, and J. Pannetier, Revue Phys. Appl. 19, 807 (1984).
15. Z. Hiroi, N. Nakayama, and Y. Bando, J. Appl. Phys. 61, 206 (1987); Z. Hiroi, Phil. Magazine B 61, 895 (1990).
16. Y. Ohishi, Y. Fujii, Z. Hiroi, N. Nakayama, Y. Bando, and T. Shinjo, (private commun.).
17. Y. Fujii, Y. Ohishi, and J.D. Axe, (private commun.).
18. M. Imafuku, Y. Sasajima, R. Yamamoto, and M. Doyama, J. Phys. F 16, 823 (1986).

Magnetic and Structural Characteristics of Multi-layered
Films Composed of Fe and Si Ultra-thin Layers

K.Kubota, [*] M.Nagakubo, and M.Naoe
Dept. of Physical Electronics, Tokyo Institute of Technology [*]
2-12-1 O-okayama, Meguro-ku, Tokyo 152, Japan. Osaka Vacuum
Ltd., 775, 7-cho Ohtori-Higashi-machi, Sakai 593, Japan

ABSTRACT

Fe and Si layers were deposited alternately by using ion beam
sputtering apparatus and the relationship between crystal structure and soft
magnetic properties of these multi-layered films have been investigated in
detail. The clear periodicity of multi-layered films was confirmed even at
the thicknesses of Fe and Si layers δ_{Fe} and δ_{Si} as small as 8.5 Å.
The saturation magnetization $4\pi Ms$ for all Fe layers decreased with
decrease of δ_{Fe} and δ_{Si}, and the coercivity Hc of these films took minimum
of 1.0 Oe at δ_{Fe} of 8.5 Å.
Such a significant decrease of $4\pi Ms$ may be attributed to the formation of
nonmagnetic regions at both side of each Fe layers. The thickness of these
nonmagnetic regions may be estimated at approximately 1.5 Å from the
measured value of $4\pi Ms$. This thickness seems to be very small because it is
almost equal to that of one monolayer of bcc α-Fe. The low Hc of the films
with δ_{Fe} and δ_{Si} of 8.5 Å may be due to the formation of ultra-fine
crystallites in Fe layer by insertion of amorphous Si layer and the direct
magnetostatic interaction among Fe layers.

INTRODUCTION

Studies on multilayered films composed of ferromagnetic and non-
magnetic ultra-thin layers has become very popular since they may possess
exhibit magnetic properties hopeful for new applications.[1,2] The ion beam
sputtering method was used in this study because those films are prepared on
the substrates free from plasma by this method and it is easy to get
multilayered films under the strict control of preparation condition.   Fe
and Si layers were deposited alternately by using the ion beam sputtering
apparatus and the relationship between crystal structure and soft magnetic
properties of these multilayered films have been investigated in detail.

EXPERIMENT

The dual ion beam sputtering apparatus used in this study is shown in Figure 1. Ar gas as pure as 99.999 % was introduced into the sputtering ion source at pressure of 1.5×10^{-4} Torr. The planar targets of Fe and Si with purity of higher than 99.99 % were alternately sputtered in turn by a fixed beam of argon ions extracted from sputtering ion source at the accelerating voltage Vs of 500 V and the total ion current of 3 mA.

The saturation magnetization 4πMs and the coercivity Hc were determined on M-H hysteresis loops measured by using a vibrating sample magnetometer. The microstructure and the crystal structure of the multilayered films were analyzed by X-ray diffractometry.
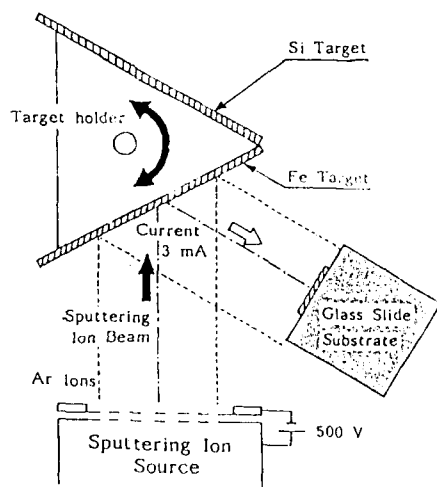
Fig.1 Schematic diagram of layout in
ion beam sputtering apparatus.

RESULTS AND DISCUSSION

Microstructure

Figure 2 shows a typical low angle X-ray diffraction diagram of Fe/Si multilayered films. For the films with δ_{Fe} and δ_{Si} of 8.5 Å, clear multilayer structure was confirmed from the first peak at 2θ as low as about 5.3 deg. Those results shows that the Fe/Si multilayered films with δ_{Fe} and δ_{Si} for each layer thickness below 10 Å can be easily fabricated by ion beam sputtering because the substrate is free from plasma.

Figure 3 shows the high angle X-ray diffraction diagrams for the films with δ_{Si} of 20 Å. For all films, only one peak at 2θ of about 45 deg. corresponding to (110) plane of α-Fe was observed. Figure 4 shows the dependence of the average crystallite size <D> determined from half value width of (110) peak on δ_{Fe}, where <D> was smaller than δ_{Fe}. This implies that the crystallite growth in Fe layers during deposition was effectively interrupted by insertion of Si layers.
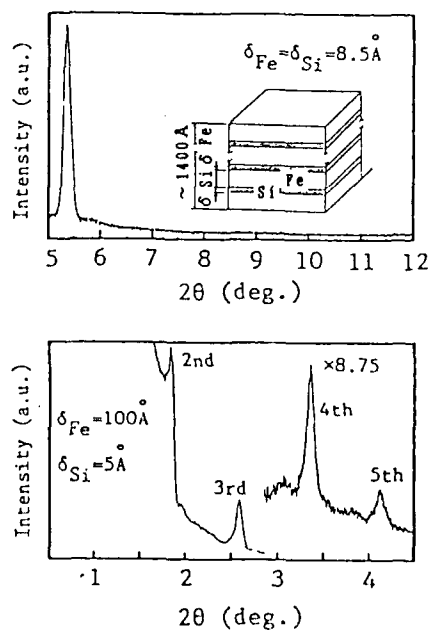
Fig.2 Low angle X-ray diffraction diagram.
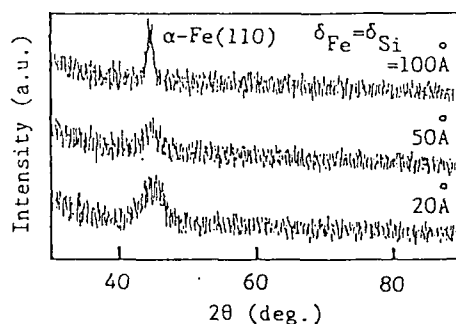
Fig.3 High angle X-ray
diffraction diagram.
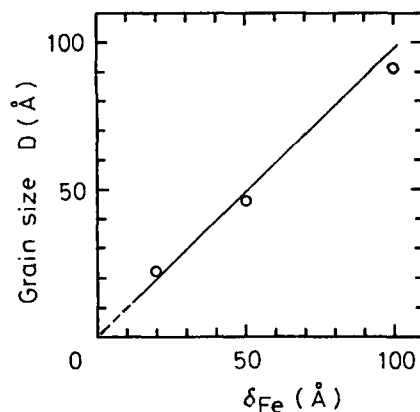
Fig.4 Dependence of average
crystallite size $\langle D \rangle$ on δ_{Fe}.

Magnetic Properties

Figure 5 shows the dependences of $4\pi Ms$ of all Fe layers and Hc on δ_{Fe} and δ_{Si}. $4\pi Ms$ estimated for all Fe layers decreased with decrease of δ_{Fe} and δ_{Si} and Hc took minimum of 1.0 Oe at δ_{Fe} of about 8.5 Å. Such a drastic decrease of $4\pi Ms$ may be attributed to formation of the nonmagnetic Si diffused region in Fe layers adjacent to Si layers.[3] Figure 6 shows the δ_{Fe} dependence of $4\pi Ms$ estimated by assuming the existence of nonmagnetic region with their thickness δa Å at both side of each Fe layer. The measured values fits very well to the estimated ones when δa was assumed to be 1.5 Å. This value of a seems to be very small because it is almost equal to that of one monolayer of bcc α-Fe. Consequently, this ion beam sputtering method may be very useful for fabrication of Fe/Si multilayered films without significant interdiffusion between each Fe and Si layer.
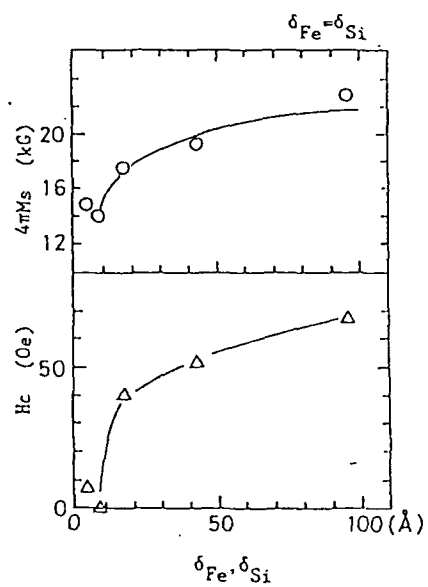
Fig.5 Dependence of 4πMs estimated
for all Fe layers and Hc on δ_{Fe}
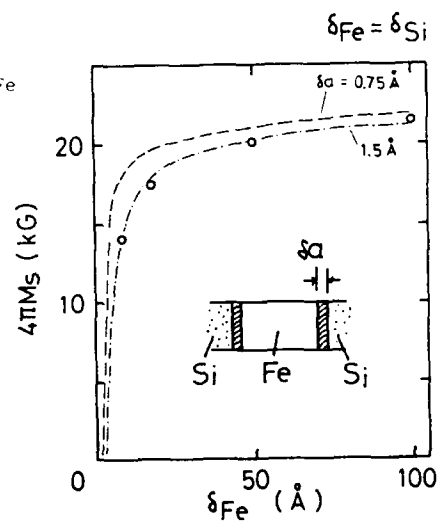
Fig.6 Dependence of 4πMs estimated
for all Fe layers on δ_{Fe}.

CONCLUSION

The clearly multilayered films composed of Fe and Si layers with their thickness of δ_{Fe} and δ_{Si} as small as 8.5 Å were fabricated by ion beam sputtering. Their coercivity was as low as 1.0 Oe. The decrease of 4πMs with decrease of δ_{Fe} and δ_{Si} agreed well with the estimated decrease of 4πMs when the thickness of nonmagnetic region existing at both side of each Fe layer was assumed at 1.5 Å. So, it may be concluded that the formation of ultra-fine crystallites in Fe layers by insertion of the ultra-thin Si interlayers can sufficiently improve the soft magnetic properties of Fe/Si multilayered films.

REFERENCE

[1] Y.Shimada, IEEE Trans. Magn., vol.24 No.6 (1988) 3075.

[2] N.Kumasaka, J. Appl. Phys. 55(6). 15 (1984) 2238.

[3] N.S.Kazama, H.Fujimori, I.Yuito, and H.Kronmuller,
    IEEE Trans. Magn., vol.20, No.5 (1988) 1296.

STRUCTURE AND MAGNETISM OF NI/FE MULTILAYERS.

NIGEL M. JENNETT* and D.J. DINGLEY*
*Bristol University, H.H.Wills Physics Laboratory, Tyndall Ave, Bristol, BS8 1TL, England.

ABSTRACT

X-ray diffractometry at grazing incidence has been performed upon Ni_n/Fe_n multilayers with 6<2n<30mpl (n = no. of monolayers per layer, mpl), as a further test that the observed reduction in magnetisation (as n decreases) was not due to interfacial alloying. The results show that the interfaces are terraced to the extent that pinholes occur in the thinner layers. The layers became continuous for modulations 2n>10mpl. Each X-ray scan revealed a series of peaks which corresponded to integer monolayer differences in modulation periodicity. In contrast, interfacial alloying would have produced a broad single peak.

M-H loops were performed on the samples for the range of temperatures 6<T<300K using a vibrating sample magnetometer with the field always applied in the plane of the sample. The sample coercivity was observed to vary with modulation wavelength such that at a modulation of 2n=16mpl it was about a factor of three greater than at either 2n=6mpl or 2n=30mpl. The coercivity peak occurs at a value of n equal to the critical layer thickness for the transformation of the Fe from FCC to BCC. High angle X-ray diffractometry shows an apparent change in planar spacing at the same modulation layer thickness (n=8mpl).

The ratio of remnant magnetisation at low temperature to that at room temperature, RT, was greater than unity for all the samples measured. The ratio increased as the modulation period of the samples decreased. This is consistent with a modulation period dependence of the Curie temperature of the Ni/Fe multilayers.

INTRODUCTION

Previous work by the authors has shown that $Ni_s Fe_n$ multilayers grown in UHV conditions, exhibit a layer thickness dependent structural transition in the Fe from FCC at small n, to BCC at large n. This structural change is matched by a change in sample magnetisation, multilayers with FCC Fe having a magnetisation up to three times less than multilayers with BCC Fe [1]. Further structural characterisation by cross sectional transmission electron microscopy (TEM) and X-ray diffractometry has demonstrated that all the samples grown were modulated, including the n=3mpl sample. However, extra satellite peaks around the X-ray Bragg peaks indicated terracing of the interfaces and some pinholing in the thinner layers [2]. A more direct method of measuring the modulation period of a multilayer is to look for "zero order" Bragg peaks at low angles, ϕ, such that 2kSinϕ = 1/2n (k = 1/X-ray wavelength). We report here the results of applying such a method.

There is mounting evidence that Fe on an appropriate FCC lattice is antiferromagnetic (AFM) [3-6] and the low magnetisation of the Ni/Fe(FCC) multilayers is consistent with this. Proving the Fe is AFM is difficult with techniques that do not probe the moment per site or the nearest neighbour magnetic coupling directly. However, by using the assumption that FCC Fe is AFM, it is possible to predict the macroscopic magnetic properties of Ni/Fe(FCC, AFM) multilayers. In this paper we report our investigation of the effect of temperature on the magnetic properties of Ni/Fe multilayers. The results are then compared with the predictions of a Monte Carlo simple Ising spin model developed by Taylor and Gyorffy [8].

EXPERIMENTAL METHOD

X-ray measurements were made in a Rigaku double crystal powder diffractometer using a Molybdenum source filtered by 0.075mm of Zirconium to reduce the KB line to 2 per cent of the KA1 intensity. The angle step size was 0.01 deg. Samples were rotated 180 degrees in the plane of the diffractometer's reference surface and the positions of the Bragg peaks (for 0° and 180° rotation) were averaged to eliminate any mounting errors. The alignment of the diffractometer was calibrated against a standard Si powder sample. Any offsets had to be known accurately before X-ray scans were performed at low angles, since small absolute errors in angle cause proportionately larger errors in the determination of the modulation period as the angle of reflection is reduced.

Magnetic measurements were made using the vibrating sample magnetometer (VSM) at the Laboratoire de Magnetisme C.N.R.S. Bellvue Paris. The main components of this machine were an Oxford Instruments gas circulation cryostat, a water-cooled electromagnet capable of 17kOe and a Princeton Applied Research EG+G model 5206 2-phase lock-in amplifier. Every sample was subjected to the maximum field in each direction for every loop, regardless of whether data at high fields was recorded. The field was always applied in the plane of the multilayers. The output from the VSM was fed directly into an X-Y plotter. Precision in measuring coercivity, Hc, and remnant magnetisation, Mr, therefore depended on the scale selected. The mica substrate of the multilayers created a further problem. As the temperature was reduced, the paramagnetic susceptibility of the mica substrate, only a small fraction of the sample signal at room temperature, increased as $1/T$ (and deviated slightly from perfect Curie law dependence at high fields). The low temperature M-H loops therefore always had strongly paramagnetic tails which prevented the direct determination of the saturation magnetisation, Ms. At best Ms could be found by extrapolating the tails of the loop back to zero applied field. To avoid the possibility of errors in fitting the tails causing, when extrapolated, large errors in Ms, the values of the remnant magnetisation, Mr, were used to compare the effect of temperature on magnetisation. Even so, the small absolute values of moment recorded for the small n multilayers resulted in the errors in remnant magnetisation ratio, Mr(T)/Mr(RT), being as much as +/-10% for some samples.

RESULTS
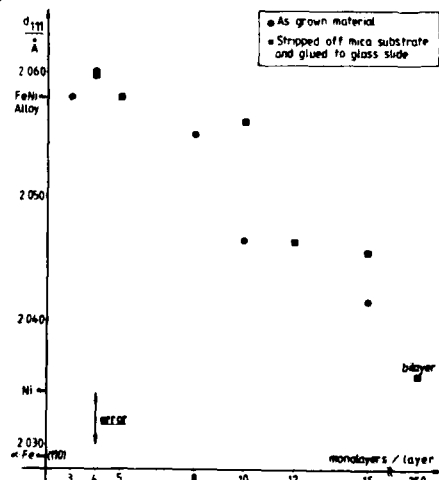
Figure 1. Graph of planar spacing vs modulation layer thickness as calculated from the Bragg peak positions at more than one reflection (eg. <111>, <222>, <333>). Circles represent measurements made on "as-grown" samples, ie multilayers still on the mica substrate. Squares represent measurements made on samples stripped off the mica substrate.

X-ray diffractometry yielded the Bragg angles for a number of relections in each multilayer. Each reflection corresponded to a different order of the fundamental <111> planar spacing. The average of the equivalent <111> spacings for each set of reflections is plotted against modulation layer thickness in figure 1.

X-ray diffractometry at low angles revealed peaks at 'Bragg' angles corresponding to the modulation period of the multilayers. The main peak observed corresponded to a modulation period within 1mpl of the design modulation. A weaker set of peaks corresponding to different modulation periods were also observed. Each of these peaks could be easily resolved. The differences in period of adjacent peaks was 1 monolayer, which is characteristic of sharp but terraced interfaces. The multilayers with modulations n<5mpl, however, also had peaks corresponding to there being significant amounts of the multilayer with a modulation period of 3n instead of 2n characteristic of pinholing of one layer.

The magnetisation of the Ni_nFe_n multilayers, at both low temperatures and room temperature, followed the same pattern as previously published [1]: The totally FCC multilayers had magnetisations which were over a factor of three less than that of the Ni/Fe(BCC) multilayers regardless of whether Mr, or Ms, were compared. The ratio of Mr(T)/Mr(RT) was greater than one for all samples and increased progressively for samples with shorter modulation periods (see figure 3).
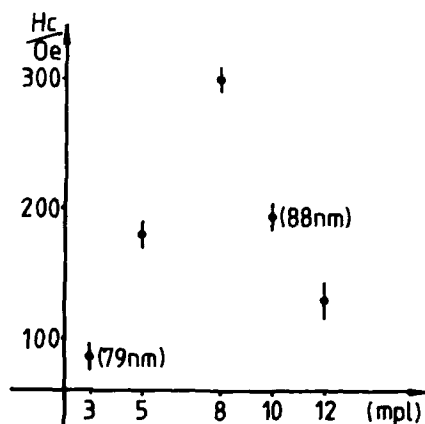
Figure 2(a). Graph of room temperature Hc vs modulation layer thickness for "as grown" Ni_nFe_n multilayers (total modulation thickness = 100nm unless otherwise indicated).
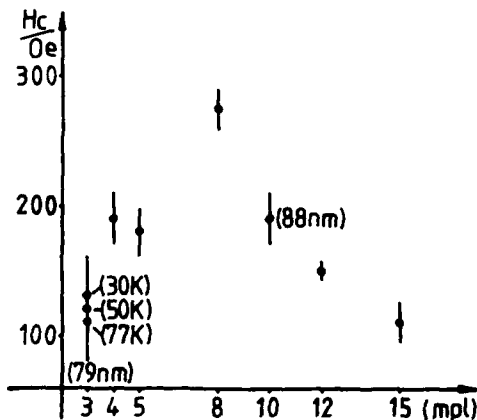
Figure 2(b). Graph of Hc at 6.5K (unless otherwise indicated) vs modulation layer thickness for the same Ni_nFe_n multilayers.

376
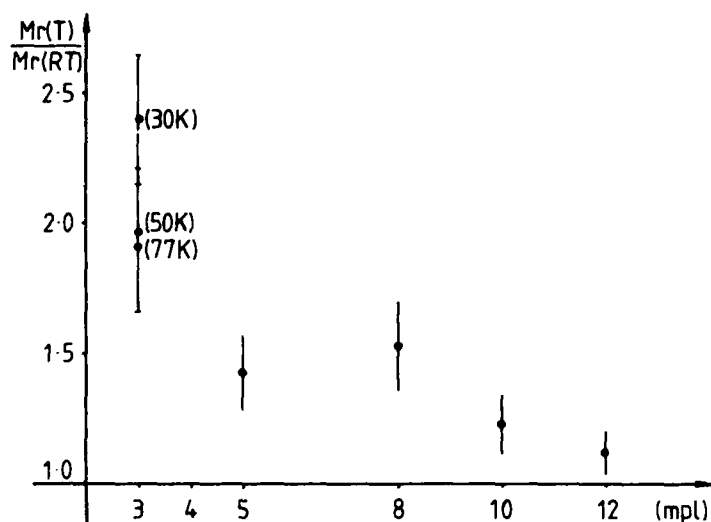
Figure 3. Graph of Mr(T)/Mr(RT) vs modulation layer thickness for Ni_nFe_n multilayers.

DISCUSSION

The low angle X-ray data discounts any possibility that the reduction in magnetisation observed in the Ni/Fe(FCC) multilayers is due to interfacial alloying. Quantisation of the modulation period can only occur if the interfaces are stepped. A graded composition interface (eg due to alloying) would create a continuum of modulation periods. This would have the effect of broadening the Bragg peaks and reducing their peak intensity, but could not produce the discrete peaks observed.

In figure 1, the error margin marked is quite large for X-ray determinations of lattice parameter. This was because the computer interface used was not capable of driving the diffractometer at its maximum resolution. The apparent step in planar spacing is therefore only twice the error margin allowing a straight line (least squares) to be a reasonable fit. However, plan view transmission electron microscopy (TEM) already published [1] has shown there to be a structural transition in the Fe layers in the layer thickness range 8<n<12mpl. Over this range of n, the Fe changes the lattice it adopts from FCC to BCC. It is, therefore, not unreasonable for a change in the planar spacing of the multilayers to occur in the same layer thickness range.

It is striking that the in plane coercivity, Hc, also peaks at n=8mpl. Factors affecting the coercivity of thin films are legion, including dislocation and defect density and total film thickness. However we recall data for Cu/Fe multilayers which show a similar coercivity anomaly [7]. In the Cu_n/Fe_n system the peak in Hc occurs at n=5mpl. Now the lattice mismatch is greater between Cu(111) and Fe(110) than between Ni(111) and Fe(110) and therefore the critical thickness for the introduction of interfacial dislocations should be less for Cu/Fe than for Ni/Fe. It is thus possible that the anomaly in Hc is due to some magnetic mechanism (eg. inverse magnetostriction) driven by misfit-stress(dependance of Hc on vs mpl in Fig.2)

In figure 3 it can be seen that Mr was observed to increase for all samples on reducing the measurement temperature. This was to be expected as

most ferromagnets have a magnetisation which varies with temperature. A schematic M vs T/Tc curve is shown in figure 4. It can be seen that, for all temperature intervals below Tc, the low temperature magnetisation is higher than at the higher temperature.
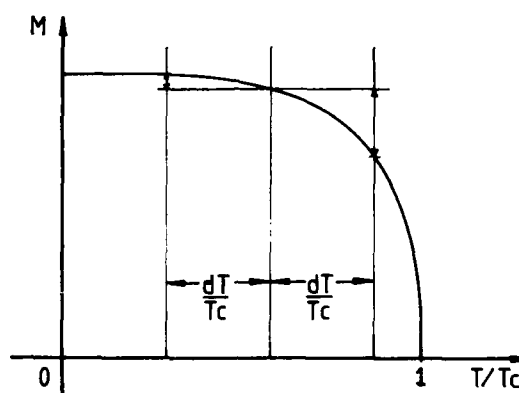
Figure 4. Schematic graph of magnetisation vs T/Tc.

Figure 3 has a further trend. As the modulation layer thickness decreases, the ratio of Mr at low temperature to that at room temperature, $Mr(T)/Mr(RT)$, increases. The effect is most apparent for the n=3mpl sample, where there is a marked variation in Mr with T. This behaviour is consistent with there being a decrease in Tc as the modulation period decreases. If Tc is reduced, RT/Tc is closer to unity. The rate of change in magnetisation with temperature is therefore much greater and $Mr(T)/Mr(RT)$ larger despite RT and T being fixed.

A modulation layer thickness dependence in Tc is possible. Monte Carlo Ising spin model calculations by Taylor and Gyorffy [8] have shown that antiferromagnetic ordering of the Fe spins in an FCC lattice reduces Tc of a Ni_n/Fe_n (FCC) multilayer from 620K for n=12mpl to 550K for n=3mpl. The model also predicts that the M vs T curves will have a less pronounced 'knee' as the modulation layer thickness of the multilayer decreases. This latter effect would have the consequence of increasing the $Mr(T)/Mr(RT)$ ratio for shorter modulation multilayers even for RT/Tc << 1. Most importantly, the model predicts the dramatic reduction in magnetisation already reported by us for Ni/Fe(FCC) multilayers at room temperature [1] and observed again here at temperatures down to 6K.

CONCLUSIONS

X-ray diffractometry at grazing incidence has provided further proof that the Ni_nFe_n multilayers, which have a magnetisation much less than expected for an homogenous NiFe alloy, have well ordered layering and are not significantly interdiffused. There is some terracing and pinholing in the thinner layers (n<5mpl) which causes a variation in modulation period but the main modulation period detected is within 1mpl of the design aim.

There is a difference in the close packed planar spacing between the multilayers with totally FCC Fe and those with the Fe in its BCC form. The apparent sudden change in planar spacing which occurs in the modulation range 8<n<12mpl is consistent with the previously reported structural transformation of the Fe from FCC to BCC which occurs in the same modulation range [1].

378

The coercivity (in plane) of the multilayers increases with layer thickness until, at the critical thickness for transformation to BCC, it is over a factor of three larger than at the smallest layer thicknesses. It is suggested that misfit stress may play a role in this anomaly.

The variation in the ratio of remnant magnetisations at low temperature and room temperature can be interpreted as the Curie temperature varying with modulation layer thickness. The conclusion that Tc decreases as the modulation layer thickness decreases, such that RT/Tc is closer to unity for the shorter modulation period multilayers, is consistent with the Monte Carlo simple Ising spin model of Taylor and Gyorffy. This model predicts that antiferromagnetic Fe-Fe coupling in FCC Fe will result in a low magnetisation for Ni/Fe(FCC) multilayers and a reduction in the multilayer Tc as layer thicknesses is reduced.

Clearly a VSM is not the ideal instrument to use to investigate magnetic coupling on an atomic level. There is, however, a growing consistency of experimental observation with the theoretical predictions of models which assume antiferromagnetic Fe in Ni/Fe(FCC) multilayers.

REFERENCES

1. N.M. Jennett, D.J. Dingley and Y. Ando in Layered Structures (Mater. Res. Soc. Proc. 160, Boston, MA 1989) pp183-189
2. N.M. Jennett and D.J. Dingley, presented at 1990 EMRS Spring Meeting, Strasbourg, France, to be published in J.Mag.Mag.Mater.
3. R.J. Weiss, Proc. Phys. Soc. 82, 281 (1963).
4. F.J.Pinski, J. Staunton, B.L. Gyorffy, D.D. Johnson and G.M. Stocks, Phys. Rev. Lett. 56, 2096 (1986).
5. M.B. Taylor, B.L. Gyorffy and C.J. Walden, J. Phys. Cond. Matter. 1991.
6. E.F. Wassermann, Festkörperprobleme 27, 85 (1987).
7. D.J. Dingley, N.M. Jennett and Y. Ando, Proc. MICRO'90. Trans. Royal Microscopy Society 1, 123 (1990).
8. M.B. Taylor and B.L. Gyorffy, J. Phys. Cond. Matter (to be published).

MAGNETIC PROPERTIES OF SPUTTERED Ni/Al MULTILAYERS

E. Tsang*, J.C. Cates**, M. Tan***, A. Waknis***, C. Alexander, Jr.**, M.R. Parker****, and J.A. Barnard***,
*University of South Alabama, Department of Mechanical Engineering, Mobile, AL 36688.
The University of Alabama, **Department of Physics, ***Department of Metallurgical and Materials Engineering, and ****Department of Electrical Engineering, Tuscaloosa, AL 35487-0202.

ABSTRACT

Magnetic properties of sputtered Ni/Al multilayers have been investigated by vibrating sample magnetometry and ferromagnetic resonance. In these compositionally modulated films (CMFs) the Al 'spacer' layer thickness was fixed at 3.5 nm while the total Ni content of each film was held constant at 308 nm. The thickness of the individual Ni layers was varied from 4.8 to 154 nm. The CMFs showed a variety of magnetic characteristics which were dependent on the thickness of the Ni layers. CMFs with Ni layer thickness 30 nm and above showed clear evidence of perpendicular anisotropy. This anisotropy is characterized by low-remanence perpendicular hysteresis loops of the type commonly found in CoCr alloy films. As the Ni layer thickness diminishes the perpendicular anisotropy decreases and is eventually lost. Simultaneously, the CMFs show increasing in-plane remanence, rising to a peak squareness of greater than 0.5 at a Ni layer thickness of 11 nm. As the Ni thickness continues to decrease, the remanence again declines. At Ni thicknesses of a few nm the CMFs become quasi-superparamagnetic. These CMFs do not show a monotonic reduction in saturation magnetization, M_s, with decreasing Ni layer thickness. Instead, both M_s and the coercivity, H_c, pass through a maximum in the region of 40-80 nm Ni layer thickness. FMR measurements were also made on these films. A plot of the effective anisotropy field produces data of a similar form to the M_s versus Ni layer thickness plot, again with a clear maximum. The FMR data also reveals interesting resonances in the films exhibiting perpendicular anisotropy. The presence of satellite resonances adjacent to the principal resonance peaks seems to suggest, in structural terms, a two-phase system as the basis of the observed anisotropy.

1. INTRODUCTION

Studies on compositionally modulated films of alternatively deposited ferromagnetic and nonmagnetic layers have attracted considerable attention because these CMFs exhibit unusual magnetic properties, some arising from apparent mixing at the interfaces. Work on CMFs in which the nonmagnetic layer is composed of Al had been carried out for Co and Fe forming the ferromagnetic layers. Grundy et al [1] reported that a perpendicular anisotropy exists for the Co/Al system as well as a preferred growth of the Co (0001) plane as the Co layer thickness decreases. Such preferred orientation is also found by Nagakubo et al [2] in the Fe/Al system which they attributed to an alternate epitaxial growth between the Fe and Al layers. In both the Co/Al and Fe/Al systems, the saturation magnetization, M_s, at first decreased gradually as the thickness of the ferromagnetic layer decreased, but then the drop in M_s values became abrupt. This paper, which reports the magnetic properties of sputtered Ni/Al CMFs, is part of an on-going investigation of Ni/Al multilayers [3].

2. EXPERIMENTAL METHODS AND MATERIALS

A series of compositionally modulated thin films of the form $(xAl/yNi)_n$ were prepared at room temperature by sequential dc-magnetron sputtering from 8" diameter elemental targets (99.97% pure Al and Ni) in a Vac-Tec Model 250 Batch Side Sputtering System. Corning Glass 7059 was used as a substrate. The thicknesses of the individual Al and Ni layers are given by x and y, respectively, measured in nm. The total number of bilayer units, $(xAl/yNi)_1$, in a given CMF is n. The wavelength, λ, (or bilayer thickness) is x+y and the total thickness of the multilayer is $n(x+y)=T$. Sputtering conditions were 100W power control and 2.5 mTorr Ar (99.99%) gas pressure. Bias voltage was not applied. The targets were pre-sputtered for 10-15 minutes before the deposition to remove contamination. The base pressure in the deposition chamber was in the range $1-5 \times 10^{-6}$ torr.

The magnetic behavior of the CMFs was investigated at room temperature by vibrating sample magnetometry (VSM) using a Digital Measurement Systems VSM Model 880 with a maximum applied field of 10kOe. Crystal structure was analyzed by XRD using a Philips APD 3600 diffractometer. A Dektak IIa surface profilometer was used to measure film thicknesses and to calibrate deposition rates.

Ferromagnetic resonance experiments were carried out in a home-built spectrometer operating at 34.5 GHz. Samples of approximately 1 X 3 mm were mounted (substrate intact) at the center of a TE_{011} microwave cavity for measurements at room temperature. The magnet was rotated about the sample cavity, and spectra taken for a number of different angular orientations of the magnetic field for each sample. Spectra were recorded as the first derivative of the absorption signal. A Cr^{3+} marker was placed in the microwave cavity with the Ni/Al samples. This marker has a g-value of 1.98, and its absorption line occurs at the same magnetic field for fixed microwave frequency. The variations in magnetic field position were measured with respect to this marker to correct for any variations that might occur during the rotation studies.

3. EXPERIMENTAL RESULTS

3.1 Crystal Structure

For a nickel layer thickness between 154 nm and 38 nm X-ray diffraction patterns show the presence of Ni (111), (200) and (220) diffractions, and the relative intensities of the diffraction peaks indicate that Ni is present in textured (111) as well as randomly-oriented polycrystalline structure with a fairly small grain size. Evidence of Al_3Ni is first detected in the sample with a Ni layer thickness of 77 nm, and as the Ni layer thickness decreases, Al_3Ni diffraction peaks increase in intensity since the number of Ni on Al interfaces, where Al_3Ni is formed, increases [3]. For samples with a Ni layer thickness less than about 20 nm, only the Ni (111) diffraction is detected, which reaches a maximum (the sharpest and narrowest diffraction peak) around a Ni layer thickness of about 11 nm (Figure 1). This variation in the intensity of the textured Ni (111) with layer thickness corresponds with the variation of in-plane remanence (given here as squareness) and coercive field, which also show a maximum at this Ni layer thickness of 11 nm (Figure 3).

3.2 Vibrating Sample Magnetometry

The VSM results show a variety of magnetic characteristics which were dependent on the thickness of the Ni layers (Figure 2). CMFs with Ni layers of 30 nm or more showed clear evidence of perpendicular anisotropy, which is characterized
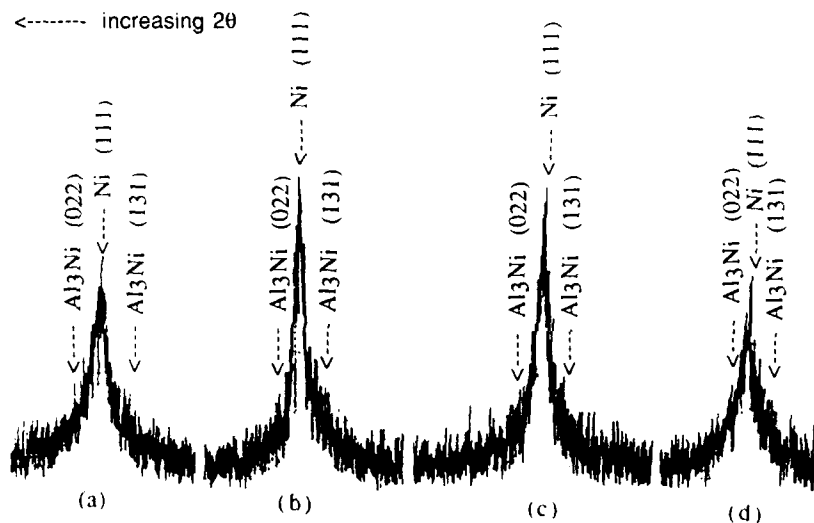
Figure 1. X-ray diffraction patterns with Ni layer thickness (a) 15 nm;
(b) 13 nm; (c) 11 nm; and (d) 9.6 nm.

by low remanence perpendicular hysteresis loops of the type commonly found in
CoCr alloy films [1,4]. As the Ni layer thickness diminishes the perpendicular
anisotropy decreases and is eventually lost when d_{Ni} is less than 19 nm. At the
same time the CMFs show increasing in-plane remanence rising to a peak
squareness of 0.55 at a Ni layer thickness of 11 nm (Figure 3). (For CMFs deposited
on Fisher Scientific glass slides, this maximum in squareness has a value of greater
than 0.7.) As the Ni layer thickness continues to decrease, the remanence again
declines. This change in the characteristics of magnetic hyeteresis loop from
perpendicular anisotropy to in-plane magnetization as Ni layer thickness decreases
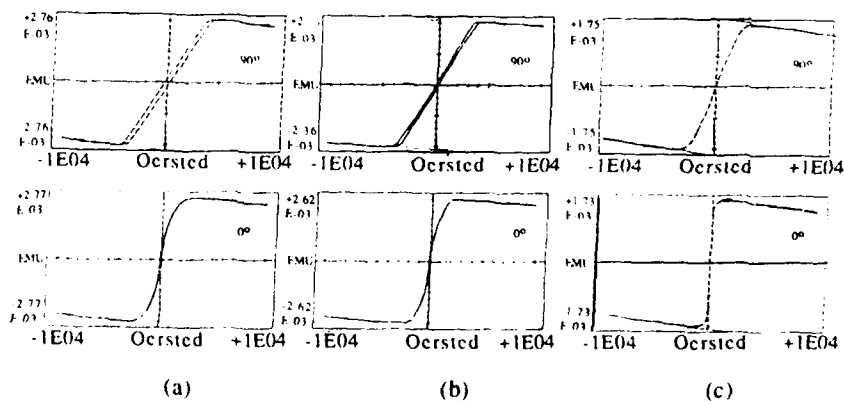
Figure 2. Hysteresis loop for Ni layer thickness (a) 154 nm; (b) 39 nm;
and (c) 11 nm.

is opposite to that found in Fe-SiO2 multilayers, where the hysteresis loops go from in-plane magnetization to perpendicular anisotropy as the Fe layer thickness decreases for a fixed thickness of the SiO2 layer [5] The maximum in in-plane remanence is accompanied by a local maximum in coercivity, H_C, at this value of Ni layer thickness (Figure 3).

The CMF Ni-Al layers do not show a monotonic reduction in saturation magnetization. M_S, with decreasing Ni layer thickness. Instead, both M_S and H_C pass through a maximum in the region of 40 to 80 nm Ni layer thickness, indicating coupling across the Al spacer in this Ni thickness regime. For Ni layer thickness less than 40 nm, the decrease in M_S can be explained by the presence of a magnetically dead layer of about 2.9 nm at the Ni-Al interface [6].
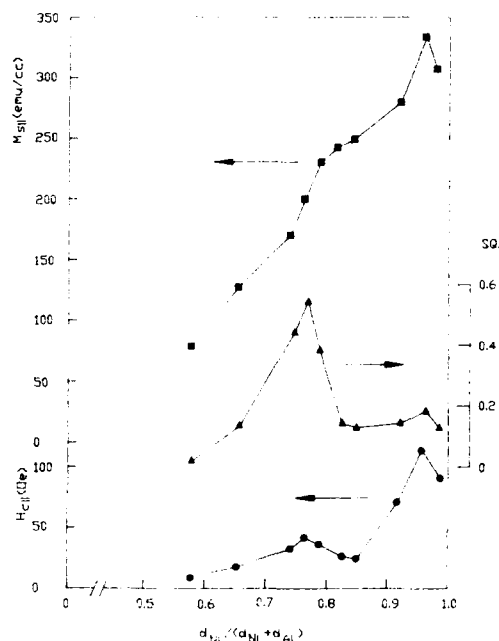
Figure 3. Plot of M_S, SQ., and H_C vs. d_{Ni}/λ

3.3 Ferromagnetic Resonance

A main absorption line was found for all samples in the Ni/Al series. Additional resonance lines appeared in samples with Ni layer thickness greater than 13nm. Observed resonances occurred between 10 and 16 kOe. The FMR spectra of each film, with the applied magnetic field perpendicular to the sample plane, are shown in Figure 4. Additional resonances appear at slightly lower fields than main resonances. Both the main and secondary resonances exhibited negative anisotropy for all samples.

Anisotropy parameters for the individual samples were determined by varying the angle of the external field with the sample axis. For samples exhibiting uniaxial anisotropy, such as the Ni/Al multilayers in this study, the angular variation of the absorption line position, H, can be fitted to the expression:

$$H = \frac{1}{2} \sqrt{H_k^2(\cos^2\theta - 1)^2 + \frac{4\omega^2}{\gamma^2}} - H_k \ (3\cos^2\theta - 1) \tag{1}$$

A summary of the FMR results with values of anisotropy field, H_k and $\gamma/2\pi$ are given in Table 1.

The multilayer Ni/Al films with d_{Ni} greater than 77 nm clearly showed very large multiple resonances caused by regions in the films with different magnetic characteristics. This second resonance was most prominent in the sample with d_{Ni} = 77 nm. In this sample, the anisotropy field, H_k, for the main resonance was -3.231

kOe and for the second resonance was -2.000 kOe. By comparing the relative areas under the absorption peak, we determined that the volume of material in these regions are approximately equal. Samples with d_{Ni} = 154 nm and 77 nm also demonstrated a magnetocrystalline anisotropy in addition to demagnetization effects.

By plotting the magnitude of the anisotropy field determined from equation (1) as a fucntion of d_{Ni}/λ, we see that for d_{Ni} between 154 nm to 39 nm, not all the field difference can be explained by demagnetization fields. This additional anisotropy could be strain-induced or caused by significant coupling between Ni layers.

4. Summary

In Ni/Al multilayers with a Ni layer thickness greater than about 20 nm, the perpendicular anisotropy as well as the presence of satellite resonances adjacent to the principal resonance peaks in FMR is due to a two-phase system, which is consisted of texture Ni (111) and randomly-oriented polycrystalline Ni with a fairly small grain size. As the Ni layer thickness decreases further, the perpendicular anisotropy disappeared and the CMFs show increasing in-plane remanence, reaching a peak when the multilayers consisted of only textured Ni (111).

d_{Ni} = 308 nm

d_{Ni} = 154 nm

d_{Ni} = 77 nm

d_{Ni} = 38.5 nm

d_{Ni} = 19 nm

d_{Ni} = 15.4 nm

d_{Ni} = 12.8 nm

d_{Ni} = 11 nm

d_{Ni} = 9.6 nm

d_{Ni} = 6.4 nm

d_{Ni} = 4.8 nm

6 KG   17KG
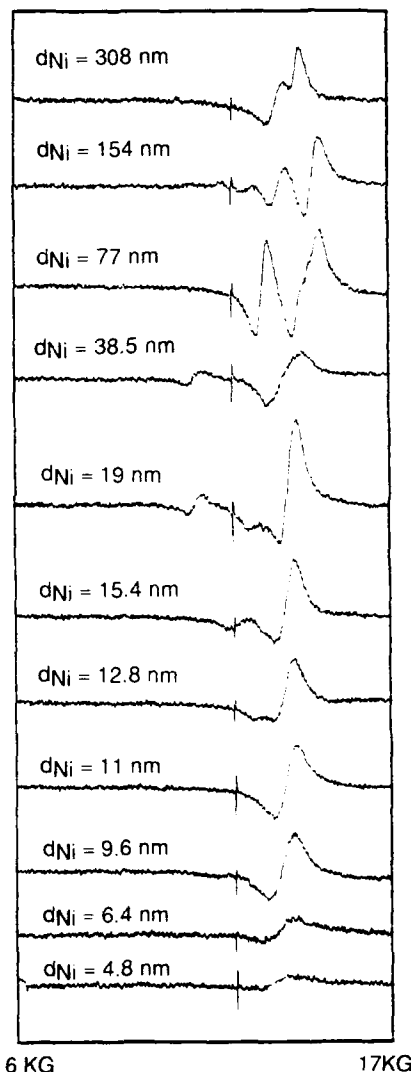
Figure 4. FMR spectra for the applied magnetic field perpendicular to the sample plane

Table I. Summary of FMR results for all samples.

dNi (nm)	Main Resonance		Secondary Resonance	
	H_k (KOe)	$\gamma/2\pi$ (GHz/KOe)	H_k (KOe)	$\gamma/2\pi$ (GHz/KOe)
308	-2.615	2.97	-2.090	2.95
154	-3.406	3.00	-2.297	2.99
77	-3.231	3.03	-2.000	3.04
38.5	-2.643	3.05		
19	-2.774	3.04		
15	-2.734	3.05		
12.8	-2.638	3.05		
11	-2.634	3.04		
9.6	-2.520	3.05		
6.4	-2.528	3.05		
4.8	-2.242	3.05		
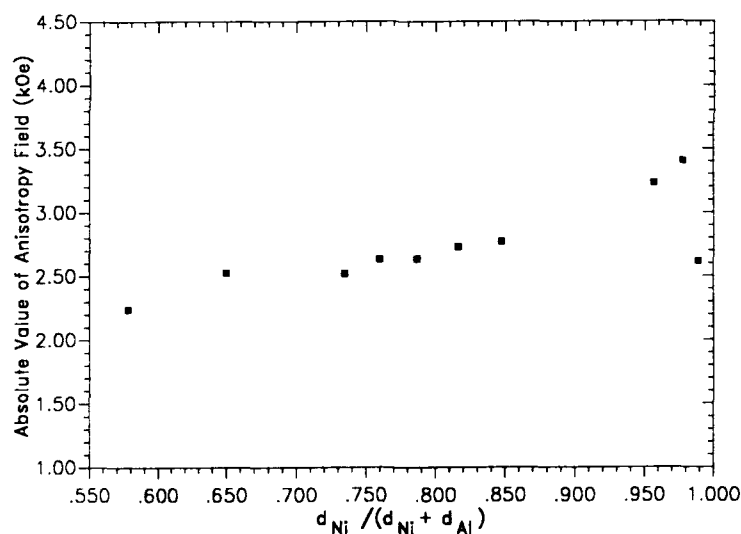
Figure 5. Anisotropy Field versus d_{Ni}/λ

References

1. P.J. Grundy, S.S. Babkair, and M. Ohkoshi, IEEE Trans. Magn., 25, 3626 (1989).
2. M. Nagakubo, T. Yamamoto, and M. Naoe, J. Appl. Phys., 64, 5751 (1988).
3. J.A. Barnard, E. Haftek, A. Waknis, and M. Tan, "Microstructural Evolution of Al/Ni and Ni/Al Bilayer Thin Films," Mat. Res. Soc. Symp. Proc. (in press).
4. N. Sato, J. Appl. Phys., 61, 1979 (1987).
5. S. Honda, M. Ohtsu and T. Kusuda, IEEE Trans. Magn., Vol. 25, No. 5, pp. 3848 (1989).
6. A. Waknis, E. Haftek, M. Tan, J.A. Barnard, and E. Tsang, (to be presented at the Spring 91 MSR Conference).

MBE-GROWN EPITAXIAL Co/Cr SUPERLATTICES

W. VAVRA, S. ELAGOZ, ROY CLARKE AND C. UHER
Department of Physics, University of Michigan, Ann Arbor, MI 48109

ABSTRACT

A series of epitaxial Co/Cr superlattices has been grown by molecular beam epitaxy. The Cr is in a metastable hcp phase as confirmed by transmission electron microscopy, selected area diffraction, and reflection high energy electron diffraction. The Cr layers are 10Å thick in all samples while the Co layers are varied from 12Å to 40Å. The diffusion between Co and Cr is studied by SQUID magnetometry and indicates step-like interfaces in the best samples. Interfacial sharpness has also been found to be unusually sensitive to Co deposition rates, and in contrast with other superlattice systems, we find that sharper interfaces enhance *parallel* anisotropy. Hall effect measurements of the saturation field are within 10% of SQUID values. Magnetoresistance at 4.2K is only 1/3% which we believe is a consequence of the high density of states at the Fermi level of hcp Cr.

INTRODUCTION

One of the more exciting aspects of using molecular beam epitaxy (MBE) for thin-film growth is the possibility of synthesizing phases of metals which do not occur in nature. MBE has proven to be very effective for this purpose since it allows the operator fine control over growth conditions and immediate feedback on the growth process via reflection high energy electron diffraction (RHEED). An especially fruitful and promising direction for research in these metastable materials has been the study of surface or thin-film magnetism. In this paper we describe the epitaxial growth of hcp Cr in Co/Cr superlattices along with the magnetic and transport properties. For details of the structural characterization we refer the reader to the accompanying paper by Elagoz et al.[1]

SAMPLE GROWTH

The samples were grown on (110) GaAs in a Vacuum Generators V80 MBE chamber. Cr was evaporated from a high-temperature effusion cell made by EPI Systems. The crucible was pyrolytic boron nitride (PBN) and an alumina insert was needed since the PBN reacted with Cr and outgased nitrogen above 1200° C. The effusion cell was held at 1550° C, however the actual temperature of the Cr was probably 100° to 150° C lower due to the insert. This gave a deposition rate of 0.21Å/s. The Co was evaporated from an electron beam hearth at various rates to be discussed in the following sections.

To establish a smooth (0001) Co surface on which to begin superlattice growth the following buffer layers were grown on a commercial (110) GaAs substrate: first, 500Å of (110) Ge, then 25Å (110) bcc Co, and finally 20Å (111) Au. The desired thickness of hcp Co was then deposited on the Au. Cr grew in the (0001) hcp orientation on Co and the (0001) hcp epitaxy of subsequent Co and Cr layers was maintained even after 68 superlattice periods of 10Å Cr - 12Å Co. A 10Å Au cap was deposited on top of the

superlattice to reduce oxidation. The Ge was grown at 550° C and all metals at 50° C. Chamber pressure during growth was $2x10^{-9}$ mbar and the total thickness of each superlattice is 1500Å.

As more samples were grown and analyzed it became evident that increasing the Co deposition rate led to remarkable improvement in the interface sharpness of the superlattices. This was evident in both RHEED and particularly magnetometer measurements. RHEED patterns of the 54'th bilayer of a sample with 10Å Cr and 18Å Co layers are shown in Fig. 1. The Co layers in this sample were deposited at 0.35Å/s. Another sample in which the Co was deposited at 0.2 to 0.25Å/s (all other growth parameters held fixed) had more diffuse RHEED streaks and even more dramatic differences in the magnetic properties.

Fig. 1 RHEED patterns of the 54'th bilayer of a superlattice with 18Å Co (left), and 10Å Cr (right) layers. The electron beam is parallel to $[11\bar{2}0]$, i.e. diffraction is from $(1\bar{1}00)$ planes.

MAGNETIC PROPERTIES

From studies of Co-Cr alloys[2] it is known that the saturation moment M_s of Co is quickly suppressed by the addition of even small percentages of Cr. Specifically, it takes only 12% Cr to reduce the M_s of Co to *half* its bulk value of 1422 emu/cm^3, and 25% Cr renders the moment negligible at 30 emu/cm^3. Therefore the M_s values of our superlattices provide useful information regarding the abruptness of the Co-Cr interface. Magnetic measurements presented here were carried out with a superconducting quantum interference device (SQUID) magnetometer at temperatures of 5K and 295K.

In Fig. 2a the saturation moment per unit volume of Co is plotted versus the Co layer thickness of the samples and different symbols are used to denote the various Co deposition rates. The samples exhibit a consistent trend toward higher moments and hence sharper interfaces as the Co deposition rate is increased. The magnitude of this change is remarkable considering the Co deposition rate was only varied by a fraction of an Å/sec. The following simple, but instructive approximation can account for the observed moments in the two samples with the sharpest interfaces (the samples with 12Å and 18Å Co layers). First, we assume the monolayer of Co atoms in contact with the Cr at each interface has negligible contribution to the net moment; this is reasonable given the above discussion on alloys. Then if we assign the bulk moment to the remainder of the Co in each layer we obtain values of M_s within 4% of the SQUID results. This also
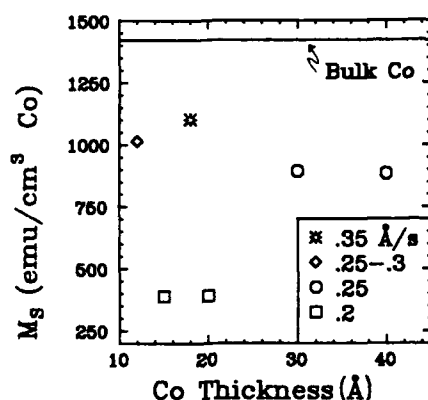
Fig.2a Saturation moment per Co volume. The legend denotes Co deposition rate.
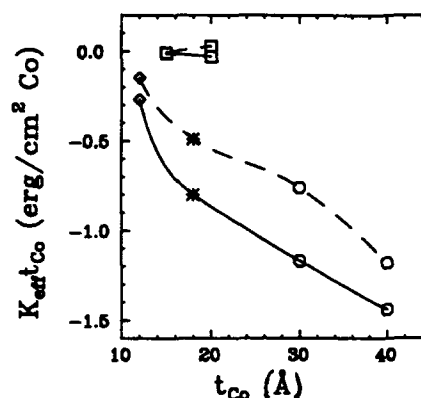
Fig.2b Anisotropy energy per Co area. Symbols follow from Fig. 2a, the solid line is for 295K and dashes are 5K.

leads us to believe that the Cr is paramagnetic which is interesting in the context of a recent prediction that hcp Cr is close to being ferromagnetic.[3]

The magnetic anisotropy energy (shown in Fig. 2b) also shows significant differences with respect to Co deposition rate. The anisotropy energy is defined as the difference in area under the M-vs-H curve for H applied parallel and perpendicular to the film plane. Each area is normalized to the M_s of that sample, and in our convention a negative value means the film plane is the easy plane. The most interesting aspect of the anisotropy data is its correlation with the saturation moments of Fig. 2a. The samples with low moments (diffuse interfaces) shift toward *perpendicular* anisotropy whereas the samples with sharper interfaces exhibit stronger *parallel* anisotropy. This is unusual in that it is opposite of what has been observed in other superlattice systems. Perpendicular anisotropy and low moments are both characteristic of Co-Cr *alloys* so we have additional confirmation that the Co and Cr are well seperated in the high-moment superlattices.

TRANSPORT PROPERTIES

Magnetotransport properties of layered magnetic structures have attracted attention recently as sensitive probes of anisotropy and interlayer magnetic coupling. In this section we present Hall effect and magnetoresistance results of measurements at 4.2K. The samples were photolithographically etched into a standard four-probe pattern for resistance plus two terminals for Hall voltage. Current channels were 1 mm wide and leads were attached with indium.

Hall resistivity is defined as the Hall voltage times the sample thickness divided by the sample current and our results (shown in Fig. 3a) have the characteristic shape for magnetic materials. The steep initial slope corresponds to the magnetic moments being lifted out of the film plane, and the intersection of the two linear parts of each plot occurs at the perpendicular saturation field. The saturation fields H_s from Hall measurements

are within 10% of those from the SQUID magnetometer. Note that the 10Å Cr - 20Å Co sample has a non-zero Hall voltage at H=0. This is the sample that had a small perpendicular anisotropy and hence retained part of its perpendicular magnetization at H=0. We have also observed this behavior in Co-Au superlattices.[4]

We now turn our attention to magnetoresistance (MR). Fig. 3b shows longitudinal MR (current parallel to H) measured at 4.2K. The kinks in the MR correspond to the parallel saturation field from SQUID measurements in all samples except the one with 20Å Co layers. This sample has a low moment and hence diffuse interfaces. The most interesting aspect of the data is that the magnitude of the MR is less than 1/3 %. This was unexpected considering a superlattice with 9Å (bcc)Cr - 30Å Fe had an MR of 45% at this temperature.[5] The 45% MR of the Cr-Fe superlattice can be understood phenomenologically by assuming alternate Fe layers have their magnetic moments in opposite directions, and spin-dependent scattering occurs as electrons move from one Fe layer to the next. As of this writing there is disagreement regarding the mechanism that causes the magnetic layers to couple, however it is clear that the spacer materials which have shown the strongest coupling such as Ru, Cu, and bcc Cr[6] all have a *low* density of states (DOS) at the Fermi energy E_F. The DOS of bcc Cr is 9.63 states/Ry atom, however in our superlattices the Cr is hcp which has a much higher DOS. Using the band structure of Sc, Ti, and Co the DOS at E_F of hcp Cr has been calculated to be 30, 33, and 45 states/Ry atom respectively.[3] We believe the high DOS is responsible for suppressing the coupling mechanism and hence diminishing the MR.
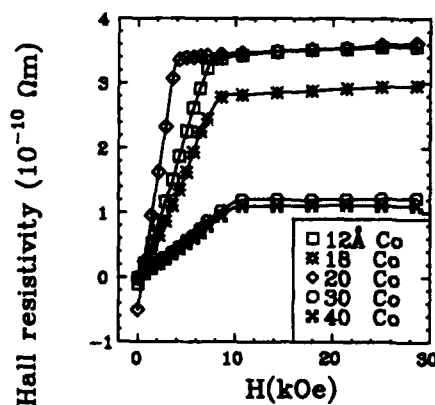
Fig.3b Hall resistivity at 4.2K. Legend denotes Co thickness, all Cr layers are 10Å.
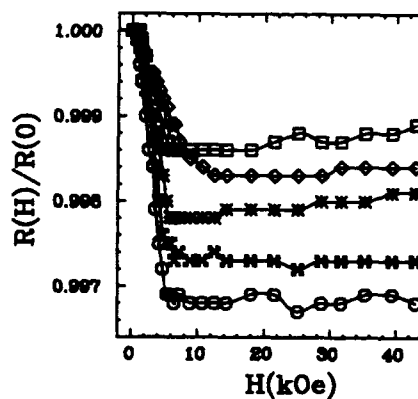
Fig.3b Longitudinal magnetoresistance at 4.2K. Symbols follow from Fig. 3a.

CONCLUSION

We have grown epitaxial hcp Cr in Co-Cr superlattices. The Cr appears to be paramagnetic. SQUID magnetometer measurements reveal that the abruptness of the Co-Cr interface is dependent on the Co deposition rate. In addition, the samples with sharper interfaces have an *in-plane* anisotropy whereas those with diffuse interfaces shift

toward *perpendicular* anisotropy. This is opposite of what has been observed in other superlattice systems. Hall effect and longitudinal magnetoresistance measurements at 4.2K yield perpendicular and parallel saturation fields within 10% of SQUID values. Furtherrmore, the magnitude of the magnetoresistance is only 1/3% which we believe is a consequence of the high density of states at the Fermi energy of the hcp Cr.

ACKNOWLEDGEMENTS

REFERENCES

1. S. Elagoz, W. Vavra, C. Uher, and Roy Clarke, in these proceedings.

2. S. Iwasaki, and K. Ouchi, IEEE Trans. Magn. **MAG-14**, 849 (1978).

3. D.A. Papaconstantopoulos, J.L. Fry, and N.E. Brener, Phys. Rev. B **39**, 2526 (1989).

4. W. Vavra, C.H. Lee, F.J. Lamelas, Hui He, Roy Clarke, and C. Uher, Phys. Rev. B **42**, 4889 (1990).

5. M.N. Baibich, J.M. Broto, A. Fert, F. Nguyen Van Dau, F. Petroff, P. Etienne, G. Creuzet, A. Friederich, and J. Chazelas, Phys. Rev. Lett. **61**, 2472 (1988).

6. S.S.P. Parkin, N. More, and K.P. Roche, Phys. Rev. Lett. **64**, 2304 (1990).

STRUCTURAL PROPERTIES OF EPITAXIAL Co-Cr SUPERLATTICES

S. ELAGOZ, W. VAVRA, C. UHER and ROY CLARKE
Department of Physics, The University of Michigan, Ann Arbor, Michigan 48109

ABSTRACT

We demonstrate the growth of epitaxially ordered Cobalt-Chromium (Co-Cr) superlattices by ultrahigh-vacuum deposition techniques. The superlattices, consisting of hcp Co (00.1) and hcp Cr (00.1) layers with their [11.0] crystallographic axes parallel to GaAs [1$\bar{1}$0] have a hexagonal closed packed (hcp) structure with the c-axis normal to the film plane.

INTRODUCTION

One of the most exciting applications of molecular beam epitaxy (MBE) is to grow heteroepitaxial structures which, due to the registry imposed at the epitaxial interface, are stabilized in phases that have no counterpart in the bulk [1, 2]. The growth, characterization, and properties of these metastable structures are especially appealing in the context of novel magnetic materials.

In this paper we describe the growth of epitaxial Co-Cr superlattices . We find that Cr is in a metastable hcp phase for Co thicknesses varying from 12 Å to 40 Å while Cr was held at a constant thickness of 10 Å for all the samples. The total thickness of the superlattices was approximately 1500 Å.

GROWTH

The superlattices were prepared in a Vacuum Generators V-80M MBE system on annealed GaAs (110) substrates. We used an e-beam hearth for deposition of Co at a rate of approximately 0.3 Å/sec. A high temperature effusion cell was utilized to evaporate Cr with a deposition rate of 0.21 Å/sec. During the growth the chamber pressure was better than 10^{-9} mBar.

For a growth orientation along close-packed planes, the following buffer layers were used: 500 Å (110) Ge, 25 Å (110) bcc Co [2] and finally 20 Å (111) fcc Au.

Deposition rates for these layers were 0.35 Å/sec, 0.25 Å/sec and 0.08 Å/sec, respectively. The substrate temperature was kept at 50 °C during the entire growth process except during the Ge buffer layer deposition, where it was held at 550 °C.

After growing the buffer layers, sequential layers of Co and Cr were deposited. Reflection high energy diffraction (RHEED) patterns observed during and after the growth indicated that the films consist of well oriented close-packed planes (see Fig. 1). Finally, a 10 Å Au cap was grown on the top Cr layer of the superlattices to inhibit surface oxidation.
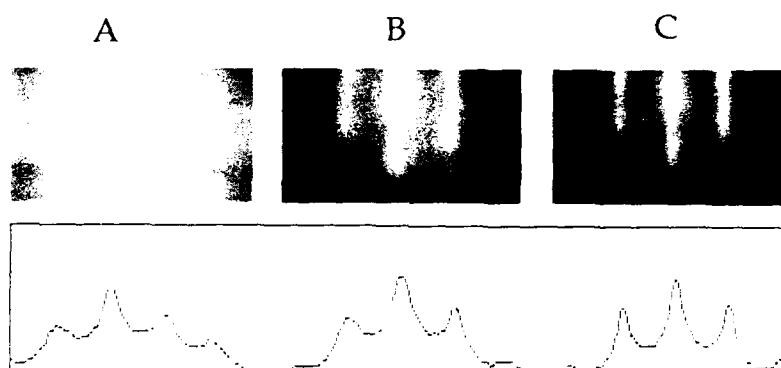
Fig. 1 RHEED photographs illustrating the effects of different growth rates and different thicknesses. RHEED patterns transform from spotty to streaky and become sharper (see RHEED intensity plot in lower panel) as Co deposition rates increase and as Cr thickness approaches 10 Å. Table I summarizes the deposition parameters for these particular samples.

SAMPLE	THICKNESS (Å)		DEP. RATE (Å/sec)	
	Co	Cr	Co	Cr
A	25	15	0.15	0.06
B	20	10	0.25	0.21
C	18	10	0.35	0.21

Table I: Growth parameters of Co-Cr superlattices referred to in Fig. 1.

The data presented in Fig. 1 show that the epitaxial growth of Co/Cr layers is very sensitive to the Co deposition rate and Cr thickness. The latter effect was demonstrated by several unsuccessful attempts to grow thicker Cr layers despite the systematic adjustment of various parameters such as Co thickness, substrate temperature and deposition rates . For thicker Cr and/or lower Co deposition rates (less than 0.3 Å/sec), *in situ* RHEED observations revealed line broadening and spotty patterns immediately after the deposition of the first Cr layer (Fig. 1). Further continuation of the growth resulted in polycrystalline films after approximately 10 bilayers.

RESULTS AND DISCUSSION

The RHEED patterns show close-packed planes but fall short of distinguishing whether these planes are hcp (00.1) or fcc (111). Complementary information is provided via x-ray measurements with a Huber 4-circle diffractometer and a 12kW Rigaku x-ray source. We used a molybdenum target and a graphite monochromator.

The Co-Cr phase diagram indicates that these elements are miscible and thus are able to form alloys. Therefore, we probed the structure by means of low-angle out-of-plane x-ray measurements to check that alloying was not the case. A one-dimensional x-ray scattering model [3], which simulates discrete layer fluctuations and interfacial diffusion, was used to analyze the data. The results are shown in Fig. 2.
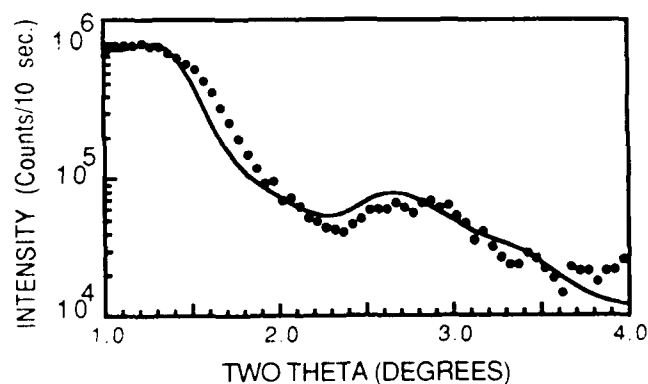
Fig. 2 Low-angle out-of-plane x-ray data. Continuous line indicates a fit to a model with ideal interfaces. Sample- (18 Å Co- 10 Å Cr)

394

We conclude from the simulation parameters that there is negligible diffusion for Co layers of thickness 18 Å. As the Co thickness increases, some roughening is evident in the superlattice. The best values of interface diffusion are found to be 0 monolayer for 18 Å Co and 0.5 monolayer for 40 Å Co. Nevertheless, a layered structure existed in all cases. We have seen up to 3rd order well-separated satellite peaks for all the samples that were grown with the particular deposition and thickness parameters discussed earlier. The superlattices described here provide an interesting comparison with Co-Cr alloy films which are of interest for their strong perpendicular anisotropy [4].

High angle out-of-plane scans were also performed. However, all the interesting reflections of Co and Cr (i.e, Co (00.2), Cr (00.2) etc,.) were overlapped by an intense GaAs (220) peak.

The close-packed nature of the superlattices is confirmed by in-plane contour maps (Fig. 3). The epitaxial orientation of the superlattice with respect to the substrate (shown in Fig. 4) is obtained via in-plane chi scans.
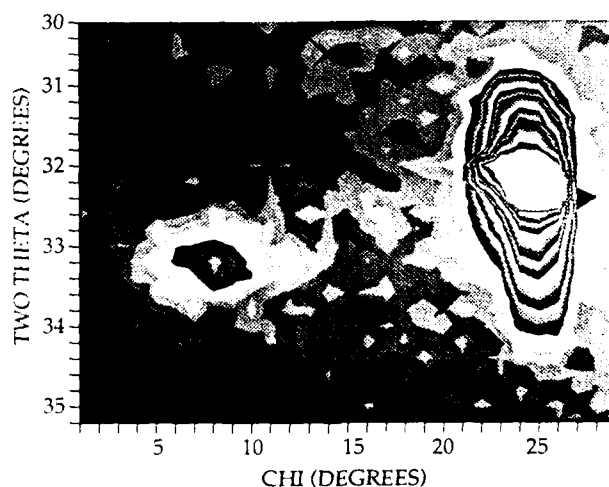
Fig. 3 In-plane x-ray intensity contour map of 20 Å Co- 10 Å Cr superlattice sample. The strong feature on the right is a tail of GaAs $(4\bar{2}0)$ peak which is rotated approximately 18.4 degrees (in chi) from GaAs $[1\bar{1}0]$. The peak on the left is the Co-Cr (11.0) hcp peak. High resolution contour scans around this peak did not show any splittings indicative of incoherent interfaces.

X-ray scans parallel to c^* resolve whether a close-packed structure stacks according to the fcc (ABCABC...) sequence or the hcp sequence (ABAB...) [5]. We have performed scans along the (10.l) direction in which fcc peaks occur at scattering vectors $\pm 2\pi/3d_{111}$ whereas hcp peaks occur at $\pm 2\pi/2d_{00.1}$ as well as at (10.0). This latter peak is unique to the hcp arrangement since there is no fcc contribution at this reciprocal lattice point.

Fig. 4 The epitaxial orientation of the superlattice with respect to the substrate.

GaAs [001]*

hcp (11.0) (Metal)

GaAs [1$\bar{1}$0]*
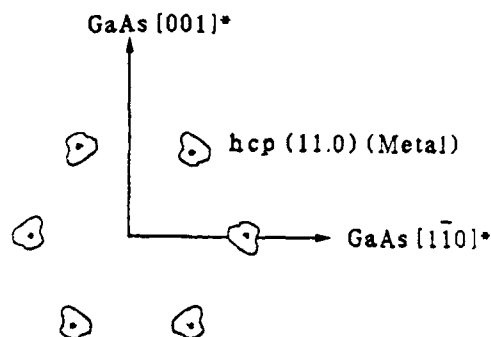
The expected values of the lattice parameters for the hcp and fcc phases of Cr were calculated by finding the ratio of the spacings of bcc Co and bcc Cr for a particular direction then applying the result to hcp/fcc Co to obtain hcp/fcc lattice parameters of Cr. Fig. 5 shows the results of a typical c^* scan.
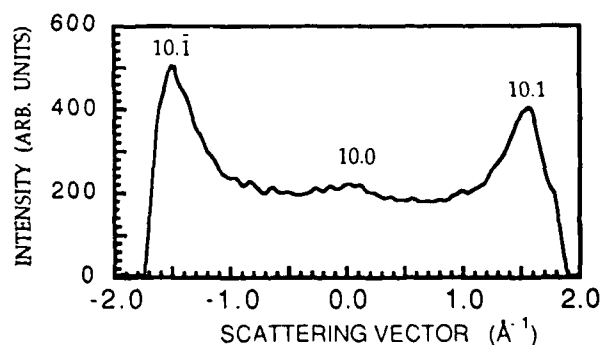
Fig. 5 c^* scan for 10 Å Cr- 40 Å Co sample. The sudden decrease in intensity on both sides is an experimental artifact of the diffractometer geometry.

Only hcp peaks are observed and the stacking coherence lengths obtained from the peaks (10.1) and ($10.\bar{1}$) give values that are greater than the Co layer thickness, establishing that the hcp structure extends beyond one Co layer. Furthermore, no splittings are observed in these peaks, nor in the contour maps, indicating that the Co and Cr layers are strained into coherence within the plane of the substrate.

CONCLUSION

We have grown Co-Cr superlattices having a coherent artificial hcp structure with the c-axis normal to the film plane. Various x-ray measurements show that films are layered and epitaxial and that interface alloying occurs at low deposition rates. Magnetic measurements on this metastable structure of Cr are underway. There is preliminary evidence that hcp Cr is paramagnetic down to the lowest temperatures (5 K). A recent calculation [6] based on the Stoner density-of-states criterion has predicted that hcp Cr is at the borderline of stability as a ferromagnetic phase.

ACKNOWLEDGMENTS

REFERENCES

1. See, for example, *Thin Films Growth Techniques for Low-dimensional Structures*, edited by R.F.C. Farrow, S.S.P. Parkin, P.J. Dobson, J.H. Neave and A.S. Arrott. (Plenum, New York, 1987)

2. G.A. Prinz, Phys. Rev. Lett. 54, 1051 (1985); R. Walmsley, J. Thompson, D. Friedman, R. M. White and T. H. Geballe, IEEE Trans. Magn. 19, 1992 (1983)

3. F. J. Lamelas, H. D. He and Roy Clarke, Phys. Rev. B 43, (1991) (in press)

4. S. Iwasaki and R. Ouchi, IEEE Trans. Mag. MAG-14, 849 (1978).

5. F. J. Lamelas, C. H. Lee, H. D. He, W. Vavra and Roy Clarke, Phys. Rev. B 40, 5837 (1989)

6. D.A. Papaconstantopoulos, J.L. Fry and N.E. Brenner, Phys. Rev. B 39, 2526 (1989).

MICRO- AND NANOSTRUCTURE OF Co/Pd AND Co/Au MULTILAYERS STUDIED WITH TRANSMISSION ELECTRON MICROSCOPY

F. HAKKENS, W. COENE AND F.J.A. DEN BROEDER
Philips Research Laboratories, P.O. Box 80000, 5600 JA Eindhoven, The Netherlands

ABSTRACT

Several metallic multilayers with very thin magnetic Co layers display a preferred magnetization perpendicular to the interfaces. There are strong indications that the magnitude of this anisotropy depends critically on details of the microstructure of the multilayers, and especially on the atomic structure of the interfaces. The micro- and nanostructure of Co/Pd and Co/Au multilayers, which exhibit a large difference in lattice parameter (9% and 14% respectively), was studied by conventional transmission electron microscopy (TEM) and high resolution TEM (HREM). The multilayers, grown by vapor deposition, show a columnar structure and have a convex curvature in the growth direction. In Co/Au multilayers also the Au lattice is bent. Misfit dislocations are observed at the interfaces even for Co layers of one atomic layer thickness. Generally the interfaces show atomic roughness, which is more severe for Co/Au than for Co/Pd.

INTRODUCTION

It is well known that some Co containing multilayers, as Co/Pd (1,2), Co/Pt (3) and Co/Au (4), exhibit a perpendicular magnetic anisotropy below certain Co layer thicknesses. The origin of this effect has been ascribed (1,5) to Néel-surface anisotropy (6), as a result of the reduced symmetry of interface atoms. Chappert et al. (7) suggested that in the case of semi-coherent multilayers, lattice misfit strain may significantly contribute to the interface anisotropy via magnetostriction. The magnitude of the perpendicular anisotropy is affected by the structural properties of the multilayers such as interface roughness, chemical intermixing and misfit relaxation by introduction of dislocations (4,8). Cross-sectional TEM is an indispensable tool to study structural details on a micro- and nano-scale.

EXPERIMENTAL

The preparation of the Co/Pd and Co/Au multilayers as well as their magnetic properties have been described elsewhere (8). Shortly, the multilayers were grown by vapor deposition in UHV. The Co/Pd films were deposited onto mica substrates at a substrate temperature $T(s) = 20$ °C and 200 °C, after prior deposition of a 100 nm Pd base layer at 450 °C. This base layer promoted a sharp [111] texture for the multilayer (rocking curve $\Delta\theta = 2.5$ deg.). The Co/Au multilayers were deposited on glass substrates at $T(s) = 20$ °C, after deposition of a 100 nm Au base layer at 20 °C and a subsequent recrystallization treatment at 150 °C for 20 min. These layers also had a [111] texture, with $\Delta\theta = 10$ deg.

TEM planar and cross-sectional specimens were prepared by argon ion-milling at 4 kV until perforation, and half an hour at 1 kV to reduce damage. The specimens were analysed in a Philips CM30/Super Twin microscope operated at 300 kV.

RESULTS AND DISCUSSION

Microstructure

Fig. 1 shows a TEM bright-field (BF) image of a Co/Pd [111] multilayer, deposited at $T(s) = 200$ °C. Due to their smaller atomic scattering factor the Co layers are imaged as narrow bright bands as compared to the darker Pd layers. Very striking is the rather periodic black and white contrast of the Co layers. This oscillating contrast is due to misfit dislocations as will be discussed later. Near the column boundaries which are grooved at the top surface, the Co-Pd interfaces show a sharp kink towards the {200} and other {111} habit planes. The column width is about 50 nm.

Fig. 1 Cross-section BF image of 0.6 nm Co / 2.2 nm Pd multilayer, T(s) = 200 °C. The uppermost area of the image represents the multilayer top surface. Two columns are visible.
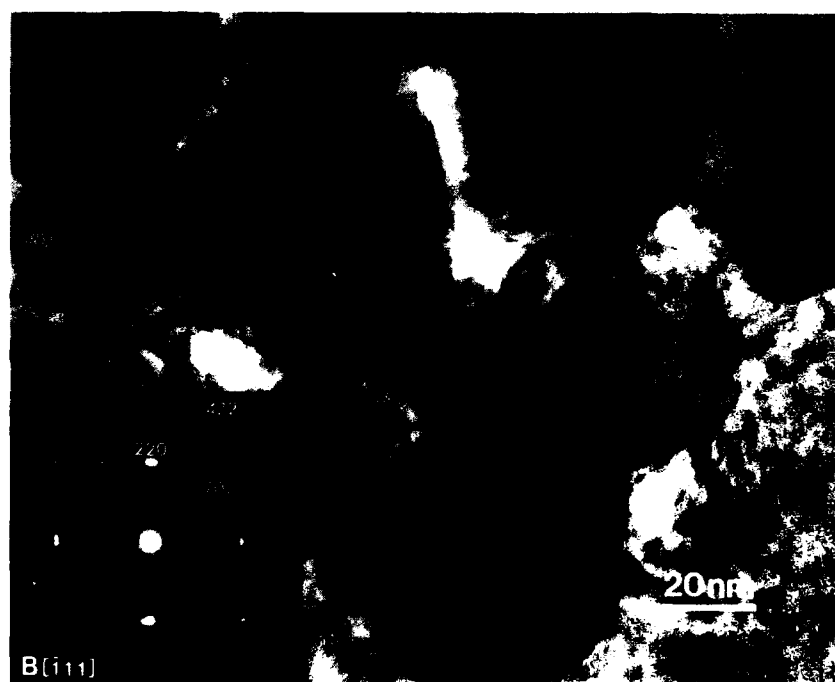
Fig. 2 Planar BF image of 0.4 nm Co / 2.2 nm Pd multilayer, T(s) = 200 °C.

In the planar BF image of fig. 2 the columnar morphology is also visible. The columns have a quasi-hexagonal shape. At some of the boundaries a periodic line contrast is visible, which results from a locally sharply inclined multilayer structure. The column width varies between 40 and 80 nm. The diffraction pattern shows diffraction spots which are split up. This is due to small rotation angles between the different columns of about 4 deg. It also shows "forbidden" 1/3 (422) spots, presumably caused by incomplete ending of perfect ABCABC stackings of (111) Pd layers at the interfaces, in combination with the difference in scattering power and lattice parameter for Co and Pd.

A Co/Pd multilayer, grown at a lower substrate temperature, T(s) = 20 °C, is shown in fig. 3. Again a variation of the interface orientation within the columns is obvious. The average column size is reduced from 50 to 20 nm. The bending of the superlattice has become more continuous, so that the area in which the interface normal deviates from the growth direction is markedly enlarged compared to T(s) = 200 °C. This might be the cause of a lower effective interface anisotropy for Co/Pd grown at T(s) = 20 °C (8). It thus appears that a lower mobility of the atoms during growth decreases the average column size and increases the bending of the multilayer. In general the multilayer bending increased gradually from the Pd base layer to the top surface.

Nanostucture

A HREM image taken from the top-right Co/Pd column in fig. 1 is shown in fig. 4. The Pd layers have the perfect ABC or CBA twinned f.c.c. stacking. The slightly bent Co layers show an oscillating contrast and appear to be thicker than 0.6 nm, which is probably the result of interface roughness, interface mixing and/or island growth. Dislocations are present at the Co-Pd interfaces, and one of them is indicated by a white arrow. A clear ABA hexagonal stacking of the Co layer can only be seen at one point indicated by a black arrow. The inset shows a numerical diffractogram which reveals the spatial frequencies of the Co and Pd lattice planes in the image of fig. 4. Spots in the diffractogram from lattice planes which are not perpendicular to the [111] growth direction, are clearly split up as the result of relaxation of the Co layers in the lateral direction. From the diffractogram we calculate a ratio between the lattice constants of the Co and the Pd layers of f = 0.925, which is slightly more than for the bulk metals, f = 0.910.

Fig. 5 is a HREM image of a Co/Au multilayer and clearly shows that not only the superlattice but also the basic crystal lattice is bent. However, the bending of the superlattice is more pronounced. The origin of this effect is believed to be an atomic "self-shadowing" mechanism due to limited surface diffusion (9) which leads to layer growth inclined towards the vapor sources. Again ABC and CBA stacking sequences of the non-magnetic layers can be distinguished. The Co layers are very rough and seem to be islands in a gold matrix. Two misfit dislocations at the Co/Au interface are indicated by arrows. Here the extra half planes ending at the Au/Co interfaces extend in the upper Au layers accommodating misfit at only one interface. The edge component of the Burgers vector can be derived from the image resulting in bedge = a/4 [112], most likely being part of a complete a/2[101] dislocation with screw component in the [110] direction. Strain perpendicular to the layers due to island growth, roughness, layer and lattice bending, is probably relaxed by dislocations being the end of extra (111) half planes parallel to the multilayer interfaces.

A 2.4 nm Co layer between two Au layers of 2.4 nm, is shown in the HREM image of fig. 6. The Co/Au interfaces are still very rough. In the Co layer the h.c.p. stacking sequence ABAB is identified. A stacking fault can be observed in the middle. Again misfit dislocations are located at the Co/Au interface.

Misfit Dislocations

HREM images reveal misfit dislocations at the multilayer interfaces. Fig. 7 shows a BF image of a Co/Pd multilayer in the [110] zone axis orientation. In the diffraction pattern spot splitting indicates again relaxation of the Co layer. An oscillating contrast of alternating dark and bright streaks is observed with a period of d(1) = 2.7 nm. A BF image in the [112] zone axis orientation is shown in fig. 8. Here the contrast is different and appears as dark dots rather than streaks, having a period d(2) = 1.6 nm.

The contrast oscillations are due to misfit dislocations. Their periodicity and their type of contrast can be explained by a two-dimensional hexagonal coincidence lattice in the (111) interface plane, schematically illustrated in fig. 9, neglecting the individual atom displacements. Using bulk parameters for Co and Pd, a coincidence lattice can be formed with 11 lattice
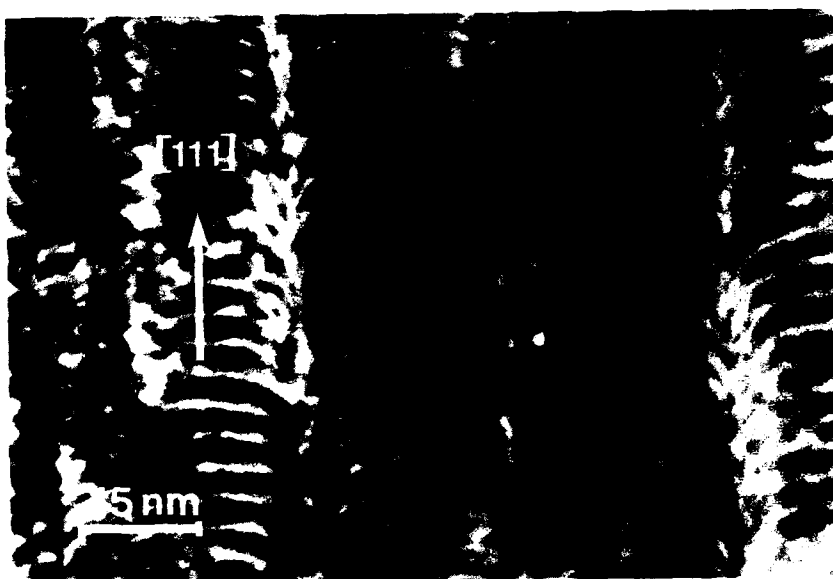
Fig. 3 Cross-section BF image of 0.8 nm Co / 2.2 nm Pd multilayer, T(s) = 20 °C.
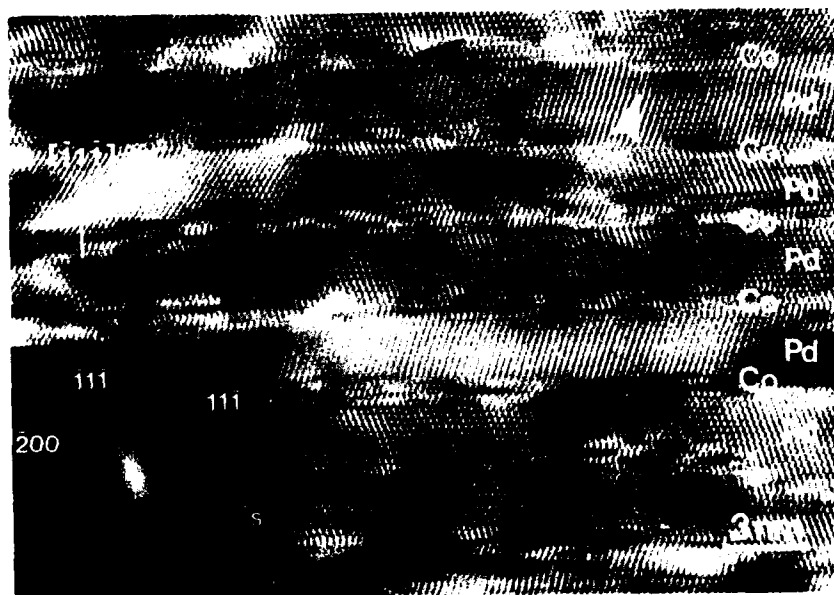
Fig. 4 Cross-section HREM image of 0.6 nm Co / 2.2 nm Pd multilayer, T(s) = 200 °C, [110] zone axis orientation. Notice the spot splitting "s" as result of lateral relaxation.

401

Fig. 5 Cross-section HREM image of 0.4 nm Co / 2.4 nm Au multilayer, T(s) = 20 °C. |110| zone axis orientation. Note the curvature of both the interfaces and the f.c.c. lattice. The mutually twinned ABC and ACB stacking sequences are indicated.

Fig. 6 Cross-section HREM image of 2.4 nm Co / 2.4 nm Au multilayer, T(s) = 20 °C, [110] zone axis orientation.

Fig. 7 Cross-section BF image of 1.2 nm Co / 2.2 nm Pd multilayer, T(s) = 200 °C, [110] zone axis orientation.
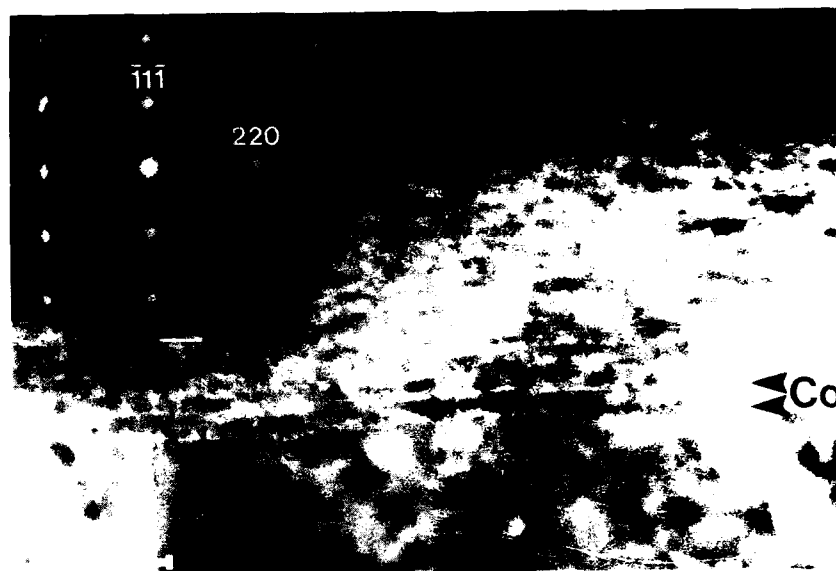
Fig. 8 Cross-section BF image of 0.8 nm Co / 2.2 nm Pd multilayer, T(s) = 200 °C, [112] zone axis orientation.
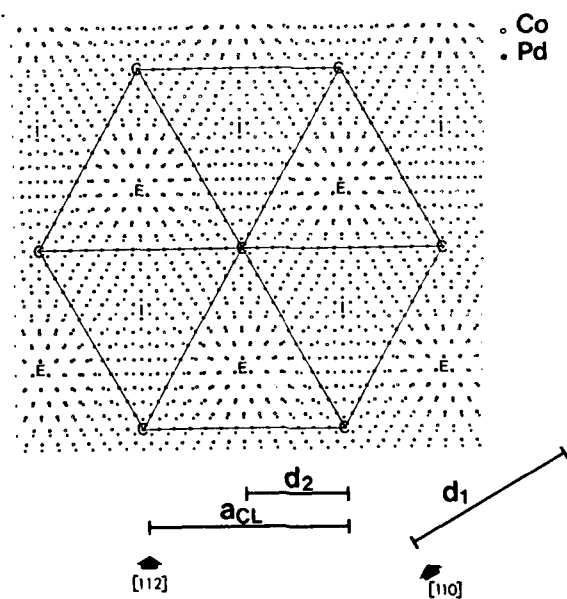
Fig. 9 Schematical representation of a hexagonal coincidence lattice at a Co/Pd [111] interface, with a coincidence lattice parameter a(CL). Only two successive Co and Pd layers right at the interface are drawn. Dislocations are formed, resulting in a periodic contrast with repeat distance d(1) when viewed in the [110] direction, and with repeat distance d(2) when projected in the [112] direction.

404

parameters of Co and 10 of Pd with the smallest possible coincidence lattice misfit and a coincidence lattice constant of a(CL) = 2.75 nm. Besides coincidence points C, the interface shows centres of bad fit E and I, which are local extrinsic and intrinsic stacking sequences, respectively (10). Lines connecting E or I points are dislocation lines along <110> directions, with a periodicity of a(CL) × 1/2 √3 = 2.75 nm. Their pairwise succession is thought to explain the asymmetric streak contrast in the [110] BF image. Along <112> directions the C,E and I points ly on rows with a repeat distance of a(CL)/2 = 1.375 nm. These rows cause a symmetric "dot" contrast in the [112] BF image. The experimentally observed dislocation distances are larger than calculated above, that is 2.7 nm in the [110] and 1.6 nm in the [112] direction. However, using the ratio f = 0.925 between the lattice parameters of the Co and Pd layers (fig. 4), we arrive at a 13 × 12 coincidence lattice with a(CL) = 3.3 nm. The dislocation distances projected in the [110] and [112] directions then become d(1) = 2.85 nm and d(2) = 1.65 nm, respectively. These values are in better agreement with the experimental observations. This model applies to both the upper and lower Co/Pd interface. The reason for the larger dislocation distances than expected for bulk Co and Pd might either be some residual lattice misfit strain, or chemical mixing due to interdiffusion. The same model, applied to Co/Au multilayers, results in a coincidence lattice formed by 8 lattice parameters of Co, and 7 lattice parameters of Au. This leads to strain contrast with a period of 1.75 nm viewed in the [110] and 1.0 nm projected in the [112] direction. These results were experimentally confirmed.

Misfit dislocations have been observed for Co/Pd and Co/Au multilayers with t(Co) ≥ 0.2 nm. This implies that the critical thickness, at which the coherent to semi-coherent transformation occurs (11), is smaller than one atomic layer for the multilayers studied. RHEED observations (12) also indicate that sub-monolayers of Co on Pd(111) already have a lattice spacing near the bulk value.

CONCLUSIONS

The multilayers show a pronounced columnar growth mode. For Co/Pd, higher T(s) leads to wider columns, probably by an increased surface diffusion during growth. Within the columns the multilayers have a convex curvature in the growth direction. HREM of a Co/Au multilayer shows that even the basic Au lattice is bent. Layer bending is probably caused by a "self-shadowing" mechanism. For Co/Pd multilayers grown at higher T(s) the layer bending is localized at the column boundaries. Variation of the multilayer interface orientation is thought to affect the magnitude of the perpendicular anisotropy through an angular dispersion of the preferred magnetization axis.

From image processing on HREM images, the presence of residual lattice misfit strain or some chemical intermixing in Co/Pd multilayers is deduced. HREM further shows the presence of h.c.p. Co in thicker Co/Au multilayers (2.4 nm Co, 2.4 nm Au).

Misfit relaxation occurs in the form of misfit dislocations, which form a two-dimensional hexagonal network in the (111) interface plane. The contrast of the dislocations depends on the viewing direction. The critical thickness is found to be below one monolayer for the studied Co/Pd and Co/Au multilayers.

References

1   P.F. Carcia, A.D. Meinhaldt and A. Suna, Appl. Phys. Lett. 47, 178 (1985)
2   F.J.A. den Broeder, H.C. Donkersloot, H.J.G. Draaisma and W.J.M. de Jonge, J. Appl. Phys. 61, 4317 (1987)
3   P.F. Carcia, J. Appl. Phys. 63, 5066 (1988)
4   F.J.A. den Broeder, D. Kuiper, A.P. van den Mosselaer and W. Hoving, Phys. Rev. Lett. 60, 2769 (1988)
5   H.J.G. Draaisma, F.J.A. den Broeder and W.J.M. de Jonge, J. M. M. M. 66, 351 (1987)
6   L. Néel, J. Phys. Rad. 15, 225 (1954)
7   C. Chappert and P. Bruno, J. Appl. Phys. 64, 5736 (1988)
8   F.J.A. den Broeder, W. Hoving and P.J.H. Bloemen, J. M. M. M., in press (1991)
9   A.G. Dirks and H.J. Leamy, Thin Solid Films 47, 219 (1977)
10 Y. Gao, P.G. Shewmon and S.A. Dregia, Acta Met. 37, 3165 (1989)
11 F.C. Frank and J.H. van der Merwe, Proc. R. Soc. London Ser. A198, 216 (1949)
12 S.T. Purcell, H.W. van Kesteren, E.C. Cosman and W. Hoving, J. M. M. M., in press (1991)

MÖSSBAUER MEASUREMENTS OF INTERFACIAL MAGNETISM OF MBE GROWN FE(100)/AG(100) MULTILAYERS

H. Tang, M.D. Wieczorek, D.J. Keavney, D.F. Storm, C.J. Gutierrez[1], Z.Q. Qiu[2], and J.C. Walker
The Henry A. Rowland Department of Physics and Astronomy, Johns Hopkins University, Baltimore, MD

[1] Presently at the Naval Research Laboratory
[2] Presently at Argonne National Laboratory

ABSTRACT

Multilayers of Fe(100)/Ag(100) were grown by MBE and analyzed with *in situ* RHEED and Mössbauer spectroscopy. These films had a constant Ag layer thickness of 40 monolayers (ML) and varying Fe layer thicknesses of 3, 6, and 9 ML. Using Mössbauer spectroscopy the presence of three Fe sites was inferred. From considerations of the hyperfine parameters and the relative intensities of the sextets, we assign one site to the bulk, and one to each interface: Fe on Ag and Ag on Fe. We believe that one explanation of this is differing tetragonal distortions at the two interfaces. Consequently, another series of films was grown in an attempt to distinguish these sites. These films were essentially identical to the 9 ML film above, but the Fe layers were composed of ^{56}Fe, with a 2 ML ^{57}Fe probe layer effused at the bulk and at each interface in turn. At this point ^{57}Fe Mössbauer spectroscopy was used to determine the hyperfine field and its temperature dependence for each of the three sites.

INTRODUCTION

Several groups [1-4] have studied Fe(100)/Ag(100) multilayers using a wide variety of characterization techniques such as Mössbauer spectroscopy, forward electron scattering, etc. These investigations have produced results suggestive of interesting interfacial properties. Most interestingly, an apparent difference in the magnetic properties of the Fe/Ag interface and the Ag/Fe interface has been observed. This is quite unlike anything observed in the Fe(110)/Ag(111) system, where a one bulk site, one interface site model has always been sufficient.

This paper reports on a study of Fe(100)/Ag(100) multilayers using a Mössbauer depth profiling technique that was pioneered by this group [5]. This technique allows us to probe the magnetic properties of the two interfaces and the interior site *individually*. We begin by reviewing previous work by this group on Fe(100)/Ag(100) multilayers that were not depth profiled. We then describe the magnetically probed film and compare their magnetic properties to those of the previous non-probed films.

GROWTH AND CHARACTERIZATION

Two series of Fe(100)/Ag(100) multilayers were grown in a Perkin-Elmer PHI 430B MBE system equipped with *in-situ* reflection high energy electron diffraction (RHEED). All multilayers were grown on polished, single-crystal NaCl(001) substrates. NaCl was chosen because of the good lattice match with

Ag(100) and the ease of film removal for purposes of transmission Mössbauer spectroscopy. The substrates were outgassed in UHV at 400 °C for 3 hours. A fresh 200 - 300 Å epilayer was deposited at 250 °C to provide a clean, flat surface for growth. Approximately 5000 Å of Ag were deposited at 250 °C as a base on which to grow all our multilayers. This base was then annealed at 375 °C for 3 hours. Earlier work [4] and our own RHEED analysis has shown that this annealing produces a dramatic improvement in film crystallinity and flatness. All the multilayers were grown at as low a substrate temperature as possible, however, our system does not have a substrate cooling capability, so the substrate experienced a ramping of temperature from 30 to 80 °C during the growths due to radiative heating from the effusion cells. We expect that we do not obtain layer-by-layer growth of Fe(100) on Ag(100) at these elevated temperatures [6]. RHEED observations of our Fe bilayer components show streaks that are somewhat broadened compared to those of the Ag base, suggesting a roughened yet still crystalline character even after 20 repetitions. Typical growth rates were 20 Å/min for Ag and 5 Å/min for Fe. After the multilayers were grown they were covered with a very thick Ag layer to protect them from oxidation upon removal from the UHV environment. The pressure in the MBE growth region was kept below 5×10^{-9} Torr during the growths. The films were removed from the NaCl substrate and analyzed with Mössbauer spectroscopy in a transmission geometry with the film normal parallel to the gamma ray propagation direction. A cryogenic refrigerator was used to vary the temperature of the samples from 12.5 K to room temperature. The samples were immersed in liquid He to obtain the 4.2 K data points.

The first series of multilayers was of the form $[Fe_xAg_{40}]_z$, where x=3, 6, and 9 ML, and z= 10 to 15 repetitions. The Ag thickness was kept at a constant 40 ML to insure that the Fe bilayer components were magnetically isolated. The second series of films was essentially identical to the 9 ML film mentioned above, except for the composition of the Fe bilayer component. In this case pure ^{56}Fe was used, and a 2 ML ^{57}Fe layer was effused at the top interface, at the bottom interface, and at the interior site, each in turn. One of these films, with the ^{57}Fe at the bottom interface, is shown schematically in figure 1. This ^{57}Fe probing was done because when the first series of films was analyzed with transmission Mössbauer spectroscopy, several interesting features were identified, most notably the existence of three Fe sites with very different hyperfine parameters in the 6 and 9 ML films. These sites were tentatively assigned as follows: two different interface sites and one interior site. Because the Mössbauer effect is only sensitive to ^{57}Fe, the 2 ML ^{57}Fe probe layer allows each site to be probed specifically. Using this technique we can verify our site assignment and study the magnetic behavior of each of the sites individually.

RESULTS AND DISCUSSION

The Mössbauer results at 4.2 K for the first series of films are shown in figure 2. The spectra consist of three magnetically split sextet components for the 6 and 9 ML films, and two such components for the 3 ML film. We assign the labels "A" and "B" to the two components in the 3 ML film and "C" to the additional component in the 6 and 9 ML films. Because the C component in the 6 and 9 ML films has bulk-like hyperfine parameters and its intensity grows with increasing Fe bilayer component thickness, we assign this component to the interior Fe site. The other two sites show hyperfine parameters that are

very different from bulk and are assigned to the two interface regions: Fe on Ag and Ag on Fe. The interface sites also show very large quadrupole splittings, which indicates a highly non-cubic environment at the interfaces. We attribute this to tetragonal distortions caused by the large mismatch in perpendicular lattice spacing between Fe(100) and Ag(100). Forward electron scattering measurements done on this system by Egelhoff et al. [7] confirm the existence of such tetragonal distortions and strongly support the two-interface site assignment.

40 ML Ag(100)

7 ML Fe 56 (100)

2 ML Fe 57 (100)

40 ML Ag(100)
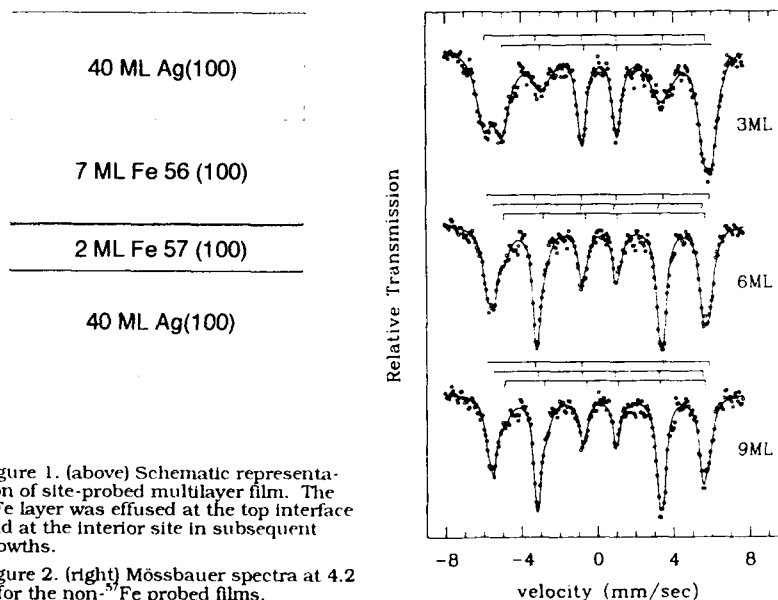
Figure 1. (above) Schematic representation of site-probed multilayer film. The ⁵⁷Fe layer was effused at the top interface and at the interior site in subsequent growths.

Figure 2. (right) Mössbauer spectra at 4.2 K for the non-⁵⁷Fe probed films.

The high temperature magnetic behavior of these films is also of interest. At room temperature the 6 ML spectrum consists of a sharp sextet, a significantly broadened sextet suggestive of magnetic relaxation, and a collapsed doublet. The 3 ML spectrum is completely collapsed, and the 9 ML spectrum remains completely magnetically split. We still obtain two sites in the 3 ML film and three sites in the 6 and 9 ML films, as at 4.2 K. The 3 and 6 ML films could be collapsed due to magnetic relaxation or a reduced Curie temperature (T_c). In order to distinguish between these two causes, Mössbauer measurements were made with a 5 kG field applied in the film plane. This completely splits the 6 ML spectrum, but does very little to the 3 ML spectrum. At 77 K the 6 ML sample is completely split even in the absence of a field, and the 3 ML spectrum is still collapsed. We can conclude from this that the 6 ML sample is strongly magnetically relaxed at elevated temperatures and that T_c for the 3 ML sample is greatly reduced from the value for bulk Fe of 1043 K.

408

All three films showed a large perpendicular surface anisotropy at 4.2 K, in agreement with previous results [1,4]. As expected the magnetization is most heavily canted out of the plane of the film in the 3 ML film, and gradually turns toward the film plane as the Fe bilayer thickness increases. However, even at x= 9 ML the magnetization is still, on the average, about 17 degrees out of plane.

The Mössbauer results at room temperature for the second series of films are shown in Fig. 3 along with the corresponding spectrum from the earlier 9 ML film. These spectra are all magnetically split, and contain mainly a single sextet component. As expected, each probed film shows a distinct spectrum that is significantly different from the spectra of the other two probed samples. Their hyperfine parameters can be well-matched with those of the 3 components in the earlier 9 ML film (see Table I). These agreements strongly support our initial 3 site assignments. However, it should be pointed out that the linewidths of these spectra are noticeably broadened. There are several possible reasons for the line broadening. As we do not have the capability for substrate cooling, the growth of Fe(100) on Ag(100) is expected to be somewhat roughened. Also, as our multilayer samples have 20 repetitions, a slight variation from one layer to another is probable. These two factors complicate the scrutiny of a single Fe site for the 2 ML ^{57}Fe probes used, especially as it is likely the magnetic and structural properties of the two monolayers are slightly different (in fact, it is expected to be).
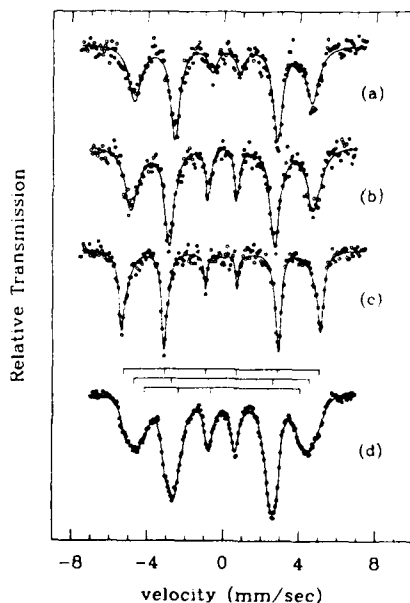
Figure 3. Room temperature Mössbauer spectra for the top (a), middle (b), bottom (c), and (d) the 9 ML non-probed film.
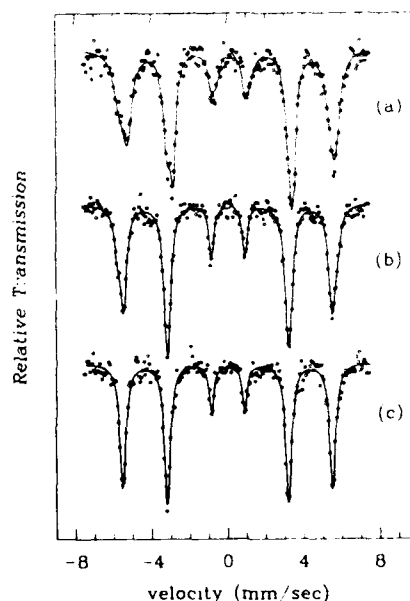
Figure 4. Mössbauer spectra at 13 K for probed films (a) top (b) middle and (c) bottom.

Table I
Summary of Hyperfine Parameters for the
Sites Obtained in the Films

Film	Site	Hyperfine Field H [kOe]	Quadrupole Splitting Δ [mm/s]	Isomer Shift δ [mm/s]
9 ML non-probed film	A	255.5	-0.05	0.09
	B	320.6	0.00	0.02
	C	287.9	-0.03	0.06
9 ML Probed Film	Top	287.1	-0.07	0.17
	Middle	299.6	0.01	0.04
	Bottom	324.1	-0.01	0.01

In order to determine the low temperature magnetic properties and the temperature dependence of the hyperfine field, Mössbauer measurements were performed at low temperatures (down to 13 K) for all three probed samples. The agreement (of the hyperfine parameters) between the previous 9 ML film and these detailed probed samples is not as good at these temperatures, but is still evident particularly in terms of isomer shift and quadrupole splitting. These spectra are shown in Fig. 4. The temperature dependence of the hyperfine field at the bottom probe can be described by a $T^{3/2}$ relation. For the other two samples with the probe at the top interface and at the interior, however, the temperature

Figure 5. Hyperfine field vs T for the probed films (a) top (b) middle and (c) bottom.

dependence follows a $T^{3/2}$ relation for temperatures above 100 K and changes to a roughly linear T dependence at lower temperatures (see Fig. 5). These latter results are preliminary and are presently being refined.

REFERENCES

[1] F.A. Volkening, B.T. Jonker, J.J. Krebs, N.C. Koon, and G.A. Prinz, J. Appl. Phys. 63, 3869 (1988)

[2] G. Lugert and G. Bayreuther, Phys. Rev. B 38, 11068 (1988); G. Bayreuther and G. Lugert, J. Magn. Magn. Mater. 35, 50 (1983)

[3] J. Korecki and U. Gradmann, Phys. Rev. Lett. 55, 2491 (1985)

[4] C.J. Gutierrez, S.H. Mayer, and J.C. Walker, J. Magn. Magn. Mater. 80, 299 (1989); Z.Q. Qiu, S.H. Mayer, C.J. Gutierrez, H. Tang, and J.C. Walker, Phys. Rev. Lett. 63, 1649 (1989); C.J. Gutierrez, S.H. Mayer. Z.Q. Qiu, H. Tang, and J.C. Walker, in Magnetic Properties of Low-Dimensional Systems II, ed. L.M. Falicov, F. Mejia-Lira, and J.L. Morán-López (Springer-Verlag, Berlin, 1990), p. 139; C.J. Gutierrez, M.D. Wieczorek, H. Tang, Z.Q. Qiu, and J.C. Walker, accepted in J. Magn. Magn. Mater.

[5] J. Tyson, A. Owens, J.C. Walker, and G. Bayreuther, J. Appl. Phys. 52 2487, (1981)

[6] B. Heinrich, K.B. Urquhart, J.R. Dutcher, S.T. Purcell, J.F. Cochran, A.S. Arrott, D.A. Steigerwald, and W.F. Egelhoff, Jr., J. Appl. Phys. 63 3863 (1988)

[7] W.F. Egelhoff, Jr., I. Jacob, J.M. Rudd, J.F. Cochran, and B. Heinrich, J. Vac. Sci. Technol. A 8 (3), 1582 (1990)

A COMPARISON OF GROWTH AND MAGNETIC PROPERTIES OF FE(110)/AG(111) AND FE(100)/AG(100) MULTILAYERS

J.C. Walker, H. Tang, M.D. Wieczorek, D.J. Keavney, D.F. Storm, Z.Q. Qiu[a], and C.J. Gutierrez[b], Johns Hopkins University, Baltimore, MD.

ABSTRACT

Two series of Fe/Ag multilayers were grown in a Perkin-Elmer 430B MBE system, one of the Fe(110)/Ag(111) orientation and another of the Fe(100)/Ag(100) orientation. Vastly different techniques were developed by this group and others to achieve epitaxial growth of both of these systems. Using RHEED, it was inferred that the optimal growth of Fe(110) on Ag(111) occurred at a substrate temperature of 180° C. In contrast, the growth of Fe(100)/Ag(100) proceeded with the sharpest RHEED streaks at a reduced substrate temperature. We believe that these fundamentally different growth parameters are the result of physically different growth modes, conjectured to be: edge growth (Fe 110), and a more nucleated growth (Fe 100). Accordingly, dissimilar magnetic interfacial properties are also strongly in evidence, accounted for by the structural differences associated with the different Fe planes. Furthermore, Fe(110) layers as thin as 3 ML were grown on Ag(111) and showed no superparamagnetism and a genuine 2-dimensional behavior of M(T). However, the Fe(100) on Ag(100) multilayers in a similar thickness range exhibited strong relaxation and a comparatively reduced Curie temperature.

INTRODUCTION

Our group has long been interested in the magnetic properties of ultrathin iron and silver layered structures, and we have worked on a method of growing high-quality, epitaxial Fe(110)/Ag(111) heterostructures and multilayers. Due to the mutual immiscibility of the two component metals and our ability to investigate microscopic magnetic properties using ^{57}Fe transmission Mössbauer spectroscopy, the iron/silver multilayer structures are ideal for our study of low-dimensional magnetism.

We have recently developed a method for growing likewise high-quality, epitaxial iron/silver multilayers in the Fe(100)/Ag(100) orientation. While other groups have grown and studied either the Fe(110)/Ag(111) or the Fe(100)/Ag(100) system [1-6], we are the first to fabricate multilayers in both orientations and directly compare their magnetic properties.

For this work we grew two series of Fe/Ag multilayers with approximately parallel structure. That is, if one denotes the structure of a given film as $(Fe_xAg_y)_z$, where x and y are the component thicknesses in monolayers and z is the number of bilayer repetitions, then for the Fe(100)/Ag(100) series, x= 3, 6, and 9; z= 15, 10, and 15, respectively, and y= 40. Likewise, for the Fe(110)/Ag(111) films, x= 3, 5, and 8; z= 8, 30, and 30, respectively, and y= 20.

Growth of the Fe(100)/Ag(100) systems differs enormously from growth of the Fe(110)/Ag(111) systems. Choice of substrate, substrate preparation prior to growth, and substrate temperature during growth are widely different for the two orientations, and accordingly, we expect that there is a difference between the two growth modes.

Mössbauer spectroscopy of these films revealed magnetic properties which vary greatly between the two orientations. Although we saw evidence of magnetic ordering in all films, the Mössbauer spectra of the Fe(100) films

412

(a)   (c)

(b)   (d)
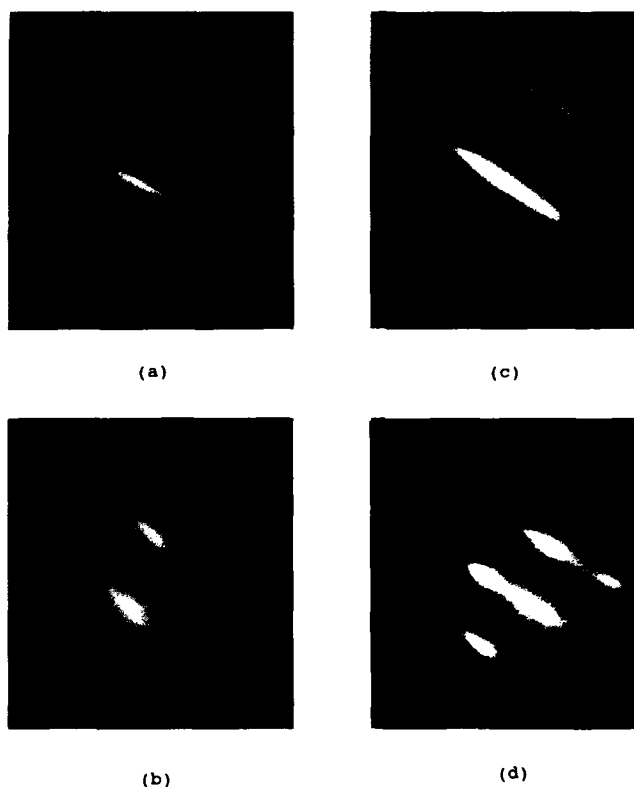
Figure 1   RHEED patterns of: (a) Ag(111) 1st layer, (b) Fe(110) 1st layer, (c) Ag(100) base layer, (d) Fe(100) 1st layer

improved patterns compare well with those of Ag(100) on GaAs(100) seen by other groups [11].

Upon completion of the silver base, the substrate was allowed to cool to room temperature. We grew the Fe(100)/Ag(100) multilayers at this reduced substrate temperature, but owing to our lack of substrate cooling, the temperature gradually ramped from about 30° C to 80° C over the course of the multilayer growth. RHEED confirmed that the iron growth was epitaxial and of the (100) orientation *(Figure 1d)*. Deposition proceeded at 3.8 Å/min for the iron and 20 Å/min for the silver.

We grew three films, each having iron layers of constant thickness equal to 3, 6, and 9 ML. The intervening silver spacer layers were 40 ML thick in all three films. The 3 and 9 ML Fe films consisted of 15 bilayer repetitions each, while the bilayer structure of the 6 ML Fe film was repeated ten times. The RHEED patterns produced by the surface of the final bilayer of each film showed little or no degradation, confirming that our multilayers are indeed of a very high quality. Finally, the multilayers

showed considerable out-of-plane alignment of the magnetization at low temperatures and thin iron layers, asymmetric and broadened lines characteristic of multiple magnetic environments, and prominent central features suggestive of magnetic relaxation or a reduced Curie temperature. By contrast the spectra of the Fe(110) films consisted of sharp, well-defined sextets which showed no evidence of magnetic relaxation or a reduced T_c. We believe this variation arises from lattice distortions which appear at the iron-silver interfaces of the Fe(100) orientation [7], but are absent in the Fe(110) films.

GROWTH AND CHARACTERIZATION

Both series of films were grown under UHV conditions in a Perkin-Elmer 430B MBE system equipped with residual gas analysis and *in situ* reflection high-energy electron diffraction (RHEED). The deposition rates were monitored by a commercially available quartz crystal oscillator (Inficon XTC).

Fe(110)/Ag(111). For the Fe(110)/Ag(111) orientation we used either natural or air-cleaved, iron-free, synthetic mica substrates. The advantage of using synthetic mica is its transparency to the gamma rays used in ^{57}Fe transmission Mössbauer spectroscopy; thus these substrates need no other preparation than outgassing for four hours at 300° C immediately prior to growth. Unfortunately, large, substrate-quality pieces of synthetic, iron-free mica are difficult to find. Following the example of Koch *et. al.* [8], we developed a method of removing our films from the much more readily available, though iron-contaminated, natural mica. After outgasssing the mica substrate, we deposited a buffer layer of about 300 Å of NaCl before commencing the silver growth. This NaCl epilayer allowed us to completely remove our films from the mica substrates using only transparent tape and a few drops of UHP water.

Upon completion of the necessary substrate preparation, we grew a silver base approximately 2.5 - 5 kÅ thick. Optimal growth of Ag(111) seems to occur at a substrate temperature of 180° C and at a deposition rate of about 20 Å/min: the presence of well-defined, multiple-order streaks on our RHEED patterns *(Figure 1a)* are evidence of the high degree of flatness and single-crystallinity effected by these growth parameters. Growth of the iron layers, which proceeded at a deposition rate of 3.8 Å/min and at the same substrate temperature as for the silver, was epitaxial and of the (110) orientation, as shown by RHEED *(Figure 1b)*. For each of the three films the iron component thicknesses were held constant at 3, 5, or 8 monolayers (ML). In all films the iron layers were separated by 20 ML of silver. (1 ML of Fe(110) - 2.00 Å; 1 ML of Ag(111) - 2.36 Å). This bilayer structure was repeated 30 times in the 5 and 8 ML Fe films and eight times in the 3 ML film.

Finally, the multilayer was capped with several thousand angstroms of additional silver to inhibit oxidation.

Fe(100)/Ag(100). For Fe(100)/Ag(100) growth we used commercially available, high-quality NaCl substrates, which were air-cleaved along the (100) plane. Immediately after outgassing the substrate in UHV for one hour at 300° C, we effused a fresh NaCl epilayer several hundred angstroms thick at the same substrate temperature and at a deposition rate of approximately 2 - 5 Å/s, following the example of Gutmann and Hayek [9] and Köster *et. al.* [10]. We then allowed the substrate to cool slightly to 250° C and commenced growth of the silver base. The silver deposition rate was about 15 - 20 Å/min for the first 1000 angstroms of accumulation, after which we increased the rate to 3 Å/s until the total silver thickness reached 1.5 kÅ. Examination of the silver surface by RHEED produced weak-intensity patterns of (100) streaks. The patterns were greatly improved, however, by a four-hour anneal at 400° C followed by an additional 2.5 kÅ layer of silver grown at a substrate temperature of 250° C *(Figure 1c)*. These
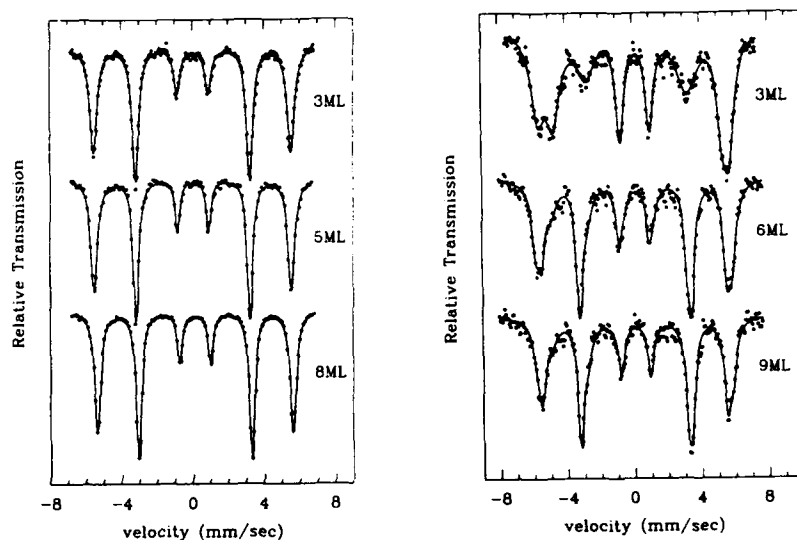
Figure 2 4.2 K Mössbauer spectra of $Fe_x(110)/Ag_{20}(111)$ *(left)* and $Fe_x(100)/Ag_{40}(100)$ *(right)*
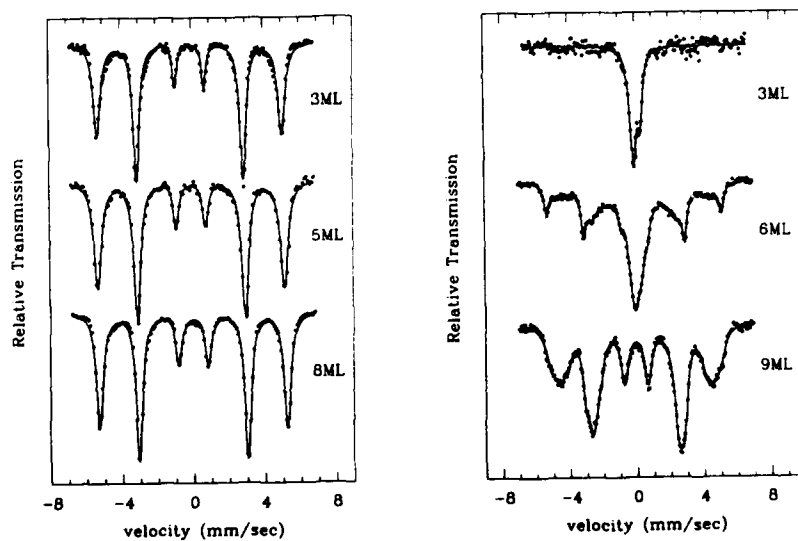
Figure 3 300 K Mössbauer spectra of $Fe_x(110)/Ag_{20}(111)$ *(left)* and $Fe_x(100)/Ag_{40}(100)$ *(right)*

were capped with 5 kÅ of Ag(100).

MAGNETIC PROPERTIES

Mössbauer spectroscopy reveals striking differences between the magnetic properties of the two orientations. The spectra of the Fe(100) films imply significant structural distortion and perpendicular anisotropy, neither of which is present in the Fe(110) films: the Mössbauer spectra of the latter show sharp, single-sextet structure and in-plane magnetization at all temperatures between 4.2 K and room temperature. The (100) Mössbauer spectra evidence significant out-of-plane canting of the magnetization, which decreases not only with increasing iron layer thickness, but also with increasing temperature, and broad, asymmetric absorption lines, which strongly suggest multiple environments. We hypothesize the existence ιf two distinct interface sites in each of the three films, plus one bulk-like site in each of the 6 and 9 ML films. As detailed elsewhere [12], we believe the appearance of multiple sites in the (100) films is due to a tetragonal lattice distortion at the iron-silver interfaces (such as has been reported by Egelhoff et. al. [13]) which is not present in the (110) films.

In addition, there is a total absence of central components in the Mossbauer spectra of the Fe(110) films, even for those of only 3 ML thickness (Figures 2 & 3). By contrast, the 3 and 6 ML Fe(100) films exhibited significant central features. We normally interpret these central components to be indicative of magnetic relaxation caused by the presence of large, flat, iron islands rather than a continuous film [14]. As detailed elsewhere [15], the central feature of the 6 ML film is due to magnetic relaxation, while that of the 3 ML film is due to a reduced Curie temperature. In the case of the 3 ML Fe(100) film, the reduction in T_c is likely due to the non-close-packed arrangement of the iron atoms.

CONCLUSION

We have succeeded in fabricating two series of high-quality, epitaxial iron/silver multilayers, Fe(110)/Ag(111) and Fe(100)/Ag(100). Growth of the two orientations proceeded under vastly different conditions, and we conjecture different growth modes as well. Mössbauer spectroscopy revealed vastly different magnetic properties, which we believe arise from different lattice distortions at the various iron/silver interfaces.

REFERENCES

(a) Currently at Argonne National Laboratory
(b) Currently at Naval Research Laboratory, Washington, DC

1. F.A. Volkening, B.T. Jonker, J.J. Krebs, N.C. Koon, and G.A. Prinz, J. Appl. Phys. 63, 3869 (1988).
2. G. Lugert and G. Bayreuther, Phys. Rev. B 38 (16), 11068 (1988)
3. G. Bayreuther and G. Lugert, J. Magn. Magn. Mat. 35, 50 (1983)
4. J. Korecki and U. Gradmann, Phys. Rev. Lett. 55, 2491 (1985)
5. C.J. Gutierrez, S.H. Mayer, and J.C. Walker, J. Magn. Magn. Mat. 80, 299 (1989)
6. C.J. Gutierrez, S.H. Mayer, Z.Q. Qiu, H. Tang, and J.C. Walker, in Magnetic Properties of Low-Dimensional Systems II, edited by L.M. Falicov, F. Mejía-Lira, and J.L. Morán-López (Springer-Verlag Berlin, Heidelberg 1990), pp. 139-148.
7. C.J. Gutierrez, Z.Q. Qiu, H. Tang, M.D. Wieczorek, S.H. Mayer, and J.C. Walker (submitted to Phys. Rev. B).

416

8. F.A. Koch, C.T. Horng, and R.W. Vook, J. Vac. Sci. Technol. 9 (1), 511 (1971)
9. A. Gutmann and K. Hayek, Thin Solid Films 58, 145 (1979)
10. S. Köster, N. Herres, M. Rey, and K. Reichelt, J. Appl. Phys. 59 (1), 278 (1986)
11. G.A. Prinz (private communication)
12. J.C. Walker, H. Tang, M.D. Wieczorek, D.J. Keavney, D.F. Storm, Z.Q. Qiu, and C.J. Gutierrez (submitted to this conference).
13. W.F. Egelhoff, Jr., I. Jacob, J.M. Rudd, J.F. Cochran, and B. Heinrich, J. Vac. Sci. Technol. A 8 (3), 1582 (1990)
14. Z.Q. Qiu, S.H. Mayer, C.J. Gutierrez, H. Tang, and J.C. Walker, Phys. Rev. Lett. 63 (15), 1649 (1989)
15. J.C. Walker, H. Tang, M.D. Wieczorek, D.J. Keavney, D.F. Storm, Z.Q. Qiu, and C.J. Gutierrez (submitted to this conference).

THE ENHANCED MAGNETIZATION OBSERVED IN FE/MO MULTILAYERS DEPOSITED BY ION-BEAM SPUTTERING

Y. Wang, F.Z. Cui, W.Z. Li, and Y.D. Fan
Department of Materials Science and Engineering, Tsinghua
University, Beijing 100084, China

ABSTRACT

Fe/Mo multilayers, with varied Fe single layer thickness, t_{Fe}, and Mo single layer thickness, t_{Mo}, were deposited by using a focusing ion-beam sputtering technique. Their structural and magnetic properties were studied. The periodic modulated structure was observed for all samples. An enhancement of magnetization over the value of bulk Fe was noticed for some samples. The change of lattice spacing of Fe layers, as a result of compress stress in the film plane, was considered to be responsible for the increase of the magnetization for Fe/Mo multilayers.

INTRODUCTION

There is an increasing interest in the studying of magnetic multilayers because of their novel magnetic properties[1-3]. Besides the perpendicular anisotropy, which leads to the potential application of the magnetic multilayers in perpendicular magnetic recording, the change of magnetization is also one of the most important aspects of magnetic multilayers. An enhancement of magnetization over that of bulk magnetic materials has been observed for some systems such as Co/Pd[3], Fe/Co[4], and Fe/Ag[5]. The enhancement of the saturation magnetization had been attributed mainly to the increase of magnetic moment for the ferromagnetic atoms at the interfaces[6]. In our work, Fe/Mo multilayers with varies modulation period were prepared by using an ion-beam sputtering technique. An enhancement of the magnetization for Fe atoms was observed in Fe/Mo multilayer systems for the first time. The author attributed the enhancement of the magnetization to the expansion of the interatomic distance between Fe atoms in Fe/Mo multilayers.

EXPERIMENT

Fe/Mo multilayers were prepared by alternate depositing Fe and Mo onto water-cooled glass or silicon wafer substrates using an ion-beam sputtering technique described before[7]. All samples were grown on prior deposited buffer layer of pure Mo with the thickness of 200 A, and were covered with a Mo layer on the outer surface. Since the single layer thickness of Fe (t_{Fe}) and Mo (t_{Mo}) was controlled by adjusting the deposition time, the determination

of the deposition rates for both Fe and Mo was a crucial procedure for the sample preparation. Two methods, i.e. Rutherford back-scattering spectroscopy (RBS) and optical interferometer, were used to calibrate the deposition rate. By choosing the proper deposition parameters, as shown in Table I, Fe/Mo multilayers with t_{Fe} in the range 10-60 A and t_{Mo} 10-80 A were prepared. The number of period for each sample was adjusted according to t_{Fe} to maintain the total thickness of Fe to be a constant as 1000 A.

Standard X-ray diffraction (XRD) using monochromatic Cu Kα radiation was deployed to measure the periodic layered structure and the crystallography structure of Fe/Mo multilayers.

The magnetic properties of Fe/Mo multilayers were measured using the vibrating sample magnetometer (VSM) with an applied magnetic field up to 2000 Oe.

Table I. The deposition parameters

Base Pressure:	$<1 \times 10^{-6}$ Torr
Working Pressure:	5×10^{-5} Torr
Ion-Beam Accelerating Voltage :	2.8 keV
Beam Current:	100 mA
Deposition Rate:	1.1 A/sec for Fe
	1.2 A/sec for Mo

RESULT AND DISCUSSION

The X-ray diffraction peaks, resulted from the periodic layered structure in Fe/Mo multilayers, were observed in the small angle $(2\theta=1.5-10°)$ XRD spectra (see Fig.1). From the position of small angle XRD peaks, the modulation period of Fe/Mo multilayers could be calculated. The exact value of t_{Fe} and t_{Mo} was determined from the atom ratio of Fe and Mo obtained with RBS. The results agreed well with our designed value within an experiment error of less than 5%.

Fig.2 shows the large angle $(2\theta=35-55°)$ XRD spectra for samples with different modulation period. From these spectra, the diffraction peaks for both BCC Fe(110) and BCC Mo(110) planes could be observed, indicating that Fe/Mo
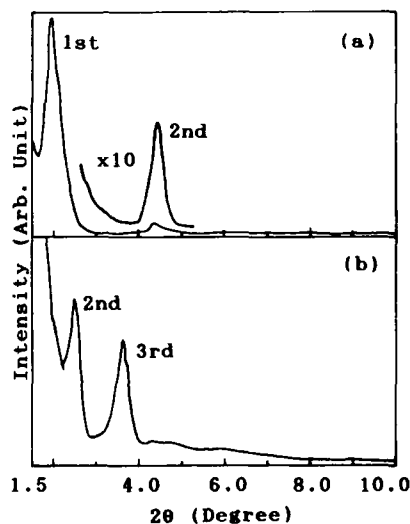
Figure 1

The small angle XRD specta for samples with:

(a) $t_{Mo}=25$ A, $t_{Fe}=11$ A

(b) $t_{Mo}=37$ A, $t_{Fe}=33$ A
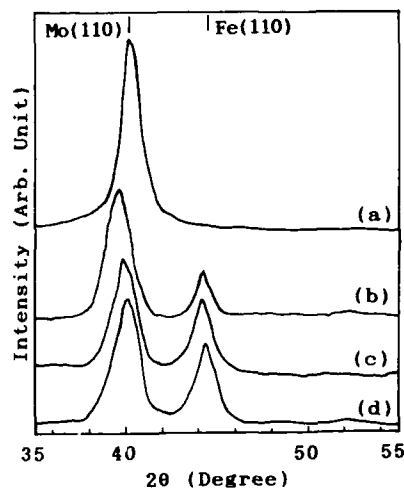
Figure 2

The large angle XRD spectra for samples with:

(a) t_{Mo} =25 A, t_{Fe} =11 A

(b) t_{Mo} =23 A, t_{Fe} =26 A

(c) t_{Mo} =37 A, t_{Fe} =33 A

(d) t_{Mo} =26 A, t_{Fe} =50 A

multilayer was composed of BCC crystalline Fe and Mo layers with a crystal orientation of Fe(110)//Mo(110). For samples with t_{Fe} and t_{Mo} larger than 20 A, a small shift towards lower angle direction could be noticed for the diffraction peaks of both Fe(110) and Mo(110) (see Fig.2 (b) and (c)). This indicated that the lattice spacing of the Fe(110) and Mo(110) planes was a little larger than that of bulk materials. The expansion of the lattice spacing of Fe was partly attributed to the lattice mismatch because the lattice spacing of Mo is 9.8% larger than that of Fe. Since the ion-beam accelerating voltage we used was 2.8 kV, which was higher than that used by other authors, the bombard-ment effects on the samples by the reflected Ar* was stronger. During the sample preparation, the reflected Ar atoms could penetrate into the film during and enlarged the interatomic distance of Fe and Mo layers. This could result in large compressive stress in the film plane[8,9].

For samples with t_{Fe} ≤10 A, only Mo(110) diffraction peak could observed at 2θ=40.5° in the XRD spectra (see Fig.2 (a)). In this case, the Fe layers were no longer continuous and became small islands scattered in Mo matrix. The Mo layers grown through the discontinuous Fe layers to form columnar crystals with Mo(110) texture.

The magnetic properties of Fe/Mo multilayers were measured at room temperature by using VSM. All samples were ferromagnetic with the easy axis in the film plane. The saturation magnetization for unit volume Fe atoms, $4\pi Ms$, was shown in Table II. For samples with t_{Fe} <20 A, $4\pi Ms$ was very low, and decreased with the decreasing t_{Fe}. For samples with t_{Fe} >50 A, $4\pi Ms$ was closing to that of single layer Fe films of 1000 A in thickness. For samples with 20 A< t_{Fe} <45 A, a remarkable enhancement of $4\pi Ms$ over that of bulk Fe could be noticed. The highest value of $4\pi Ms$ was 2.60 T, about 20% over that of bulk Fe. It was found that the samples which had enhanced $4\pi Ms$ were those with large compressive stress, as mentioned above. The lattice spacing of Fe(110) expanded because of the lattice mismatch between Fe an Mo layers and Ar atoms absorbed in the film during the deposition. The magnetic properties of ferromagnetic elements relate closely to the atomic volume or the interatomic distance[4]. It has been point out by

420

the energy-bound calculation[10,11] that the magnetic moment of the atom increases as the atomic volume increases. Therefor an appropriate expansion of the interatomic distance could result in larger exchanging forces between Fe atoms, and lead to the enhanced magnetic moment for Fe atoms. For samples with $t_{Fe} < 20$ A, $4\pi Ms$ decreased because the Fe layer became poorly crystallized and no longer continuous as t_{Fe} decreased.

Table II. The saturation magnetization, $4\pi Ms$,
measure by VSM

Sample	$4\pi Ms$ (T/cm^3)
Bulk Fe	2.15
Fe Thin Film (1000 A)	1.83
Fe(5A)/Mo(24A)	0.46
Fe(11A)/Mo(25A)	0.87
Fe(15A)/Mo(25A)	1.42
Fe(20A)/Mo(26A)	1.84
Fe(21A)/Mo(24A)	2.07
Fe(26A)/Mo(11A)	2.37
Fe(26A)/Mo(23A)	2.31
Fe(28A)/Mo(43A)	1.98
Fe(29A)/Mo(38A)	2.07
Fe(32A)/Mo(52A)	2.14
Fe(33A)/Mo(37A)	2.54
Fe(34A)/Mo(70A)	2.60
Fe(45A)/Mo(26A)	1.96
Fe(50A)/Mo(26A)	1.84

CONCLUSIONS

All Fe/Mo multilayers prepared by ion-beam sputtering exhibited good periodic modulated structures.

A remarkable enhancement of saturation magnetization over that of bulk Fe was observed for samples with 20 A$< t_{Fe} <$40 A. This phenomena was attributed to the appropriate expansion of interatomic distance between Fe atoms, which was caused by the lattice mismatch and the absorbed Ar atoms in the film.

ACKNOWLEDGEMENT

REFERENCES

1. M.B. Stearns, C.H. Lee, and T.L. Groy, Phys. Rev. B 40, 8256 (1989).
2. F.Z. Cui, Y.D. Fan, Y. Wang, A.M. Vredenberg, H.J.D. Draaisma, and R. Xu, J. Appl. Phys. 68, 701 (1990).
3. F.J.A. den Broeder, H.C. Donfersloot, H.J.G. Draaisma, and W.J.M. de Jonge, J. Appl. Phys. 63, 3479 (1988).
4. B. Sato, J. Appl. Phys. 67, 4462 (1990).
5. R. Krishnan, and M. Tessier, J. Appl. Phys. 67, 5391 (1990).
6. A.J. Freeman, and C.L. Fu, J. Appl. Phys. 61, 3356 (1987).
7. Y. Wang, F.Z. Cui, W.Z. Li and Y.D. Fan, in Thin Films and Beam-Solid Interaction, edited by H.D. Li (Elsevier Science Publishers B.V. 1991) pp.119-122.
8. B. Windows, and F. Sharples, J. Mater. Res. 3, 856 (1988).
9. J.A. Thornton, J. Vac. Technol. A4, 3059 (1986).
10. O.K. Andersen, J. Madsen, U.K. Poulsen, O. Jepsen, and J. Kollar, Physica 86-88B, 249 (1977).
11. L. Moruzzi, P.M. Schwarz, and P. Mohn, Phys. Rev. B 34,1784 (1986).

INVESTIGATION OF MAGNETIC ORDER IN IRON OXIDE-NICKEL OXIDE SUPERLATTICES WITH MODULATION WAVELENGTH LESS THAN 80 Å

S. D. BERRY, D. M. LIND, G. CHERN, H. MATHIAS AND L. R. TESTARDI
Florida State University, Department of Physics and the Center for
Materials Research and Technology, Tallahassee, FL 32306-3016

ABSTRACT

We have investigated the magnetic order, using SQUID magneto-
metry, for short modulation wavelength Fe_3O_4/NiO superlattices,
grown on single crystal MgO. Ferrimagnetic Fe_3O_4 has a saturation
moment of ~500 emu/cm^3 at 0 K and a Curie temperature of 858 K,
while bulk NiO is antiferromagnetic with a Néel temperature of
525 K. Very high crystalline quality with little interdiffusion
is indicated by X-ray diffraction, SEM, optical microscopy, and
in-situ RHEED, and the samples show highly anisotropic electrical
conductivity which also indicates the strong modulation present.
Long wavelength samples ($\Lambda_{mod} > 200$ Å) have a behavior only slight-
ly different from that expected from bulk Fe_3O_4, but for $\Lambda_{mod} < 80$ Å,
spontaneous magnetization is replaced by paramagnetism, with weak
temperature dependence (not $1/T$) from 5 K to 400 K.

INTRODUCTION

We have prepared Fe_3O_4/NiO superlattices on MgO single crystal
substrates, with a range of modulation wavelengths 16 Å$<\Lambda_{mod}<258$ Å.
The components all share a cubic oxygen lattice which are nearly
lattice matched (mismatch is ~0.3 % for Fe_3O_4/NiO, ~0.7 % for
NiO/MgO, and ~0.4 % for Fe_3O_4/MgO). The thicknesses of each compo-
nent was nominally equal, but in general the films had Fe_3O_4 mea-
sured layer thicknesses comprising ~45 % of the bilayer thickness.
The films were found to be of high quality by in-situ RHEED, X-ray
diffraction (XRD), SEM, and optical microscopy.

Growth procedures and characterization of the film structure
have been reported[1], and will only be reviewed briefly here. The
superlattices were grown in a MBE system using dual electron beam
evaporation sources with elemental Fe and Ni, respectively, which
were alternately shuttered under the control of a film thickness
monitor. Oxygen was incorporated via a oxygen plasma-assisted ECR
source. Pressure during deposition was about 2×10^{-5} Torr (entirely
oxygen); the background pressure was in the high 10^{-9} Torr to low
10^{-8} Torr range. Grown films were typically 1 μ thick.

In-situ RHEED served as a monitor of crystal quality during
the growths. RHEED patterns alternated between those for a cubic
rocksalt pattern for NiO and MgO, and the pattern for the spinel
Fe_3O_4 layers which had extra streaks midway between the ones for
NiO/MgO due to the doubled periodicity of the spinel structure.

The X-ray diffraction (XRD) measurements for the films show
no evidence of other crystal orientations than the (001) direction
of the single crystal substrate and for the films reported here.
A sampling of typical XRD spectra are presented in Figure 1, show-
ing the low angle scans for Λ_{mod} = 53 Å and Λ_{mod} = 75 Å. The large
number of lines present indicates the high crystalline quality in
these films (which are among our worst ones). We do not believe

424
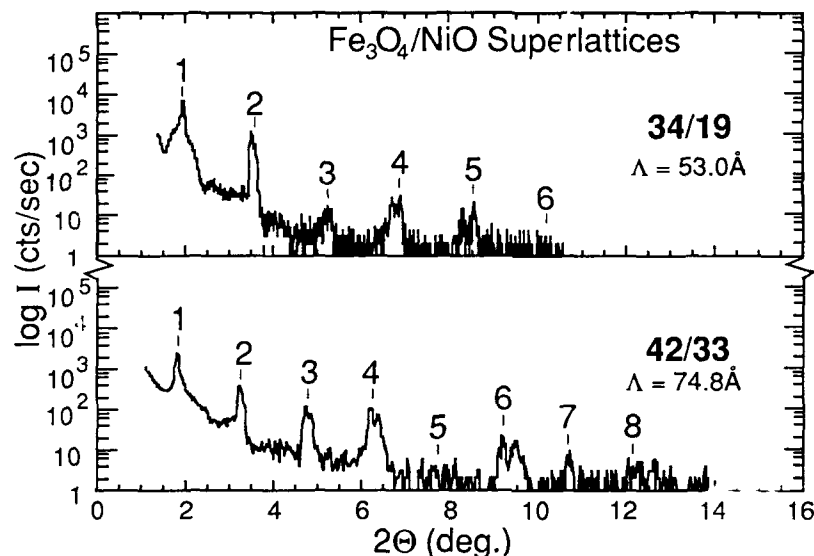
Figure 1. Low angle XRD results for Λ_{mod}=53 Å and Λ_{mod}=75 Å super-
lattices.

that significant interfacial interdiffusion is consistent with
both the XRD results or the alternating RHEED patterns found dur-
ing growth; we are presently attempting to model the XRD results.

We have also measured in-plane conductivity of these super-
lattices and the transverse (out-of-plane) conductivity in similar
modulated structures grown on nickel-coated mica[2]. The I-V mea-
surements show non-linear behavior similar to the Poole-Frenkel
effect[3], and we find very high anisotropy (approaching 10^6) in the
measured conductivity. For Fe_3O_4 single crystal films we observe
the Verwey transition[4] near its normal temperature of 120K.

MAGNETIZATION

We have also previously reported on the direct magnetic char-
acterization of these superlattices through the measurement of
hysteresis loops (magnetization in-plane) in a SQUID magnetome-
ter[5]. Measurements were made of both the substrate with no super-
lattice, and the combined substrate/superlattice system to allow
for an appropriate substrate background subtraction.

Single crystal Fe_3O_4 films grown on MgO substrates showed a
behavior consistent with bulk Fe_3O_4, but when Λ_{mod} is decreased
below 80 Å, the measurements showed loops with little hysteresis,
which behave approximately linearly (paramagnetism) with applied
field, and without reaching saturation at applied fields of 55 kOe
(the maximum of our superconducting magnet). There are essential-
ly no directional differences found (in-plane, out-of plane, and
in the body diagonal direction) for fields exceeding about 40 kOe.

Hysteresis measurements were performed at three temperatures
in Reference 5: 5 K, 10 K, and 300 K. The linear response found

at both 5 K and 10 K were nearly identical over the entire ±55 kOe applied field range. For 300 K, the slope of the response often increased (about 5-10 %), which is **not** the 1/T behavior expected for Curie type paramagnetism.

M versus T Scans

To understand the temperature behavior in greater detail, we made measurements of a subset of the grown superlattices for a 55 kOe applied field, allowing the temperature to vary from 5 K to ~320 K. Since our background measurements were performed at fixed temperatures, and we did not yet desire to destroy these films, we resorted to a simulation of the MgO substrate background.

We have previously found that the substrates we have used have both the normal diamagnetism expected of MgO, but also a paramagnetic contribution, presumably from Mg vacancies in the crystal lattice acting as paramagnetic centers. By modelling the paramagnetic contribution using a J=1/2 Brillouin function, and a room temperature measurement of the substrate to measure the diamagnetic moment of the substrate, we have found we can completely characterize the substrate signal as a function of ambient temperature and applied field.

Using this procedure, we have measured the magnetization M versus temperature T for Fe_3O_4 single crystal films, and for $\Lambda_{mod}=75$ Å and $\Lambda_{mod}=53$ Å superlattices at an applied field H of 55 kOe. The results are shown in Figure 2. The Verwey transition is clearly visible in the curve for the Fe_3O_4 film. The other curve for short wavelength superlattices show no such behavior (we have not seen the Verwey transition in any of our superlattices), and clearly do not show significant temperature variation (such as 1/T). Increasing M with T is clearly seen in the Λ=53 Å film for T<200 K. These scans are qualitively similar to previous results obtained from the endpoints of hysteresis curves.

Discussion

The temperature dependence of the M, since it does not obey the 1/T form, is not consistent of normal paramagnetism due to independent magnetic moments in a thermal bath. A possible explanation for the M versus T behavior is if there is significant coupling at the Fe_3O_4/NiO interfaces, the strong anisotropy found by antiferromagnetic resonance measurements in NiO[6] may be locking the Fe_3O_4 moments to the NiO (111) spin axis direction, with neighboring Fe_3O_4 layers antiferromagnetically coupled.

The fact that M increases with T (at least over some temperature range) then may be due to a slight softening of the NiO anisotropy with temperature. At higher temperatures the Fe_3O_4 magnetization will begin to decrease more rapidly with temperature and the total M of the superlattice (in-plane) will then decrease. Interesting effects may also be observed closer to the Néel temperature when the NiO layers disorder; this measurement is now impossible in our SQUID for our large samples.

The above suggestion is only speculation, however, since we have not yet performed any microscopic measurements on these films. This might allow us to make definite conclusions regarding the origin of the linear hysteresis. We are planning experiments in the near future (FMR and neutron scattering) which we hope will

426
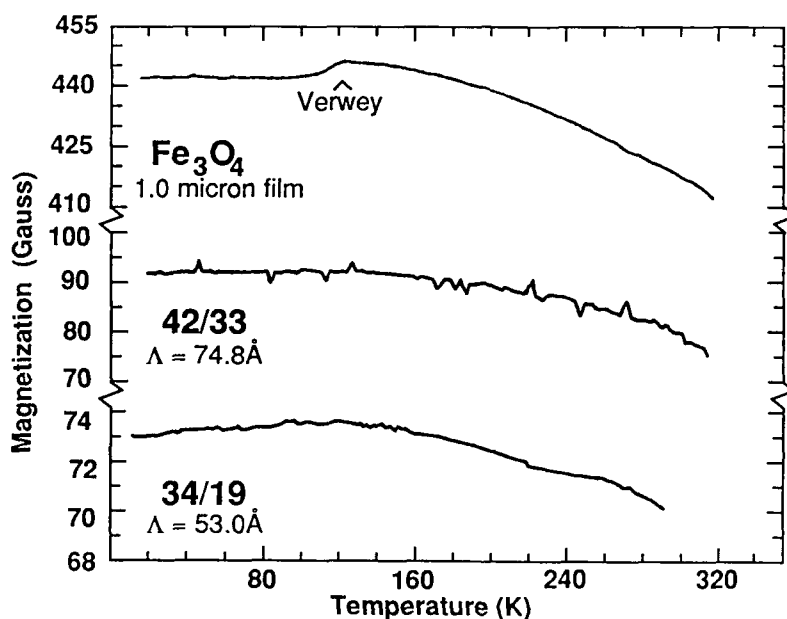
Figure 2. Magnetization plotted against temperature for Fe_3O_4 film, 53 Å superlattice and 75 Å superlattice.

provide us with more definitive conclusions.

REFERENCES

1. D. M. Lind, S. D. Berry, G. Chern, H. Mathias, and L. R. Testardi, March meeting of the American Physical Society; prepared for publication elsewhere.

2. G. Chern, S. D. Berry, D. M. Lind, H. Mathias, and L. R. Testardi, to be published, Appl. Phys. Lett., June, 1991; prepared for publication elsewhere.

3. N. F. Mott, Phil. Mag. **24**, 911 (1971).

4. J. M. Honig, in **The Metal and Nonmetallic States of Matter**, P. P. Edwards and C. N. R. Rao, eds., 261 (London: Taylor and Francis, 1985).

5. S. D. Berry, D. M. Lind, G. Chern, H. Mathias, and L. R. Testardi, March Meeting of the American Physical Society; prepared for publication elsewhere.

6. J. Kanamori, **Magnetism**, G. T. Rado and H. Suhl, eds, (Academic Press, New York, 1963).

PREPARATION AND MAGNETISM OF CuO/Al_2O_3 AND CuO/MgO ARTIFICIAL SUPERSTRUCTURED FILMS

MITSUGU SOHMA AND KENJI KAWAGUCHI
National Chemical Laboratory for Industry, 1-1 Higashi, Tsukuba, Ibaraki
305, Japan

ABSTRACT

Three kinds of copper oxide (CuO) films, that is, CuO mono-layer films (MLFs), CuO/Al_2O_3 artificial superstructured films (ASFs) and CuO/MgO ASFs were prepared by a reactive vapor deposition method. Magnetic susceptibility of the MLFs is almost constant against temperature and the Neel temperature (T_N) is a little lower than that of bulk CuO. There is paramagnetic contribution proportional to the number of the interfaces for both kinds of ASFs. It is considered to be caused by imperfect -Cu-O-Cu- antiferromagnetic superexchange interactions located in the vicinity of interfaces.

INTRODUCTION

A copper oxide (CuO) is an essential component in oxide high-Tc superconductors. It is well known that the antiferromagnetic properties of CuO differ from other 3-d transition metal mono-oxides that show a typical antiferromagnetic behavior [1-4]. It will give us useful information concerning the high-Tc mechanism to study the magnetic properties of CuO. Several attempts to prepare CuO films have been reported [5-9], however the magnetic properties have not been investigated yet. In this work, we present the preparation and the magnetic properties of CuO mono-layer films (MLFs), CuO/Al_2O_3 artificial superstructured films (ASFs) and CuO/MgO ASFs.

EXPERIMENTAL

A reactive vapor deposition process was used to fabricate the sample films. The deposition chamber was first evacuated to the base pressure of about 5×10^{-7} Torr. using oil diffusion pumping system. The source materials were metallic Cu, α-Al_2O_3 and MgO. They were evaporated by electron beam guns in the oxygen atmosphere activated by radio frequency (RF) plasma. The atmospheric pressure was kept 2×10^{-4} Torr. during deposition. Polyimide films and cleaved MgO(100) single crystal plates were used as substrates. The sample discussed in this report were prepared at substrate temperature of 300°C. The deposition rate was controlled by automatically using a quartz thickness control system. It was kept at 0.02nm/sec. because very low deposition rate was found favorable for full oxidation of the samples. Structural analysis was performed by a conventional powder X-ray diffraction (XRD) system. The magnetization of the samples was measured by a SQUID susceptometer (HOXAN HSM-2000) in the temperature range between 4.3K and 300K. An external field of 10kOe was applied horizontally to the film plane. Microscopic magnetic properties of the films were investigated through the hyperfine fields of ^{57}Fe doped in CuO by a Moessbauer method. The Moessbauer samples were prepared using a 2-at% ^{57}Fe doped Cu ingot as a source material. The Doppler shift velocity was calibrated with the spectrum of pure iron metal. These magnetic properties were examined for the samples deposited on very thin ($7.5\mu m$) polyimide substrates (UPILEX S, trade name by Ube Industries, Ltd.,), because the sub-

strate was effective for minimization of background signal in SQUID meas-
urements and high γ-ray transmission in Moessbauer measurements.

CuO MLFs

        Single phase CuO MLFs were successfully prepared with the RF plasma
activation of oxygen atmosphere.   Typical XRD patterns are shown in Fig.1
for the samples (RF power: 20W) deposited on polyimide and MgO substrates.
The sample on a polyimide substrate has a polycrystalline structure, while
that on a MgO(100) substrate exhibits a preferred orientation   as reported
in the reference [7].
        The temperature dependence of magnetic susceptibility of the CuO MLF
on polyimide is shown in Fig.2.   The magnetic susceptibility value of the
substrate is comparable to that of the sample film.   However the suscepti-
bility of the substrate showed a small and monotonous change in tempera-
ture, and the reliable true value of the sample was evaluated.   Such an
anomaly as measured for typical antiferromagnetic materials was not ob-
served and we could not determine the Neel temperature (T_N) from the re-
sults.
        The temperature dependence of the Moessbauer spectra has been inves-
tigated [10] for the sample deposited on a polyimide substrate (RF power:
60W) as shown in Fig.3.   A paramagnetic doublet spectrum is seen above
180K.   The values of the isomer shift (IS) and the quadrupole splitting
(QS) are 0.41 mm/sec and 1.37 mm/sec, respectively at 180K.   A signifi-
cant broadening of the spectrum is shown below 150K.   When the broadening
is due to the hyperfine field (HF) induced by the matrix CuO molecular
field, T_N was estimated to be about 160K from the relation between the HF
and the temperature [10].   This temperature is a little lower than the
reported bulk value of 230K [1-4].   The Moessbauer spectrum at 4.2K shows a
relatively clear hyperfine sextet.   A two components fitting result is
illustrated by a solid curve (a) (both components of (b):sextet and
(c):doublet are drawn together).   Those of calculated magnetic HF and IS
of the sextet are 426 kOe and 0.50 mm/sec, respectively.   The broad peak
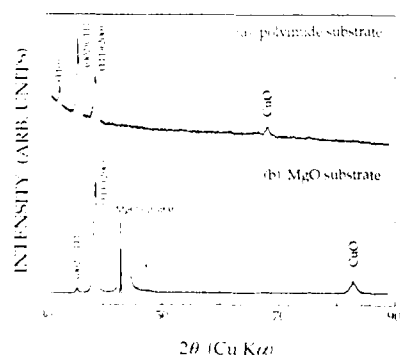
Fig.1. XRD patterns of CuO MLFs (300nm)
prepared under a RF plasma power of 20W.
Both samples were deposited on (a) a
polyimide substrate and (b) a cleaved
MgO(100) single crystal at 300°C.
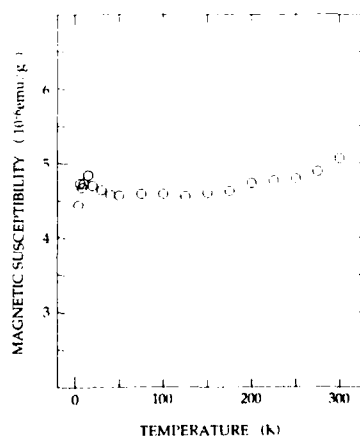
Fig.2. Net magnetic susceptibility of the
same CuO MLF used in Fig.1(a).   An exter-
nal field of 10kOe was applied horizontal-
ly to the film.

width of the sextet indicates a little distribution of HF values. It would probably reflects the structural imperfection of the CuO film. The values of IS and QS of the doublet component are 0.55 mm/sec and 2.1 mm/sec. The doublet suggests that there is a small nonmagnetic component. However there has not been additional information to support it yet. Further investigation is necessary.

CuO/Al$_2$O$_3$ ASFs

A typical XRD pattern of a CuO/Al$_2$O$_3$ ASF deposited on polyimide substrate is shown in Fig.4. Artificial superstructural periodicity is clearly confirmed from the low angle XRD pattern. No Bragg peaks of Al$_2$O$_3$ were observed for ASFs with various artificial periods in the middle angle region. Whereas the ASFs with CuO layers thicker than 5nm showed a polycrystalline CuO pattern.

A Curie like paramagnetic component was observed obviously in the magnetization curves of CuO/Al$_2$O$_3$ ASFs. When the thickness of Al$_2$O$_3$ layers and the number of artificial periods (NAP) are constant, there are no remarkable differences in the magnetization in the low temperature region. It means that the thickness of the CuO layers is not correlated with the paramagnetic behavior in thelow temperature region. The temperature dependence of magnetization for Al$_2$O$_3$/CuO ASFs is given in Fig.5 for various artificial periods. In these ASFs, the total thickness of CuO and Al$_2$O$_3$ are constant. The magnetization in low temperature region increases with decreasing the thickness of artificial periods. Note that such a Curie like behavior is not significant for the CuO MLF prepared under the same condition as ASFs as shown in Fig.2. To evaluate the contribution from the interfaces, the magnetization data of Fig.5(a)-(c) were subtracted by those of Fig.5(d) at several temperatures. The magnetization in the low temperature region is proportional to the number of interfaces. It is reasonable to consider that the paramagnetic components are derived from the interfaces where -Cu-O-Cu- antiferromagnetic superexchange interactions are cut off.
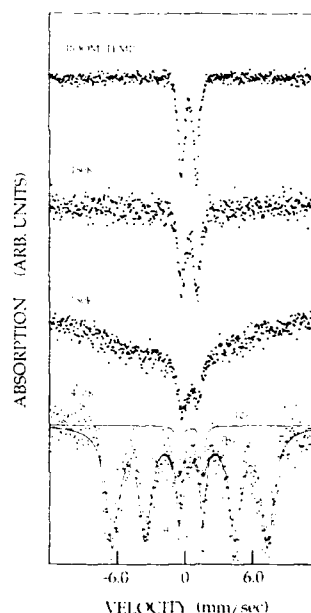
Fig.3. Temperature dependence of Moessbauer spectra of an ^{57}Fe-doped CuO MLF (100nm) deposited on a polyimide substrate at 300°C under a RF plasma power of 60W. The solid curve (a) is the least squares fitting result with Lorenzian lines for the spectrum at 4.2K, and (b),(c) are the sextet component and the doublet component of (a), respectively.
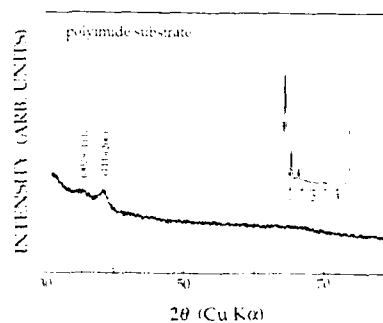
Fig.4. XRD patterns of a CuO(10nm)/Al$_2$O$_3$(15nm) ASF prepared under a RF power of 20W on a polyimide substrate at 300°C. The NAP is twenty.
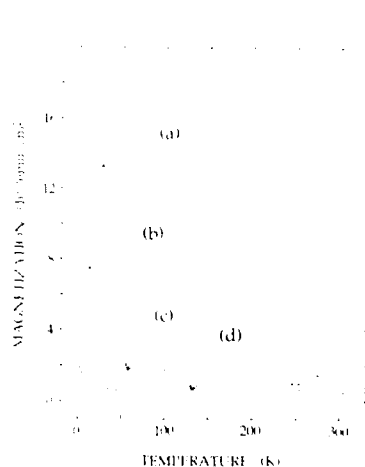
Fig.5. Net magnetization of ASFs per square centimeter. The preparing conditions are the same as those in Fig.4. An external field of 10kOe was applied horizontally to the film.
(a) [CuO(2nm)/Al₂O₃(3nm)]×100,
(b) [(5nm)/(7.5nm)]×40,
(c) [(10nm)/(15nm)]×20,
(d) Al₂O₃(150nm)/CuO(200nm)/Al₂O₃(150nm)

2θ (Cu Kα)
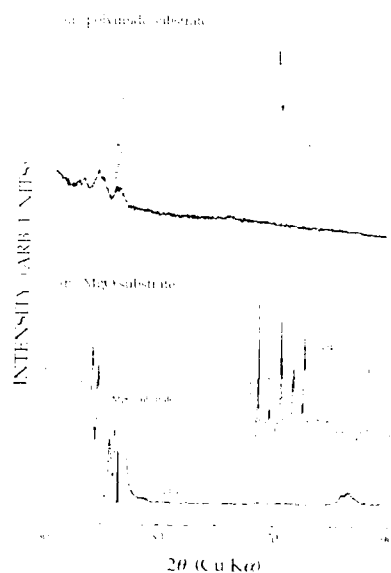
Fig.6. XRD patterns of CuO(5nm)/MgO(4nm) ASFs on (a) a polyimide substrate and (b) a cleaved MgO(100) single crystal. The preparing conditions are the same as those in Fig.4. The MP is twenty.

CuO/MgO ASFs

XRD patterns of CuO/MgO ASFs deposited on a polyimide and a MgO(100) substrate are shown in Fig.6. A few Bragg peaks of Cu_2O are clearly observed as illustrated in Fig.6(a), when the thickness of CuO layers is less than about 5nm. It is supposed that the existence of Cu_2O phase is attributed to oxygen defects at interfaces. While the ASF deposited on a MgO(100) substrate shows no Cu_2O peaks in Fig.6(b). The CuO/MgO ASFs are expected to grow epitaxially with the direction of CuO[111]//MgO[100] [7]. Actually, the ASFs exhibits higher order satellite peaks around CuO(111) in the figure. It suggests a good structural quality at the interfaces.

Magnetization as a function of temperature shows a similar tendency to that of CuO/Al$_2$O$_3$ ASF in the low temperature region. The magnetization in the low temperature region increases remarkably for the ASFs containing a Cu_2O phase. The magnetic properties of Cu_2O is believed to be a diamagnetic material, probably unpaired spins arise from oxygen defects.

REFERENCES

1. M.O'Keeffe and F.S.Stone, J. Phys.Chem. Solids **23**, 261 (1962)

2. J.B.Forsyth, P.J.Brown and B.M.Wanklyn. J.Phys.C: Solid State Phys. **21**, 2917 (1988)
3. M.S.Sheeha, Z.Feng and R.Gopalakrishnan, ibid. **21**, L1051 (1988)
4. B.X.Yang, T.R.Thurston, J.M.Tranquada and G.Shirane, Phys.Rev.**B 39**, 4343 (1989)
5. T.Nakamura, H.Yamamoto and M.Tanaka, Physica B **165&166**, 1489 (1990)
6. W.Klein, H.Schmitt and M.Boeffgen, Thin Solid Films **191**, 247 (1990)
7. J.P.Locquet, J. Less-Common Met. **164&165**, 300 (1990)
8. A.B.Laurie, M.L.Norton, Mat.Res.Bull. **24**, 1521 (1989)
9. H.Holzschuh, H.Suhr, Appl.Phys.A **51**,486 (1990)
10. M.Sohma, K.Kawaguchi, to be published in Solid State Commun.

ABSORPTION OF RADIATION BY MAGNETIC SUPERLATTICES

J.G. LePage and R.E. Camley
University of Colorado, Physics Department, Colorado Springs, CO 80933-7150

ABSTRACT

We calculate the absorption of infra-red radiation by a magnetic superlattice composed of alternating ferromagnetic films. Although the films are ferromagnetic, the interfacial interaction is antiferromagnetic (i.e. Fe/Gd or Co/Gd). As has been shown previously, such a system can exist in several distinct phases, and we calculate the power absorption for these different phases. The spin wave modes of the system were found and used to construct a Green's function via an eigenvector expansion. The incoming radiation was modeled as an oscillating magnetic field which was assumed to decay into the material. Given this driving field, the Green's function yields the response of the system. Our results indicate that a simple absorption measurement can be used to probe for surface and bulk magnetic phase transitions. Additionally, we can find the response of the system to a spatially uniform driving field and thus calculate the local susceptibility. We discuss the possibility of using such a susceptibility to find dipole-exchange modes in magnetic superlattices.

INTRODUCTION

Magnetic multilayers have shown a stimulating richness of behaviour. In particular we have seen a set of structures (Dy/Y, Gd/Y[1], Gd/Dy[2], Fe/Cr[3], Co/Gd[4] and Fe/Gd[5]) which exhibit a series of magnetic phase transitions at relatively low temperatures and applied fields. These new materials are likely to have new and unusual dynamic properties as well. In this paper we will explore the electromagnetic properties of a simple, and yet characteristic, magnetic superlattice.

We consider a model system composed of alternating films of iron (thirteen ML) and gadolinium (five ML) arranged in a bcc structure. While both materials are ferromagnetic, the coupling at the interface is antiferromagnetic. The geometry is shown in figure 1. The structure is finite in the y-direction and infinitely extended in the x- and z-directions. This system can exist in a number of different magnetic phases[5]. As illustrated in Fig. 1, the Gd-aligned state occurs when the Gd spins are aligned with the external field. There is also an Fe-aligned state and a canted state (in which the spins are rotated away from the z-axis in the x-z plane).
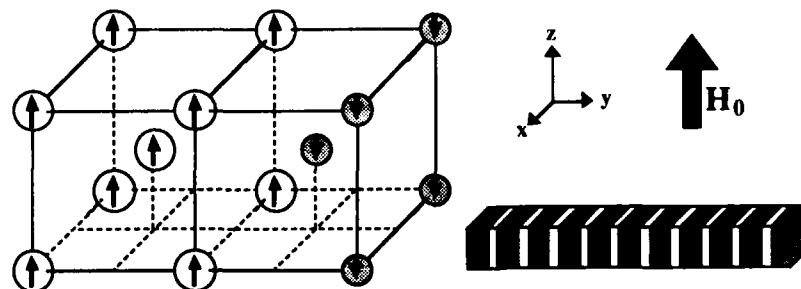
Fig. 1. The crystalline structure of our system is shown on the left. The Gd atoms are represented by white circles; the Fe atoms by shaded circles. Note the direction of the magnetic moments. A slice through the entire crystal is shown on the right. The Fe layers are shaded. The orientation of the coordinate axis and the direction of the external field are shown above.

In addition, the structure can also have either Fe or Gd at the surfaces. The choice of this outermost film radically alters the nature of the magnetic phase transition[6]. If Fe is chosen, the phase transition from the Gd-aligned state to the canted state nucleates at the surface and the transition takes place at a field about 5 times lower than that required for the bulk transition. On the other hand, if gadolinium is chosen, the phase transition begins in the interior of the crystal. In this paper we concentrate on a finite multilayer with Fe at both surfaces; the complete system is a symmetric structure made up of eleven *films* of Fe and 10 *films* of Gd.

THEORY: POWER ABSORPTION

We are concerned primarily with the response of our superlattice to an externally applied driving field. To begin, consider the magnetic field that acts on a spin in the nth layer of the superlattice. In a bcc structure each spin (except for those spins at the surface) has a total of eight nearest neighbors. Therefore, each spin is immersed in a effective field given by

$$H_{eff,n} = 4J_{n,n-1}S_{n-1} + 4J_{n,n+1}S_{n+1} + H_0 + h_n \qquad (1)$$

$J_{n,p}$ is the exchange constant that operates between spins in the nth and pth layer. For ease of notation, we use J in this paper to represent the true exchange constant divided by $(-g\mu_B)$; g is the landé factor and μ_B is the Bohr magneton). Thus JS has units of magnetic field. H_0 is a static externally applied field which always acts along the positive z-direction. h_n is a small oscillating field that acts within the plane perpendicular to H_0. Naturally, each spin is aligned with the static component of its effective field. Of course, this effective field is, in the general case, *not* aligned with the externally applied field. In the most general case, the spins are canted away from the external z-axis by some angle θ but remain within the x-z plane. Each spin is given its own z'-axis which corresponds to the orientation of its static configuration vector. The equations of motion are the Bloch equations:

$$\frac{dS_n}{dt} = \gamma\, S_n \times H_{eff,n} - \frac{S_n}{\tau} \qquad (2)$$

We assume a time dependence for S_n and h_n of the form of $e^{-i\omega t}$. τ is the transverse relaxation time. After some manipulation, we get the following equations of motion

$$-i\omega S_n^{x'} = \gamma\left[H_0\cos\theta_n + 4J_{n-1,n}S_{n-1}^{z'}\cos(\theta_{n-1} - \theta_n) + 4J_{n,n+1}S_{n+1}^{z'}\cos(\theta_{n+1} - \theta_n)\right]S_n^y$$

$$-\gamma\left[4J_{n-1,n}S_n^{z'}\right]S_{n-1}^y - \gamma\left[4J_{n,n+1}S_n^{z'}\right]S_{n+1}^y - \frac{S_n^{x'}}{\tau} - \gamma h_n^y S_n^{z'} \qquad (3)$$

$$-i\omega S_n^y = -\gamma\left[H_0\cos\theta_n + 4J_{n-1,n}S_{n-1}^{z'}\cos(\theta_{n-1} - \theta_n) + 4J_{n,n+1}S_{n+1}^{z'}\cos(\theta_{n+1} - \theta_n)\right]S_n^{x'}$$

$$+\gamma\left[4J_{n-1,n}S_n^{z'}\cos(\theta_{n-1} - \theta_n)\right]S_{n-1}^{x'} + \gamma\left[4J_{n,n+1}S_n^{z'}\cos(\theta_{n+1} - \theta_n)\right]S_{n+1}^{x'}$$

$$-\frac{S_n^y}{\tau} + \gamma h_n^x S_n^{z'}\cos\theta_n \qquad (4)$$

If we write the equations of motion for each spin in the system, we get a system of linear equations which we can rewrite as a matrix equation:

$$- i\omega S = \overleftrightarrow{A} S + \gamma c \tag{5}$$

where S is a vector that contains the x'- and y-components of the spins and c contains the inhomogenous terms found in equations (3) and (4). Once we have solved the homogenous problem for the left and right eigenvectors and their associated eigenvalues, we can form the response S via an eigenvector expansion [7]. Thus, we can write S as a sum over the eigenvectors:

$$S = \sum_{i=1}^{2N} a_i S_i^{(r)} \tag{6}$$

where $S_i^{(r)}$ is the ith (right) eigenvector of the matrix $\overleftrightarrow{A}$. The a_i are given by

$$a_i = \frac{\gamma S_i^{(l)} \cdot c}{\left(i\omega - \Omega_i\right) S_i^{(l)} \cdot S_i^{(r)}} \tag{7}$$

where Ω_i is the ith eigenvalue of the matrix $\overleftrightarrow{A}$ while $S_i^{(l)}$ is the ith left eigenvector. Thus we form the response of the system to an externally applied oscillating magnetic field from the eigenvectors of the matrix A. The a_i's effectively provide the Green's function for the system. The time averaged power absorbed is proportional to the real portion of

$$\frac{1}{2} \sum_{n=1}^{\cdot} \frac{1}{T} \int_0^T \left[\frac{dM_n^x}{dt} (h_n^x)^* + \frac{dM_n^y}{dt} (h_n^y)^* \right] dt = -\frac{i\omega}{2} \sum_{n=1}^{N} \left[\gamma \hbar S_n^x (h_n^x)^* \cos\theta_n + \gamma \hbar S_n^y (h_n^y)^* \right] \tag{8}$$

Note that this is the power absorbed by a columnar section of the slab with a cross-sectional area of b^2 where b is the lattice constant in the x and z directions. Note that infra-red radiation falling on the surface of the multilayer with an incident angle of zero can be modeled by an oscillating magnetic field subject to the conditions

$$h_n^y = 0 \quad \text{and} \quad h_n^x = h_0 e^{-\alpha n} \tag{9}$$

where α is positive. In this case, the time averaged power absorbed is given by

$$P_{Total} = Re\left(-\frac{i\omega}{2} \sum_{n=1}^{N} \gamma \hbar S_n^x h_0^* e^{-\alpha n} \cos\theta_n \right) \tag{10}$$

RESULTS: POWER ABSORPTION

When we began this project, our aim was to determine in general terms the effects of magnetic phase transitions on the absorption of infra-red light. When the system undergoes a phase transition, one of the spin wave modes is driven to zero; the mode goes "soft". Thus, near a phase transition point, we expect to see one of the absorption peaks move towards zero frequency. Conversely, as the system enters a new phase, we expect to see a mode appear near zero frequency and move away from zero as the system moves away from the phase transition point. We do, in fact, see this type of behavior. However, we had also hoped to see an abrupt change in the power absorption spectra as the system makes magnetic phase transitions. Our results show that, in most cases, the change is more subtle. One of the most easily detected transitions is the field-driven phase change from the Gd-aligned state to the twisted configuration. This effect can be seen in figure 2. Note that a relatively small change
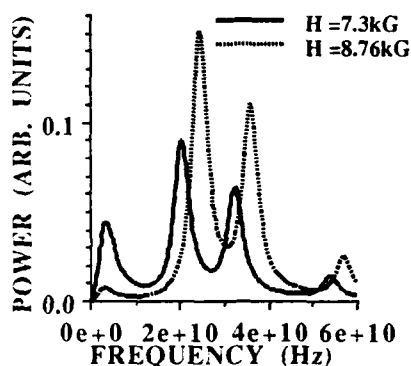
Fig. 2. Power absorption spectrums for the system at T=0K for two different values of magnetic field. At 7.3 kG the sytem is in the Gd-aligned state; at 8.76 kG the system is in the twisted state.
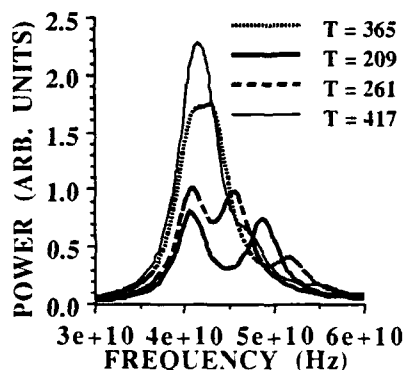
Fig. 3. Power absorption spectrums for the system at four different temperatures. H_0=14.6 kG. At T=365,417 K the system is in the Fe-aligned state. At T=261,209 the system is in the twisted state.

in the magnitude of the external field (from H_0 = 7.3 kG to H_0 = 8.76 kG) results in a much larger increase in the power absorption (from about 0.09 at 20.38 GHz to about 0.15 at 24.45 GHz). Note also the two small peaks near zero frequency; these peaks are the manifestations in the power absorption spectra of the "soft" modes mentioned above. Another detectable phase transition occurs as the temperature increases from 261 K while the magnetic field remains at a value of H_0=14.6 kG (see figure 3). Note that at temperatures of 209 K and 261 K, the system is in the twisted state. At values of T = 365 K and 417 K, the system is in the Fe-aligned phase. When the system is in the twisted state, there are two distinct peaks. As the system makes the transition into the Fe-aligned phase, these peaks merge and the power absorption increases significantly. A few generalizations can be made on the basis of these two examples (as well as other cases not included in this paper). First of all, we see that the power absorption curves are strongly dependent on the values of temperature and applied field; this is to be expected. Second, there tend to be significant changes in power absorption near phase transitions. Finally, close observation of the peaks due to the "soft" modes can reveal the occurence of a phase transition.

It should be possible to experimentally detect phase transitions if the spin configuration of the system is known in sufficient detail and, therefore, the calculations (which are based on these data) are sufficiently accurate. Of course, real materials can be quite complicated and many processes may be responsible for the absorption of infra-red light. We modeled only the absorption of light via the excitation of magnons. Despite this inherent limitation, the calculated power vs. frequency curves do serve to highlight many of the unusual properties of our material. For instance, this system's seeming similarity to a ferrimagnet is underscored by the dominant role that the "ferrimagnetic-like" mode usually plays in power absorption. (This mode,identified by the fact that its frequency is equal to γH_0 at k=0, is similar to one of the normal modes of a bulk ferrimagnet.) Absorption due to this mode is particularly pronounced in the Fe-aligned phase but also occurs in the twisted phase. However, a careful analysis of the absorption curves shows that there is a much smaller contribution from this mode when the system is in the Gd-aligned phase. This behavior can be easily explained. First, recall that since infra-red light decays rather rapidly into the material, such a probe is necessarily very surface sensitive. A simple calculation shows that the power absorption due to this mode is proportional to the square of the "effective" magnetization:

$$\sum_{n=1}^{N} M_n^z e^{-\alpha n} \tag{11}$$

where M_n^z is the magnetization in the nth layer. Notice that the magnetization of layers near the surface figure prominently in this sum while layers deeper in the material play a much less significant role. With this in mind consider the first unit cell of the system when it is in the Fe-aligned phase. The Fe moments in the first thirteen layers are aligned with the static field and so contribute a positive term to the effective magnetization while the Gd moments in the next five layers are aligned anti-parallel with the static field and so contribute a much smaller negative term. Therefore, the effective magnetization is relatively large in the Fe-aligned phase and so the power absorption due to the ferrimagnetic-like mode is relatively large. Using similar reasoning, we find that in the Gd-aligned phase, the effective magnetization is considerably smaller. To carry our analysis one step further, consider what happens when Gd makes up the outermost film. In this case, the effective magnetization is largest in the Gd-aligned phase and we expect the power absorption to be greater in this phase than in the Fe-aligned phase; this is precisely the result that we find.

SUSCEPTIBILITY

Our formalism can be easily applied to the calculation of the magnetic susceptibility. As is well known, the dynamic susceptibility governs the long-wavelength "dipolar" spin wave modes which often find application in magnetostatic devices. The strategy is simple. We begin by considering a spatially uniform driving field oriented in the x-y plane with a time dependence of the form $e^{-i\omega t}$. The magnetization can be related to this driving field via

$$\mathbf{M} = \overset{\leftrightarrow}{\chi} \mathbf{h} \tag{12}$$

where the x- and y-components of the magnetization are defined as

$$M^x = \frac{1}{V} \sum_{unit\ cell} \gamma \hbar S_n^{x'} \cos\theta_n \quad \text{and} \quad M^y = \frac{1}{V} \sum_{unit\ cell} \gamma \hbar S_n^y \tag{13}$$

wher V is the volume of a unit cell. As it happens, only one mode is excited by a spatially uniform magnetic field; therefore, the sum in equation (6) is particularly simple. This mode is analogous to one of the k=0 modes of a simple ferrimagnet and has $\omega = \gamma H_0$. It is mathematically convenient to treat this one mode as two physically equivalent eigenvectors specified by

$$S_n^{x'} = S_n^z \quad \text{and} \quad S_n^y = \pm i S_n^{z'} \cos\theta_n \tag{14}$$

where the upper sign refers to "mode 1" while the lower sign refers to "mode 2." Mode 1 has a time dependence of the form $e^{-i\omega t}$ while mode 2 has a time dependence of the form $e^{+i\omega t}$. After applying all this information to equation (7) we find that the coefficients of these modes are

$$a_1 = \gamma \frac{ih^y - h^x}{2(\omega - \gamma H_0)} \tag{15}$$

and

$$a_2 = \gamma \frac{h^x + ih^y}{2(\omega + \gamma H_0)} \tag{16}$$

438

We can now construct the x and y components of the magnetization:

$$M^x = \gamma \left[\frac{i\omega h^y - \gamma H_0 h^x}{\omega^2 - \gamma^2 H_0^2} \right] M^z \qquad (17)$$

and

$$M^y = \gamma \left[\frac{i\omega h^x + \gamma H_0 h^y}{\gamma^2 H_0^2 - \omega^2} \right] M^z \qquad (18)$$

Note that we have used the fact that

$$M^z = \frac{1}{V} \sum_{unit\ cell} \gamma \hbar S_n^{z'} \cos\theta_n \qquad (19)$$

After substituting the equations for the magnetization into equation (12) and solving for the components of the susceptibility tensor we find

$$\overleftrightarrow{\chi} = \frac{4\pi\gamma M^z}{\gamma^2 H_0^2 - \omega^2} \begin{bmatrix} \gamma H_0 & -i\omega \\ +i\omega & \gamma H_0 \end{bmatrix} \qquad (20)$$

This is remarkably similar **in form** to the result for a ferromagnet. However, since M^z varies from unit cell to unit cell in our superlattice, the magnetic susceptibility of our material is position dependent. More importantly M itself is now field dependent since it can be adjusted by varying the applied field.

As mentioned earlier the susceptibility above is a good starting point for including dipolar fields and we can obtain the magnetostatic long-wavelength spin waves. Similar calculations have been done previously for a variety of systems[8]. We should note however that the susceptibility **does not** provide a complete description of the system. In particular, in the zero temperature limit one can produce a phase transition from the Gd-aligned state to the twisted state by increasing the magnetic field. In contrast, the spin waves calculated from the susceptibility above do not show a soft mode at the phase transition. In the future it will be necessary to explore the validity of including dipolar fields into the problem through the use of the susceptibility calculated above.

REFERENCES

1) J. Kwo et. al. Phys. Rev. B 35, 7925 (1987); C. F. Majkrzak et al. Phys. Rev. Lett., 56 2700 (1986); M. B. Salamon et al. Phys. Rev. Lett., 56 259 (1986); J. J. Rhyne et al. J. Appl. Phys. 61, 4043 (1987)
2) R. E. Camley, J. Kwo, M. Hong and C. L. Chien, Phys. Rev. Lett., 64, 2703 (1990)
3) P. Grünberg. R. Schreiber, Y. Pang, M. B. Brodsky and H. Sowers, Phys. Rev. Lett., 57, 2442 (1986)
4) S. Tsunashima, T. Ichikawa, M. Nawate, and S. Uchiyama, J. Phys. (Paris) Colloq. 49 C8-1803 (1988)
5) R. E. Camley, Phys. Rev. B 39 12316 (1989)
6) J. G. LePage and R. E. Camley, Phys. Rev. Lett., 65 1152 (1990)
7) L.L. Hinchey and D. L. Mills, Phys. Rev. B 33, 3329 (1986); Phys. Rev. B 34, 1689 (1986)
8) N. S. Almeida and D. L. Mills, Phys. Rev. B 37 3400 (1988)

Perpendicular Magnetic Anisotropy and Magneto-Optics

PERPENDICULAR MAGNETIC ANISOTROPY OF Pd/Co AND RELATED MULTILAYERS

S. TSUNASHIMA, K. NAKAMURA, H. TAKAHASHI, S. FUKATSU AND S. UCHIYAMA
Nagoya University, Dept. of Electronics, Nagoya, 464-01 Japan

ABSTRACT

Multilayer films consists of noble metal (Pd, Pt, Cu, Au, PdSi) and transition metal(Co, Ni, PdCo, PtCo, CoZr) layers were prepared by rf sputtering method on glass and/or MgO single crystal substrates. The perpendicular magnetic anisotropy was examined in relation to the magnetostriction, lattice misfits, crystallinity and crystal orientations. The results suggest that the perpendicular magnetic anisotropy in noble metal/PdCo alloy multilayers originates from the magnetoelastic energy of the PdCo layers under a stress due to the lattice misfits. In both Pd/Co and Pd/Ni multilayers, the anisotropy was found to depend on the crystal orientation, and the dependence is discussed from the view point of the magnetoelastic surface anisotropy.

INTRODUCTION

Various noble metal/Co multilayered films, such as Pd/Co, Pt/Co and Au/Co have large magnetic anisotropy with the easy axis perpendicular to the film plane.[1-3] The physical origin of the anisotropy can be classified into at least two categories. One is the magnetocrystalline surface anisotropy and the other is the magnetoelastic surface anisotropy.[4]

For Pd/Co multilayers, we have pointed out the possibility of the contribution of the magnetoelastic surface anisotropy since the magnetostriction of PdCo alloys is extremely large.[5,6] However, it is difficult to prove the contribution of the magnetoelastic surface anisotropy through an experiment since the structure and the strain at the interface are not well known.

In this paper, we present a series of experiments on the magnetic anisotropy of multilayers consist of noble metal and PdCo alloy layers including other related multilayers. We will further discuss the relation between the crystal orientation and the anisotropy in Pd/Co and Pd/Ni multilayers from the view point of the magnetoelastic surface anisotropy.

FILM PREPARATION

Multilayered films(MLs) were prepared by rf sputtering from separated two targets onto glass and/or MgO(100) substrates at ambient temperature. Deposition rates were 2 to 5 Å/s and the Ar pressure during sputtering is 10 to 30 mTorr. The bilayer periods were controlled by adjusting the rotation rate of the substrate holder which turns around above the targets. The thickness ratio of Magnetic layers to noble metal(NM) ones was kept constant for each multilayer system. Thus the thickness of NM layers was varied in proportion to the magnetic layer thickness. This is different from other

442

experiments where NM layer thickness was kept constant.[1-3] The thickness
of MLs is around 1000 Å when not mentioned.

To examine the influence of the crystal orientation, some of MLs were
sputtered on MgO (100) substrates with Ag buffer layers.

RESULTS AND DISCUSSION

Noble metal/PdCo multilayers

Typical x-ray diffraction patterns are shown in Fig. 1 for Pt/PdCo MLs
comparing with Pd/Co MLs. In the low angle diffraction, the 1st and 2nd peak
intensities of Pt/PdCo are nearly the same with those of Pd/Co. In the high
angle diffraction, the satellite peaks of Pt/PdCo are also similar to those
of Pd/Co in their intensity. These results indicate that the sharpness of
the interface in both multilayers are similar to each other since both types
of MLs have nearly the same structural parameters contributing to the super-
lattice diffractions, namely they have nearly the same values of the total
thickness, the sublayer period, the sublayer thickness ratio and the
difference in the scattering factor between sublayers.

Figure 2 shows magnetization curves of various NM/PdCo MLs together
with PdCo single layered film. Pt/PdCo and Pd/PdCo MLs show the
perpendicular magnetization while Cu/PdCo ML shows the in-plane
magnetization. In these MLs, the composition of PdCo alloy layers are the
same and therefore the MLs are similar in the demagnetization energy. Thus
the perpendicular magnetic anisotropy of PdCo layer seems to be enhanced in
Pt/PdCo and Pd/PdCo MLs while reduced in Cu/PdCo MLs.
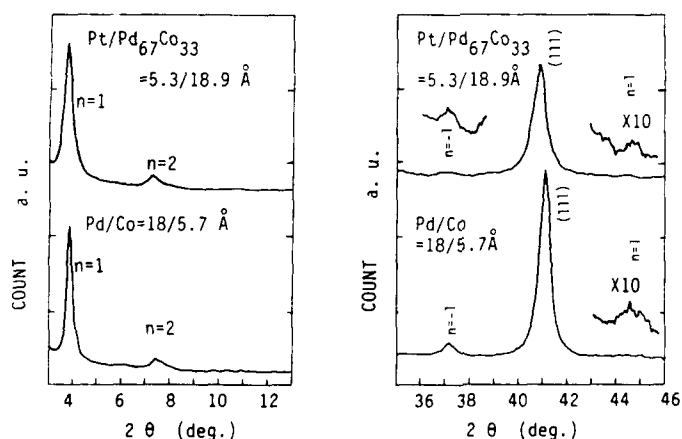
Fig.1 Low and high angle x-ray diffractogram of Pt/PdCo and Pd/Co
       multilayers.[5]
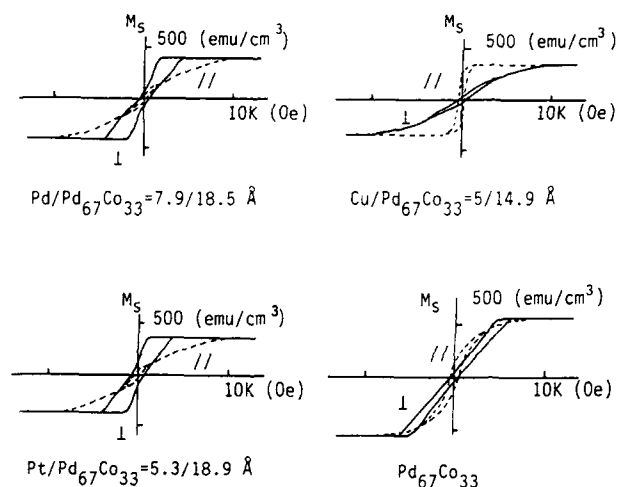
Fig.2 Magnetization curves of NM(NM=Pd,Pt,Cu)/PdCo multilayered and
PdCo single layered films. ($\parallel$) and ($\perp$) indicate fields parallel and
perpendicular to the film plane, respectively.[5]
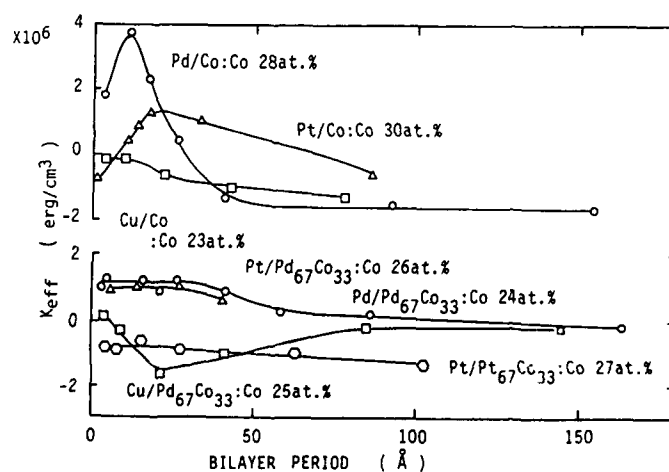
Fig. 3 Effective perpendicular anisotropy K_{eff} of NM(NM=Pt,Pd,Cu)/Co
(upper figure) and NM(NM=Pt,Pd,Cu,Au)/PdCo, Pt/PtCo multilayers
(lower figure) as a function of bilayer periods.

The effective anisotropy of various MLs including Pt/Co, Pd/Co and Cu/Co are shown in Fig.3 as a function of bilayer thickness. In Pd/Co and Pt/Co MLs, K_{eff} has a clear maximum at a bilayer thickness less than 20Å, which suggests the contribution of the interface to the anisotropy. On the other hand, in Pd/PdCo and Pt/PdCo, K_{eff} is positive in a wide range of λ up to 50 Å and then decreases with increasing λ. The behavior of Cu/PdCo is a little curious; a negative peak is seen at $\lambda = 20$Å, and with increasing λ, the anisotropy approaches gradually to the same value with Pd/PdCo MLs.

Figure 4 shows λK_{eff} as a function of the thickness of the magnetic layers t for various MLs. In Pd/Co and Pt/Co MLs, the plots of λK_{eff} for large λ becomes a straight line with a negative gradient and a positive extrapolation at t = 0, which correspond to a negative volume anisotropy and a positive surface anisotropy of 0.3 to 0.5 erg/cm^2. The maximum of λK_{eff} was obtained at t=3 and t=8 Å for Pd/Co and Pt/Co MLs, respectively. These results are quite similar to previous experiments.[1,2]
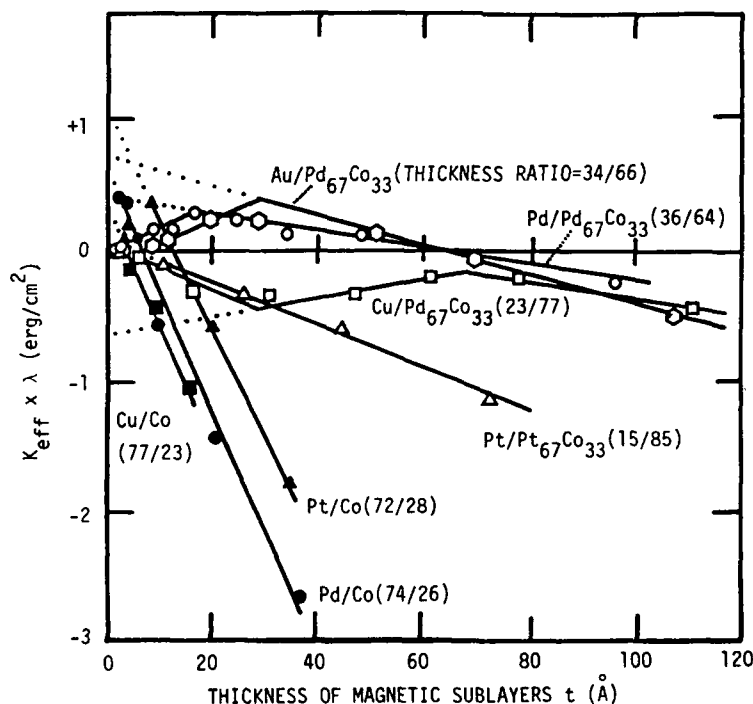
Fig. 4 Effective anisotropy K_{eff} multiplied by bilayer period λ for NM/PdCo (NM=Pt,Pd,Au,Cu) and Pt/PtCo multilayers as a function of magnetic sublayer thickness.

In Cu/Co MLs, λ K$_{eff}$ is always negative, but the linear extrapolation suggests also a positive surface anisotropy. Data obtained for smaller t than 10 $\AA$ deviate from the straight line, which is similar to the case of Pd/Co or Pt/Co MLs.

In NM/PdCo MLs, the surface anisotropy K$_s$ obtained from the extrapolation strongly depends on the kind of NM. For Pt, Pd and Au, Ks is positive, while for Cu it is negative. In all the NM/PdCo MLs, the critical thickness of magnetic layers t$_c$ where λ K$_{eff}$ begins to deviate from the straight line, is about 20 $\AA$, which is much thicker than the case of Pd/Co MLs.

Negative Ks in Cu/PdCo and positive Ks in both Pd/PdCo and Pt/PdCo can be explained by assuming the magnetoelastic surface anisotropy[4] induced at the interface between the NM and PdCo alloy layers. This surface anisotropy seems to originate from the magnetoelastic energy in PdCo layers under a planar stress due to the misfit of lattice constants between PdCo and NM layers. Since the magnetostriction λ_{111} of PdCo alloy is negative, a larger lattice constant of noble metal than PdCo will give rise to a positive Ks and smaller one negative Ks.

If the ML is free from dislocations, the anisotropy should be independent of the bilayer period and is only proportional to the amount of the misfit and to the magnetostriction λ_s of magnetic layers. In these situation, the anisotropy has volume character rather than surface one, namely K$_{eff}$ becomes independent of the bilayer thickness. Actually, in Pd/PdCo and Pt/PdCo MLs, the effective anisotropy shown in Fig.3 is rather constant up to λ = 20 $\AA$. Above this critical thickness (magnetic layer thickness t$_c$), the stress may be relaxed by introducing dislocations near the interface and as a result K$_{eff}$ gradually decreases with increasing λ. For magnetic layers thicker than t$_c$, the magnetoelastic energy stored near the interface can be expressed by the surface anisotropy as have been discussed in Fig.4.

The magnetoelastic anisotropy calculated from the value of λ_{111} (= 1.7 $\times$ 10^{-4}) [6] together with the strain to be assumed in the pseudomorphic structure is about two times larger than that obtained by experiment. This discrepancy may be due to the incomplete crystal orientation and/or the release of the strain at the interface.

The anisotropy of Pt/PtCo MLs is also shown in Figs.3 and 4. In Pt/PtCo MLs, we cannot expect such a large magnetoelastic anisotropy as in Pd/Co MLs since the magnetostriction of PtCo alloy is only about 2.6$\times$10^{-5} [7] which is much smaller than PdCo. The effective anisotropy shown in Fig. 3 is very weekly dependent on the bilayer thickness, and the surface anisotropy estimated from Fig.4 is much smaller than that of Pt/PdCo MLs. These results show the absence of the anisotropy source which exists in Pt/PdCo and Pd/PdCo MLs, and suggest the magnetoelastic origin of Ks in NM/PdCo MLs.

From the results described above, we can deduce that some or most part of K$_s$ in Pd/Co multilayers also originates from the magnetoelastic energy. In Pd/Co MLs, K$_{eff}$ shows maximum at very small t$_{co}$ of 3 $\AA$, where Co layers sandwiched between Pd layers are equivalent to PdCo alloys in the sence of short range order and actually the MLs show the magnetostriction comparable

to that of PdCo alloys[7]. Thus the situation in Pd/Co MLs is considered to be similar to Pd/PdCo MLs. Furthermore, recent transmission X-ray diffractometry revealed that the lattice constants of Pd and Co in the film plane change gradually approaching to the value of alloys with decreasing bilayer thickness.[8] Therefore, a large part of K_s may originate from the magnetoelastic anisotropy although the magnetocrystalline surface anisotropy cannot be excluded from the origin in actual Pd/Co MLs as well as in ideal superlattices, .

For further discussion, however, we need more precise knowledge not only of the strain but also of the magnetostriction for the atomic layers just at the interface. Since the measurement of such parameters must be very difficult, theoretical estimation of the magnetoelastic energy will help the understanding of Pd/Co interface. Recent band calculation which obtained the magnetic anisotropy of Pt/Co interface [9] might become useful to understand the origin of the perpendicular aniosotropy if the anisotropy could be obtained as a function of lattice distortion in Pd/Co MLs.

(100) Pd/Co multilayers

X-ray diffraction pattern of Pd/Co ML prepared on (100) MgO is shown in Figure 5. It is seen that the ML has (100) preferred orientation. The interface of (100) MLs seems sharper than (111) MLs deposited on glass substrates since higher order diffraction peaks were observed in both low and high angle patterns.
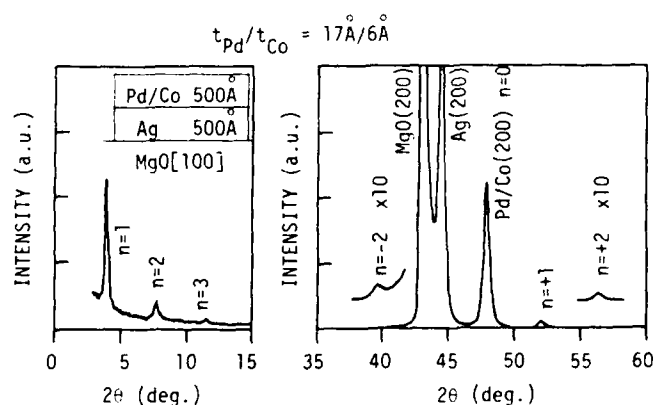
Fig. 5 X-ray diffractogram of Pd/Co multilayers prepared on (100) MgO substrates.

Figure 6 shows λ K_{eff} as a function of Co layer thickness t_{Co}. For (100) Pd/Co, it is difficult to estimate the surface anisotropy from the extrapolation of a straight line. Dotted line is drawn using data points for large t_{Co}. As seen from the figure, λ K_{eff} is enhanced deviating from the straight line when Co layers are thinner than 10 Å, and it becomes positive for the Co thickness of one or two monolayers. This behavior was already reported for (100) Pd/Co MLs grown by MBE on GaAs substrates.[10] Here, we point out that this is explainable in terms of the anisotropic magneto-striction constants of PdCo alloys.

As shown in Fig 7(a), λ_{111} of PdCo alloys is negative in a wide range of the alloy composition, while λ_{100} is negative only in the range of high Pd concentration.[6] If we may assume that very thin Co layers sandwiched between Pd layers have magnetostriction constants similar to Pd rich alloys, namely both negative λ_{111} and λ_{100}, while a little thicker Co layers have negative λ_{111} but positive λ_{100}, then we can expect positive magnetoelastic anisotropy in both (111) and (100) MLs when Co layers are very thin, while negative anisotropy in (100) MLs when rather thick.
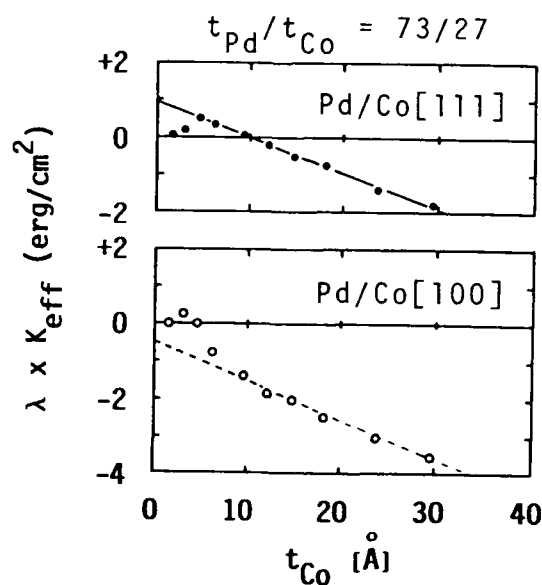
Fig. 6   Effective anisotropy K_{eff} multiplied by bilayer periods λ for Pd/Co multilayers prepared on glass and (100)MgO substrates as a function of Co layer thickness t_{Co}.

448

(a)Pd/Co alloys   (b)PdNi alloys
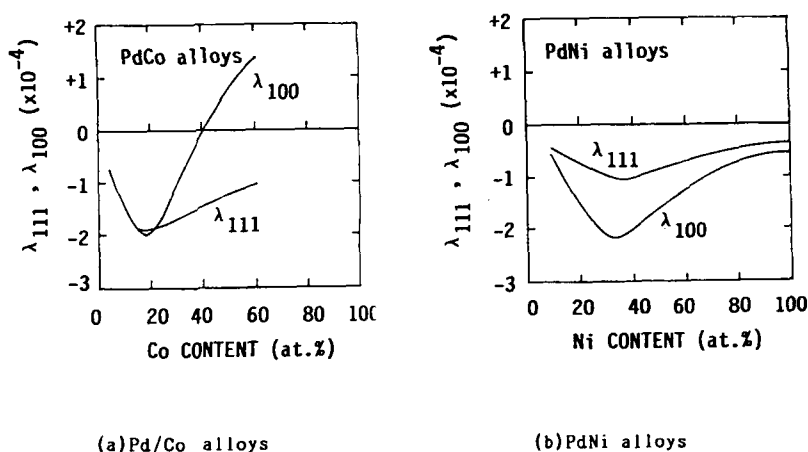
Fig. 7 Magnetostriction constants of (a)Pd/Co and (b)PdNi alloys at 0 K.
[6]

For the relation between the crystal orientation and the anisotropy, an
alternative explanation might be possible: The values of the surface ani-
sotropy might be the same in both orientations but the volume anisotropy,
namely, the magnetocrystalline anisotropy of Co layers, varies with the
crystal orientation. This explanation, however, has a difficulty since we
must assume an extremely large crystalline anisotropy of about 1.5×10^7
erg/cc to account for the large difference in K_u between (111) and (100) MLs
at $t_{co}= 10$ Å.(See Fig. 6)

Pd/CoZr, PdSi/Co and PdSi/CoZr multilayers

As described above, both (111) and (100) Pd/Co MLs show perpendicular
magnetization when Co layers are very thin. Then we examined the influence
of the crystallinity on the anisotropy by introducing amorphous Pd and/or
Co. For amorphous Pd and Co, $Pd_{82}Si_{18}$ and $Co_{90}Zr_{10}$ alloy layers were
utilized, respectively. The thickness of Co or CoZr layers were chosen at
about 2 Å so as to obtain positive Ku regardless of the crystal orientation
or possibly even in amorphous.

Figure 8 shows the X-ray diffractogram and the Kerr hystereris loops of Pd/Co, Pd/CoZr, PdSi/Co and PdSi/CoZr MLs. As seen from the figure, (111) diffraction peaks are observed in Pd/CoZr while not in PdSi/Co and PdSi/CoZr. Perpendicular anisotropy similar to Pd/Co was obtained only in the Pd/CoZr ML. This means that ordered Pd is necessary for the appearance of the anisotropy. From the magnetoelastic point of view, ordered Pd will give rise to a misfit strain in PdCo alloy formed at the interface and result in the magnetoelastic surface anisotropy. On the other hand, disordered interfaces will not give any misfit strain and hence any anisotropy.

Pd layer / Co layer = (8Å / 2Å)X 100
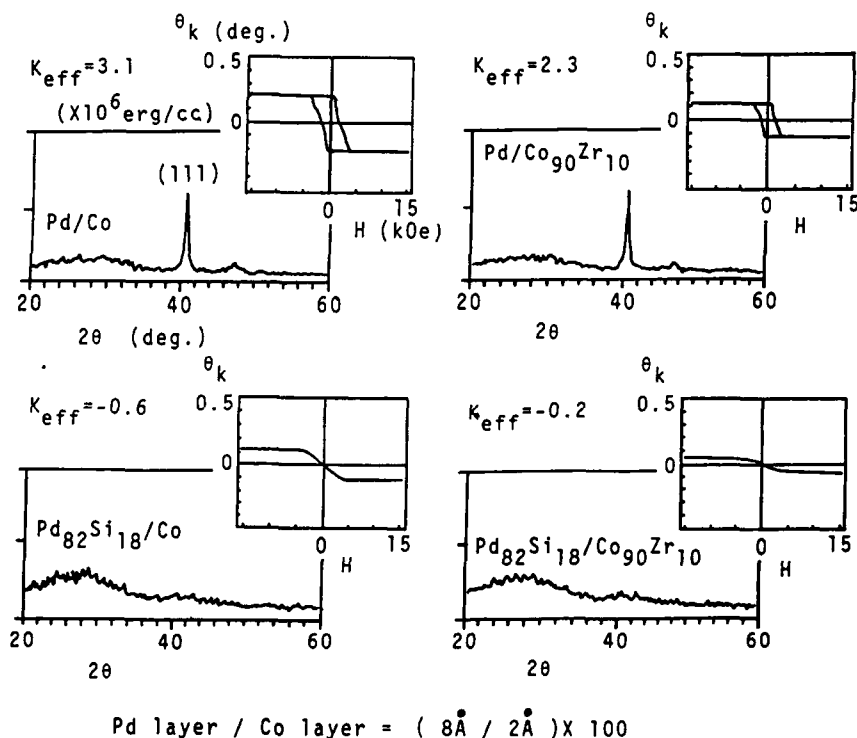
Fig. 8   X-ray diffractogram and Kerr hysteresis loops of Pd/Co, Pd/CoZr, PdSi/Co and PdSi/CoZr multilayers.

Pd/Ni multilayers

As shown in Fig.7(b), PdNi alloys exhibit large and negative magneto-striction constants comparable to those of PdNi alloys.[6] In order to examine the mechanism of the anisotropy suggested for Pd/Co MLs, multilayers were also prepared for Pd/Ni system.

Pd/Ni MLs prepared on MgO(100) and glass substrates showed X-ray diffractogram similar to Pd/Co MLs on respective substrates. Fig. 9 shows a X-ray diffractogram of Pd/Ni ML prepared on (100) MgO. From the figure, (100) preferred orientation can be observed.

Figure 10 shows magnetization curves of (111) and (100) Pd/Ni MLs. (111) Pd/Ni MLs exhibit very weak effective anisotropy around 1×10^5 erg/cc or less.[11] On the other hand, (100) Pd/Ni MLs show stronger anisotropy up to 5×10^5 erg/cc. This difference in the perpendicular anisotropy might be also related to the anisotropic magnetostriction constans of PdNi alloys; since λ_{100} is about two times larger than λ_{111} as shown in Fig. 8, we can expect larger anisotropy in (100) MLs.

At present we have not succeeded to make (100) MLs for wide range of Ni layer thickness, but it was confirmed that (100) MLs with Ni layer thinner than 8 Å exhibit perpendicular magnetization ($K_{eff} > 0$).

The surface anisotropy estimated for (111) Pd/Ni MLs at room temperature is only about one tenth of (111) Pd/Co MLs although λ_{111} of PdNi is as large as one half of PdCo. This seems to be due to the following two reasons. One is the low Curie temperature of PdNi system which results in lower anisotropy at room temperature. The other is smaller strain in Pd/Ni MLs than in Pd/Co MLs. This difference has been recently confirmed from the RHEED experiments for Ni and Co overlayers grown by MBE on (111) Pd.[12]
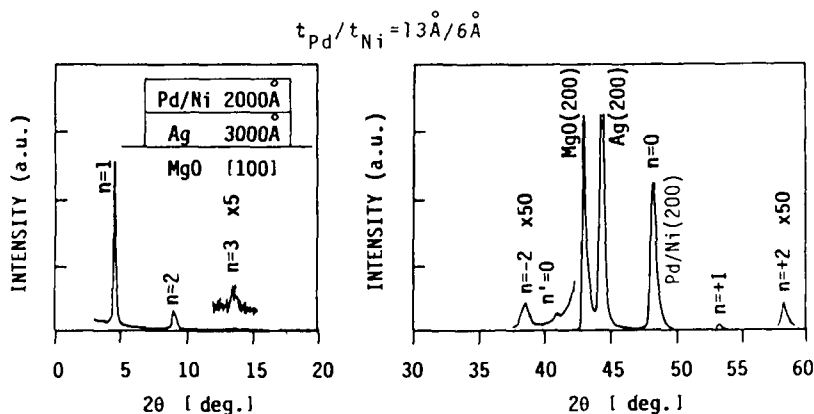
Fig. 9 X-ray diffractogram of Pd/Ni multilayers prepared on MgO(100).

Pd/Ni [111]   Pd/Ni [100]
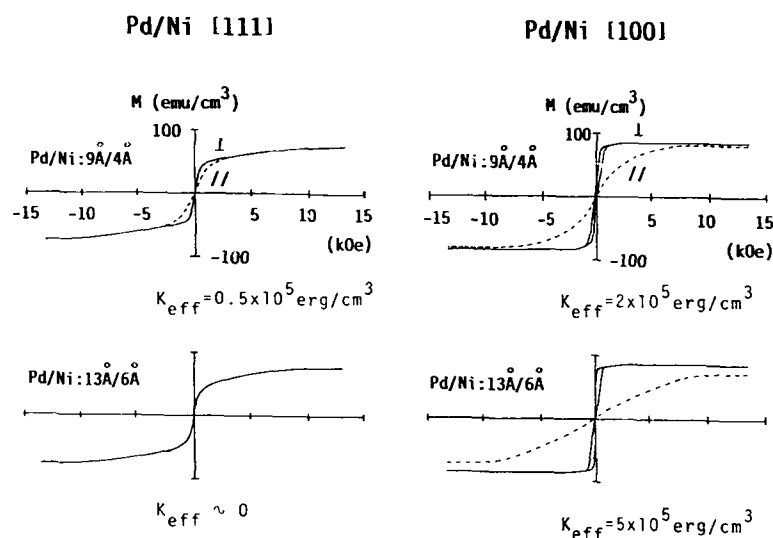
Fig. 10 Magnetization curves of Pd/Ni multilayers prepared on glass and
(100) MgO substrates. Solid and dotted curves with a field
perpendicular and parallel to the film plane, respectively.

CONCLUSION

In NM/PdCo multilayer (NM = Pt,Pd,Cu,Au), perpendicular anisotropy is
induced depending on the lattice constant of NM. The surface anisotropy K_s
is estimated to be positive in Pd/PdCo, Pt/PdCo and Au/PdCo where the
lattice constants of the NMs are larger than PdCo, while it is negative in
Cu/PdCo where Cu has a smaller lattice constant. The origin of K_s is
inferred to be the magnetoelastic energy due to the lattice misfit between
PdCo and NM layers. In Pt/PtCo multilayers, K_s is much smaller than those in
Pt/PdCo and Pd/PdCo MLs, which shows the lack of magnetoelastic surface
anisotropy in PtCo based MLs.

In (100) Pd/Co MLs, perpendicular anisotropy is induced only when Co
layers are very thin. This peculiar behavior can be attributed or at least
is related to the compositional dependence of magnetostriction constant λ_{100}
of PdCo alloys.

Perpendicular anisotropy comparable to that of Pd/Co MLs was obtained
in Pd/CoZr ML but not in amorphous PdSi/Co ML, which suggests that ordered
Pd is necessary for the appearance of the anisotropy.

In Pd/Ni MLs, perpendicular anisotropy is stronger in (100) orientation
than in (111). This could be also attributed to the anisotropic magneto-
striction constants of PdNi alloys.

452

REFERENCES

1. P. F. Carcia, A. D. Meinhald and A. Suna, Appl. Phys. Lett. 47, 178 (1985)
2. P. F. Carcia, J. Appl. Phys. 63, 5066 (1988)
3. F. J. A. den Broeder, D. Kuiper, A. P. van de Mosselaer and W. Hoving, Phys. Rev. Lett. 60, 2769 (1988)
4. P. Bruno and J. Seiden, J. de Phys. c8, 1645 (1988)
5. S. Tsunashima, K. Nagase, K. Nakamura and S. Uchiyama, IEEE Trans magn. 25, 3761 (1989); S. Tsunashima, K. Nakamura and S. Uchiyama: IEEE Trans magn. 26, 2724 (1990)
6. T. Tokunaga, M. Kohri, H. Kadomatsu and H. Fujiwara, J. Phys. Soc. Jpn. 50, 1411 (1988)
7. S. Hashimoto, Y. Ochiai and K. Aso, J. Appl. Phys. 66, 4909 (1989)
8. H. Takahashi, S. Fukatsu, T. Asanuma, S. Tsunashima and S. Uchiyama, (unpublished)
9. Ruqian Wu, Chun Li, A.J. Freeman, presented at American Phys. Soc. March Meeting, Cincinnati, OH, 1991
10. F. J. A. den Broeder, D. Kuiper and W. Hoving, in Growth, Characterization and Properties of Ultrathin Magnetic Films and Multilayers, edited by B. T. Jonker, J. P. Heremans and E. L. Marinero (Mater. Res. Soc. Proc. 151,(Pittsburgh, PA, 1989) pp.105-109.
11. H. Takahashi, S. Tsunashima, S. Fukatsu and S. Uchiyama, presented at E-MRS Spring Meeting, Strasbourg, France, 1990 (to be published in J. Magn. Magn. Mater.)
12. T. Yamasaki, M. Taninaka, K. Nakagawa, A. Itoh, Y. Suzuki and K. Katayama,(private communication)

THE ROLE OF NEXT-NEAREST NEIGHBORS IN THE NEÉL MODEL OF SURFACE ANISOTROPY FOR BCC CRYSTALS

Robert L. White and Bruce M. Clemens
Stanford University, Department of Materials Science and Engineering, Stanford, CA 94305

ABSTRACT

We have extended the Neél model of surface anisotropy in b.c.c. crystals to include next nearest neighbor interaction. Fitting the experimental data for Fe (001) and (110) surfaces leads to some pradoxes which cast doubt on the Neél surface anisotropy as the dominant source of surface anisotropy in thin films.

(A) Introduction

Measurements of the magnetic anisotropy for magnetic thin films and for multilayer arrays of thin films yield values significantly different from those of bulk crystals of similar composition. Furthermore, such measurements show a dependence on film thickness (in general with a component linearly inverse in the film thickness) which allows the experimental separation of the anisotropy into a volume component and a surface or interface component. The surface anisotropy can be very strong, strong enough that for many films (especially in the cobalt family) the normal component of the anisotropy is strong enough to overcome the demagnetization effects and to result in a film magnitization perpendicular to the film.

The surface magnetic anisotropy may have several sources. Stresses relieved in the first few atomic layers will, with magnetostriction, produce a surface-like anisotropy. The stress associated with crystallographically oriented dislocation caused by lattice mismatch at the interface may also cause surface magnetic anisotropy. Perhaps the most obvious cause of surface magnetic anisotropy, however, is the breaking of symmetry which occurs at an interface. An iron atom, for instance, in a bulk crystal of iron, has an environment of cubic symmetry not permitting an axial component of magnetic anisotropy. At an interface, by contrast, there is clearly a breaking of symmetry normal to the interface and, if the interfacial plane is one of low symmetry, also a breaking of symmetry in the interfacial plane. Many years ago L Neél proposed a simple pseudodipolar pair model for computing interfacial anisotropy [1]. That model has produced surprisingly good quantitative results when applied to magnetic surface anisotropy [2] and even when applied to the effect on anisotropy of interface morphology features such as atomic plane steps. Neél's original model, and applications since, have taken cognizance only of nearest magnetic neighbors when making the pseudodipolar energy calculations. We show in this paper that for bcc crystals, where the next nearest neighbor distance is only 13% larger than the nearest neighbor separation, the inclusion of next nearest neighbors into the Neél calculation produces significant differences from the nearest neighbor only calculations.

(B) Computational Procedures.

The crux of the Neél surface anisotropy model is the assumption that for every pair of magnetic atoms in a solid there is an energy of interaction with the magnetization of the sample which depends on the angle, ϕ, between the magnetization and the pair axis and is of the form

$$W = \ell\left(\cos^2\phi - \frac{1}{3}\right)$$

(1)

454

The origin of this energy, as Van Vleck has pointed out, is from the combined action of the effective exchange field and the spin-orbit interaction of the atoms involved. If, only one class of atomic pairs exists, and only one ℓ need be considered, both ℓ and $\partial \ell / \partial r$ can be computed from magnetostriction data. If two classes of neighbor pairs (for instance nearest neighbor and next nearest neighbor) are included and two values of ℓ (ℓ_1 and ℓ_2) required they cannot both be deduced from magnetostriction data without additional assumptions.

Given expression (1), the calculation of anisotropy energies is quite straight - forward. One defines for each magnetic neighbor a radius vector r_i expressed in a coordinate system fixed in the crystal lattice, for cubic crystals the obvious <100> frame. The direction of magnetization relative to the same coordinate frame is specified by the direction cosines β_1, β_2 and β_3. One can then compute W_i for each neighbor pair by forming the dot product of r_i with M_o, followed by a summation over the r_i characterizing the magnetic neighbors. For a magnetic atom in a site of cubic symmetry in the bulk of the crystal, the W_i sum to zero (or more accurately, to a constant) and no axial anisotropy results. For a surface atom, on the other hand, the summation over the W_i in general leads to an axial contribution to magnetic anisotropy.

(C) Surface Anisotropy, {100} plane, BCC crystal

We assume here that both the magnetic film and the film with which it interfaces are body-centered cubic crystals. Figure 1 shows the environment of an iron atom, S, on the (001) interface. Such an atom has eight nearest neighbors and six next nearest neighbors at
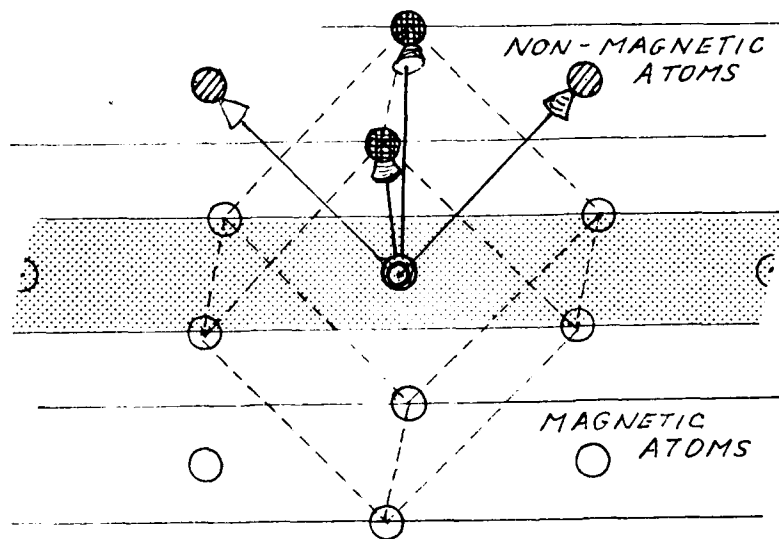
Fig.1 (011) interface plane for BCC crystal showing interface atom ⊚ , nearest neighbor non-magnetic atom ⊕ , and next nearest neighbor non -magnetic atom ⊘ .

distances of $\sqrt{3}/2\ \underline{a} = 0.866\ \underline{a}$ and $\underline{a}$ respectively, where $\underline{a}$ is the lattice constant. The iron film is assumed to be below the interface plane and the non-magnetic interlayer material above the plane. The central surface iron atom has four magnetic nearest neighbor atoms over which the Neél sum must be made (and is missing four equivalent neighbors). For the (001) surface shown

$$W_{tot} = \sum_{i=1}^{4} W_i = \frac{8}{3}\ell_1 \tag{2}$$

This energy is a constant independent of the orientation of the magnitization, so, in agreement with Neél's early calculation, nearest neighbors produce no surface anisotropy, neither in plane nor perpendicular to the plane, for this case.

If we move now to next nearest neighbors (with interaction parameter ℓ_2), one of the six neighbors is missing, and we can arrive at the total pseudodipolar energy either by summing over the five magnetic neighbors or taking the negative sum over the missing (one) nearest neighbor. In either case, we obtain

$$W_{tot} = \ell_2\left(\frac{1}{3} - \beta_3^2\right) \tag{3}$$

Since there are $2/a^2$ surface atoms per square centimeter of the (001) face of a bcc crystal, we have (dropping the constant term)

$$W_{anis} = -\frac{2}{a^2}\ell_2 \cos^2\theta \tag{4}$$

If we compare this expression with the standard expression for surface anisotropy

$$K_{anis} = K_s \cos^2\theta + K_{sp} \sin^2\theta \cos^2\phi \tag{5}$$

where K_s specifies the anisotropy perpendicular to the interface and K_{sp} specifies the in plane anisotropy, we conclude that second nearest neighbors produce surface anisotropy

$$K_s = -\frac{2}{a^2}\ell_2 \quad K_{sp} = 0 \tag{6}$$

That $K_{sp} = 0$ is not surprising; the fourfold symmetry of the (001) plane requires it.

We conclude that nearest neighbors do not produce surface anisotropy for the bcc (001) interface, but that next nearest neighbors do in fact yield a perpendicular component of anisotropy.

(D) Surface Anisotropy, (110) plane, BCC Crystal

The computational procedure in this case is exactly the same as in the preceding section. Figure 2 shows the configuration of nearest neighbors and next nearest neighbors of a surface atom, S, in a (011) plane. The S atom has two magnetic neighbors in a (011) plane replaced by non-magnetic atoms, and two next nearest neighbors in a (100) plane replaced by non-magnetic atoms.
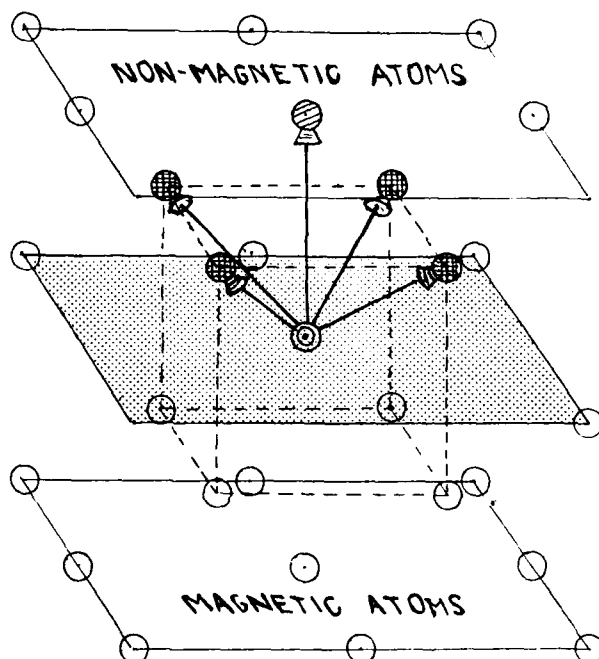
Fig.2 (001) interface plane for BCC crystal showing
interface atom ⊚ , nearest neighbor non-magnetic atom ⊕ ,
and next nearest neighbor non-magnetic atom ⊘ .

Doing first the sum of the energies W_i over the nearest neighbors we obtain

$$W_{tot} = -\frac{4}{3}\ell_2\beta_2\beta_3$$

$$(7)$$

where the angles β_2 and β_3 are expressed with reference to the cubic axis of the crystal.
Rotating this expression into a primed set of axes, which has the z' axis normal to the
interface (therefore in a crystal [011] direction), the, x axis unchanged, and the y' axis in a
crystal [011] direction, we have

$$W_{tot} = -\frac{2}{3}\ell_1\left(\beta_3^{'2}-\beta_2^{'2}\right)$$

$$(8)$$

Recognizing that there are $\sqrt{2}/a^2$ atoms per square centimeter in the (011) plane, and
converting our direction cosines into spherical coordinates, we obtain

$$W_{tot} = -\frac{2\sqrt{2}}{3a^2}\ell_1\left(2\cos^2\theta + \sin^2\theta\cos^2\phi - 1\right)$$

$$(9)$$

Giving us the surface anisotropy constants

$$K_s = -\frac{4\sqrt{2}}{3a^2}\ell_1 \qquad K_{sp} = -\frac{2\sqrt{2}}{3a^2}\ell_1 \tag{10}$$

These results are in full agreement with those of Elmers and Gradmann, who have made precisely the same calculation. We reproduce the calculation here only because we wish to consider these results in the context of considering both nearest and next-nearest neighbors.

Moving now to the next nearest neighbor calculation, we obtain

$$W_{tot} = -\ell_2\left(\beta_2^2 + \beta_3^2 - \frac{2}{3}\right) \tag{11}$$

Rotating to the primed coordinate frame, we obtain

$$W_{tot} = -\ell_2\left(\frac{1}{3} - \beta_1^{'2}\right) \tag{12}$$

or again introducing the number of surface atoms per square centimeter at the interface, and expressing the energy in spherical coordinator, we have

$$W_{tot} = -\frac{\sqrt{2}}{a^2}\ell_2\left(\frac{1}{3} - \sin^2\theta\cos^2\phi\right) \tag{13}$$

Giving anisotropy constants

$$K_s = 0 \qquad K_{sp} = \frac{\sqrt{2}}{a^2}\ell_2 \tag{14}$$

(E) Discussion and comparison with experiment.

When we attempt to fit the results of the above calculations to the experimental data we encounter several difficulties. We note that for the (001) face K_s depends only on nearest neighbors whereas for the (110) face, it depends only on next nearest neighbors. Experimentally K_s (001) $\approx$ -1 erg/cm^2 [2] and K_s(110) $\approx$ +1 erg/cm^2 [3]. We would deduce, then, that ℓ_1 is positive, ℓ_2 negative, and of nearly equal magnitude. This is surprising. One would intuitively expect that ℓ_1 and ℓ_2 would be of the same sign. Their origin, as remarked above, is in the joint action of the exchange field and the spin orbit coupling. For nearest and next nearest neighbors we have the same atoms, same sign of exchange field, and sign of spin -orbit coupling, same crystal field environment, and only 13% difference in spacing. We note further that including second nearest neighbor makes the in-plane environment of a surface atom in the (110) plane nearly fourfold, as compared to the strongly axial in-plane environment if only nearest neighbors are included. We would therefore expect inclusion of next nearest neighbor to reduce K_{sp}, which would in fact be the case if ℓ_1 and ℓ_2 were of the same sign. If ℓ_1 and ℓ_2 are of opposite sign, as obtained by fitting K_s for the (110) and (001) planes, symmetrizing the environment increases the uniaxiality of the anisotropy, which is surprising.

A related difficulty with the Neél model arises for nickel $K_s(111)$, where the sign of ℓ deduced from magnetostriction data is opposite from what is required to fit the surface anisotropy observed [4].

If it were possible to compute ℓ_1 and ℓ_2 from first principles these difficulties could be resolved. Unfortunately only heuristic models are available. The calculations of surface anisotropy and the deduction of the ℓ values from magnetostriction data all proceed from the assumption that a pair interaction of the form of Eq. 1 is the dominant source of anisotropy in the transition metals. If this assumption is not true, and other sources are important, single ion anisotropy, for instance, the logic of all the above calculations collapse.

Our present calculations suggest that the Neél pair model of anisotropy is not valid for the calculation of surface anisotropics. Given, however, the difficulty of measuring surface anisotropies and the number of effects potentially confounding the measurement (magnetostriction, ordered arrays of misfit dislocations, surface relaxation) it is premature to conclude with any confidence that the Neél model is in general not valid.

(F) Conclusions

We conclude that there are significant difficulties in explaining the surface magnetic anisotropy of cubic thin films on the Neél surface anisotropy model.

References

(1)   L. Neél, J. Phys. Radium $\underline{15}$, 225 (1954).

(2)   H.S. Elmers and U. Gradmann, Appl. Phys. $\underline{A51}$, 1582 (1990).

(3)   B. Heinrich, J. D. Cochran, A. S. Arrott, S. T. Purcell, K. B. Urquhart, J. R. Dutcher, and W. F. Egelhoff, Jr., Appl. Phys. $\underline{A49}$, 473 (1989).

(4)   E. Bergter, U. Gradmann and R. Bergholz, Solid State Comm. $\underline{53}$, 565 (1985).

MAGNETIC ANISOTROPY OF CRYSTALLINE DEFECTS

B.M. Clemens, R.L. White, W.D. Nix, and J.A. Bain, Department of Materials Science and Engineering, Stanford University, Stanford, CA 94305-2205

ABSTRACT

We consider the anisotropies due to coherency strains and the inhomogeneous strains associated with misfit dislocations, both of which give rise to anisotropy through the magnetostrictive coupling. Coherency strains can give rise to an apparent surface anisotropy due to the decrease in coherency strain with the film thickness. This anisotropy is comparable in magnitude to that observed experimentally for Fe [110] epitaxial thin films on W [110]. The strain field associated with misfit dislocations produces a surface anisotropy which is also comparable in magnitude to experimentally observed anisotropies. Dislocations along the *in-plane* [001] and [110] directions both produce the same preferred direction of magnetization orientation.

INTRODUCTION

The magnetic anisotropy of thin films and multilayered materials has been the subject of considerable recent interest[1,2,3,4]. Much of this stems from the importance of anisotropy for applications such as magnetooptic recording media and microwave devices. Several sources for the observed *out-of-plane* and *in-plane* anisotropy have been suggested, including electronic structure effects[1], shape, coherency strain[2], and the broken symmetry of nearest neighbor environments at surfaces and defects. The Néel ion pair model has frequently been used to calculate surface anisotropies, and has in some cases produced reasonable agreement with experimental results. However, recently we have calculated the Néel anisotropy for several surfaces and found qualitative disagreement with experiments, pointing out the general failability of the Néel model[5]. In this paper, we examine the magnetic anisotropy associated with thickness dependent strains. We present analysis of elastic coherency strains, and we introduce a new mechanism for magnetic anisotropy, the stress fields associated with misfit dislocations. Each can produce an anisotropy which can be interpreted as a surface or interface effect. For the example of epitaxial Fe thin films on W, we find both an *in-plane* and *out-of-plane* anisotropy which are of magnitude comparable with that observed experimentally by others[2].

THIN FILM ANISOTROPY

Magnetic anisotropy arises from the dependence of the magnetic energy, F_m, on the direction of magnetization. For epitaxial thin films, it is convenient to express this directional dependence in terms of the laboratory or film frame angles. For purposes of illustrating the phenomena discussed in this paper, we will be considering epitaxial [110] Fe films on W, and in Fig.1 we define the film frame angles θ and ϕ relative to the crystallographic directions. The angular dependence of the magnetic energy is then expressed as:

$$F_m = K^{\perp} \cos^2 \theta + K^{\parallel} \sin^2 \theta \cos^2 \phi \qquad (1)$$

where $K^{\perp}$ and $K^{\parallel}$ are the perpendicular and parallel anisotropy constants. If $K^{\perp} < 0$, the easy axis of magnetization will be perpendicular to the film plane, and if $K^{\perp} > 0$ and $K^{\parallel} < 0$ the easy axis of magnetization will be in the plane along the [001] direction.

The total anisotropy constants are a sum of surface and bulk contributions:

$$K = V k_b + S k_s$$
$$\frac{K}{V} = k_b + \frac{k_s}{t} \qquad (2)$$

where V is the sample volume, S is the surface area, t is the film thickness, k_b is the bulk anisotropy per unit volume, and k_s is the surface or interface anisotropy per unit area. The

460

Figure 1: Schematic showing crystallographic directions of a [110] oriented film and the angles θ and φ of the magnetization relative to the crystallographic directions.
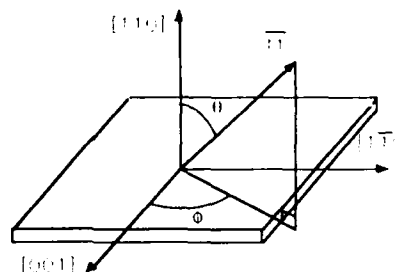
simplicity of this distinction between surface and bulk effects is deceptive. Homogeneous strains in thin films lead to bulk anisotropy, but, as discussed below, the $1/t$ dependence of the strains can lead to the misinterpretation of the resulting anisotropies as a surface effect. The local strains associated with misfit dislocations do give rise to an interface anisotropy, but the changes in misfit dislocation density with film thickness can obscure the anisotropy origin. The discussion of both these effects relies on a common magnetoelastic formalism.

STRAIN INDUCED ANISOTROPY

The magnetoelastic energy can be expressed as a function of the cubic reference frame elastic strains ϵ_{ij}^{cf} and the direction cosines, α_{ij}, of the magnetization relative to the cubic reference frame[6]:

$$f_{m-el} = B_1\left[\epsilon_{11}\left(\alpha_1 - \frac{1}{3}\right) + \epsilon_{22}\left(\alpha_2 - \frac{1}{3}\right) + \epsilon_{33}\left(\alpha_3 - \frac{1}{3}\right)\right] + B_2(\epsilon_{12}\alpha_1\alpha_2 + \epsilon_{23}\alpha_2\alpha_3 + \epsilon_{31}\alpha_3\alpha_1)$$

where B_1 and B_2 can be found in terms of the magnetoelastic constants λ_{100} and λ_{111}. For BCC we find:

$$B_1 = -\frac{3(c_{11} - c_{12})\rho_a\lambda_{100}}{2}$$

$$B_2 = -6c_{11}\rho_a\lambda_{111}$$

where c_{11}, c_{12}, and c_{11} are the components of the stiffness tensor (in the cubic reference frame), and ρ_a is the atomic density.

The elastic strain state associated with either epitaxy or misfit dislocations is most conveniently expressed in the reference frame of the principal strains, which, for the cases considered here, coincides with the film reference frame shown in Fig.1. In this case we can write:

$$\epsilon_{ij}^{ff} = \begin{pmatrix} \epsilon_1 & 0 & 0 \\ 0 & \epsilon_2 & 0 \\ 0 & 0 & \epsilon_3 \end{pmatrix}$$

where the subscripts 1, 2, and 3 refer to the directions [001], [110] and [1$\bar{1}$0] respectively.

The cubic reference frame strains for Eqn. 3 can be found by matrix rotation of the film reference frame strains. Writing the direction cosines α_i's in terms of the film frame angles θ and φ allows identification of the anisotropy constants of Eqn. 1:

$$k_s^\perp = \frac{3}{2}c_{11}\lambda_{111}(\epsilon_2 - \epsilon_3)$$

$$k_s^\parallel = \frac{3}{4}\{\lambda_{100}[(c_{11} - c_{12})(2\epsilon_1 - \epsilon_2 - \epsilon_3)] - \lambda_{111}[c_{11}(\epsilon_2 - \epsilon_3)]\}$$

These are bulk anisotropy constants in that they must be multiplied by the film volume to obtain the total magnetoelastic energy.

EPITAXIAL STRAINS

For a film with bulk lattice parameter a_0^f on a substrate with bulk lattice parameter a_0^s, the total *in-plane* mismatch strain, $\epsilon_m^{\parallel}$, will be accommodated by a combination of *in-plane* elastic strain $\epsilon_e^{\parallel}$ and plastic deformation $\epsilon_p^{\parallel}$ which occurs through the generation of misfit dislocations. We can write:

$$\epsilon_m^{\parallel} = \frac{a_0^f - a_0^s}{a_0^s}$$

$$= \epsilon_e^{\parallel} + \frac{b}{s} \tag{7}$$

where b is the dislocation Burger's vector and s is the dislocation spacing.

The balance between elastic strain and misfit dislocation density represented by Eqn. 7 changes as the film thickness increases. At small film thicknesses, $\epsilon_m^{\parallel}$ is accommodated entirely by elastic strain, and above a critical thickness, there will be misfit dislocation formation, and the elastic strain and misfit dislocation spacing will decrease with $1/t[7]$. This change in stress state of the film can contribute to changes in the bulk anisotropy which can be misinterpreted as a surface anisotropy effect. Considering the energy associated with dislocation motion, Nix has found[7]:

$$\epsilon_e^{\parallel} = \frac{1.9b}{4\pi M(1-\nu)}\frac{2\mu_f\mu_s}{(\mu_f+\mu_s)}\left(\frac{1}{t}\right)\ln\left(\frac{\beta t}{b}\right) \tag{8}$$

where μ_f and μ_s are the shear moduli for the film and substrate, ν is Poisson's ratio, β is a dislocation core energy parameter ($\beta \sim 0.75$), and M is the biaxial modulus. Figure 2 shows the prediction of Eqn. 8 for a Fe film. Note the nearly linear dependence on $1/t$.

The magnetic anisotropy constants due to epitaxial strains can be obtained from Eqn. 1 by setting $\epsilon_1 = \epsilon_2 = \epsilon_e^{\parallel}$ and $\epsilon_3 = \epsilon_e^{\perp}$, where $\epsilon_e^{\parallel}$ is the *in-plane* strain component, imposed by the substrate, and $\epsilon_e^{\perp}$ is the *out-of-plane* component which results from the Poisson effect. For BCC (110) oriented films the two components are related through:

$$\epsilon_e^{\perp} = -\frac{c_{11} + 3c_{12} - 2c_{44}}{c_{11} + c_{12} + 2c_{44}}\epsilon_e^{\parallel} \tag{9}$$

Eqns. 6 then give:

$$k_e^{\perp} = \frac{3}{2}c_{44}\lambda_{111}\left(\epsilon_e^{\parallel} - \epsilon_e^{\perp}\right)$$

$$k_e^{\parallel} = -\frac{3}{4}\left[(c_{11} - c_{12})\lambda_{100} - c_{44}\lambda_{111}\right]\left(\epsilon_e^{\parallel} - \epsilon_e^{\perp}\right) \tag{10}$$

Note that this differs from the results of Ref. [2]. If we plug in numbers[6], we find:

$$\frac{k_e^{\perp}}{\epsilon_e^{\parallel}} = -5.6 \times 10^6 \text{J/m}^3$$

$$\frac{k_e^{\parallel}}{\epsilon_e^{\parallel}} = -6.2 \times 10^6 \text{J/m}^3 \tag{11}$$

These bulk anisotropy constants are comprable in magnitude (but opposite in sign) to those observed for Fe on W by Elmers and Gradman[2]. More importantly if we consider the thickness dependence of the strain shown in Fig. 2, we find a thickness dependent anisotropy constants (shown in Fig. 3). If one were to naively take the slope of the anisotropy in Fig. 3 and assign it to a surface anisotropy one would find:

$$k_s^{\perp} = -5.6 \times 10^{-4} \text{J/m}^2$$

$$k_s^{\parallel} = -6.2 \times 10^{-4} \text{J/m}^2 \tag{12}$$

These apparent surface anisotropies are comparable to those observed experimentally[2].

462
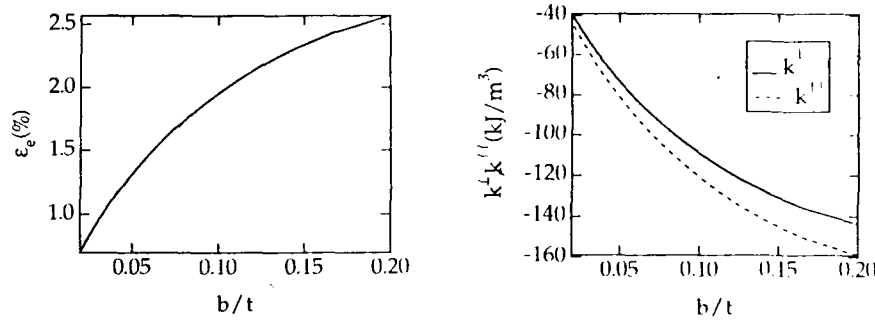
Figure 2: Elastic coherency strain vs b/t for a Fe film.

Figure 3: Bulk anisotropy constants arising from thickness dependent coherency stresses.

MISFIT DISLOCATION ANISOTROPY

To calculate the anisotropy associated with misfit dislocation strains, we utilized the Peierls-Nabarro dislocation model[8] adapted to describe an array of misfit dislocations in an isotropic medium. The situation is shown schematically in Fig 1. We impose the constraint that the traction forces must go to zero on the surfaces of cylinders of radius of $s/2$ where s is the dislocation spacing. The resulting stresses are:

$$\sigma_{xx} = -A\left\{\frac{3y + 2\xi}{x^2 + (y+\xi)^2} - \frac{2y(y+\xi)^2}{[x^2 + (y+\xi)^2]^2}\right\} + \frac{12Ay}{s^2}$$

$$\sigma_{yy} = -A\left\{\frac{y}{x^2 + (y+\xi)^2} - \frac{2x^2y}{[x^2 + (y+\xi)^2]^2}\right\} + \frac{4Ay}{s^2}$$

$$\sigma_{xy} = -A\left\{\frac{x}{x^2 + (y+\xi)^2} - \frac{2xy(y+\xi)}{[x^2 + (y+\xi)^2]^2}\right\} + \frac{4Ax}{s^2} \tag{13}$$

$$\sigma_{zz} = -2A\nu\frac{y+\xi}{x^2 + (y+\xi)^2} + \frac{16A\nu y}{s^2} \tag{14}$$

ξ is the dislocation width, $(\xi \sim b)$ and ν is the Poisson's ratio. Here A is a material dependent parameter given by:

$$A = \frac{b}{2\pi(1 - \nu)}\frac{2\mu_f\mu_s}{\mu_f + \mu_s} \tag{15}$$

where μ_f and μ_s are the film and substrate shear moduli.

To calculate the total anisotropy due to these stresses, we can take advantage of linear elasticity and the linear dependence on strain of the anisotropy constants (Eqn. 6). We find the average stress in the film by integrating the stresses over the cylinders shown in Fig 1 and dividing by the film cross section area $s \cdot t$. In performing this average, we assumed that the film thickness, t was greater than the cylinder radius $s/2$, thus our results will break down for thin films with large dislocation spacings. We use isotropic elasticity analysis to find the average film frame strains, which can then be inserted into Eqn. 6 to find the total anisotropy per unit volume. In doing this we note that for a dislocation in a bulk material, the spatial average of the strains would be zero. However, for a misfit dislocation at the interface between the magnetic film and non magnetic substrate only the strain in the film will contribute to the anisotropy. The spatial average over the top half of the strain field

of a dislocation is *not* necessarily zero, so that there can be anisotropy associated with the elastic strains around misfit dislocations.
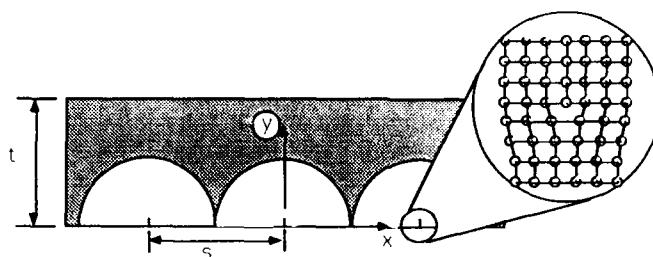
Figure 4: Schematic showing dislocation array with spacing *s*

We considered dislocations pointing along the [001] and [1$\bar{1}$0] *in-plane* crystallographic directions. Fig. 5 shows the resulting average principal strains (multiplied by the film thickness *t*) as a function of dislocation spacing, *b/s*. Since the stresses are localized to the interface, the average stress in the film falls off as $1/t$. The *out-of-plane* strains are tensile and the *in-plane* stresses perpendicular to the dislocation lines are compressive.

Fig. 6 shows the anisotropy constants $k_s^{\perp}$ and $k_s^{\parallel}$ which result from the strains in Fig. 5. The first thing to notice is that the magnitudes of these anisotropies are of the same magnitude as surface anisotropies observed in Fe thin films on W[2]. Both $k_s^{\perp}$ and $k_s^{\parallel}$ are positive, indicating that the preferred direction for the magnetization is along the *in-plane* [110] direction. It is interesting to note that the dislocation arrays pointing along the [001] and the [110] both produce this same anisotropy direction, indicating that the anisotropy in the magentostriction constants dominates in this case. A further point of interest is that the anisotropy decreases as the dislocation spacing decreases. This reflects the smaller spatial extent of the strain fields of more closely spaced dislocations.
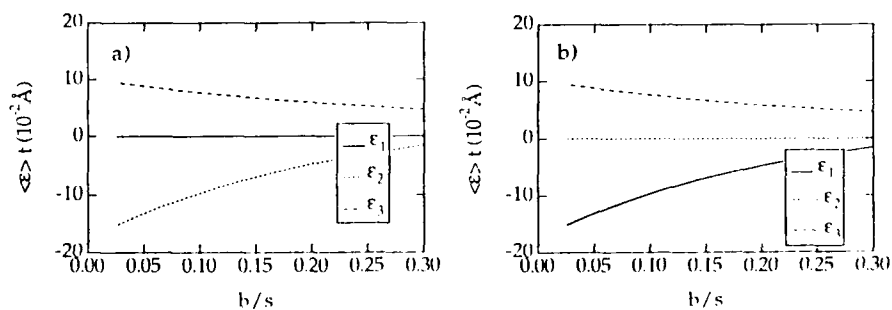
Figure 5: Averaged strains which result from misfit dislocation arrays in the a) [001] and b) [110] directions plotted as a function of the misfit dislocation density *b/s*.

464
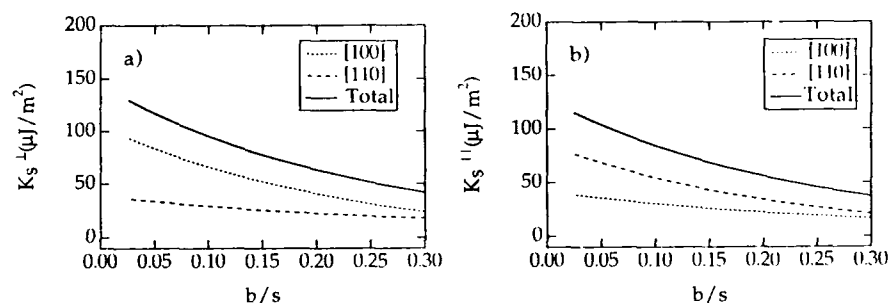
Figure 6: Anisotropy constants, $K^\perp$ a), and $K^\parallel$ b), which result from the misfit dislocation strains in Fig. 5.

We observe that thickness dependent epitaxial strains can result in an apparent surface anisotropy which is comparable in magnitude to those observed. We also find that the elastic strains associated with misfit dislocations can give rise to a surface anisotropy. Dislocations along the [001] and [110] directions in Fe [110] thin films contribute the anisotropy with the same preferred orientation of the magnetization. This is due to the dominance of the anisotropy of the magnetoelastic effect.

References

[1] J.G. Gay and R. Richter. *Phys. Rev. Lett.*, **56**, 2728, (1986).

[2] H.J. Elmers and U. Gradmann. *Appl. Phys.*, **A51**, 1 9, (1990).

[3] B. Heinrich, K.B. Urquhart, J.R. Dutcher, S.T. Purcell, J.F. Cochran, A.S. Arrott, D.A. Steigerwald, and W.F. Egelhoff. *J. of Appl. Phys.*, **63**, 3863 8, (1988).

[4] N.C. Koon, B.T. Jonker, F.A. Volkening, J.J. Krebs, and G.A. Prinz. *Phys. Rev. Lett.*, **59**, 2463–6, (1987).

[5] R.L. White and B.M. Clemens. *Mat. Res. Soc. Proc. Spring Meeting*, 1991.

[6] S. Chikazumi and S.H. Charap. *Physics of Magnetism*. Kreiger, Malabar, Florida, 1964.

[7] W.D. Nix. *Met. Trans. A*, **20A**, 2217–45, (1989).

[8] J.P. Hirth and J. Lothe. *Theory of Dislocations*. McGraw-Hill, New York, 1968.

MAGNETIC ANISOTROPY OF EPITAXIAL Co/Pt SUPERLATTICES

C.J. Chien, B.M. Clemens, S.B. Hagstrom
Department of Materials Science and Engineering, Stanford University, Stanford, CA 94305-2205
R.F.C. Farrow, C.H. Lee, E.E. Marinero, C.J. Lin
IBM Research Division, Almaden Research Center, 650 Harry Road, San Jose, CA 95120-6099

ABSTRACT

Selected orientations of epitaxial Co/Pt superlattices were grown on GaAs substrates in [001], [110], and [111] orientations using seeded epitaxy techniques. The microstructural and magnetic properties of Co/Pt superlattices are presented. The magnetic anisotropies of Co/Pt superlattices are found strongly dependent on the crystallographic orientation of the growth axis. High-resolution cross-sectional transmission electron microscopy (HRXTEM) investigation of the Co/Pt interfaces has revealed the presence of a large number of planar defects in the [111] Co/Pt superlattice. HRXTEM shows that the interface of Co/Pt is wavy and is not atomically abrupt. These findings suggest that models for the magnetic anisotropy should not be based on idealized, chemically abrupt interfaces but should incorporate magnetocrystalline anisotropy in the alloy region. We propose a model for the magnetic anisotropy based on the Néel magnetic surface anisotropy and the existence of defects in the alloy region. The easy axis of the magnetic anisotropy predicted by the model agrees with the magnetic and structural data for the superlattices.

1. INTRODUCTION

Recently, there has been an increasing interest in the magnetic anisotropy of ultrathin magnetic multilayers. Understanding of the contributing sources to magnetic anisotropy in magnetic thin films is essential to applications and to fundamental thin film magnetism. For magnetic thin films, aside from the magnetocrystalline anisotropy, the magneto-elastic anisotropy, and the shape anisotropy (which favors the spontaneous magnetization to lie in the film plane), the magnetic surface plays an important role in magnetic thin film anisotropy. Néel proposed the magnetic surface anisotropy resulting from the reduced symmetry in the environment for an atom at the surface[1]. In magnetic multilayer structures, comprising alternate magnetic and non-magnetic layers, interface anisotropy due to the broken symmetry is expected, too. The thermodynamic stability of the interface in multilayers then is of crucial importance in determining the magnetic interface anisotropy. Especially, in ultrathin magnetic multilayers, the magnetic interface anisotropy can be more dominant than the volume type anisotropy, since the ratio of surface to volume increases.

In magnetic multilayers, the effective magnetic anisotropy K_{eff} per unit volume of the magnetic layers with thickness t is defined to be the difference in energy required to saturate the multilayers by applying the magnetic field perpendicular and parallel to the film plane. Experimentally, the effective magnetic anisotropy can be described by a phenomenological formula, including a volume and an interface type anisotropy:

$$K_{eff} = K_v + 2K_s/t \qquad (1)$$

The contributing sources to the volume type anisotropy, K_v, are at least threefold: (1) Shape anisotropy, which tends to force the spontaneous magnetization to lie in the film plane, due to the demagnetizing field, (2) magnetocrystalline anisotropy, and (3) magnetostriction due to induced stress. The most interesting and important anisotropy in magnetic multilayers is magnetic surface (or interface) anisotropy, K_s, but its origin is still unclear.

2. EXPERIMENTAL TECHNIQUES

The Co/Pt superlattices were prepared in a VG 80-M MBE system(VG Semicon Ltd.). (001) orientation of GaAs substrates were used to seed the (001) and (110) Co/Pt superlattice orientations. For (111) Co/Pt superlattices, the GaAs substrate with surface normal inclined within 0.5° of [$\overline{1}\overline{1}\overline{1}$] direction was used. After etching in a 1:1:100 solution of

$H_2O_2/NH_4OH/H_2O$, the substrate was heated to ~600°C in a background pressure of $< 10^{-10}$ mbar to desorb surface impurities and to generate a 1×1 reflection high-energy electron diffraction (RHEED) pattern. The Ag seed layer was deposited at a rate of 0.4Å/sec from a knudsen cell held at 1050°C. The Co and Pt films were deposited at a rate of ~0.15 and ~0.25 Å/sec from e-gun sources, respectively. The deposition rate and beam-interrupt shutter were computer controlled. The fluctuation in the film thickness was less than 2%. The background pressure before film deposition was approximately ~2×10^{-11} mbar, while during the film growth was ~2×10^{-10} mbar or lower.

To prepare cross-sectional specimens for transmission electron microscopy observations a sample was first cut into 5×3 mm rectangles. Samples were sandwiched together and sliced to produce wafers ~1 mm thick. After grinding and polishing to a thickness of 200μm, 3mm diameter discs were cut and dimpled. The final thinning to obtain electron transparent regions was achieved by ion milling with 5-6 kev Ar ions using a liquid nitrogen cooled stage of a Gatan dual ion miller. High-resolution cross-sectional transmission electron microscopy (HRXTEM) investigations were performed in a Philips EM430-ST electron microscope operating at 300 kev.

The spontaneous magnetization direction were obtained from the torque curve. The perpendicular polar and the in-plane longitudinal Kerr hysteresis loops were used to confirm the easy directions, and also obtain the coercivity.

3. SELECTED SEEDED EPITAXY OF Co/Pt SUPERLATTICES

The key to successful growth of Co/Pt superlattices in three different orientations depends on the epitaxy of Ag buffer layers. Direct deposition of Ag on (001)GaAs results in an epitaxial Ag film with [110] direction along the film normal, i.e., [001] of GaAs substrate. In the film plane, the orientation relationships are [001] Ag parallel to [110] GaAs and [110] Ag parallel to [110] GaAs. The Co and Pt films were then grown epitaxially on this (110) Ag buffer layer to form the (110) Co/Pt superlattice. If several monolayers of Fe, Co or Pt were deposited before Ag buffer layers were grown, the epitaxial relationships were (001) Ag parallel to (001) Fe and GaAs, but with Ag unit cell rotated 45° about the [001] axis relative to the substrate normal. This seeded the Ag and the Co/Pt superlattice along the [001] orientation. The (001) Co/Pt superlattice was formed by depositing Pt films first on the (001) Ag buffer layer. For (111) Co/Pt superlattices, (111) GaAs substrates were used to seed the (111) Ag epitaxial film. (111) Co/Pt superlattices were grown epitaxially on Ag beginning with the Pt layer.

4. RESULTS

4.1 Microstructures

High-resolution cross-sectional transmission electron microscopy (HRXTEM) studies have been carried out on the (001), (110) and (111) Co/Pt superlattices to determine the microstructure of the samples. In (001), (110) and (111) orientations of Co/Pt superlattices, the 3.6Å Co, whose stable phase is hexagonal-closed-pack (hcp) structure at room temperature, forms a face-centered-cubic (fcc) solid solution with Pt. No evidence of hcp Co was found, and the Co/Pt layering can not be seen from the atomic image contrast. Figure 1 shows a high-resolution, cross-sectional transmission electron micrograph of a 2×(50Å Co/50Å Pt) structure showing the Co/Pt interface. Clearly, the interface is wavy and is not atomically abrupt. The dominant defects in the [111] oriented superlattices are stacking faults and twins on Co/Pt(111) planes. Figure 2 shows a HRXTEM of (111) Co/Pt superlattice. In this case the superlattice consisted of 30 periods of Co(3.2Å)/Pt(16.7Å). It shows a high density of planar defects, stacking faults and twins, in the Co/Pt superlattices. Both the Ag film and superlattice are free of stacking faults or twins for [110] and [001] oriented superlattices.

Figure 1 High-resolution, cross-sectional transmission electron micrograph of a 4×(50Å Co/50Å Pt) structure showing the Co/Pt interface. The interface is wavy and is not atomically abrupt.

Figure 2 High-resolution, cross-sectional transmission electron micrograph of (111) Co/Pt superlattice. In this case it was a 30 periods of Co(3.2Å)/Pt(16.7Å) superlattice. It shows a high density of planar defects, stacking faults and twins, in the Co/Pt superlattices.

468

4.2 Magnetic Properties

Figure 3 shows the perpendicular polar Kerr hysteresis loops for (001), (110), and (111) Co(3Å)/Pt(16.8Å) superlattices. Clearly the (111) Co/Pt superlattice has a large perpendicular magnetic anisotropy. The (001) Co/Pt has a hard axis along the film normal. Figure 4 shows the in-plane longitudinal Kerr hysteresis loop for the (110) Co/Pt superlattice. It shows that there is an easy axis in the film plane, and normal to it is a hard axis in the film plane. The in-plane easy axis of (110) Co/Pt superlattices has also been confirmed by the measurement of the torque curve, and is identified by cross-sectional transmission electron microscopy to be along [001] axis of Co/Pt superlattices.

5. PAIR ENERGY MODEL

Neel[1] described the magnetic surface anisotropy in a phenomenological pair model. He assumed the pair energy is dependent on the angle, θ, between the direction of magnetization and the bond. The pair energy between two magnetic atoms can be expressed by Legendre polynomials:

$$w(r, \cos\theta) = g(r) + l(r)(\cos^2\theta - 1/3) + q(r)(\cos^4\theta - 6/7\cos^2\theta + 3/35) + ... \qquad (2)$$

where r is the interatomic distance. For simplicity, we neglect the higher order terms and express the interaction energy as

$$w(r, \cos\theta) = l(r)(\cos^2\theta - 1/3) \qquad (3)$$

If $(M_x\ M_y\ M_z)$ are the direction cosines of the magnetization and $(Ax\ Ay\ Az)$ are those of bond direction, the pair energy becomes

$$w(r, \cos\theta) = l(r)[(M_xAx + M_yAy + M_zAz)^2 - 1/3] \qquad (4)$$
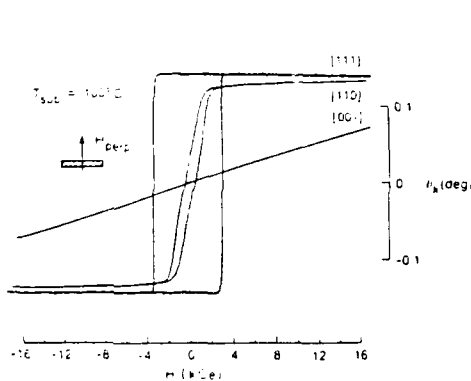
Figure 3. Perpendicular polar Kerr hysteresis loops for (001), (110), and (111) 15×(~3ÅCo /16.8ÅPt) superlattices. Magnetic field was applied normal to the sample surface.
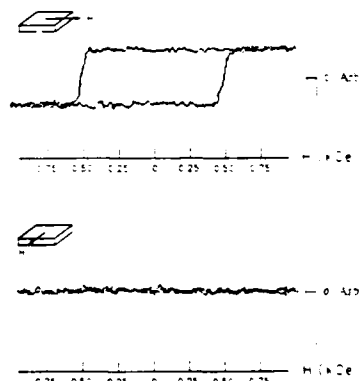
Figure 4. In-plane longitudinal Kerr hysteresis loop for the (110) Co/Pt superlattice.
(a). The magnetic field was applied along the easy axis in the film plane.
(b). The magnetic field was applied normal to the easy axis in the film plane.

6. THERMODYNAMIC STABILITY OF Co/Pt INTERFACES

According to the Co/Pt binary phase diagram, Co and Pt form a solid solution at room temperature, and two ordered phases, CoPt and CoPt3 exist at 1:1 and 1:3 atomic composition in a wide atomic concentration range. From the X-ray diffraction and XPD (x-ray photoelectron diffraction) studies[2], it suggests Co and Pt are mixing at interfaces. Cross-sectional high resolution electron microscopy also showed that Co/Pt interfaces were not atomically abrupt, and revealed a high density of stacking faults and twins parallel to film surface in (111) Co/Pt superlattices. Previous x-ray scattering measurements on quench disordered alloy containing high concentration of Pt revealed a preference for unlike nearest neighbors[3].

Based on the observations and studies above, we assumed that limited interdiffusion occurred at Co/Pt interfaces and local ordered phases, CoPt3, formed within the mixed region. This phase is favored by the Pt-rich composition of the superlattice and by the Pt-rich environment of arriving Co atoms.

7. CALCULATION

(001) Co/Pt Superlattices

Figure 5(a) shows the (001) surface of an ordered CoPt3 which has the CuAu3 structure. The surface energy per Co atom is due to the missing Co atom at the (001) Pt/CoPt3 interface. It shows that each Co atom on the interface has five nearest neighbor Co atoms: A1 = (100), A2 = (010), A3 = (100), A4 = (010), A5 = (001). If the magnetization direction cosines are $M = (M_x, M_y, M_z)$, and we sum over these five pair energy, using Neel pair energy model, it results

$$W = \sum w = L(1/3 - M_z^2) \qquad (5)$$

L is pair energy anisotropy constant and is negative for Co, i.e., the magnetic moment of Co atom favors to align along the bond direction. This can be confirmed by the magneto-elastic constant of bulk Co and Co alloy[4]. This shows that the [001], the film normal, is the hard axis.

(110) Co/Pt Superlattices

For a (110) surface of an ordered CoPt3, see Figure 5(b), the surface energy is then due to the broken symmetry at the (110) Pt/CoPt3 interface. It shows that each Co atom at the interface has four nearest neighbor Co atoms: A1 = (100), A2 = (010), A3 = (001), A4 = (001). The energy per Co atom is then

$$W = L(M_z^2 - 1/3) \qquad (6)$$

It shows that the [001] direction in the film plane is the spontaneous magnetization direction.
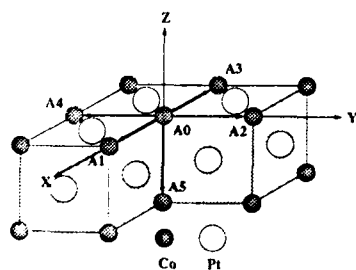
Figure 5(a). The (001) surface of ordered CoPt3.
It shows that each Co atom at the interface has
five nearest neighbor Co atoms.
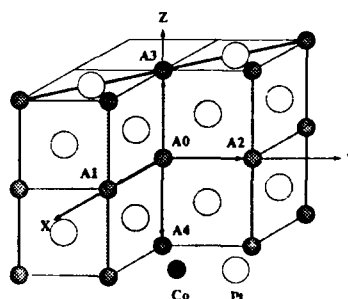
Figure 5(b). The (110) surface of ordered
CoPt3. It shows that each Co atom at the
interface has four nearest neighbor Co atoms.

(111) Co/Pt Superlattices

Figure 5(c) shows the (111) surface of an ordered $CoPt_3$. It shows that each Co atom at the surface has three first nearest neighbor Co atoms. These first nearest neighbors contribute no anisotropy, since the sum of the pair energy, W, is independent of magnetization directions. Now we consider the second nearest neighbors, see Figure 5(d). It shows that there are three second nearest neighbor Co atoms: A1 = ($\bar{1}$10), A2 = (0$\bar{1}$1), and A3 = ($\bar{1}$0$\bar{1}$). The energy per Co atom due to the second nearest neighbor Co atoms is then

$$W = L'(M_x+M_y+M_z)^2 \tag{7}$$

where L' is the pair energy constant due to the second nearest Co atoms. It predicts the easy axis is along [111], the surface normal.

In the case of (111) Co/Pt superlattices, a large number of stacking faults were found which can generate Co-Co pairs along <110> directions. These <110> Co-Co pairs can combine to form an easy axis along [111], the film normal, by a similar mechanism to that proposed by Chikazumi[5] in the case of partially ordered $FeNi_3$ alloy containing stacking faults. Figure 5(e) shows that <110> Co-Co pairs were generated by (111) plane stacking faults. Figure 5(f) shows that the sum of these <110> Co-Co pairs can form a net [111] easy axis. Again, applying the Neel pair energy model, we get

$$W = (1/2)PL[(M_x + M_y + M_z)^2 - 1] \tag{8}$$

where P is a density function of Co-Co pairs. It shows that the [111] direction, the film normal, is the easy axis.
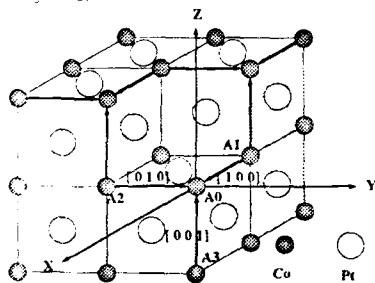
Figure 5(c). The (111) surface of ordered $CoPt_3$. It shows that each Co atom at the surface has three first nearest neighbor Co atoms.
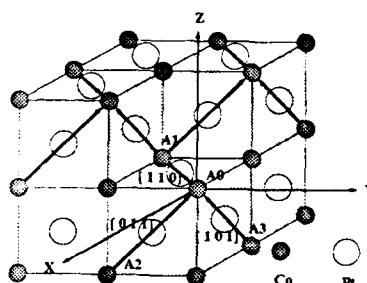
Figure 5(d). It shows that there are three second nearest neighbor Co atoms at the (111) $CoPt_3$ surface.
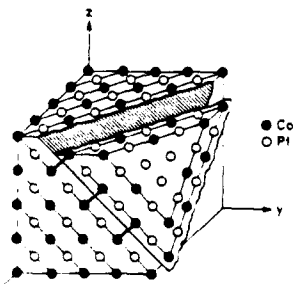
Figure 5(e). <110> Co-Co pairs are generated by (111) plane stacking faults.[5]
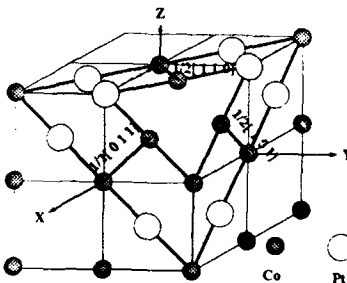
Figure 5(f). The sum of these <110> Co-Co pairs can form a net [111] easy axis.

8. CONCLUSIONS

The microstructural and magnetic properties of Co/Pt superlattices are presented. Superlattices with 3.2Å Co / 16.8Å Pt are grown by seeded molecular-beam epitaxy technique, oriented along the [001], [110], and [111] directions of Pt. We find that the magnetic property of the superlattice is strongly dependent on the growth orientation. For structures with [111] growth orientation the easy axis of magnetization is perpendicular to the film plane, but in the film plane for [001] growth orientation. The [110] oriented superlattices have intermediate behavior and show strong in-plan anisotropy. X-ray diffraction, x-ray photoelectron diffraction, and high-resolution cross-sectional transmission electron microscopy analysis of the superlattices show significant differences in interface quality and defect structure for different growth orientations. High-resolution cross-sectional electron microscopy reveals a high density of stacking faults and twins in the [111] oriented superlattices. It is suggested that a combination of limited interdiffusion, partial ordering of the alloy and stacking faults may contribute to the origin of the perpendicular anisotropy for the [111] oriented superlattices. Neel's phenomenological pair energy model combined with the thermodynamic stability at the Co/Pt interface provides a surprisingly good prediction for the magnetization easy axes of (001), (110) and (111) orientations of Co/Pt superlattices. Though this phenomenological model is tentative and needs more experimental support, it may provide a microscopic picture to the magnetic interface anisotropy.

REFERENCES

1. Neel, J. Phys. Rad 15, 225 (1954)

2. B.D. Hermsmeier, R.F.C. Farrow, C.H. Lee, E.E. Marinero, C.J. Lin, R.F. Marks, and C.J. Chien, in press: J. Magn. Magn. Mat., (1990)

3. P.S. Rudman and B.L. Averbach, Acta Met., 5, 65 (1957)

4. S. Chikazumi in "Physics of magnetism", Wily, New York, (1964), Chapter 8, page 174.

5. S. Chikazumi in "Physics of magnetism", Wily, New York, (1964), Chapter 17, page 359.

THE PERPENDICULAR MAGNETIC ANISOTROPY AND STRUCTURE OF SPUTTERED Ag/Co, Pd/Co, AND AgPd/Co MULTILAYERED FILMS

AKIRA YAMAGUCHI*, WE-HYO SOE*, RYOICHI YAMAMOTO*, and MASONOBU KOBAYASHI**
*Research Center for Advanced Science and Technology, University of Tokyo, 4-6-1, Komaba, Meguro-ku, Tokyo 153, Japan
**Research Laboratory, Oki Electric Industry Co., Ltd., 550-5 Higashiasakawa-cho, Hachioji, Tokyo 193, Japan

ABSTRACT

The structural and magnetic properties of sputtered Ag/Co, Pd/Co, and AgPd/Co multilayered films were investigated. When substrate temperature during deposition (Ts) was set at room temperature, the easy magnetization axis of the Pd/Co films with Co thickness less than 7Å was normal to the film plane and that of the Ag/Co films was parallel. AgPd/Co multilayered films showed a transition of the preferred direction of magnetic moment from lying in the film plane towards lying along the film normal when increasing the Pd concentration above 81 at%. Moreover, an anomalous reduction of the saturation magnetization was found. The perpendicular magnetic anisotropy of Pd/Co films with low Ts increased with decreasing the thickness of Co layer. However, the Pd/Co films with high Ts showed opposite tendency.

INTRODUCTION

The magnetic properties of metallic multilayered films are of great interest both from fundamental and technological view points. Especially, the perpendicular magnetic anisotropy of multilayered films have been attracting much attention in relation to magnetic and magneto-optical recording media[1-4]. As has been reported in several systems, Co/Pd[1,2], Co/Au[3], and Co/Pt[4], a large positive uniaxial magnetic anisotropy (Ku) can be observed when the magnetic layer thickness is smaller than a few monolayers. However, the origin of this anisotropy remains unclear. The physical mechanism has been generally believed to be a change in the magnetic anisotropy of the interface atoms as a consequence of the reduced symmetry in there surroundings which was predicted by Néel[5]. Nevertheless, recent studies[6,7] indicate that the origin of the perpendicular anisotropy can not be explained only by the Néel's surface anisotropy. Moreover, strain and mixing at magnetic-nonmagnetic interfaces have been suggested as possible mechanisms[8]. If the perpendicular anisotropy arises from the strain, one can expect that Ag/Co multilayers may also show the positive Ku, because the lattice constant of Ag is nearly equal to that of Au.

In this paper, we report the structural and magnetic properties, especially the perpendicular magnetic anisotropies, of Ag/Co, Pd/Co, and AgPd/Co multilayered films and discuss the origin of these anisotropies.

SAMPLE PREPERATION AND CARACTERIZATION

Ag/Co, Pd/Co, and AgPd/Co multilayers were prepared by a dual cathodes rf-magnetron sputtering system. Co, Ag, and Pd targets and Ag19%Pd81% and Ag44%Pd56% alloy targets were placed on two cathodes and shields were arranged around these targets so as to prevent mixing of sputtered fluxes. The substrates are fixed on a rotating table, which alternately moves them from one flux to the other. The sputtering was performed with high-purity Ar at 20×10^{-3} Torr, after pumping the chamber up to below 2×10^{-6} Torr. The glass substrates were used and the substrate temperature (Ts) during the deposition of Ag/Co and Pd/Co multilayered films, was controlled between room temperature (R.T.) and 200°C using two infrared image heaters.

The bilayer thickness of multilayered films can be determined from x-ray diffraction analysis and showed good agreement with the designed value. The Co layer thickness ranged between 2.5-34Å for Ag/Co, 2.4-9.6Å for Pd/Co and 3.1-15Å for AgPd/Co respectively.

Extensive x-ray characterization has been made using high- and low-angle x-ray diffraction techniques. The details of these studies will be the subject of a future publication. Briefly, Ag/Co and Pd/Co multilayers with Ts = R.T multilayers showed several satellite reflections in high-angle range and superlattice reflections in low-angle range. In the Pd/Co multilayers, the number of satellite and superlattice reflections decreased and the peak widths became narrower with an increase in the Ts. This shows that the grain size coarsening and the mixing at the Pd-Co interfaces were accelerated with high Ts. Ag/Co multilayers with Ts ≥ 70°C did not show any satellite and superlattice reflections, and AgPd/Co multilayers showed weak and broad peaks in high-angle range and the only 1st order superlattice reflection at low-angle range were observed. These results indicate that: (a) in Ag/Co multilayers, the higher Ts destroys the compositionally modulated structures (CMS), (b) Pd/Co multilayers have the CMS even if the Ts is 200°C, and (c) AgPd/Co multilayers have highly disordered lattice structures, but CMS still remain.

The magnetization measurements of multilayered films were made at room temperature with the VSM (vibrating sample magnetometer), applying the magnetic field up to 15kOe, both parallel and normal to the film plane.

MAGNETIC PROPERTIES

Ag/Co multilayers

The uniaxial anisotropy, Ku, is defined as the area between the perpendicular and the parallel magnetization curve per unit Co-volume. Ku is taken positive when the magnetization is preferably oriented perpendicular to the film. If we denote Ks as the anisotropy originating from the interface per unit area and Kv as the contribution to the anisotropy per volume unit Co, the uniaxial anisotropy can phenomenologically be described as

$$Ku = 2Ks / t_{Co} + Kv \qquad (1)$$

(a) Ts = R.T.   (b) Ts ≥ 70°C
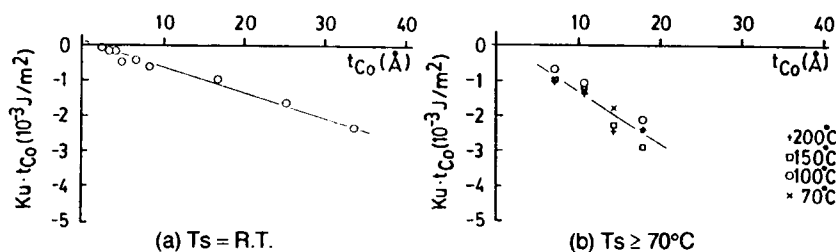
Fig.1 The t_{Co} dependence of $Ku \cdot t_{Co}$ of Ag/Co multilayers.

Here t_{Co} denotes the Co layer thickness and the factor 2 arises from the two interfaces of each Co layer. The volume anisotropy Kv consists of magnetostatic or demagnetization energy, and magnetocrystalline anisotropy.

In Fig.1 the uniaxial magnetic anisotropies of the Ag/Co multilayers with Ts = R.T. (a) and Ts ≥ 70°C (b) are shown as a function of the thickness of Co. In both cases the uniaxial magnetic anisotropies are well described by eq.(1) and can be considered to be independent of Ts in the range from 70°C to 200°C. These plots yield an interface contribution Ks = $(0.03\pm0.05) \times 10^{-3}$ J/m^2, a volume contribution Kv = $(-0.69\pm0.32) \times 10^6$ J/m^3 when Ts is R.T., and Ks = $(0.12\pm0.13) \times 10^{-3}$ J/m^2, $Kv = (-1.52\pm0.16) \times 10^6$ J/m^3 for Ts ≥ 70°C. For pure Co film with hexagonal axis perpendicular to the film, the demagnetization energy Kd would be Kd = $-1/2\mu_0 M^2$ = -1.23×10^6 J/m^3 and magnetocrystalline energy K1 = 0.41×10^6 J/m^3, K2 = 0.10×10^6 J/m^3. This results in a volume contribution Kd + K1 + K2 = -0.72×10^6 J/m^3, which is nearly equal to the Kv for Ts = R.T. Since Ks for both Ts = R.T. and Ts ≥ 70°C can be regarded as almost zero, we believe that the surface magnetic anisotropy energy is very small, if exists. Furthermore, the Kv for Ts ≥ 70°C showed considerably large value compared with other Co-based multilayered films whose easy magnetization axis is normal to the film plane, and the reason is uncertain. The most possible explanation is that the magnetoelastic effect presented due to the large thermal stress.

Pd/Co multilayers

The Co layer thickness dependence of the remanent magnetization ratio Mr/Ms for Ts = R.T., 50, 75, 100, 150, and
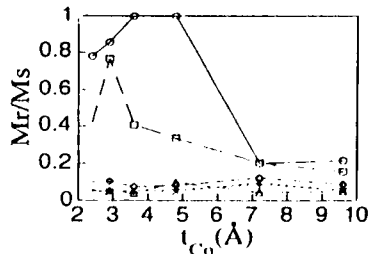
Fig.2 The remanent magnetization
ratio Mr/Ms of Pd/Co multilayers.
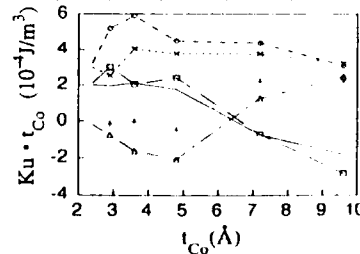
Fig.3 The t_{Co} dependence of $Ku \cdot t_{Co}$
of Pd/Co multilayers.

200°C with the magnetic field normal to the film plane are shown in Fig.2. It shows that in order to obtain the high remanent magnetization, lower Ts and $3Å \leq t_{Co} \leq 5Å$ are preferable and the higher Ts seems to make its performance worse. The behavior of the uniaxial magnetic anisotropy exhibited an entirely different picture (Fig.3). The $Ku \cdot t_{Co}$ for Ts = R.T. and 50°C, increased almost linearly with a decrease in t_{Co} and this dependence agrees with the previous results. Nevertheless, in the case of Ts = 75°C and 100°C, the values of the $Ku \cdot t_{Co}$ were larger than those for Ts = R.T. and 50°C, and were positive up to t_{Co} = 9.6Å. Moreover, the $Ku \cdot t_{Co}$ for Ts = 150 and 200°C increased with the t_{Co} and its sign changed from negative to positive.

The magnetic surface anisotropy predicted by Néel is considered to become smaller with the intermixing[9]. Since this mixing progressed at higher Ts, we can not explain the Ts dependence of Ku only by the Néel's anisotropy. In these complex behaviors of Ku, two or more mechanisms seem to operate.

In table I, the sign of Ku and the larger remanent magnetization axis are summarized. This table demonstrates that the lower Ts in the case of $t_{Co} \leq 4.8Å$ and the higher Ts in the case of $t_{Co} \geq 7.2Å$ yield positive Ku and especially, the former condition is desirable in order to turn the easy magnetization axis normal to the film plane.

AgPd/Co multilayers

Typical hysteresis loops of the $Ag_{19}Pd_8 13Å/Co3.1Å$, $Ag_{44}Pd_5 16Å/Co3.0Å$ and $Pd21Å/Co3.1Å$ films are shown in Fig.4. The preferred direction of magnetic moment changed from lying in the film plane towards lying along the film normal when increasing the Pd concentration above 81 at%. Moreover, saturation magnetization (Ms) decreased with an increase in the Ag concentration. Fig.5 shows the t_{Co} dependence of the saturation magnetization. An enhancement of Ms in Pd/Co multilayers with $t_{Co} \leq 10Å$ was observed and this enhancement is

	R.T.	50°C	75°C	100°C	150°C	200°C
Co2.4Å/Pd11.4Å	PM	PM	PM	P	P	N
Co2.9Å/Pd13.7Å	PM	PM	PM	P	N	N
Co3.6Å/Pd16.8Å	PM	P	P	P	N	N
Co4.8Å/Pd22.8Å	PM	P	P	P	N	N
Co7.2Å/Pd34.1Å	N	N	P	P	P	P
Co9.4Å/Pd45.5Å	N	N	P	P	P	P

PM: Perpendicular magnetization ($Mr_\perp / Mr_{//} > 1$)
P : Positive Ku, but in plane magnetization ($Mr_\perp / Mr_{//} < 1$)
N : Negative Ku

Table I. Sign of Ku and the larger remanent magnetization axis of Pd/Co multilayers.

(a) Pd21Å/Co3.1Å

(b) Ag$_{19}$Pd$_{81}$13Å/Co3.1Å

(c) Ag$_{44}$Pd$_{56}$16Å/Co3.0Å
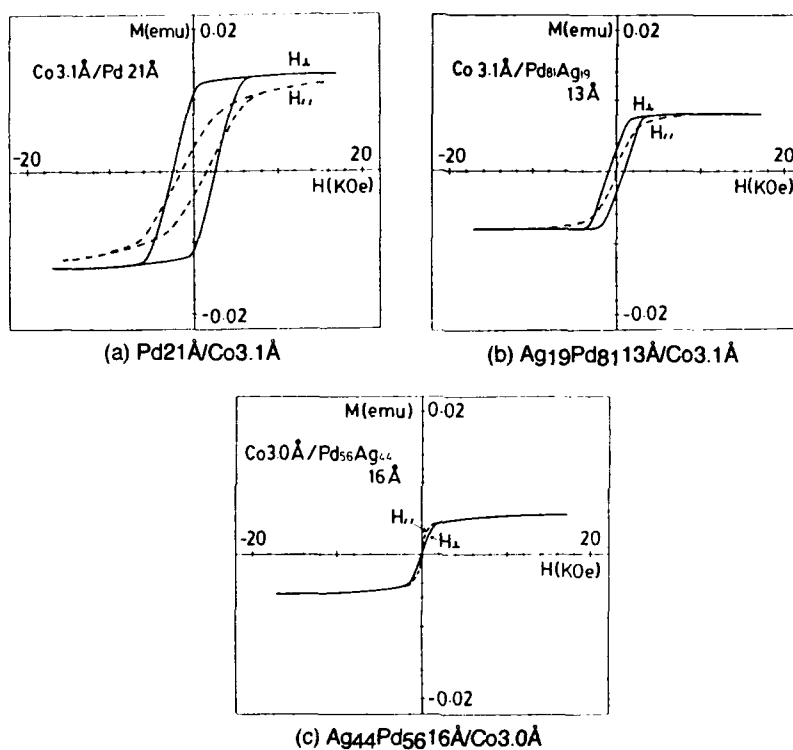
Fig.4 Typical hysteresis loops for the Pd/Co and AgPd/Co.

believed to arise from polarization of Pd atoms at interfaces[10].

On the contrary, an anomalous reduction of Ms was observed in AgPd/Co multilayers. In the case of Ag$_{44}$Pd$_{56}$/Co multilayers,
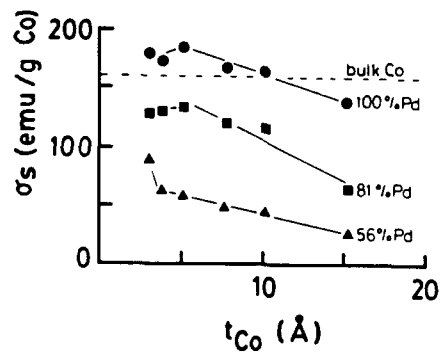
Fig.5 The t_{Co} dependence of Ms of AgPd/Co multilayers.

Ms decreased up to 84% while the reduction of Ms of the Pd/Co multilayers was within 14% and that of Ag/Co was within 9%. As mentioned above, the AgPd/Co multilayers contains many lattice defects. Therefore, it is considered that the abnormal reduction was resulted from the effect of superparamagnetism.

CONCLUSIONS

We have shown that Ag/Co, Pd/Co, and AgPd/Co multilayers have different magnetic anisotropies, respectively. These differences seem to support the existence of two or more mechanisms which may influence the perpendicular magnetic anisotropy. Whereas many studies have been reported so far, the values of Kv and Ks do not always agree with each other even in the case of same systems. These disagreements should be attributed to the differences in the microscopic structures and strains of the films.

ACKNOWLEDGMENTS

REFERENCES

1. P.F.Carcia, A.D.Meinhalt, and A.Suna, Appl. Phys. Lett. **47**, 178 (1985).
2. H.J.G.Draaisma, W.J.M.de Jonge, and F.J.A.den Broeder, J. Magn. Magn. Mater. **66**, 351 (1987).
3. F.J.A.den Broeder, D.Kuiper, A.P.van de Mosselaer, and W.Hoving, Phys. Rev. Lett. **60**, 2769 (1988).
4. F.J.A.den Broeder, D.Kuiper, H.C.Donkersloot, and W.Hoving, Appl. Phys A., **A49**, 507 (1989).
5. M.L.Néel, J. Phys. Rad. **15**, 225 (1954).
6. K.Spörl and D.Weller, E-MRS, Strasbourg 1990, paper C-VI/P6.
7. C.H.Lee, R.F.C.Farrow, B.D.Hermsmeier, R.F.Marks, W.R.Bennet, C.J.Lin, E.Marinero, P.D.Kirchner, and C.J.Chien, E-MRS, Strasbourg 1990, paper C-VIII/P7.
8. C.Chappert and P.Bruno, J. Phys. **64**, 55736 (1988).
9. H.J.G.Draaisma, F.J.A.den Broeder, and W.J.M.de Jonge, J. Appl. Phys. **63**, 3479 (1988).
10. P.F.Carcia, A.Suna, D.G.Onn, and R.van Antwerp, J. Superlattices and Microstructures **1**, 101 (1985).

Magnetic anisotropy determined from angular dependent magnetization measurements

P.J.H. BLOEMEN, E.A.M. VAN ALPHEN, W.J.M. DE JONGE,
Department of Physics, Eindhoven University of Technology,
5600 MB Eindhoven, The Netherlands

F.J.A. DEN BROEDER,
Philips Research Laboratories,
5600 JA Eindhoven, The Netherlands

Abstract

It is shown that a (biaxial) vibrating sample magnetometer (VSM) can be used to determine the magnetic anisotropy of thin films. Besides the commonly measured component along the magnetic field also the component perpendicular to the magnetic field was measured. Experiments were performed in a magnetic field of fixed magnitude as a function of the angle between the field and the film plane. These type of measurements give both an accurate estimate of the magnetic anisotropy and also show when domains are formed during rotation of the magnetization. The method has been applied to determine the magnetic anisotropy of Co/Pd and Co/Cu multilayers. The results are compared to those obtained with alternative methods.

Introduction

In the magnetism of ultrathin films and multilayers the magnetic anisotropy plays an important role. Through the vast amount of research in this field in the past few decades, it is now well known that the preferential orientation of the magnetization in multilayers can be manipulated by choosing appropriate combinations of ferromagnetic and non-magnetic metals with suitable thicknesses. In Co/Pt and Co/Pd(111) multilayers for example, perpendicular magnetic anisotropy can be achieved for small Co-thicknesses [1-2]. It is clear that an accurate determination of the magnetic anisotropy energy is important. To obtain the anisotropy, various techniques are used such as ferromagnetic resonance, torque magnetometry and magnetization measurements, for instance with a vibrating sample magnetometer (VSM). In the latter technique, which is rather common, the hysteresis loops are measured with the field parallel and perpendicular to the film plane. The total effective magnetic anisotropy energy, in this report defined as the sum of the intrinsic and shape anisotropy, is then determined from the area enclosed between the two loops.

In the following sections we will first discuss this method and related problems and propose an alternative method of using a magnetometer to determine the anisotropy.

Considerations

In the absence of hysteresis the area method is correct, for layers with in-plane anisotropy as well as for very thin layers with strong perpendicular anisotropy. In the latter case

this is however, not as obvious as sometimes is suggested.

From simple continuum theory it can be derived that the perpendicular $M(H)$ curve saturates at the demagnetizing field $\mu_0 M_s$ and that the in-plane loop saturates at an anisotropy field containing only the intrinsic magnetic anisotropy. It is generally assumed that for the in-plane loop the demagnetizing field does not play a role because the total component of the magnetization perpendicular to the film is zero. However this derivation is only correct for thick films. For very thin films with perpendicular anisotropy Malèk [3], Kooy [4] and Draaisma [5] et al. have shown, from an energy minimalization including magnetostatic and domain wall energies, that the (up-down oriented) domains in these films are very large. Consequently, the magneto*'atic energy, in zero field for example, of an up-down domain structure with zero average perpendicular magnetization, is nearly equal to the full magnetostatic, or demagnetizing energy, of the same film saturated perpendicularly. Saturating the film with a perpendicular field therefore costs very little demagnetizing energy $\frac{1}{2}\mu_0 M_s^2 \cdot (1 - f)$ and saturation is reached at relatively low fields. Here f is a number close to 1 depending on the domain size and film thickness which can be calculated easily within Malèk's model. Furthermore, in saturating the film in-plane, the spins feel almost the full demagnetizing field since they are in large domains. Therefore, the in-plane loop is, besides the intrinsic anisotropy, also affected by the nearly full amount of shape anisotropy $\frac{1}{2}\mu_0 M_s^2 \cdot f$. In calculating the area between the perpendicular and in-plane loop however, the terms with f cancel and the area again represents the total effective anisotropy. As mentioned, for films with an in-plane preferential orientation no complications arise and the correctness of the area method is understood easily.

However a fundamental problem of the area method is encountered when hysteresis is present in one or both loops. The area between the loops then is not well defined and one is forced to average the branches of the loops in some way. The thus obtained area might then contain, besides the total effective magnetic anisotropy, also unknown energy contributions associated with domain processes. This leads to an uncertainty in the anisotropy value obtained with this method. Furthermore, a practical difficulty is encountered when the available field is too small to saturate the films in the hard direction. An extrapolation of the hard axis loop is then used to get an estimate of the area, which is sometimes rather arbitrary for non linear M(H) curves.

In this report an alternative method for measuring anisotropy energies *using a VSM* is proposed which circumvents the problems mentioned above.

Experiments

The experimental geometry of the measurement is shown in Fig. 1. For details concerning the VSM we refer to Bernards et al. [6].
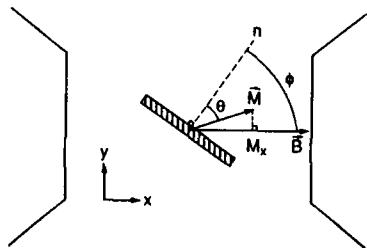
Figure 1 : Top view of a sample positioned between the poles of an electromagnet generating a magnetic field $B = \mu_0 H$ in the x-direction. The sample can be rotated in the x-y-plane while the x and y component of the magnetization can be measured simultaneously.

The applied field is set at a constant value, large enough to assure a uniform magnetization in the sample but not necessarily larger than the anisotropy field i.e. saturation in the hard direction is not needed. In this field the sample is rotated in the x-y-plane. At each angle the component of the magnetization M_x along the field and M_y perpendicular to the field, can be measured. It is clear that the magnetic anisotropy affects the angular dependence of these components.

To calculate the dependence of M_x and M_y on ϕ, uniaxial anisotropy and uniform magnetization are assumed. For given magnetic field H and effective magnetic anisotropy K, first the energy of the magnetization given by $K \sin^2 \theta - \mu_0 M_s H \cos(\phi - \theta)$ is minimized for each ϕ with respect to θ. This yields the equilibrium orientation θ_{eq} of M as a function of ϕ. Then $M_x(\phi)$ and $M_y(\phi)$ are calculated easily using $M_x = M_s \cos(\theta_{eq} - \phi)$ and $M_y = M_s \sin(\theta_{eq} - \phi)$. For zero anisotropy the magnetization simply follows the field and no angular dependence occurs, i.e. $M_x = M_s$ and $M_y = 0$, whereas for very strong anisotropy the magnetization rotates only slightly from the easy axis resulting in a cosine like behavior for M_x and M_y. As long as the basic assumption about the uniform magnetization is satisfied, the normalized length of the magnetization vector $\sqrt{M_x^2 + M_y^2}/M_s$ will be constant. Formation of domains at a certain angle, yielding a non-uniform magnetization, can be monitored by a decrease of $\sqrt{M_x^2 + M_y^2}/M_s$. Data in this regime cannot be used in the context of the present method to obtain the anisotropy.

Examples of experimental rotation diagrams are shown in Figures 2 and 3, where the measured M_x normalized to the saturation magnetization is plotted as a function of the angle between the applied field and the film plane.
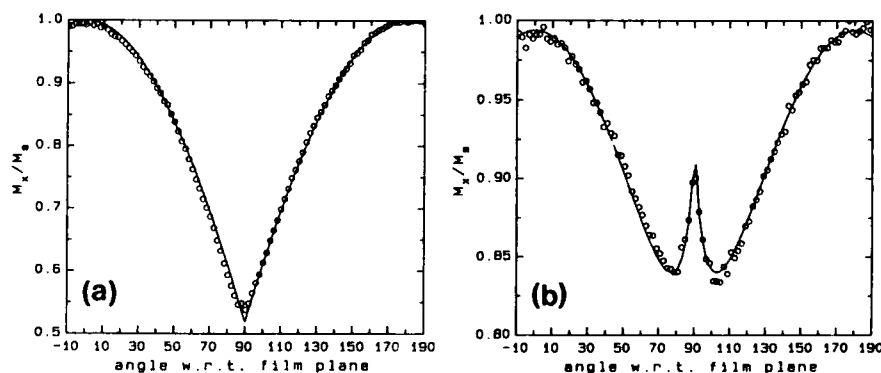
Figure 2 : Normalized x-component of the magnetization measured as a function of the angle between the applied field and the film plane. The measurements were performed on glass/200 Å Cu/ 40x(20 Å Co + 21 Å Cu) at fields of 0.79 T (a) and 1.43 T (b). The solid line represents a fit assuming uniform rotation of the magnetization.

Figure 2 displays the data obtained for a fcc Co/Cu(111) multilayer. This multilayer has an in-plane preferential orientation as can be inferred from the fact that saturation only occurs at 0^0 and 180^0 i.e. with the field along the film plane. When rotating the field away from the film plane a decrease in M_x/M_s is observed, meaning that the magnetization lags behind more and more. The solid line is a fit of the model assuming uniaxial anisotropy and uniform rotation of the magnetization, as discussed above. The length of the magnetization vector was observed to be constant in the whole range except very near the perpendicular direction. Fitting the data (Fig. 2a), obtained with an applied field of $\mu_0 H = 0.79T$, over all angles, gives $K = -1.09$ MJ/m^3. Within experimental accuracy (5%) this is in agreement with torque measurements and with the value obtained from the area between the two loops, which showed no hysteresis in this case. The data at a higher field $\mu_0 H = 1.43T$ (Fig. 2b) also yield -1.09 MJ/m^3. The submaximum observed for this field at the perpendicular orientation (90^0) can be understood if we realize that $M(H)$ curves for angles near perpendicular, cross each other for fields near the anisotropy field.
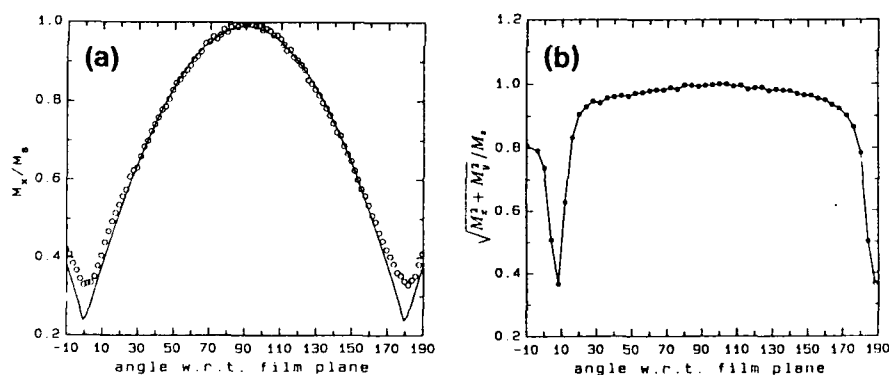
Figure 3 : Magnetization measurements as a function of the angle between the field and the film plane at 1.43 T on glass/1000 Å Pd/200x(2 Å Co + 22 Å Pd). (a) Component of the magnetization along the field. (b) The normalized length of the average magnetization vector.

In Fig. 3a the rotation diagram for M_x is shown for a Co/Pd(111) multilayer with strong *perpendicular* anisotropy. The normalized length of the magnetization vector $\sqrt{M_x^2 + M_y^2}/M_s$ versus the orientation of the field is shown in Fig. 3b. As can be seen, serious deviations from 1 (uniform magnetization) occur near the in-plane direction. As quoted before these are attributed to the formation of domains. It is therefore not correct to include the data in this angular range in the fitting process. Leaving out these data gives us a K value of 4.39 MJ/m^3, again in agreement with torque measurements, which were also fitted in the domain free range.

In conclusion, we have shown that the magnetic anisotropy can be determined from magnetization measurements as a function of the angle between the applied magnetic field and the easy direction, provided that no domains are present. Biaxial VSM measurements for an in-plane preferential Co/Cu multilayer and a strongly perpendicular easy Co/Pd multilayer gave good agreement with torque experiments.

References

1. F.J.A. den Broeder, W. Hoving and P.J.H. Bloemen,
   Proc. of the EMRS Spring Meeting 1990, May 29-June 1,
   Strasbourg (J. Magn. Magn. Mat, in press)

2. H.J.G. Draaisma, W.J.M. de Jonge and F.J.A. den Broeder,
   J. Magn. Magn. Mat. **26**, 351 (1987)

3. Z. Malèk and V. Kambersky,
   Czechosl. J. Phys. **8**, 416 (1958)

4. C. Kooy and U. Enz, Philips Res. Repts. **15**, 7 (1960)

5. H.J.G. Draaisma and W.J.M. de Jonge,
   J. Appl. Phys. **62**, 3318 (1987)

6. J.P.C. Bernards, G.J.P. van Engelen, C.P.G. Schrauwen,
   H.A.J. Cramer, S.B. Luitjens, IEEE Trans. Magn. **26**, 216 (1990),
   J.P.C. Bernards, C.P.G. Schrauwen, Thesis, University of Twente,
   The Netherlands (1990)

MAGNETOELASTIC INTERACTIONS AT SURFACES AND INTERFACES

R. C. O'HANDLEY AND S. SUN
Department of Materials Science and Engineering, Massachusetts Institute of Technology, 77 Massachusetts Ave., Cambridge, MA. 02139

ABSTRACT

The contribution of strains to anomalous surface and interface magnetic anisotropies cannot be analyzed quantitatively without knowledge of the ME coupling coefficients there. We have measured the ME coupling coefficients B^s near the surface (~0.5nm) of two amorphous alloys, $Fe_{77}Cr_6B_{17}$ (with bulk magnetostriction $\lambda_s = +7 \times 10^{-6}$) and $Co_{76}Cr_4B_{20}$ ($\lambda_s = -3.8 \times 10^{-6}$) and found them to differ significantly from the bulk values B^b: Fe-base. $B^s = -1.7 \times 10^5 J/m^3$ (57% of B^b) and Co-base. $B^s = 5.8 \times 10^5 J/m^3$ (three times B^b).

Background

Numerous studies have focussed attention on magnetic surface anisotropy in ultrathin films [1,2], multilayers [3], and at bulk surfaces [4]. These effects can sometimes be isolated from bulk anisotropy by studying the thickness dependence of the effective anisotropy:

$$K_{eff} = K^v + 2\pi M_z^2 + 2K_s/t \qquad (1)$$

where K^v is the volume magnetocrystalline anisotropy constant, $2\pi M_z^2$ is the demagnetization energy density and K^s is the surface magnetic anisotropy. When $K_{eff} > 0$ the magnetization lies in plane. Experimental plots of $K_{eff} \cdot t$ vs. t generally show linear behavior with the slope giving the bulk crystal and shape anisotropy and the intercept giving the surface anisotropy.

Neel [5] first drew attention to the fact that the reduced symmetry at a surface causes the familiar phenomenological expression for cubic anisotropy energy density to require terms of lower order:

$$K^s = K_s \alpha_z^2 + K_{ss} \alpha_x^2 \alpha_y^2 = K_s \cos^2\theta + K_{ss}\sin^2\theta\cos^2\varphi \qquad (2)$$

K_s in this expression is the uniaxial surface energy per unit area that enters Eq. 1.

It should be clear that magnetoelastic (ME) energies could be treated in a way similar to crystal anisotropy. In fact Neel [5] attributed surface magnetic anisotropy primarily to ME effects. The familiar expansion of volume magnetic anisotropy energy density in powers of strain gives:

$$f_m = K_{ij} \alpha_i \alpha_j + B_{ij} \alpha_i \alpha_j e_{ij} + D_{ijkl} \alpha_i \alpha_j e_{ij} e_{kl} \quad \ldots \quad (3)$$

Here K_{ij} is the crystal anisotropy, independent of strain, B_{ij} is the first order ME coefficient coupling the strain e_{ij} to the direction of magnetization described by $\alpha_i\alpha_j$. B_{ij} is related to the more familiar magnetostriction coefficient by an elastic stiffness constant: $B_{ij} = -C_{ijkl}\lambda_{kl}$. D_{ijkl} is a second order ME coefficient. Eq. 3 shows that a surface strain relative to the bulk may contribute to magnetic anisotropy through B_{ij}.

If bulk parameters were to apply near the surface, the first order ME energy due to a 1% strain in Ni would give rise to a uniaxial anisotropy energy density of order $1.6 \times 10^5 J/m^3$. This is 40 times the bulk magnetocrystalline anisotropy energy density of Ni. For the large strains near surfaces and interfaces, it is expected that second order effects (described by D_{ijkl}) would be important. Such strains effectively make B_{ij} strain dependent if we can write Eq. 3 as

$$f_m = K_{ij} \alpha_i \alpha_j + B^s \alpha_i \alpha_j e_{ij} \quad (4)$$

where $B^s = B_{ij} + D_{ijkl}e_{kl}$. It is clear that a large strain e_{kl} can alter the measured ME coefficient B^s through the second order ME coefficient. In fact Barandiaran et al. [6] have shown that strains up to 1% applied to a cobalt-rich amorphous alloy change the saturation magnetostriction coefficient λ_s linearly from its unstrained value of $\lambda_s(0) = +0.09 \times 10^{-6}$ at a rate $d\lambda_s/de = -12 \times 10^{-6}$.

Pure metals are known to experience localized strains of up to 10% normal to their surface due to the unique electronic structure there [7]. Similarly, epitaxial films and multilayers experience in-plane misfit strains of a comparable magnitude. So it is to be expected that the ME coefficients in these cases may differ from their bulk values. In fact strain-modulated FMR measurements on Ni-C and Ni-Ag multilayers [8] show that the effective magnetostriction coefficient λ_{eff} can be measured as a function of Ni layer thickness and analyzed with an expression analogous to Eq. 1. In this case λ_{eff} shows a bulk contribution $\lambda^b = -36 \times 10^{-6}$, close to that of polycrystalline Ni, and a surface contribution which drives λ_{eff} toward positive values with decreasing thickness.

It is interesting to note that ultrathin epitaxial films of Ni/Cu (001) [9] (where the Ni layers may be stretched by as much as 2.6%) show in-plane magnetization for thicknesses up to 4.5 ML. At this thickness dislocations nucleate to relieve much of the misfit strain [10] and the magnetization immediately takes on a large out-of-plane component. This behavior cannot be explained on the basis of nickel's negative λ_{100} coefficient but it is consistent with the positive surface magnetostrictive coupling implied by Zubarek et al.'s measurements.

Surface ME coefficients

We have made careful measurements of the strain dependence of surface magnetization in amorphous ribbons (using secondary electron spin polarization analysis to probe the surface behavior) in order to determine the surface ME coupling coefficient [11] B^s. The B^s we measure is not a surface ME coefficient in the same sense that K^s is a surface anisotropy (energy/area). Our B^s has units of energy/volume because it is the surface ME coefficient integrated over the probe depth of the secondary electrons [12], namely about 0.5nm.

The surface magnetization is measured from the polarization of secondary electrons with kinetic energy above the low-E_K anomalous polarization enhancement range [13, 14]. We use a diffuse-scattering, gold-film, spin polarimeter [15] and a repeller grid (between the extraction lens and the drift tube) to remove the polarization-enhanced cascade electrons. This technique has been shown to give a reliable measure of valence band magnetization [13].

We chose to study amorphous materials for two reasons: 1) only one ME coefficient is required to describe the effects of interest and 2) alloys having bulk magnetostriction constants λ_s^b of opposite sign can be obtained in materials of similar structure. The amorphous alloys were $Co_{76}Cr_4B_{20}$ (λ_s^b = -3.8 x 10^{-6}) and $Fe_{77}Cr_6B_{17}$ (λ_s^b = +7 x 10^{-6}). The amorphous ribbons can be wound into a continuous loop to minimize stray fields, the bane of low-energy electron experiments.

Figure 1 shows the P-H loops of the sputter-cleaned, annealed cobalt-base and iron-base alloys. The integrated Sherman function of our plarimeter is 0.14 ±0.01. Surface saturation polarization values P_s^S obtained by extrapolation to $1/H = 0$ are indicated as well as the bulk valence band saturation polarizations P_s^b. For the cobalt-base glass, $P_s^S = P_s^b$ within experimental error. The surface magnetization of the iron-base glass is strongly suppressed relative to the bulk value. This is not due to surface oxidation but rather to boron surface segregation. After sputter cleaning, the Auger spectrum of the Fe-base sample shows a boron peak that increases as $[1-e^{-t/\tau}]$ with τ = 90 min. Annealing causes a further steep increase in boron concentration so that the equilibrium surface composition determined by quantitative Auger analysis is $Fe_{51}Cr_5B_{42}$. In light of this, the reduced surface magnetization observed for the iron-base alloy is not unreasonable.

We determine the ME coupling coefficient in the usual way, by taking the strain derivative of the M-H curve [16]. Using the thermodynamic definition of the magnetostrictivity **d** that couples magnetic and elastic responses to field H and stress σ, respectively, we have:

$$\mathbf{d} = \left(\frac{\partial e}{\partial H}\right)_\sigma$$

(5a)

$$= \mu_o\left(\frac{\partial M}{\partial \sigma}\right)_H$$

(5b)
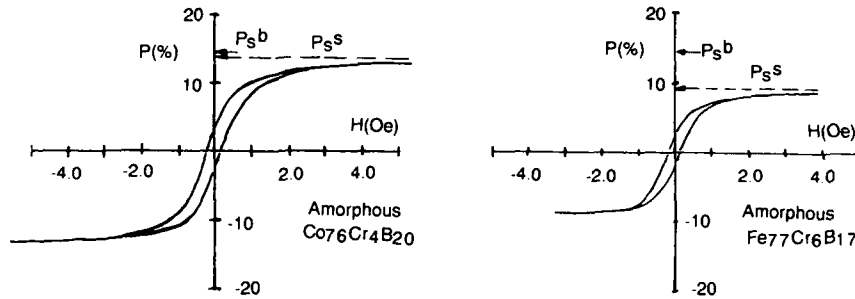
Figure 1. Secondary electron polarization vs applied field. Surface saturation polarization P_s^s and bulk saturation polarization P_s^b are indicated.

Integration of Eq. 5a and substitution from Eq. 5b gives:

$$e(H) - e(0) = \int_0^H d\, dH = \int_0^H \varepsilon_0 \left(\frac{\partial}{\partial} \frac{M}{\sigma} \right)_H dH \tag{6}$$

A standard elastic treatment [11] for tensile stress relates B to e(H) giving finally:

$$B^s = - \frac{3 D / 4}{m^2(H) - m^2(0)} \int_0^H \left(\frac{\partial}{\partial} \frac{A}{e} \right)_H dH \tag{7}$$

Here m(H) is the reduced magnetization in the field direction $M_x(H)/M_s$, A is the electron asymmetry measured at the polarimeter in the field direction $A = A_x = (N^+ - N^-)/(N^+ + N^-)$ and D is $\mu_0 n_v \mu_B \rho f N_A/(Sw)$ with n_v the number of valence electrons, ρ the mass density, f the fraction of atoms present that are magnetic, N_A is Avogadro's number, S is the polarimeter efficiency, and w is the weight per formula unit.

Figure 2 shows the strain dependence of A for the two samples. The increase in polarization P=A/S with compressive strain for the cobalt base alloy indicates that its surface magnetostriction coefficient λ_s^s is negative just as is the bulk coefficient, λ_s^b. For the Fe base alloy the decrease in A with strain also indicates the same positive sign for λ_s^s as for λ_s^b. We approximate the integral in Eq. 8 by the sum of differentials

$$\int_0^H \left(\frac{\partial}{\partial} \frac{A}{e} \right)_H dH = \sum_{i=1}^N \left(\frac{\Delta}{\Delta} \frac{A}{e} \right)_H \Delta H \tag{8}$$

in order to calculate the ME coefficients integrated over the secondary electron probe depth.

Figure 3 summarizes the results by showing the relation of the
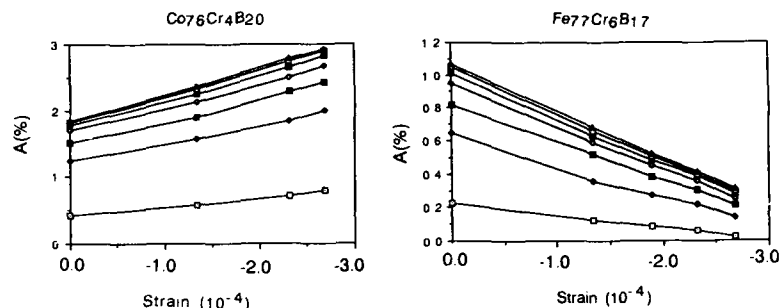
Figure 2. Strain dependence of asymmetry A for various field strengths for the two samples.

measured surface ME coefficients to the bulk ME coefficients. For the cobalt-base glass, B^s is more than three times greater than B^b and of the same sign. For the iron-base alloy the magnitude of B^s is slightly more than half that of the bulk value and also of the same sign. But the surface composition was determined to be $Fe_{51}Cr_5B_{42}$. If the value of B^s were to scale with $(M_s^s)^2$, as is generally the case, we would expect B^s of a surface with the composition $Fe_{77}Cr_6B_{17}$ to be about $-3.9 \times 10^5 J/m^3$, larger in magnitude than that of the bulk.

These results show that it is not necessasrily a good approximation to use bulk ME coefficients when estimating the elastic contribution to magnetic surface anisotropy. A clean surface may be subject to surface segregation which changes its composition. Even in the absence of surface segregation B^s may differ significantly from B^b, mainly due to the reduced symmetry and unique electronic structure at the surface.

Figure 3. Bulk and surface ME coupling coefficients B^b and B^s.

490

References

1) U. Gradmann. J. Korecki and G. Waller. Appl. Phys. **A 39**. 101 (1986);
M. Stampanoni. A. Vaterlaus. M. Aeschlimann. and F. Meier,
Phys. Rev. Lett. **59**. 2483 (1987);   N.C. Koon. B.T. Jonker. F.A.
Volkening. J.J. Krebs. and G.A. Prinz. Phys. Rev. Lett. **59**. 2463 (1987);
B. Heinrich. K.B. Urquhart, A.S. Arrott. J.F. Cochran. K. Myrtle. and S.T.
Purcell. Phys. Rev. Lett. **59**. 1756 (1987); C. Liu. E. R. Moog and S. D.
Bader. Phys. Rev. Lett.**60**. 2422 (1988); R.J. Hicken. G.T. Rado. Gang
Xiao. and C.L. Chien. Phys. Rev. Lett. **64**. 1820 (1990); D. P. Pappas. K.
P. Kamper and H. Hopster. Phys. Rev. Lett. **64**. 3179 (1990).

2) J.G. Gay and R. Richter. Phys. Rev. Lett. **56**. 2728 (1986); H. Fu. M.
Mansuripur and P. Meystre. Phys. rev. Lett. **66**. 1086 (1991).

3) H. J. G. Draasma. W. J. M. de Jong and F. J. A. den Broeder, J. Magn.
Mag. Mtls. **66**. 351 (1987) and F. J. A. den Broeder. K. Kuiper. A. P.
van de Mosselaer. and W. Hoving. Phys. Rev. Lett.**60**. 2769 (1988).

4) D. Mauri. R. Allenspach. and M. Landolt. J. Appl. Phys. **58**.
906 (1985); R. C. O'Handley and J. P. Woods. Phys. Rev. **B42**. 6568
(1990).

5) L. Neel. Compt. rend. **237**. 1468 (1953).

6) J. M. Barandiaran. A. Hernando. V. Madurga. O.V. Nielsen. M. Vasquez
and M. Vasquez-Lopez. Phys. Rev. **B35**. 5066 (1987).

7) A.J. Freeman and C.L. Fu. J. Appl. Phys. **61**. 3356 (1987).

8) R. Zuberek. H. Szymczak. R. Krishnan and M. Tessier. J. de Phys.
C8. **49** 1761 (1988).

9) C. Ballentine PhD Thesis. Physics. U. Texas (Dec. 1989).

10) J. S. Gidley et al. Phys. Rev. Lett. **62**. 811 (1989).

11) S. Sun and R. C. O'Handley. submitted for publication.

12) D. L. Abraham and H. Hopster. Phys. Rev. Lett. **58**. 1352 (1987); T.
Van Zandt and R. Browning. J. Appl. Phys. **68**. 5835 (1990); D.P.
Pappas, K.P. Kamper. B.P. Miller. H. Hopster. D.E. Fowler. C.R. Brundle.
A.C. Luntz. and Z. X. Shen. Phys. Rev. Lett. **66**. 504. 1991.

13) E. Kisker. W. Gudat and K. Schroder. Sol. St. Comm. **44**. 591.
(1982) and G. Chrobok and M. Hoffmann. Phys. Rev. Lett. **57A**.
257 (1976).

14) D. R. Penn. S. P. Apell and S. M. Girvin. Phys. Rev. Lett. **55**. 518
(1985).

15) J. Unguris. D.T. Pierce and R.J. Celotta. Rev. Sci. Instrum. **57**.
1314 (1988); M. R. Scheinfein. D. T. Pierce. J. Unguris. J. J. McClellend.
and R. J. Celotta. Rev. Sci. Instrum. **60**. 1 (1989); M. R. Scheinfein. J.
Unguris. M. H. Kelley. D. T. Pierce. and R. J. Celotta. Rev. Sci. Instrum.
61. 2501 (1990).

16) M. Wun-Fogle and A.E. Clark. I.E.E.E. Trans. Mag. **25**. 3611 (1989).

MAGNETO-OPTICAL ENHANCEMENT OF TbFeCo/Al FILMS
AT SHORT WAVELENGTH

Kibong SONG, Hiroshi ITO[*] and Masahiko NAOE

Tokyo Institute of Technology,
Department of physical Electronics,Tokyo 152,Japan.
* Corporate R&d Laboratory,
Pioneer Electronic corporate,
Saitama 350-02, Japan

ABSTRACT

The bilayered films composed of magneto-optical(MO) amorphous Tb-Fe-Co alloy and reflective Al layers were deposited successively on glass slide substrates without plasma exposure by using the facing targets sputtering system. The specimen films with the thickness of MO layer t_{MO} below 5 nm showed apparent perpendicular magnetic anisotropy constant Ku of 2 to 3×10^6 erg/cm^3 and rectangular Kerr loop. The specimen film with t_{MO} of 14 nm took the Kerr rotation angle θ_K as large as about 0.36 degree, at the wavelength λ as short as about 400 nm. These values of θ_K is considerably larger than those of the bilayered films in the conventional MO media. Normally, the bilayered films with t_{MO} above 50 nm took θ_K of about 0.25 degree at θ_K of 400 nm.

INTRODUCTION

Nowadays, MO disks were used for erasable high density recording media. According to the exploring quantity of information and intelligence, it is necessary to develop higher density recording media. So, many researchers and engineers have been engaged in developing high density MO media at short wavelength. In order to obtain higher recording density and C/N ratio, it is essential to make media noise as low as possible, especially at short wavelength. In order to examine the possibility of high density MO media, the amorphous thin films of Tb-Fe-Co alloy (a-TbFeCo) with noncrystalline interface have been chosen.

In this study, the bilayered films composed of a-TbFeCo and pure Al layers have been prepared on "plasma-free" substrate by the facing targets sputtering(FTS) apparatus[1,2]. In order to deposit excellent a-TbFeCo thin films with proper short-range ordering, the relationship between the sputtering conditions and their properties have been investigated, and it also have been attempted to optimize the conditions[2-4].

EXPERIMENT

The bilayered films composed of a-TbFeCo and pure Al layers were deposited sequentially on glass slide substrate without plasma exposure by using FTS apparatus. As illustrated in Fig.1, this apparatus has two pairs of facing targets and rotatable substrate holder. So the bilayered films can be deposited successively without breaking the vacuum. For con-

492

finement of plasma, magnetic field of about 220 G were applied normally to both target planes at the central position of two facing targets. Targets were a pair of $Fe_{90}Co_{10}$ alloy plates with Tb chips and a pair of pure Al ones. The composition of a-TbFeCo layers were mainly controled by alternating the number of Tb chips mounted on $Fe_{90}Co_{10}$ targets. The a-TbFeCo layers with the thickness of MO layer t_{MO} of 5 to 300 nm were deposited on glass side substrates at the argon pressure P_{Ar} of 0.5 to 7.5 mTorr and the deposition rate Rd of 100 nm/min. The Al layers with the thickness t_{Al} of 100 nm were deposited successively on a-TbFeCo layer at P_{Ar} of 0.5mTorr and R_d of 50 nm/min. The microstructure was observed by means of scanning electron microscopy(SEM), scanning tunnel microscopy(STM) and transmission electron microscopy(TEM). The Kerr rotation angle θ_K and the coercivity He were determined by with observing Kerr loop tracer from the substrate side at the wavelength in the range of 400 to 900 nm.
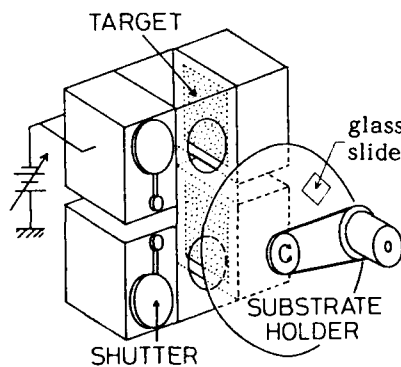
Fig.1 Facing Targets Sputtering Apparatus
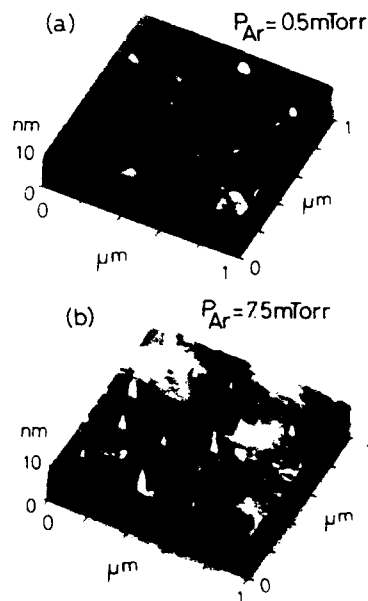
Fig.2 STM images of surface appearance
in the a-TbFeCo films

RESULTS AND DISCUSSION

Figure 2 (a) and (b) shows the STM images of surface appearance in the a-TbFeCo films deposited at P_{Ar} of 0.5 and 7.5 mTorr, respectively, and at R_d of 100 nm/min. The a-TbFeCo film deposited at lower P_{Ar} of 0.5 mTorr revealed very flat surface appearance than that of the film deposited at higher P_{Ar} of 7.5 mTorr. As the authors reported previously [3,1], the films deposited at lower P_{Ar} and higher R_d showed very flat

surface appearance and revealed uniform, dense and columnless cross-sectional morphology. Such a high quality films exhibited good resistance against corrosion and oxidation, too. So the MO layers in a-TbFeCo/Al bilayered films have been prepared by lower P_{Ar} of 0.5 mTorr and higher R_d of 100 nm/min in this study.

Figure 3 shows the torque curve of a-TbFeCo/Al bilayered films with very small t_{MO} of less than 5 nm. The effective perpendicular magnetic anisotropy constant Ku measured by Miyajima's method[5] was in the range of 2 to 3×10^6 erg/cm^3 as large as that of the films with large t_{MO} and the films revealed sharply rectangular polar Kerr loop.

Figure 4 (a) and (b) shows the Kerr loops of a-TbFeCo/Al bilayered films with t_{MO} of 100 and 14 nm, respectively. The specimen films with large t_{MO} of 100 nm showed monotonous increase of θ_K with increase of the measurement wavelength λ . On the other hand, the specimen films with small t_{MO} of 14 nm showed monotonous decrease of θ_k with increase of λ . Such an enhancement of MO effect at short λ may be caused not only by the significant interference of the reflected light at upper and under interfaces of MO layer, but also by the striking perpendicular magnetic anisotropy at the clear and uniform interface between a-TbFeCo and Al layers.

Figure 5 shows the wavelength λ dependencies of the reflectivity R of a-TbFeCo/Al bilayered films with t_{Al} of 100 nm and t_{MO} of 100 and 14 nm. R of both films measured from substrate side increased monotonously with increase of λ , but the specimen film with small t_{MO} of 14 nm exhibited larger R. The difference between them may be due to the effect of reflected light at Al layer[6].

The figure of merits(FOM) was calculated on the basis of the observed data as shown in Fig.4 and 5. FOM of a-TbFeCo/Al bilayered films with small t_{MO} of 14 nm was 0.25 degree. This value is larger than that of the film with large t_{MO} of 100 nm. So, the bilayered films with extremely flat surface composed of uniform, dense and columnless a-TbFeCo and Al thin layers have certain possibilities for high density MO media,especially at short λ .

Fig.3 Torque curve of a-TbFeCo/Al by layered films

TbFeCo/Al(100nm)

λ(nm)	(a)t_{MO}=100nm	(b)t_{MO}=14nm
830		
700		
550		
400		
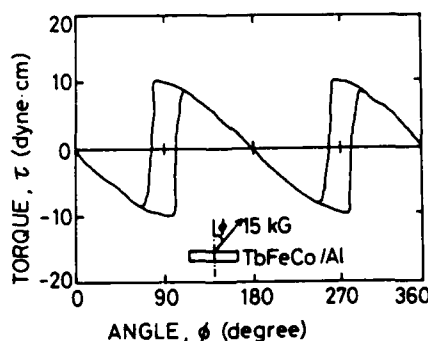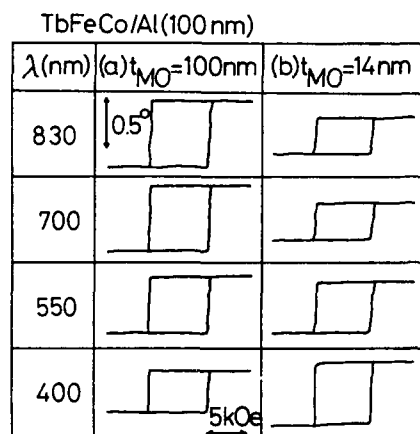
Fig.4 Kerr loops of a-TbFeCo/Al
bilayered films
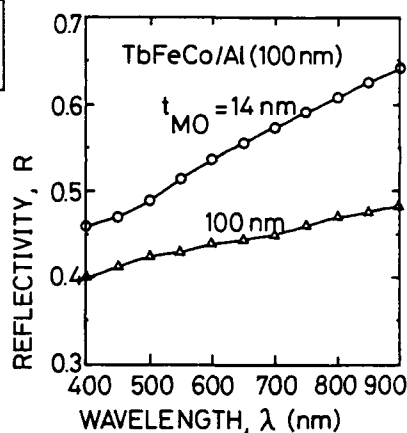
Fig.5 Wavelength dependence of
the reflectivity R of
a-TbFeCo/Al bilayered films

CONCLUSION

The bilayered films composed of amorphous Tb-Fe-Co alloy and pure Al layers were deposited sequentially by facing targets sputtering(FTS) apparatus. A-TbFeCo layers have been prepared at the Ar pressure P_{Ar} in the range of 0.5 to 7.5 mTorr and the deposition rate R_d of 100 nm/min. Al layers have been prepared at P_{Ar} of 0.5 mTorr and R_d of 50 nm/min. The obtained conclusions are as follows;

(1) The a-TbFeCo films deposited at lower P_{Ar} and higher R_d showed very flat surface and revealed dense, uniform and columnless cross-sectional morphology.

(2) The bilayered films composed of such excellent a-TbFeCo and Al layers possessed large perpendicular magnetic anisotropy constant and revealed sharply rectangular polar Kerr loop, even for small t_{MO} below 5 nm.

(3) The films with the thickness of MO layer t_{MO} of about 14 nm exhibited significant increase of the Kerr rotation angle θ_K and the figure of merit FOM at the short wavelength λ. θ_K and FOM of at λ of 400 nm were 0.36 and 0.25 degree, respectively.

REFERENCES

1. Y.Niimura, S.Nakagawa, and M.Naoe, Mater.Sci.and Engineeing, 98, 53(1988).
2. M.Naoe, N.Kitamura and H.Ito, J.Appl.phys., 63,3850(1988)
3. H.Ito and M.Naoe, ICCC Trans.Magn., 26,181(1990)
4. K.Song, H.Ito and M.Naoe, Materials Science and Engineering, A132, to be published(1991)
5. H.Miyajima, K.Sato and T.Mizoguchi, J.Appl.Phys., 4669(1976)
6. H.Ito, M.Yamaguchi and M.Naoe, Mat.Res.Soc.Symp.Proc.,150, 171(1989)

OPTICAL AND MAGNETO-OPTICAL MODELING OF
ULTRA-THIN FILM MULTILAYERS*

WILLIAM A. McGAHAN, PING HE, and JOHN A. WOOLLAM
Center for Microelectronic and Optical Materials Research, and Departments of
Electrical Engineering and Physics, University of Nebraska-Lincoln, Lincoln NE 65808.
*Research Supported by NSF Grant #CMR8918889.

ABSTRACT

A method for calculation of the optical and magneto-optical response of multilayered structures in which the layers are atomically thick is presented. The method can be used to calculate the response of any film which has arbitrary compositional variation in the direction normal to the film plane as well. Calculations are presented for Tb/Co compositionally modulated alloys.

INTRODUCTION

Previous attempts at calculation of the optical and magneto-optical specular scattering from multilayers in which the individual layers were a few atoms thick have been based on the assumption that the individual layers were perfect in that the nominal interior of each layer was considered to be homogenous. Often, the optical and magneto-optical constants of the layers are then assigned to be those of bulk samples or thick films of the same material, an assumption which is certain to fail in the limit of very thin layers. The model presented herein provides a somewhat more physically realistic way to calculate the properties of so-called 'nano-scale' multilayers, at the expense of requiring measurements of the optical and magneto-optical constants of the binary alloys involved over a fairly broad range of compositions. This model is based on the theory of sinusoidal composition variation in very thin multilayers developed by Shan to describe the magnetic properties of compositionally modulated rare-earth transition metal alloys. The model could be used to calculate the properties of discrete layers with compositionally varying interfaces, but this has not been done at the present time.

498

The characteristic matrix approach

The model used to calculate multilayer properties is based on the definition of the characteristic matrix, or transfer matrix for thin films, which may or may not be magneto-optically active. We assume that the magnetization in the films is directed normal to the plane of the sample, defined to be the $\hat{z}$ axis, such that the dielectric tensor for a magneto-optic layer has the form:

$$\overline{\epsilon} = \begin{bmatrix} \epsilon_{xx} & -\epsilon_{xy} & 0 \\ \epsilon_{xy} & \epsilon_{xx} & 0 \\ 0 & 0 & \epsilon_{zz} \end{bmatrix} \tag{1}$$

where ϵ_{xx} is the complex dielectric constant and we assume $\epsilon_{zz}=\epsilon_{xx}$. Maxwell's equations are then solved in a material having this dielectric tensor. This solution can be matched to solutions in adjacent films at the upper and lower boundaries of a film, such that a transfer matrix can be defined which will relate the electric and magnetic field components (only four are independent, hence 4x4 matrices are used, and the x and y components of the fields are used for a basis) at the top surface of the film to those at the bottom. To find the response of a stack of films, it is then only necessary to calculate the characteristic matrix for each film, and then multiply these matrices together in sequence from the top of the stack to the bottom to find the total characteristic matrix for the stack. For materials having the dielectric tensor (1), (off-diagonal elements may be zero), the characteristic matrix in the basis (E_x, H_y, E_y, H_x) is[1]:

$$[C] = \begin{bmatrix} c & -iMs & \frac{1}{2}is\delta\tilde{Q} & \frac{1}{2}\tilde{Q}N(c\delta - s) \\ \dfrac{-is}{M} & c & \dfrac{-\tilde{Q}(c\delta + s)}{2M} & \dfrac{-i\tilde{Q}Ns\delta}{2M} \\ \dfrac{-i\tilde{Q}Ns\delta}{2M} & \frac{1}{2}\tilde{Q}N(c\delta - s) & c & iNs \\ \dfrac{-\tilde{Q}(c\delta+s)}{2M} & \frac{1}{2}i\tilde{Q}s\delta & \dfrac{is}{N} & c \end{bmatrix} \tag{2}$$

where $c=\cos\theta$, $s=\sin\theta$, $M=m\gamma$, and $N=m/\gamma$. Also, γ is the cosine of the angle of propagation of the light beam in the layer, calculated from Snell's law and the isotropic indices of refraction of the layer of interest and the incident medium, θ is the isotropic phase thickness of the film:

$$\theta = \frac{2\pi}{\lambda}\cdot\tilde{n}\gamma d \tag{3}$$

and m is the isotropic wave impedance of the medium $\sqrt{\frac{\mu}{\epsilon}}$. Given the complex index of refraction $\tilde{n}$, the magneto-optic Voigt parameter $\dot{Q}$, the thickness of the film d, and the direction cosine γ of the incident light wavevector with respect to the the y-z plane, the characteristic matrix (2) of the film can be calculated.

When the total characteristic matrix of a stack of films has been found, it is relatively simple to calculate optical properties of the stack (reflectance, transmittance, ellipsometric parameters ψ and Δ) as well as magneto-optic properties (Kerr rotation, Kerr ellipticity) from the elements of the matrix [C]. The reader is referred to reference [1] for details.

Modeling of ultra-thin multilayer structures

The above described theory has been used extensively for the analysis of experimental optical and magneto-optical data on multilayers in which the individual layers are tens of Angstroms to thousands of Angstroms thick. However, implicit in a layered model such as this is the assumption that there is no interdiffusion between layers. i. e. that all interfaces between layers are perfect. It is possible to include interfacial effects by addition of another layer to the model to describe a different material formed at the interface, but it is unreasonable to expect this to work if the composition of the material varies across the interface.

The model used for ultra-thin multilayers in this work is based on a similar model used to calculate the magnetic properties of rare-earth transition metal multilayers by Z. S. Shan. The (local) composition C(z) of the film at a depth z in the stack (measured from the top of the stack) is to be given by

$$C(z) = C_0 + AC_0\cos\left(2\pi\cdot\frac{z}{d_1+d_2}\right) \tag{4}$$

where d_1 and d_2 are the nominal thicknesses of the individual layers which make up the bilayer, C_0 is the center composition, and the parameter A, ranging from zero to one, represents the degree to which the composition is modulated. Note that in the following discussion, arbitrary choices for the function $C(z)$ could be allowed, but we have chosen (4) as being most physical for the TbCo multilayer system, for which calculations are presented.

The bilayer is then divided into a large number ($\simeq 100$) of thin slabs, each of which are assumed to be compositionally homogeneous with an alloy composition given by equation (4). The procedure for calculation of the characteristic matrix of the total stack is as follows: first, calculate [C] for each slab in a single bilayer. A bilayer is defined as extending from a peak in the concentration of one constituent to the next adjacent peak. The optical and magneto-optical constants of each slab are interpolated from the constants of alloys of known composition, where the composition of the slab of interest is given by (4), with z equal to the depth in the bilayer measured from the top. The [C] matrices for each slab are then multiplied together in sequence to produce the characteristic matrix for a single bilayer. Then, if there are n bilayers in the structure, the characteristic matrix for the entire stack is given by

$$[C]_{stack} = [C]_{top}[C]^{n-1}_{bilayer}[C]_{\frac{1}{2}bilayer}[C]_{bottom}[C]_{substrate} \qquad (5)$$

where the 'top' and 'bottom' matrices represent layers of thickness $d_1/2$ and $d_2/2$, with compositions C_0+AC_0 and C_0-AC_0, respectively. These additional matrices, plus the $\frac{1}{2}$bilayer matrix, are included to account for the fact that the top layer will not have interdiffusion of the second species from the top, nor will the bottom. If samples are overcoated, a [C] matrix for the overcoat should premultiply the right side of (5). We expect this model to work best for magneto-optic properties (and constants) which are measured at saturation, with the applied field along the z-axis, as the magnetization in the multilayer should everywhere be directed along z in this case, and expression (1) for the dielectric tensor of the slabs will be valid.

Results of calculations for TbCo multilayers

The use of this model for calculations is severely hindered by the lack of published optical and magneto-optical constants for binary alloys as a function of composition and photon wavelength. We are currently measuring these constants for various TbCo alloys as a function of composition, but unless the alloy composition of interest has a

significant degree of perpendicular anisotropy, it can be very difficult to saturate the sample in the z-direction for measurement of the saturation magneto-optical constants. The following calculations are based on constants measured in the composition range (Tb_xCo_{1-x}) .04 $\leq$ x $\leq$ .31 However, samples in the lower range of composition could not be saturated (x $\leq$ .085). Also, as the compensation composition lies within this composition range (x $\simeq$ .23), the magneto-optical constants for these materials undergo an abrupt change in sign at this composition. As the compositionally modulated alloys of Tb/Co appear to behave as magnetically homogeneous systems, we multiply all magneto-optic constants for x $\geq$ .23 by (-1), such that each subnetwork is aligned in the same direction everywhere in the stack, although the magnetization of the subnetwork can vary as a function of z. Finally, compositionally modulated alloys of Tb/Co tend to show perpendicular anisotropy in the region where the individually layer thicknesses are equal, such that we cannot measure the saturation Kerr rotation for samples with layer thicknesses corresponding to alloy fractions within the range for which optical and magneto-optical constants have been obtained. Only when magnetization measurements on the multilayers are made such that the measured Kerr rotation and ellipticity can be corrected to their saturation values can direct comparison to experiment be made for this model. Such measurements are in progress.

The calculated reflectance and saturation Kerr rotation and ellipticity as a function of modulation amplitude are shown in figures 1 and 2. For this calculation, the center composition was $Tb_{.23}Co_{.77}$, with the bilayer thickness fixed at 10.0 Angstroms. The data are presented as a function of the modulation amplitude, and are calculated at normal incidence with an illuminating beam of wavelength 6328 Angstroms. Similar results are obtained when the modulation amplitude is fixed and the layer thicknesses are allowed to vary, such that the composition remains fixed. Note the relative insensitivity of both the reflectance and the Kerr parameters to the modulation amplitude. This is probably a consequence of the relative smallness of the bilayers with respect to the wavelength of the probing light beam. As the beam tends to average over a fair number of bilayers, the calculated properties tend to resemble those of the alloy having the center composition C_0, with relatively little dependence on the modulation or layer thickness. This is seen experimentally in that the optical properties of compositionally modulated alloys, when modeled as bulk films, do not depend strongly on the layer thicknesses as compared to the magneto-optical properties.
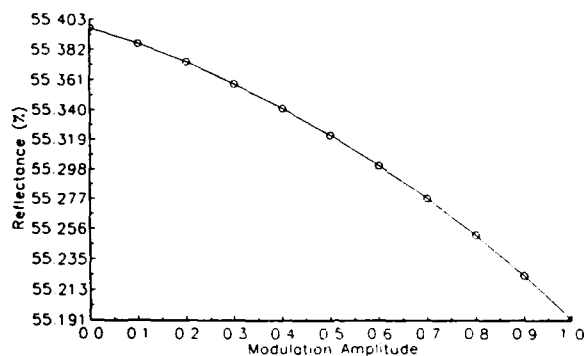
Figure 1. Calculated reflectance as a function of modulation amplitude for
multilayer described in text.
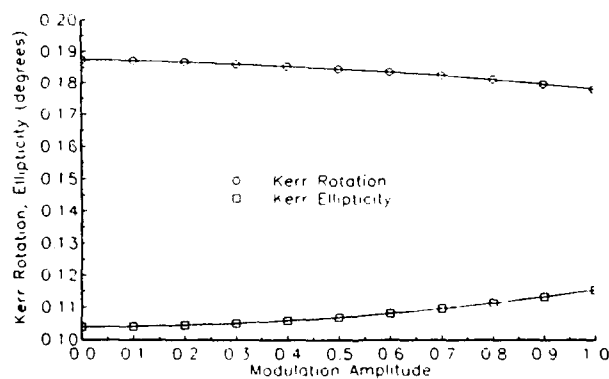
Figure 2. Calculated dependence of Kerr Rotation and Ellipticity on modulation
amplitude for sample described in text.

Conclusions

We have described a model which can be used to calculate the optical and
magneto-optical response of compositionally modulated films. We are currently
acquiring necessary additional experimental data to check this model against
experimental data for TbCo multilayers. Finally, we find the optical and magneto-
optical responses calculated from this model to be weak functions of the modulation
amplitude and layer thicknesses in the ultra-thin film regime.

References

1. William A. McGahan and John A. Woollam, Appl. Phys. Comm, 9(1&2), 1 (1989).

Author Index

Subject Index